

PACIFIC EARTHQUAKE ENGINEERING RESEARCH CENTER

NGA-East: Median Ground-Motion Models for the Central and Eastern North America Region

PEER Report No. 2015/04
Pacific Earthquake Engineering Research Center
Headquarters at the University of California, Berkeley

April 2015

Disclaimer

The opinions, findings, and conclusions or recommendations expressed in this publication are those of the author(s) and do not necessarily reflect the views of the study sponsor(s) or the Pacific Earthquake Engineering Research Center.

NGA-East: Median Ground-Motion Models for the Central and Eastern North America Region

PEER Report No. 2015/04
Pacific Earthquake Engineering Research Center
Headquarters at the University of California, Berkeley

April 2015

ABSTRACT

This report documents recent ground motion models (GMMs) developed as part of the Next Generation Attenuation for Central and Eastern North America (CENA) project (NGA-East). NGA-East is a multi-disciplinary research project coordinated by the Pacific Earthquake Engineering Research Center (PEER) that involves a large number of participating junior and senior researchers, practitioners, and end-users. Various organizations have provided technical input to the project from academia, industry, and government agencies. The objective of NGA-East is to develop a new ground motion characterization (GMC) model for the Central and Eastern North America (CENA) region. The tectonic region of interest reaches across into Canada; thus, the term CENA instead of CEUS is used. The GMC consists in a set of new models (GMMs, a.k.a. GMPEs) for median, ground motions a set of standard deviation models, and their associated weights in the logic-trees, for use in probabilistic seismic hazard analyses (PSHA).

The current report documents the development of new median candidate GMMs. Models for standard deviations of ground motions are developed through a separate set of tasks within NGA-East and are published separately.

The GMMs have been developed using various tasks previously completed in NGA-East, notably the path regionalization, finite-fault simulations, and database development tasks. This report consists of eleven chapters. Each chapter has its own GMM developer team and may include multiple new GMMs. In all, a total of 20 GMMs are described in this report, covering a range of alternative approaches for modeling ground motions, building on empirical relations for CENA and WNA, using recorded ground motions and collected intensity data, and incorporating point-source and finite-fault simulations.

ACKNOWLEDGMENTS

This study was sponsored by the Pacific Earthquake Engineering Research center (PEER), as part of the NGA-East research project, and was funded by the U.S. Nuclear Regulatory Commission (NRC), the U.S. Department of Energy (DOE), and the Electric Power Research Institute (EPRI), with the participation of the U.S. Geological Survey (USGS).

Any opinions, findings, and conclusions or recommendations expressed in this material are those of the authors and do not necessarily reflect those of the sponsoring agencies.

LIST OF ACRONYMS

We have made an attempt to make the terminology as uniform as possible throughout the report. However, since each chapter is written by a different author or group of authors, we also tried to accommodate their personal style (e.g., passive versus active voice) and preferences. Some acronyms and symbols are also preferred by specific authors and reflected in their figure labels. We provide a list of the most common acronyms and symbols below and provide alternative notations when applicable.

ACR	Active Crustal Region
CBR	Center, body and range
CENA	Central and Eastern North America
GMC	Ground Motion Characterization
CEUS	Central and Eastern United States
CEUS SSC	Central and Eastern U.S. Seismic Source Characterization for Nuclear Facilities Project
DNFSB	Defense Nuclear Facilities Safety Board
DOE	United States Department of Energy
ENA	Eastern North America
EPRI	Electric Power Research Institute
FAS	Fourier Amplitude Spectra
FF, FFM	Finite Fault, Finite Fault Model
GM	Ground Motion
GMC	Ground Motion Characterization
GMM	Ground Motion Model is used preferably in the report, GMMs includes GMPEs and other model formats
GMPE	Ground Motion Prediction Equation is used for GMMs that have been parameterized into equations
GMIM	Ground Motion Intensity Measure (PSA, PGA, PGV)
M	Moment magnitude
NGA	Next Generation Attenuation
NGA-East	Next Generation Attenuation Relationship for the Central and Eastern North American Region
NGA-West	Next Generation Attenuation Relationship for shallow crustal earthquakes in active tectonic regions (original project)
NGA-West2	Next Generation Attenuation Relationship for shallow crustal earthquakes in active tectonic regions (phase 2 of NGA-West project)
NRC	United States Nuclear Regulatory Commission
NUREG	Regulatory guides, reports and brochures from the U.S. Nuclear Regulatory Commission
PGA	Peak Ground Acceleration
PGV	Peak Ground Velocity
PIE	Potentially-Induced Event
PS, PSM	Point-Source, Point-Source Model
PSA, SA	Pseudo-Spectral Acceleration (5% damping in this report), some modelers use SA (Spectral Acceleration) instead

PSHA	Probabilistic Seismic Hazard Analysis
Q	Quality factor
R_{HYP}, R_{hyp}	Hypocentral distance (km)
R_{JB}, R_{jb}	Joyner-Boore distance: closest distance to horizontal projection of fault trace (km)
R_X	Equivalent to Joyner-Boore distance measured perpendicularly to the fault trace (km). R_X is negative on the footwall side of the fault and positive on the hanging-wall side
$R_{RUP}, R_{rup}, R_{clst}$	Rupture distance: closest distance to the fault trace (km)
RotD50	Median value of resultants of two horizontal components of ground motions as computed over each angle of rotation from 1 to 180°
SCR	Stable Continental Region
SSC	Seismic Source Characterization
SSHAC	Senior Seismic Hazard Assessment Committee
T	Spectral period (in seconds)
TDI	Technically Defensible Interpretations
TI	Technical Integrator
U.S.	United States
USGS	United States Geological Survey
V_S	Shear-wave velocity
V_{S30}	Time-averaged shear-wave velocity in top 30 meters of geomaterial
WG	Working Group
WUS	Western United States
Z_{HYP}, Z_{hyp}	Depth to hypocenter (km)
Z_{TOR}	Depth to top of rupture (km)

CONTENTS

ABSTRACT.....	iii
ACKNOWLEDGMENTS	v
LIST OF ACRONYMS	vii
TABLE OF CONTENTS	ix
1 INTRODUCTION ♦ Christine A. Goulet, Yousef Bozorgnia & Norman A. Abrahamson	1
1.1 Background	1
1.2 NGA-East Model Development Constraints	1
1.3 Datasets and Model Building Tools.....	3
1.3.1 NGA-East Database	3
1.3.1.1 <i>Summary and Attributes</i>	3
1.3.1.2 <i>Regionalization</i>	3
1.3.2 NGA-East Site Conditions Corrections	4
1.3.3 CENA Models for Attenuation	5
1.3.4 CENA Finite-Fault Simulations and Data	7
1.3.5 NGA-West2 Database.....	7
1.4 Modeling Approaches and Report Organization.....	7
1.4.1 Organization by Type of Modeling Approach.....	7
1.4.2 Electronic Appendices	9
1.5 Acknowledgments	9
1.6 List of Electronic Appendices for Chapter 1.....	9
2 POINT-SOURCE STOCHASTIC-METHOD SIMULATIONS OF GROUND MOTIONS FOR THE PEER NGA-EAST PROJECT ♦ David M. Boore	11
2.1 Introduction.....	11
2.2 Simulation Method	12
2.2.1 Path Parameters.....	12
2.3 Source Properties	17
2.4 Simulated Motions for the PEER NGA-East Project.....	33
2.5 Summary and Discussion	48
2.6 Acknowledgments	48
2.7 List of Electronic Appendices for Chapter 2.....	49

3	DEVELOPMENT OF HARD ROCK GROUND-MOTION MODELS FOR REGION 2 OF CENTRAL AND EASTERN NORTH AMERICA ♦ Robert B. Darragh, Norman A. Abrahamson, Walter J. Silva & Nick Gregor.....	51
3.1	Background	52
3.2	Model Parameters.....	52
	3.2.1 Magnitude Saturation.....	63
	3.2.2 Kappa	66
	3.2.3 Duration	68
	3.2.4 $Q(f)$ and Source Depth	68
	3.2.5 Parameter Correlation.....	68
3.3	Development of Ground-Motion Model.....	68
3.4	Acknowledgments	69
3.5	List of Electronic Appendices for Chapter 3.....	84
4	REGIONALLY-ADJUSTABLE GENERIC GROUND-MOTION PREDICTION EQUATION BASED ON EQUIVALENT POINT-SOURCE SIMULATIONS: APPLICATION TO CENTRAL AND EASTERN NORTH AMERICA ♦ Emrah Yenier & Gail M. Atkinson	85
4.1	Introduction.....	85
4.2	Functional Form of the Generic GMPE	87
4.3	Determination of Model Coefficients	90
4.4	An Example Application: Adjustment of the Generic GMPE for CENA	102
	4.4.1 Regional Attenuation	105
	4.4.2 Regional Stress Parameter	107
	4.4.3 Calibration Factor	109
	4.4.4 CENA-Adjusted GMPE.....	115
4.5	Conclusions.....	118
4.6	Acknowledgments	118
4.7	Electronic Appendix for Chapter 4.....	118
5	GROUND-MOTION PREDICTION EQUATIONS FOR CENA USING THE HYBRID EMPIRICAL METHOD IN CONJUNCTION WITH NGA-WEST2 EMPIRICAL GROUND-MOTION MODELS ♦ Shahram Pezeshk, Arash Zandieh, Kenneth W. Campbell & Behrooz Tavakoli.....	119
5.1	Introduction.....	120
5.2	Stochastic Ground-Motion Simulations.....	120
	5.2.1 Effective Point-Source Distance	121
	5.2.2 Site Response	122

5.2.2.1	<i>Site Characterization in CENA</i>	122
5.2.2.2	<i>Site Characterization in WNA</i>	123
5.2.3	Source Model.....	125
5.2.3.1	<i>Stress Parameter in CENA</i>	125
5.2.3.2	<i>Stress Parameter in WNA</i>	126
5.2.4	Source and Path Duration.....	127
5.2.5	Path Attenuation.....	128
5.2.5.1	<i>Path Attenuation for CENA</i>	128
5.2.5.2	<i>Path Attenuation for WNA</i>	130
5.3	Empirical GMPEs for WNA	131
5.4	HEM-Based GMPEs for CENA	132
5.4.1	Median Model.....	132
5.4.1.1	<i>Small-to-Moderate Events</i>	132
5.4.1.2	<i>Large-Magnitude Scaling</i>	133
5.4.2	Variability and Uncertainty.....	134
5.5	Comparison with Previous GMPEs	134
5.6	Comparison with Observations	139
5.7	Summary and Conclusions	145
5.8	Acknowledgements	147
5.9	List of Electronic Appendices for Chapter 5	147
6	GROUND-MOTION PREDICTIONS FOR EASTERN NORTH AMERICAN EARTHQUAKES USING HYBRID BROADBAND SEISMOGRAMS FROM FINITE-FAULT SIMULATIONS WITH CONSTANT STRESS-DROP SCALING ♦ Arthur D. Frankel	149
6.1	Methodology	149
6.2	Results	154
6.3	Conclusions	163
6.4	Acknowledgments	163
6.5	Electronic Appendix for Chapter 6	163
7	HYBRID EMPIRICAL GROUND-MOTION MODEL FOR CENTRAL AND EASTERN NORTH AMERICA USING HYBRID BROADBAND SIMULATIONS AND NGA-WEST2 GMPES ♦ Alireza Shahjouei & Shahram Pezeshk	165
7.1	Introduction	166
7.2	Review of Hybrid Empirical Method	168
7.2.1	Framework.....	168

7.3	Ground-Motion Simulation.....	168
7.3.1	Long-Period Simulation Parameters	169
7.3.1.1	<i>Fault Areas.....</i>	<i>169</i>
7.3.1.2	<i>Slip, Rise Time, and Slip Rate Distributions.....</i>	<i>170</i>
7.3.1.3	<i>Hypocenter Location and Seismogenic Zone.....</i>	<i>171</i>
7.3.2	High-Frequency Simulation Parameters	172
7.3.2.1	<i>Earthquake Source Term</i>	<i>174</i>
7.3.2.2	<i>Path Effects</i>	<i>175</i>
7.3.2.3	<i>Site Effects.....</i>	<i>175</i>
7.4	Hybrid Broadband.....	176
7.5	Empirical Ground-Motion Models in WNA.....	178
7.6	Proposed Ground-Motion Prediction Equations for CENA.....	179
7.6.1	Hybrid Empirical Ground-Motion Estimates in CENA.....	179
7.7	The Functional Form	180
7.8	Results and Model Evaluation	183
7.8.1	Comparison with Previous Models.....	183
7.8.2	Comparison with Recorded Ground Motions.....	185
7.9	Discussions and Conclusions.....	191
7.10	Data and Resources.....	191
7.11	Acknowledgments	192
7.12	List of Electronic Appendices for Chapter 7.....	192
8	EMPIRICAL GROUND-MOTION PREDICTION EQUATIONS FOR EASTERN NORTH AMERICA ♦ Md. Nayeem Al Noman & Chris H. Cramer	193
8.1	Introduction.....	193
8.2	Dataset.....	194
8.2.1	NGA-East Database	194
8.2.2	Intensity Data	195
8.2.3	Data Distribution.....	199
8.3	Methodology and Functional Form.....	200
8.4	Results	200
8.4.1	Scaling.....	204
8.4.2	Comparison to other GMPEs	209
8.5	Summary.....	212
8.6	Acknowledgments	212
8.7	Electronic Appendix for Chapter 8.....	212

9	GROUND-MOTION PREDICTION EQUATIONS FOR THE CENTRAL AND EASTERN UNITED STATES ♦ Vladimir Graizer	213
9.1	Introduction.....	214
9.2	PGA Attenuation Model.....	216
9.3	Site Correction	220
9.4	PGA-Based Predictive Model for Spectral Acceleration	221
9.5	Residuals	244
9.6	Results	248
9.7	Acknowledgments	249
9.8	Disclaimer	249
9.9	Electronic Appendix for Chapter 9.....	249
10	REFERENCED EMPIRICAL GROUND-MOTION MODEL FOR EASTERN NORTH AMERICA ♦ Behzad Hassani & Gail M. Atkinson	251
10.1	Introduction.....	251
10.2	The Ground-Motion Database for ENA	253
10.3	Referenced Empirical Method.....	255
10.4	Conclusions.....	271
10.5	Data and Resources.....	271
10.6	Acknowledgments	271
10.7	Electronic Appendix for Chapter 10.....	272
11	PEER NGA-EAST MEDIAN GROUND-MOTION MODELS ♦ Justin Hollenback, Nicolas Kuehn, Christine A. Goulet & Norman A. Abrahamson.....	273
11.1	Introduction.....	274
11.1.1	Approach and Motivation	274
11.1.2	Effective Amplitude Spectrum: Orientation-Independent Average Fourier Amplitude Spectrum	274
11.2	Development of Empirical EAS Model.....	275
11.2.1	Selected Data and Regional Constraints	275
11.2.2	Regression Approach.....	276
11.2.3	Empirical EAS Model.....	276
11.3	Extension of Empirical EAS Model Using Seismological Theory and Models	290
11.3.1	Extension of Empirical EAS Model from 0.6 Hz down to 0.01 Hz	290
11.3.2	Extension of Empirical EAS Model to Large M from 0.01 to 10 Hz.....	291

11.3.3	Extension of Empirical EAS Model from 10 to 400 Hz.....	295
11.3.4	Correction to Reference Site Conditions	297
11.4	Random Vibration Theory and Calibrated Duration Model	300
11.4.1	RVT Overview.....	300
11.4.2	Development of Calibrated RVT-Duration Model	301
11.5	Final Model Results: PSA, PGA, and PGV	303
11.6	Conclusions.....	309
11.7	Acknowledgements	309
11.8	Electronic Appendix for Chapter 11	309
12	REFERENCES.....	311

1 Introduction

Christine A. Goulet, Yousef Bozorgnia

**Pacific Earthquake Engineering Research Center (PEER)
University of California, Berkeley**

Norman A. Abrahamson

**Pacific Gas and Electric Company
San Francisco, California**

1.1 BACKGROUND

This report documents recent ground motion models (GMMs) developed as part of the Next Generation Attenuation for Central and Eastern North America (CENA) project (NGA-East). NGA-East is a multi-disciplinary research project coordinated by the Pacific Earthquake Engineering Research Center (PEER) that involves a large number of participating researchers, practitioners, and end-users from various organizations in academia, industry, and government.

The objective of NGA-East is to develop a new ground motion characterization (GMC) for the CENA region. The GMC consists of a set of new GMMs (a.k.a. GMPEs) for median ground motions, a set of standard deviation models, and their associated weights in the logic-trees, for use in probabilistic seismic hazard analyses (PSHA). The current report documents the development of new median GMMs. Models for standard deviations of ground motions are developed through a separate set of tasks within NGA-East and are published separately. The term GMM is used as the general term in this report. Some models have been parameterized into equations, and the term “ground-motion prediction equations (GMPE)” is applicable, and other models consist of sets of ground-motions tables. The term GMM is general and applicable to all the models.

1.2 NGA-EAST MODEL DEVELOPMENT CONSTRAINTS

The NGA-East objective is to develop a comprehensive GMC for CENA. The project constraints have been developed to address the key earthquake scenarios identified in the CEUS Seismic Source Characterization project [EPRI/DOE/NRC 2012].

The magnitude used in NGA-East is the Moment Magnitude, M . M is related to seismic moment, M_0 , by Hanks and Kanamori [1979] as:

$$M = 2/3 \log(M_0 \text{ in dyne-cm}) - 10.7 \quad (1.1)$$

Median GMMs are to provide “average” horizontal ground motions on very hard-rock (VHR) sites located up to 1200 km from future earthquakes in CENA, with M in the 4.0 to 8.2 range. The VHR reference site conditions have been defined by the NGA-East Geotechnical Working Group as corresponding to shear-wave velocity $V_S = 3000$ m/sec and a kappa (κ) of 0.006 sec. The development of the reference sites conditions is detailed in two PEER reports: Hashash et al. [2014a] and Campbell et al. [2014]. In addition, the GMM developers have focused the development of their models on the CENA region that excludes the Gulf Coast (see Region 1, or GROUP 2; see Section 1.3.1.2). The GMMs for the Gulf Coast are developed in separate NGA-East tasks. Also, the GMMs documented in this report are for footwall condition, and adjustments for hanging-wall condition are developed in a separate task.

The preferred “average” horizontal ground-motion intensity measure (GMIM) is RotD50 [Boore 2010]. RotD50 is the median value of resultants of two horizontal components of ground motions as computed over each angle of rotation from 1 to 180°. RotD50 is computed independently for each spectral period/frequency. The minimum requested GMIMs are peak ground acceleration (PGA), peak ground velocity (PGV), and 5%-damped linear pseudo-spectral acceleration (PSA) for oscillator periods listed in Table 1.1.

Table 1.1 Minimum 5%-damped PSA periods (and frequencies) for NGA-East GMM development

<i>T</i> (sec)	<i>F</i> (Hz)
0.01	100
0.02	50
0.025	40
0.03	33.33
0.04	25
0.05	20
0.075	13.33
0.1	10
0.15	6.67
0.2	5
0.25	4
0.3	3.33
0.4	2.5
0.5	2
0.75	1.33
1	1
1.5	0.67
2	0.5
3	0.33
4	0.25
5	0.2
7.5	0.13
10	0.1

1.3 DATASETS AND MODEL BUILDING TOOLS

The NGA-East GMM developers had access to a series of datasets and modeling tools. Specific references to those are provided within the different chapters. Summary of the key products are elaborated in the following sub-sections.

1.3.1 NGA-East Database

1.3.1.1 Summary and Attributes

The NGA-East ground-motion database includes the two- and three-component ground-motion recordings from numerous selected events ($M > 2.5$, distances of 2000 km or more) recorded in the CENA region since 1988 [Goulet et al. 2014]. This is the largest database of processed ground motions recorded in stable continental regions (SCRs). It contains over 29,000 records from 81 earthquake events at 1379 recording stations. The database includes PSA for the 5%-damped elastic oscillators, with periods ranging from 0.01 to 10 sec. As indicated Section 1.2, the preferred GMIM used for the NGA-East GMM development is RotD50, which is also provided for the same period range. The NGA-East database consists of three groups of complementary products: the summary file referred to as the “flatfile,” which contains metadata, ground-motion information and GMIM, the time series (acceleration, velocity, and displacement), and the corresponding Fourier spectra files. The flatfile as well as additional requested products were shared with all the GMM developers.

1.3.1.2 Regionalization

A separate task in NGA-East was to regionalize CENA on the basis of systematic differences in simulated ground motions and their attenuation. From this task four distinct regions were defined as follows [Dreiling et al. 2014]:

1. Mississippi Embayment/Gulf Coast region (MEM)
2. Central North America (CNA)
3. The Appalachian Province (APP)
4. The Atlantic Coastal Plain (ACP)

These four regions are shown in Figure 1.2, with the numbering used in the NGA-East flatfile (Section 1.3.1.1). The flatfile includes three separate fields for regionalization. The first two, correspond to the “Event and Station Region Number,” respectively. For these two fields, the number directly corresponds to the region containing the epicenter (Event Field) and the station (Station Field). If the epicenter or the station is outside these four regions, the flag is set to -999.

The third and last regionalization field is called “Path Region Number” and aims to define a region containing the full propagation path (from the epicenter to the Station). If the full path is contained within any of the four regions above, the field is populated with the region number directly. If either or both of the Event or Station Region Number are outside the four regions (at least one of the fields is -999), then the Event Station Field is also -999.

The regionalization task also demonstrated that the four regions could be aggregated into two distinct attenuation groups:

GROUP 1: Central North America (CNA), Appalachians (APP), and Atlantic Coastal Plain (ACP)

GROUP 2: Mississippi Embayment/Gulf Coast (MEM or GC)

Two new regions were created to accommodate this grouping of regions. Region 5 includes paths that cross any or many of the regions' 2, 3, and 4 boundaries. To fully populate the attenuation Group 1 from above, one would have to combine data with Path Region numbers 2, 3, 4, and 5. Region 6 allows for paths crossing between any sub-region of Group 1 into region 1 (MEM/GC).

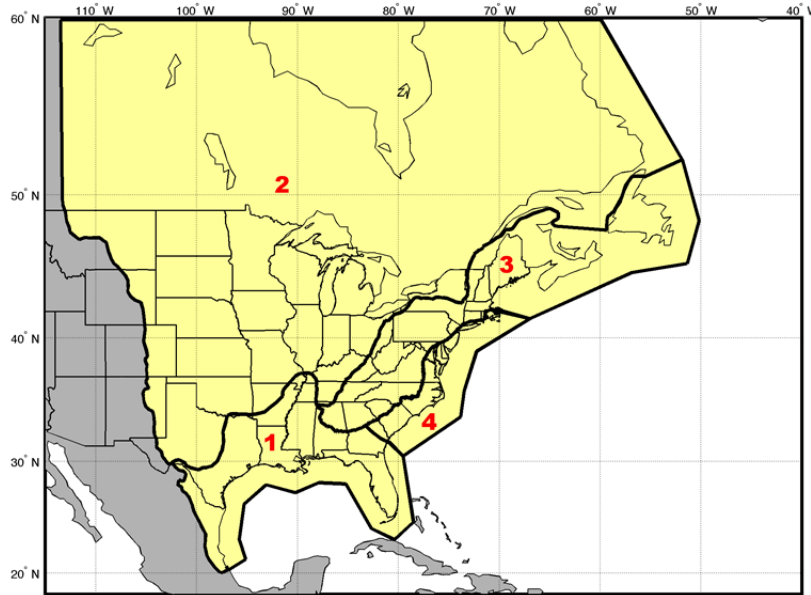


Figure 1.2 Four regions defined for Central and Eastern North America (CENA). The regions have been numbered as follows for the NGA-East database: (1) Mississippi Embayment/Gulf Coast region; (2) central North America; (3) the Appalachian Province; and (4) the Atlantic Coastal Plain.

1.3.2 NGA-East Site Conditions Corrections

The NGA-East database includes V_{S30} estimates for all the recording stations. However, only about 100 sites have V_{S30} values from *in situ* measurements. The vast majority of stations were assigned an inferred V_{S30} value based on various proxy methods described in Chapter 5 of Goulet et al. [2014]. Therefore, there is a certain level of uncertainty on the estimated V_{S30} values, rendering the correction to reference rock also uncertain.

The approach favored by NGA-East was to let each GMM modeling group use their own site correction methods for correcting the as-recorded ground motions to the reference site condition. With this approach, a wider range of ground motions is essentially captured. The GMM developers were nonetheless provided with a draft version of the Boore [2015] report on

site correction models for Fourier amplitude spectra (FAS) and PSA. This was used as a verification tool or as part of the model building process by the different GMM modeling teams.

1.3.3 CENA Models for Attenuation

NGA-East compiled a series of attenuation models from the literature. By attenuation models, we refer to correlated models of geometrical spreading and anelastic attenuation (Q) from ground-motions studies and not to complete GMMs. Expecting to have GMMs based on the point-source stochastic model developed as part of the project, the NGA-East team wanted to select a subset of attenuation models that would (1) span the range of models available and (2) be small enough to be manageable.

The initial literature review contained over 40 models developed between 1983 and 2014 (see Appendix 1A). From this list, a subset of 22 models was selected based on the quality and age of the data used in the published studies. Another review of these 22 models was completed, and six models were selected as representative of the range of available models (see Appendix 1A). The six selected models are listed in Table 1.2.

Table 1.2 Summary of the selected representative attenuation models.

Model and Reference	Geometric Spreading $G(R)$	What is “ R ”? ¹	Attenuation $\exp(-\pi f R / Q\beta)$	Applicable Range ²
AB95 (J97) [Atkinson and Boore 1995]	$G(R) = \begin{cases} R^{-1}, & R \leq 70 \text{ km} \\ C_0 R^0, & 70 \text{ km} < R \leq 130 \text{ km} \\ C_1 R^{-0.5}, & R > 130 \text{ km} \end{cases}$ $C_0 = (1/70), C_1 = (130^{0.5}/70)$	$R = R_{hyp}$	$Q(f) = 680f^{0.36}$ $\beta = 3.8 \text{ km/sec}$	$4.0 \leq M \leq 7.25$ $10 \leq R \leq 500 \text{ km}$ $0.5 \leq f \leq 20 \text{ Hz}$
SGD02 (S02sc, EPRI93) [Silva et al. 2002]	$G(R) = \begin{cases} R^{-(a+b(M-6.5))}, & R \leq 80 \text{ km} \\ C_0 R^{-0.5(a+b(M-6.5))}, & R > 80 \text{ km} \end{cases}$ $a = 1.0296, b = -0.0422, C_0 = 80^{-0.5(a+b(M-6.5))}$	$R = R_{hyp}$	$Q(f) = 351f^{0.84}$ $\beta = 3.52 \text{ km/sec}$	$4.5 \leq M \leq 8.5$ $1 \leq R \leq 400 \text{ km}$ $0.1 \leq f \leq 100 \text{ Hz}$
A04 (BCA10a) [Atkinson 2004]	$G(R) = \begin{cases} R^{-1.3}, & R \leq 70 \text{ km} \\ C_0 R^{0.2}, & 70 \text{ km} < R \leq 140 \text{ km} \\ C_1 R^{-0.5}, & R > 140 \text{ km} \end{cases}$ $C_0 = (70^{-0.2}/70^{1.3}), C_1 = C_0(140^{0.5}/140^{-0.2})$	$R = R_{hyp}$	$Q(f) = \max(1000, 893f^{0.32})$ $\beta = 3.7 \text{ km/sec}$	$4.4 \leq M \leq 6.8$ $10 \leq R \leq 800 \text{ km}$ $0.05 \leq f \leq 20 \text{ Hz}$
BCA10d [Boore et al. 2010]	$G(R) = R^{-1}$ all R	$R = R_{PS}$	$Q(f) = 2850$ $\beta = 3.7 \text{ km/sec}$	$4.4 \leq M \leq 6.8$ $10 \leq R \leq 800 \text{ km}$ $0.05 \leq f \leq 20 \text{ Hz}$
BS11 [Boatwright and Seekins 2011]	$G(R) = \begin{cases} R^{-1}, & R \leq 50 \text{ km} \\ C_0 R^{-0.5}, & R > 50 \text{ km} \end{cases}$ $C_0 = (50^{0.5}/50)$	$R = R_{hyp}$	$Q(f) = 410f^{0.5}$ $\beta = 3.5 \text{ km/sec}$	$4.4 \leq M \leq 5.0$ $23 \leq R \leq 602 \text{ km}$ $0.2 \leq f \leq 20 \text{ Hz}$
AB14 [Atkinson and Boore 2014]	$G(R) = \begin{cases} 10^{T_c C_{LF}} R^{-1.3}, & R \leq 50 \text{ km} \\ C_0 R^{-0.5}, & R > 50 \text{ km} \end{cases}$ $T_c = \begin{cases} 1, & f \leq 1 \text{ Hz} \\ 1 - 1.429 \log_{10}(f), & 1 \text{ Hz} < f < 5 \text{ Hz} \\ 0, & f \geq 5 \text{ Hz} \end{cases}$ $C_{LF} = \begin{cases} 0.2 \cos \left[\frac{\pi}{2} \left(\frac{R-h}{1-h} \right) \right], & R \leq h \\ 0.2 \cos \left[\frac{\pi}{2} \left(\frac{R-h}{50-h} \right) \right], & h < R < 50 \text{ km} \end{cases}$ $h = \text{focal depth (km)}, C_0 = (50^{0.5}/50^{1.3})$	$R = R_{PS}$	$Q(f) = 525f^{0.45}$ $\beta = 3.7 \text{ km/sec}$	$3.5 \leq M \leq 6$ $10 \leq R \leq 500 \text{ km}$ $0.2 \leq f \leq 20 \text{ Hz}$

¹ R_{hyp} = hypocentral distance; R_{PS} = effective point source distance
 $R_{PS} = [R_{hyp}^2 + h_{FF}^2]^{1/2}$, $\log_{10}(h_{FF}) = -0.405 + 0.235M$ [Yenier and Atkinson 2015a]

²When applicable range not explicitly stated in paper it was inferred from data comparisons.

1.3.4 CENA Finite-Fault Simulations and Data

Following a large finite-fault validation exercise, three finite-fault simulations modeling approaches passed the acceptance criteria and were selected for the generation of CENA ground-motion data. The methodologies are implemented on the Southern California Earthquake Center Broadband Platform (SCEC BBP), version 14.6, and are documented, along with the validation exercise itself, in a Focus Section in *Seismological Research Letters* (Volume 86, Issue 1). The simulations methodologies were evaluated for applicability to Western U.S. (WUS), Japanese, and CENA events, as detailed in Goulet et al. [2015], Maechling et al. [2015] and Dreger et al. [2015].

The EXSIM (EX), Graves and Pitarka (GP) and San Diego State University (SD) methodologies were selected for NGA-East and are described in detail in Atkinson and Assatourians [2015], Graves and Pitarka [2015], and Olsen and Takedatsu [2015]. The NGA-East project was in agreement with Dreger et al. [2015] that the ground motions from these methods should not be used for their absolute values, but instead for their relative magnitude scaling effects on ground motions. NGA-East developed a set of simulation scenarios for that purpose. The different earthquake scenarios and station layouts were defined to capture the effect of M -scaling relative to $M=5$, for a range of distances.

Appendix 1B summarizes the simulations process and links to data files for the M -scaling models.

1.3.5 NGA-West2 Database

A subset of GMM developers used data from active crustal regions (ACRs) and developed parts of their model using the NGA-West2 database [Ancheta et al. 2014]. The NGA-West2 database includes earthquake events from multiple ACRs, such as from the WUS, Middle East, Japan, and China, among others. The key NGA-West2 product used in the NGA-East GMM development was the flatfile, which includes metadata on source, propagation and site effects as well as 5%-damped PSA $RotD_{50}$ values.

1.4 MODELING APPROACHES AND REPORT ORGANIZATION

1.4.1 Organization by Type of Modeling Approach

This report consists of a collection of individual chapters, each authored by the GMM developer teams (or groups of developers). Each chapter, therefore, provides a self-contained documentation of the models and suites of models. The NGA-East project organized the methods by a general type, based on the approach used in the development, as briefly summarized below.

Table 1.3 summarizes the outline of the report, with each GMM or suite of GMMs organized based on the modeling approach, the set of seismological constraints, and the extrapolation approach for large M , close-in distance and higher frequencies.

Approach: This column summarizes the general underlying modeling approach. For example, we distinguish models that are essentially empirical, based on point-source (PS) or finite-fault (FF) simulations, from those that use the hybrid empirical method (HEM).

Constraints: This provides further information on how the model development is constrained, which can be based on seismological models or on ground-motion data.

Extrapolation: This refers to how the models extrapolate beyond the NGA-East database.

Table 1.3 Summary of GMM approaches covered in this report.

Approach	Constraints	Extrapolation	Chapter Number, Title (Authorship)
Traditional Point-Source (PS) Stochastic (FAS-based)	PS model, published sets of empirical attenuation models, NGA-East database	PS model	2. Point-Source Stochastic-Method Simulations of Ground Motions for the PEER NGA-East Project (D.M. Boore)
	PS model, broadband inversion of NGA-East database	PS model	3. Development of Hard Rock Ground-Motion Models for Region 2 of Central and Eastern North America (R.B. Darragh, N.A. Abrahamson, W.J. Silva, and N. Gregor)
Regionally-Adjustable Generic GMM based on Point-Source model (PS Referenced Empirical)	PS model used to develop generic GMM, parameters defined from data-rich host region, adjustments using NGA-East database	Generic GMM adjusted to CENA data	4. Regionally-Adjustable Generic Ground-Motion Prediction Equation based on Equivalent Point-Source Simulations: Application to Central and Eastern North America (E. Yenier and G.M. Atkinson)
Hybrid Empirical (FAS- and PSA-based)	Published sets of CENA and WUS PS models	GMM host region (WUS)	5. Ground-Motion Prediction Equations for Eastern North America using a Hybrid Empirical Method (S. Pezeshk, A. Zandieh, K.W. Campbell, and B. Tavakoli)
Finite-Fault (FF) Simulations (PSA-based)	FF model, NGA-East database	FF model	6. Ground-Motion Predictions for Eastern North American Earthquakes Using Hybrid Broadband Seismograms from Finite-Fault Simulations with Constant Stress-Drop Scaling (A. Frankel)
			7. Hybrid Empirical Ground-Motion Model for Central and Eastern North America using Hybrid Broadband Simulations and NGA-West2 GMPEs (A. Shahjouei and S. Pezeshk)
Traditional Empirical (PSA-based)	NGA-East database	Intensity	8. Empirical Ground -otion Prediction Equations for Eastern North America (M.N. Al Noman and C.H. Cramer)
		Imposed spectral shape	9. Ground-Motion Prediction Equations for the Central and Eastern United States (V. Graizer)
Referenced Empirical (PSA-based)	NGA-East database	GMM host region (WUS)	10. Referenced Empirical Ground-Motion Model for Eastern North America (B. Hassani and G.M. Atkinson)
FAS-RVT-PSA Empirical (require FAS and duration models)	NGA-East database	PS and FF models for scaling, Global GMs for extrapolation of duration model	11. PEER NGA-East Median Ground-Motion Models (J. Hollenbeck, N. Kuehn, C.A. Goulet and N.A. Abrahamson)

1.4.2 Electronic Appendices

A suite of electronic appendices is organized for each chapter. The last section of each chapter lists the electronic appendices associated to that chapter. For Chapters 2 to 11, some of appendices are the output tables from the model as provided by the GMM developers.

1.5 ACKNOWLEDGMENTS

NGA-East, like other NGA projects, has greatly benefitted from strong interactions among junior and senior researchers, practitioners, and end-users. We thank all the participants for their dedication and efforts.

1.6 LIST OF ELECTRONIC APPENDICES FOR CHAPTER 1

- 1A Selection of representative attenuation models (PDF document)
- 1B Finite fault simulations (PDF document)
 - 1B.1 Finite fault simulations, M-scaling Model 1 coefficients for PSA (Excel workbook)
 - 1B.2 Finite fault simulations, M-scaling Model 2 coefficients for PSA (Excel workbook)
 - 1B.3 Finite fault simulations, M-scaling Model 2 coefficients for FAS (Excel workbook)

2 Point-Source Stochastic-Method Simulations of Ground Motions for the PEER NGA-East Project

David M. Boore

**U.S. Geological Survey
Menlo Park, California**

Abstract

Ground-motions for the PEER NGA-East project were simulated using a stochastic method. The simulated motions are provided for most of the stipulated distances between R_{RUP} of 0 and 1200 km, M from 4 to 8, and 25 ground-motion intensity measures: peak ground velocity (PGV), peak ground acceleration (PGA), and 5%-damped pseudo-absolute response spectral acceleration (PSA) from 0.01 sec to 10.0 sec. Tables of motions are provided for each of six attenuation models (Section 1.3.3). The attenuation-model-dependent stress parameters used in the stochastic-method simulations were derived from inversion of PSA data from eight earthquakes in eastern North America (ENA).

2.1 INTRODUCTION

This report describes point-source, stochastic-method simulations of ground motions for ground-motion intensity measures (GMIMs), moment magnitudes (M), and rupture distances specified by the Management Team of the NGA-East project. The simulations are for a site for which $V_{S30} = 3.0$ km/sec. The Management Team specified the attenuation models (geometric spreading and Q) to be used, but I chose the other parameters needed in the simulations: (1) I describe the simulation method and the parameters used in the simulations (in particular, the stress parameter for each attenuation model, the finite-fault (FF) factor used to convert from R_{RUP} to the effective point-source distance R_{PS} , the path duration, and the crustal amplifications, as well as the average radiation pattern and the velocity and density in the source region); (2) I show the results of the simulations [the results are in the form of tables of motion, not ground-motion prediction equations [GMPEs]]; and (3) I conclude with some comments about the range of applicability of the motions and limitations of the simulations.

2.2 SIMULATION METHOD

The point-source (PS) stochastic method for simulating earthquake ground motions is well known and will not be discussed here (see Boore [2003] for more information, and Boore and Thompson [2015] [BT15] for some recent revisions to the method as implemented in the SMSIM suite of programs [Boore 2005]). What will be discussed here are the parameters to be used in the simulations (a sample file containing the parameters used in the SMSIM simulations is given in Appendix 2A). The parameters fall into several general categories: source, path, and site. The discussions in this section are organized by these categories. Although it is usual to start with the source, I begin the discussion with the path parameters, because the stress parameters of the source are dependent on the path parameters.

The inversions for the stress parameters used my program *stress_param_from_psa*, and the forward simulations used *tmrs_loop_rv_drvr*. These programs use random-vibration simulations with the Der Kiureghian [1980] rms-to-peak factors and the BT15 D_{rms} coefficients. The program *tmrs_loop_rv_drvr* is part of my SMSIM suite of programs, available from the online software page of www.daveboore.com [Boore 2005]. The version of SMSIM used for the simulations in this chapter is dated October 15, 2014.

2.2.1 Path Parameters

Attenuation Models:

Six attenuation models (by which I mean a specification of the distance-dependent geometric spreading and the frequency-dependent Q) were provided by the Management Team and are described in Section 1.3.3 and Appendix 1A. These models are summarized in Table 2.1 for convenience. Two of the models (A04 and AB14) are characterized by a geometrical spreading of $1/R^{1.3}$ within the first 70 km and 50 km, respectively, whereas most of the other models have a decay of $1/R$ for these distance ranges. The simplest model is BCA10D, which has $1/R$ geometrical spreading at all distances. As I will show, the difference in the geometrical spreading functions has a large impact on the stress parameters derived from data, as well as the ability to fit the data at a wide range of periods. It is important to note that I am not endorsing any of the models, although I find that the best overall model is BS11, closely followed by the BCA10D and AB95 models; the two models with $1/R^{1.3}$ geometrical spreading cannot fit the data at periods of 1 sec and 2 sec, no matter what stress parameter is used.

Path-Dependent Durations:

One of the main changes relative to parameters used in my previous simulations for ground motions in ENA is the path duration, as shown in Figure 2.1. Details regarding the derivation of the new durations are in Boore and Thompson [2015]. The much longer durations than those used before (the previous durations are shown by the gray line in Figure 2.1) will result in lower ground motions for a given stress parameter and attenuation model; therefore, I needed to determine the stress parameter to be used for each attenuation model—I cannot simply use the stress parameters in Boore [2012]. The duration function is given in Table 2.2.

Table 2.1 Summary of attenuation models from Section 1.3.3.

Model	Geometrical spreading*	Q	Reference
A04	-1.3(70)0.2(140)-0.5	$\max(1000, 893 f^{0.32})$	Atkinson [2004]
AB14	-1.3(50)-0.5	$525 f^{0.45}$	Atkinson and Boore [2014]
AB95	-1.0(70)0.0(130)-0.5	$680 f^{0.36}$	Atkinson and Boore [1995]
BCA10D	-1.0	2850	Boore et al. [2010]
BS11	-1.0(50)-0.5	$410 f^{0.5}$	Boatwright and Seekins [2011]
SGD02	-1.1(80)-0.55	$351 f^{0.84}$	Silva et al. [2002]

* The entries are shorthand for the geometrical spreading function; the numbers in parenthesis are the breakpoint distances, with the exponent of R being given by the numbers on either side of the breakpoint distance. Note that the AB14 geometrical spreading is frequency dependent--the function shown is for frequencies of 5 Hz and above; for lower frequencies the equivalent power is negative with an absolute value greater than 1.3 for distances within 50 km, except at distances less than about 10 km. The SGD02 model is magnitude dependent; the coefficients given in the table are for $M=5$.

Table 2.2 The path duration model for stable continental regions* (from Boore and Thompson [2015]).

R_{PS} (km)	D_P (sec)
0.0	0.0
15.0	2.6
35.0	17.5
50.0	25.1
125.0	25.1
200.0	28.5
392.0	46.0
600.0	69.1
Slope of last segment	0.111

*Values for non-tabulated distances are given by linear interpolation of the tabulated values (in terms of duration and distance, not logarithms of these quantities). Durations for distance beyond the last tabulated distance are given by

$$D_P(R) = D_P(R_{last}) + slope \times (R - R_{last})$$

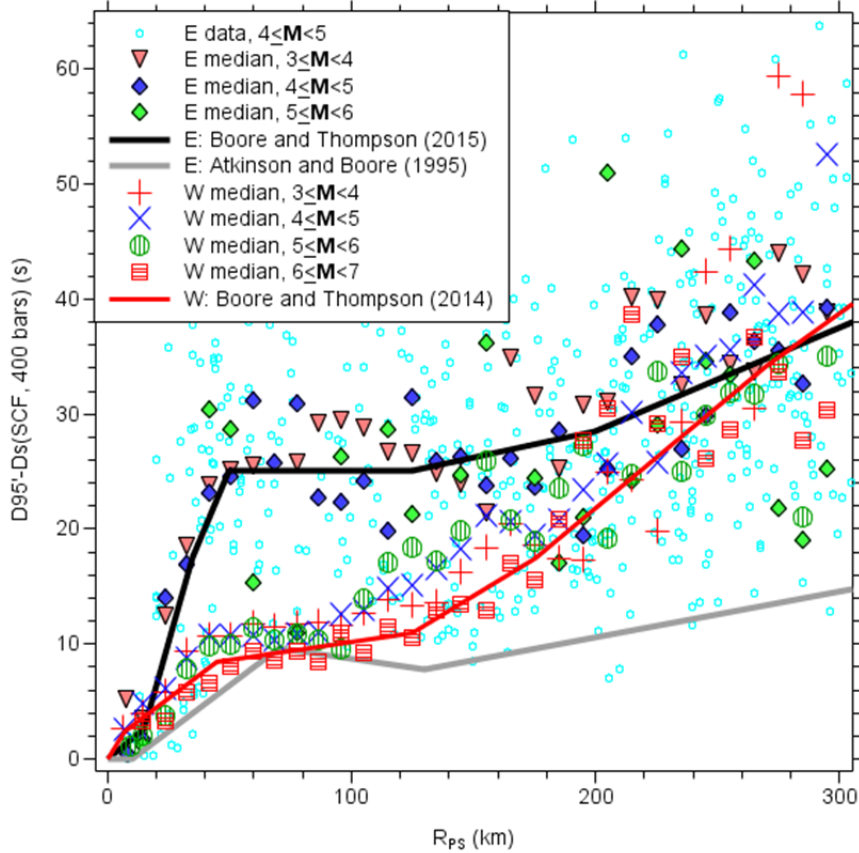


Figure 2.1 The medians in various magnitude (\mathbf{M}) and point-source distance (R_{PS}) bins of the path duration $D_p = D'_{95} - D_S$ for data both from ENA (“E”) and active crustal regions (ACRs) (“W”). The source duration D_S is given by $1/f_c$, in which the corner frequency f_c is given by the single-corner frequency model with a stress parameter of 400 bars. Guided primarily by the medians for the $\mathbf{M} = 4$ to 5 range (the individual data points for this magnitude range are shown by the small open circles), Boore and Thompson [2015] subjectively derived a path duration function consisting of joined linear segments. For comparison, D_p used in some previous simulations of motions in ENA [Atkinson and Boore 1995] and the recent path duration for ACRs [Boore and Thompson 2014] are also shown. Modified from Boore and Thompson [2015], which should be consulted for more details.

Crustal Amplification:

Two crustal amplification models were used in the simulations, one for the final simulations, for which it was stipulated that the velocity model had $V_{S30} = 3.0$ km/sec [Hashash et al. 2014a, b] and one with $V_{S30} = 2.0$ km/sec for the inversion of data for the stress parameters to be used in the final simulations. Table 2.3 contains the amplifications. The data used in the inversions were

intended to be from hard rock sites, but according to the NGA-East flatfile, the V_{s30} at the sites is probably closer to 2.0 km/sec than 3.0 km/sec. The two amplifications are shown in Figure 2.2, which also shows the effect of applying a diminution operator $\exp(-\pi\kappa f)$ with $\kappa = 0.006$ sec. The amplifications were computed using the square-root-impedance method [Boore 2013], assuming a source density of 2.8 g/cc and a shear-wave velocity of 3.7 km/sec, a vertical angle of incidence, and no attenuation (see BT15). The velocity profiles used in the amplification calculations are based on the very hard rock profile of Boore and Joyner [1997] (BJ97). For $V_{s30} = 3000$ m/sec, the top 300 m of the Boore and Joyner profile was replaced by a layer with a velocity of 3000 m/sec (see BT15). The profile for which $V_{s30} = 2000$ m/sec was constructed by replacing the top 300 m of the standard hard rock profile of BJ97 with a 30-m-thick layer with a constant velocity of 2000 m/sec, underlain by material with a linear gradient that connected the 2000 m/sec value at 30 m with the 3000 m/sec value at a depth of 300 m in the BJ97 very hard rock profile. More information can be found in Boore [2015].

Table 2.3 Crustal amplification (A) and frequency (f) pairs for stable continental regions (SCRs) for velocity models for which and $V_{S30} = 3.0$ km/sec (the latter modified from Table 4 in Boore and Joyner [1997]*.

f	$A(V_{S30} = 2.0 \text{ km/sec})$	f	$A(V_{S30} = 3.0 \text{ km/sec})$
0.010	1.000	0.001	1.000
0.015	1.008	0.008	1.003
0.032	1.015	0.023	1.010
0.054	1.026	0.040	1.017
0.078	1.038	0.061	1.026
0.111	1.055	0.108	1.047
0.168	1.069	0.234	1.069
0.245	1.086	0.345	1.084
0.387	1.116	0.508	1.101
0.647	1.159	1.090	1.135
0.950	1.202	1.370	1.143
1.556	1.270	1.690	1.148
2.333	1.342	1.970	1.150
3.156	1.386	2.420	1.151
4.333	1.420	—	—
6.126	1.445	—	—
8.662	1.461	—	—
11.376	1.467	—	—
15.164	1.471	—	—
25.586	1.471	—	—

*Values for non-tabulated frequencies are given by linear interpolation of the logarithms of the tabulated values. Amplifications for frequencies less than and greater than the tabulated frequencies take on the values at the closest tabulated frequencies.

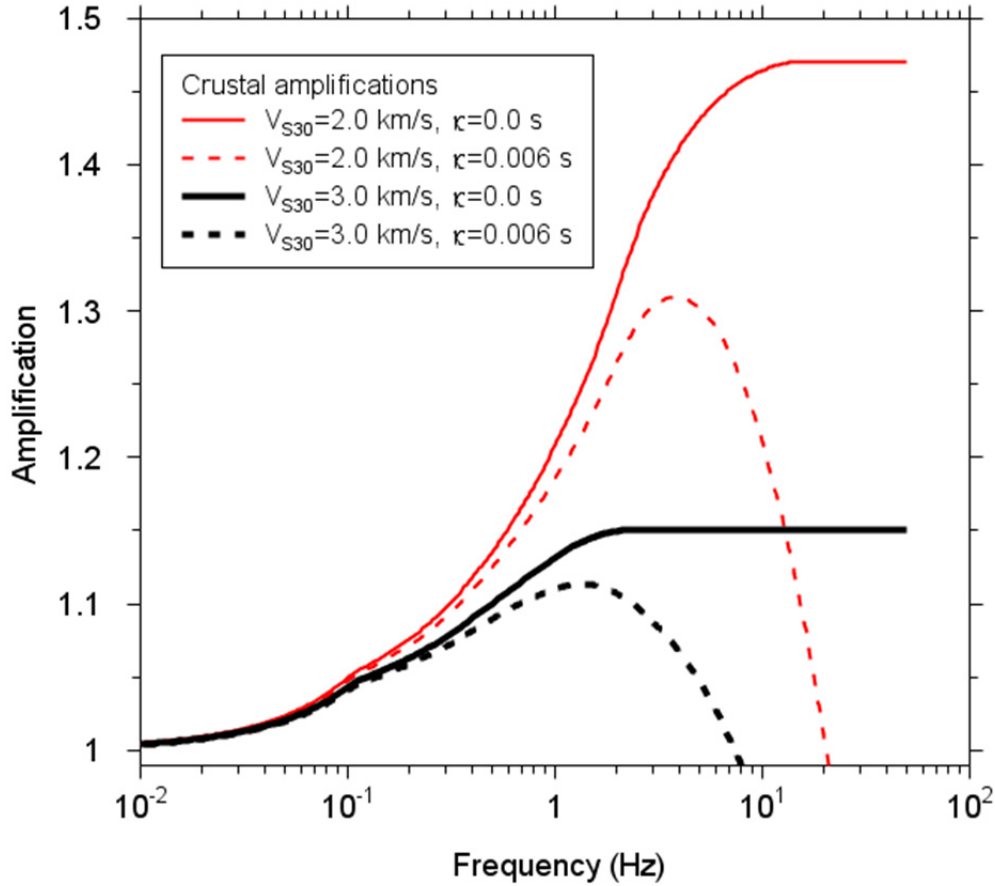


Figure 2.2 Crustal amplifications for sites with two values of V_{S30} : 2.0 km/sec and 3.0 km/sec. Shown are the amplifications without attenuation (solid curves) and with attenuation, as modeled by the diminution operator $\exp(-\pi\kappa f)$, where $\kappa = 0.006$ sec. See Boore and Thompson [2015] for more details.

Diminution Parameter κ :

The stipulated value of 0.006 sec [Campbell et al. 2014] was used in the simulations.

2.3 SOURCE PROPERTIES

The properties that need to be specified are the spectral shape of the source and how it changes with magnitude, the average radiation pattern, and the adjustment of distance to account for the finite size of the source.

Average Radiation Pattern and Density, and Shear-Wave Velocity near the Source:

The simulations used a value of 55 for the average radiation pattern (e.g., Boore and Boatwright [1984]), and a shear-wave velocity and density in the source region of 3.7 km/sec and 2.8 g/cc. These primarily enter into the simulations as part of a frequency-independent constant, and

because these parameters were used in the inversion of data for the stress parameters and then in forward calculations using the stress parameters, the effect of any changes in the average radiation pattern or source velocity or density would be canceled out.

Source Spectral Shape:

I used a single-corner frequency (SCF), constant stress parameter model. Using a more general, double-corner frequency model (e.g., Boore et al. [2014]) would require choosing the values of more parameters. There are barely sufficient data to estimate the single stress parameter ($\Delta\sigma$) needed in the SCF model, however, and for that reason I used the SCF model.

Finite-Fault Adjustment to Distance:

The ground-motion predictions used in hazard calculations usually use the closest distance to the rupture surface (R_{RUP}) as the distance metric in the calculations. As discussed in detail in BT15, however, the distance to be used in point-source stochastic method simulations should be R_{PS} , where

$$R_{PS} = \sqrt{R_{RUP}^2 + h(\mathbf{M})^2} \tag{2.1}$$

and $h(\mathbf{M})$ is a factor that accounts for the finiteness of the rupture surface of a fault. In this study, I use the equations of BT15 for $h(\mathbf{M})$; these are a combination of the relations of Yenier and Atkinson [2014; 2015a]. The relations are shown in Figure 2.3 as a function of magnitude.

Stress Parameter:

For a given attenuation model, the most important parameter that must be specified is the stress parameter $\Delta\sigma$. To obtain a feeling for the stress parameters needed to fit data for each of the attenuation models, as well as to judge the ability of the models to fit data over a range of distances and periods, Figures 2.4–2.9 compare the data from the Riviere du Loup earthquake with simulations for a wide range of stress parameters (centered at 800 bars) for oscillator periods of 0.1, 0.2, 1.0, and 2.0 sec, $V_{S30} = 2.0$ km/sec, and the six models of attenuation. Careful inspection of these figures leads to these conclusions:

1. The two models that have $1/R^{1.3}$ within the first 70 to 50 km (A04 and AB14; Figures 4 and 5) require a large value of the stress parameter to match the response spectral observations at $T = 0.1$ sec and $T = 0.2$ sec; no values of the stress parameter will allow the simulations to match the observations at periods of 1.0 sec and 2.0 sec.
2. At short periods and for most of the attenuation models, the stress parameter that leads to the best match of the data for distances within about 200 km leads to an overestimation of the data at greater distances. The one clear exception to this is the BS11 model. This is subjectively the best of the six models in terms of its ability to match data at a wide range of distances and periods.

3. The simplest model (BCA10D), with $1/R$ spreading at all distances, can match the data for a wide range of periods for distances less than about 400 km, but unlike the BS11 model, it seems to require different stress parameters to match the short-period data at different distances.
4. Both the BS11 and the BCA10D models underestimate the bulk of the longer-period data beyond about 400 km, no matter what stress parameter is used.

Similar conclusions can be drawn from similar comparisons for the Saguenay and Val des Bois earthquakes (figures comparable to Figures 2.4–2.9 for those earthquakes are not shown here because of space limitations).

With this background in the ability of the six attenuation models to match the data, I inverted the data of Boore (2012) for $\Delta\sigma$, using the SMSIM parameters previously discussed (Appendix 2A shows one of the SMSIM parameter files used in the analysis). I followed the methodology of Boore et al. [2010], for each attenuation model. I did separate inversions for the data within 200 km and within 600 km. The results are in Table 2.4–Table 2.9 (one table for each attenuation model; all tables have the same format). In those tables I also include the geometric means and the factor corresponding to 10 raised to the power of the standard deviation of the log mean of the stress parameters. The individual stress parameters as well as the geometric means are shown in Figure 2.10 for the six attenuation models. I used the geometric means obtained from the inversions of data within 200 km for the simulations of ground motions for the NGA-East project, as I felt that it is more important in applications to match the data at closer than at greater distances. The geometric means used in the simulations excluded the stress parameters from the Saguenay earthquake. The main reason for doing this was that the stress parameter from that earthquake is quite high and seems to be an outlier, rather than being part of a normal distribution of $\ln\Delta\sigma$. On the other hand, the stress parameter from the Nahanni earthquake also seems to be a low outlier, at least for some of the attenuation models. In retrospect I should have included the stress parameter for the Saguenay earthquake, and more importantly, because the number of events is so small I should have used the median of the stress parameters for each attenuation model rather than the geometric mean, which equals the median of $\Delta\sigma$ only if $\Delta\sigma$ is log normally distributed. For the BS11 attenuation model, the median stress parameter for all earthquakes inverted from data within 200 km is 172 bars, compared with the 185 bars used in the simulations. I compared the simulations for these two stress parameters for all GMIMs and a subset of magnitudes from 5 to 8 and distances from 10 to 1000 km. The motions for the lower stress parameter are always lower than for the higher stress parameter, but by no more than 5%. This is much less than any reasonable estimate of either aleatory or epistemic uncertainty, and therefore I judge that no changes need to be made in my reported ground motions.

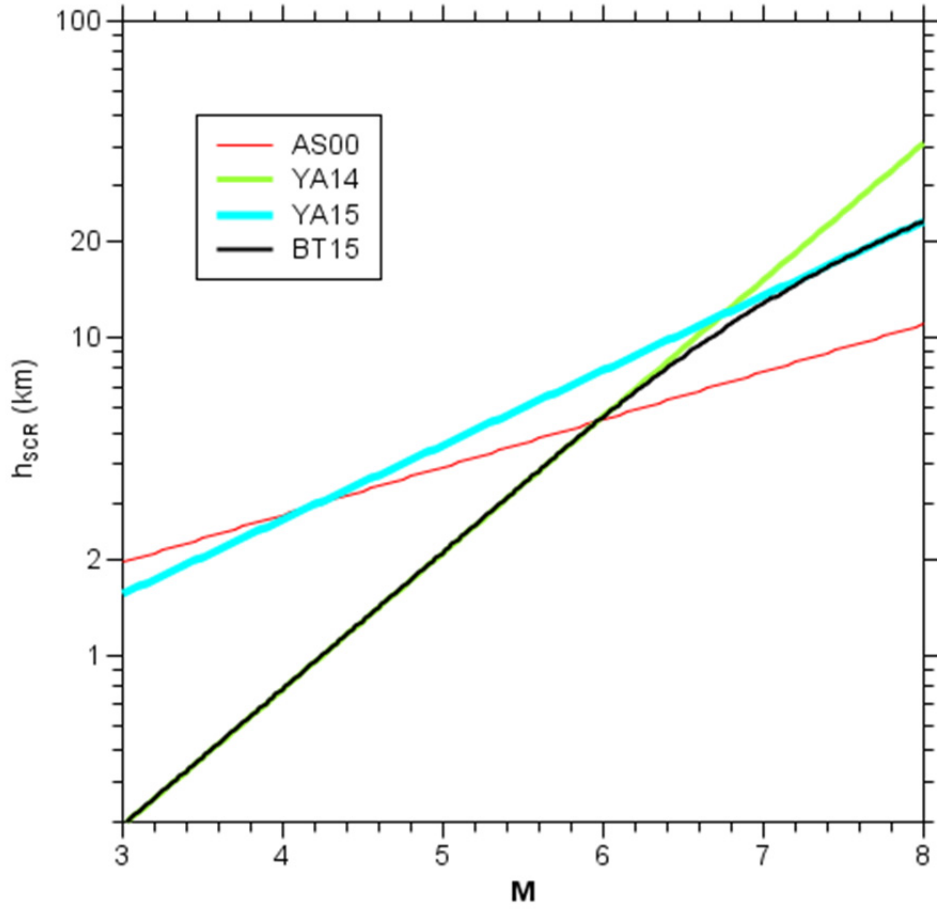


Figure 2.3 The finite-fault (FF) factor h_{SCR} (where “SCR” stands for “stable continental region”) used in converting the closest distance to the rupture surface (R_{RUP}) to the distance to be used in the point-source calculations (R_{PS}) Shown are the h_{SCR} functions for Atkinson and Silva [2000] (AS00), Yenier and Atkinson [2014] (YA14), Yenier and Atkinson [2015a] (YA15), and Boore and Thompson [2015] (BT15). The FF factors for AS00, YA14, and YA15 are intended for use in ACRs; they have been reduced by a factor of 0.68 to account for the likely higher stress drops for earthquakes in SCRs than in ACRs. Modified from BT15, which should be consulted for more details.

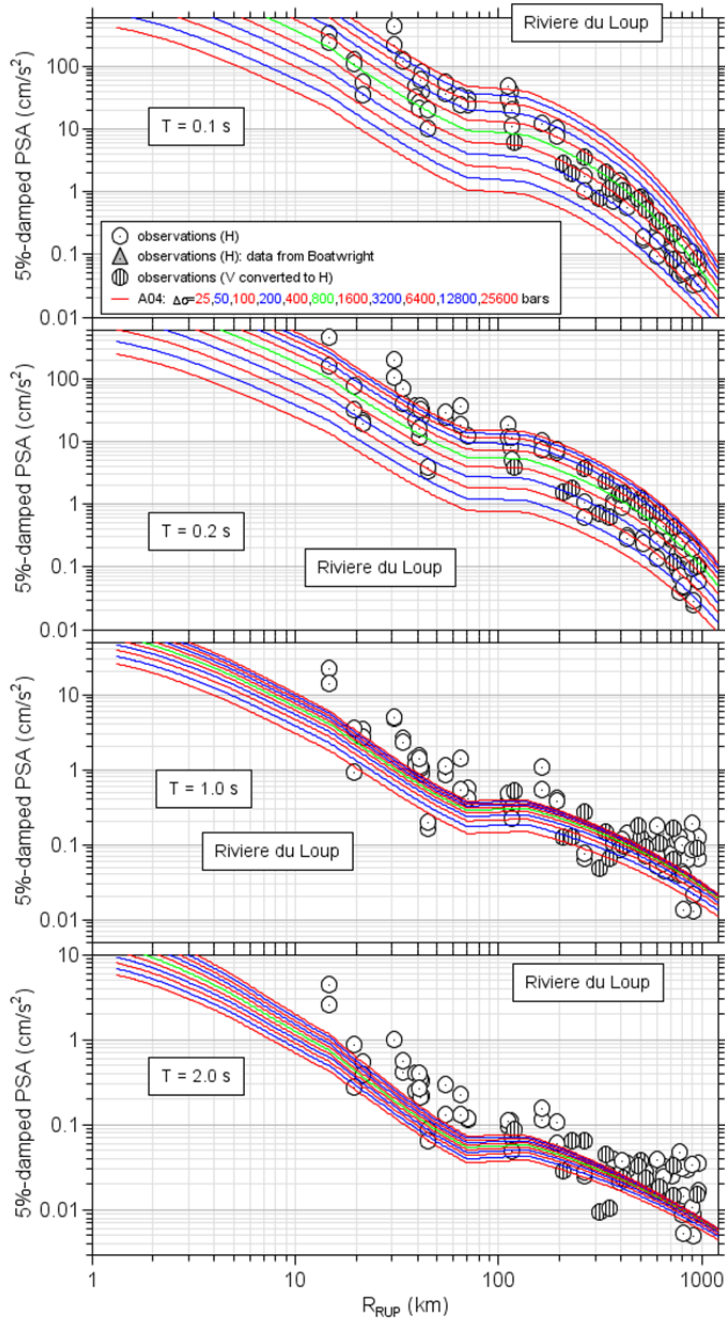


Figure 2.4 Observations from the 2005 Riviere du Loup earthquake (symbols) and simulated PSA for a suite of stress parameters, using crustal amplifications for $V_{S30} = 2.0$ km/sec and the Atkinson [2004] (A04) attenuation model. See Boore [2012] for details regarding the observations.

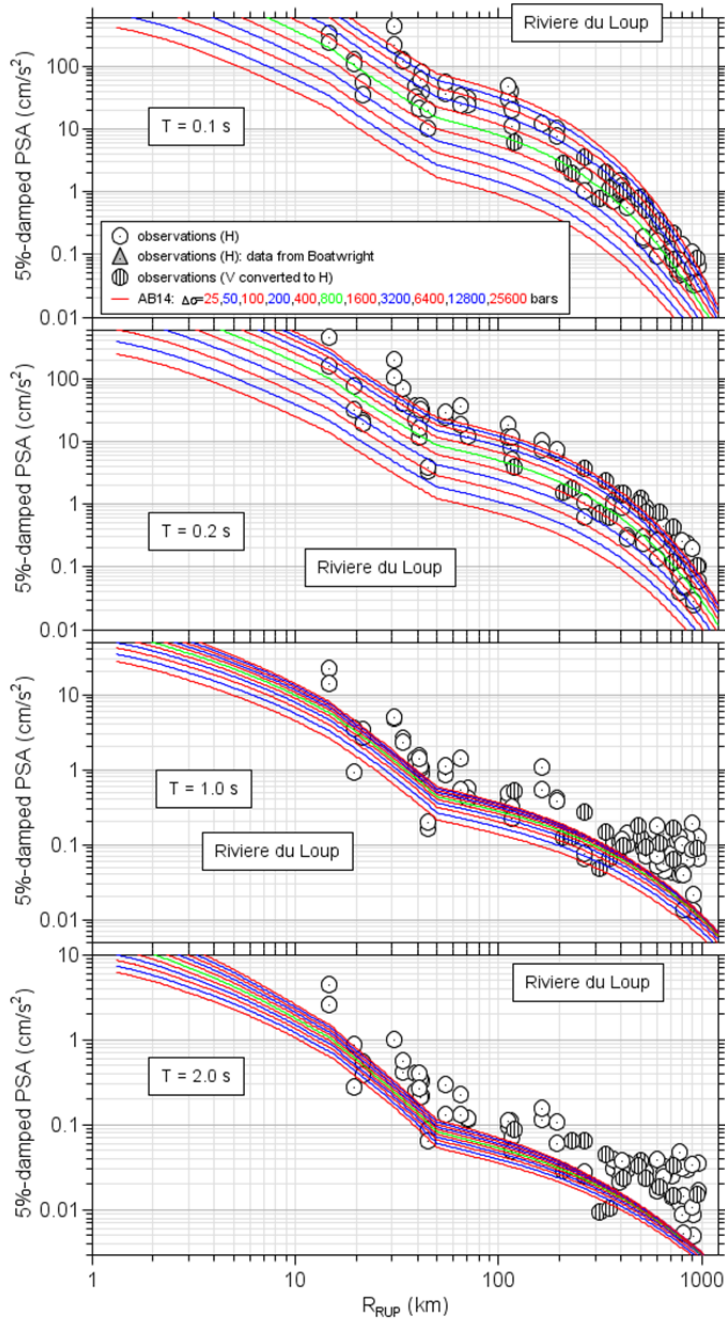


Figure 2.5 Observations from the 2005 Riviere du Loup earthquake (symbols) and simulated PSA for a suite of stress parameters, using crustal amplifications for $V_{S30} = 2.0$ km/sec and the Atkinson and Boore [2014] (AB14) attenuation model. See Boore [2012] for details regarding the observations.

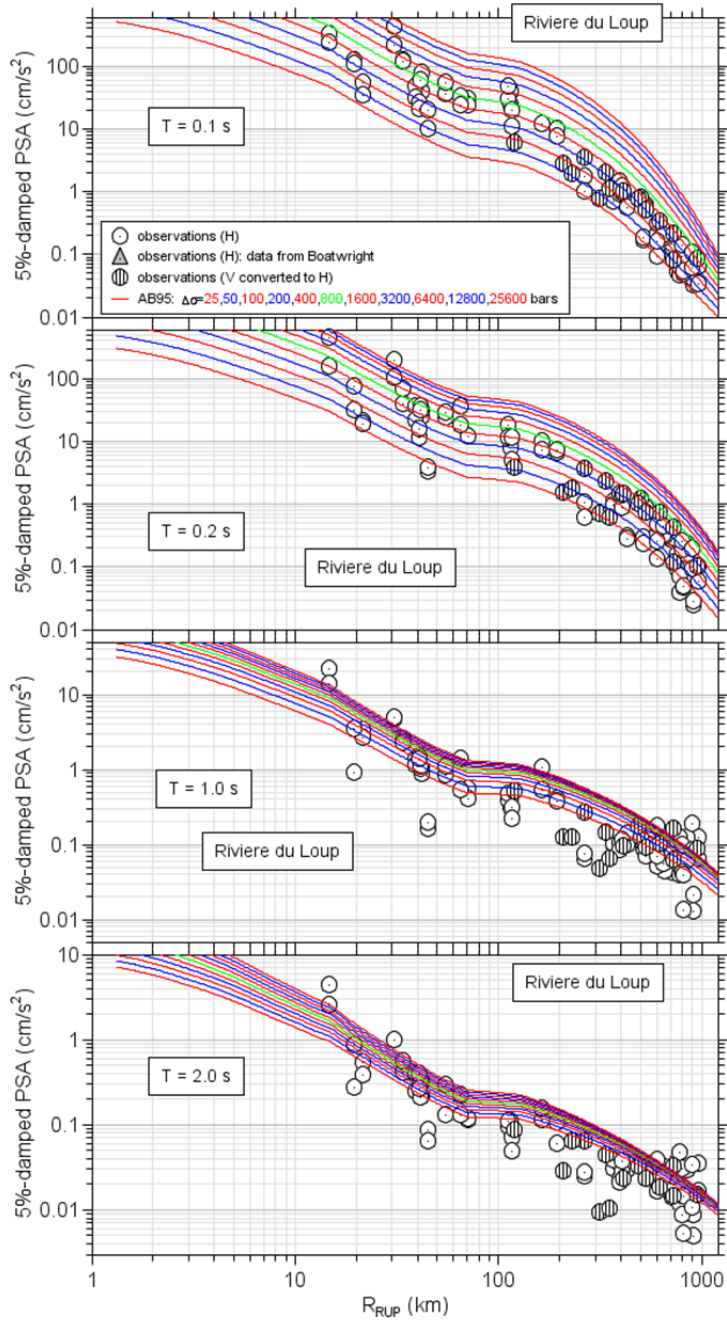


Figure 2.6 Observations from the 2005 Riviere du Loup earthquake (symbols) and simulated PSA for a suite of stress parameters, using crustal amplifications for $V_{S30} = 2.0$ km/sec and the Atkinson and Boore [1995] (AB95) attenuation model. See Boore [2012] for details regarding the observations.

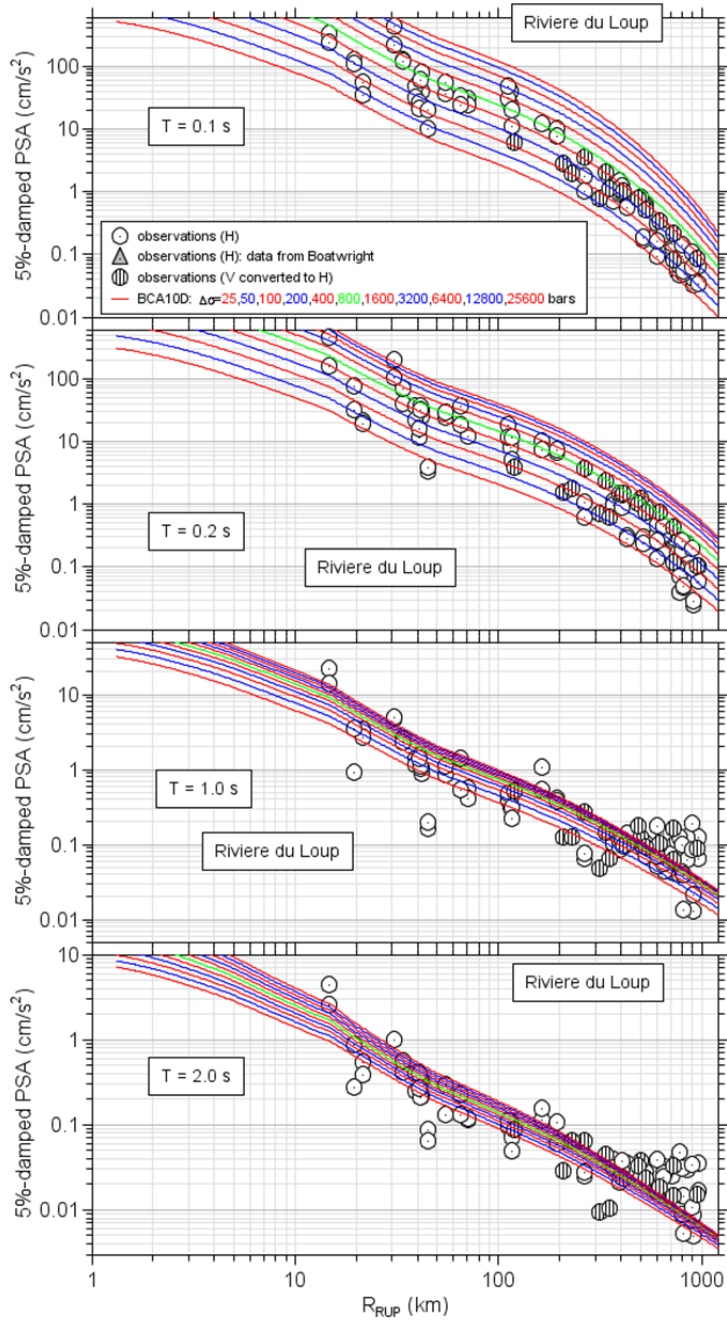


Figure 2.7 Observations from the 2005 Riviere du Loup earthquake (symbols) and simulated PSA for a suite of stress parameters, using crustal amplifications for $V_{S30} = 2.0$ km/sec and the Boore et al. [2010] (BCA10D) attenuation model. See Boore [2012] for details regarding the observations.

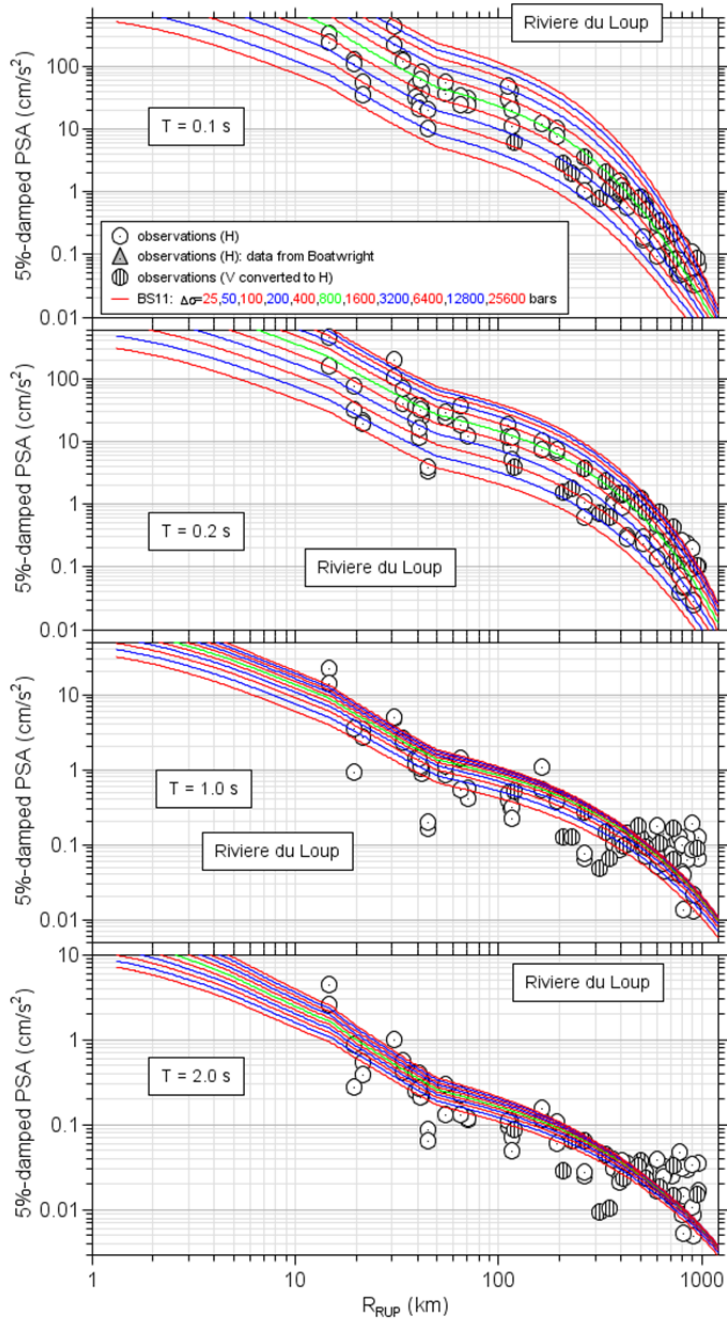


Figure 2.8 Observations from the 2005 Riviere du Loup earthquake (symbols) and simulated PSA for a suite of stress parameters, using crustal amplifications for $V_{S30} = 2.0$ km/sec and the Boatwright and Seekins [2011] (BS11) attenuation model. See Boore [2012] for details regarding the observations.

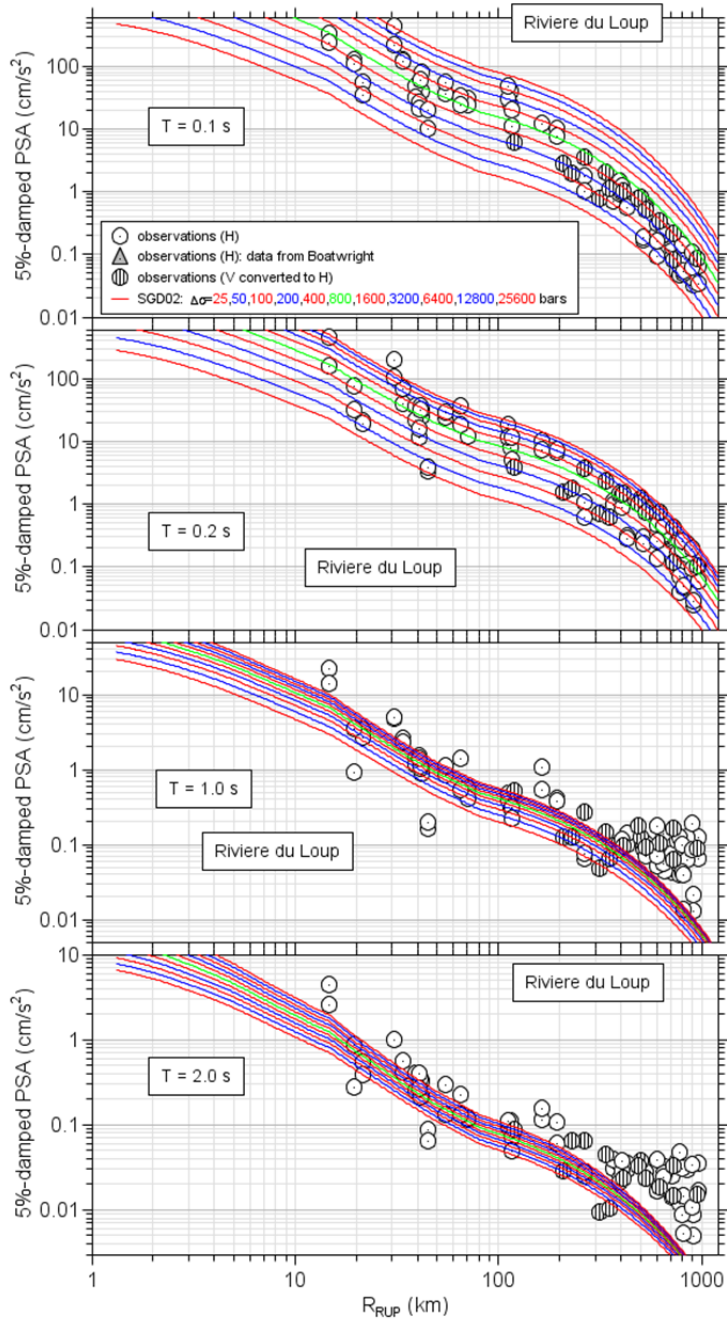


Figure 2.9 Observations from the 2005 Riviere du Loup earthquake (symbols) and simulated PSA for a suite of stress parameters, using crustal amplifications for $V_{S30} = 2000$ m/sec and the Silva et al. [2002] (SGD02) attenuation model. See Boore [2012] for details regarding the observations.

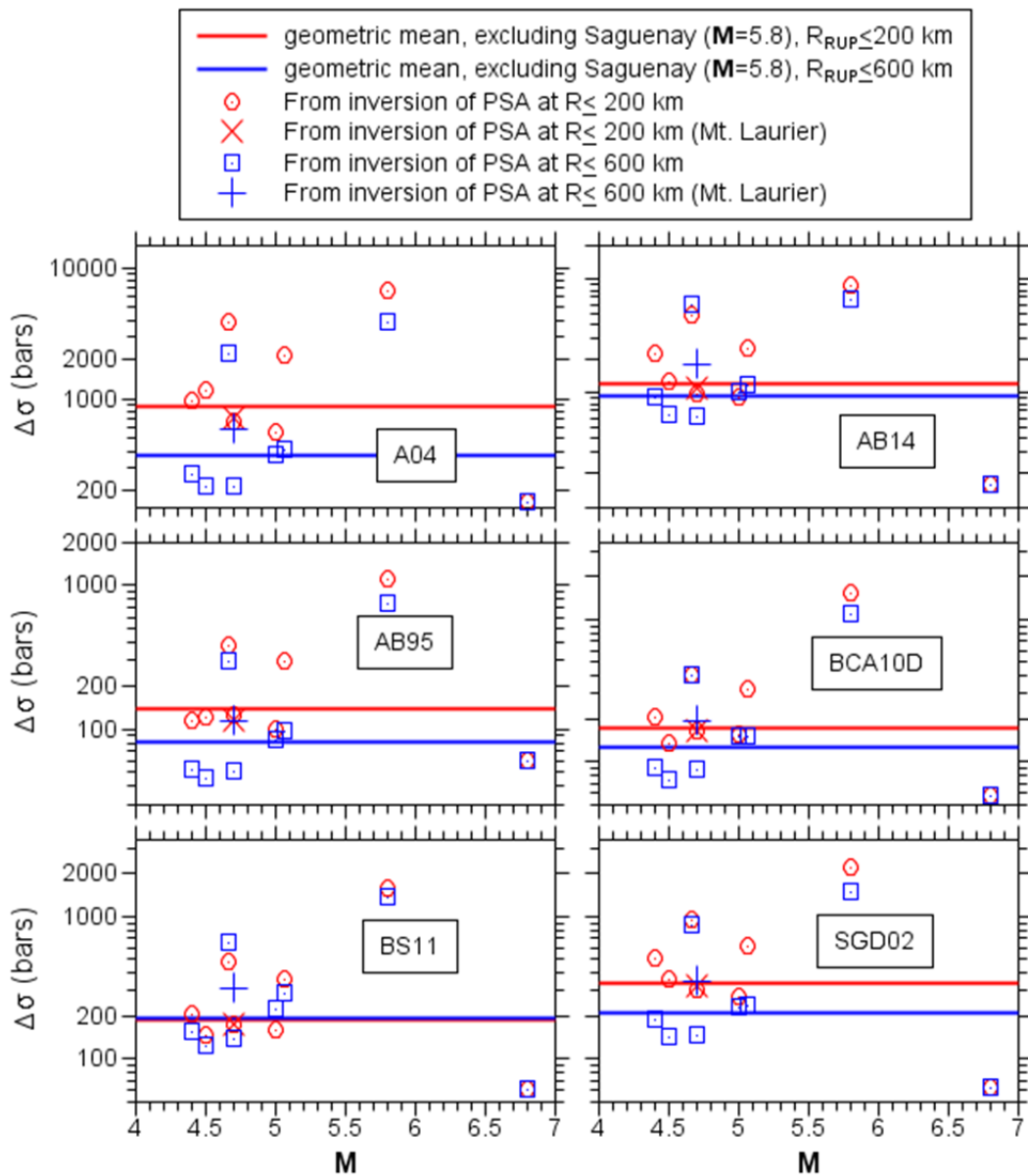


Figure 2.10 Summary of stress parameters obtained from inversions of observed PSA for the six attenuation models. The results from inversions using data within 200 km and within 600 km are shown separately. The stress parameters from recording of the Mt. Laurier earthquake are shown as separate symbols to distinguish those results from the other event (Kipawa) with the same M .

Table 2.4 Stress parameters from inverting the 0.1 sec and 0.2 sec PSA from recordings of the indicated events, using the Atkinson [2004] (A04) attenuation model. Two sets of data were used, for maximum distances of 200 km and 600 km. The geometric mean (*gmean*) was computed from the inverted stress parameters, excluding the stress parameter from the Saguenay earthquake; *sdevfctr* is the standard deviation of the mean log stress, expressed as a factor (i.e., 10 raised to the power given by the standard deviation of the mean log stress).

Event	Date (M/D/Y)	M	Attenuation model	Stress (bars)	
				$(R_{RUP} < 200 \text{ km})(F_M)(F_Z)T(\text{sec})M_h\Delta\sigma$	$(R_{RUP} < 600 \text{ km})$
Nahanni	12/23/1985	6.80	a04	162	162
Saguenay	11/25/1988	5.80	a04	6565	3818
Mt. Laurier	10/19/1990	4.70	a04	703	597
Cap Rouge	11/06/1997	4.41	a04	961	265
St. Anne	03/16/1999	4.50	a04	1155	214
Kipawa	01/01/2000	4.70	a04	668	217
Ausable	04/20/2002	5.00	a04	547	375
Riviere du Loup	03/06/2005	4.67	a04	3848	2225
Val des Bois	06/23/2010	5.07	a04	2165	404
<i>gmean</i>				887	376
<i>sdevfctr</i>				2.6	2.3

Table 2.5 Stress parameters from inverting the 0.1sec and 0.2 sec PSA from recordings of the indicated events, using the Atkinson and Boore [2014] (AB14) attenuation model. Two sets of data were used, for maximum distances of 200 km and 600 km. The geometric mean (*gmean*) was computed from the inverted stress parameters, excluding the stress parameter from the Saguenay earthquake; *sdevfctr* is the standard deviation of the mean log stress, expressed as a factor (i.e., 10 raised to the power given by the standard deviation of the mean log stress).

Event	Date (M/D/Y)	M	Attenuation model	Stress (bars) ($R_{RUP} < 200$ km)	Stress (bars) ($R_{RUP} < 600$ km)
Nahanni	12/23/1985	6.80	ab14	157	157
Saguenay	11/25/1988	5.80	ab14	8720	6559
Mt. Laurier	10/19/1990	4.70	ab14	1100	1811
Cap Rouge	11/06/1997	4.41	ab14	2206	923
St. Anne	03/16/1999	4.50	ab14	1236	635
Kipawa	01/01/2000	4.70	ab14	989	625
Ausable	04/20/2002	5.00	ab14	896	1001
Riviere du Loup	03/06/2005	4.67	ab14	4731	5888
Val des Bois	06/23/2010	5.07	ab14	2461	1181
<i>gmean</i>				1219	961
<i>sdevfctr</i>				2.7	2.8

Table 2.6 Stress parameters from inverting the 0.1sec and 0.2 sec PSA from recordings of the indicated events, using the Atkinson and Boore [1995] (AB95) attenuation model. Two sets of data were used, for maximum distances of 200 km and 600 km. The geometric mean (*gmean*) was computed from the inverted stress parameters, excluding the stress parameter from the Saguenay earthquake; *sdevfctr* is the standard deviation of the mean log stress, expressed as a factor (i.e., 10 raised to the power given by the standard deviation of the mean log stress).

Event	Date (M/D/Y)	M	Attenuation model	Stress (bars) ($R_{RUP} < 200$ km)	Stress (bars) ($R_{RUP} < 600$ km)
Nahanni	12/23/1985	6.80	ab95	59	59
Saguenay	11/25/1988	5.80	ab95	1109	738
Mt. Laurier	10/19/1990	4.70	ab95	113	115
Cap Rouge	11/06/1997	4.41	ab95	113	52
St. Anne	03/16/1999	4.50	ab95	119	45
Kipawa	01/01/2000	4.70	ab95	124	51
Ausable	04/20/2002	5.00	ab95	98	84
Riviere du Loup	03/06/2005	4.67	ab95	382	296
Val des Bois	06/23/2010	5.07	ab95	296	95
<i>gmean</i>				137	81
<i>sdevfctr</i>				1.8	1.9

Table 2.7 Stress parameters from inverting the 0.1sec and 0.2 sec PSA from recordings of the indicated events, using the Boore et al. [2010] (BCA10D) attenuation model. Two sets of data were used, for maximum distances of 200 km and 600 km. The geometric mean (*gmean*) was computed from the inverted stress parameters, excluding the stress parameter from the Saguenay earthquake; *sdevfctr* is the standard deviation of the mean log stress, expressed as a factor (i.e., 10 raised to the power given by the standard deviation of the mean log stress).

Event	Date (M/D/Y)	M	Attenuation model	Stress (bars) ($R_{RUP} < 200$ km)	Stress (bars) ($R_{RUP} < 600$ km)
Nahanni	12/23/1985	6.80	bca10d	57	57
Saguenay	11/25/1988	5.80	bca10d	1499	1082
Mt. Laurier	10/19/1990	4.70	bca10d	162	193
Cap Rouge	11/06/1997	4.41	bca10d	202	91
St. Anne	03/16/1999	4.50	bca10d	134	74
Kipawa	01/01/2000	4.70	bca10d	162	88
Ausable	04/20/2002	5.00	bca10d	155	150
Riviere du Loup	03/06/2005	4.67	bca10d	405	399
Val des Bois	06/23/2010	5.07	bca10d	319	150
<i>gmean</i>				173	125
<i>sdevfctr</i>				1.8	1.9

Table 2.8 Stress parameters from inverting the 0.1sec and 0.2 sec PSA from recordings of the indicated events, using the Boatwright and Seekins [2011] (BS11) attenuation model. Two sets of data were used, for maximum distances of 200 km and 600 km. The geometric mean (*gmean*) was computed from the inverted stress parameters, excluding the stress parameter from the Saguenay earthquake; *sdevfctr* is the standard deviation of the mean log stress, expressed as a factor (i.e., 10 raised to the power given by the standard deviation of the mean log stress).

Event	Date (M/D/Y)	M	Attenuation model	Stress (bars) ($R_{RUP} < 200$ km)	Stress (bars) ($R_{RUP} < 600$ km)
Nahanni	12/23/1985	6.80	bs11	61	61
Saguenay	11/25/1988	5.80	bs11	1563	1361
Mt. Laurier	10/19/1990	4.70	bs11	170	313
Cap Rouge	11/06/1997	4.41	bs11	202	151
St. Anne	03/16/1999	4.50	bs11	144	123
Kipawa	01/01/2000	4.70	bs11	172	138
Ausable	04/20/2002	5.00	bs11	156	220
Riviere du Loup	03/06/2005	4.67	bs11	472	656
Val des Bois	06/23/2010	5.07	bs11	361	288
<i>gmean</i>				185	194
<i>sdevfctr</i>				1.9	2.1

Table 2.9 Stress parameters from inverting the 0.1sec and 0.2 sec PSA from recordings of the indicated events, using the Silva et al. [2002] (SGD02) attenuation model. Two sets of data were used, for maximum distances of 200 km and 600 km. The geometric mean (*gmean*) was computed from the inverted stress parameters, excluding the stress parameter from the Saguenay earthquake; *sdevfctr* is the standard deviation of the mean log stress, expressed as a factor (i.e., 10 raised to the power given by the standard deviation of the mean log stress).

Event	Date (M/D/Y)	M	Attenuation Model	Stress (bars) ($R_{RUP} < 200$ km)	Stress (bars) ($R_{RUP} < 600$ km)
Nahanni	12/23/1985	6.80	sgd02	62	62
Saguenay	11/25/1988	5.80	sgd02	2193	1459
Mt. Laurier	10/19/1990	4.70	sgd02	320	352
Cap Rouge	11/06/1997	4.41	sgd02	511	187
St. Anne	03/16/1999	4.50	sgd02	355	141
Kipawa	01/01/2000	4.70	sgd02	300	146
Ausable	04/20/2002	5.00	sgd02	272	229
Riviere du Loup	03/06/2005	4.67	sgd02	939	851
Val des Bois	06/23/2010	5.07	sgd02	621	233
<i>gmean</i>				338	210
<i>sdevfctr</i>				2.2	2.1

2.4 SIMULATED MOTIONS FOR THE PEER NGA-EAST PROJECT

In addition to the stress parameters just discussed, other parameters used in the simulations included crustal amplifications for sites with $V_{S30} = 3.0$ km/sec, as specified by the Management Team, with $\kappa = 0.006$ sec, and the BT15 FF factors; other parameters are given in Appendix 2A. The peak motions were obtained from random-vibration theory, using the Der Kiureghian [1980] rms-to-peak factors and the BT15 D_{RMS} equations. The SMSIM program *tmrs_loop_rv_drvr* was used to do the simulations. The results have been aggregated into six workbooks (appendices 2A-2G) comprising 150 tables, each table being for a given attenuation model and a given GMIM (6 models \times 25 GMIMs = 150). Plots of 5%-damped PSA versus R_{RUP} are shown in Figures 2.11–2.17 for periods of 0.01 sec, 0.1 sec, 0.2 sec, 1.0 sec, 2.0 sec, 5 sec, and 10 sec. Each figure shows the motions for all attenuation models, with one magnitude per graph in each figure (magnitudes 5, 6, 7, and 8). Note that all of the attenuation models yield similar motions at distances between about 30 km and 200 km for magnitudes near 5 and for periods of 0.1 sec and 0.2 sec; this makes sense since the stress parameters for each attenuation model were chosen to

give a match to data for these distances, magnitude, and periods. At short distances, the steep decay of the A04 and AB14 models yields higher short-period motions than the other models. The larger motions for the SGD02 attenuation model for larger magnitudes is a consequence of the magnitude-dependent geometrical spreading in that model, something that is not a factor in the other models (but because of the effect of the FF factor, there is an apparent magnitude-dependent decay with distance for these other models—see Figures 2.18–22 for examples). The larger motions for the AB14 model at close distances and long periods is due to the period-dependent geometrical spreading in that model. This period dependence is such that the geometrical spreading is more rapid than $1/R^{1.3}$ at distances between about 10 km and 50 km for period of 1 sec and longer.

Direct comparisons of the distance dependence of the motions from the BS11 model for the four magnitudes are shown in Figures 2.18–2.22 for periods of 0.01 sec, 0.1 sec, 0.2 sec, 1.0 sec, and 2.0 sec. As mentioned earlier, notice the apparent magnitude dependence of the distance decay of the motions. This is largely, if not entirely, due to the magnitude-dependent FF factor. Also note that there is some oversaturation of motions at close distances and short periods. This oversaturation is not present using the Yenier and Atkinson [2015a] FF factors, as shown by the dashed curves in the figures. The difference in the motions using the BT15 and the YA15 FF factors is a result of the stronger magnitude dependence of the FF factors at small magnitudes for BT15 than for YA15. (This discussion will be easier to follow with reference to Equation (2.1) and Figure 2.3, realizing that the simulations use R_{PS} and not R_{RUP} when evaluating all distance-dependent components of the stochastic model.) For a fixed R_{RUP} this stronger dependence leads to an apparent negative magnitude scaling, because at short periods the positive magnitude scaling due to the source scaling is not enough to compensate for the effect of the FF factor. At longer periods the source-scaling effect is strong enough to counter the negative scaling due to the FF factor (e.g., compare Figures 2.18 and 2.22).

The period dependence of the simulations is shown in Figure 2.23 for a wide range of magnitudes and distances. The simulated motions vary smoothly with changes in the predictor variables. The strong distance-dependent changes in the shape of the spectra are a result of the stronger attenuation of the motions with distance at short periods than at long periods.

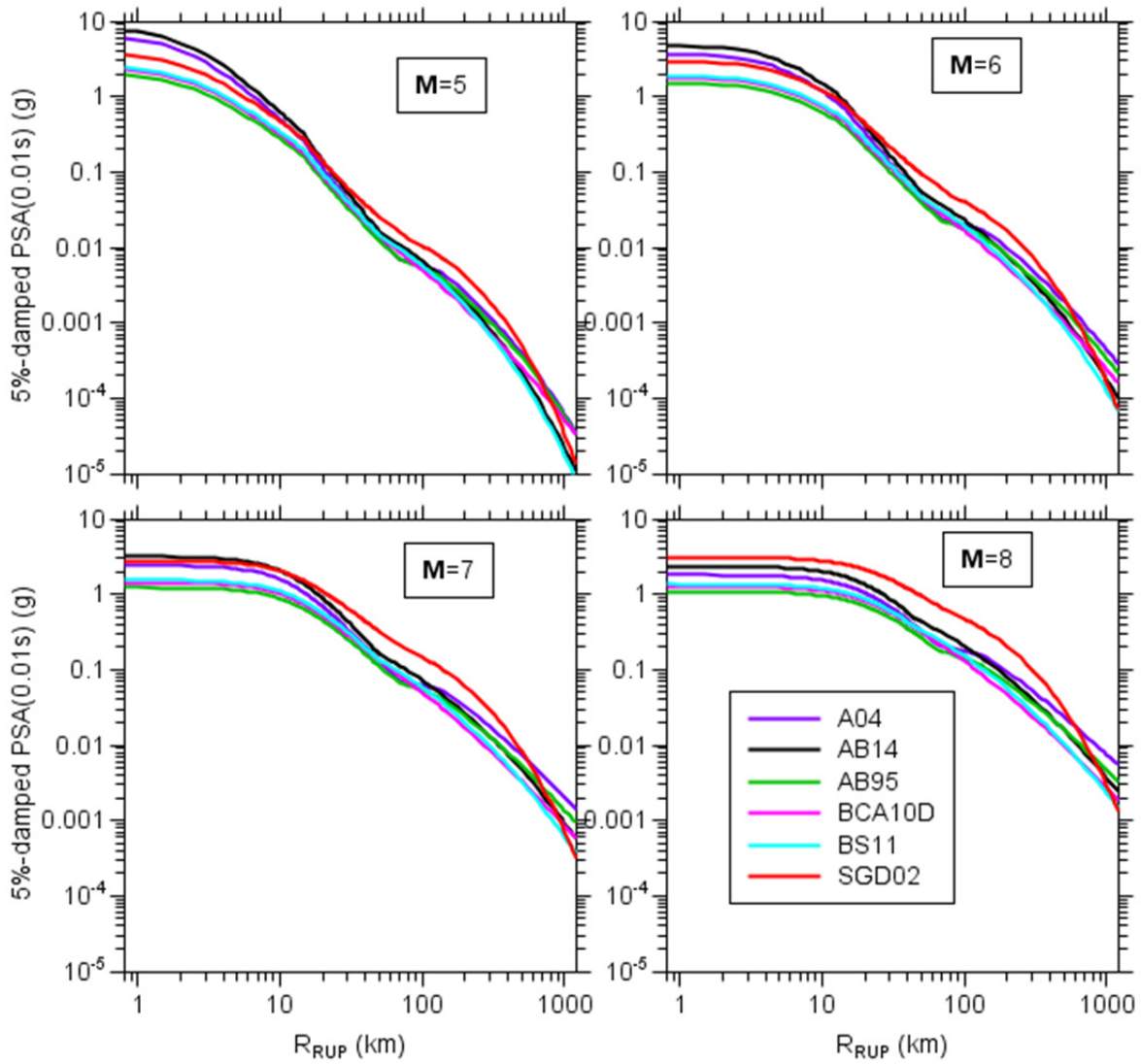


Figure 2.11 A comparison of simulated 5%-damped response spectra from the six attenuation models for a period of 0.01 sec as a function of distance for four magnitudes. The crustal amplifications used in the simulations were for sites with $V_{S30} = 3.0$ km/sec .

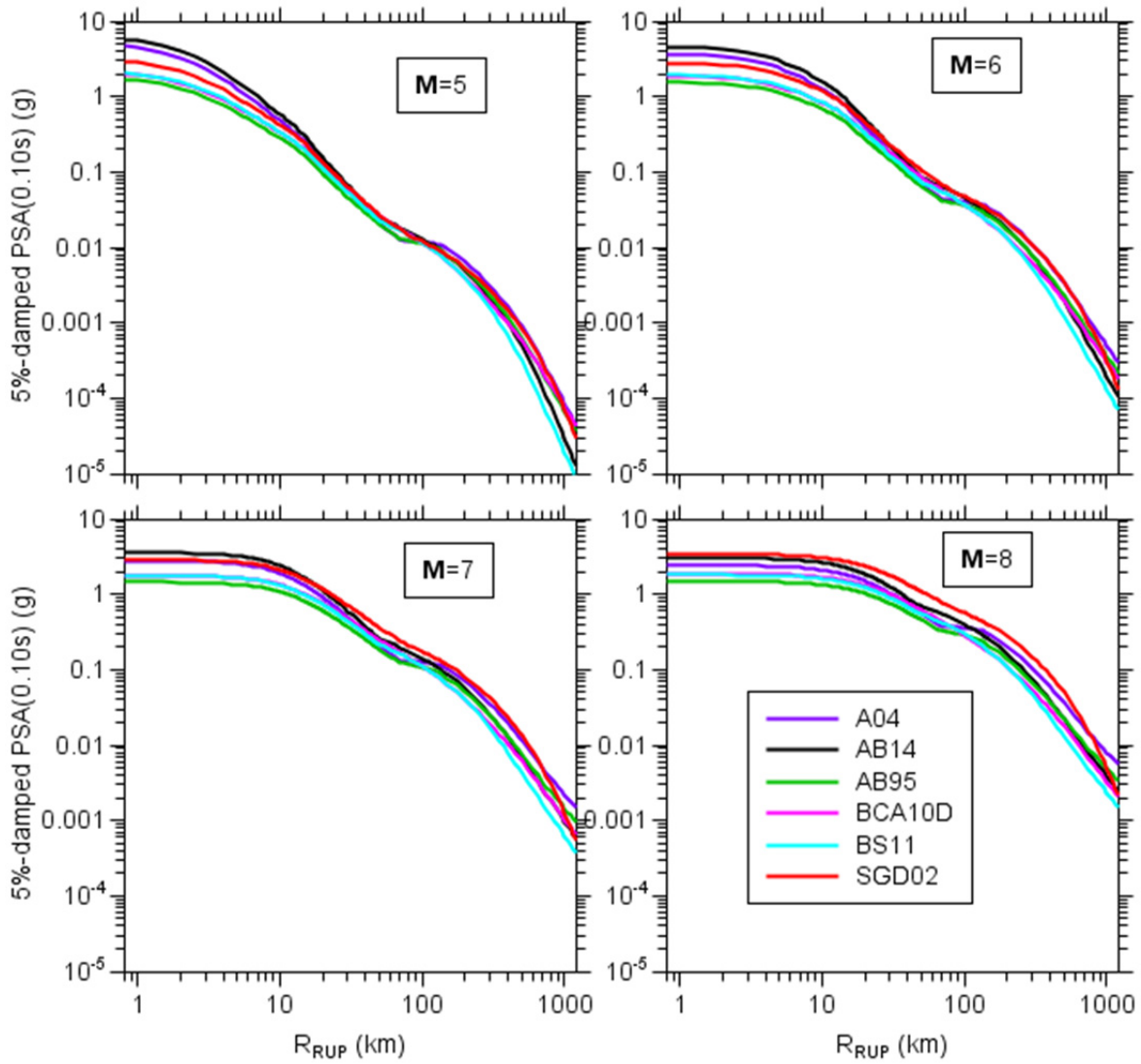


Figure 2.12 A comparison of simulated 5%-damped response spectra from the six attenuation models for a period of 0.1 sec as a function of distance for four magnitudes. The crustal amplifications used in the simulations were for sites with $V_{S30} = 3.0$ km/sec .

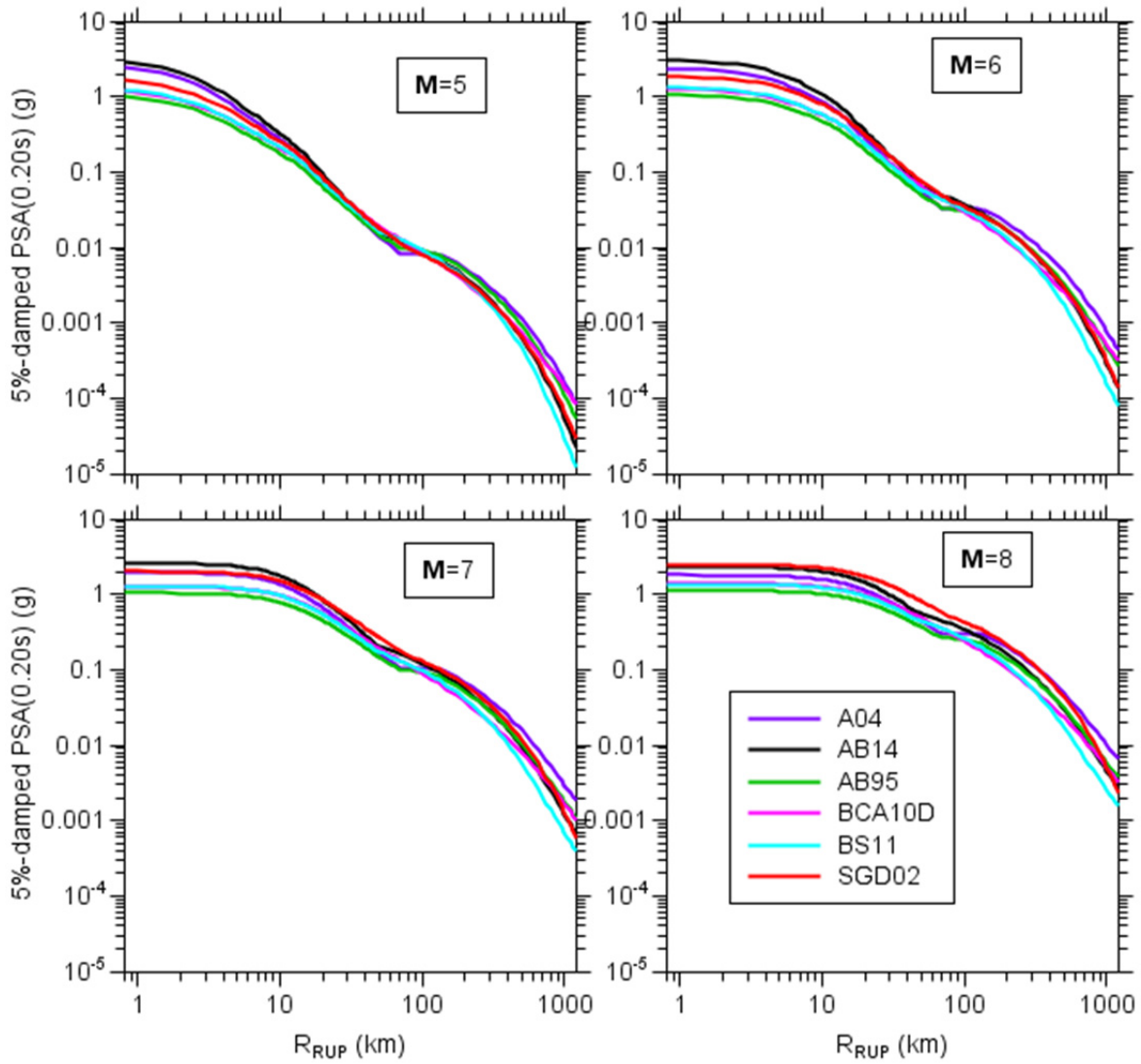


Figure 2.13 A comparison of simulated 5%-damped response spectra from the six attenuation models for a period of 0.2 sec as a function of distance for four magnitudes. The crustal amplifications used in the simulations were for sites with $V_{S30} = 3.0$ km/sec .

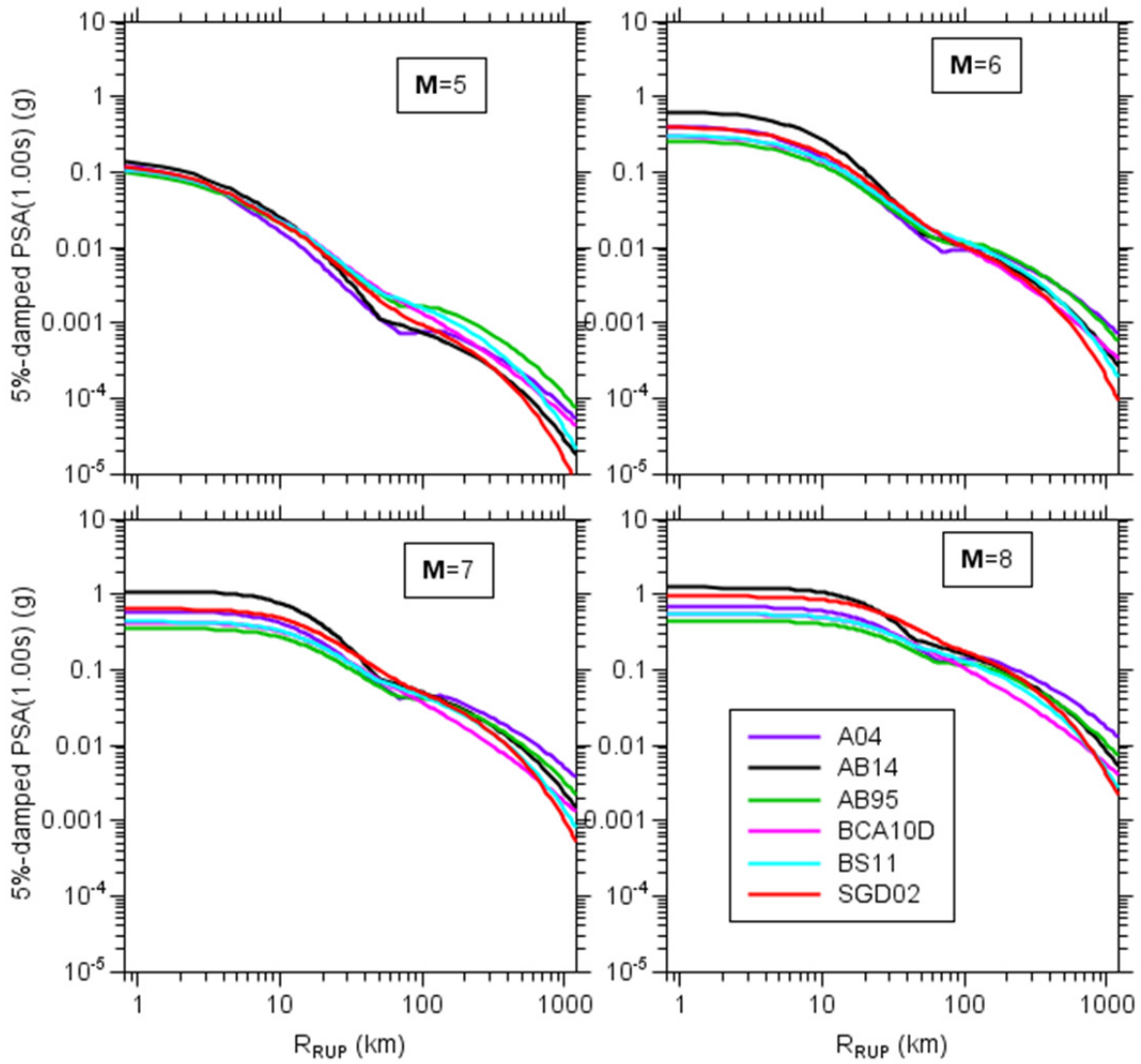


Figure 2.14 A comparison of simulated 5%-damped response spectra from the six attenuation models for a period of 1.0 sec as a function of distance for four magnitudes. The crustal amplifications used in the simulations were for sites with $V_{S30} = 3.0$ km/sec .

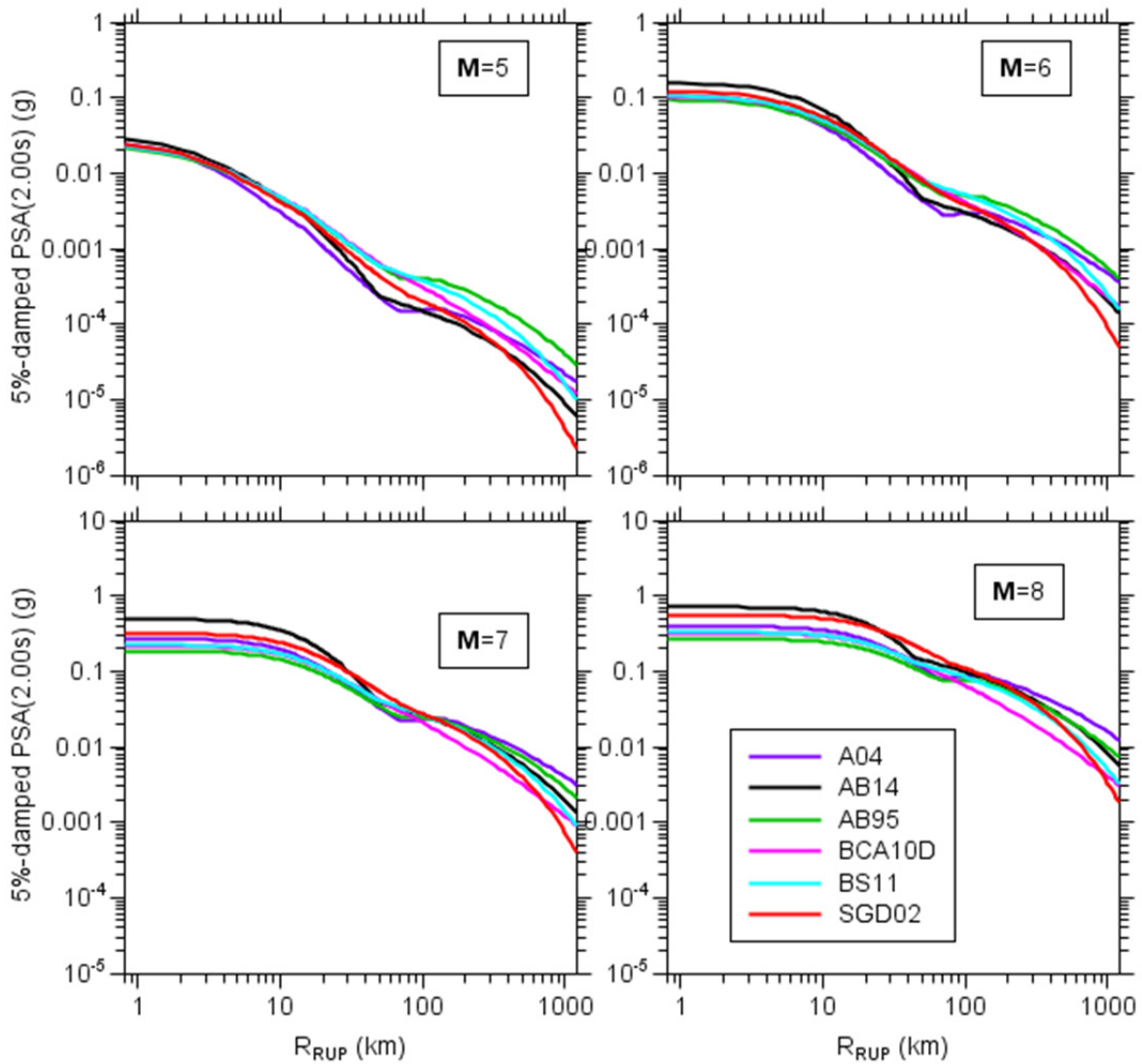


Figure 2.15 A comparison of simulated 5%-damped response spectra from the six attenuation models for a period of 2.0 sec as a function of distance for four magnitudes. The crustal amplifications used in the simulations were for sites with $V_{S30} = 3.0$ km/sec .

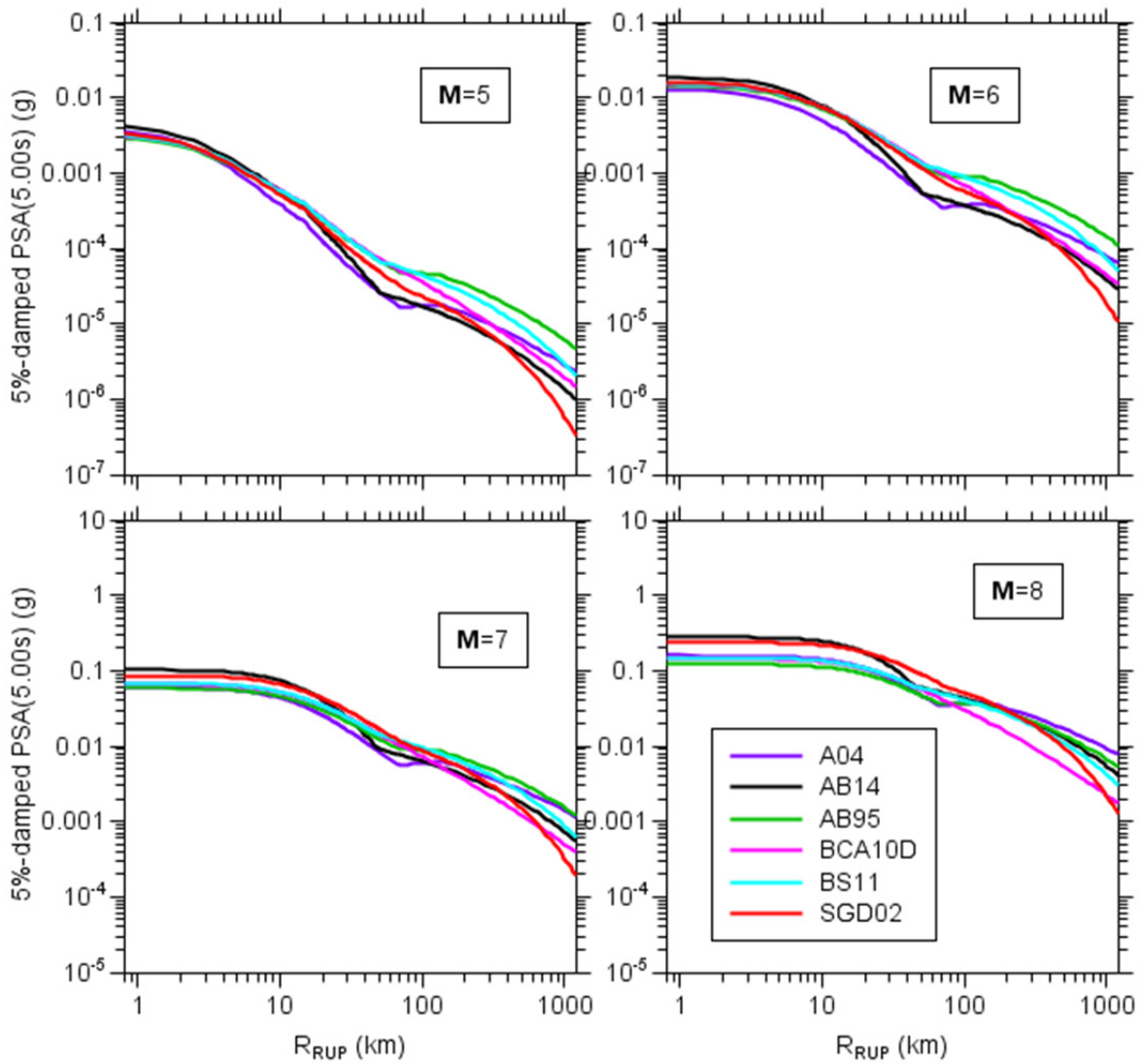


Figure 2.16 A comparison of simulated 5%-damped response spectra from the six attenuation models for a period of 5.0 sec as a function of distance for four magnitudes. The crustal amplifications used in the simulations were for sites with $V_{S30} = 3.0$ km/sec .

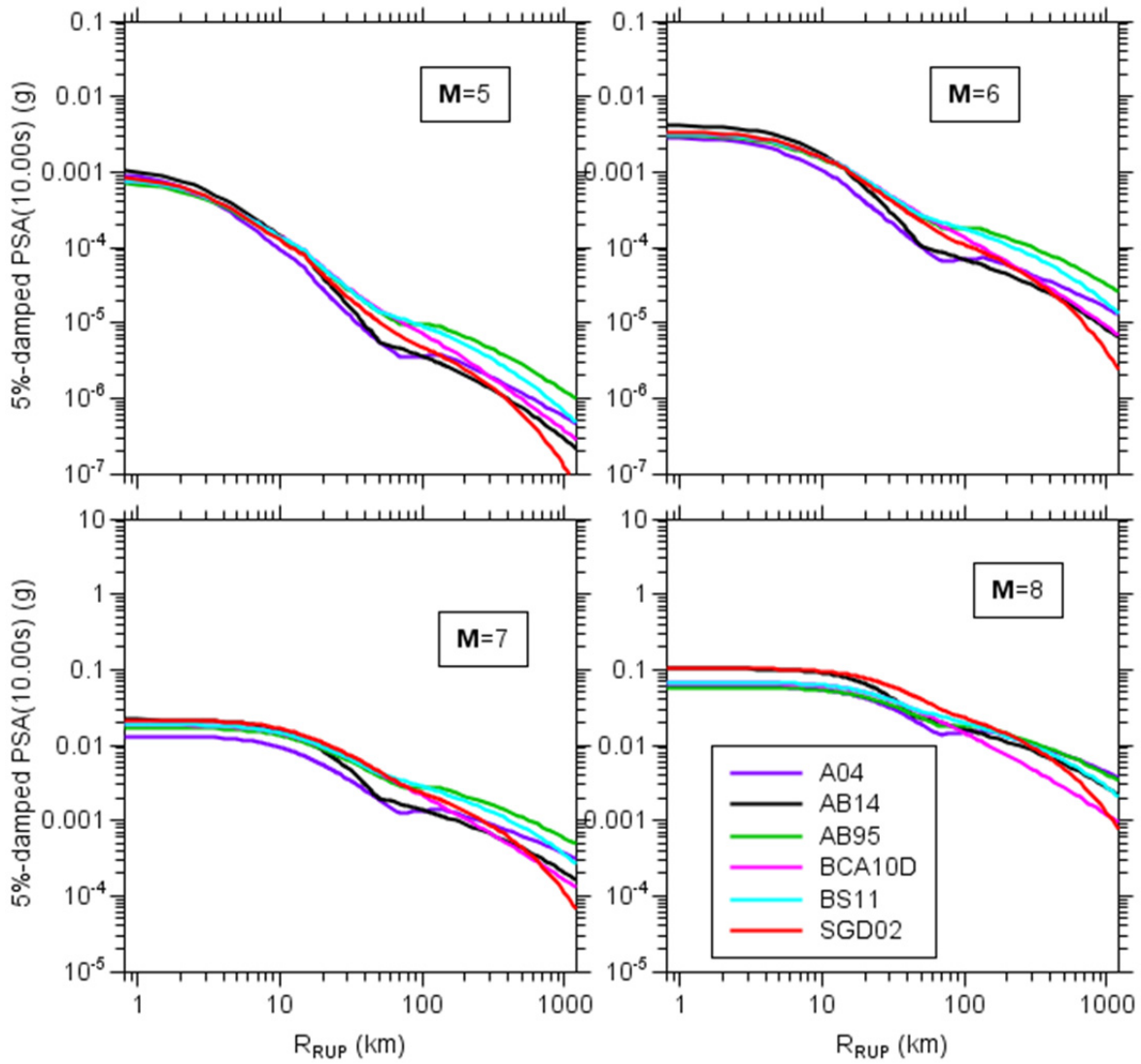


Figure 2.17 A comparison of simulated 5%-damped response spectra from the six attenuation models for a period of 10.0 sec as a function of distance for four magnitudes. The crustal amplifications used in the simulations were for sites with $V_{S30} = 3.0$ km/sec .

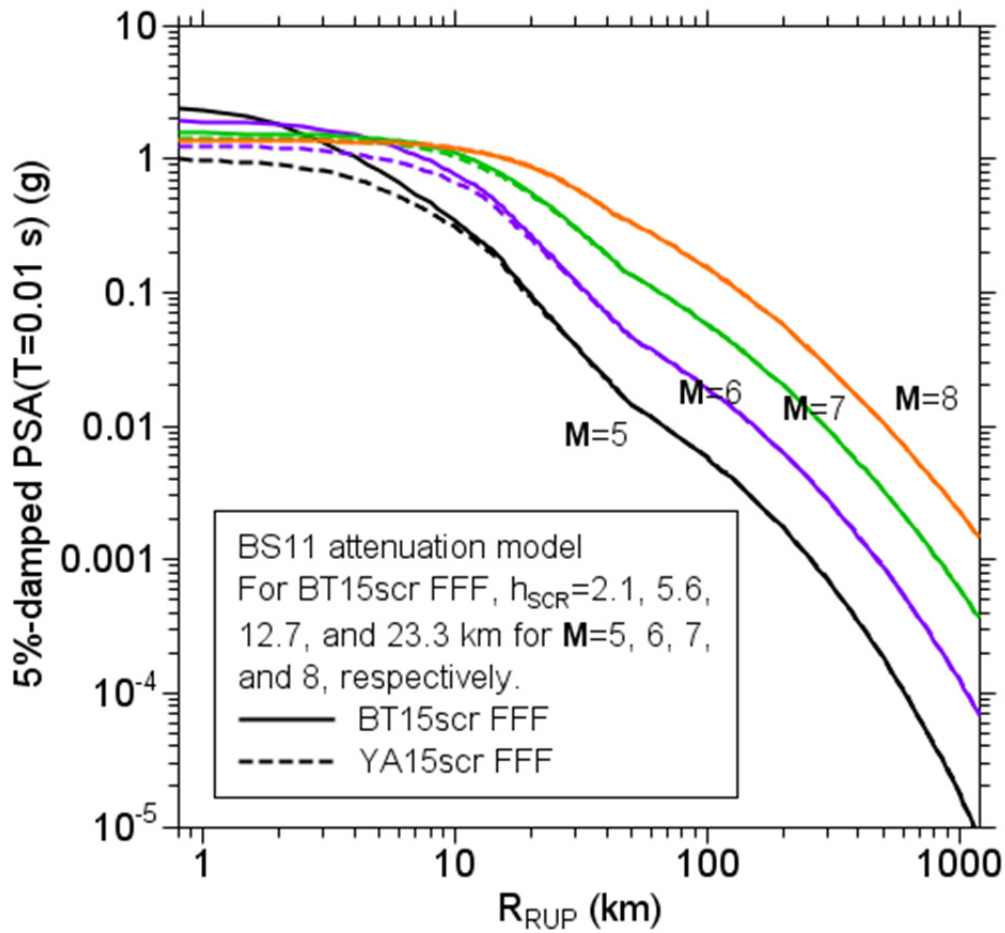


Figure 2.18 Simulated 5%-damped response spectra at a period of 0.01 sec for the Boatwright and Seekins [2011] (BS11) attenuation model as a function of distance to the rupture surface (R_{RUP}) for four magnitudes. Two magnitude-dependent functions for the finite-fault factor (FFF) were used to convert R_{RUP} to the distance R_{PS} used in the point-source simulations: Boore and Thompson [2015] solid lines and Yenier and Atkinson [2015a] dashed lines. The “scr” after BT15 and YA15 indicate that the FFFs were adjusted for SCRs, following BT15. The crustal amplifications used in the simulations were for sites with $V_{S30} = 3.0$ km/sec .

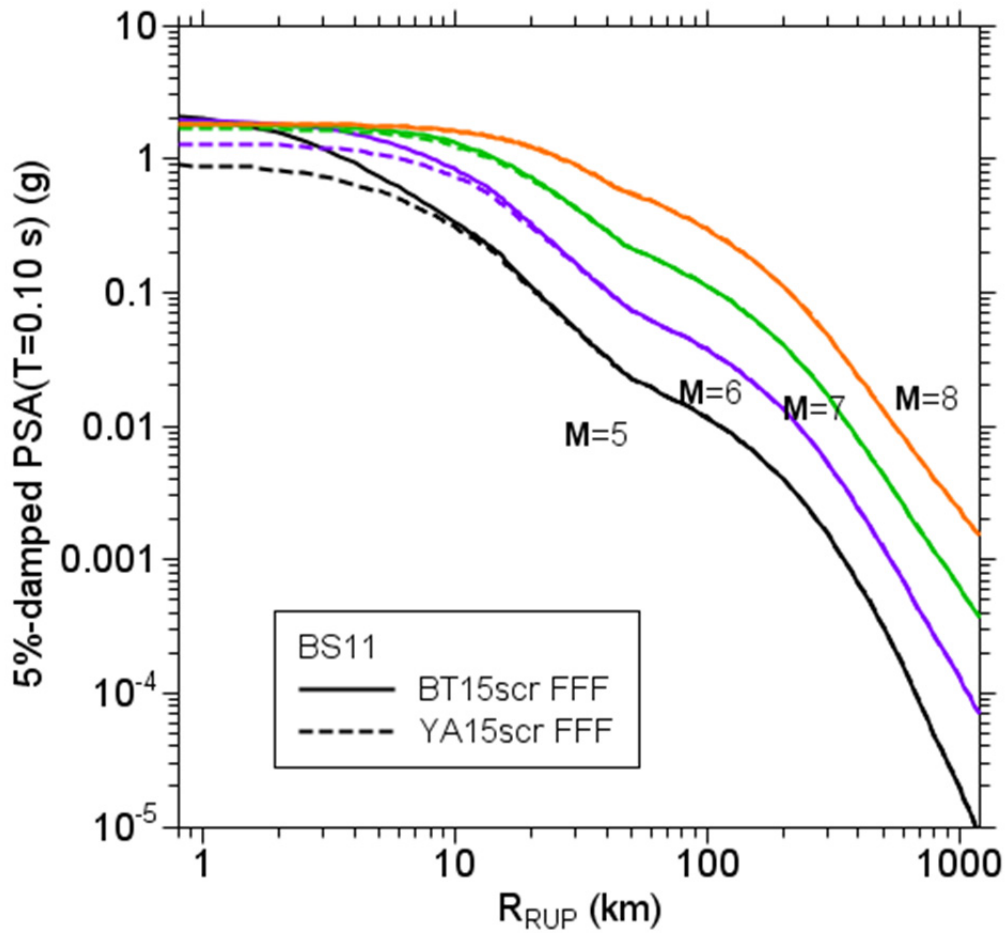


Figure 2.19 Simulated 5%-damped response spectra at a period of 0.1 sec for the Boatwright and Seekins [2011] (BS11) attenuation model as a function of distance to the rupture surface (R_{RUP}) for four magnitudes. Two magnitude-dependent functions for the finite-fault factor (FFF) were used to convert R_{RUP} to the distance R_{PS} used in the point-source simulations: Boore and Thompson [2015] solid lines and Yenier and Atkinson [2015a] dashed lines. The “scr” after BT15 and YA15 indicate that the FFFs were adjusted for stable continental regions (scr), following BT15. The crustal amplifications used in the simulations were for sites with $V_{S30} = 3.0$ km/sec .

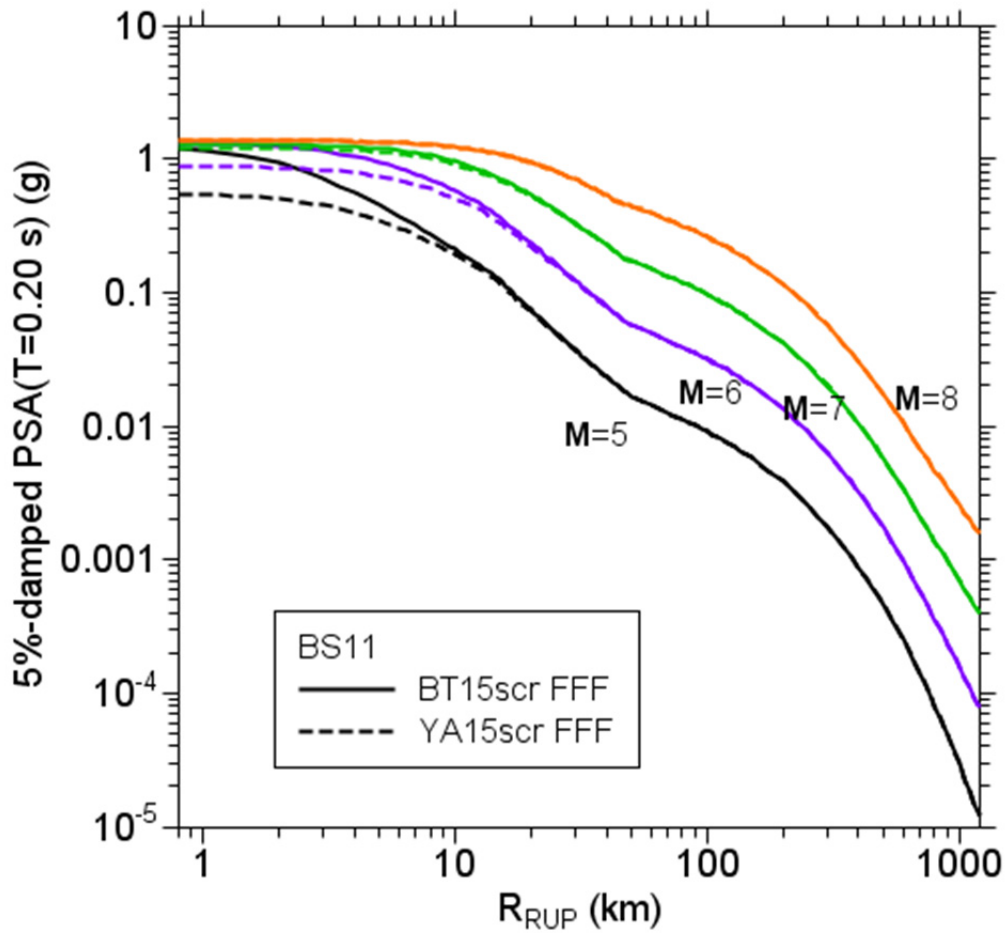


Figure 2.20 Simulated 5%-damped response spectra at a period of 0.2 sec for the Boatwright and Seekins [2011] (BS11) attenuation model as a function of distance to the rupture surface (R_{RUP}) for four magnitudes. Two magnitude-dependent functions for the finite-fault factor (FFF) were used to convert R_{RUP} to the distance R_{PS} used in the point-source simulations: Boore and Thompson [2015] solid lines and Yenier and Atkinson [2015a] dashed lines. The “scr” after BT15 and YA15 indicate that the FFFs were adjusted for stable continental regions (scr), following BT15. The crustal amplifications used in the simulations were for sites with $V_{S30} = 3.0$ km/sec .

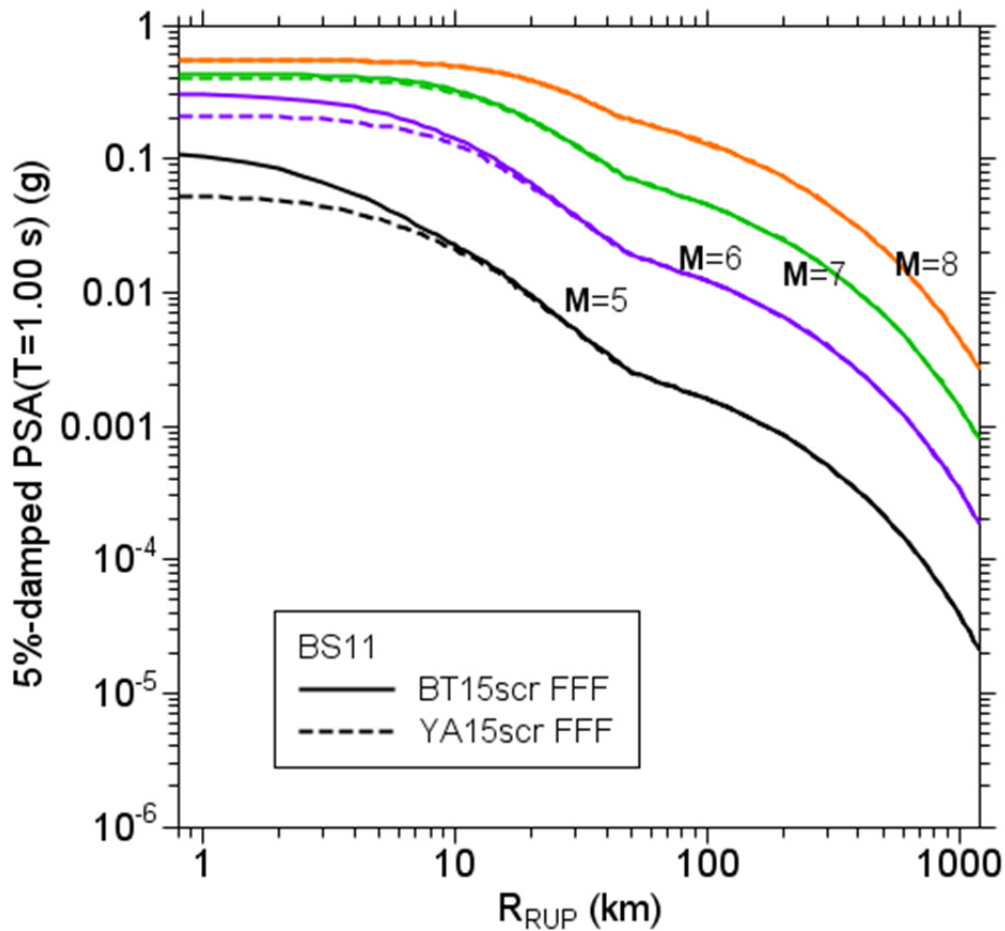


Figure 2.21 Simulated 5%-damped response spectra at a period of 1.0 sec for the Boatwright and Seekins [2011] (BS11) attenuation model as a function of distance to the rupture surface (R_{RUP}) for four magnitudes. Two magnitude-dependent functions for the finite-fault factor (FFF) were used to convert R_{RUP} to the distance R_{PS} used in the point-source simulations: Boore and Thompson [2015] solid lines and Yenier and Atkinson [2015a] dashed lines. The “scr” after BT15 and YA15 indicate that the FFF were adjusted for stable continental regions (scr), following BT15. The crustal amplifications used in the simulations were for sites with $V_{S30} = 3.0$ km/sec .

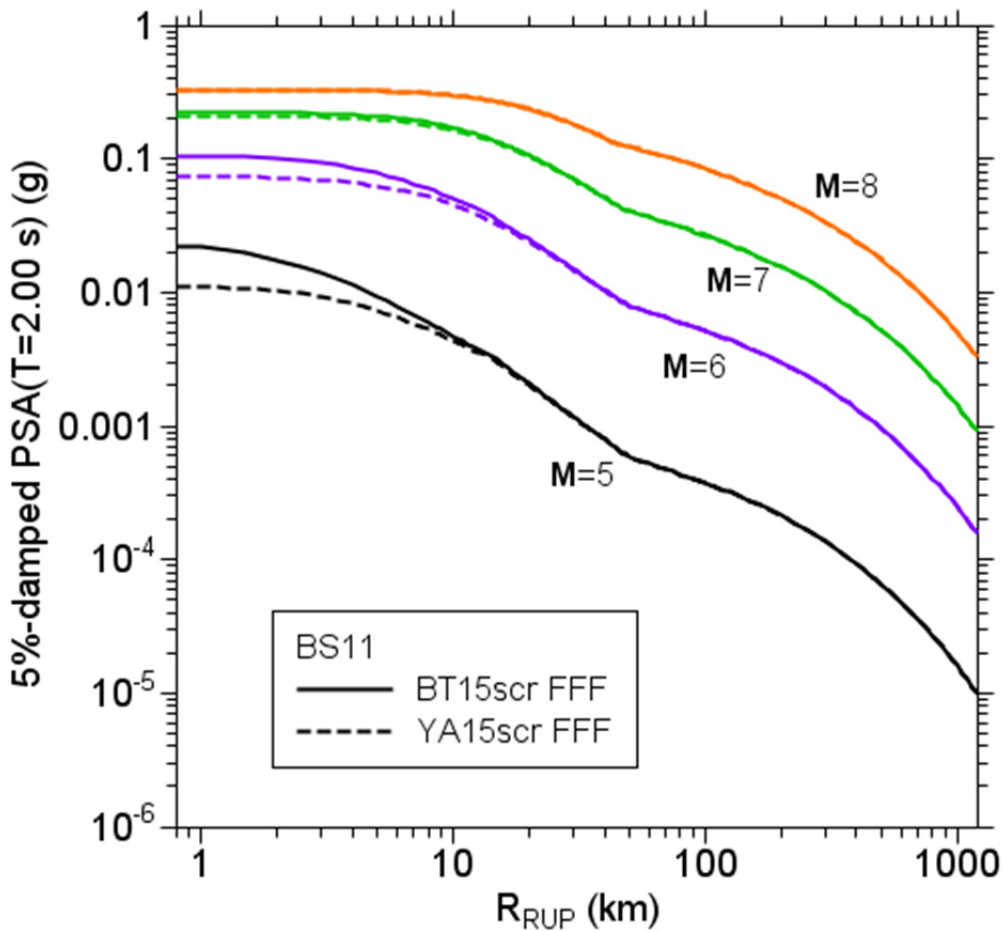


Figure 2.22 Simulated 5%-damped response spectra at a period of 2.0 sec for the Boatwright and Seekins [2011] (BS11) attenuation model as a function of distance to the rupture surface (R_{RUP}) for four magnitudes. Two magnitude-dependent functions for the finite-fault factor (FFF) were used to convert R_{RUP} to the distance R_{PS} used in the point-source simulations: Boore and Thompson [2015] solid lines) and Yenier and Atkinson [2015a] dashed lines). The “scr” after BT15 and YA15 indicate that the FFF were adjusted for stable continental regions (scr), following BT15. The crustal amplifications used in the simulations were for sites with $V_{S30} = 3.0$ km/sec .

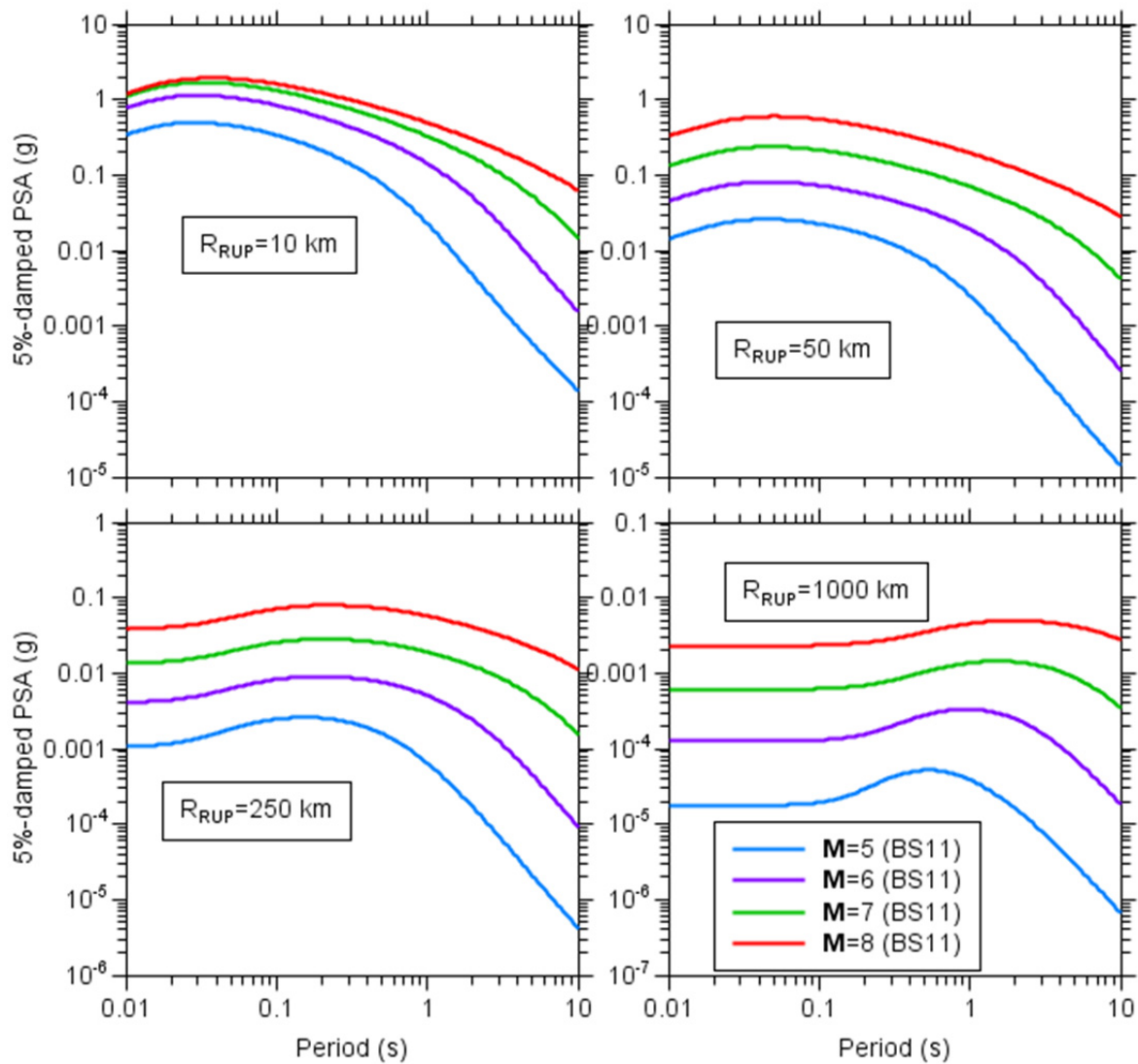


Figure 2.23 Simulated 5%-damped response spectra for the Boatwright and Seekins [2011] (BS11) attenuation model as a function of period for four magnitudes and four distances. The Boore and Thompson [2015] finite-fault factor for stable continental regions was used to convert R_{RUP} to the distance R_{PS} used in the point-source simulations. The crustal amplifications used in the simulations were for sites with $V_{S30} = 3.0$ km/sec .

2.5 SUMMARY AND DISCUSSION

In order to fulfill my commitment to the PEER NGA-East project, I have provided motions from point-source stochastic-method simulations for almost the whole stipulated range of \mathbf{M} , R , and T for the six specified attenuation models. Motions are not provided at all stipulated distances (R_{rup} from 0 to 1500 km) or magnitudes (up to 8.2), however, because the BT15 D_{RMS} coefficients are not defined for $R_{PS} < 2$ km and for $R_{PS} > 1262$ km and for $\mathbf{M} > 8.0$. The first distance condition means that motions are not provided for very short distances and small magnitudes, for which R_{PS} for the specified R_{RUP} is less than 2 km. The second distance condition means that no motions are provided for distances beyond 1262 km; because $R_{PS} \approx R_{RUP}$ at this distance, independent of magnitude, the exclusion applies for all magnitudes.

Even though I show that the models with $1/R^{1.3}$ geometrical spreading cannot fit longer period data no matter what stress parameter is used, I provide motions for those models anyway. Although I am not endorsing any one model, if I had to choose one, it would be the BS11 model. If I were allowed to choose three, they would be AB95, BCA10D, and BS11.

What Is Missing?

There are two obvious things missing from this report:

- a consideration of depth on the stress parameter
- a discussion of the uncertainty in the motions

There are some studies that find a depth dependence to the stress parameter, not only for potentially-induced earthquakes, but also for regular tectonic earthquakes (e.g., J. Boatwright, presentation given at a NGA-East workshop). I have not attempted to include such a dependence in this study, although it would be easy to do so. The second limitation—no discussion of uncertainty—would require more work, such as doing many simulations using distributions of the model parameters. These distributions would include the “static” parameters such as average radiation pattern, as well as “dynamic” parameters such as the stress parameter, whose distribution could be guided by *sdevfctr* in Tables 2.5–2.9.

2.6 ACKNOWLEDGMENTS

This paper was prepared as an account of work sponsored by an agency of the U.S. Government. Neither the U.S. Government nor any agency thereof, nor any of their employees, makes any warranty, expressed or implied, or assumes any legal liability or responsibility for any third party’s use, or the results of such use, of any information, apparatus, product, or process disclosed in this report, or represents that its use by such third party would not infringe privately owned rights. The views expressed in this paper are not necessarily those of the U.S. Nuclear Regulatory Commission. I thank the Nuclear Regulatory Commission for supporting this work, and Christine Goulet for her stellar management of the project; without her timely persistence and appeals to my ego, it is unlikely that I would have done any of the work described herein. I also thank Rasool Anooshehpour, Eric Thompson, and Brad Aagaard for their useful comments on the paper.

2.7 LIST OF ELECTRONIC APPENDICES FOR CHAPTER 2

- 2A Sample Input file for SMSIM (PDF document)
- 2B Model Output for A04 attenuation (Excel workbook)
- 2C Model Output for AB14 attenuation (Excel workbook)
- 2D Model Output for AB95 attenuation (Excel workbook)
- 2E Model Output for BCA10D attenuation (Excel workbook)
- 2F Model Output for BS11 attenuation (Excel workbook)
- 2G Model Output for SGD02attenuation (Excel workbook)

3 Development of Hard Rock Ground-Motion Models for Region 2 of Central and Eastern North America

Robert B. Darragh

**Pacific Engineering and Analysis
El Cerrito, California**

Norman A. Abrahamson

**Pacific Gas & Electric Company
San Francisco, California**

Walter J. Silva

**Pacific Engineering and Analysis
El Cerrito, California**

Nick Gregor

**Bechtel, Inc.
San Francisco, California**

Abstract

Due to the low rates of seismicity, a significant and currently unresolvable issue exists in the estimation of strong ground motions for specified magnitude, distance, and site conditions in Central and Eastern North America (CENA). The preferred approach to estimating design ground motions is through the use of empirical attenuation relations, perhaps augmented with a model-based relation to capture regional influences, beyond the range of available data. In this chapter, we summarize the features of four proposed ground-motion models (GMMs) based on the point-source stochastic simulation method. The methodology essentially consists in three steps. Step one involves the inversion of recorded data using selected assumptions for a subset of point-source (PS) parameters. The second step consists in generating simulations beyond the magnitude and distance range covered by the empirical data. The last step is the parameterization of the simulations into ground-motion prediction equations (GMPEs). The four models are

grouped into single- and double-corner PS models (1C or 2C), each group including a version with the stress parameter that is either constant or variable as a function of magnitude (CSP or VSP). The models are developed for peak ground acceleration and peak particle velocity (PGA and PGV), and 5%-damped pseudo-spectral acceleration (PSA) for a wide range of frequencies from event to events with $M_{4.5-8.5}$ at distances up to 1000 km.

3.1 BACKGROUND

Due to the low rates of seismicity, a significant and currently unresolvable issue exists in the estimation of strong ground motions for specified magnitude, distance, and site conditions in Central and Eastern North America (CENA). The preferred approach to estimating design ground motions is through the use of empirical attenuation relations, perhaps augmented with a model-based relation to capture regional influences. For Western North America (WNA), particularly California, seismicity rates are such that sufficient strong-motion recordings are available for ranges in magnitudes and distances to properly constrain regression analyses. Naturally, not enough recorded data are available at close distances (≤ 10 km) to large magnitude earthquakes ($M \geq 6 \frac{3}{4}$) so large uncertainty exists for these design conditions but, in general, ground motions are reasonably well defined. For CENA however, very few data exist and nearly all are for $M \leq 5.8$ and distances exceeding about 50 km. Although this is a fortunate circumstance in terms of hazard, the potential exists for large, though infrequent, earthquakes in certain areas of CENA, and the actual risk to life and structures is comparable to that which exists in seismically active WNA. As a result, the need to characterize strong ground motions is significant and considerable effort has been directed to developing appropriate ground-motion models (GMMs) for CENA conditions [Boore and Atkinson 1987; Toro and McGuire 1987; EPRI 1993; Toro et al. 1997; Atkinson and Boore 1997; Silva et al. 2003; and Atkinson 2012a]. Because the strong-motion dataset is sparse in CENA, numerical simulations represent the only available approach, and the stochastic PS model (see Appendix 3A) has generally been the preferred model used to develop attenuation relations. The process involves repeatedly exercising the model for a range in magnitude and distance as well as expected parameter values, adopting a functional form for a regression equation, and finally performing regression analyses to determine coefficients for median predictions as well as variability about the median. Essential elements in this process include: (1) a physically realistic, reasonably robust, and well-validated model [Silva et al. 1996; Schneider et al. 1993]; (2) appropriate parameter values and their distributions; and (3) a statistically stable estimate of model variability (Appendix 3A). The model variability is added to the variability resulting from the regression analyses (parametric plus regression variability) to represent the total variability associated with median estimates of ground motions; see Appendix 3A.

3.2 MODEL PARAMETERS

For the PS model implemented here, parameters include stress drop or stress parameter ($\Delta\sigma$), source depth (H), path damping $\left[Q(f) = Q_0 f^n\right]$, shallow crustal damping (κ), and crustal amplification. The PS model parameters were based on inversions of Fourier amplitude spectra (FAS) computed from recordings within Region 2. To the extent permitted by the distribution of

M , distance, and site conditions, model parameters $\Delta\sigma$ (bars), $Q(f)$, $G(R)$, and κ were based on the inversions. The inversions included 53 earthquakes [10 potentially-induced events (PIES)] at 241 different sites for a total of 1133 recordings spanning the hypocentral distance range of about 10 km to 1000 km. The inversion dataset is listed in Table 3.1. To model crustal amplification, the mid-continental crustal model [EPRI 1993] was updated to be consistent with the CENA model and is listed in Table 3.2. To sample as wide a geographical area as possible within Region 2, the full range in site conditions was included using the PEER specified \bar{V}_s (30 m) values for each recording site. To provide analytical amplification factors, recording sites were grouped into NEHRP categories using single within-bin elastic amplification factors for each category. The distributions of sites in terms of NEHRP site category and hypocentral distance are given in Table 3.1.

Table 3.1a Natural earthquakes used in inversions.

EQ I.D.	Mag	Hypo Depth (km)	Stress Parameter (bars)	N	No. in NEHRP class					No. in the distance range (km)				EQ Name
					A	B	C	D	E	0 to 50	50 to 100	100 to 250	>250	
5	5.81	21.47	.120248E+03	19	12	3	4	0	0	0	7	8	4	Saguenay
6	3.27	7.5	.479283E+01	5	5	0	0	0	0	5	0	0	0	La Malbaie, QC
7	4.29	5.0	.149995E+02	6	6	0	0	0	0	5	1	0	0	La Malbaie, QC
8	4.46	22.0	.960367E+02	7	7	0	0	0	0	1	1	5	0	Cap-Rouge, QC
9	4.44	20.0	.445649E+02	5	5	0	0	0	0	0	0	0	5	CoteNord, QC
10	4.63	13.0	.280121E+02	3	3	0	0	0	0	0	0	1	2	Kipawa QC
11	3.29	11.4	.298068E+02	6	6	0	0	0	0	5	1	0	0	La Malbaie, QC
12	3.65	18.0	.393395E+02	8	7	0	1	0	0	1	6	1	0	Laurentide, QC
13	3.11	18.0	.200520E+02	6	6	0	0	0	0	0	5	1	0	Laurentide, QC
16	5.00	5.0	.500944E+02	19	5	7	4	3	0	0	2	8	9	Au Sable Forks, NY
17	3.78	2.0	.222921E+02	8	8	0	0	0	0	0	0	0	8	Lac Laratelle, QC
18	4.55	17.0	.898737E+02	7	0	4	2	1	0	0	0	1	6	Caborn, IN
24	3.56	11.1	.220950E+02	23	12	5	4	2	0	7	1	0	15	La Malbaie, QC
25	3.82	18.0	.437482E+02	35	17	7	8	2	0	0	0	8	26	Bark Lake, QC
28	2.87	22.0	.156672E+02	6	6	0	0	0	0	0	6	0	0	La Baie, QC
29	3.10	4.0	.360408E+02	33	8	11	10	4	0	0	0	1	32	Prairie Center, IL
30	3.10	4.0	.275646E+02	28	8	10	7	3	0	1	3	15	9	Port Hope, ON
32	4.60	12.3	.844457E+02	43	23	9	10	1	0	11	4	2	26	Riviere Du Loop, QC
35	3.75	16.0	.499614E+02	46	20	14	7	5	0	5	1	12	28	Thurso, ON
36	2.59	18.0	.154505E+02	16	7	4	4	1	0	1	3	7	5	Hawkesbury, ON
37	3.77	25.0	.184712E+02	36	21	7	6	2	0	7	4	0	25	Baie Saint Paul
44	2.80	5.0	.773180E+01	26	7	8	8	3	0	3	5	11	7	Cobourg, ON
45	2.77	13.5	.552924E+02	8	8	0	0	0	0	5	2	1	0	Baie Saint Paul
46	5.27	14.0	.452120E+02	16	0	4	8	4	0	3	3	9	1	Mt Carmel, IL
47	4.64	14.0	.922446E+02	14	0	3	8	3	0	2	3	8	1	Mt Carmel, IL AS
48	4.03	15.0	.744346E+02	14	0	3	8	3	0	2	3	8	1	Mt Carmel, IL AS
49	3.75	13.0	.874276E+02	13	0	3	7	1	0	2	3	6	2	Mt Carmel, IL AS
50	2.97	18.0	.537396E+01	24	7	7	6	3	1	3	0	6	15	Buckingham, QC

EQ I.D.	Mag	Hypo Depth (km)	Stress Parameter (bars)	N	No. in NEHRP class					No. in the distance range (km)				EQ Name
					A	B	C	D	E	0 to 50	50 to 100	100 to 250	>250	
51	3.60	13.3	.222090E+02	32	17	7	5	2	1	4	2	1	25	Riviere Du Loop, AS
55	2.57	26.1	.356591E+02	21	5	7	7	1	1	3	1	6	11	Constance Bay, ON
59	2.62	20.8	.268509E+01	5	0	1	2	2	0	4	1	0	0	Lebanon, IL
60	5.10	22.0	.833965E+02	52	21	8	19	3	1	0	8	11	33	Val-des-Bois
61	3.51	13.0	.172812E+02	22	8	6	6	2	0	0	0	4	18	St. Flavien, QC
63	4.48	11.0	.895439E+02	8	5	2	1	0	0	0	0	3	5	Mont Lauier, QC
75	3.85	14.0	.374737E+02	31	4	7	16	4	0	0	0	4	27	Greentown, IN
81	3.89	27.0	.235651E+02	38	1	11	19	7	0	1	3	23	11	Sullivan, MO
85	3.63	7.0	.350954E+02	46	19	11	13	3	1	1	4	5	36	Hawkesbury, ON
86	3.60	11.4	.278455E+01	8	8	0	0	0	0	7	1	0	0	Charlevoix
87	3.24	13.3	.351055E+02	16	8	3	3	2	0	4	3	0	9	Baie Saint Paul
116	4.19	28.0	.766712E+01	6	6	0	0	0	0	0	2	4	0	Saguenay, FS
117	3.50	30.0	.577445E+01	6	6	0	0	0	0	0	0	6	0	Saguenay, AS
83	2.57	16.7	*	36	14	12	9	1	0	8	2	7	19	Val-des-Bois, AS
84	2.37	19.9	*	24	9	11	2	1	1	8	1	8	7	Val-des-Bois, AS

* Unresolved corner frequency fixed at 20 Hz, beyond bandwidth

Table 3.1b Potentially-induced earthquakes (PIEs) used in inversions.

EQ I.D.	Mag	HypoDepth (km)	Stress Parameter (bars)	N	No. in NEHRP class					No. in the distance range (km)				EQ Name
					A	B	C	D	E	0 to 50	50 to 100	100 to 250	>250	
56	3.84	8.0	.587968E+01	22	1	1	19	1	0	1	3	18	0	Jones, OK PIE
57	4.18	4.0	.959584E+01	23	0	2	20	1	0	4	5	12	2	Lincoln, OK PIE
66	4.36	14.0	.346318E+02	52	1	6	42	4	0	10	6	32	4	Slaughterville, OK, PIE
67	3.86	5.0	.112731E+02	10	0	3	7	0	0	2	1	7	0	Guy, AR, PIE
73	3.96	3.0	.594909E+01	47	1	5	39	2	0	9	5	33	0	Arcadia, OK, PIE
74	3.23	4.0	.544403A+01	44	1	6	35	2	0	9	3	32	0	Bethel Acres, OK, PIE
76	3.90	5.0	.701690E+01	12	0	4	7	1	0	3	1	7	1	Guy, AR, PIE
80	4.68	4.0	.152482E+02	25	0	12	9	3	0	3	3	14	5	Greenbrier, AR, PIE
90	4.73	3.0	.175376E+02	43	1	9	32	1	0	3	5	21	14	Sparks, OK, PIE
91	5.68	8.0	.201170E+02	24	1	5	17	1	0	4	1	15	4	Sparks, OK, PIE

Table 3.2 Central North America

Thickness (km)	V_S (km/sec)	Density (g/cm ³)
1.0	3.00	2.52
11.0	3.52	2.71
28.0	3.80	2.78
-----	4.68	3.35

Category specific shear-wave velocity profiles were based on \overline{V}_s (30 m) taken at 2032 m/sec, 1170 m/sec, 560 m/sec, 270 m/sec, and 180 m/sec for NEHRP site categories A, B, C, D, and E, respectively [Kamai et al. 2013], and reflect a WNA crustal structure. For application to CENA, the profiles were placed on top of the hard rock crustal model (Table 3.2), with the implicit assumption that the deep soils and soft-to-firm rock conditions for WNA and CENA reflect generally similar dynamic material properties at low loading levels. While the relative distributions of material types and ages may be somewhat different, e.g., more till and loess soils in CENA compared to WNA, similarity in deep soil and soft-to-firm rock implies generally similar overall category specific amplification, at least for the current application. The profiles are shown in Figure 3.1 to a depth of 500 ft, with the resulting elastic amplification factors shown in Figure 3.2. See Appendix 3B for a summary of the site response approach.

Results of initial inversions suggested a simple bilinear model for geometrical attenuation may adequately capture the distribution of residuals with distance. The final bilinear model has a simple $1/R$ geometrical attenuation with a transition to $1/\sqrt{R}$ beyond 50 km (R_0), where R is hypocentral distance. Geometrical attenuation of FAS was previously found to have a weak magnitude dependence [Silva et al. 1996; Silva et al. 2003]. The magnitude dependence was based on inversions of FAS developed by spectrally matching response spectra (5% damped) at suites of \mathbf{M} and distance from the Abrahamson and Silva [1997] empirical GMPE [Silva et al. 1996] using random vibration theory (RVT) [Boore 1983]. The magnitude dependency was updated using the same process applied to the NGA-West2 GMPEs. The model for the geometrical attenuation including magnitude dependency is given by

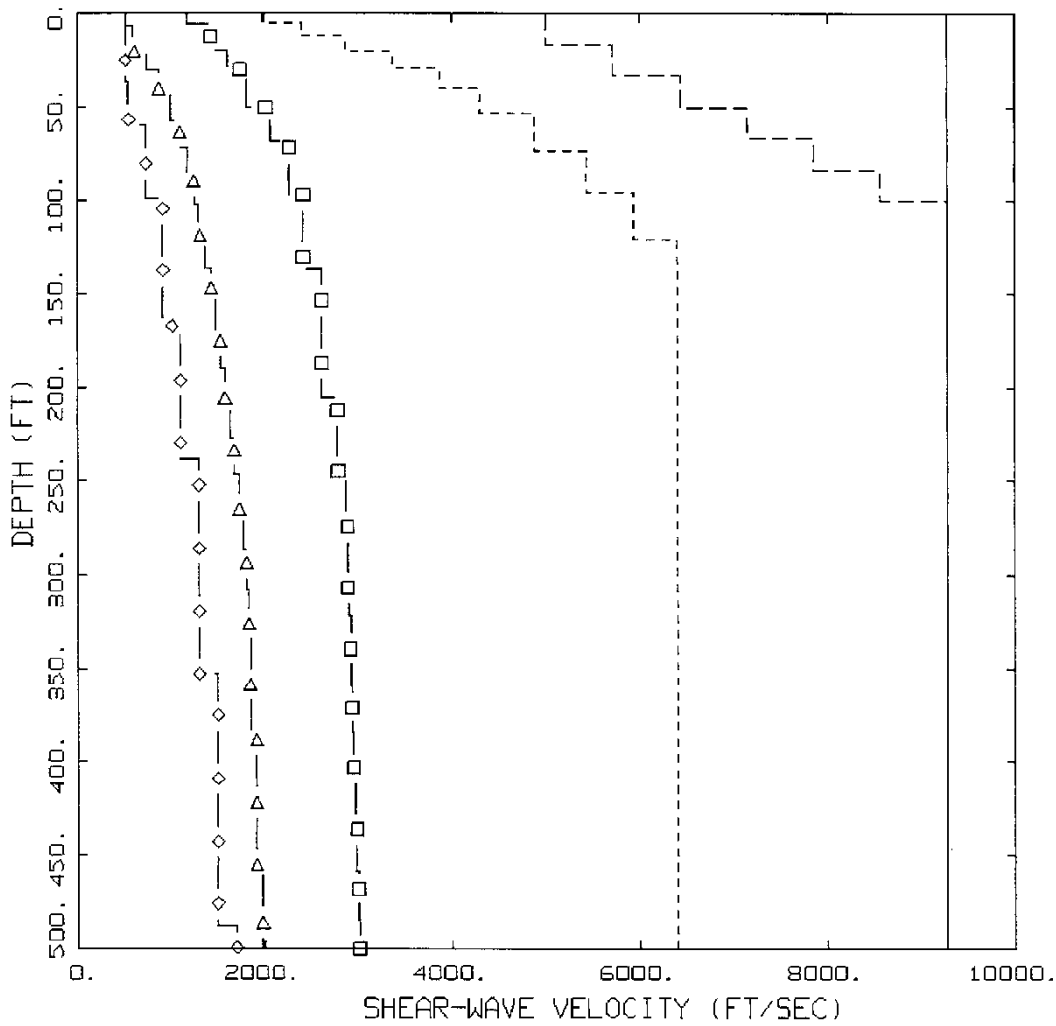
$$\begin{aligned} R^{-[a+b(\mathbf{M}-5.0)]}, & \quad R \leq 50 \text{ km} \\ R^{-[a+b(\mathbf{M}-5.0)]/2}, & \quad R > 50 \text{ km} \end{aligned} \tag{3.1}$$

with $a = 1.0$ based on FAS inversions of Region 2 recordings and $b = -0.03$ based on the NGA-West2 FAS inversions.

For the final inversion, residuals verses distance to 1000 km are shown in Figure 3.3, with the associated stress parameters listed in Table 3.1. Fixed parameters for the inversion include geometrical attenuation [Equation (3.1)] and fixed frequency dependence of $Q(f)$ at 0.5 (Section 3.2.4). Inversion parameters were stress parameter, Q_0 at 629.0, and κ estimates for NEHRP categories A, B, C, D, and E at 0.005 sec, 0.005 sec, 0.013 sec, 0.011 sec, and 0.002 sec, respectively. The NEHRP category E κ estimate reflects a single site and is not considered reliable. Note that the NEHRP category C and D sites, soft rock to firm soil, have unexpectedly low κ estimates. This may reflect relatively shallow soft rock and till sites as well as shallow soils representative of the glaciated region of North America, as few sites are located within the Michigan and Ohio basins or at deep soil locations in Canada.

Overall the distributions of residuals are considered acceptable across site condition and frequency, as well as with distance for a very simple model. The distribution of residuals spanning the frequency range of 0.5 Hz to 20.0 Hz also suggest the NEHRP category

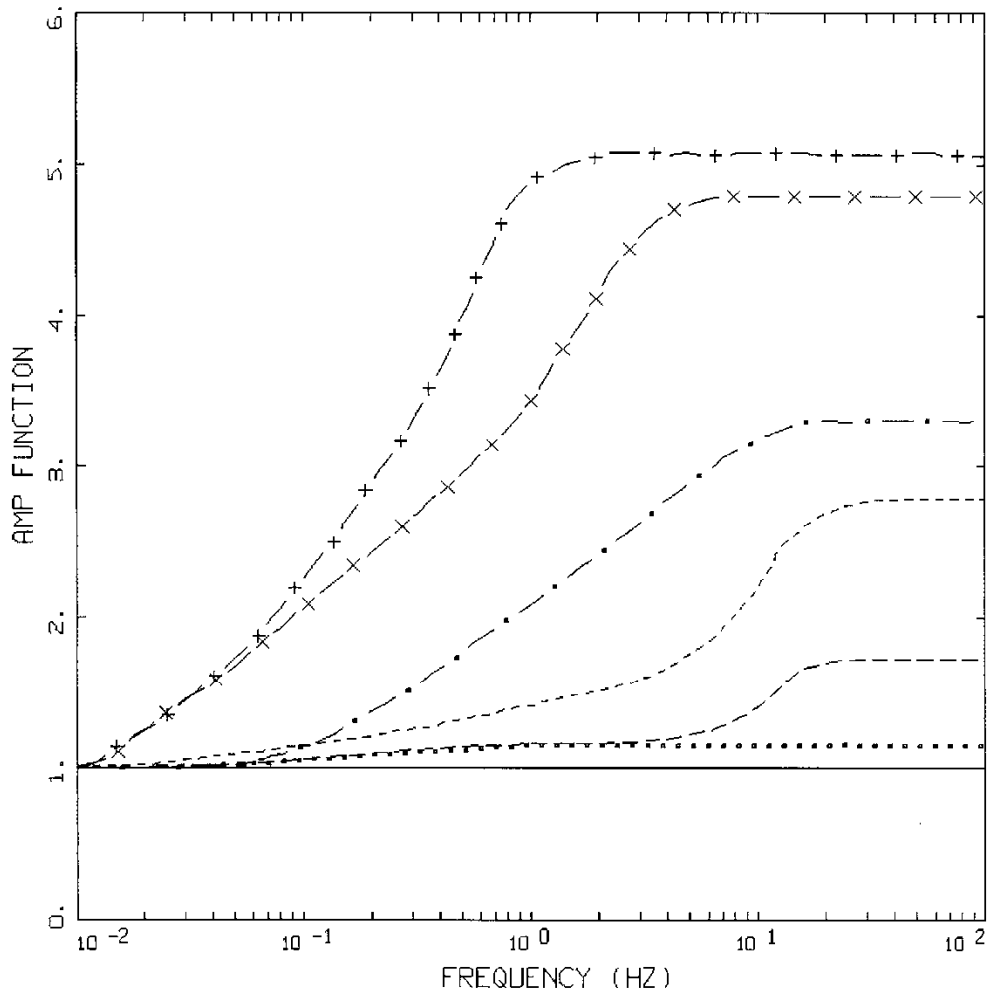
amplification factors reflect little bias across frequency, and the \bar{V}_s (30 m) assignments are sufficiently accurate at least for the binning used here.



CENA SHEAR WAVE PROFILES

- LEGEND
- 3,000 M/SEC, NEHRP A, HARD ROCK
 - 2,032 M/SEC, NEHRP A
 - 1,170 M/SEC, NEHRP B
 - 560 M/SEC, NEHRP C
 - △— 270 M/SEC, NEHRP D
 - ◇— 180 M/SEC, NEHRP E

Figure 3.1 NEHRP category specific shear-wave velocity profiles a depth of plotted to 500 ft. Profile B reaches hard rock (Table 3.2) at an assumed depth of about 1500 ft, while profiles C, D, and E reach hard rock (Table 3.2) at an assumed depth of about 4000 ft.



AMPLIFICATION FACTORS

- LEGEND
- 3,000 M/S, NEHRP A, HARD ROCK
 - 2,032 M/S, NEHRP A
 - 1,170 M/S, NEHRP B
 - . - 560 M/S, NEHRP C
 - x - 270 M/S, NEHRP D
 - + - 180 M/S, NEHRP E
 - _____ UNITY

Figure 3.2 Linear elastic amplification factors (FAS) developed for NEHRP site categories A, B, C, D, and E (Figure 3.1).

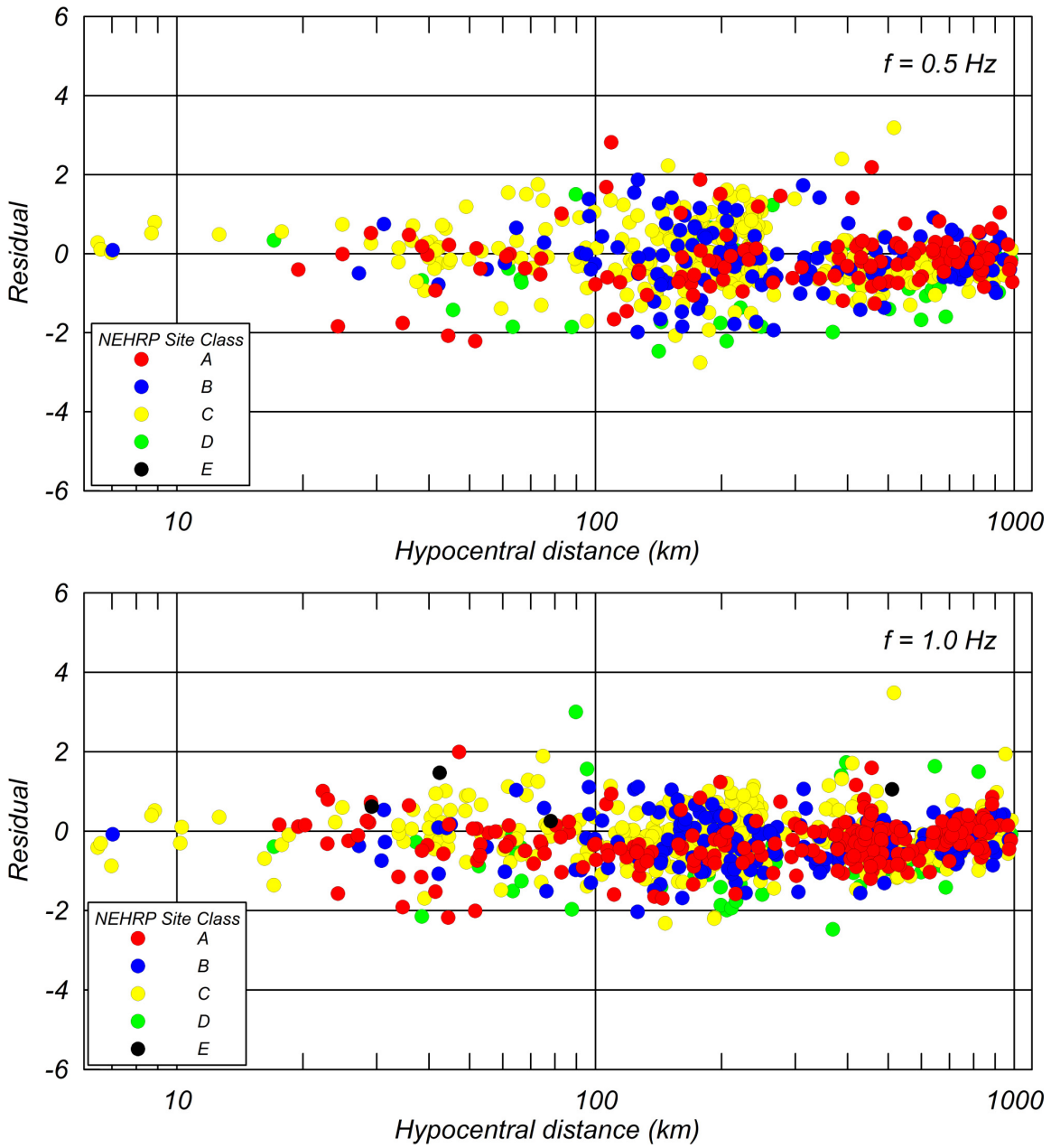


Figure 3.3 Residuals versus distance for the five NEHRP site categories and Region 2 earthquakes listed in Table 3.1: 0.5 Hz, 1.0 Hz, 2.0 Hz, 5.0 Hz, 10.0 Hz, 15.0 Hz, and 20.0 Hz.

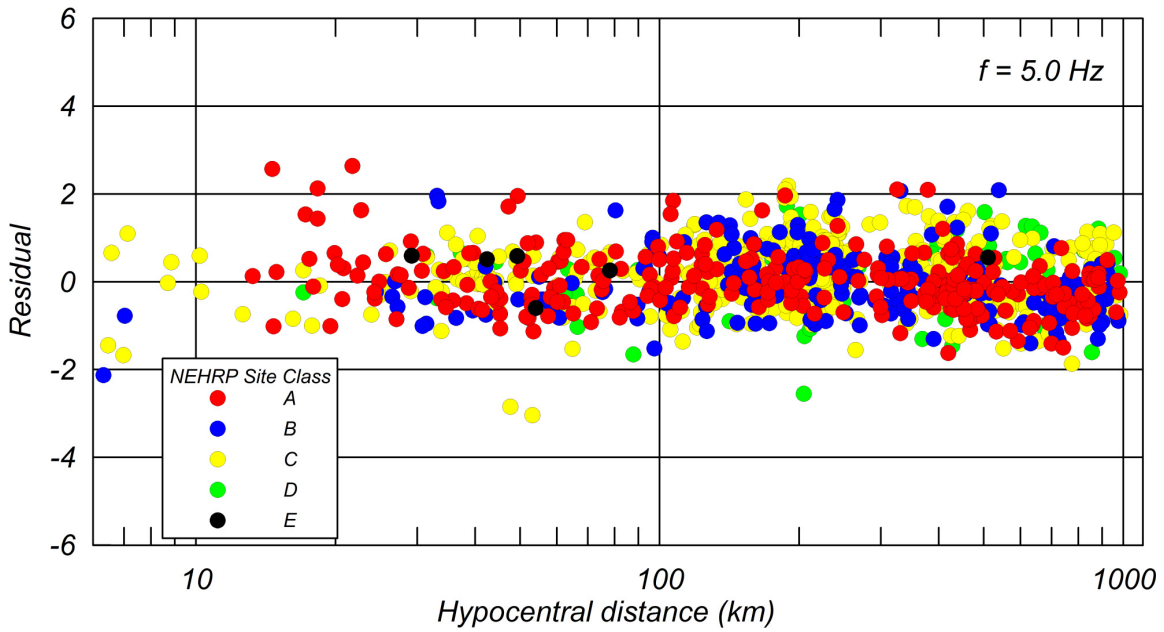
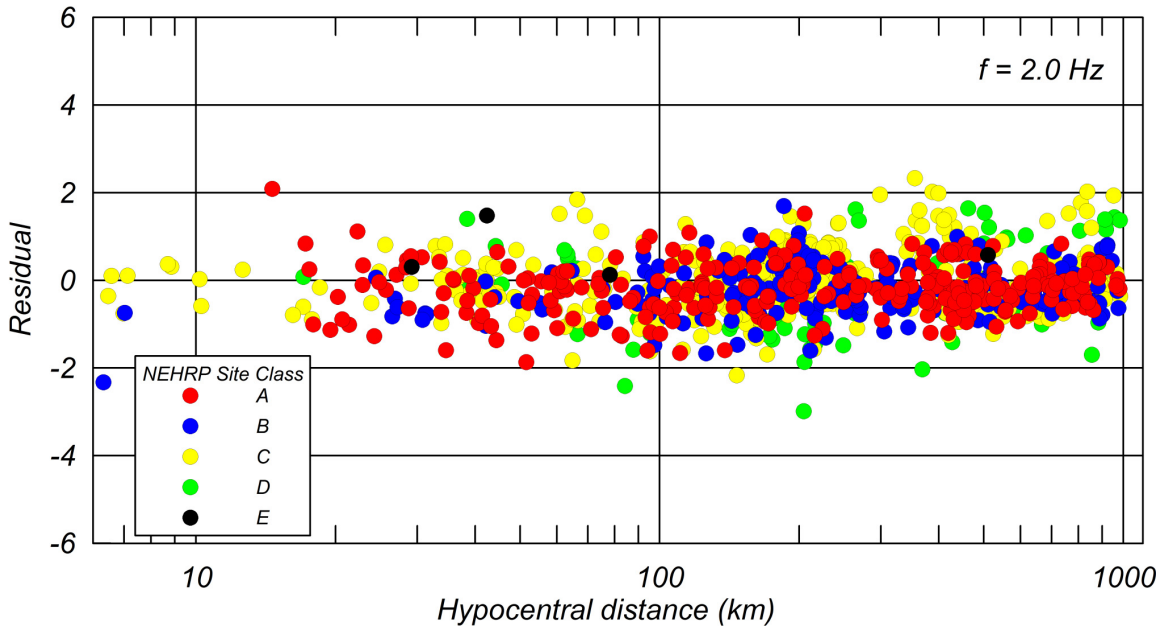


Figure 3.3 Continued.

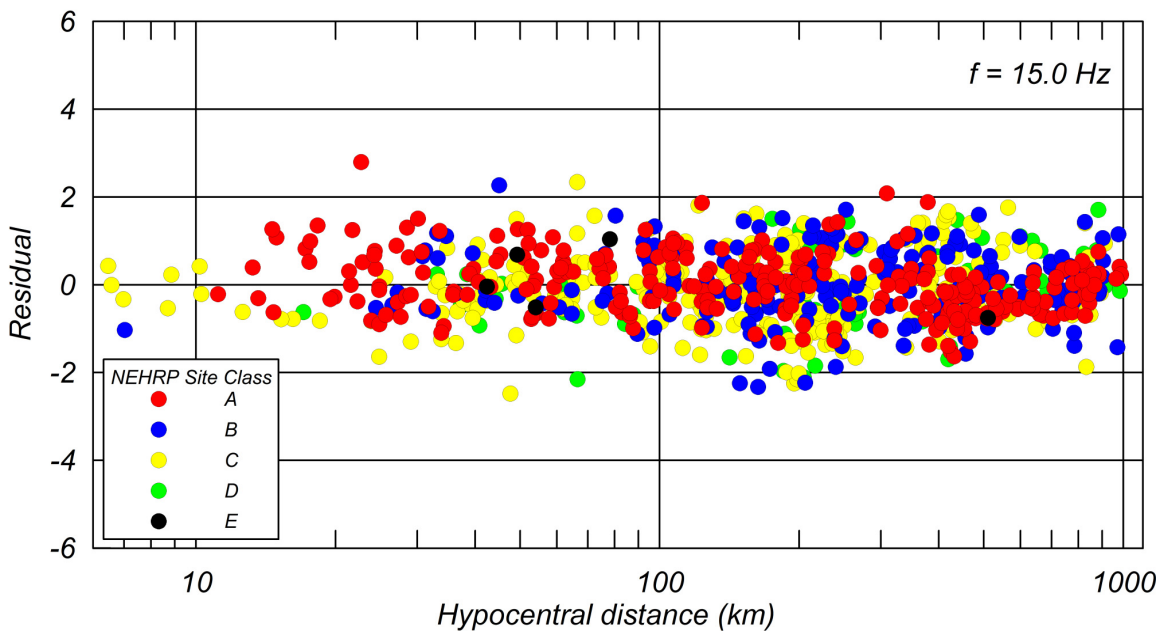
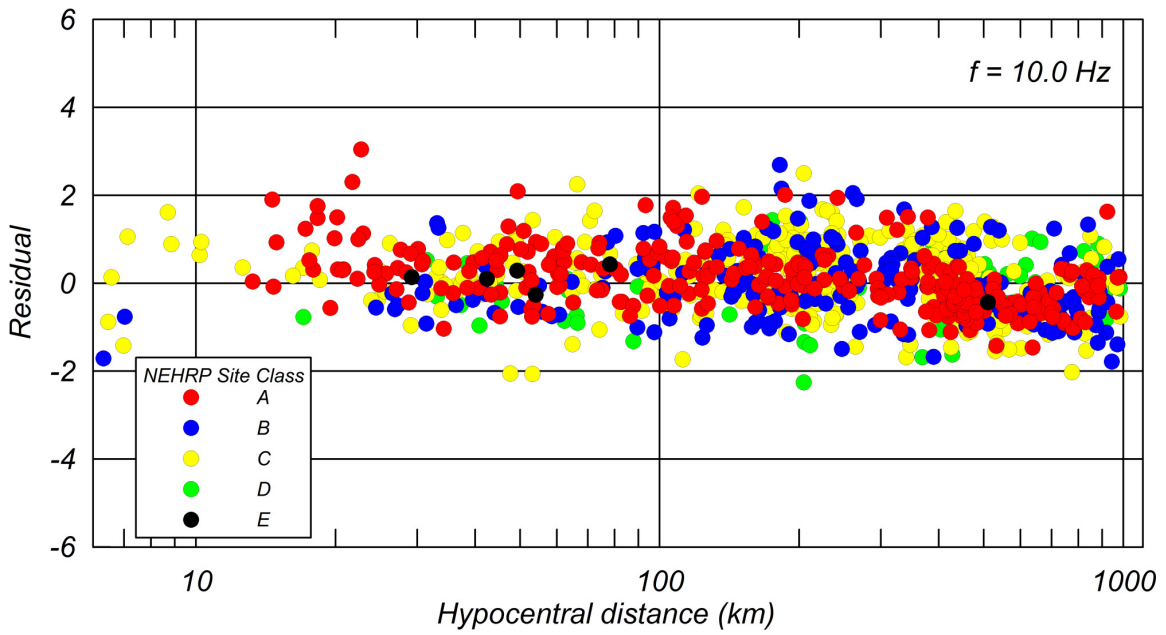


Figure 3.3 Continued.

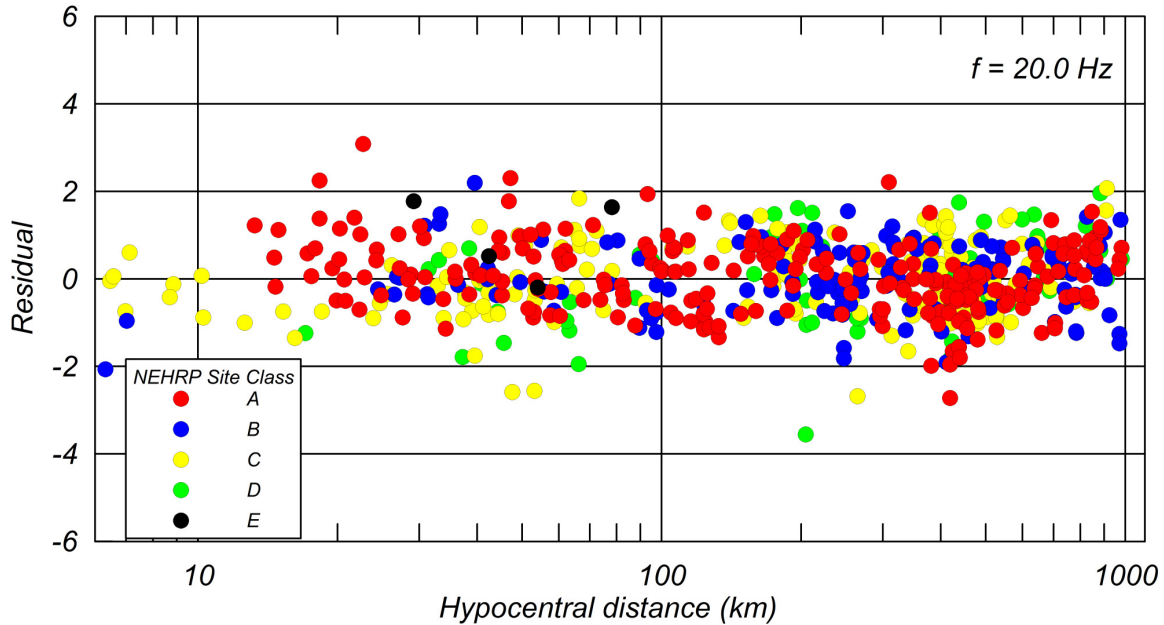


Figure 3.3 Continued.

3.2.1 Magnitude Saturation

Beginning at small magnitude, for a fixed increase in magnitude, ground motions naturally increase, but observationally the rate of increase reduces significantly at the larger magnitudes. To accommodate for uncertainty in the causative mechanism, saturation is modeled in two distinct ways: (1) variable stress parameter, decreasing with increasing magnitude; or, separately, (2) inclusion of a constant stress parameter with an additional (fictitious) depth term that increases with magnitude [Silva et al. 2003]. In principal, these artifices are necessary to accommodate a shortcoming in the PS model, as saturation is generally considered an effect of source finiteness due to an extended rupture surface. However, as noted in Silva et al. [1996] and now accommodated in NGA-West-1 and -2 GMPEs in source depth terms, larger magnitude sources tend to have more shallow slip, resulting in lower motions, especially at higher frequencies, suggesting lower stress parameters. The variable stress parameter model was intended to capture such trends within the simplicity of the point-source model. Based on inversions of FAS determined from the NGA-West2 empirical GMPEs, models for a variable stress parameter and fictional depth were developed. The point-source inversions used a suite of magnitudes ($M4.5$, 5.5 , 6.5 , and 7.5) as well as rupture distances (1, 5, 10, 20, 50, 100, and 200 km). To maintain linearity in site response, rock site conditions were used with \bar{V}_s (30 m) values as low as 550 m/sec to ensure the GMPEs were reasonably well constrained. The resulting stress parameters showed, as previously [Silva et al. 2003], a strong monotonic decreasing magnitude dependence at $M5.5$ and above, but with the updated GMPEs extending to $M4.5$, the inversions showed a clear break in scaling below $M5.5$. The stress parameter for $M5.5$ was 53 bars with that of $M4.5$ about a factor of two lower at 26 bars. Above $M5.5$, the decrease in stress parameter with increasing magnitude was about a factor of two for a unit increase in magnitude, as shown in Table 3.3. The magnitude dependence may be expressed as

$$\ln \Delta \sigma_w = 6.83 - 0.52M \quad (3.2)$$

Assuming the WNA magnitude scaling of stress parameter is appropriate for CENA earthquake source processes, the mean stress parameter for CENA Region 2 earthquakes in the **M4.5** magnitude range was used to scale the WNA stress parameters using the ratio at **M4.5**. The mean stress parameter was used to provide PS estimates of mean power spectra, consistent with the use of RVT to provide estimates of peak time domain ground motions [Ou and Herrmann 1990]. Considering the stress parameters for natural earthquakes in the magnitude range of **M4.0** to **M5.0** (Table 3.1a), the mean magnitude was **M4.41** and the estimate for the mean stress parameter was 59.9 bars (taken as 60 bars). The distribution of stress parameters with magnitude is shown on Figure 3.4. For WNA the stress parameter for **M4.5** was 26 bars (Table 3.3), suggesting a factor of about 2 between WNA and CENA, which may be parameterized by

$$\ln \Delta \sigma_E = 7.64 - 0.52M \quad (3.3)$$

The magnitude dependencies (Equations 3.2 and 3.3) are considered appropriate for **M** ranging from **M 5.5** to **M 8.5**.

Table 3.3 Inversions of NGA-West2 GMPES for stress parameter.

M	Stress parameter (bars)
4.5	26
5.5	53
6.5	35
7.5	19
8.5	11*

*Extrapolated using $\ln \Delta \sigma = 6.83 - 0.52M$

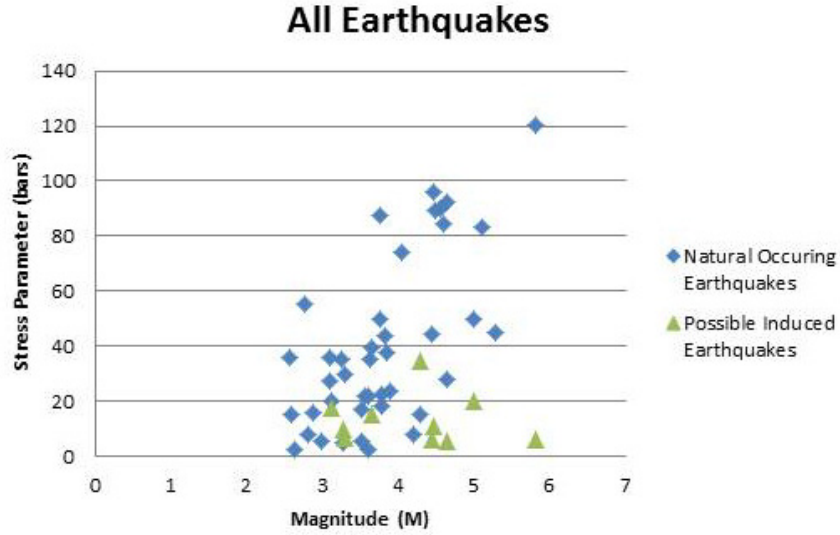


Figure 3.4 Region 2 stress parameter verses magnitude.

For the constant stress parameter model, the mean stress parameter for **M5.5** and above was taken as 120 bars, thus preserving the break in scaling near **M5** with a factor-of-two increase in stress parameter between **M4.5** and **M5.5** and above. This jump in stress parameter at **M5.5** preserves the observed **M4.5** stress parameter of 60 bars and a constant stress parameter from **M5.5** to **M8.5**. The resulting 120 bar stress parameter above **M5.5** exceeds the mean CENA stress parameter of about 64 bars for **M5.5** and above, but it is compensated for at close-to-moderate Joyner–Boore distances by inclusions of the fictitious depth term [Silva et al. 2003; Yenier and Atkinson 2014]. Because the fictitious depth term is coupled to the magnitude-dependent geometrical attenuation term [Equation (3.1)] leading to non-unique inversion estimates, the model was developed by forcing the PS model to reflect magnitude scaling at peak acceleration to be similar to the NGA-West2 empirical GMPEs at close distance and above **M5.5**. The resulting model is described by

$$\ln h = -5 + \mathbf{M} \quad (3.4)$$

This model is similar to that of Yenier and Atkinson [2014] in natural logarithmic units:

$$\ln h = -4 + \mathbf{M} \quad (3.5)$$

Coupled with the magnitude-dependent geometrical attenuation [Equation (3.1)], the model of Yenier and Atkinson [2014] resulted in too much saturation above **M7.5**.

For the two-corner frequency manifestation of the PS model, the additive functional form and parameters of Atkinson and Boore [1995] was implemented. For consistency with the single-corner frequency model, the high-frequency levels were constrained to be equivalent to those of the single-corner frequency model [Boore et al. 2015] for both variable and constant stress parameter simulations.

3.2.2 Kappa

For kappa (κ), inversions of sites combined into NEHRP categories resulted in hard and firm rock site Categories A and B estimates of about 0.005 sec for each. Since these values were close to the typically adopted value of 0.006 sec, the latter was used in the simulations. Table 3.4 lists the PS parameters.

Table 3.4 Source and path parameters and standard errors used in the PS simulations.

Parameter(s)	Value	Standard Error σ_{In}	
Moment Magnitude (M)	4.5, 5.5, 6.5, 7.5, 8.5		
Epicentral Distance (km)	1, 5, 10, 20, 50, 75, 100, 200, 400, 700, 1000		
M	Magnitude-Independent Point-Source Depth (km)		
4.5	8 (2, 15) ^a	0.6	
5.5	8 (2, 15) ^a		
6.5	8 (2, 15) ^a		
7.5	8 (2, 15) ^a		
8.5	8 (2, 15) ^a		
M	Mean magnitude-dependent and independent stress parameter ^b (bars)		
4.5	60	60	0.5
5.5	120	120	
6.5	70	120	
7.5	40	120	
8.5	25	120	
Crustal Attenuation			
Q_0	630 ^c		0.4
η	0.50		-----
Near-Surface Crustal Damping			
κ (sec)	0.006		-----
Crustal Model			
Profiles	Central North America		Toro [1996] rock correlation model
Geometrical Attenuation			
Hypocentral Distance	$a = 1.00^c$		
$R^{-[a+b(M-5.0)]}, R \leq RC$	$b = -0.03^b$		
$R^{-[a+b(M-5.0)]}, R > RC$	$RC = 50 \text{ km}^c$		

a. (2, 15) Indicates lower- and upper-bound values, respectively.

b. Magnitude scaling based on inversions of the NGA GMPEs; Power et al. [2008], M 4.5 based on Region 2 non-PIE recordings (Table 3.1)

c. Based on Region 2 recordings

3.2.3 Duration

To provide estimates of duration in developing peak time domain estimates of PSA (5% damped), PGA and peak particle velocity (PGV) using RVT, in keeping with a simple geometrical attenuation model, duration was taken as the inverse of the corner-frequency. To this was added a simple distance term of 0.05 times the hypocentral distance [Herrmann 1985]. In this application the single- and double-corner source models had the same estimates of duration defined by the single-corner stress parameters and fixed source region shear-wave velocity of 3800 m/sec (Table 3.2).

3.2.4 $Q(f)$ and Source Depth

The $Q(f)$ model was taken as $630f^{0.5}$ with Q_0 based on the inversions and the frequency dependence constrained to 0.5 from Boatwright and Seekins [2011]. While initial inversions resulted in a similar value, 0.63, significant parameter coupling in this method existed between η and Q_0 . As a result, η was fixed at the Boatwright and Seekins [2011] value of 0.5, who found that a similar simple geometrical attenuation was consistent with the recordings they analyzed.

Source depths were randomized centered on 8 km, independent of magnitude, with a σ_{in} of 0.6 [EPRI 1993]. Upper and lower bounds on depths were set at 2 km and 15 km, respectively, and were independent of magnitude as well, recognizing that such shallow depths (e.g., 2 km) for large magnitude earthquakes may be unrealistic but in this case reflect shallow asperities.

3.2.5 Parameter Correlation

Finally it is important to point out, because all of the point-source parameters are correlated—some highly and some weakly—the suite of parameters are fundamentally relative to each other. As a result, none of the parameters may be taken separately as absolute values: the family must be kept together. The suite of point-source model parameters is summarized in Table 3.4.

3.3 DEVELOPMENT OF GROUND-MOTION MODEL

The functional form selected for the regressions is given by

$$\ln y = C_1 + C_2 \mathbf{M} + (C_6 + C_7 \mathbf{M}) \ln(R_{JB} + e^{C_4}) + C_{10} (\mathbf{M} - 6)^2 + C_8 R_{JB} \quad (3.6)$$

where R_{JB} is the closest distance to the surface projection of the rupture surface, consistent with the validation exercises [Silva et al. 1996]. The functional form does not contain a bilinear geometrical attenuation term [Equation (3.1)], rather the regressions were used to smooth through the change in slope of the simulated motions near R_{JB} of 50 km. A smooth trend in geometrical attenuation was considered to reflect an appropriate characterization of geometrical attenuation over a wide region, reflecting varying crustal structures that are not well sampled by recorded motions (see illustration in Figure 3.5).

Regression coefficients are listed in Tables 3.5a–3.5d for the single-corner variable stress parameter (1CVSP), single-corner constant stress parameter (1CCSP), double-corner variable stress parameter (2CVSP), and double-corner constant stress parameter (2CCSP) models, respectively, together with the corresponding parametric and total variabilities. Examples of the four models are illustrated in Figures 3.6–3.13 in terms of peak acceleration versus Joyner–Boore distance and PSA (5% damped) at a distance of 1 km. Figures 3.6–3.13 show results for the 1CVSP, 1CCSP, 2CVSP, and 2CCSP models respectively.

An example of the aleatory variability is shown in Figure 3.14 and is based on summing the variances associated with parameter variations (Table 3.4), single-corner frequency point-source modeling of past earthquakes (Appendix 3A), and regression fit. Since the two-corner frequency source model was not available when the validations were performed [Silva et al. 1996], the model variability for the single-corner frequency source model was used. This is considered conservative as the total aleatory variability for the two-corner model is likely to be lower than that of the single-corner model; comparisons using WUS data show it provides a better fit to recorded motions at low frequencies (≤ 1 Hz); see Atkinson and Silva [1997; 2000]. This is, of course, assuming the aleatory parametric variability associated with the two-corner frequencies is not significantly larger than that associated with the single-corner frequency model. At long periods (> 1 sec) the total variability is largely empirical, being driven by the modeling component or comparisons to recorded motions. The large long-period uncertainty is due to the tendency of the point-source model to over predict low-frequency motions at large magnitudes ($M > 6.5$) [EPRI 1993]. This trend led Atkinson and Silva [1997; 2000] to introduce a double-corner point-source model for WUS crustal sources, suggesting a similarity in source processes for WUS and CEUS crustal sources, but with CEUS sources being more energetic, on average, by about a factor of two (twice WUS stress parameters). Additionally, while this variability may be considered large, it includes about 17 earthquakes with magnitudes ranging from $M_{5.3}$ to 7.4, distances out to 500 km, and both rock and soil sites. The average M for the validation earthquakes is about 6.5, near the magnitude where empirical aleatory variability has a significant reduction. The magnitude-independent PS variability may then reflect the generally higher variability associated with lower magnitude ($M \leq 6.5$) earthquakes, over-estimating aleatory variability for larger magnitude earthquakes. Additionally, the model variability at long periods is not well constrained due to bandwidth limitations with the value at 1 sec used for longer periods. For PGV, the variability for PSA at 1 Hz is recommended.

3.4 ACKNOWLEDGMENTS

We wish to acknowledge the assistance and sound technical advice given to us by Christine Goulet, Tadahiro Kishida, and Justin Hollenback. Support from and data supplied by PEER is gratefully acknowledged.

Table 3.5a Central North America regression coefficients for the single-corner model with variable medium stress parameter (1CVSP) as a function of moment magnitude (**M**).

Freq. Hz	C_1	C_2	C_4	C_5	C_6	C_7	C_8	C_{10}	Parametric	Total
									σ	σ
0.1	-20.70170	2.64538	1.60	.00000	-0.85386	0.02092	-0.00023	-0.38364	0.3196	1.3150
0.133	-19.30977	2.53810	1.60	.00000	-0.86799	0.02244	-0.00034	-0.41943	0.3243	1.3031
0.2	-17.01765	2.32837	1.70	.00000	-0.93219	0.02833	-0.00047	-0.44801	0.3412	1.1859
0.25	-15.73256	2.19970	1.70	.00000	-0.96422	0.03205	-0.00056	-0.45339	0.3590	1.1112
0.333	-13.89546	2.01650	1.80	.00000	-1.03622	0.03823	-0.00063	-0.44922	0.3957	1.0458
0.5	-11.26706	1.73920	1.90	.00000	-1.14531	0.04845	-0.00073	-0.42325	0.4573	0.9777
0.667	-9.59010	1.54206	1.90	.00000	-1.20890	0.05576	-0.00086	-0.39430	0.4675	0.8800
1.0	-7.33709	1.26868	1.90	.00000	-1.32346	0.06678	-0.00095	-0.34391	0.5214	0.8432
1.333	-5.83157	1.09737	1.90	.00000	-1.40241	0.07373	-0.00102	-0.30599	0.5589	0.8647
2.0	-4.09245	0.88722	2.00	.00000	-1.50436	0.08564	-0.00134	-0.26170	0.5569	0.8112
2.5	-3.46576	0.79958	1.90	.00000	-1.54090	0.09067	-0.00147	-0.24159	0.5743	0.8055
3.333	-2.27943	0.67456	2.10	.00000	-1.66666	0.10278	-0.00168	-0.22071	0.6090	0.8252
4.167	-1.68615	0.61083	2.10	.00000	-1.72606	0.10891	-0.00182	-0.20919	0.6278	0.8266
5.0	-1.27961	0.57066	2.10	.00000	-1.75957	0.11297	-0.00200	-0.20216	0.6636	0.8436
6.667	-0.43074	0.49884	2.20	.00000	-1.88995	0.12337	-0.00206	-0.19533	0.6844	0.8544
10.0	0.81886	0.40572	2.40	.00000	-2.09616	0.13905	-0.00215	-0.19106	0.6931	0.8545
13.333	1.66658	0.35160	2.50	.00000	-2.25798	0.14913	-0.00207	-0.19038	0.6881	0.8424
20.0	3.06366	0.26819	2.70	.00000	-2.53997	0.16495	-0.00178	-0.19095	0.6845	0.8413
25.	3.79191	0.22335	2.80	.00000	-2.69737	0.17359	-0.00155	-0.19172	0.6805	0.8355
34.0	4.67247	0.17652	2.90	.00000	-2.88566	0.18254	-0.00124	-0.19270	0.6644	0.8188
40.0	4.86888	0.16674	2.90	.00000	-2.94101	0.18475	-0.00109	-0.19325	0.6550	0.8086
50.0	4.43661	0.18214	2.80	.00000	-2.89516	0.18320	-0.00101	-0.19443	0.6419	0.7996
100,0	1.89577	0.26924	2.50	.00000	-2.50321	0.17152	-0.00121	-0.19894	0.6202	0.7827
PGA	1.62570	0.28192	2.50	.00000	-2.46237	0.16942	-0.00120	-0.19953	0.6160	0.7793
PGV	1.19632	0.79454	2.20	.00000	-2.21916	0.17493	-0.00041	-0.24587	0.4437	-----

Table 3.5b Central North America regression coefficients for the single-corner model with constant medium stress parameter (1CCSP) as a function of moment magnitude (**M**).

Freq. Hz	C_1	C_2	C_4	C_5	C_6	C_7	C_8	C_{10}	Parametric	Total
									σ	σ
0.1	-20.06107	2.50246	1.80	.00000	-1.13010	0.08057	-0.00055	-0.32349	0.3039	1.3113
0.133	-18.66299	2.41186	1.90	.00000	-1.16052	0.08208	-0.00063	-0.36373	0.3119	1.3000
0.2	-16.58806	2.23360	1.90	.00000	-1.19869	0.08625	-0.00080	-0.40189	0.3274	1.1820
0.25	-15.22512	2.11094	2.00	.00000	-1.25398	0.09062	-0.00085	-0.41303	0.3423	1.1059
0.333	-13.39925	1.93667	2.10	.00000	-1.33056	0.09702	-0.00091	-0.41576	0.3745	1.0380
0.5	-10.92487	1.67642	2.10	.00000	-1.41670	0.10615	-0.00105	-0.39729	0.4311	0.9658
0.667	-9.08872	1.47527	2.20	.00000	-1.51519	0.11500	-0.00112	-0.37210	0.4384	0.8649
1.0	-7.00883	1.21785	2.10	.00000	-1.60080	0.12434	-0.00126	-0.32552	0.4924	0.8256
1.333	-5.67931	1.05981	2.00	.00000	-1.64755	0.12953	-0.00137	-0.28936	0.5308	0.8468
2.0	-3.92569	0.84817	2.10	.00000	-1.75261	0.14192	-0.00170	-0.24602	0.5332	0.7952
2.5	-3.12602	0.75319	2.10	.00000	-1.82434	0.14839	-0.00177	-0.22649	0.5515	0.7894
3.333	-2.09571	0.63331	2.20	.00000	-1.91756	0.15954	-0.00204	-0.20556	0.5886	0.8103
4.167	-1.50171	0.57010	2.20	.00000	-1.97730	0.16564	-0.00219	-0.19419	0.6077	0.8114
5.0	-0.85507	0.51403	2.30	.00000	-2.05632	0.17230	-0.00229	-0.18721	0.6448	0.8289
6.667	-0.21847	0.45405	2.30	.00000	-2.14517	0.18072	-0.00243	-0.18035	0.6674	0.8408
10.0	1.41516	0.32933	2.60	.00000	-2.41950	0.20126	-0.00244	-0.17581	0.6784	0.8426
13.333	2.34381	0.26746	2.70	.00000	-2.59432	0.21244	-0.00235	-0.17499	0.6738	0.8308
20.0	3.90932	0.16773	2.90	.00000	-2.90264	0.23054	-0.00204	-0.17525	0.6712	0.8305
25.0	4.73824	0.11380	3.00	.00000	-3.07586	0.24039	-0.00179	-0.17566	0.6672	0.8247
34.0	5.73551	0.05753	3.10	.00000	-3.28259	0.25061	-0.00147	-0.17635	0.6518	0.8086
40.0	5.95074	0.04757	3.10	.00000	-3.34144	0.25283	-0.00131	-0.17681	0.6415	0.7977
50.0	5.44598	0.07177	3.00	.00000	-3.28537	0.25005	-0.00123	-0.17790	0.6263	0.7871
100	2.62409	0.18314	2.70	.00000	-2.84813	0.23496	-0.00147	-0.18265	0.6020	0.7683
PGA	1.94816	0.22231	2.60	.00000	-2.73230	0.22861	-0.00157	-0.18324	0.5976	0.7649
PGV	1.55019	0.71702	2.30	.00000	-2.47087	0.23173	-0.00080	-0.21838	0.4205	-----

Table 3.5c Central North America regression coefficients for the double-corner model with variable medium stress parameter (2CVSP) as a function of moment magnitude (**M**).

Freq. Hz	C_1	C_2	C_4	C_5	C_6	C_7	C_8	C_{10}	Parametric	Total
									σ	σ
0.1	-19.62771	2.37863	1.60	.00000	-0.81479	0.01546	-0.00027	-0.35171	0.2066	1.2922
0.133	-18.18962	2.24940	1.60	.00000	-0.83277	0.01769	-0.00039	-0.35266	0.2113	1.2797
0.2	-15.96589	2.03343	1.70	.00000	-0.90334	0.02432	-0.00053	-0.33114	0.2401	1.1609
0.25	-14.68409	1.91250	1.80	.00000	-0.96082	0.02900	-0.00057	-0.31279	0.2654	1.0846
0.333	-13.16400	1.76172	1.80	.00000	-1.01410	0.03516	-0.00069	-0.28684	0.3083	1.0160
0.5	-10.91115	1.54906	1.90	.00000	-1.12846	0.04624	-0.00080	-0.25449	0.3712	0.9405
0.667	-9.34243	1.39827	2.00	.00000	-1.22858	0.05550	-0.00087	-0.23866	0.3724	0.8334
1.0	-7.51876	1.20223	1.90	.00000	-1.32362	0.06660	-0.00101	-0.22526	0.4257	0.7876
1.333	-6.15054	1.07271	1.90	.00000	-1.40319	0.07370	-0.00108	-0.21826	0.4800	0.8159
2.0	-4.46949	0.89608	2.00	.00000	-1.50124	0.08528	-0.00142	-0.20949	0.4916	0.7679
2.5	-3.83347	0.81740	1.90	.00000	-1.53149	0.08956	-0.00156	-0.20336	0.5256	0.7715
3.333	-2.80897	0.70732	2.00	.00000	-1.60718	0.09870	-0.00187	-0.19505	0.5815	0.8052
4.167	-1.98749	0.63335	2.10	.00000	-1.69694	0.10571	-0.00197	-0.18939	0.6132	0.8156
5.0	-1.54722	0.59123	2.10	.00000	-1.72652	0.10941	-0.00216	-0.18555	0.6568	0.8382
6.667	-0.88020	0.52752	2.10	.00000	-1.80627	0.11725	-0.00235	-0.18091	0.6894	0.8584
10.0	0.36600	0.43107	2.30	.00000	-1.99842	0.13239	-0.00252	-0.17722	0.7075	0.8662
13.333	1.21055	0.37380	2.40	.00000	-2.15434	0.14259	-0.00249	-0.17602	0.7054	0.8566
20.0	2.57488	0.28755	2.60	.00000	-2.42736	0.15866	-0.00226	-0.17541	0.7011	0.8548
25.0	3.70933	0.21903	2.80	.00000	-2.66156	0.17117	-0.00193	-0.17538	0.6951	0.8474
34.0	4.62521	0.16851	2.90	.00000	-2.85735	0.18073	-0.00162	-0.17545	0.6774	0.8294
40.0	4.84234	0.15701	2.90	.00000	-2.91740	0.18321	-0.00146	-0.17557	0.6668	0.8182
50.0	4.93563	0.14508	2.90	.00000	-2.97179	0.18610	-0.00122	-0.17584	0.6516	0.8074
100	2.27065	0.23507	2.60	.00000	-2.56256	0.17363	-0.00142	-0.17617	0.6241	0.7858
PGA	1.62848	0.26802	2.50	.00000	-2.45195	0.16823	-0.00151	-0.17639	0.6192	0.7819
PGV	1.67528	0.63277	2.20	.00000	-2.18201	0.16725	-0.00056	-0.17732	0.3689	-----

Table 3.5d Central North America regression coefficients for the double-corner model with constant medium stress parameter (2CCSP) as a function of moment magnitude (**M**).

Freq. Hz	C_1	C_2	C_4	C_5	C_6	C_7	C_8	C_{10}	Parametric	Total
									σ	σ
0.1	-18.24018	2.10561	1.80	.00000	-1.07045	0.07176	-0.00061	-0.37267	0.2012	1.2914
0.133	-16.75026	1.98135	1.90	.00000	-1.10434	0.07381	-0.00069	-0.37073	0.2041	1.2785
0.2	-14.57945	1.77734	2.00	.00000	-1.17552	0.07997	-0.00082	-0.34212	0.2307	1.1590
0.25	-13.45277	1.66940	2.00	.00000	-1.21152	0.08382	-0.00091	-0.31745	0.2550	1.0821
0.333	-11.88050	1.52775	2.10	.00000	-1.29302	0.09093	-0.00097	-0.28094	0.2961	1.0124
0.5	-9.74168	1.33996	2.20	.00000	-1.41702	0.10275	-0.00108	-0.23252	0.3551	0.9343
0.667	-8.43417	1.21946	2.20	.00000	-1.49228	0.11125	-0.00120	-0.20809	0.3524	0.8247
1.0	-6.63613	1.05600	2.20	.00000	-1.62243	0.12365	-0.00127	-0.19037	0.4022	0.7752
1.333	-5.56253	0.96293	2.10	.00000	-1.66906	0.12914	-0.00140	-0.18511	0.4573	0.8028
2.0	-4.17571	0.82286	2.10	.00000	-1.73283	0.13913	-0.00180	-0.18128	0.4738	0.7566
2.5	-3.42601	0.74918	2.10	.00000	-1.79502	0.14445	-0.00189	-0.17866	0.5095	0.7607
3.333	-2.44019	0.64886	2.20	.00000	-1.86842	0.15332	-0.00221	-0.17377	0.5698	0.7967
4.167	-1.85629	0.59401	2.20	.00000	-1.91425	0.15783	-0.00239	-0.17036	0.6031	0.8080
5.0	-1.44487	0.55767	2.20	.00000	-1.93988	0.16095	-0.00259	-0.16781	0.6483	0.8316
6.667	-0.82411	0.50288	2.20	.00000	-2.01066	0.16743	-0.00280	-0.16475	0.6842	0.8542
10.0	0.40372	0.40864	2.40	.00000	-2.19435	0.18173	-0.00299	-0.16203	0.7057	0.8647
13.333	1.24086	0.35309	2.50	.00000	-2.34543	0.19120	-0.00298	-0.16121	0.7047	0.8560
20.0	3.01971	0.24082	2.80	.00000	-2.68885	0.21059	-0.00265	-0.16069	0.7024	0.8559
25.0	3.79614	0.19089	2.90	.00000	-2.85195	0.21950	-0.00243	-0.16031	0.6966	0.8486
34.0	4.74380	0.13842	3.00	.00000	-3.05053	0.22882	-0.00212	-0.16000	0.6804	0.8318
40.0	5.51652	0.09726	3.10	.00000	-3.21104	0.23577	-0.00182	-0.16004	0.6690	0.8200
50.0	5.06614	0.11708	3.00	.00000	-3.16617	0.23348	-0.00171	-0.16010	0.6520	0.8077
100	2.33150	0.21424	2.70	.00000	-2.74751	0.21991	-0.00190	-0.16029	0.6220	0.7841
PGA	1.67665	0.24894	2.60	.00000	-2.63644	0.21441	-0.00199	-0.16044	0.6168	0.7800
PGV	2.13579	0.52982	2.30	.00000	-2.34136	0.20847	-0.00103	-0.17735	0.3711	-----

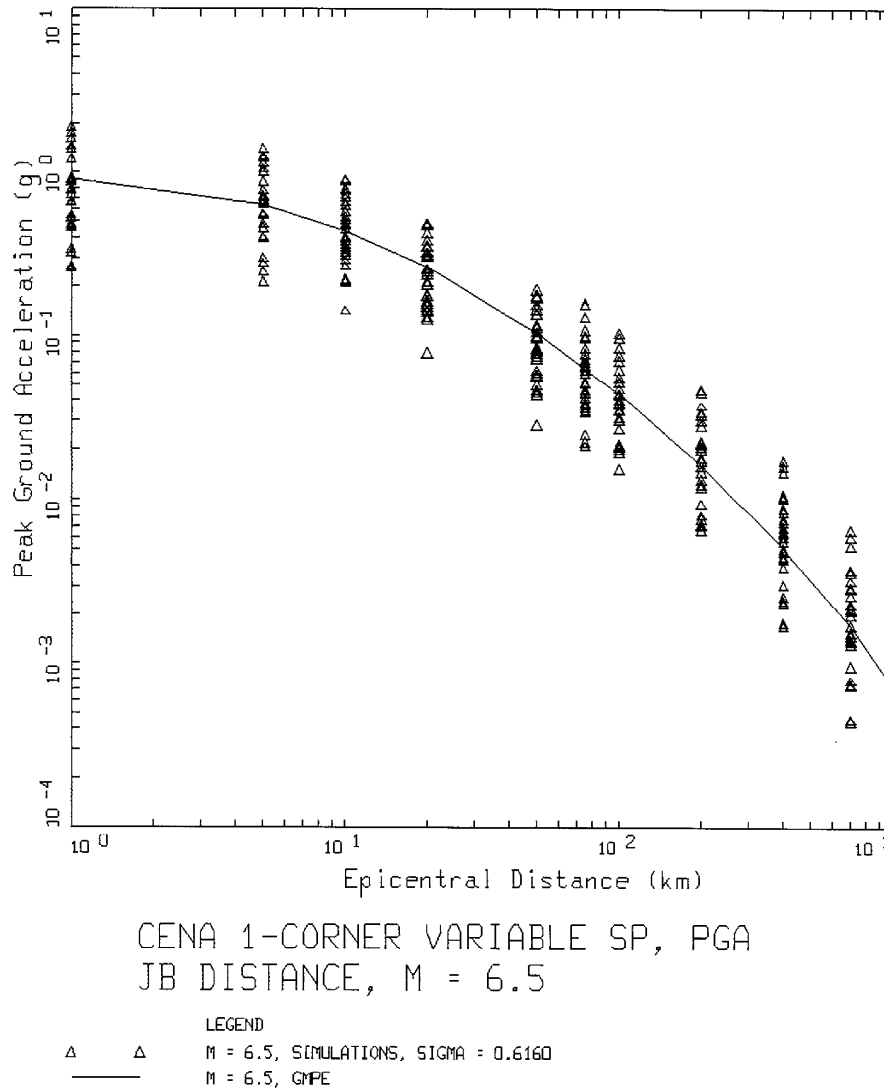
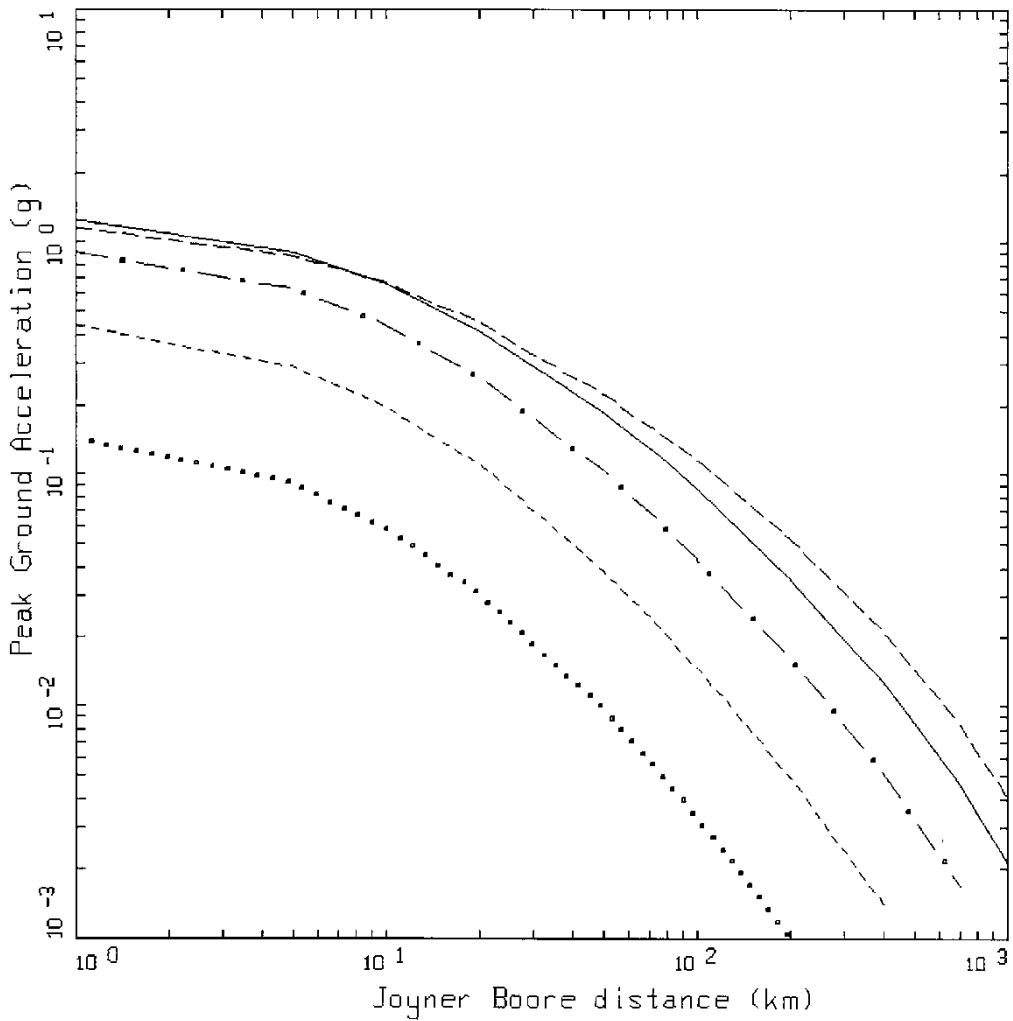


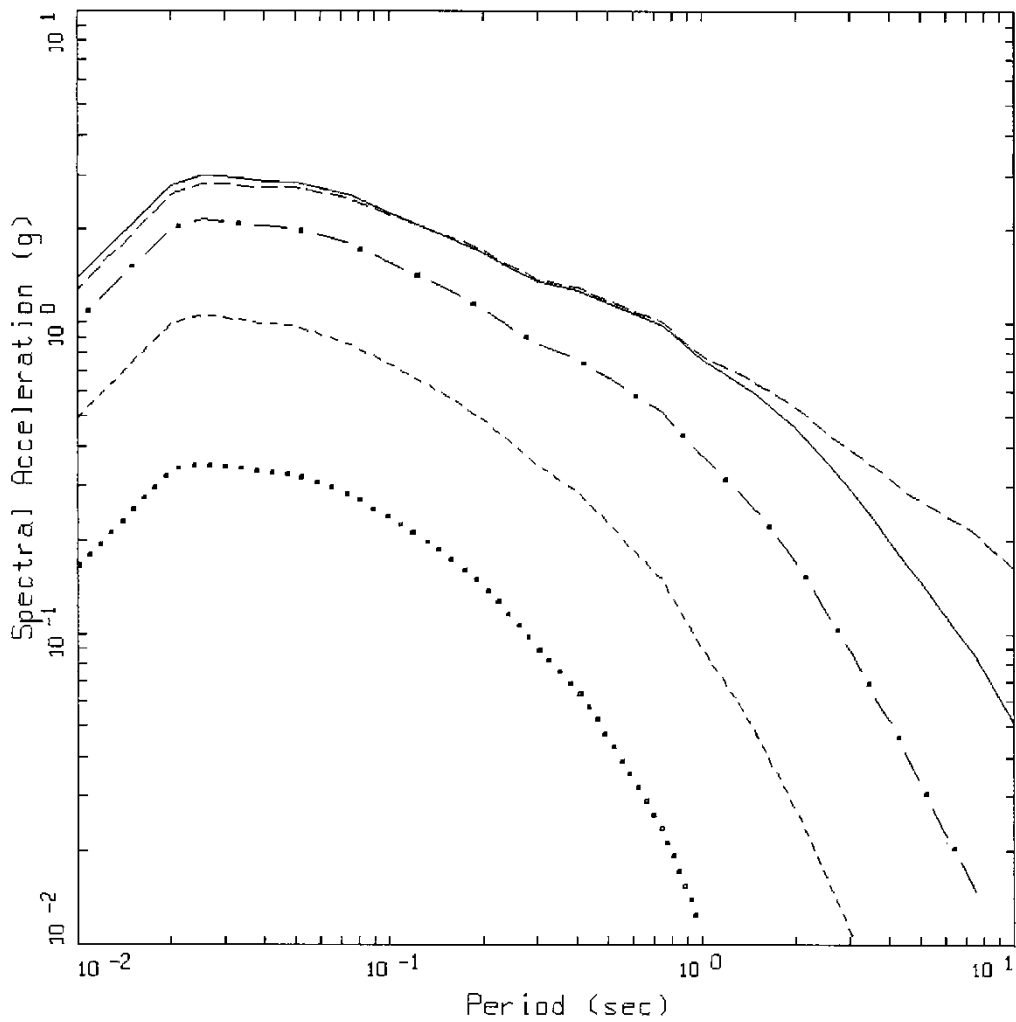
Figure 3.5 Example of model [Equation (3.6)] fit to single-corner variable stress parameter (1CVSP) simulated motions for M 6.5 (Table 3.4).



CENA 1-CORNER VARIABLE SP, PGA
JB DISTANCE

LEGEND
 M=4.5
 ----- M=5.5
 - . - . M=6.5
 _____ M=7.5
 - - - - M=8.5

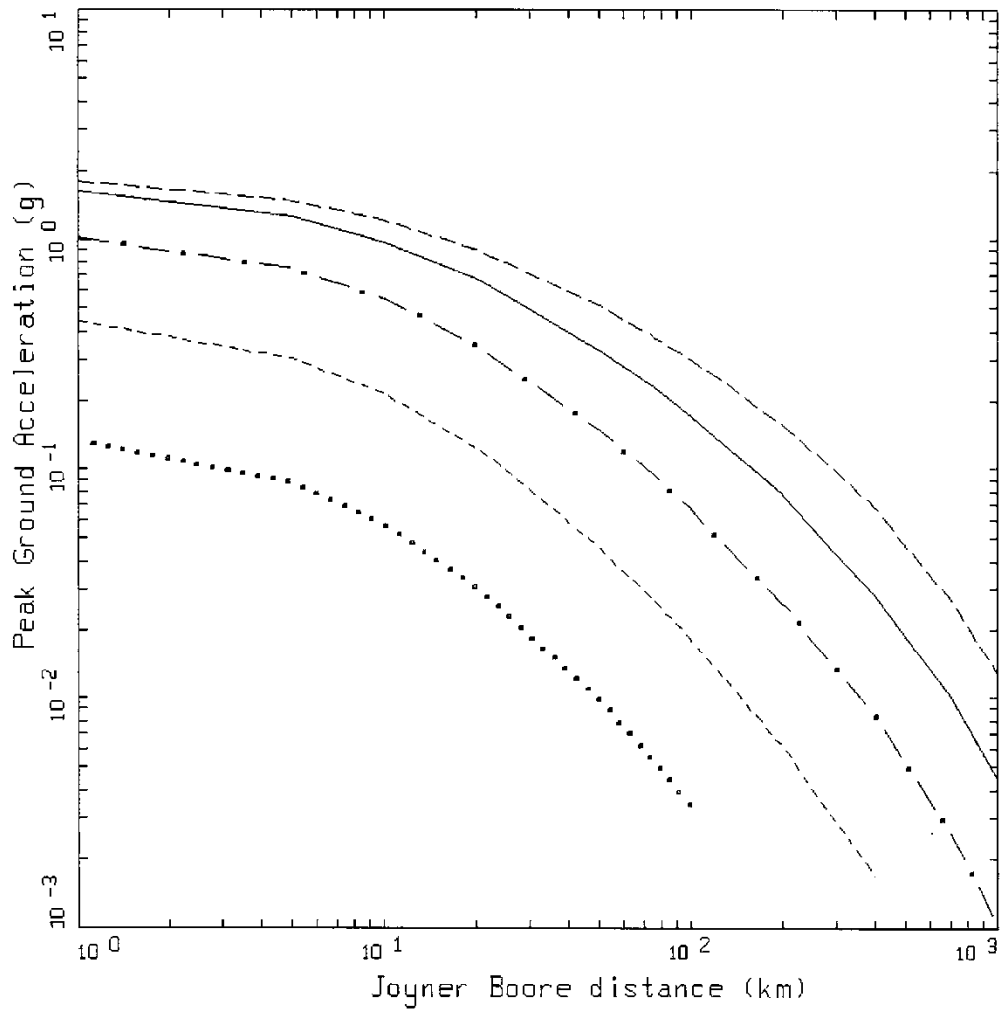
Figure 3.6 Plot of PGA values versus Joyner–Boore distance: single-corner variable stress parameter (1CVSP).



CENA 1-CORNER VARIABLE SP, PSa
 JB DISTANCE = 1 KM

- LEGEND
- M=4.5
 - M=5.5
 - . - . M=6.5
 - M=7.5
 - M=8.5

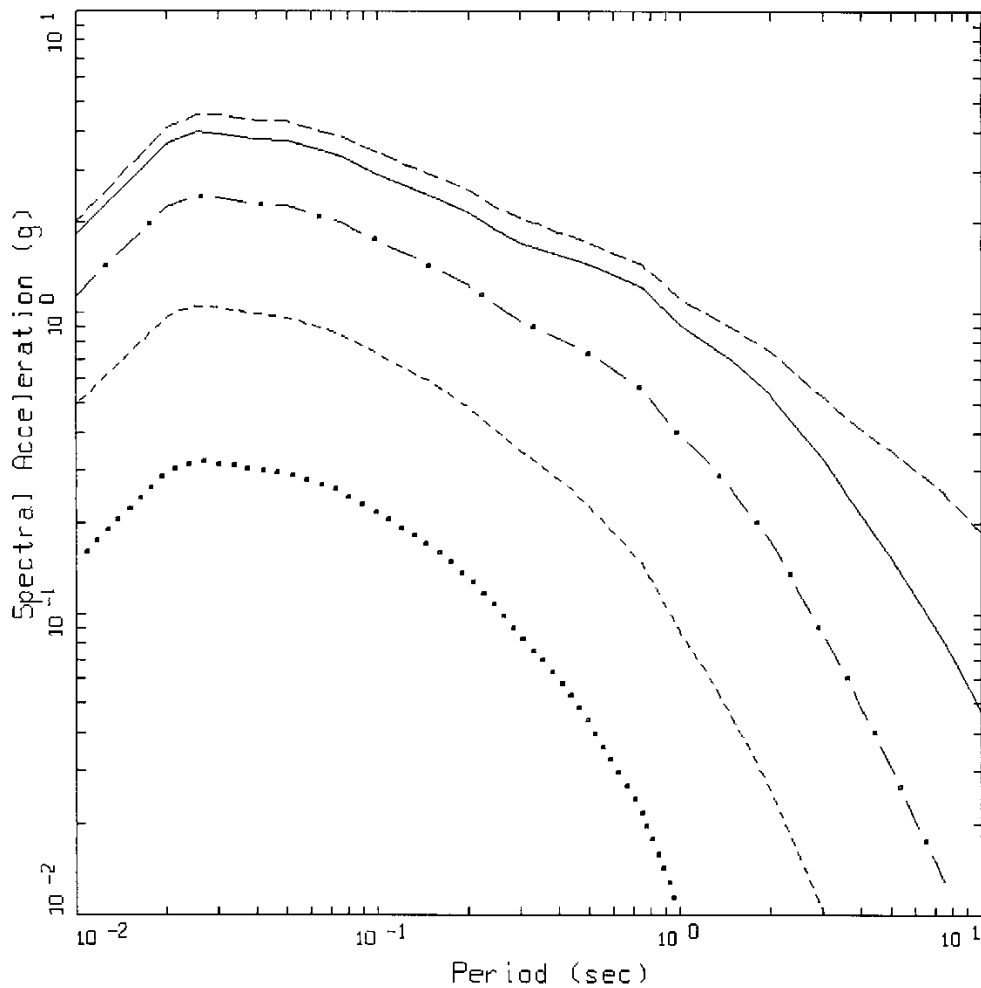
Figure 3.7 Plot of PSA (5% damped) at a distance of 1 km: single-corner variable stress parameter (1CVSP).



CENA 1-CORNER CONSTANT SP, PGA
JB DISTANCE

LEGEND
 M=4.5
 ----- M=5.5
 - . - . M=6.5
 _____ M=7.5
 - - - - M=8.5

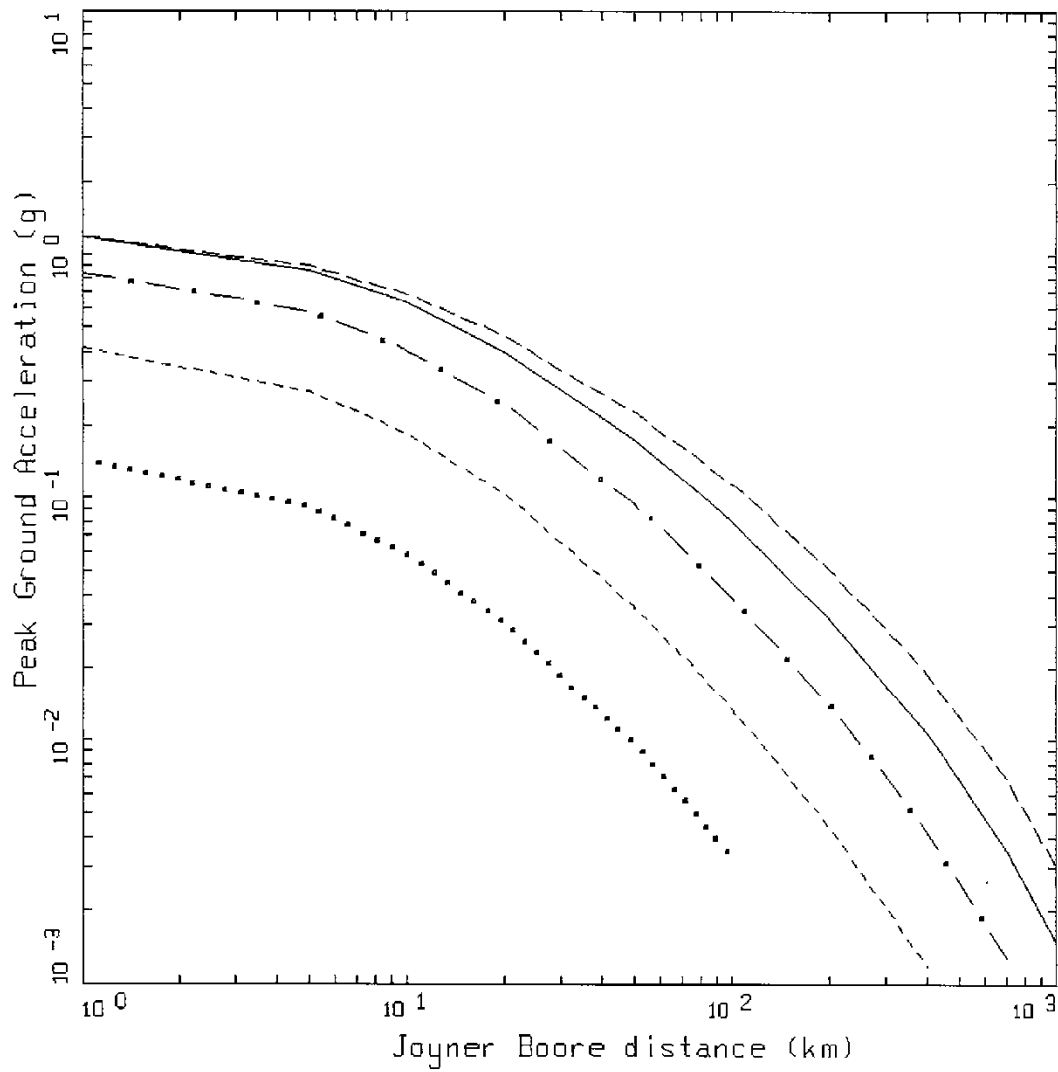
Figure 3.8 Plot of PGA values versus Joyner–Boore distance: single-corner constant stress parameter (1CCSP).



CENA 1-CORNER CONSTANT SP, PSa
 JB DISTANCE = 1 KM

- LEGEND
- M=4.5
 - M=5.5
 - . - . M=6.5
 - M=7.5
 - M=8.5

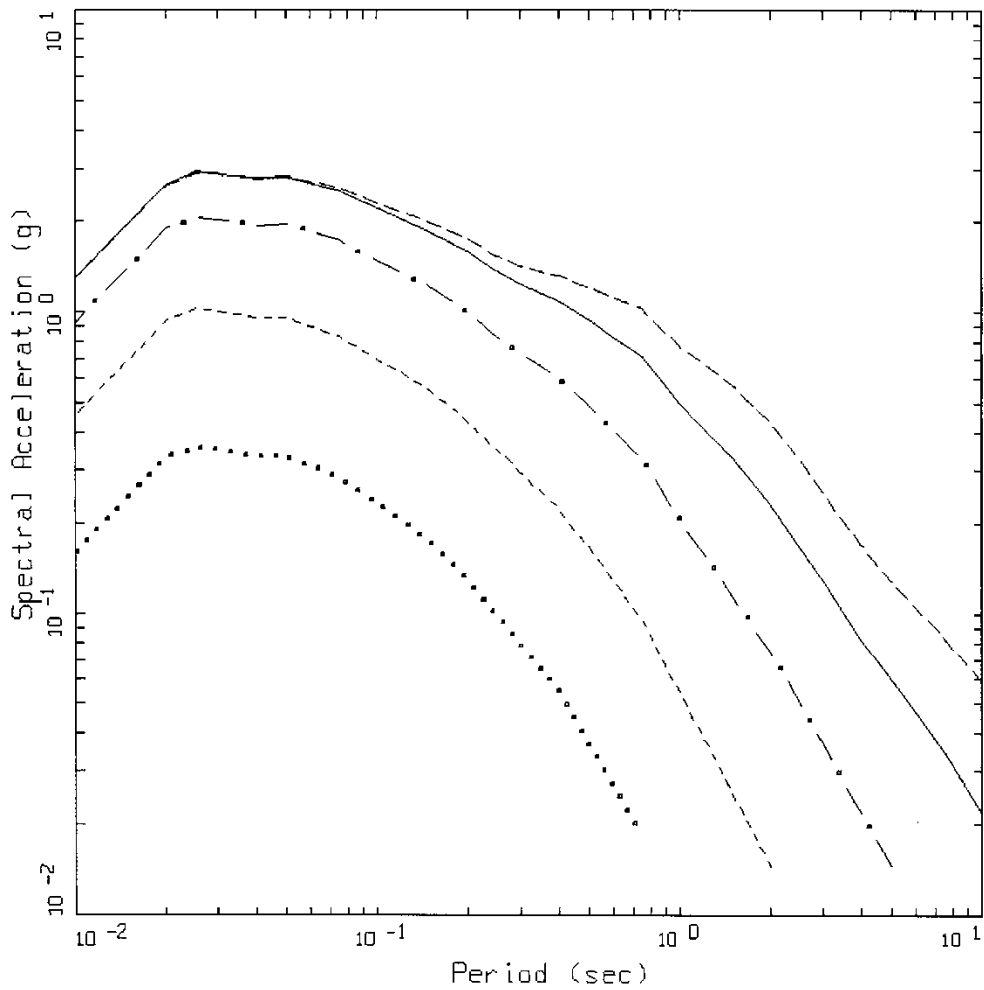
Figure 3.9 Plot of PSA (5% damped) at a distance of 1 km: single-corner constant stress parameter (1CCSP).



CENA 2-CORNER VARIABLE SP, PGA
JB DISTANCE

LEGEND
 M=4.5
 ----- M=5.5
 - . - . M=6.5
 _____ M=7.5
 - - - - M=8.5

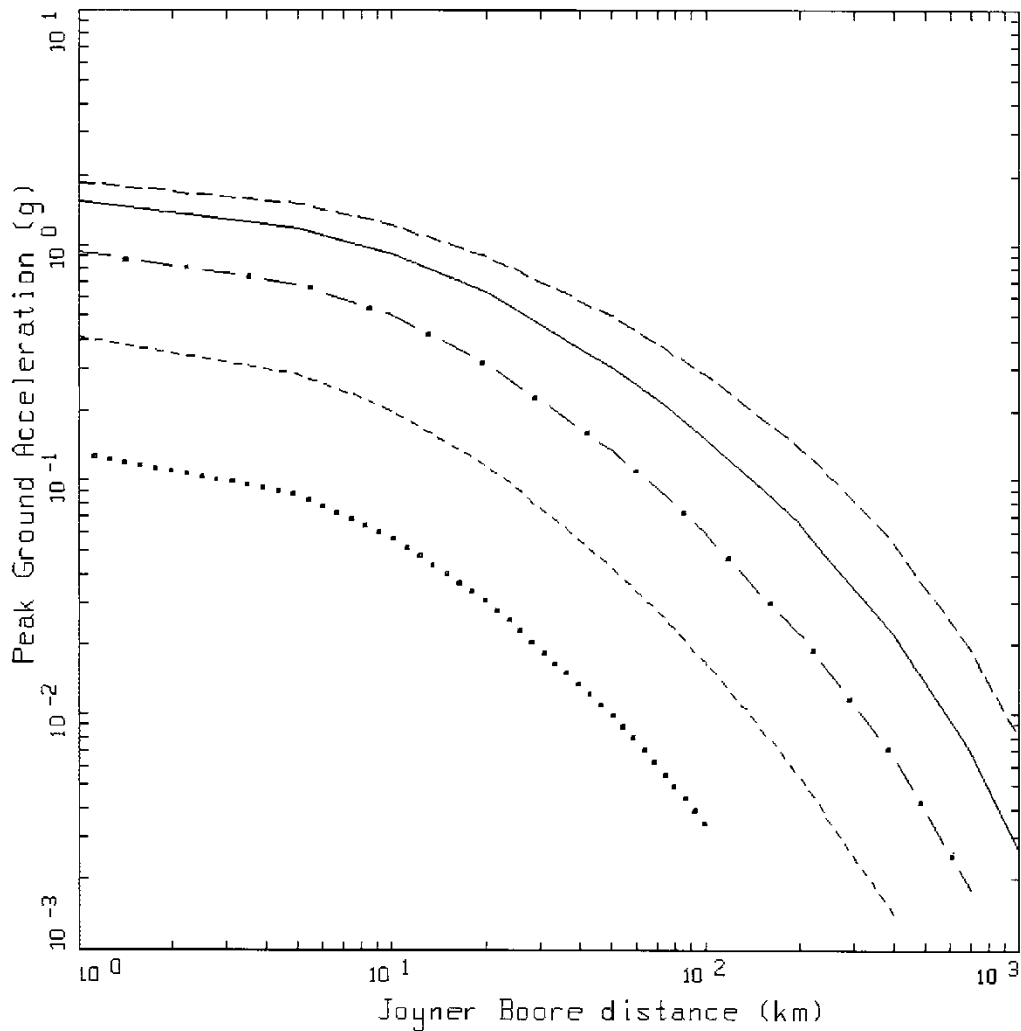
Figure 3.10 Plot of PGA values versus Joyner–Boore distance: double-corner variable stress parameter (2CVSP).



CENA 2-CORNER VARIABLE SP, PSa
 JB DISTANCE = 1 KM

LEGEND
 M=4.5
 - - - - M=5.5
 - . - . M=6.5
 _____ M=7.5
 - - - - M=8.5

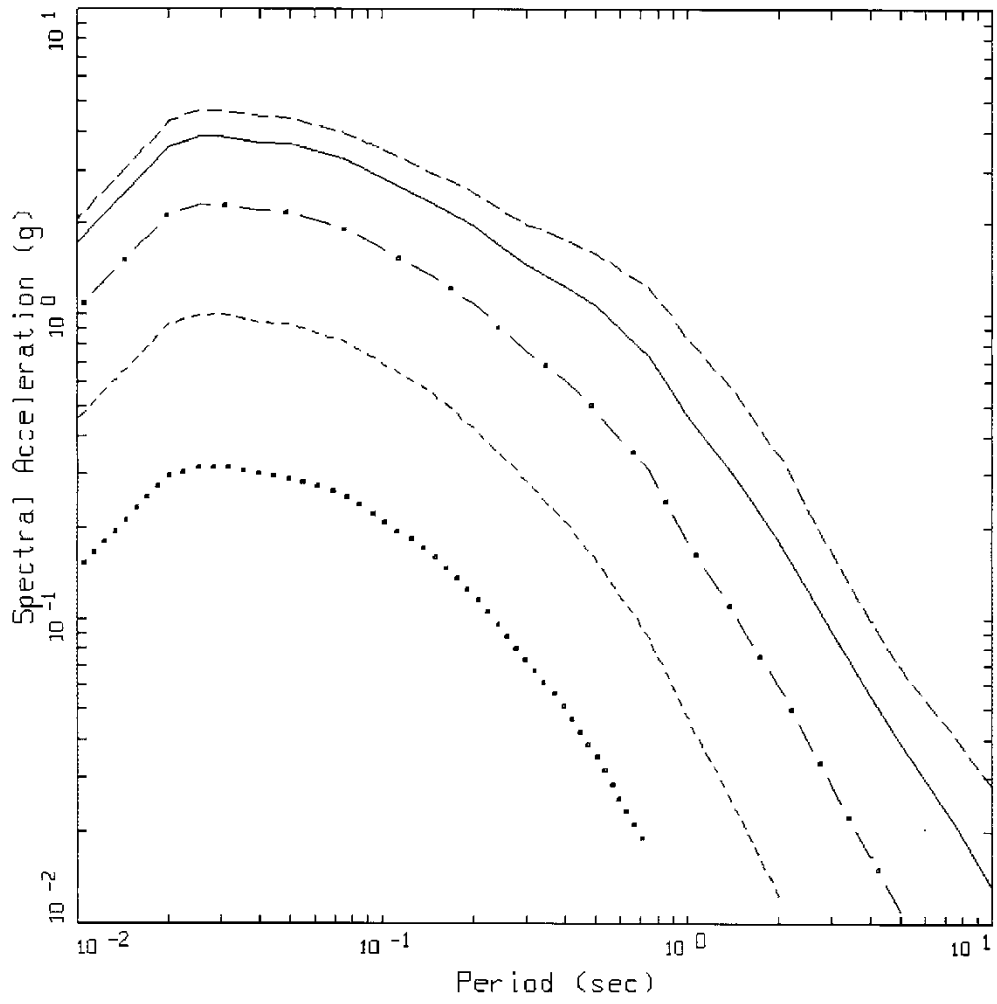
Figure 3.11 Plot of PSA (5% damped) at a distance of 1 km: double-corner variable stress parameter (2CVSP).



CENA 2-CORNER CONSTANT SP, PGA
JB DISTANCE

LEGEND	
.....	M=4.5
-----	M=5.5
- . - . -	M=6.5
————	M=7.5
-----	M=8.5

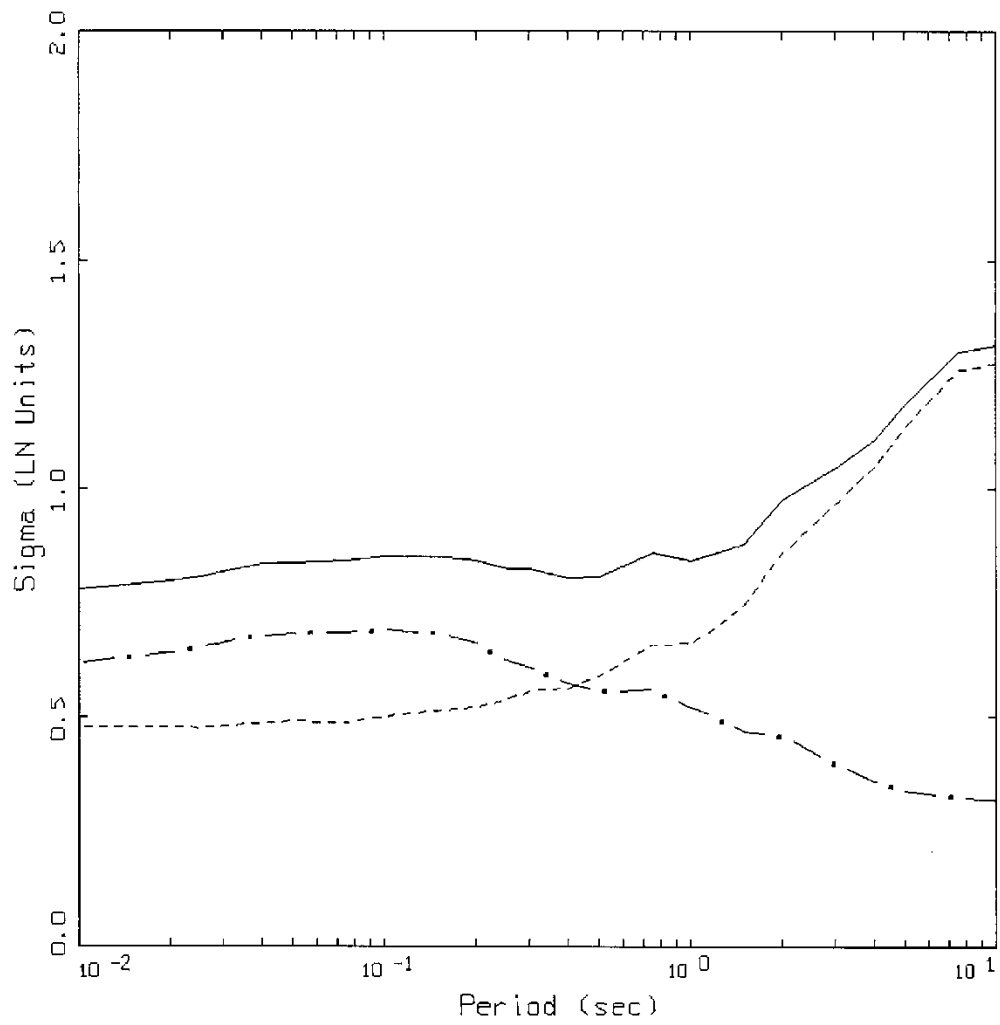
Figure 3.12 Plot of PGA values versus Joyner–Boore distance: double-corner constant stress parameter (2CCSP).



CENA 2-CORNER CONSTANT SP, PSa
 JB DISTANCE = 1 KM

- LEGEND
- M=4.5
 - M=5.5
 - . - . M=6.5
 - M=7.5
 - M=8.5

Figure 3.13 Plot of PSA (5% damped) at a distance of 1 km: double-corner constant stress parameter (2CCSP).



CENA 1-CORNER VARIABLE SP
VARIABILITY

- LEGEND
- PARAMETRIC SIGMA
 - MODELING SIGMA (BIAS CORRECTED)
 - TOTAL SIGMA

Figure 3.14 Modeling and parametric variability computed for the single-corner-frequency point-source model with variable stress parameters.

3.5 LIST OF ELECTRONIC APPENDICES FOR CHAPTER 3

- 3A Stochastic Ground-Motion Model Description (PDF document)
- 3B Site Response Analysis Method (PDF document)
- 3C Model Output: single corner, variable medium stress drop, 1CVSD (Excel workbook)
- 3D Model Output: single corner, constant medium stress drop, 1CCSD (Excel workbook)
- 3E Model Output: double corner, variable medium stress drop, 1CVSD (Excel workbook)
- 3F Model Output: double corner, constant medium stress drop, 2CCSD (Excel workbook)

4 Regionally-Adjustable Generic Ground-Motion Prediction Equation based on Equivalent Point-Source Simulations: Application to Central and Eastern North America

Emrah Yenier

Gail M. Atkinson

**Western University
Ontario, Canada**

Abstract

We develop a generic ground-motion prediction equation (GMPE) that can be adjusted for use in any region by modifying a few key model parameters. The basis of the GMPE is an equivalent point-source simulation model whose parameters have been calibrated to empirical data in California in such a way as to determine the decoupled effects of basic source and attenuation parameters on ground-motion amplitudes. We formulate the generic GMPE as a function of magnitude, distance, stress parameter, geometrical spreading rate, and anelastic attenuation coefficient. This provides a fully adjustable predictive model, allowing users to calibrate its parameters using observed motions in the target region. We also include an empirical calibration factor to account for residual effects that are different and/or missing in simulations compared to observed motions in the target region. As an example application, we show how the generic GMPE can be adjusted for use in Central and Eastern North America (CENA), and calibrated with the NGA-East database. We provide median predictions of ground motions in CENA for average horizontal-component peak ground motions and 5%-damped pseudo spectral acceleration (periods up to $T = 10$ sec), for magnitudes **M3** to **M8** and distance up to 600 km.

4.1 INTRODUCTION

Reliable estimates of ground motions that may be produced by future earthquakes require robust modeling of the earthquake source and attenuation attributes in the region of interest. Ground-motion observations from past events provide a valuable empirical basis to develop ground-

motion prediction equations (GMPEs) that describe amplitudes as a function of variables such as magnitude, distance and site condition. However, with the exception of well-monitored active regions such as California and Japan, empirical ground-motion data are generally sparse in the magnitude-distance range of engineering interest. Thus, there are insufficient data for development of reliable GMPEs in many regions, with Central and Eastern North America (CENA) being a classic example.

There are several alternative methods used for derivation of GMPEs in data-poor regions. A widely used method is the simulation-based approach, in which synthetic ground motions are generated over a wide magnitude and distance range, and the GMPE is developed based on the simulated amplitude data. The simulations are based on a seismological model of the source, path, and site effects, with the parameters being calibrated using the available empirical data for the region. Simulations can be performed using a variety of techniques ranging from simple stochastic point-source (PS) methods to more sophisticated finite-source broadband simulations [e.g., Atkinson and Boore 1995, 2006; Toro et al. 1997; Silva et al. 2002; Somerville et al. 2001, 2009; and Frankel 2009]. Another common approach is the hybrid empirical method [Campbell 2002; 2003]. This method calibrates an empirically well-constrained GMPE in a data-rich host region (e.g., western North America, WNA) for use in a data-poor target region (e.g., CENA) based on adjustment factors obtained from response-spectral ratios of stochastic simulations in the host and target regions [e.g., Campbell 2002, 2003; Scherbaum et al. 2005; and Pezeshk et al. 2011]. A third method is the referenced empirical approach introduced by Atkinson [2008]. It is similar to the hybrid empirical method in concept, but adjustment factors are determined empirically using spectral ratios of observed motions in the target region to predictions of an empirical GMPE in the host region [e.g., Atkinson, 2008, 2010; Atkinson and Boore 2011, Atkinson and Motazedian 2013; and Hassani and Atkinson, 2014].

Both the hybrid empirical method and the referenced empirical approach anchor their predictions to magnitude scaling and saturation effects observed in data-rich regions, assuming that these effects are transferable. Although the magnitude scaling is assumed to be similar between regions, no such assumption is made regarding the overall level of ground-motion amplitudes. Differences in overall amplitude level and distance scaling between regions are attributed to regional differences in fundamental source and attenuation parameters. The hybrid empirical method requires sound knowledge of these parameters in both host and target regions in order to determine host-to-target adjustment factors via simulations reliably. This may restrict the applicability of the method [Campbell 2003]. The referenced empirical approach resolves this issue by determining the adjustment factors empirically, avoiding the need for assumptions of the source and attenuation parameters for the host and target regions. An important limitation of the referenced empirical approach, however, is that the available ground-motion data in the target region may not sufficiently represent all important regional characteristics [Atkinson 2008].

In this study, we take advantage of key concepts from both the hybrid empirical and referenced empirical approaches to develop a robust simulation-based generic GMPE. The generic GMPE can be adjusted for use in any region by modifying a few key modeling parameters, and calibrated for regional use from limited empirical data. The basic idea is that we first develop a well-calibrated simulation-based GMPE for active tectonic regions, using the NGA-West2 database [Ancheta et al. 2014]. We parameterize this generic GMPE so as to isolate the effects of the basic source and attenuation parameters on peak ground motions and response

spectra. This provides effective and transparent control over the transferable factors between regions. The fundamental seismological parameters used as predictive variables in the generic GMPE include magnitude, distance, stress parameter, geometrical spreading rate, and the anelastic attenuation coefficient. This provides an adjustable predictive model that is readily calibrated with minimal regional data. In the generic GMPE, we also consider an empirical calibration factor to account for residual effects that are different and/or missing in simulations compared to empirical data. This closes any remaining gap between simulated and observed motions.

As an example implementation of the generic model, we use it to develop a GMPE for CENA by adjusting the stress and anelastic attenuation, and calibrate the model using the NGA-East database. During the calibration exercise, we infer a magnitude- and depth-dependent stress parameter model based on the values obtained from study events. We provided median predictions of ground motions in CENA for average horizontal-component peak ground motions and 5%-damped pseudo spectral acceleration (periods up to $T = 10$ sec), for wide ranges of magnitude (**M3–M8**) and distance (< 600 km).

4.2 FUNCTIONAL FORM OF THE GENERIC GMPE

A regionally-adjustable generic prediction equation requires a robust yet simple functional form that successfully decouples the effects of fundamental source and attenuation parameters on ground-motion amplitudes. We defined the generic GMPE as

$$\ln Y = F_E + F_Z + F_\gamma + F_S + C \quad (4.1)$$

where $\ln Y$ is the natural logarithm of a ground-motion intensity measure. F_E , F_Z , F_γ , and F_S represent functions for earthquake source, geometrical spreading, anelastic attenuation, and site effects, respectively. The C term is an empirical calibration factor that accounts for the residual differences between simulations and empirical data. We formulated the source and geometrical spreading effects (F_E and F_Z) in an equivalent PS sense, using ground-motion simulations with parameters calibrated to observations in California, obtained from the NGA-West2 database [Ancheta et al. 2014]. The anelastic attenuation (F_γ) was adjusted to optimize observed frequency-dependent attenuation effects. In this study, we provide predictions for the orientation-independent horizontal component of peak ground acceleration (PGA), peak ground velocity (PGV) and 5%-damped pseudo-spectral acceleration (PSA), where PGA and PSA are given in units of g and PGV is in cm/sec.

The source function (F_E) describes the effects of magnitude and stress parameter on ground-motion amplitudes as:

$$F_E = F_M + F_{\Delta\sigma} \quad (4.2)$$

where F_M represents the ground motions (for moment magnitude **M**) that would be observed at the source—if there were no distance-saturation effects—for the reference stress ($\Delta\sigma$) and

kappa (κ_0) parameters for the reference site condition. We chose $\Delta\sigma = 100$ bar and $\kappa_0 = 0.025$ sec as the reference modeling parameters based on the findings of Yenier and Atkinson [2015c] for California earthquakes. In Equation (4.2), $F_{\Delta\sigma}$ represents the stress adjustment factor that is needed when $\Delta\sigma$ is different than 100 bars.

The F_M term is defined as a function of moment magnitude (\mathbf{M}), using a hinged-quadratic function:

$$F_M = \begin{cases} e_0 + e_1(\mathbf{M} - \mathbf{M}_h) + e_2(\mathbf{M} - \mathbf{M}_h)^2 & \mathbf{M} \leq \mathbf{M}_h \\ e_0 + e_3(\mathbf{M} - \mathbf{M}_h) & \mathbf{M} > \mathbf{M}_h \end{cases} \quad (4.3)$$

where the hinge magnitude, \mathbf{M}_h , and model coefficients, e_0 to e_3 , are period-dependent. This mimics the functional form of magnitude scaling used by Boore et al. [2014b] in their NGA-West2 empirical GMPE.

The stress adjustment term is defined as:

$$F_{\Delta\sigma} = e_{\Delta\sigma} \ln(\Delta\sigma/100) \quad (4.4)$$

where $e_{\Delta\sigma}$ describes the rate of the ground-motion scaling with $\Delta\sigma$. Equation (4.4) describes the relationship between stress parameter and response spectral amplitudes, facilitating the determination of $\Delta\sigma$ from PSA data in the target region.

We model the geometrical spreading effects based on the equivalent PS method. Seismic waves are assumed to radiate from a virtual PS placed at an overall effective distance from the site, such that the empirically-observed saturation effects are successfully reproduced. The effective distance (R) is given as

$$R = \sqrt{D_{RUP}^2 + h^2} \quad (4.5)$$

where D_{RUP} is the closest distance from the site to the fault-rupture surface, and h is a pseudo-depth term that accounts for distance saturation effects. The pseudo-depth is generally defined as a function of magnitude to account for the extension of distance-saturation effects to larger distances with increasing magnitude. In this study, we define the pseudo-depth as [Yenier and Atkinson 2015a]:

$$h = 10^{-0.405 + 0.235\mathbf{M}} \quad (4.6)$$

We define the geometrical spreading function (F_Z) as

$$F_Z = \ln(Z) + (b_3 + b_4\mathbf{M}) \ln(R/R_{ref}) \quad (4.7)$$

where Z represents the geometrical attenuation of Fourier amplitudes, while the multiplicative component, $(b_3 + b_4 \mathbf{M}) \ln(R/R_{ref})$, accounts for the change in the apparent attenuation that occurs when ground motions are modeled in the response spectral domain rather than the Fourier domain. The coefficients b_3 and b_4 are period-dependent, and R_{ref} is the reference effective distance, given as $R_{ref} = \sqrt{1+h^2}$.

In ground-motion modeling, Z is generally considered as a piecewise continuous function that describes the distance-dependent attributes of geometrical spreading, considering the contributions of direct waves at close distances, and multiple reflections and refractions at larger distances. Babaie Mahani and Atkinson [2012] evaluated the ability of various functional forms to describe the geometrical attenuation in North America, and concluded that a bilinear model provides a good balance between simplicity and ability to capture the key attenuation attributes over a broad distance range. In this study, we define Z using a hinged bilinear model that provides for a transition from direct-wave spreading to surface-wave spreading of reflected and refracted waves:

$$Z = \begin{cases} R^{b_1} & R \leq R_t \\ R_t^{b_1} (R/R_t)^{b_2} & R > R_t \end{cases} \quad (4.8)$$

where R_t represents the transition distance, and b_1 and b_2 are the geometrical attenuation rates of Fourier amplitudes at $R \leq R_t$ and $R > R_t$, respectively. In the generic GMPE, we fix the transition distance at $R_t = 50$ km based on the findings of Yenier and Atkinson [2014].

The geometrical spreading rate at close distances is often assumed to be given by $b_1 = -1.0$, based on the homogeneous whole-space approximation. However, theoretical waveform simulations suggest faster spreading rates, about $b_1 \approx -1.3$ for typical layered earth models [Ojo and Mereu 1986; Burger et al. 1987; Ou and Herrmann 1990; Somerville et al. 1990; Chapman and Godbee 2012; and Chapman 2013]. Empirical modeling of ground motions in various regions, including WNA, CENA, and Australia also support this finding [Atkinson 2004; Allen et al. 2007; Babaie Mahani and Atkinson 2012; and Yenier and Atkinson, 2014, 2015c]. Therefore, we define the geometrical spreading rate at $R \leq 50$ km as $b_1 = -1.3$ in the generic model. The geometrical spreading rate at $R > 50$ km is fixed at the widely-used value of $b_2 = -0.5$, which is consistent with attenuation of surface waves in a half-space [Ou and Herrmann 1990; Atkinson 2012a].

Equation (4.7) effectively decouples the geometrical spreading of Fourier amplitudes (Z) and the change in observed decay of amplitudes when convolved by the response transfer function. Although the descriptive parameters of Z are fixed at their generic values in the model, Equation (4.7) allows modification of the shape and rates of Z if there is compelling evidence supporting such a change. In such a case, the preferred model as given in Equation (4.8) can be replaced with an alternative geometrical spreading model that is compatible with the decay of the Fourier amplitudes in the target region.

The anelastic attenuation function (F_γ) is given as:

$$F_\gamma = \gamma D_{RUP} \quad (4.9)$$

where γ is a period-dependent anelastic attenuation coefficient that is empirically determined from regional ground-motion data.

In the generic GMPE, we describe site effects relative to a reference condition of NEHRP (National Earthquake Hazards Reduction Program) B/C boundary, for which the travel-time weighted average shear-wave velocity over the top 30 m is $V_{S30} = 760$ m/sec. In this study, we adopt the site effects model of BSSA14 [Boore et al. 2014b]:

$$F_S = F_{lin} + F_{nl} \quad (4.10)$$

where F_{lin} represents the linear site effects, and F_{nl} represents the nonlinear site effects. The linear site response is defined as a function of V_{S30} :

$$F_{nl} = \begin{cases} c \ln(V_{S30}/760) & V_{S30} \leq V_c \\ c \ln(V_c/760) & V_{S30} > V_c \end{cases} \quad (4.11)$$

where c describes the V_{S30} -scaling and V_c is the limiting velocity beyond which ground motions no longer scale with V_{S30} . The nonlinear site response is given as

$$F_{nl} = f_1 + f_2 \ln \left[\frac{PGA_r + f_3}{f_c} \right] \quad (4.12)$$

where f_2 represents the degree of nonlinearity as a function of V_{S30} :

$$f_2 = f_4 \left[\exp \{ f_5 (\min(V_{S30}, 760) - 360) \} - \exp \{ f_5 (760 - 360) \} \right] \quad (4.13)$$

In Equations (4.11)–(4.13), parameters c , V_c , f_1 , f_3 , f_4 , and f_5 are model coefficients given in BSSA14 and PGA_r is the median peak horizontal acceleration predicted for the reference condition ($V_{S30} = 760$ m/sec).

4.3 DETERMINATION OF MODEL COEFFICIENTS

We calculate model coefficients of the magnitude effect (F_M), geometrical spreading function (F_Z) and stress adjustment factor ($F_{\Delta\sigma}$) from amplitude data generated from ground-motion simulations. The simulations are based on the equivalent point-source stochastic method with parameters calibrated to observed motions in California as described by Yenier and Atkinson [2015c]; simulation parameters are summarized in Table 4.1. Briefly, we use the additive double-corner-frequency source model of Boore et al. [2014a] with a spectral-sag parameter (ϵ) suggested by Yenier and Atkinson [2015c]. In simulations, the geometrical decay of Fourier

amplitudes (Z) is defined in terms of effective distance, as given in Equation (4.8) ($b_1 = -1.3$, $b_2 = -0.5$, and $R_i = 50$ km). We use the pseudo-depth model given in Equation (4.6) to account for near-distance saturation effects. The simulations do not include anelastic attenuation, because we will determine these effects empirically from regional ground-motion data (shown later). We simulate ground motions at NEHRP B/C site conditions assuming the generic crustal amplification factors given by Atkinson and Boore [2006]. We assume that the near-surface high-frequency attenuation parameter is $\kappa_0 = 0.025$ sec for this site class. Yenier and Atkinson [2015c] showed that equivalent point-source simulations with these modeling parameters (but also including regional anelastic attenuation effects) can reproduce average observed spectral amplitudes of earthquakes in California, for magnitudes up to **M**7.5 and distances less than 400 km. Any inadequacies or misfits between the simulations and empirical data will map into unresolved residuals, which will be taken into account through the calibration factor, C .

We perform time-domain equivalent point-source stochastic simulations using the widely-cited SMSIM software [Boore 2003; 2005], for magnitudes from **M**3 to **M**8 (with increments of 0.1 **M** units) and distances from 1 km to 400 km (with increments of 0.1 log₁₀ units), for a fixed stress parameter of $\Delta\sigma = 100$ bar. We generate 100 synthetic ground motions for each combination of **M**, D_{RUP} . For each simulated time series we calculate PGA, PGV, and PSA at 31 periods from 0.01 sec to 10 sec, then take the geometric mean for each parameter over the 100 simulations.

The coefficients of the magnitude-scaling term F_M are computed from the regression of simulations obtained at $D_{RUP} = 1$ km ($Y_{sim,1km}$). Recall that F_M represents the magnitude scaling of ground motions that would be observed at the source if there were no saturation effects. Therefore, we need to remove the saturation effects that we imposed in the simulations at 1km to extract the unsaturated magnitude effects, F_M ; this is easily done:

$$\ln Y_{sim,1km} = F_M - 1.3 \ln \left(\sqrt{1 + h^2} \right) \quad (4.14)$$

where the last term accounts for the saturation effects imposed in the simulations (i.e., F_Z at $D_{RUP} = 1$ km). We use a grid search to determine the hinge magnitude (\mathbf{M}_h), where we determine the coefficients e_0 to e_3 by regression of the amplitudes at 1 km, for each trial value of \mathbf{M}_h . We select the best-fitting \mathbf{M}_h and the associated coefficients (e_0 to e_3) based on minimizing the residuals of the simulated amplitudes with respect to the model equation. Figure 4.1 compares ground motions simulated at $D_{RUP} = 1$ km and the fitted model [Equation (4.14)] as a function of magnitude, for peak ground motions and response spectra. As seen in the figure, the fitted functional form captures the magnitude scaling and saturation effects implied by simulations very well.

Table 4.1 Parameter values used in stochastic equivalent point-source simulations (from Yenier and Atkinson, [2015c])

Parameter	Value
Shear-wave velocity	$\beta = 3.7 \text{ km/sec}$
Density	$\rho = 2.8 \text{ g/cm}^3$
Source model	Generalized additive double-corner-frequency source model of Boore et al. [2014a]
Spectral sag	$\varepsilon = \min(1, 10^{1.2-0.3M})$
Effective distance	$R = (D_{rup}^2 + h^2)^{0.5}$
Pseudo-depth	$h = 10^{-0.405+0.235M}$
Geometrical attenuation	$R^{-1.3}$ for $R \leq 50 \text{ km}$, and $50^{-1.3} (R/50)^{-0.5}$ for $R > 50 \text{ km}$
Anelastic attenuation	Not considered in simulations (determined empirically)
Site amplification (NEHRP B/C)	Table 4 of Atkinson and Boore [2006] Frequency-amplification pairs delimited by semicolons: 0.0001Hz-1; 0.1Hz-1.07; 0.24Hz-1.15; 0.45Hz-1.24; 0.79Hz-1.39; 1.38Hz-1.67; 1.93Hz-1.88; 2.85Hz-2.08; 4.03Hz-2.2; 6.34Hz-2.31; 12.5Hz-2.41; 21.2Hz-2.45; 33.4Hz-2.47; 82Hz-2.50
Kappa factor	$\kappa_0 = 0.025 \text{ sec}$
Source duration	$0.5/f_a + 0.5/f_b$ where f_a and f_b are the corner frequencies
Path duration*	Table 1 of Boore and Thompson [2014] Rupture distance-path duration pairs delimited by semicolons: 0 km-0 sec; 7 km-2.4 sec; 45 km-8.4 sec; 125 km-10.9 sec; 175 km-17.4 sec; 270 km-34.2 sec. Path duration increases with distance at a rate of 0.156 sec/km after the last nodal point.
Simulation calibration factor for California†	$C_{sim} = 3.16$

* The nodal rupture distances of Boore and Thompson [2014] are converted to effective distance using the pseudo depths (h) for each magnitude level.

† Factor applied to simulations for matching simulations to observed response spectra in California with zero bias. (Reader is referred to Yenier and Atkinson [2015c] for more information regarding the C_{sim} parameter)

We determined the model coefficients of the geometrical spreading function from regression of simulated amplitudes at variable distances, after playing back the magnitude effects (i.e., $\ln Y_{sim,1km} - F_M$). We use the form:

$$\ln Y_{sim,1km} = F_M = \ln(Z) + (b_3 + b_4 \mathbf{M}) \ln(R/R_{ref}) \quad (4.15)$$

In this regression, we constrain the Z to the decay shape used in the simulations (i.e., $b_1 = -1.3$, $b_2 = -0.5$, and $R_t = 50$ km). This forces the differences between the decay rates of Fourier and response spectral amplitudes to map into $b_3 + b_4 \mathbf{M} \ln(R/R_{ref})$. In Figure 4.2, we compare the generic GMPE (i.e., $F_M + F_Z$) against simulations to assess the performance of the fitted F_Z model. This shows that the generic GMPE is in good agreement with the behavior of the simulated amplitudes. The values of model coefficients for F_M and F_Z are listed in Table 4.2. This specifies the generic GMPE for California for the reference stress parameter (100 bars) and the reference site condition (B/C), but without anelastic attenuation or overall amplitude calibration factor. These factors can be determined empirically for the target region, as described below.

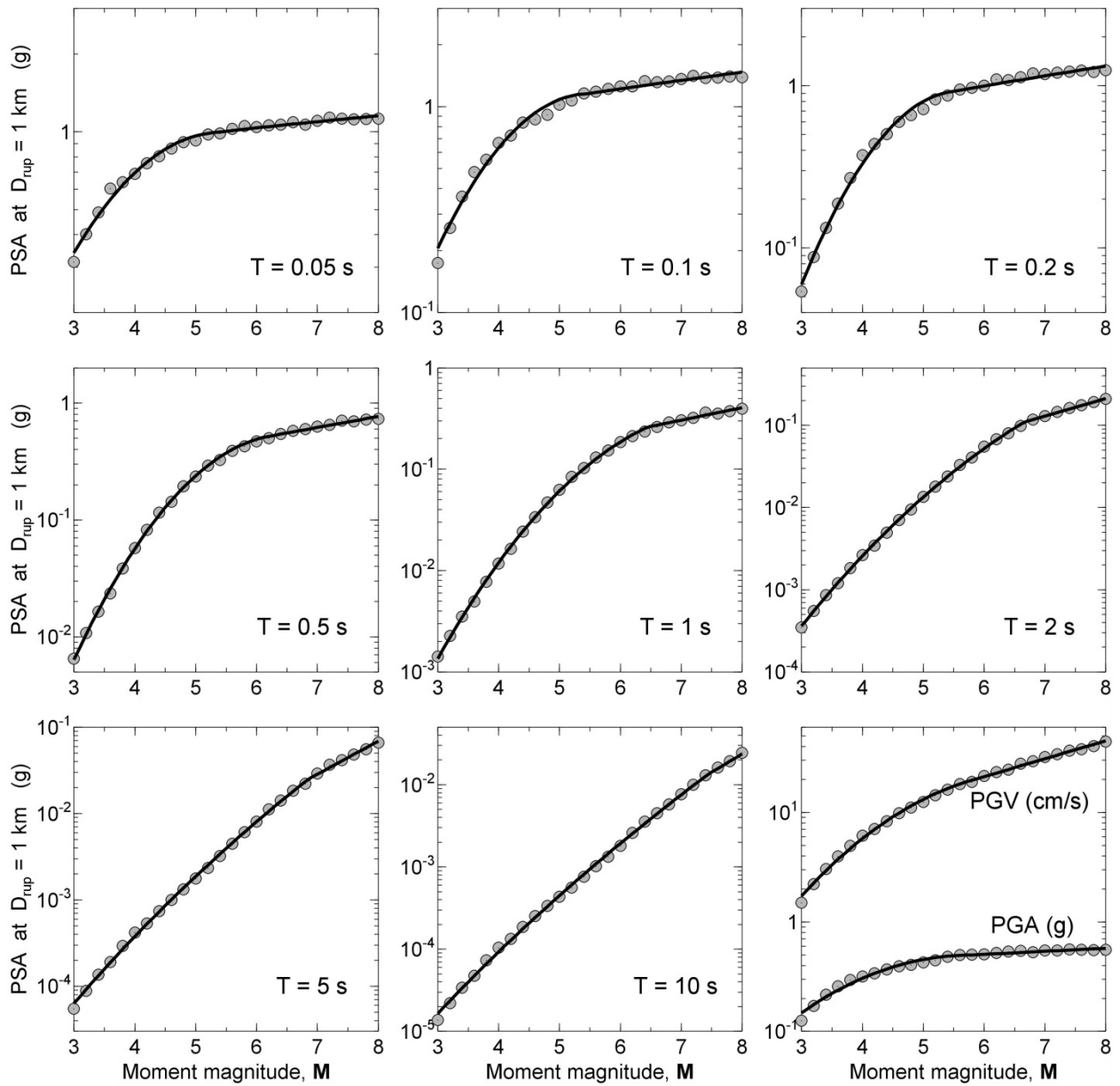


Figure 4.1 Ground motions simulated at $D_{RUP} = 1$ km (circles), and the fitted model (lines) as a function of magnitude.

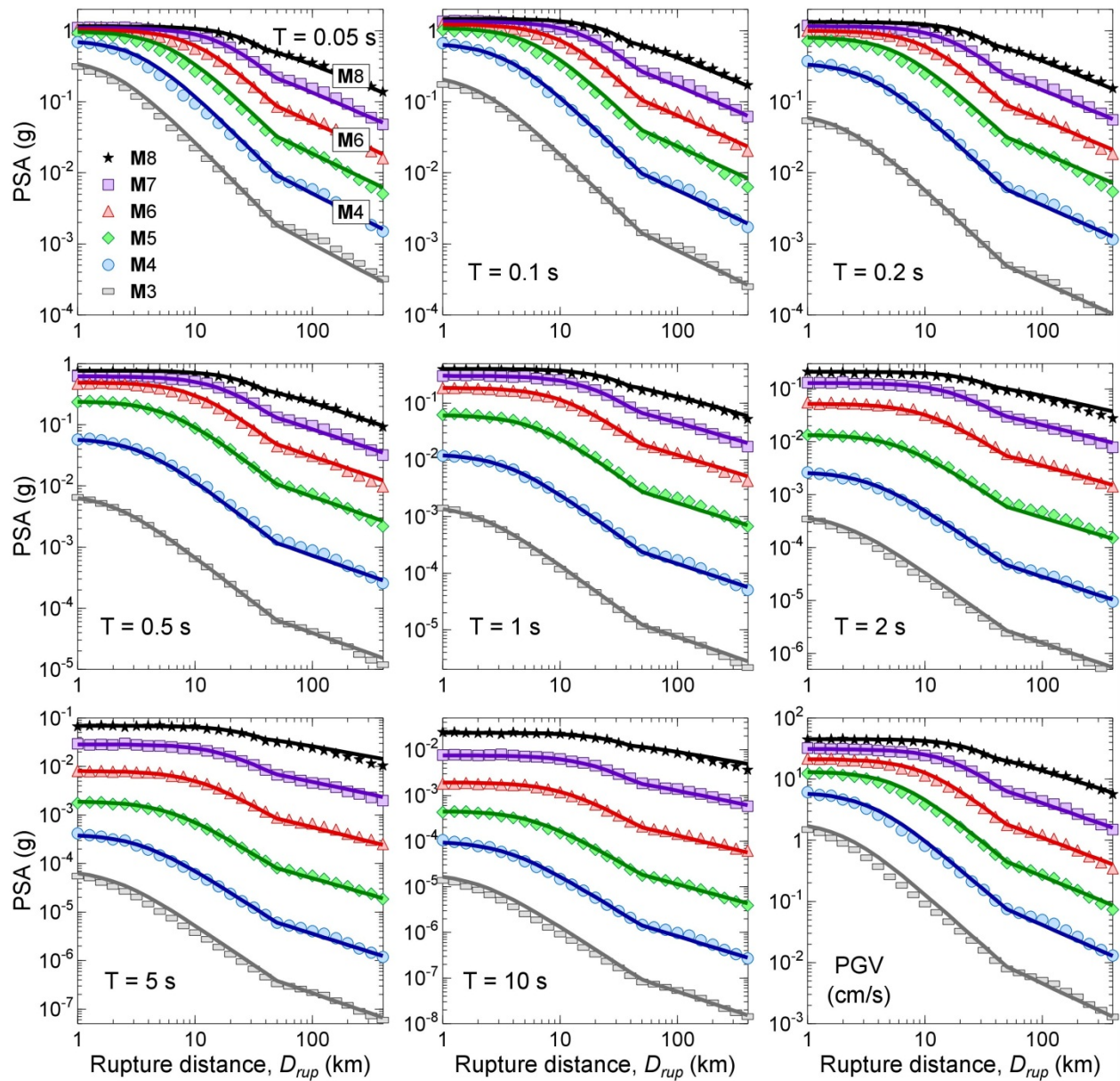


Figure 4.2 Simulations (symbols) in comparison to predictions of the generic GMPE (lines), as a function of rupture distance, for magnitudes **M3** to **M8**. $\Delta\sigma = 100$, $V_{S30} = 760$ m/sec. Note that no anelastic attenuation is included in either simulations or the generic GMPE because this effect is determined empirically.

Table 4.2 Model coefficients of the magnitude term (F_M) and geometrical spreading function (F_Z) in the generic GMPE.

T (sec)	M_h	e_0	e_1	e_2	e_3	b_3	b_4
0.010	5.85	2.23A+0	6.87E-1	-1.36E-1	7.64E-1	-6.21E-1	6.06E-2
0.013	5.90	2.28E+0	6.85E-1	-1.29E-1	7.62E-1	-6.26E-1	6.13A-2
0.016	5.85	2.27E+0	6.97E-1	-1.23A-1	7.59E-1	-6.31E-1	6.19E-2
0.020	5.90	2.38E+0	7.00E-1	-1.07E-1	7.49E-1	-6.38E-1	6.25E-2
0.025	6.00	2.56E+0	6.84E-1	-9.42E-2	7.41E-1	-6.31E-1	6.10E-2
0.030	6.15	2.81E+0	6.61E-1	-9.09E-2	7.39E-1	-6.03A-1	5.64E-2
0.040	5.75	2.73A+0	7.03A-1	-1.09E-1	7.38E-1	-5.48E-1	4.82E-2
0.050	5.35	2.56E+0	7.19E-1	-1.64E-1	7.54E-1	-5.10E-1	4.28E-2
0.065	5.75	3.00E+0	6.84E-1	-1.55E-1	7.55E-1	-4.67E-1	3.64E-2
0.080	5.20	2.58E+0	7.65E-1	-2.43A-1	7.87E-1	-4.21E-1	3.07E-2
0.100	5.45	2.78E+0	7.12E-1	-2.62E-1	7.94E-1	-3.77E-1	2.47E-2
0.130	5.35	2.64E+0	7.35E-1	-3.32E-1	8.12E-1	-3.55E-1	2.22E-2
0.160	5.25	2.47E+0	8.09E-1	-3.87E-1	8.41E-1	-3.26E-1	1.92E-2
0.200	5.45	2.55E+0	8.19E-1	-3.86E-1	8.43A-1	-2.87E-1	1.38E-2
0.250	5.60	2.52E+0	8.67E-1	-3.77E-1	8.78E-1	-2.43A-1	9.21E-3
0.300	5.85	2.63A+0	8.47E-1	-3.63A-1	8.76E-1	-2.12E-1	5.16E-3
0.400	6.15	2.67E+0	8.50E-1	-3.47E-1	8.97E-1	-1.93A-1	4.85E-3
0.500	6.25	2.54E+0	8.86E-1	-3.49E-1	9.18E-1	-2.08E-1	8.54E-3
0.650	6.60	2.62E+0	8.76E-1	-3.16E-1	9.25E-1	-2.28E-1	1.37E-2
0.800	6.85	2.66E+0	9.05E-1	-2.89E-1	8.94E-1	-2.52E-1	1.91E-2
1.000	6.45	1.99E+0	1.34E+0	-2.46E-1	9.83A-1	-2.97E-1	2.76E-2
1.300	6.75	2.01E+0	1.39E+0	-2.06E-1	1.00E+0	-3.50E-1	3.78E-2
1.600	6.75	1.75E+0	1.56E+0	-1.68E-1	1.05E+0	-3.85E-1	4.43A-2
2.000	6.65	1.25E+0	1.75E+0	-1.32E-1	1.19E+0	-4.35E-1	5.36E-2
2.500	6.70	9.31E-1	1.82E+0	-1.09E-1	1.29E+0	-4.79E-1	6.14E-2
3.000	6.65	5.16E-1	1.91E+0	-8.98E-2	1.42E+0	-5.13A-1	6.76E-2
4.000	6.85	3.44E-1	1.93A+0	-7.47E-2	1.51E+0	-5.51E-1	7.43A-2
5.000	6.85	-7.92E-2	1.98E+0	-6.21E-2	1.59E+0	-5.80E-1	7.90E-2
6.500	7.15	-6.67E-3	1.97E+0	-5.45E-2	1.63A+0	-5.96E-1	8.12E-2
8.000	7.50	2.56E-1	1.94E+0	-5.23A-2	1.59E+0	-6.09E-1	8.30E-2
10.000	7.45	-2.76E-1	1.97E+0	-4.63A-2	1.72E+0	-6.20E-1	8.42E-2
PGA	5.85	2.22E+0	6.86E-1	-1.39E-1	7.66E-1	-6.19E-1	6.03A-2
PGV	5.90	5.96E+0	1.03A+0	-1.65E-1	1.08E+0	-5.79E-1	5.74E-2

We generate another set of simulations to calculate the stress adjustment factor. In this new set, we simulate ground motions for the same magnitude range (**M3–M8**) but for a fixed distance $D_{RUP} = 1$ km and variable stress parameters ($10 \text{ bar} \leq \Delta\sigma \leq 1000 \text{ bar}$). Similar to the first set, 100 synthetic motions are generated for each combination of **M**, D_{RUP} , and $\Delta\sigma$, and the geometric mean of the peak motions and response spectra are calculated.

The stress adjustment factor, $F_{\Delta\sigma}$, models the expected change in amplitudes when $\Delta\sigma$ is different than 100 bars. We determine $F_{\Delta\sigma}$ using simulations obtained at $D_{RUP} = 1$ km, as:

$$F_{\Delta\sigma} = \ln Y_{\text{sim},1\text{km}}(\mathbf{M}, \Delta\sigma) - \ln Y_{\text{sim},1\text{km}}(\mathbf{M}, 100 \text{ bar}) \quad (4.16)$$

where $Y_{\text{sim},1\text{km}}(\mathbf{M}, \Delta\sigma)$ is the ground motion simulated at $D_{RUP} = 1$ km for a given magnitude and stress, and $Y_{\text{sim},1\text{km}}(\mathbf{M}, 100 \text{ bar})$ represents the ground motion simulated at $D_{RUP} = 1$ km for the same magnitude, but for the reference stress ($\Delta\sigma = 100 \text{ bar}$). Figure 4.3 shows the required stress adjustment factors as a function of $\Delta\sigma$, for various magnitudes and periods. This factor has an increasing trend with the stress, where by definition $F_{\Delta\sigma} = 0$ at $\Delta\sigma = 100 \text{ bar}$. The slope of $F_{\Delta\sigma}$ which is defined by coefficient $e_{\Delta\sigma}$ in Equation (4.4), represents the strength of the ground-motion scaling with the stress parameter. The steeper the slope, the larger the influence of stress on ground motions. As seen in Figure 4.3, $\Delta\sigma$ has significant influence at short periods ($T < 0.2 \text{ sec}$), regardless of magnitude. However, its effects weaken with increasing period, particularly for small-to-moderate magnitude events ($\mathbf{M} < 6$). For large magnitudes, the $\Delta\sigma$ effects extend to longer periods due to the shifting of the two corner frequencies with magnitude.

We regress the values of $e_{\Delta\sigma}$ (calculated for each magnitude and period from the values of $F_{\Delta\sigma}$ using Equation (4.4) to the functional form:

$$e_{\Delta\sigma} = \begin{cases} s_0 + s_1\mathbf{M} + s_2\mathbf{M}^2 + s_3\mathbf{M}^3 + s_4\mathbf{M}^4 & \Delta\sigma \leq 100 \text{ bar} \\ s_5 + s_6\mathbf{M} + s_7\mathbf{M}^2 + s_8\mathbf{M}^3 + s_9\mathbf{M}^4 & \Delta\sigma > 100 \text{ bar} \end{cases} \quad (4.17)$$

where s_0 to s_9 are period-dependent model coefficients. We use two polynomials because we require a different shape for the $e_{\Delta\sigma}$ values for $\Delta\sigma \leq 100 \text{ bar}$ and $\Delta\sigma > 100 \text{ bar}$; we constrain the regressions to attain $F_{\Delta\sigma} = 0$ at $\Delta\sigma = 100 \text{ bar}$. Figure 4.4 shows how the values of $e_{\Delta\sigma}$ vary with magnitude and period. The net effect of the stress parameter is complicated because of interactions between scaling of the high-frequency source amplitudes, shifting of the two corner frequencies, and changes in spectral sag between the corner frequencies. Additionally, the stress parameter affects the source duration, which in turn influences the response spectral amplitudes. Coupling of all these factors in the response spectrum domain requires a high-order polynomial to satisfactorily model $\Delta\sigma$ -scaling over a wide period range. The values of model coefficients for the stress adjustment factor are listed in Table 4.3.

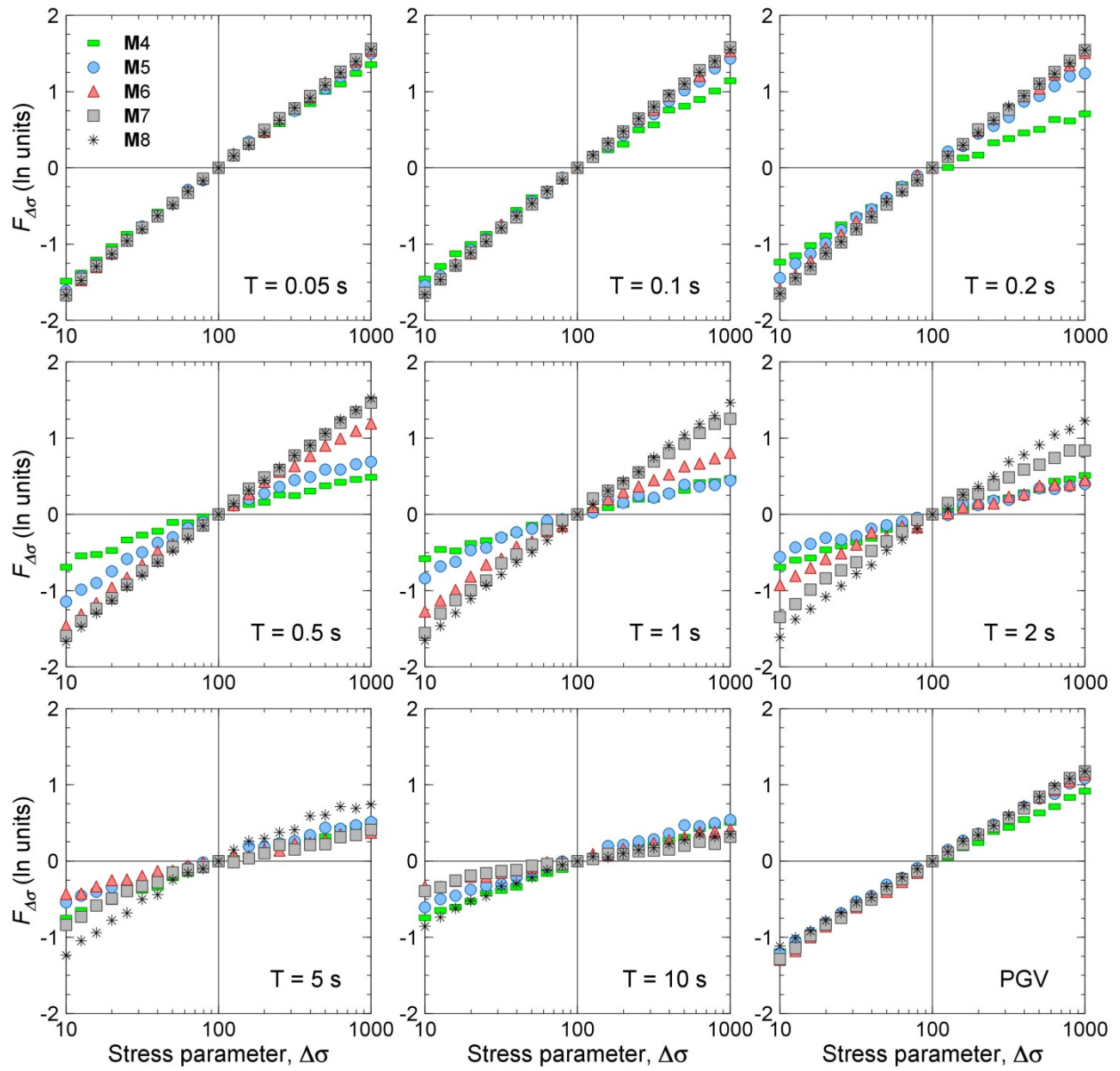


Figure 4.3 Stress adjustment factors ($F_{\Delta\sigma}$) determined from simulations.

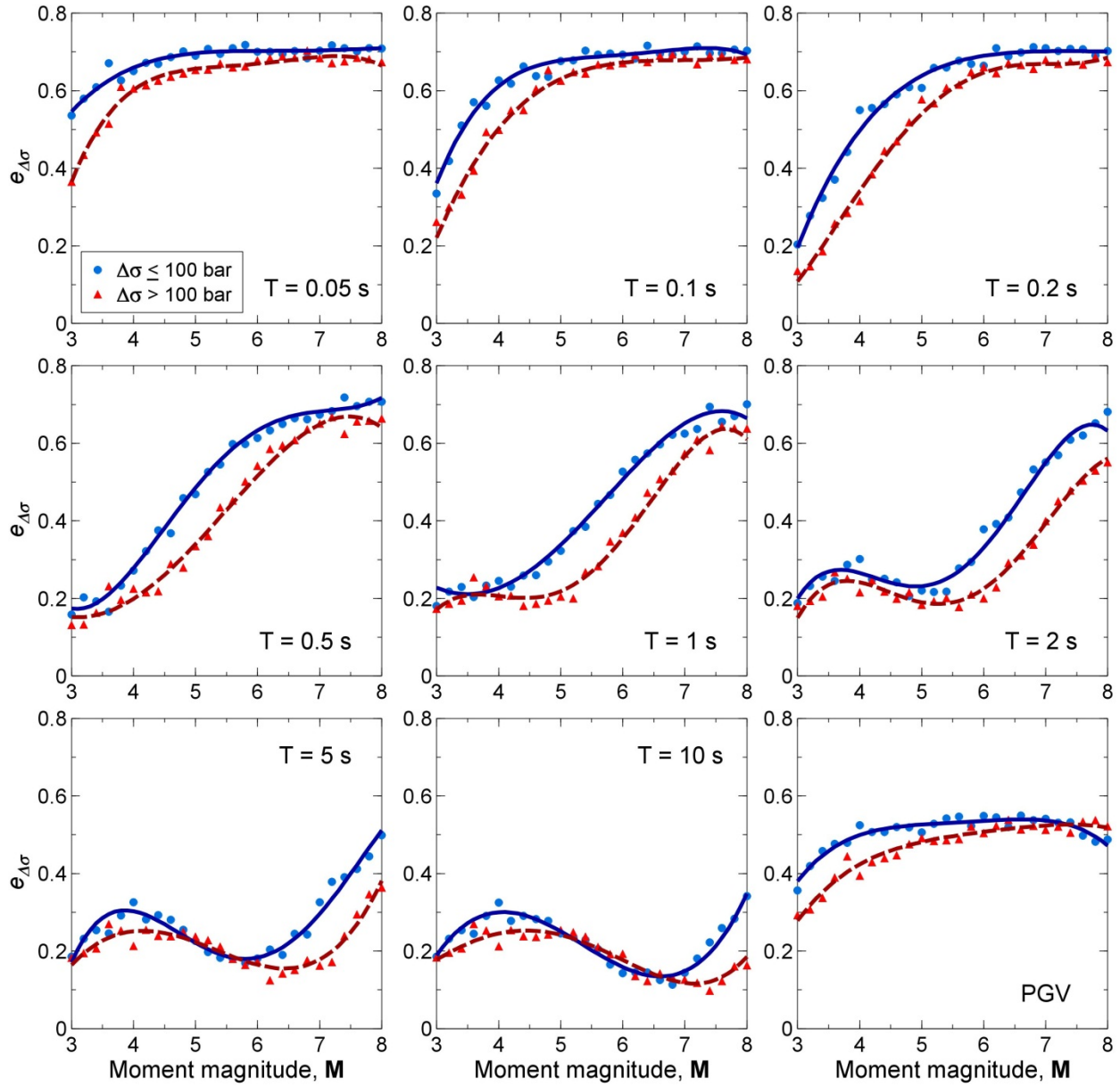


Figure 4.4 Stress-scaling coefficients ($e_{\Delta\sigma}$) obtained from simulations (symbols) and the fitted model [Equation (4.17)].

Table 4.3 Model coefficients of the stress adjustment factor ($F_{\Delta\sigma}$) in the generic GMPE

T (sec)	s_0	s_1	s_2	s_3	s_4
0.010	-2.05E+0	1.88E+0	-4.90E-1	5.67E-2	-2.43A-3
0.013	-1.92E+0	1.80E+0	-4.71E-1	5.47E-2	-2.36E-3
0.016	-1.71E+0	1.66E+0	-4.36E-1	5.09E-2	-2.20E-3
0.020	-1.16E+0	1.27E+0	-3.34E-1	3.91E-2	-1.70E-3
0.025	-1.54E+0	1.59E+0	-4.29E-1	5.10E-2	-2.24E-3
0.030	-1.06E+0	1.20E+0	-3.13A-1	3.62E-2	-1.55E-3
0.040	-8.57E-1	1.04E+0	-2.68E-1	3.08E-2	-1.33A-3
0.050	-9.63A-1	9.83A-1	-2.16E-1	2.08E-2	-7.42E-4
0.065	-2.23A+0	1.95E+0	-4.90E-1	5.49E-2	-2.29E-3
0.080	-3.68E+0	2.96E+0	-7.51E-1	8.42E-2	-3.51E-3
0.100	-4.05E+0	3.10E+0	-7.62E-1	8.33A-2	-3.39E-3
0.130	-4.17E+0	3.09E+0	-7.44E-1	7.98E-2	-3.21E-3
0.160	-3.96E+0	2.82E+0	-6.50E-1	6.72E-2	-2.61E-3
0.200	-2.71E+0	1.73A+0	-3.30E-1	2.82E-2	-9.06E-4
0.250	-1.77E+0	9.83A-1	-1.31E-1	6.00E-3	-1.16E-5
0.300	-3.18E-1	-1.39E-1	1.70E-1	-2.85E-2	1.42E-3
0.400	2.02E+0	-1.86E+0	6.12E-1	-7.67E-2	3.34E-3
0.500	3.96E+0	-3.29E+0	9.88E-1	-1.20E-1	5.14E-3
0.650	3.65E+0	-2.82E+0	7.93A-1	-8.93A-2	3.55E-3
0.800	2.40E+0	-1.65E+0	4.09E-1	-3.71E-2	1.05E-3
1.000	1.07E+0	-4.55E-1	3.74E-2	1.03A-2	-1.08E-3
1.300	-2.51E+0	2.52E+0	-8.45E-1	1.21E-1	-6.02E-3
1.600	-5.26E+0	4.74E+0	-1.48E+0	1.96E-1	-9.28E-3
2.000	-6.64E+0	5.77E+0	-1.74E+0	2.24E-1	-1.03A-2
2.500	-8.08E+0	6.84E+0	-2.02E+0	2.54E-1	-1.14E-2
3.000	-7.98E+0	6.64E+0	-1.92E+0	2.37E-1	-1.04E-2
4.000	-7.12E+0	5.78E+0	-1.61E+0	1.90E-1	-7.98E-3
5.000	-6.39E+0	5.08E+0	-1.38E+0	1.58E-1	-6.36E-3
6.500	-4.80E+0	3.68E+0	-9.37E-1	9.76E-2	-3.47E-3
8.000	-3.42E+0	2.51E+0	-5.80E-1	5.15E-2	-1.34E-3
10.000	-2.19E+0	1.51E+0	-2.87E-1	1.53A-2	2.38E-4
PGA	-2.13A+0	1.94E+0	-5.04E-1	5.82E-2	-2.50E-3
PGV	-2.25E+0	1.95E+0	-5.18E-1	6.14E-2	-2.73A-3

Table 4.3 Continued.

<i>T</i> (sec)	<i>s</i> ₅	<i>s</i> ₆	<i>s</i> ₇	<i>s</i> ₈	<i>s</i> ₉
0.010	-1.44E+0	1.24E+0	-2.89E-1	3.09E-2	-1.25E-3
0.013	-1.35E+0	1.20E+0	-2.80E-1	3.01E-2	-1.23A-3
0.016	-1.08E+0	1.04E+0	-2.47E-1	2.69E-2	-1.11E-3
0.020	-1.27E+0	1.25E+0	-3.17E-1	3.62E-2	-1.55E-3
0.025	-1.45E+0	1.37E+0	-3.37E-1	3.73A-2	-1.54E-3
0.030	-2.24E+0	1.98E+0	-5.09E-1	5.78E-2	-2.44E-3
0.040	-3.31E+0	2.66E+0	-6.68E-1	7.42E-2	-3.06E-3
0.050	-4.23A+0	3.29E+0	-8.32E-1	9.30E-2	-3.87E-3
0.065	-3.96E+0	2.87E+0	-6.67E-1	6.88E-2	-2.65E-3
0.080	-3.14E+0	2.18E+0	-4.67E-1	4.47E-2	-1.60E-3
0.100	-2.45E+0	1.57E+0	-2.89E-1	2.30E-2	-6.57E-4
0.130	-1.38E+0	6.26E-1	-1.16E-2	-1.09E-2	8.28E-4
0.160	-2.00E-1	-3.37E-1	2.57E-1	-4.25E-2	2.18E-3
0.200	8.20E-1	-1.08E+0	4.40E-1	-6.10E-2	2.85E-3
0.250	1.78E+0	-1.77E+0	6.07E-1	-7.83A-2	3.50E-3
0.300	2.25E+0	-2.00E+0	6.33A-1	-7.70E-2	3.27E-3
0.400	2.42E+0	-1.94E+0	5.56E-1	-6.17E-2	2.39E-3
0.500	8.56E-1	-4.53A-1	6.46E-2	5.22E-3	-8.30E-4
0.650	-6.67E-1	9.28E-1	-3.71E-1	6.18E-2	-3.43A-3
0.800	-2.12E+0	2.15E+0	-7.30E-1	1.05E-1	-5.29E-3
1.000	-4.47E+0	4.05E+0	-1.27E+0	1.71E-1	-8.14E-3
1.300	-5.49E+0	4.77E+0	-1.44E+0	1.85E-1	-8.46E-3
1.600	-5.88E+0	4.98E+0	-1.46E+0	1.83A-1	-8.16E-3
2.000	-6.01E+0	4.99E+0	-1.43A+0	1.75E-1	-7.59E-3
2.500	-4.88E+0	3.95E+0	-1.09E+0	1.26E-1	-5.17E-3
3.000	-4.18E+0	3.32E+0	-8.86E-1	9.89E-2	-3.85E-3
4.000	-2.63A+0	1.96E+0	-4.62E-1	4.24E-2	-1.18E-3
5.000	-1.38E+0	9.09E-1	-1.42E-1	1.32E-3	7.11E-4
6.500	-3.93A-1	9.83A-2	9.53A-2	-2.78E-2	1.96E-3
8.000	-6.87E-3	-1.89E-1	1.69E-1	-3.53A-2	2.20E-3
10.000	2.68E-1	-3.86E-1	2.17E-1	-3.97E-2	2.30E-3
PGA	-1.44E+0	1.24E+0	-2.85E-1	3.02E-2	-1.22E-3
PGV	-1.76E+0	1.38E+0	-3.26E-1	3.50E-2	-1.42E-3

Adjustment of the generic model to a specific region includes any required modifications to the source and attenuation parameters, as well as determination of an empirical calibration factor that accounts for residual effects that are missing and/or different in the simulations compared to the observed motions. In this study, we assume that the magnitude (F_M) and saturation (h) effects determined from simulations are transferable to other regions. However, the stress parameter may vary regionally; the generic GMPE is directly adjusted for this effect when the regional value of stress parameter is plugged into $F_{\Delta\sigma}$. The required modifications for regional attenuation can be done by means of Z and γ . We recommend keeping the presumed Z model (geometric spreading) as it is defined in the generic model unless there is compelling evidence for its modification. The anelastic attenuation coefficient, γ , is determined using empirical data at regional distances for the region of interest; such data can be obtained from weak-motion studies. The calibration factor, C , is calculated through the analysis of residuals between observed motions in the target region and the GMPE, after application of the regional values of $\Delta\sigma$, Z , and γ .

4.4 AN EXAMPLE APPLICATION: ADJUSTMENT OF THE GENERIC GMPE FOR CENA

As an example implementation of the method, we adjust the generic GMPE for CENA using ground motions obtained in the region. We use the database of PGA, PGV, and 5%-damped PSA from the NGA-East flatfile, for CENA earthquakes of $M \geq 3.0$ that were recorded by at least three stations within 600 km. We consider both natural and induced earthquakes in the region. However, ground motions recorded in the Gulf Coast regions were excluded due to considerably different attenuation attributes in this region [EPRI 2004]. We use the average orientation-independent horizontal-component ground motions calculated based on the RotD50 measure [Boore 2010], as provided in NGA-East flatfile; this is approximately equivalent to geometric mean motions as provided in the simulations. Figure 4.5 shows a map of the epicenters of the study events; Figure 4.6 is a map of stations and their site condition; and Figure 4.7 shows the magnitude-distance distribution of the selected records.

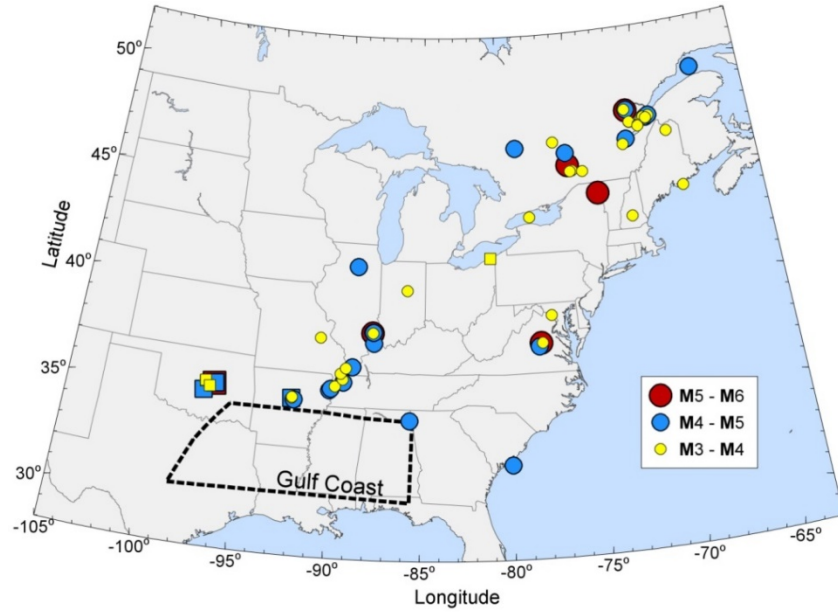


Figure 4.5 Epicenters of study events in CENA. Circles show epicenter locations of naturally-occurring earthquakes and squares indicate events that have been flagged as potentially induced in the NGA-East flatfile. Dashed line marks the Gulf Coast region.

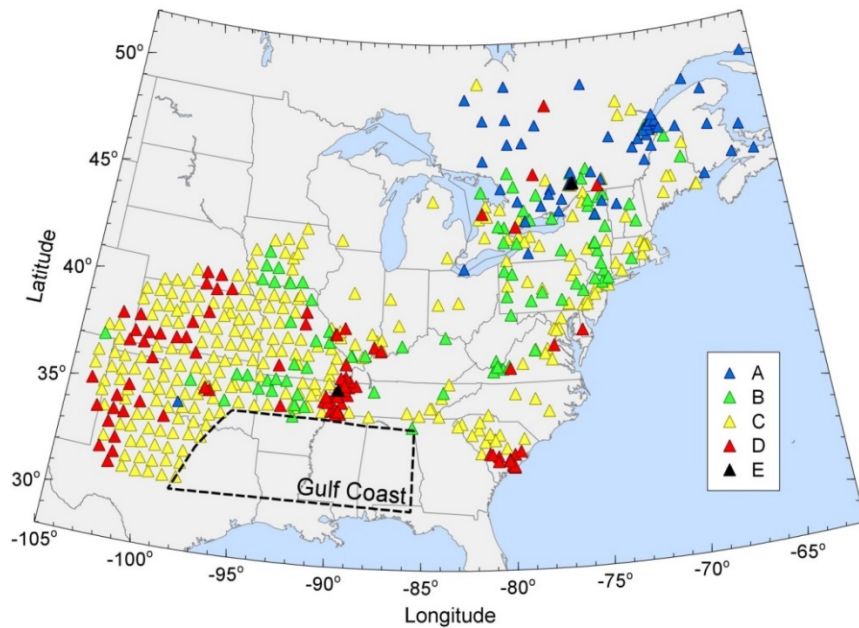


Figure 4.6 Locations of recording stations and their NEHRP site classification: (A) $V_{S30} > 1500$ m/sec; (B) 760 m/sec $< V_{S30} \leq 1500$ m/sec; (C); and (D) 180 m/sec $< V_{S30} \leq 360$ m/sec; and $V_{S30} \leq 180$ m/sec [NEHRP 2000]. We excluded stations located in the Gulf Coast region (dashed line).

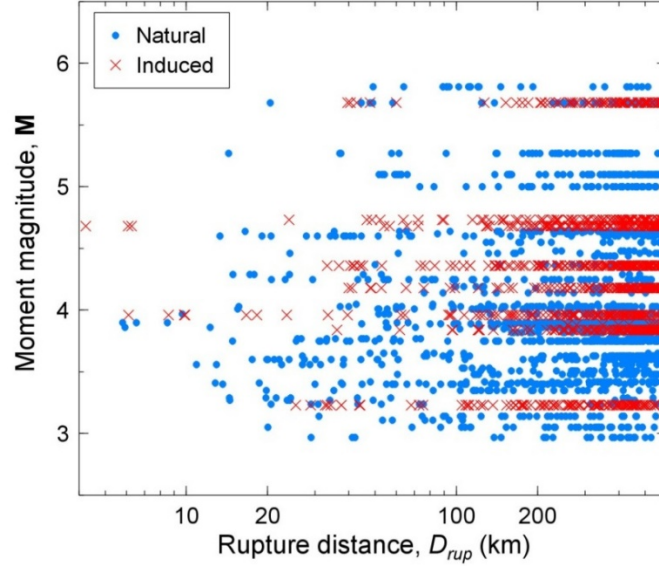


Figure 4.7 Magnitude-distance distribution of the selected ground motions in CENA. Ground motions recorded beyond 600 km are not considered.

In the analysis, we consider response spectra up to a maximum usable period to reduce the impact of long-period noise on the adjusted GMPE. For a given ground-motion record, the maximum usable period, T_{\max} , is defined as

$$T_{\max} = \frac{1}{\max[(1.25f_{lc}), (f_{\min})]} \quad (4.18)$$

where f_{\min} is the low-cut filter frequency of the record reported in the NGA-East flatfile, and f_{lc} is the limiting frequency below which spectral amplitudes are assumed to be noise-dominated. We describe f_{\min} as

$$f_{\min} = \max[(0.1), (10^{0.75-M/3})] \quad (4.19)$$

Equation (4.19) is defined such that it provides an overall agreement with the geometric mean of the factored filter frequencies (i.e., $1.25f_{lc}$), as seen in Figure 4.8. For $M < 6$, the f_{\min} model given for CENA is relatively less conservative than that was used for California by Yenier and Atkinson [2015c], because ground motions attenuate more slowly in CENA, providing useable signal to greater distances.

We correct the recorded ground-motion amplitudes to the equivalent values for NEHRP B/C site conditions ($V_{S30} = 760$ m/sec) using the F_S function adopted from BSSA14. This function is based on the values of V_{S30} and PGA_r for each record, where the V_{S30} values are given in the NGA-East flatfile, and we assume that PGA_r can be reasonably estimated from BSSA14 as

an approximation. We deliberately use BSSA14 rather than a CENA GMPE for this purpose, as we do not wish the higher frequency content in CENA to impose greater nonlinearity.

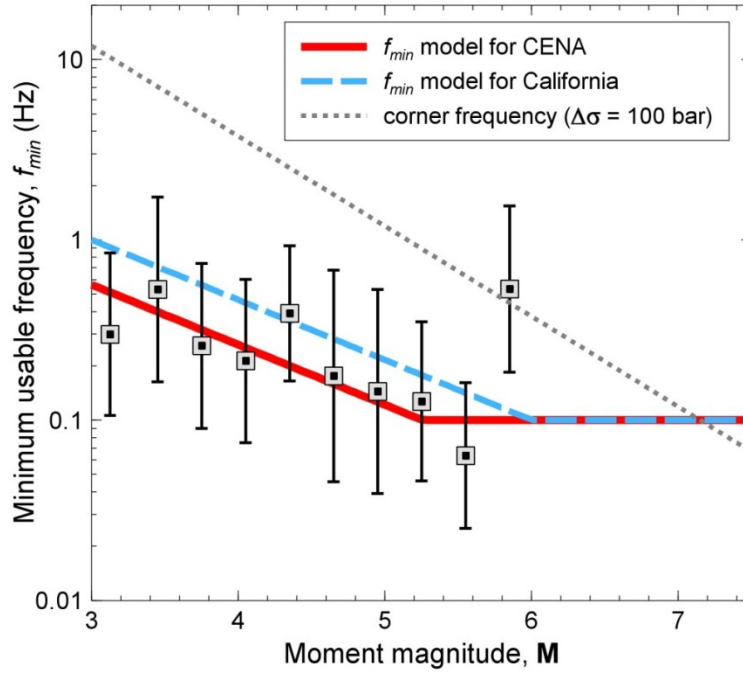


Figure 4.8 Minimum usable frequency (f_{\min}) model considered for records in CENA (solid line). Squares indicate the geometric mean of the factored low-cut filter frequencies (i.e., $1.25 f_{lc}$) determined for evenly spaced magnitude bins. The error bars represent one standard deviation about the mean values. The dashed line indicates the f_{\min} model used for California by Yenier and Atkinson [2015c]. The dotted line shows the corner frequency of the Brune [1970] source model for $\Delta\sigma = 100$ bar.

4.4.1 Regional Attenuation

Empirical studies suggest that the geometrical spreading of Fourier amplitudes in CENA can be adequately described as $R^{-1.3}$ within 50 km and $R^{-0.5}$ at further distances [Atkinson and Boore 2014; Babaie Mahani and Atkinson 2012]. We therefore use the generic bilinear Z model ($b_1 = -1.3$, $b_2 = -0.5$ and $R_t = 50$ km) without modification. The only attenuation adjustment needed is for the regional anelastic attenuation. As described in the methodology presented earlier, we determine the regional anelastic attenuation (γ_{CENA}) from the empirical data using:

$$\ln Y_{B/C,ij} - (F_{M,i} + F_{Z,ij}) = E_i + \gamma_{CENA} D_{RUP,ij} \quad (4.20)$$

where $Y_{B/C,ij}$ represents the B/C-corrected motion for event i and station j . $F_{M,i}$, and $F_{Z,ij}$ are the magnitude and geometrical spreading functions evaluated for the known magnitude and distance ($D_{RUP,ij}$) of the record, respectively. The E_i term is an event term, which provides the average

adjustment required to match observed amplitudes from event i . Its value can be attributed to two main factors: (i) the difference between the reference stress implicitly carried by the F_M function (100 bars) and its true value for the i^{th} event (modeled by $F_{\Delta\sigma}$); and (ii) the overall difference between synthetics and observed motions in CENA (modeled by C). We calculate the regional anelastic attenuation coefficient (γ_{CENA}) and event terms (E_i) for each oscillator period and ground-motion parameter; the values of the γ_{CENA} term are listed Table 4.4.

Table 4.4 Anelastic attenuation to adjust the generic GMPE for CENA.

T (sec)	γ_{CENA}
0.010	-4.66E-3
0.013	-4.69E-3
0.016	-4.69E-3
0.020	-4.67E-3
0.025	-4.88E-3
0.030	-5.11E-3
0.040	-5.27E-3
0.050	-5.47E-3
0.065	-5.71E-3
0.080	-5.79E-3
0.100	-5.64E-3
0.130	-5.24E-3
0.160	-4.77E-3
0.200	-4.20E-3
0.250	-3.65E-3
0.300	-3.12E-3
0.400	-2.44E-3
0.500	-2.04E-3
0.650	-1.64E-3
0.800	-1.43A-3
1.000	-1.26E-3
1.300	-1.06E-3
1.600	-1.17E-3
2.000	-1.02E-3
2.500	-1.06E-3
3.000	-1.09E-3
4.000	-1.30E-3
5.000	-9.35E-4
6.500	-7.87E-4
8.000	-6.43A-4
10.000	-3.65E-4
PGA	-4.67E-3
PGV	-2.79E-3

4.4.2 Regional Stress Parameter

The stress parameter is often determined by matching the predicted and observed spectral amplitudes at short periods for the specified moment. However, this approach results in a non-unique solution for $\Delta\sigma$ due to the trade-off between earthquake source and attenuation [Boore et al. 2010; Yenier and Atkinson 2014]. Moreover, $\Delta\sigma$ has little effect on the response spectrum at long periods (Figure 4.3), especially for small-to-moderate events, restricting our ability to calibrate the response spectral amplitudes at long periods. To ensure a model calibration that is consistent over a wide period range, we determine the stress parameter by matching the observed spectral shape for the known moment (i.e., the corner frequency), rather than spectral amplitudes. This breaks the trade-off between source and attenuation parameters, transferring the overall amplitude difference to the calibration factor C [Yenier and Atkinson, 2015c]. Following this technique, we use a grid search to determine $\Delta\sigma$ for each event. We select the best-fitting $\Delta\sigma$ based on the minimum standard deviation of residuals between E_i and $F_{\Delta\sigma}$, over a wide period range ($0.01 \text{ sec} \leq T \leq 10 \text{ sec}$); by minimizing the standard deviation of residuals, we are effectively finding the best shape, rather than the best level.

Figure 4.9 shows the shape-based $\Delta\sigma$ values obtained from CENA events as a function of focal depth (d). The mean stress determined for evenly spaced focal depth bins shows an increasing trend from $\Delta\sigma \approx 30 \text{ bar}$ at $d = 2.5 \text{ km}$ to $\Delta\sigma \approx 250 \text{ bar}$ at $d = 10 \text{ km}$; it remains relatively constant at greater depths. Figure 4.10 shows the best-fitting $\Delta\sigma$ as a function of magnitude. For $\mathbf{M} < 5$, the stress parameter shows large variability. Despite the large variation of $\Delta\sigma$ values at small magnitudes, the depth effect is clearly visible by the distinct separation of depth-clustered stresses. For $\mathbf{M} > 5$, the stress parameter attains a value of $\Delta\sigma \approx 300 \text{ bar}$, on average; note that this is about three times the corresponding value for California events.

We regress the best-fitting $\Delta\sigma$ values to develop a regional stress model for CENA. Based on the observations made in Figures 4.9 and 4.10, we constrain the model to attain $\Delta\sigma = 300 \text{ bar}$ for $\mathbf{M} \geq 5$ and $d \geq 10 \text{ km}$. The mean value of the stress parameter for earthquakes in CENA is expressed as:

$$\ln \Delta\sigma_{\text{CENA}} = 5.704 + \min[0, 0.29(d - 10)] + \min[0, 0.229(\mathbf{M} - 5)] \quad (4.21)$$

The estimates of Equation (4.21) for different magnitudes and depths are shown in Figures 4.9 and 4.10. The mean residuals between the observed and predicted $\Delta\sigma$ values attain values around zero, as illustrated in Figure 4.11. Overall, the proposed $\Delta\sigma$ model provides a good agreement with the $\Delta\sigma$ values determined from CENA events based on the inferred spectral shape.

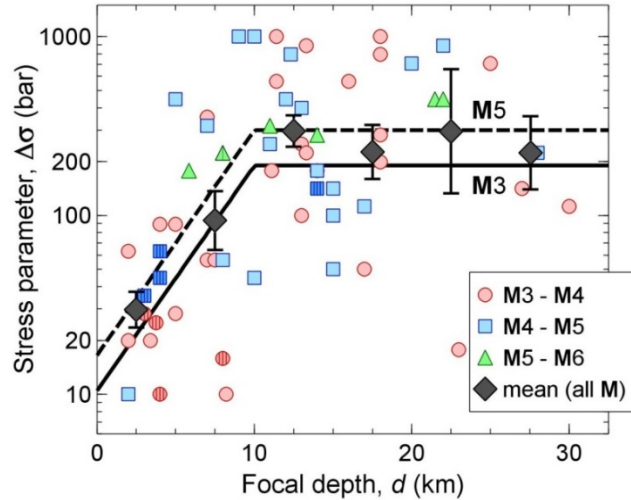


Figure 4.9 Best-fitting stress parameters ($\Delta\sigma$) determined for CENA events as a function of focal depth (d). $\Delta\sigma$ values are clustered into different magnitude bins as shown in the legend. Hatched symbols indicate $\Delta\sigma$ values obtained from the induced events. Diamonds represent the mean $\Delta\sigma$ calculated for evenly spaced focal depth bins over all magnitudes, and the error bars show standard error about the mean stress. Lines indicate the derived $\Delta\sigma$ model [Equation (4.21)] evaluated for M3 (solid) and M5 (dashed).

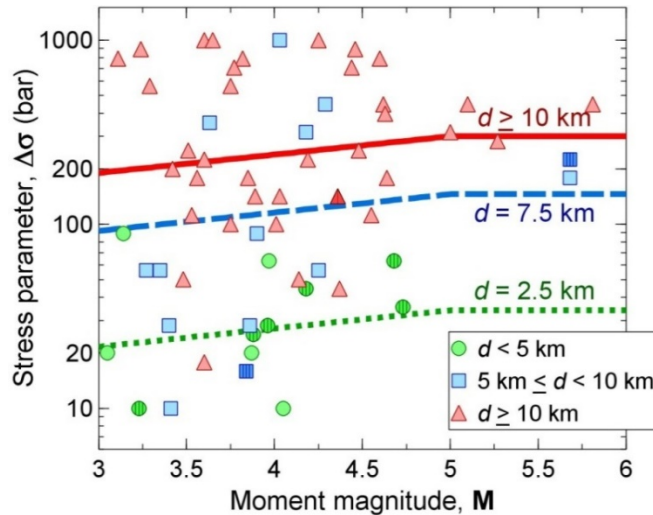


Figure 4.10 Best-fitting stress parameters ($\Delta\sigma$) determined based on matching the observed response spectral shape for CENA events, as a function of magnitude. $\Delta\sigma$ values are clustered into different focal depth (d) bins as shown in the legend. Hatched symbols show $\Delta\sigma$ values obtained from the induced events. Lines indicate the derived $\Delta\sigma$ model [Equation (4.21)] evaluated for $d = 2.5$ km (dotted), $d = 7.5$ km (dashed), and $d \geq 10$ km (solid).

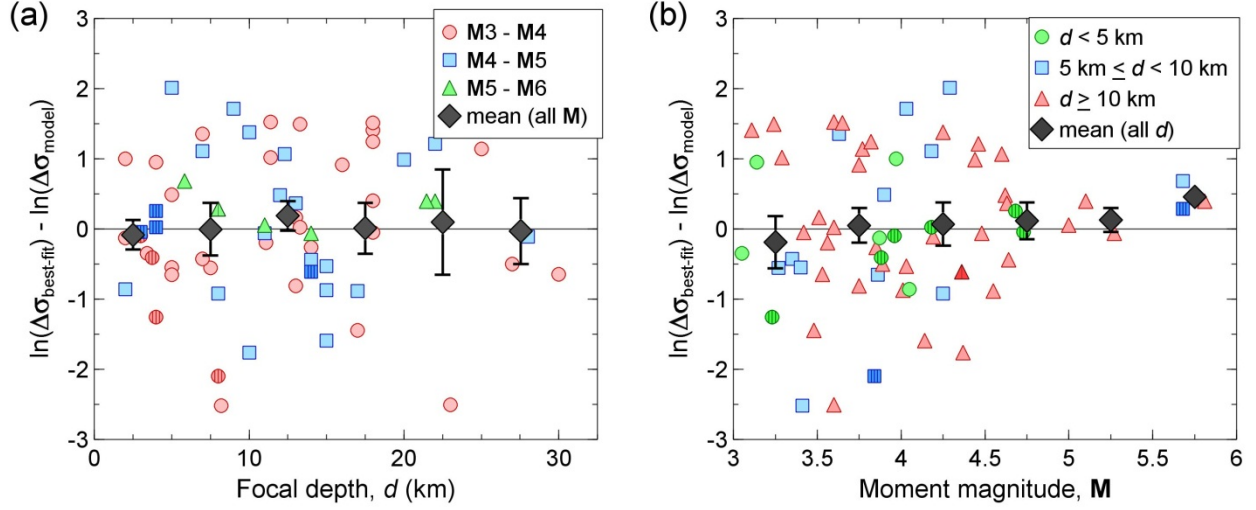


Figure 4.11 Residuals between the best-fitting $\Delta\sigma$ values obtained from CENA events and the estimates of the $\Delta\sigma$ model [Equation (4.21)] evaluated for the known magnitudes and focal depths of the study events.

4.4.3 Calibration Factor

An overall calibration factor is needed to reconcile the predictions with observed amplitudes in the target region, accounting for effects missing and/or different in simulations (e.g., discrepancies between the assumed and true values of crustal properties, site amplification, κ_0 , and path duration). We calculate the calibration factor based on the analysis of residuals:

$$\delta_{ij} = \ln Y_{B/C,ij} - \left(F_{M,i} + F_{\Delta\sigma CENA,i} + F_{Z,ij} + \gamma_{CENA} D_{RUP,ij} \right) \quad (4.22)$$

where δ_{ij} represents the residual for the ground motion obtained from event i at station j , for a given spectral period or peak motion. $F_{\Delta\sigma CENA,i}$ is the stress adjustment factor evaluated for $\Delta\sigma$ from Equation (4.21) for the known magnitude and focal depth of event i . The last term accounts for the regional anelastic attenuation determined earlier.

Figure 4.12 shows the event residuals ($\delta_i = \sum \delta_{ij} / n_i$, where n_i is the number of records obtained from event i ; $n_i \geq 3$ at a given period) as a function of magnitude. δ_i generally attains negative values and appears to be randomly distributed, showing no distinct attributes for natural and induced events. The mean that, in general, δ_i values determined at evenly spaced magnitude bins show no magnitude-dependent trend. This suggests that the magnitude scaling of ground motions in CENA is well captured by the F_M function, at least for the available data.

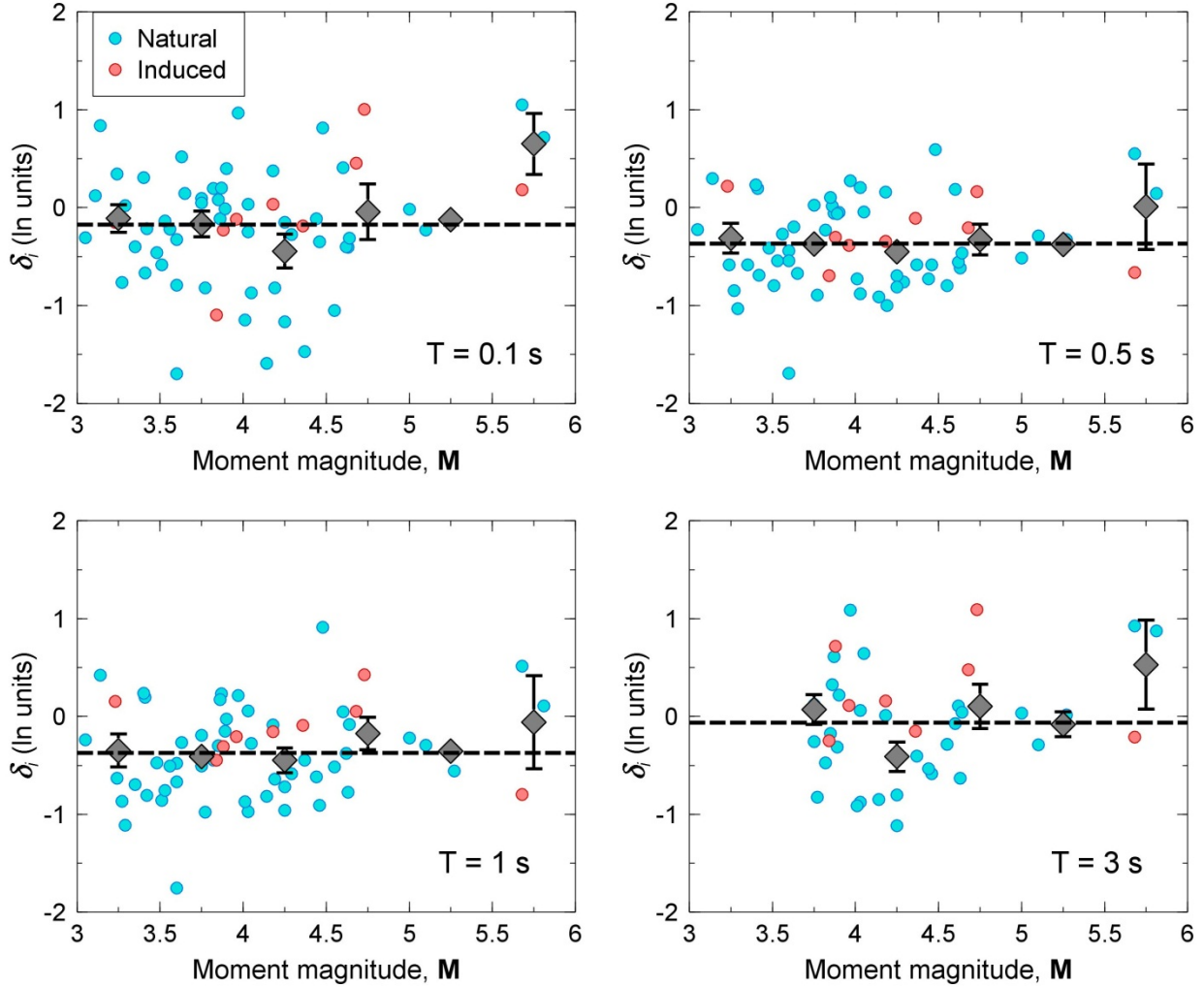


Figure 4.12 Average of residuals determined for each event that have at least 3 observations at a given period (δ_i , circles). Diamonds show mean of δ_i values determined for evenly spaced magnitude bins, and error bars represent the standard error about the mean. Dashed lines indicate the event-based calibration factor (C_e) that is defined as the average of δ_i values over all magnitudes, at a given period.

Based on the observations made in Figure 4.12, we calculate an event-based calibration factor (C_e) as the average of δ_i values over all magnitudes, for each spectral period/peak motion. The C_e term fluctuates with period between 0 and -0.5 (ln units) for periods $T < 3$ sec and attains positive values with an increasing trend at larger periods, as shown in Figure 4.13. This increasing trend at long periods may be due to the fact that stochastic simulations are inherently limited in their ability to generate the coherent motions seen at long periods. We describe C_e as:

$$C_e = \begin{cases} -0.25 + \max[0, 0.39 \ln(T/2)] & T \leq 10 \text{ sec} \\ -0.25 & \text{for PGA} \\ -0.25 & \text{for PGV} \end{cases} \quad (4.23)$$

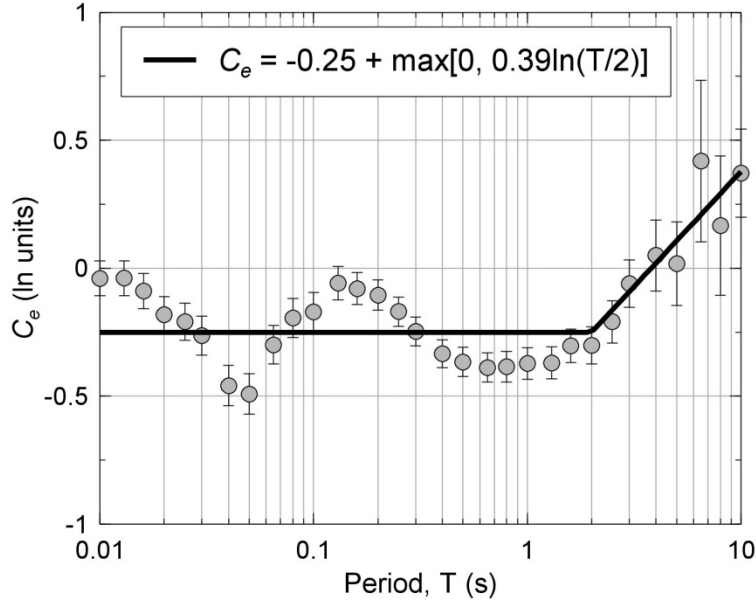


Figure 4.13 Event-based calibration factor (C_e , solid line) for CENA. Circles indicate average C_e values determined for all events at each period, and error bars represent the standard error about the mean.

We subtract the event-based δ_i term from the individual residuals to calculate the average residual at each station (i.e., $\delta_j = \sum (\delta_{ij} - \delta_i) / n_j$, where n_j is the number of observations at station j ; $n_j \geq 3$ at a given period).

Figure 4.14 illustrates the variation of δ_j as a function of V_{S30} . The mean δ_j determined for NEHRP C sites attain near zero value, in general, suggesting that the BSSA14 site amplification model is reasonable for this site class. However, ground motions on NEHRP B sites are under predicted by $\sim 15\%$ and ground motions at NEHRP D sites are over predicted by $\sim 20\%$, on average. The mean δ_j determined for NEHRP A sites is near zero, except for short periods. For $T < 0.1$ sec, ground motions at NEHRP A sites are under predicted by $\sim 20\%$, on average.

Finally, we correct the individual residuals for the event and station terms (i.e., $\delta'_{ij} = \delta_{ij} - \delta_i - \delta_j$) to assess the performance of the assumed geometrical spreading function. Figure 4.15 compares the δ'_{ij} values as a function of rupture distance. The mean δ'_{ij} determined for log-spaced distance bins attains near zero values at $D_{RUP} > 150$ km, suggesting that γ_{CENA} parameter can successfully represent the overall attenuation at far distances. However, the mean

δ'_{ij} deviates from the horizontal zero-line and decreases with distance for $D_{RUP} < 150$ km, as shown in the figure. This discrepancy might be attributable to the path-duration model. In the simulations, we used a path-duration model derived primarily from observed motions in WNA. Boore and Thompson [2015] recently reported that the path duration in ENA is much longer than that in WNA, particularly at distances less than 150 km. This difference could result in some overestimation of CENA motions for $D_{RUP} < 150$ km because the presumed WNA path-duration model is implicitly carried via the F_Z function to CENA.

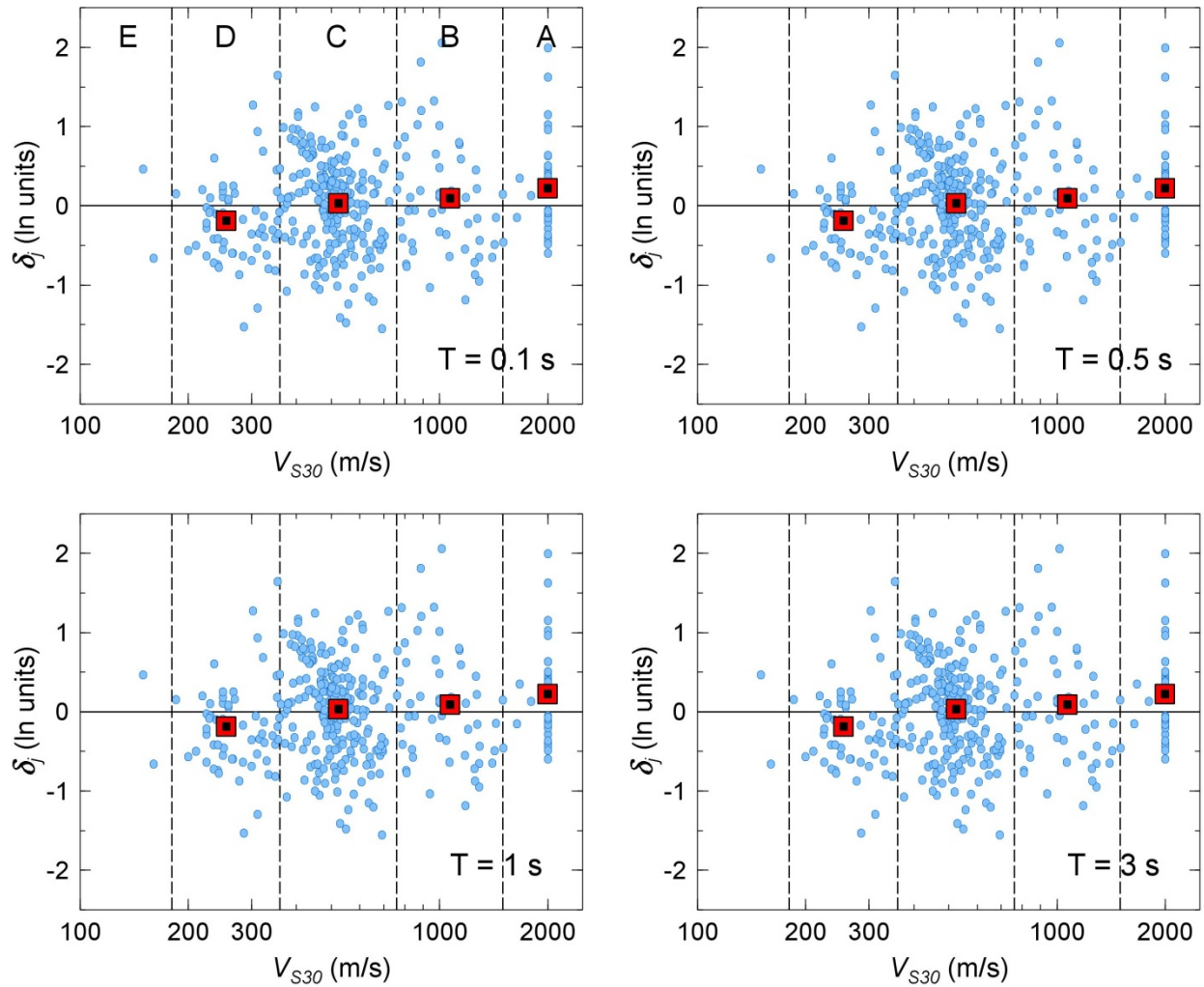


Figure 4.14 Event-corrected average residuals for each station (δ_j , circles) as a function of V_{S30} . Mean of δ_j values for NEHRP site classes are shown by squares (standard errors for the mean values are smaller than the symbols).

We consider an additional minor calibration term for regional differences in the path duration. We describe this path-related calibration (C_p) as:

$$C_p = \begin{cases} \Delta b_3 \ln(R/150) & R \leq 150 \text{ km} \\ 0 & R > 150 \text{ km} \end{cases} \quad (4.24)$$

where Δb_3 represents a calibration for the geometrical attenuation rate in response spectrum domain. We determine the Δb_3 term from the regression of δ'_{ij} based on Equation (4.24) at each period and peak motion separately. Figure 4.16 shows the variation of Δb_3 coefficients as a function of period. Its value could be determined only up to $T = 3$ sec due to the limited data at $D_{RUP} < 100$ km for longer periods. We smooth Δb_3 values as:

$$\Delta b_3 = \begin{cases} \min \{0.095, 0.030 + \max[0, 0.095 \ln(T/0.065)]\} & T \leq 10 \text{ sec} \\ 0.030 & \text{for PGA} \\ 0.052 & \text{for PGV} \end{cases} \quad (4.25)$$

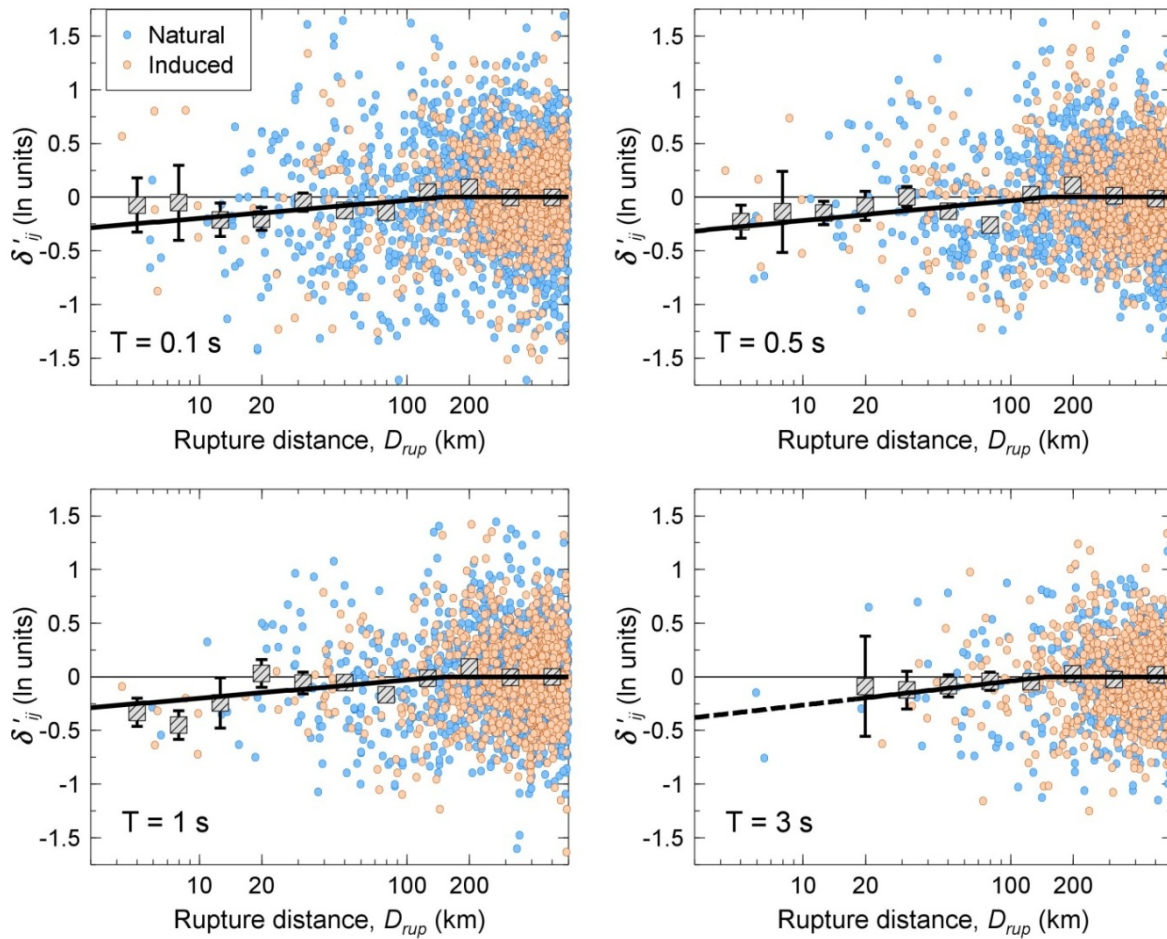


Figure 4.15 Event- and site-corrected residuals (δ'_{ij}) as a function of distance, for ground motions obtained from natural and induced events. Squares show the mean δ'_{ij} values determined for logarithmically spaced distance bins and error bars indicate the standard error about the mean. Solid line represents the fitted path-related calibration model (C_p).

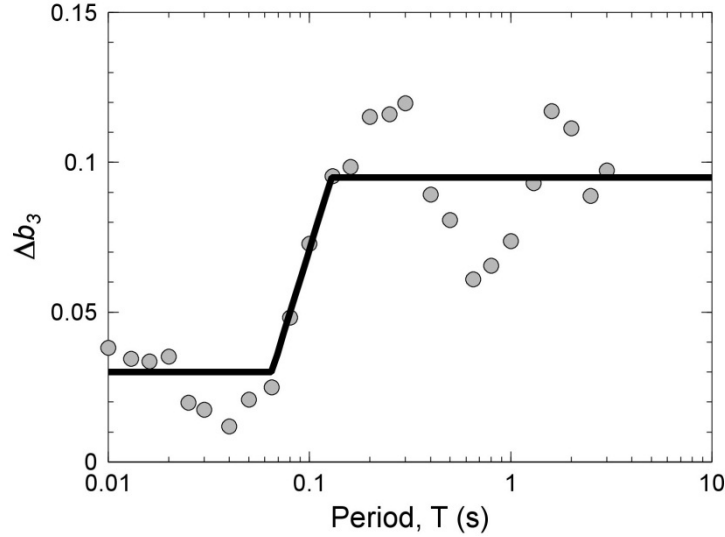


Figure 4.16 Δb_3 values determined from regression analysis (circles) and the Δb_3 smoothed model for CENA [Equation (4.25), solid line].

4.4.4 CENA-Adjusted GMPE

The total calibration needed for the adjusted GMPE is the summation of C_e and C_p terms. This closes the systematic gaps between simulation-based predictions and observed motions in CENA. The resultant CENA-adjusted prediction equation is given as:

$$\ln Y_{\text{CENA}} = F_M + F_{\Delta\sigma\text{CENA}} + F_Z + Y_{\text{CENA}} D_{\text{RUP}} + F_S + C_e + C_p \quad (4.26)$$

Figure 4.17 illustrates PSA values predicted from Equation (4.26) for magnitudes **M4** to **M8** as a function of rupture distance, for NEHRP B/C site condition ($V_{S30} = 760$ m/sec). The B/C-corrected ground motions obtained from earthquakes in CENA are also shown in the figure, for two magnitude ranges: **M3.5–M4.5** and **M4.5–M5.5**. The CENA-adjusted GMPE is in good agreement with the empirical data, where available, and provides seismologically informed predictions of average ground motions for moderate-to-large magnitudes ($M > 6$).

We also provide ground-motion predictions for very hard rock site condition ($V_{S30} = 3000$ m/sec). Atkinson [2012b] derived site factors that allow amplitude conversion between sites with $V_{S30} = 760$ m/sec and $V_{S30} \geq 2000$ m/sec, using the predictions of Atkinson and Boore [2006]. The site factors are given independent of distance, except for very short periods (Table 4.5). For $T \leq 0.025$ s, the site factor is given as a function of epicentral distance (D_{epi}). We convert ground-motion predictions for $V_{S30} = 760$ m/sec [Equation (4.26)] to the equivalent motions for $V_{S30} = 3000$ m/sec based on the site factors of Atkinson [2012b]. Here, we assume that the amplitude difference between sites with $V_{S30} \geq 2000$ m/sec and $V_{S30} = 3000$ m/sec is small enough to neglect. We use $D_{\text{RUP}}-D_{\text{epi}}$ distance conversion method described in Atkinson [2012b] to evaluate site factors for $T \leq 0.025$ sec. Figure 4.18 shows a comparison of predicted response spectra for $V_{S30} = 760$ m/sec and $V_{S30} = 3000$ m/sec.

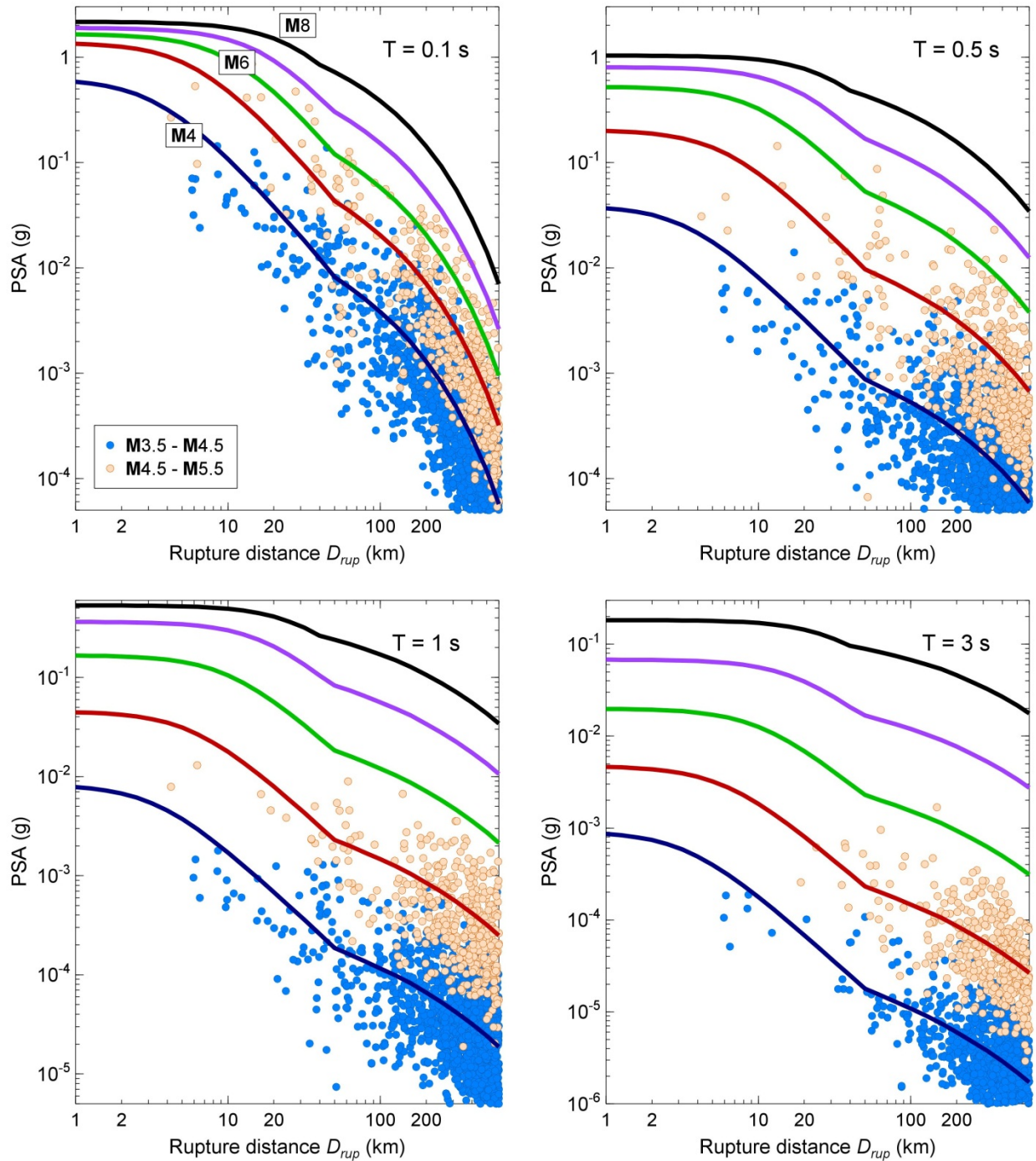


Figure 4.17 PSA predictions from the adjusted GMPE [Equation (4.26)] for magnitudes **M4** to **M8** (focal depth, $d = 10$ km), for $V_{S30} = 760$ m/sec (lines). Circles represent the B/C-corrected ground motions obtained from earthquakes in CENA for two magnitude ranges: **M3.5–M4.5** and **M4.5–M5.5**.

Table 4.5 Site conversion factors from Atkinson [2012b].

T (sec)	$\ln Y_{V_{S30}=760 \text{ m/sec}} - Y_{V_{S30} \geq 2000 \text{ m/sec}}$
≤ 0.025	$-0.69 + 0.15 \ln(D_{epi})$
0.050	-0.23
0.100	0.07
0.200	0.28
0.333	0.32
0.500	0.32
1.000	0.25
2.000	0.21
≥ 5.000	0.14
PGA	$-0.69 + 0.15 \ln(D_{epi})$
PGV	0.21

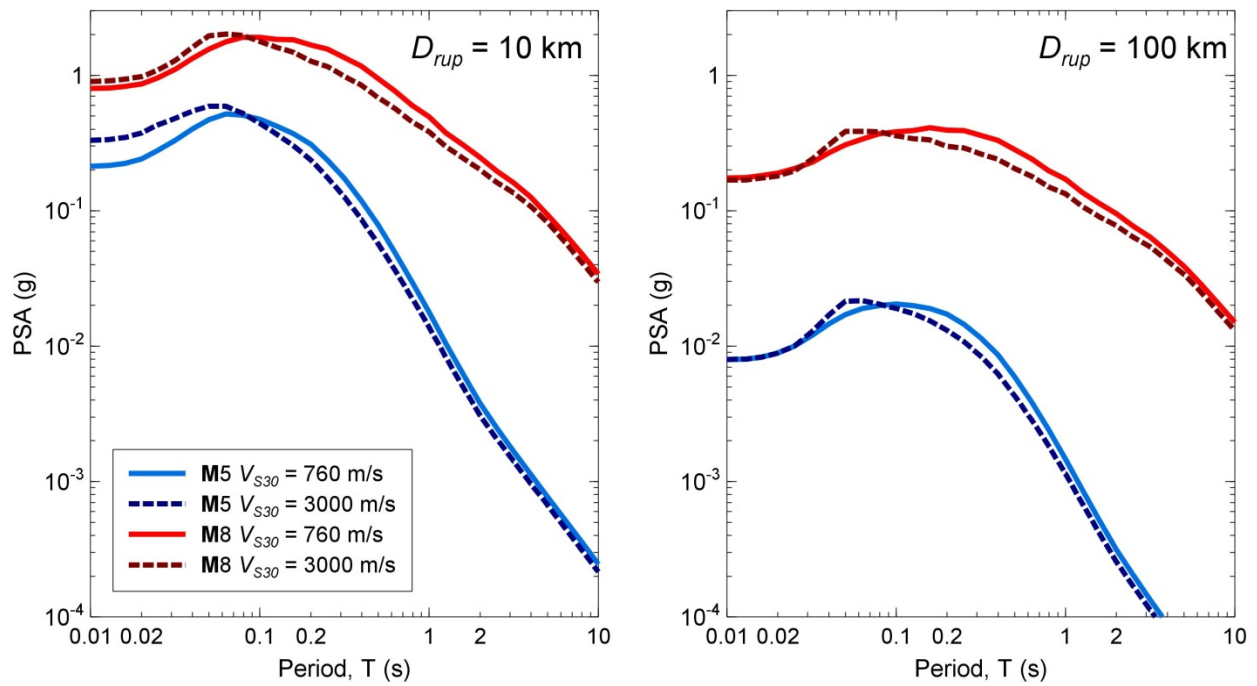


Figure 4.18 Predicted response spectra for CENA for $V_{S30} = 760$ m/sec and $V_{S30} = 3000$ m/sec.

4.5 CONCLUSIONS

We conclude that the generic GMPE approach provides a calibrated model of predicted ground motions in CENA that agrees with average motions from the NGA-East database, and is constrained by simulation-based scaling principles that have been demonstrated to work in California over a wide range of magnitudes and distances. We have provided calibrated median predictions of ground motions in CENA for average horizontal-component peak ground motions and 5%-damped response spectra (up to $T = 10$ sec), for magnitudes **M3** to **M8** and distances < 600 km. The approach that we have taken whereby we cast our model into a framework that is parameterized by the basic seismological parameters of moment, stress, and attenuation has both conceptual and practical advantages. We can create easily understandable and documentable alternative GMPEs by considering a range of possible parameter values that might be reasonable for the region (or a subset of the region). For each parameter set, we may use the empirical data to derive a new calibration factor for each frequency, such that the overall residuals are minimized for the given model. Analysis of the residual trends and their variability under the alternative models then provides information on the limitations of the alternative parameter sets.

4.6 ACKNOWLEDGMENTS

This study was supported by the Natural Sciences and Engineering Research Council of Canada, by the NGA-East project, and by the USGS NEHRP program under Grant G13AP00067. Any opinions, findings, and conclusions or recommendations expressed in this material are those of the authors and do not necessarily reflect those of the sponsoring agencies.

4.7 ELECTRONIC APPENDIX FOR CHAPTER 4

4A Model Output (Excel workbook)

5 Ground-Motion Prediction Equations for CENA Using the Hybrid Empirical Method in Conjunction with NGA-West2 Empirical Ground-Motion Models

Shahram Pezeshk

Department of Civil Engineering
The University of Memphis

Arash Zandieh

Lettis Consultants International, Inc.
Boulder, Colorado

Kenneth W. Campbell

CoreLogic EQECAT
Oakland, California

Behrooz Tavakoli

Bechtel Power Corporation
San Francisco, California

Abstract

The hybrid empirical method (HEM) of simulating ground-motion intensity measures (GMIMs) in a target region uses stochastically simulated GMIMs in the host and target regions to develop adjustment factors that are applied to empirical GMIM predictions in the host region. In this study, the HEM approach was used to develop two new ground-motion prediction equations (GMPEs) that incorporate two alternative methods of large-magnitude scaling for a target region defined as Central and Eastern North America (CENA), excluding the Gulf Coast region. The method uses five new empirical GMPEs developed as part of the PEER NGA-West2 project to estimate GMIMs in the host region and two new seismological models to stochastically simulate GMIMs in both the host and target regions. The GMIMs evaluated in this study are peak ground acceleration (PGA) and 5%-damped pseudo-acceleration response-spectral ordinates (PSA) for $T = 0.01-10$ sec, $M = 3.0-8.0$, and $R_{RUP} \leq 1000$ km, although we caution that the GMPEs are

best constrained for $R_{RUP} < 300 - 400$ km. The predicted GMIMs are for a CENA reference hard-rock site condition defined by the site parameters $V_{s30} = 3000$ m/sec and $\kappa_0 = 0.006$ sec.

5.1 INTRODUCTION

In this study, we use the hybrid empirical method (HEM) to develop ground-motion prediction equations (GMPEs) for Central and Eastern North America (CENA) as part of the NGA-East project [Goulet et al. 2014]. The HEM approach [Campbell 2003] is a well-accepted methodology to develop GMPEs in areas with limited ground-motion recordings. In the HEM approach, ground-motion intensity measures (GMIMs) in a target region (CENA in this study) are predicted from empirical GMPEs in a host region (Western North America, WNA, in this study) using seismologically-based adjustment factors between the two regions. The adjustment factors are calculated as the ratio of stochastically simulated GMIMs in the two regions.

Using appropriate regional seismological parameters in the stochastic simulations, the calculated adjustment factors take into account differences in earthquake source, wave-propagation, and site-response characteristics between the two regions. The empirically derived GMPEs for the host region are transferred to the target region by applying the regional adjustment factors to the empirical GMIM predictions and deriving a GMPE from these HEM-based estimates using standard regression analysis. The HEM approach has been used by several researchers to develop GMPEs in CENA [e.g., Campbell 2002, 2003, 2007, 2008, 2011, Tavakoli and Pezeshk 2005, Pezeshk et al. 2011], in central Europe [Scherbaum et al. 2005] and in southern Spain and southern Norway [Douglas et al. 2006]. Campbell [2014] provides a complete review of these and other applications of the HEM approach.

The purpose of this study is to update the HEM-based GMPEs of Campbell [2007, 2008, 2011] and Pezeshk et al. [2011] for CENA using the five empirical GMPEs developed in the PEER NGA-West2 project [Bozorgnia et al. 2014] for WNA other shallow crustal active tectonic regions in conjunction with the latest information on CENA and WNA seismological parameters. Although we use stochastic point-source (PS) models for both CENA and WNA to obtain simulated GMIMs for the development of the regional adjustment factors, we limit their use to $M \leq 6.0$ in order to avoid the need to include finite-fault (FF) effects. The models are then extrapolated to the larger magnitudes of greater engineering interest using two different methods. WNA seismological parameters are taken from the study of Zandieh and Pezeshk [2015], who performed a set of PS inversions intended to match the median GMIM estimates from the NGA-West2 GMPEs. They limited the PS inversions to $M \leq 6.0$ in order to avoid FF effects and to stay within the magnitude range of earthquakes in the NGA-East database [Goulet et al. 2014].

5.2 STOCHASTIC GROUND-MOTION SIMULATIONS

We developed a set of computer routines based on the random vibration theory (RVT) method of Kottke and Rathje [2008] to perform the PS stochastic simulation of GMIM amplitudes using the WNA and CENA seismological models. The output of the program is peak ground acceleration (PGA) and 5%-damped pseudo-acceleration response-spectral ordinates (PSA) at a pre-selected set of spectral periods (T). The regional adjustment factors are calculated as the ratio of the

simulated spectral values for CENA to those for WNA. In the stochastic method, the ground-motion acceleration is modeled as filtered Gaussian white noise modulated by a deterministic envelope function defined by a specified set of seismological parameters [Boore 2003]. The filter parameters are determined by either matching the properties of an empirically defined spectrum of strong ground motion with theoretical spectral shapes or using reliable physical characteristics of the earthquake source and propagation media [Hanks and McGuire 1981, Boore 1983, 2003]. Atkinson et al. [2009] and Boore [2009] investigated the relationship between the stochastic point-source model SMSIM [Boore 2005] and the stochastic finite-fault model EXSIM [Motazedian and Atkinson 2005] and suggested how the two could be aligned to give better agreement in predicted motions from small earthquakes at large distances, where the two models should provide similar results.

In the point-source model, the total Fourier amplitude spectrum (FAS) of the horizontal vibratory ground displacement $Y(M_0, R, f)$ due to shear-wave propagation in an elastic half-space can be modeled by the equation [Boore 2003]:

$$Y(M_0, R, f) = S(M_0, f)P(R, f)G(f)I(f) \quad (5.1)$$

where M_0 is seismic moment (dyne-cm), R is source-to-site distance (km), f is frequency (Hz), $S(M_0, f)$ is the source spectrum, $P(R, f)$ is the path attenuation term, $G(f)$ is the site-response term, and $I(f)$ is a filter representing the type of GMIM. The FAS of acceleration is obtained by multiplying $Y(M_0, R, f)$ by ω^2 , where $\omega = 2\pi f$ is circular frequency.

5.2.1 Effective Point-Source Distance

In the stochastic PS model, the earthquake source is assumed to be concentrated at a point within the crust, which is a reasonable assumption for small earthquakes or when the source-to-site distance is substantially larger than the earthquake source dimensions. Otherwise, FF effects in the form of magnitude and distance saturation begin to influence the ground motions. This reflects the fact that seismic waves with wavelengths much smaller than the earthquake source rupture dimensions do not increase in amplitude as the size of the earthquake and the corresponding energy release increase [e.g., Tavakoli and Pezeshk 2005, Yenier and Atkinson 2014]. It has also been suggested that when fault-rupture lengths are much greater than the closest distance from the site to the rupture surface, the motions recorded at the site will only have contributions from the closest part of the rupture, with the energy from greater distances along the fault arriving in a more attenuated form [Baltay and Hanks 2014, Boore and Thompson 2014].

Atkinson and Silva [2000] defined an effective point-source distance metric R'_{RUP} to use in PS stochastic simulations to mimic the ground-motion saturation effects from FF effects. They also defined a magnitude-dependent equivalent point-source depth h to modify this distance for magnitude saturation effects. Following these authors, we define an effective PS distance metric to use with our PS stochastic simulations with the expression:

$$R'_{RUP} = \sqrt{R_{RUP}^2 + h^2} \quad (5.2)$$

where the pseudo-depth parameter h , also referred to as the FF factor by Boore and Thompson [2014], is defined by the expression:

$$\log h = \begin{cases} \max(-0.05 + 0.15\mathbf{M}, -1.72 + 0.43\mathbf{M}) & \mathbf{M} \leq 6.75 \\ -0.405 + 0.235\mathbf{M} & \mathbf{M} > 6.75 \end{cases} \quad (5.3)$$

which combines the pseudo-depth relationships developed by Atkinson and Silva [2000] and Yenier and Atkinson [2014, 2015a,b] in order to provide a consistent set of effective distances over the entire magnitude range of interest.

We use the effective PS distance metric in the stochastic simulations to evaluate the adjustment factors for a given set of magnitude and distances. This is done by: (1) evaluating the NGA-West2 GMPEs for a given set of \mathbf{M} and R_{RUP} , (2) calculating the corresponding values of R'_{RUP} from Equations (5.2) and (5.3), (3) using the values of R'_{RUP} to determine the stochastic adjustment factors, and (4) using the adjustment factors to derive the HEM-based GMIM estimates for the original set of \mathbf{M} and R_{RUP} .

5.2.2 Site Response

The site-response term $G(f)$ is defined as the product of crustal-amplification and diminution functions [Boore 2003]. Crustal amplification is calculated using the quarter-wavelength (QWL) method, which Boore [2013] now refers to as the square-root-impedance (SRI) method. Boore [2003] proposes the maximum frequency filter parameter f_{\max} [Hanks 1982] and the kappa filter parameter κ_0 [Anderson and Hough 1984] as alternative parameters to model the site diminution (attenuation) function. The kappa filter function, $\exp(-\pi\kappa_0 f)$, can be considered the path-independent loss of energy in ground motion as it propagates through the site profile. It is defined by Anderson and Hough [1984] as the high-frequency slope of the FAS on a log-linear plot. Although kappa can be calculated from a recording at any distance, the part of kappa (κ_0) that is associated with the crustal profile beneath the site includes attenuation from both wave scattering and material damping [Campbell 2009] and can be calculated in a variety of ways depending on the size of the earthquake and the available recordings [Ktenidou et al. 2014]. We use κ_0 instead of f_{\max} to define site attenuation because of its common use in engineering seismology [Campbell 2009, Ktenidou et al. 2014].

5.2.2.1 Site Characterization in CENA

Campbell [2003] and Tavakoli and Pezeshk [2005] used a CENA reference hard-rock site condition with a time-average shear-wave velocity in the top 30 m of the site profile of $V_{S30} \approx 2800$ m/sec and $\kappa_0 = 0.006$ sec. They used the generic CENA hard-rock crustal-amplification model developed by Boore and Joyner [1997]. Pezeshk et al. [2011] and Campbell [2008, 2011] used an empirically derived CENA hard-rock crustal-amplification model proposed

by Atkinson and Boore [2006] for a hard-rock site with $V_{S30} \geq 2000$ m/sec and $\kappa_0 = 0.005$ sec. In this study, we adopted a CENA reference hard-rock site condition recommended for use in the NGA-East project that corresponds to $V_{S30} = 3000$ m/sec and $\kappa_0 = 0.006$ sec based on the comprehensive studies of Hashash et al. [2014a] and Campbell et al. [2014]. We used the crustal-amplification factors derived by Boore and Thompson [2015] using the QWL (SRI) method, which are based on the velocity profile of Boore and Joyner [1997] modified to have a shear-wave velocity of 3000 m/sec over the top 300 m of the profile, consistent with the NGA-East reference hard-rock crustal profile of Hashash et al. (2014a). These crustal-amplification factors are listed in Table 5.1.

5.2.2.2 Site Characterization in WNA

Boore and Joyner [1997] provided crustal-amplification factors for a generic-rock site profile in WNA with $V_{S30} = 620$ m/sec that were developed using the QWL (SRI) method. These amplification factors have been used by many investigators, including the authors, to conduct stochastic simulations in WNA and other active tectonic regions [e.g., Atkinson and Silva 1997, 2000, Beresnev and Atkinson 2002, Campbell 2003, 2007, 2008, 2011, Tavakoli and Pezeshk 2005, Pezeshk et al. 2011]. Boore and Thompson [2014, 2015] updated the generic-rock crustal-amplification factors of Boore and Joyner [1997] using an improved density-velocity relationship, which we adopted for our study. These updated crustal-amplification factors are listed in Table 5.1.

Anderson and Hough [1984] report typical values for κ_0 in the range 0.02–0.04 sec for rock sites in WNA. Atkinson and Silva [1997] used an average value of 0.04 sec in their stochastic model for southern California, which has been used by many other investigators, including the authors. Yenier and Atkinson [2014] found that a value of 0.025 sec was consistent with ground-motion recordings on rock in California. A summary of other investigators' estimates of κ_0 is given in Campbell [2009, 2014].

Following Al Atik et al. [2014], we used inverse random vibration theory (IRVT) to derive a value for the host site kappa in WNA that is consistent with the NGA-West2 GMPEs and the generic-rock amplification factors of Boore and Thompson [2014, 2015]. We first removed the host crustal-amplification factors from the IRVT-based near-source FAS predictions to decouple the crustal-amplification term from the determination of κ_0 at high frequencies as suggested by Al Atik et al. [2014]. The resulting FAS were analyzed to select the start and end frequencies over which plots of log FAS versus frequency could be considered linear and not impacted by high-frequency distortions from the predicted response spectra. We then fit the slope $-\pi\kappa_0$ to the selected range of frequencies. Similar to Al Atik et al. [2014], we considered six different near-source scenarios ($M = 5.0$ and 6.0 and $R_{RUP} = 5, 10$ and 20 km) to define kappa values for the median of the GMIM predictions from all five NGA-West2 GMPEs. We limited the magnitude range to 6.0 to be consistent with the range used in the inversions of the NGA-West2 GMPE. Figure 5.1 illustrates how the kappa values were calculated by the IRVT approach for the six scenarios. These results are consistent with an average κ_0 of 0.035 sec, which we used to characterize the site attenuation for the generic-rock site in WNA (Table 5.2).

Table 5.1 Crustal-amplification factors [Boore and Thompson 2015].

CENA		WNA	
f (Hz)	$A(f)$	f (Hz)	$A(f)$
1.00E-03	1.000	1.00E-03	1.00
7.83A-03	1.003	9.00E-03	1.01
2.33A-02	1.010	2.50E-02	1.03
4.00E-02	1.017	4.90E-02	1.06
6.14E-02	1.026	8.10E-02	1.10
1.08E-01	1.047	1.50E-01	1.19
2.34E-01	1.069	3.70E-01	1.39
3.45E-01	1.084	6.80E-01	1.58
5.08E-01	1.101	1.11E+00	1.77
1.09E+00	1.135	2.36E+00	2.24
1.37E+00	1.143	5.25E+00	2.75
1.69E+00	1.148	6.03E+01	4.49
1.97E+00	1.150	1.00E+02	4.49

Note: Crustal-amplification factor do not include the effects of site attenuation.

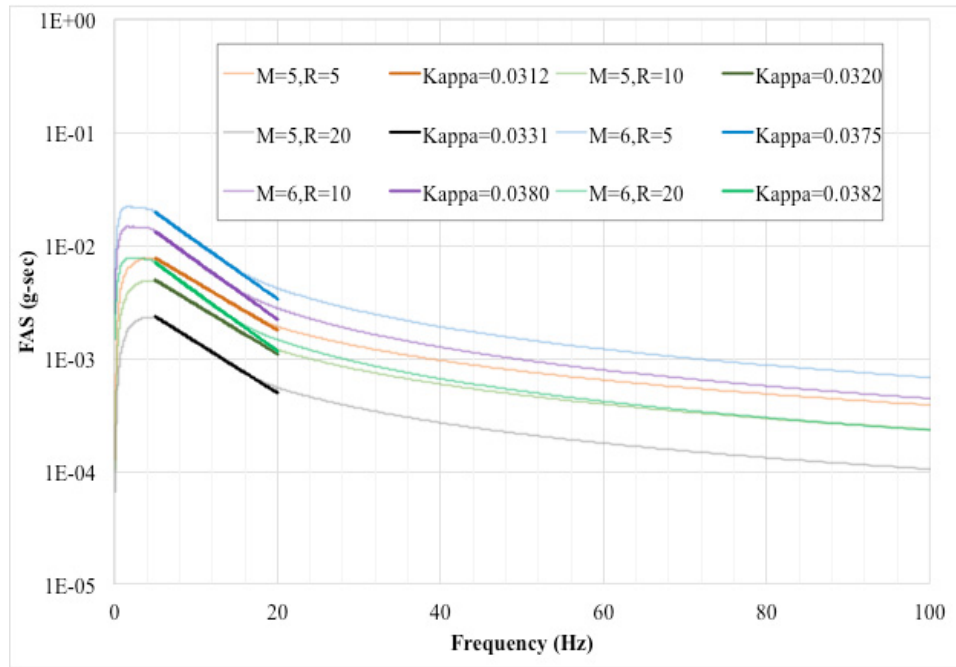


Figure 5.1 Kappa values (sec) for six scenarios computed using the IRVT approach and the median predictions from the NGA-West2 GMPEs.

Table 5.2 Median seismological parameters for WNA and CENA.

Parameter	WNA	CENA
Source spectrum	Single corner frequency ω^2	Single corner frequency ω^2
Stress parameter, $\Delta\sigma$ (bars)	135	400
Source velocity, β_s (km/sec)	3.5	3.7
Source density, ρ_s (gm/cc)	2.8	2.8
Geometric spreading, $Z(R)$	$R^{-1.03}$ $R \leq 45$ km	$R^{-1.3}$ $R \leq 60$ km
	$R^{-0.96}$ $45 < R < 125$ km	R^0 $60 < R < 120$ km
	$R^{-0.50}$ $R \geq 125$ km	$R^{-0.5}$ $R \geq 120$ km
Quality factor, Q	$202f^{0.54}$	$440f^{0.47}$
Source duration, T_s (sec)	$1/f_0$	$1/f_0$
Path duration, T_p (sec)	Table 5.3	Table 5.3
Site amplification, $A(f)$	Table 5.1	Table 5.1
Site attenuation, κ_0 (sec)	0.035	0.006

5.2.3 Source Model

We used the Brune [1970, 1971] ω^2 displacement source spectrum to represent the source model in the stochastic simulations. Brune's model is a single-corner frequency (f_0) PS spectrum in which the stress parameter $\Delta\sigma$ controls the spectral shape at high frequencies. The choice of an appropriate stress parameter in WNA and CENA has been the subject of many studies. The basis for the values of $\Delta\sigma$ we use for these regions in this study is discussed in the following sections.

5.2.3.1 Stress Parameter in CENA

Boore et al. [2010] used the PS stochastic simulation program SMSIM [Boore 2005] to determine the stress parameters for eight well-recorded earthquakes in CENA. They showed that estimates of $\Delta\sigma$ are strongly correlated to the rate of geometrical spreading in the near-source region. They estimated a geometric mean value of $\Delta\sigma = 250$ bars using the geometrical spreading and quality factor (Q) relationships of Atkinson [2004] (hereafter referred to as A04) for the case in which the 1988 Saguenay earthquake was included, and 180 bars for the case in which the Saguenay event was excluded. Atkinson et al. [2009] and Boore [2009] also found that a stress parameter of 250 bars was needed to bring the stochastic point-source results of SMSIM in line with the stochastic FF results of EXSIM [Motazedian and Atkinson 2005], which was used with a stress parameter of 140 bars to develop the GMPE of Atkinson and Boore [2006], for small distant earthquakes. Campbell [2008, 2011] had initially estimated this PS stress parameter

to be 280 bars. Atkinson and Assatourians [2010] analyzed recordings of the $M = 5.0$ Val-des-Bois, Quebec, earthquake using the A04 attenuation model and found them to be consistent with a stress parameter of 250 bars, although they note that this value is somewhat on the high side compared to other events of around the same magnitude, except for the 1988 Saguenay earthquake which had a stress parameter of around 500 bars.

In their revision of the CENA seismological model, Boore and Thompson [2015] found that a stress parameter of 400 bars was needed to approximate the amplitude of the ground motions that matched the A04 attenuation model and the Atkinson and Boore [1995] path duration when the new energy based significant duration parameter recommended by Boore and Thompson [2014] was used. A higher value of $\Delta\sigma$ was needed to compensate for the smaller amplitudes predicted from the stochastic simulations when the longer path durations of Boore and Thompson [2014] were used, which spreads the radiated energy from the point source over a longer period of time. Since we are using the new source model of Boore and Thompson [2015], we use $\Delta\sigma = 400$ bars in our CENA point-source stochastic simulations (Table 5.2).

5.2.3.2 Stress Parameter in WNA

Atkinson and Silva [1997, 2000] modeled California ground motions using the stochastic FF simulation model of Silva et al. [1990]. They used these results to introduce an equivalent double-corner frequency PS spectrum to mimic the FF effects observed at large magnitudes in lieu of using a magnitude-dependent stress parameter such as used to develop the GMPEs of Silva et al. [2002] and Yenier and Atkinson [2015c] based on a single-corner frequency spectrum. Atkinson and Silva [2000] showed that at high frequencies their double-corner source model gave similar results for events of $M < 6.0$ as a Brune single-corner model with $\Delta\sigma = 80$ bars. At larger magnitudes and lower frequencies, where finite-fault effects become significant, the two models were found to diverge due to the spectral sag in the double-corner model that was found to more realistically model the spectral shape of large-magnitude ground motions.

Yenier and Atkinson [2015c] proposed a seismological model for California that they empirically calibrated with response spectra from the NGA-West2 database [Ancheta et al. 2014]. Crustal-amplification factors were derived using the QWL (SRI) method and the NEHRP B/C ($V_{s30} = 760$ m/sec) velocity profile of Frankel et al. [1996] and site attenuation parameter was taken as $\kappa_0 = 0.025$ sec based on Yenier and Atkinson [2014]. The source was defined as a Brune single corner spectrum. Path attenuation was adopted from Raouf et al. [1999], modified to represent a different crustal shear-wave velocity and to have a minimum path attenuation of $Q = 100$. Path duration was taken from Boore and Thompson [2014]. Geometric spreading was found to be consistent with $R^{-1.3}$ out to 50 km, after which a spreading rate of $R^{-0.5}$ was used. Yenier and Atkinson [2015c] used the effective point-source distance metric of Atkinson and Silva [2000] for $M < 6.0$ and that of Yenier and Atkinson [2014] for larger magnitudes in order to model magnitude-saturation effects. They selected stress parameters that minimized the trends in the residuals, ensuring that the observed and simulated spectra had similar shapes for $f > 0.1$ Hz. These stress parameters were found to be a function of magnitude with values that increase from 15 bars at $M = 3.0$ to 100 bars at $M > 5.0$. Finally, they used a calibration factor of 4.47 in the stochastic simulations to eliminate any bias between the simulated and observed spectral amplitudes.

For our stochastic simulations in WNA, we used the seismological parameters derived by Zandieh and Pezeshk [2015] from an inversion of the NGA-West2 GMPEs for earthquake scenarios with magnitudes $\mathbf{M} < 6.0$. This model was used to ensure that the WNA host seismological model was consistent with the GMIM predictions from the host GMPEs. In order to minimize the inherent trade-off between κ_0 and $\Delta\sigma$ in these inversions, Zandieh and Pezeshk [2015] used the IRVT method of Al Atik et al. [2014] to determine the value of κ_0 from the median near-source estimates of PSA from all five NGA-West2 GMPEs, as described earlier in this chapter. The IRVT approach resulted in an average site attenuation of $\kappa_0 = 0.035$ sec. After constraining κ_0 to the average obtained from the IRVT approach and the crustal amplifications to those proposed by Boore and Thompson [2015], Zandieh and Pezeshk [2015] performed GMIM inversions to obtain the remaining seismological parameters using a genetic algorithm (GA) similar to that of Scherbaum et al. [2006]. By constraining the crustal-amplification factors and the value of κ_0 , the near-source spectral shape at high frequencies becomes only a function of the stress parameter, which helped to stabilize the inversion results.

Based on the inversions, Zandieh and Pezeshk [2015] obtained a stress parameter of 135 bars for scenarios in the magnitude range $\mathbf{M} = 4.0 - 6.0$. We used this stress parameter for all magnitudes to be consistent with the magnitude-independent stress parameter used in the CENA seismological model. Campbell [2003] and Campbell [2007, 2011] used a stress parameter of 100 bars in their WNA Brune single-corner frequency stochastic model, which they showed was generally consistent with pre-NGA and the Campbell and Bozorgnia [2008] NGA-West1 GMPE PSA predictions for $\mathbf{M} = 5.0$ and 6.0 earthquakes at $R_{RUP} = 10$ and 30 km. Pezeshk et al. [2011] used a stress parameter of 80 bars, which they showed was generally consistent with the median of the five NGA-West1 GMPE predictions [Power et al. 2008] for an $\mathbf{M} = 6.0$ earthquake at $R_{RUP} = 10$ km. The larger stress parameter of 135 bars found by Zandieh and Pezeshk [2015] is consistent with the longer path durations associated with the Boore and Thompson [2015] WNA duration model and should be considered to supersede the values used by Campbell [2007, 2008, 2011] and Pezeshk et al. [2011]. A stress parameter of 135 bars is also consistent with observations of Modified Mercalli Intensity (MMI) by Atkinson and Wald [2007], who suggested that these observations were consistent with a three-times larger stress parameter for earthquakes in CENA as compared to those in WNA as indicated in Table 5.2.

5.2.4 Source and Path Duration

The sum of the source duration T_S and path duration T_p represents the total duration of ground motion in the stochastic method. The source duration for the Brune single corner spectrum is typically defined [e.g., Boore 2003] as the inverse of the source corner frequency, or $T_S = 1/f_0$ (Table 5.2). Boore and Thompson [2014] used the NGA-West2 database to derive a new distance-dependent relationship for T_p for active crustal regions, such as WNA, that is different from relationships proposed previously. Boore and Thompson [2015] adopted this new path duration for WNA and similarly derived a distance-dependent T_p relationship for stable crustal regions, such as CENA, using the NGA-East database [Goulet et al. 2014]. We used the path-

duration models proposed by Boore and Thompson [2015] in this study (Table 5.2), which are provided in Table 5.3 and plotted in Figure 5.2 for completeness.

Table 5.3 Path duration models [Boore and Thompson 2015].

CENA		WNA	
R_{RUP} (km)	T_p (sec)	R_{RUP} (km)	T_p (sec)
0	0.0	0.0	0.0
15	2.6	7.0	2.4
35	17.5	45.0	8.4
50	25.1	125.0	10.9
125	25.1	175.0	17.4
200	28.5	270.0	34.2
392	46.0		
600	69.1		
Slope of last segment	0.111	Slope of last segment	0.156

Note: Rupture distances must be converted to effective distance using the pseudo-depth for each magnitude.

5.2.5 Path Attenuation

The path attenuation term $P(R, f)$ is separated into two components, commonly referred to as geometric attenuation (or spreading) and anelastic attenuation. Geometric attenuation models the amplitude decay due to the expanding surface area of the wave front as it propagates away from the source. Anelastic attenuation, quantified by the quality factor Q , models the amplitude decay due to the conversion of elastic wave energy to heat and is usually found to be frequency dependent. Boore et al. [2010] found that the stress parameter is strongly correlated to the choice of geometrical attenuation, which emphasizes the fact that the set of seismological parameters for a given region must be internally consistent and should not be taken from different studies with vastly different assumptions. The path attenuation parameters that we used for CENA and WNA are presented in the following sections and summarized in Table 5.2.

5.2.5.1 Path Attenuation for CENA

Boore et al. [2010] used four geometrical attenuation models ranging from a simple $R^{-1.0}$ decay for all distances to more complicated bilinear and trilinear distance decay models to determine the stress parameter for eight well-recorded earthquakes in CENA. Atkinson and Assatourians [2010] studied the attenuation of five well-recorded CENA earthquakes and found that the ground motions were better fit if the A04 geometrical attenuation model, with $R^{-1.3}$ near-source spreading, is used for hypocentral distances beyond 10 km and a $R^{-1.0}$ decay is used at shorter distances. Campbell [2007, 2008, 2011] and Pezeshk et al. [2011] used the original A04 path-attenuation model.

In this study, we used the path attenuation model developed by Chapman et al. [2014] in our CENA seismological model (Table 5.2). These authors used broadband recordings from the EarthScope Transportable (TA) Array and an iterative inversion process to derive a trilinear geometric attenuation model with $R^{-1.3}$ spreading to 60 km, R^0 (no spreading) from 60 to 120 km, and $R^{-0.5}$ or L_g -wave spreading beyond 120 km. At regional distances, the dominant phase in the ground-motion recording is the L_g phase, which is composed of multiple reflections of S -waves trapped within the crust. Chapman and Godbee [2012] also found FAS to decay with $R^{-1.3}$ spreading at short distances from physics-based ground-motion simulations. Chapman et al. [2014] found that for all CENA regions, except the Gulf Coast, the quality factor that is consistent with the above geometric attenuation term is given by the relationship $Q = 440f^{0.47}$. As illustrated in Figure 5.2, the transition distances of 60 and 120 km in the Chapman et al. [2014] geometric attenuation model are generally consistent with the transition distances of 50 and 120 km obtained by Boore and Thomson [2015] in their evaluation of path duration in CENA.

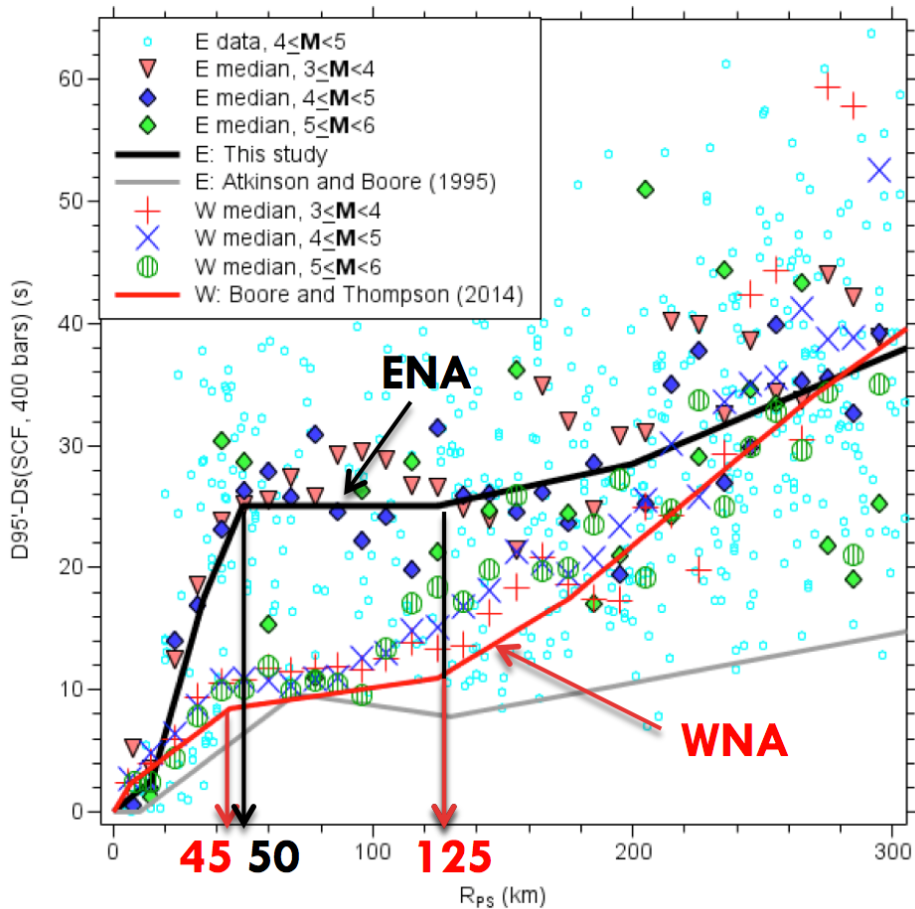


Figure 5.2 Path duration models for CENA and WNA (modified from Boore and Thompson [2015]). E, eastern North America; W, western North America.

5.2.5.2 Path Attenuation for WNA

Campbell [2007, 2008, 2011] and Pezeshk et al. [2011] used the path attenuation model of Raouf et al. [1999] developed for southern California in their stochastic point-source ground-motion simulations for WNA. Atkinson and Silva [2000] also used this path attenuation model in their stochastic finite-fault simulations. Malagnini et al. [2007] analyzed broadband waveforms from small-to-moderate events in the San Francisco Bay Area and found that the best-fitting path attenuation model was given by the relationship $Q = 180f^{0.42}$ for geometric attenuation given by $R^{-1.0}$ spreading within 30 km and $R^{-0.6}$ spreading at larger distances. This model is similar to that of Raouf et al. [1999] for southern California, who found $Q = 180f^{0.45}$ for geometric attenuation given by $R^{-1.0}$ spreading within 40 km and $R^{-0.5}$ spreading at larger distances. Fatehi and Herrmann [2008] determined high-frequency scaling in the Pacific Northwest and northern and central California by analyzing broadband waveforms in these regions. They found both geometric and anelastic attenuation to be regionally dependent. Spreading rates were found to vary between $R^{-1.0}$ and $R^{-1.1}$ within 40 km, except at very high frequencies in northern California, which had a rate of $R^{-1.3}$. Spreading rates at longer distances were found to be more variable, ranging from $R^{-0.8}$ to $R^{+0.5}$ from distances of 40 to 100 km and $R^{-0.5}$ to $R^{-0.9}$ at larger distances. Anelastic-attenuation parameters were also found to be regionally variable with $Q_0 = 210 - 280$ and $\eta = 0.35 - 0.55$ in the relation $Q = Q_0 f^\eta$.

Babaie Mahani and Atkinson [2013] investigated the geometric attenuation of ground motion from small-to-moderate earthquakes across North America and found spreading rates that varied between $R^{-1.1}$ and $R^{-1.3}$ at near-source distances. At longer distances, typically beyond 40 to 100 km, ground motions are dominated by surface waves whose path attenuation depends on fault mechanism, focal depth, and crustal structure [e.g., Burger et al. 1987, Ou and Herrmann 1990, Yenier and Atkinson 2015c]. Yenier and Atkinson [2014] found that geometric spreading from eleven well-recorded earthquakes in California is generally steeper than $R^{-1.0}$ at short distances. Yenier and Atkinson [2015c] considered a bilinear geometric spreading term and near-source spreading rates of both $R^{-1.0}$ and $R^{-1.3}$, decreasing to $R^{-0.5}$ beyond a transition distance of 50 km. They determined that both of these near-source spreading rates could be made to fit the recordings by using calibration factors of 1.08 and 3.16, respectively, to adjust the stochastic PS simulation GMIMs over all magnitudes and frequencies. They concluded that the steeper near-source spreading rate provided the best fit to the path attenuation in California. As discussed previously, Yenier and Atkinson [2015c] used the Raouf et al. [1999] anelastic attenuation term, which after scaling to a shear-wave velocity of 3.7 km/sec in the vicinity of the source, was modified to $Q = \max(100, 170.3f^{0.45})$. The maximum value of $Q = 100$ was based on the recommendations of Boore [1983] and Yenier and Atkinson [2014].

In this study, we used the path attenuation terms determined from the inversion of the NGA-West2 GMPEs by Zandieh and Pezeshk [2015]. For consistency with the WNA seismological model, a trilinear geometric attenuation term with transition distances of 45 km and 125 km were used to perform the inversions. These transition distances were selected to match the WNA transition distances used by Boore and Thompson [2015] in their path duration model (Figure 5.2). The inversion resulted in geometric spreading of $R^{-1.03}$ to a distance of 45 km and $R^{-0.96}$ between distances of 45 to 125 km (both virtually equal to $R^{-1.0}$). Beyond 125 km,

spreading rate was assumed to be equal to $R^{-0.5}$, consistent with L_g surface-wave attenuation (Table 5.2). The resulting anelastic attenuation term was found to be $Q = 202f^{0.54}$ (Table 5.2).

5.3 EMPIRICAL GMPEs FOR WNA

One important component of the HEM approach is using appropriate empirical GMPEs in the host region. Pezeshk et al. [2011] incorporated the five GMPEs from the PEER NGA-West1 project [Power et al. 2008] to derive empirical ground-motion estimates for WNA in their HEM-based GMPE for CENA. Campbell [2007, 2008, and 2011] used a single NGA-West1 GMPE [Campbell and Bozorgnia 2008] to demonstrate how the new NGA-West1 models might impact the Campbell [2003] HEM-based GMPE in CENA.

In this study, we used the five GMPEs developed as part of the PEER NGA-West2 project [Bozorgnia et al. 2014] to derive the empirical GMIM estimates in the host WNA region. These GMPEs are referred to as ASK14 [Abrahamson et al. 2014], BSSA14 [Boore et al. 2014], CB14 [Campbell and Bozorgnia 2014], CY14 [Chiou and Youngs 2014], and I14 [Idriss 2014] in the remainder of this report. These GMPEs used a vastly expanded NGA-West2 database [Ancheta et al. 2014] that included over 20,000 recordings from shallow crustal earthquakes in California (for $M < 5.5$) and in other similar active tectonic regions throughout the world (for $M \geq 5.5$). We used the weighted geometric mean of the RotD50 [Boore 2010] average horizontal GMIM predictions from the five GMPEs in order to derive empirical estimates that are consistent with those used in the inversions performed by Zandieh and Pezeshk [2015]. We assigned the same weights that were used to evaluate the NGA-West2 GMPEs for the 2014 update of the U.S. national seismic hazard model [Petersen et al. 2014]. In this scheme, the weights were distributed evenly between four of the GMPEs with I14 being given one-half the weight of the others.

Except for BSSA14, which is developed with the R_{JB} FF distance metric, the other GMPEs use the finite-fault R_{RUP} distance metric. Since the proposed model in this study is based on R_{RUP} , we converted R_{JB} to R_{RUP} for purposes of evaluating BSSA14 using the relationships developed by Scherbaum et al. [2004]. Following Campbell [2003, 2007, 2011], we used a generic style of faulting to evaluate the NGA-West2 GMPEs because there is no empirical evidence in CENA that there are differences in ground-motion amplitude between faulting styles. This generic style of faulting is an average of strike-slip and reverse faulting mechanisms, because of the predominantly compressional stress regime in CENA, and was implemented by setting $F_{RV} = 0.5$ and $F_{NM} = 0$ in ASK14, CB14, and CY14; $SS = 0.5$, $RS = 0.5$, $NS = 0$, and $U = 0$ in BSSA14, and $F = 0.5$ in I14. We did not include the hanging-wall effect in the evaluation of ASK14, CB14, and CY14 because of the unknown strike angles of earthquakes and the general absence of known faults in CENA. All the NGA-West2 GMPEs that included regional site-response and anelastic attenuation terms were evaluated for the California region and for $V_{S30} = 760$ m/sec or NEHRP B/C [BSSC 2009] site conditions. CY14 was evaluated for average directivity effects and for an “inferred” value of V_{S30} , which only affects the value of the standard deviation. We used a fault rupture dip of 90° to evaluate those GMPEs that had fault dip as a predictor variable.

ASK14, CB14, and CY14 include the depth to the top of rupture Z_{TOR} as one of the predictor variables. For each of these models, the default value of Z_{TOR} recommended by the developers for a future California earthquake was used. ASK14, BSSA14, and CY14 use $Z_{1.0}$, or the depth to the 1 km/sec shear-wave velocity (V_s) horizon beneath the site, to model sediment-depth and basin effects. CB14 uses $Z_{2.5}$, or the depth to the $V_s = 2.5$ km/sec horizon beneath the site, to model these effects. For these GMPEs, the default values of $Z_{1.0}$ and $Z_{2.5}$ recommended by the developers for a California site were used.

5.4 HEM-BASED GMPEs FOR CENA

5.4.1 Median Model

Median estimates of the desired GMIMs in CENA were obtained by scaling the NGA-West2 empirical estimates of PGA and PSA with the stochastically derived adjustment factors derived from the SMSIM computer program [Boore 2005] using the regional seismological parameters listed in Table 5.2. The GMIMs were evaluated for 11 values of magnitude ranging between $M = 3.0 - 8.0$ in 0.5 magnitude increments and 25 values of distance given by the values $R_{RUP} = 1, 2, 5, 10, 15, 20, 30, 40, 50, 60, 70, 80, 100, 120, 140, 180, 200, 250, 300, 400, 500, 600, 700, 800,$ and 1000 km. Since the GMPEs were developed for a CENA reference hard-rock site with $V_{S30} = 3000$ m/sec and $\kappa_0 = 0.006$ sec [Hashash et al. 2014b], the GMIM predictions must be modified for other site conditions using an appropriate site-response method. Such methods are being developed as part of the NGA-East project.

5.4.1.1 Small-to-Moderate Events

A limitation of the empirical GMIM estimates and, therefore, the HEM approach is the general invalidity of the NGA-West2 GMPEs beyond distances of around 300 km [Gregor et al. 2014]. Because of the lower rate of attenuation in CENA, GMIM amplitudes of engineering interest can occur at distances farther than 300 km and possibly as far as 1000 km for $M = 7.5 - 8.0$ events similar to those that occurred in New Madrid in 1811 and 1812 [Petersen et al. 2014]. To handle this limitation in the pre-NGA GMPEs, Campbell [2003] supplemented the GMIMs that were estimated in CENA for $R_{RUP} > 70$ km from the HEM approach with stochastically simulated values. He scaled the stochastically simulated GMIMs for each magnitude by a factor that made them equal to the median HEM estimate for the same magnitude at $R_{RUP} = 70$ km. Tavakoli and Pezeshk [2005] and Pezeshk et al. [2011] employed the same approach in the development of their HEM-based models. Campbell [2008; 2011] also used the same approach to scale the empirical GMIM estimates from the Campbell and Bozorgnia [2008] NGA-West1 GMPE, which was nominally valid to distances of 200 km but that was practically valid only to around 100 km.

Although the approach used previously is perfectly valid, we decided to use a different approach in this study. We used the HEM approach to estimate GMIMs to the maximum distance of 1000 km and then compared these estimates to recordings from the NGA-East database [Goulet et al. 2014]. We used a calibration factor to adjust any bias that existed between the GMIM estimates from the HEM approach and the CENA recordings. A single calibration

the GMIM estimates from the HEM approach and the CENA recordings. A single calibration factor was used for all magnitudes, distances, and spectral periods to prevent any distortions in the shape of the predicted response spectra. This calibration was done after adjusting the CENA response spectra to the reference hard-rock site condition using the method explained in a later section of this report.

After calibration, the HEM-simulated GMIMs were used together with nonlinear least-squares regression to derive the model coefficients in a parameterized GMPE defined with a specified functional form. GMPEs were developed for 5%-damped PSA for $\mathbf{M} \leq 6.0$ and $R_{RUP} \leq 1000$ km at 21 spectral periods ranging from $T = 0.01$ –10 sec, consistent with the set of periods used in the NGA-West2 models. Peak ground acceleration is assumed to be the value of PSA at $T = 0.01$ sec. Magnitude scaling for $\mathbf{M} > 6.0$ was estimated using two methods, referred to as stochastic scaling and empirical scaling. These methods are described in the next section. After trial and error, the GMPE functional form that was found to best model the HEM-based GMIM estimates is given by the expression:

$$\begin{aligned} \log(\bar{Y}) = & c_1 + c_2\mathbf{M} + c_3\mathbf{M}^2 + (c_4 + c_5\mathbf{M}) \times \min[\log(R), \log(60)] \\ & + (c_6 + c_7\mathbf{M}) \times \max[\min\{\log(R/60), \log(120/60)\}, 0] \\ & + (c_8 + c_9\mathbf{M}) \times \max[\log(R/120), 0] + c_{10}R \end{aligned} \quad (5.5)$$

where

$$R = \sqrt{R_{RUP}^2 + c_{11}^2} \quad (5.6)$$

In these equations, \bar{Y} is the median value of PGA or PSA (g), \mathbf{M} is moment magnitude, and R_{RUP} is closest distance to the fault-rupture surface (km). The coefficients in these equations are listed in Tables 5.4 and 5.5 for the stochastic-scaling and empirical-scaling methods, respectively.

5.4.1.2 Large-Magnitude Scaling

The GMIM predictions from the empirical NGA-West2 GMPEs used in the inversions performed by Zandieh and Pezeshk [2015] to develop the seismological parameters for the WNA stochastic model were limited to events with $\mathbf{M} \leq 6.0$ in order to restrict them to a range of magnitudes for which the point-source assumption used in the stochastic simulations is valid. Therefore, we believe that the HEM-based GMIM estimates and the WNA and CENA stochastic models used to derive them are well-constrained by empirical data for $\mathbf{M} \leq 6.0$, after applying an average empirical calibration factor of 0.32 (a factor of 2.09) to the HEM estimates. This calibration factor is included in the c_1 coefficient of Equation (5.5) and is explained in a later section of the report.

For events with $\mathbf{M} > 6.0$, we considered two approaches to model magnitude scaling: (1) using the HEM-based estimates for all magnitudes, assuming that the magnitude scaling from the HEM approach can be extrapolated to $\mathbf{M} > 6.0$ (hereafter referred to as the stochastic-scaling approach), and (2) using the magnitude scaling predicted by the NGA-West2 GMPEs, assuming

referred to as the empirical-scaling approach). Figures 5.3 and 5.4 display the magnitude-scaling characteristics of PSA predicted by our GMPEs for $R_{RUP} = 5, 10, 30,$ and 70 km using the stochastic-scaling and empirical-scaling approaches, respectively. These figures show that the empirical-scaling approach does not exhibit as much oversaturation at large magnitudes, short distances, and short periods as the stochastic-scaling approach. Since the consensus amongst engineering seismologists is to preclude oversaturation in GMPEs (e.g., see ASK14 and CB14), we prefer the version of the GMPE that is based on the empirical-scaling approach.

5.4.2 Variability and Uncertainty

We modeled aleatory variability as a complementary task in the development of our GMPE. We also compared our variability model to that derived directly from the selected NGA-East recordings used to calibrate our GMPEs. However, the topic of aleatory variability is outside of the scope of the current report and will be documented in a separate paper.

We did not evaluate epistemic uncertainty as part of this study. Based on the mathematical framework given in Campbell [2003], the major sources of epistemic uncertainty in the HEM approach are due to: (1) uncertainty in the seismological parameters used in the stochastic simulations, and (2) uncertainty in the median predictions from the empirical GMPEs. We did not include epistemic uncertainty in our model because, in practice, this type of uncertainty is typically evaluated by using alternative GMPEs or evaluating and selecting a representative suite of models using a variety of methods [Atkinson et al. 2014]. Furthermore, the within-model uncertainty associated with an individual GMPE, such as that proposed by Al Atik and Youngs [2014], is not generally included when using multiple models [e.g., Campbell 2007, 2014, Pezeshk et al. 2011].

5.5 COMPARISON WITH PREVIOUS GMPEs

Figure 5.5 compares the distance-scaling (attenuation) characteristics of the GMPEs developed in this study (hereafter referred to as PZCT14) with those of Pezeshk et al. [2011] (hereafter referred to as PZT11) and Campbell [2008, 2011], the hard-rock and extended large-distance version of Campbell [2007] (hereafter referred to as C07). Plots are shown for PGA and PSA at $T = 0.1, 0.2, 0.5, 1,$ and 4 sec, $M = 5.0$ and 7.0 , and $R_{RUP} = 1-1000$ km. Both C07 and PZT11 used the HEM approach to develop GMPEs for the generic CENA hard-rock site conditions defined by Atkinson and Boore [2006], which correspond to NEHRP site class A [BSSC 2009] with $V_{S30} \geq 2000$ m/sec and $\kappa_0 = 0.005$ sec. To perform a consistent comparison, the estimated GMIMs from C07 and PZT11 were adjusted to the reference hard-rock site conditions used in this study, or $V_{S30} = 3000$ m/sec and $\kappa_0 = 0.006$ sec [Hashash et al. 2014b]. This adjustment was approximated by multiplying the C07 and PZT11 GMIM predictions by the ratio of the site-amplification factors in Atkinson and Boore [2006] to those used in this study [Boore and Thompson 2015]. No adjustment for κ_0 was done due to the similarity in the two values.

Table 5.4 Coefficients of the HEM-based GMPE developed in this study using the stochastic-scaling approach.

T(s)	c1	c2	c3	c4	c5	c6	c7	c8	c9	c10	c11	σReg
PGA	-2.0429E-01	7.8051E-01	-8.0630E-02	-3.9556E+00	3.9011E-01	-3.2591E-01	8.2425E-02	-1.9280E+00	2.5112E-01	-2.3467E-03	-6.3677E+00	6.7572E-02
0.01	4.2645E-01	7.0745E-01	-7.8324E-02	-4.1840E+00	4.0911E-01	-6.4552E-01	1.0491E-01	-2.0559E+00	2.5851E-01	-2.2860E-03	6.6534E+00	6.6835E-02
0.02	6.5733E-01	6.8026E-01	-7.4441E-02	-4.0879E+00	3.9085E-01	-6.3265E-01	5.9299E-02	-2.6446E+00	2.9338E-01	-2.0452E-03	6.7235E+00	7.0188E-02
0.03	3.4203E-01	7.2048E-01	-7.4370E-02	-3.8959E+00	3.7288E-01	6.6284E-03	-1.9709E-02	-2.8483E+00	3.0255E-01	-2.0679E-03	6.5234E+00	7.6110E-02
0.04	-1.2664E-02	7.6522E-01	-7.5579E-02	-3.7526E+00	3.6439E-01	5.4789E-01	-6.7567E-02	-2.5771E+00	2.7111E-01	-2.3762E-03	-6.3318E+00	8.1391E-02
0.05	-2.6083E-01	7.9629E-01	-7.6977E-02	-3.6831E+00	3.6387E-01	7.9036E-01	-7.1234E-02	-2.0936E+00	2.2316E-01	-2.7467E-03	-6.1902E+00	8.6347E-02
0.08	-7.9950E-01	9.0874E-01	-8.4599E-02	-3.5869E+00	3.5907E-01	6.0223E-01	3.5201E-03	-1.0753E+00	1.3978E-01	-3.3186E-03	6.1052E+00	9.2628E-02
0.10	-1.3913E+00	1.0596E+00	-9.4862E-02	-3.4750E+00	3.4391E-01	2.3694E-01	6.8643E-02	-4.5169E-01	8.9673E-02	-3.4808E-03	6.1301E+00	9.0411E-02
0.15	-2.4251E+00	1.3217E+00	-1.1166E-01	-3.3222E+00	3.1772E-01	-3.2248E-01	1.4497E-01	1.8247E-01	8.0811E-03	-3.2161E-03	6.2295E+00	8.4379E-02
0.20	-3.2432E+00	1.5367E+00	-1.2620E-01	-3.2779E+00	3.0621E-01	-5.6426E-01	1.6890E-01	1.6405E-01	-4.1004E-03	-2.6381E-03	6.3660E+00	8.3346E-02
0.25	-3.8580E+00	1.6854E+00	-1.3610E-01	-3.2646E+00	3.0240E-01	-6.5142E-01	1.7420E-01	5.7603E-02	-3.2731E-03	-2.1368E-03	6.3308E+00	8.3841E-02
0.30	-4.2402E+00	1.7716E+00	-1.4189E-01	-3.2909E+00	3.0531E-01	-6.8649E-01	1.7365E-01	-6.0024E-02	2.2210E-03	-1.7435E-03	6.3176E+00	8.1633E-02
0.40	-5.0127E+00	1.9316E+00	-1.5013E-01	-3.2350E+00	2.9190E-01	-6.0955E-01	1.4809E-01	-3.7154E-01	2.4987E-02	-1.0722E-03	6.4935E+00	7.5611E-02
0.50	-5.4414E+00	2.0053E+00	-1.5317E-01	-3.2322E+00	2.8881E-01	-5.2867E-01	1.2618E-01	-6.7709E-01	5.5498E-02	-6.6423E-04	6.5578E+00	6.8966E-02
0.75	-6.0852E+00	2.0701E+00	-1.5330E-01	-3.2007E+00	2.8627E-01	-4.2659E-01	1.0139E-01	-9.8560E-01	8.4097E-02	-3.0398E-04	6.3032E+00	6.3291E-02
1.00	-6.4464E+00	2.0770E+00	-1.4983E-01	-3.1645E+00	2.8139E-01	-3.6049E-01	8.2928E-02	-1.1127E+00	9.2414E-02	-1.8571E-04	6.1868E+00	6.2594E-02
1.50	-6.7270E+00	1.9919E+00	-1.3814E-01	-3.1322E+00	2.8478E-01	-2.7117E-01	6.1717E-02	-1.2716E+00	1.1036E-01	-4.7980E-05	5.8175E+00	6.4354E-02
2.00	-6.8008E+00	1.9072E+00	-1.2889E-01	-3.1617E+00	2.9348E-01	-2.3094E-01	4.8925E-02	-1.4382E+00	1.3165E-01	-3.6122E-06	5.6552E+00	6.5045E-02
3.00	-6.7402E+00	1.7295E+00	-1.1036E-01	-3.1987E+00	3.0191E-01	-1.4433E-01	2.9331E-02	-1.6195E+00	1.5347E-01	1.3089E-05	-5.4468E+00	6.7393E-02
4.00	-6.6382E+00	1.5894E+00	-9.6466E-02	-3.2203E+00	3.0740E-01	-1.2761E-01	2.7137E-02	-1.5748E+00	1.4115E-01	-4.2019E-05	-5.5917E+00	6.5942E-02
5.00	-6.7258E+00	1.5356E+00	-8.9780E-02	-3.2314E+00	3.0888E-01	-1.0632E-01	2.3236E-02	-1.5715E+00	1.3543E-01	-9.1894E-05	5.7262E+00	6.5012E-02
7.50	-7.1935E+00	1.5138E+00	-8.4408E-02	-3.2359E+00	3.1698E-01	-1.7665E-02	1.7312E-02	-1.6579E+00	1.4943E-01	-1.3695E-04	5.8465E+00	6.2654E-02
10.0	-7.5073E+00	1.5223E+00	-8.3930E-02	-3.2898E+00	3.2569E-01	1.8068E-01	-3.0216E-03	-1.6146E+00	1.4614E-01	-1.9393E-04	5.7011E+00	6.8376E-02

Table 5.5 Coefficients of the HEM-based GMPE developed in this study using the empirical-scaling approach.

T(s)	c1	c2	c3	c4	c5	c6	c7	c8	c9	c10	c11	σReg
PGA	-7.65463E-01	8.99411E-01	-7.87391E-02	-3.53403E+00	2.94791E-01	-4.79922E-01	1.17806E-01	-2.18173E+00	3.02903E-01	-2.32654E-03	6.46122E+00	5.83553E-02
0.010	-1.87094E-01	8.31363E-01	-7.50346E-02	-3.71379E+00	3.03033E-01	-7.79339E-01	1.35992E-01	-2.30678E+00	3.09283E-01	-2.26338E-03	6.74501E+00	5.63673E-02
0.020	8.38693E-02	7.93361E-01	-7.07297E-02	-3.64067E+00	2.89796E-01	-7.69238E-01	9.12407E-02	-2.88487E+00	3.39897E-01	-2.01321E-03	6.81411E+00	5.77429E-02
0.030	-1.78641E-01	8.25599E-01	-7.14761E-02	-3.48914E+00	2.80892E-01	-1.80579E-01	2.31933E-02	-3.07234E+00	3.46923E-01	-2.04325E-03	6.61601E+00	6.48271E-02
0.040	-4.94724E-01	8.65930E-01	-7.35842E-02	-3.37796E+00	2.79637E-01	3.21834E-01	-1.61079E-02	-2.79142E+00	3.15740E-01	-2.36453E-03	6.42491E+00	7.32989E-02
0.050	-7.24554E-01	8.95917E-01	-7.56845E-02	-3.32496E+00	2.83089E-01	5.31827E-01	-1.34413E-02	-2.30051E+00	2.69315E-01	-2.75061E-03	6.27777E+00	8.15609E-02
0.075	-1.25503E+00	1.00888E+00	-8.39703E-02	-3.23738E+00	2.80880E-01	3.43213E-01	6.06517E-02	-1.28945E+00	1.93192E-01	-3.35176E-03	6.18420E+00	9.08520E-02
0.100	-1.84853E+00	1.16017E+00	-9.43571E-02	-3.12502E+00	2.65994E-01	1.61084E-02	1.16830E-01	-6.96951E-01	1.51094E-01	-3.51938E-03	-6.20508E+00	8.90813E-02
0.150	-2.86205E+00	1.41808E+00	-1.11004E-01	-2.98461E+00	2.41626E-01	-4.49375E-01	1.73581E-01	-1.47412E-01	8.22468E-02	-3.22385E-03	-6.32171E+00	8.52373E-02
0.200	-3.66596E+00	1.63158E+00	-1.25557E-01	-2.95175E+00	2.31350E-01	-6.27371E-01	1.84663E-01	-2.47049E-01	7.74139E-02	-2.59108E-03	6.47912E+00	8.30937E-02
0.250	-4.25969E+00	1.77746E+00	-1.35505E-01	-2.95507E+00	2.29811E-01	-6.68077E-01	1.81122E-01	-4.05959E-01	8.04627E-02	-2.04070E-03	6.46963E+00	8.14216E-02
0.300	-4.63036E+00	1.86380E+00	-1.41588E-01	-2.99490E+00	2.34657E-01	-6.77525E-01	1.75957E-01	-5.47859E-01	8.47313E-02	-1.61409E-03	6.47529E+00	7.69199E-02
0.400	-5.40692E+00	2.02896E+00	-1.50595E-01	-2.94995E+00	2.23086E-01	-5.91148E-01	1.49164E-01	-8.40017E-01	9.92077E-02	-9.23060E-04	6.66683E+00	6.87587E-02
0.500	-5.84273E+00	2.10822E+00	-1.54523E-01	-2.95648E+00	2.22183E-01	-5.22723E-01	1.29842E-01	-1.08614E+00	1.19416E-01	-5.30261E-04	6.73299E+00	6.33758E-02
0.750	-6.49908E+00	2.18511E+00	-1.56965E-01	-2.94753E+00	2.25893E-01	-4.59367E-01	1.12022E-01	-1.25183E+00	1.28380E-01	-2.31588E-04	6.46561E+00	6.34840E-02
1.000	-6.86922E+00	2.20396E+00	-1.55719E-01	-2.93253E+00	2.26115E-01	-4.04372E-01	9.55267E-02	-1.29734E+00	1.25976E-01	-1.51633E-04	6.35641E+00	6.57461E-02
1.500	-7.17151E+00	2.14344E+00	-1.48391E-01	-2.94011E+00	2.38686E-01	-3.05307E-01	7.18673E-02	-1.38564E+00	1.33655E-01	-4.13000E-05	5.98611E+00	6.89642E-02
2.000	-7.28730E+00	2.08549E+00	-1.43056E-01	-2.99414E+00	2.53318E-01	-2.54601E-01	5.60472E-02	-1.51930E+00	1.49438E-01	-5.53000E-06	-5.80583E+00	6.90878E-02
3.000	-7.34489E+00	1.95722E+00	-1.30032E-01	-3.03854E+00	2.64881E-01	-1.50614E-01	3.18413E-02	-1.66760E+00	1.64809E-01	7.65000E-06	-5.52790E+00	7.05972E-02
4.000	-7.38680E+00	1.86047E+00	-1.19074E-01	-3.02325E+00	2.63714E-01	-1.51449E-01	3.28799E-02	-1.60344E+00	1.47278E-01	-4.23000E-05	-5.59561E+00	7.01128E-02
5.000	-7.60677E+00	1.83922E+00	-1.13517E-01	-2.97984E+00	2.54473E-01	-1.60000E-01	3.50577E-02	-1.58277E+00	1.37396E-01	-9.03000E-05	-5.66311E+00	7.05975E-02
7.500	-8.25078E+00	1.85078E+00	-1.07189E-01	-2.87880E+00	2.40256E-01	-1.68689E-01	5.01684E-02	-1.64339E+00	1.45477E-01	-1.32983E-04	-5.72138E+00	6.98691E-02
10.000	-8.58111E+00	1.85033E+00	-1.03929E-01	-2.87577E+00	2.36240E-01	-8.46595E-02	5.49995E-02	-1.59869E+00	1.45009E-01	-2.04723E-04	5.60438E+00	7.53778E-02

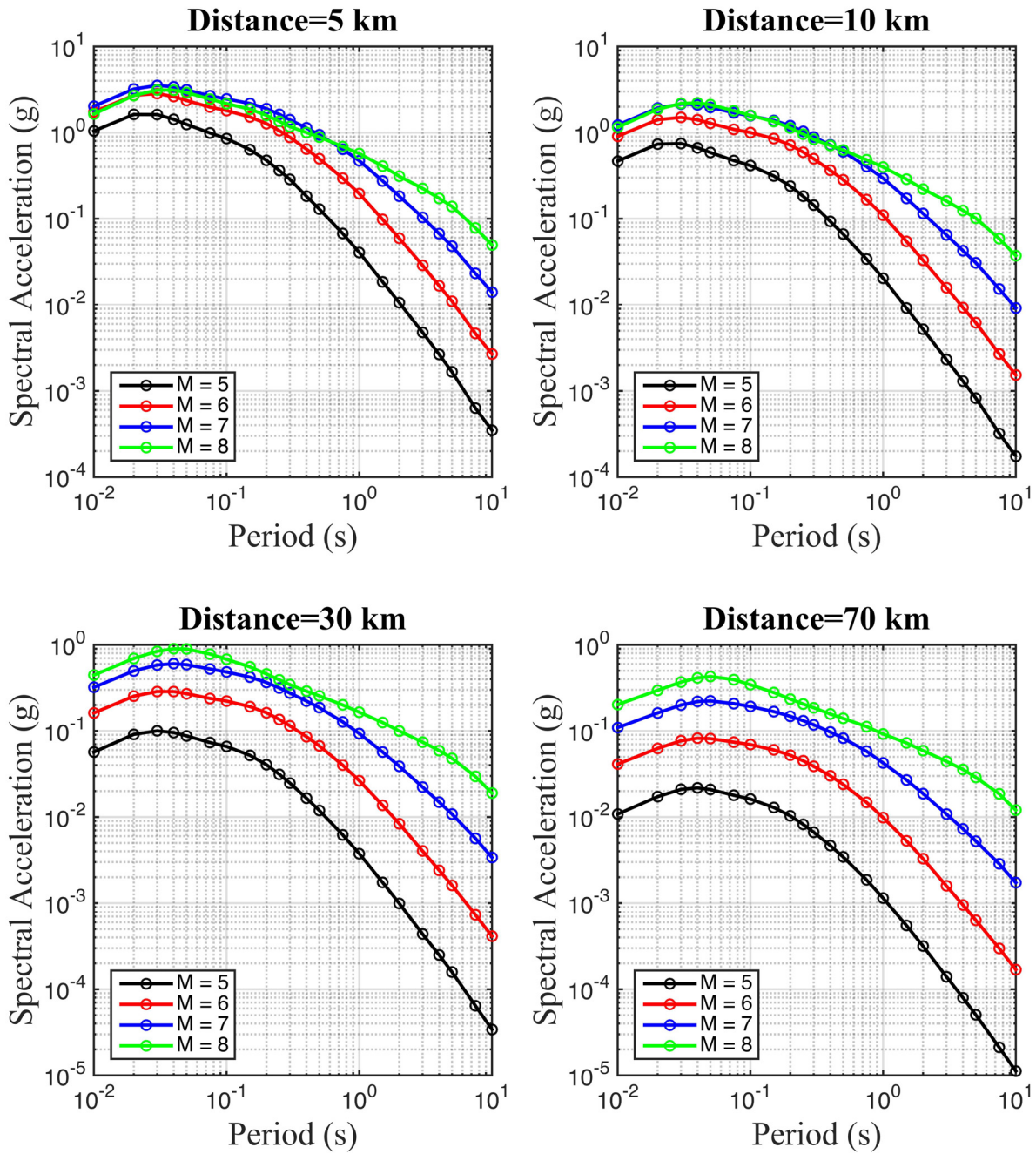


Figure 5.3 Response spectra predicted by the HEM-based GMPE developed in this study using the stochastic-scaling approach to large-magnitude scaling showing their dependence on magnitude and distance.

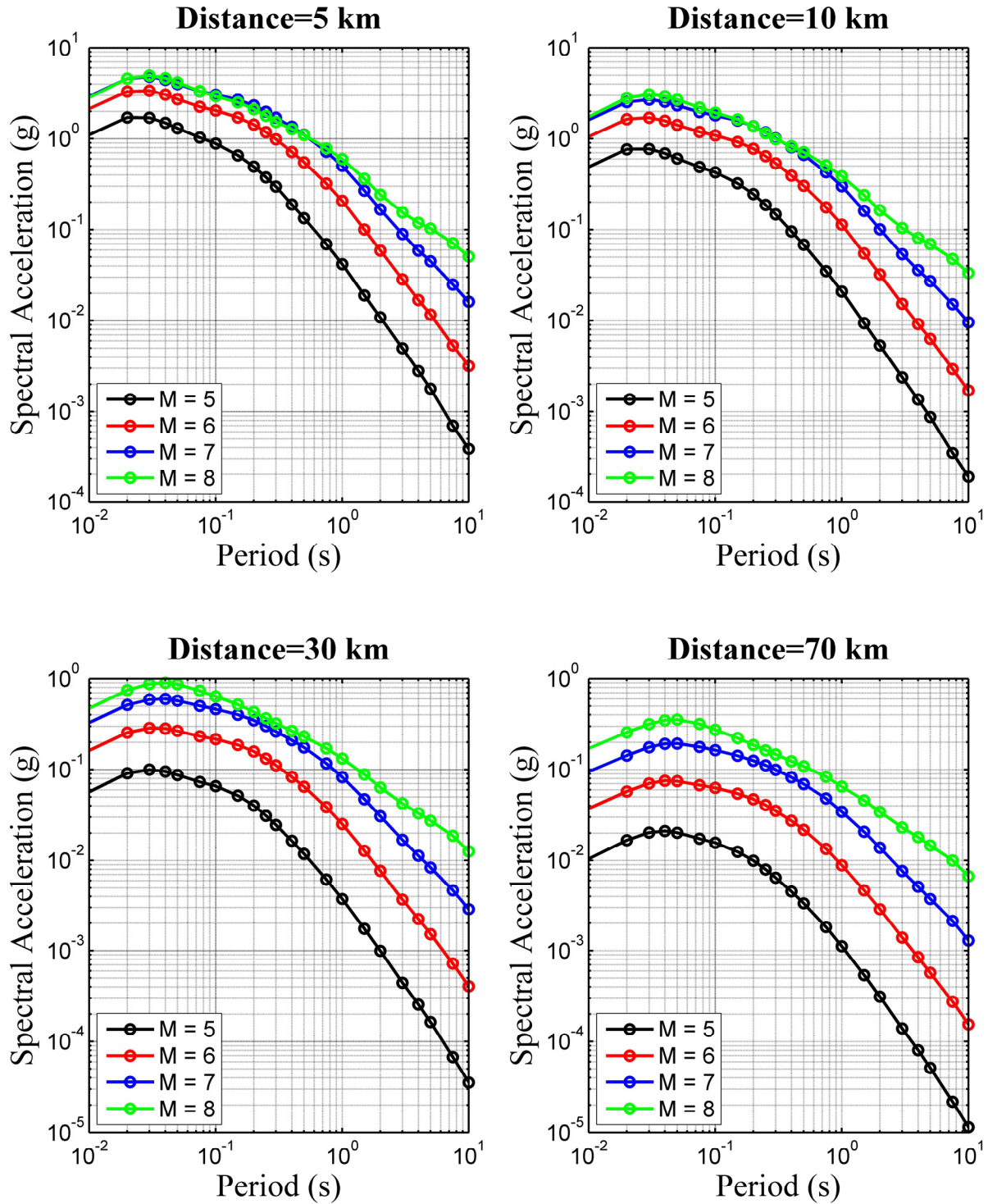


Figure 5.4 Response spectra predicted by the HEM-based GMPE developed in this study using the empirical-scaling approach to large-magnitude scaling showing their dependence on magnitude and distance.

PZT11 used a lower median stress parameter for CENA compared to this study (250 bars versus 400 bars). Similarly, C07 used a stress parameter of 280 bars. Although these stress parameters appear to be inconsistent, we note that the lower values of $\Delta\sigma$ are consistent with the findings of Atkinson et al. [2009] and Boore [2009] who noted that it is necessary to use $\Delta\sigma = 250$ bars with the PS stochastic simulation program SMSIM in order to approximate the predictions from Atkinson and Boore [2006] based on the FF stochastic simulation program EXSIM using $\Delta\sigma = 140$ bars. Since all of these models are calibrated with CENA recordings, the differences in the stress parameters are consistent with other aspects of the seismological models and computer code and do not necessarily represent a bias in the GMIM predictions.

We observe from Figure 5.5 that the GMIM predictions of C07 and PZT11 are similar to the predictions from this study at high frequencies for $\mathbf{M} = 5.0$ and $R_{RUP} = 10$ km; however, they are generally smaller for $\mathbf{M} = 7.0$. One important difference at short distances is the use of the new effective PS distance metric defined in Equations (5.2) and (5.3) that is used to model the near-source magnitude saturation effects in the stochastic-scaling approach. The use of this distance metric clearly leads to greater saturation (in fact oversaturation) at short periods, short distances, and large magnitudes compared to the empirical-scaling approach. PZT11 used a similar effective distance metric, although C07 did not [Campbell 2014]. For longer periods, the C07 and PZT11 predictions tend to be smaller even for $\mathbf{M} = 5.0$ and $R_{RUP} > 10$ km.

5.6 COMPARISON WITH OBSERVATIONS

The GMIM predictions from the GMPEs developed in this study are compared to the PGA and PSA observations from the NGA-East database [Goulet et al. 2014] for CENA recordings with $\mathbf{M} \geq 3.0$ and $R_{RUP} \leq 1000$ km. For this comparison, we only use tectonic earthquakes and not the potentially-induced events (PIEs) identified in the NGA-East database because of the scientific controversy whether PIEs have different source and/or attenuation characteristics than tectonic events [e.g., Hough 2014b]. We used the RotD_{50} average horizontal components of the GMIMs that are listed in the database to be consistent with the definition of the horizontal GMIMs used in the NGA-West2 GMPEs. We excluded earthquakes and recording stations in the Gulf Coast region, which have been shown to exhibit significantly different ground-motion attenuation because of the thick sediments in the region [Dreiling et al. 2014]. Figure 5.6 (left panel) displays a map of the recording stations with different colors representing their NEHRP site class, and Figure 5.6 (right panel) displays a map of the associated earthquakes. NEHRP site class E (soft-soil) sites were excluded from consideration because of their complex site-response characteristics and their potential for significant nonlinear site effects. Figure 5.7 displays the magnitude-distance distribution of the selected recordings.

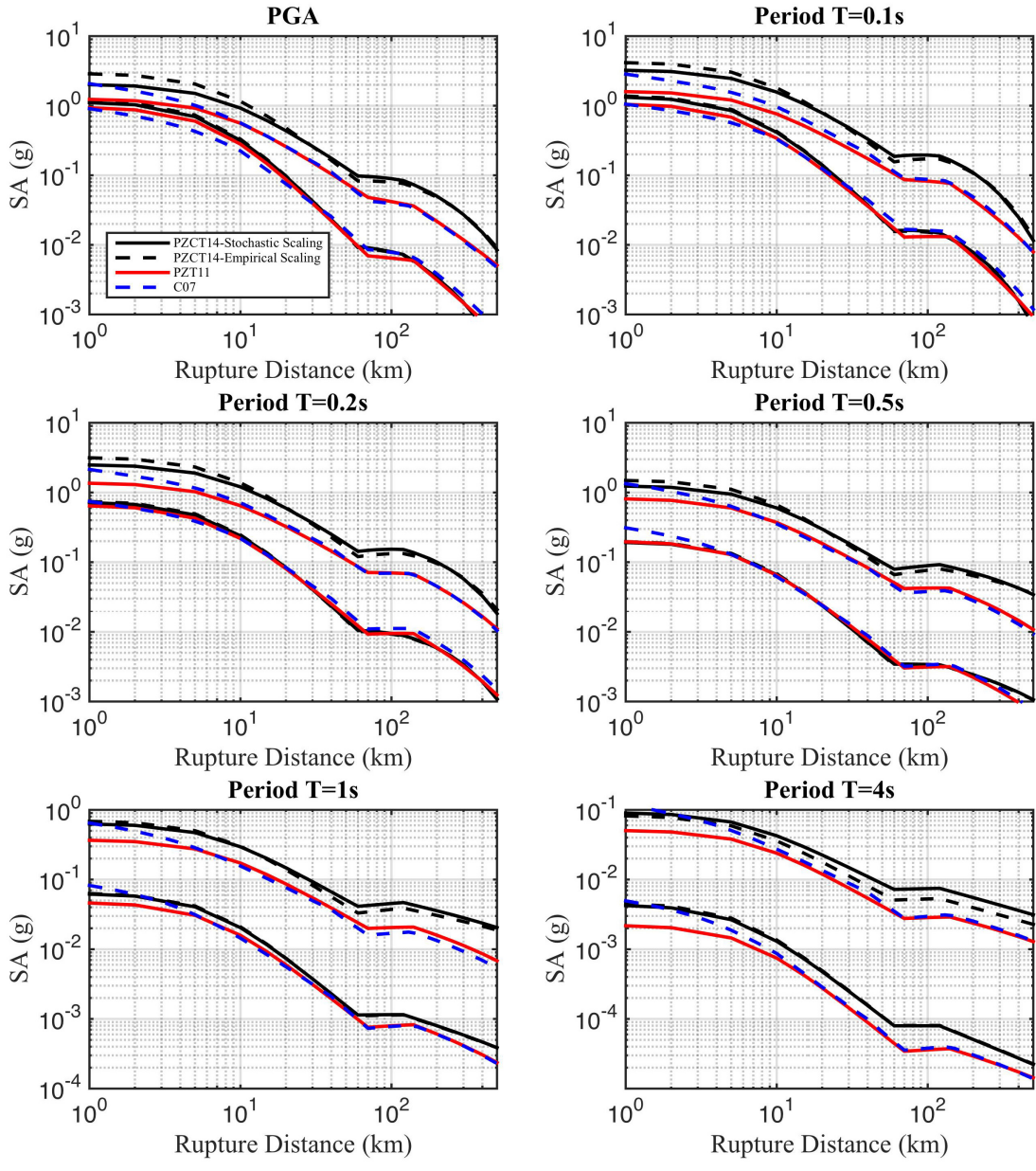


Figure 5.5 Comparison of PGA and PSA predicted by the GMPEs developed in this study with two HEM-based GMPEs developed previous by the authors for $M = 5.0$ (lower curves) and 7.0 [upper curves]; PZT11, Pezeshk et al. [2011]; C07, Campbell [2007, 2008, 2011].

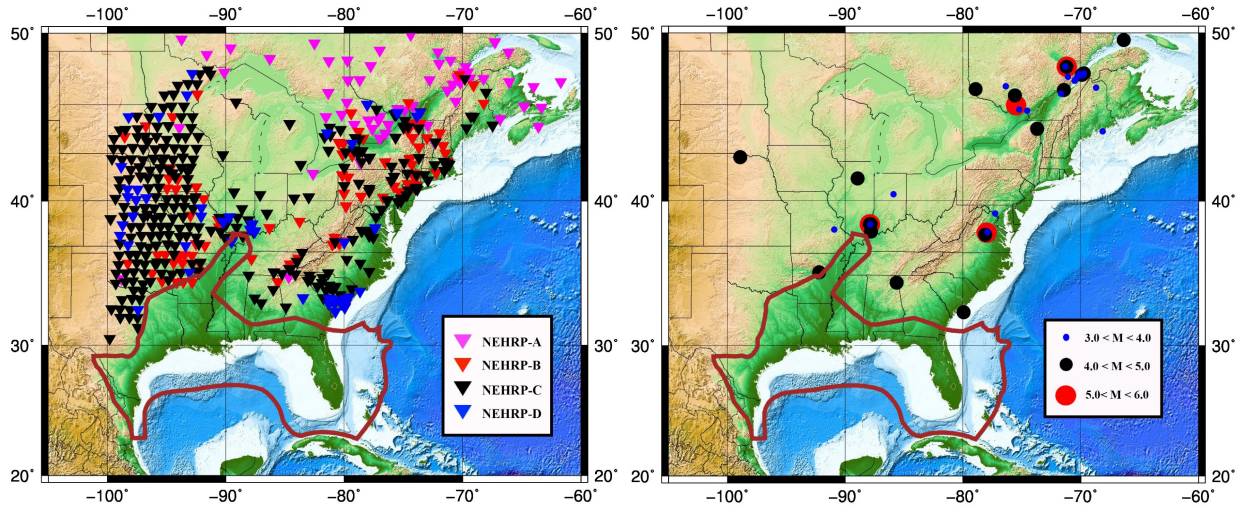


Figure 5.6 CENA recording stations (left panel) and associated earthquakes (right panel) used in the comparisons with the HEM-based GMPE developed in this study. All potentially-induced earthquakes (PIEs) and recording stations located within the Gulf Coast region are excluded.

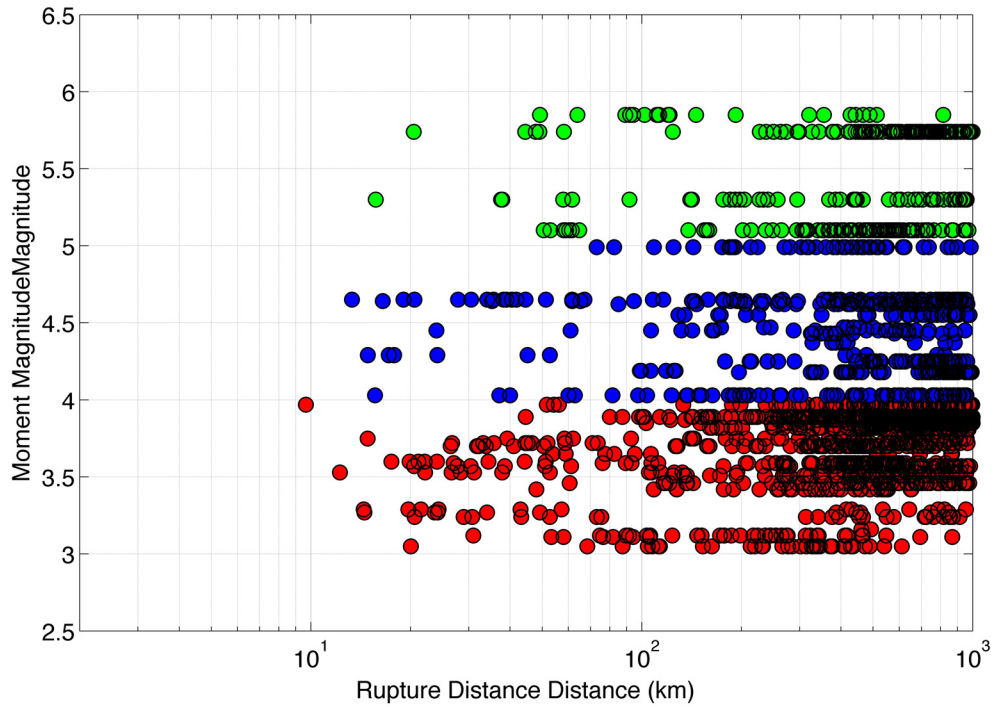


Figure 5.7 The magnitude-distance distribution of the selected CENA ground motion recordings.

As indicated in Figure 5.6, the selected recordings were obtained from a variety of site conditions. To perform a consistent comparison between the GMIM predictions from the GMPE developed in this study and the observations, the observed GMIMs were adjusted to the CENA hard-rock reference site condition used to develop the GMPE based on an approach similar to that generally used in the NGA-East project [Goulet and Boore *Personal Communication* 2014]. We first adjusted the observed PSA and PGA values for sites with $V_{S30} < 1500$ m/sec, the practical limit of the NGA-West2 GMPEs, to NEHRP B/C site conditions ($V_{S30} = 760$ m/sec) using the site term in BSSA14. This site term is a function of V_{S30} and PGA_R , the median value of PGA on NEHRP B/C site conditions.

The BSSA14 site term includes two parts: a linear term F_{LIN} that is a function of V_{S30} only and a nonlinear term F_{NL} that is a function of both V_{S30} and PGA_R . In order to avoid an iterative process, an estimate of PGA_R for each recording was obtained from a PS stochastic simulation of the recording for each magnitude, distance, and spectral period as indicated below. A summary of the method that we used to adjust the observations to the CENA reference hard-rock site condition can be described as follows:

1. Compile generic V_S and density profiles corresponding to $V_{S30} = 760$ m/sec [Atkinson and Boore 2006], $V_{S30} = 2000$ m/sec [Atkinson and Boore 2006], and $V_{S30} = 3000$ m/sec [Boore and Thompson 2015];
2. For each recording with specified \mathbf{M} , R_{RUP} , and $V_{S30} < 1500$ m/sec, correct to $V_{S30} = 760$ m/sec using the site term in BSSA14 and the value of PGA_R from the CENA stochastic simulations after adjusting to NEHRP B/C site conditions using the ratio of the crustal-amplification factors for the $V_{S30} = 760$ m/sec and $V_{S30} = 3000$ m/sec site profiles.
3. For the few sites with $1500 < V_{S30} \leq 2000$ m/sec, assume that they are representative of the $V_{S30} = 2000$ m/sec site profile.
4. Find the ratio of PGA and PSA values between the $V_{S30} = 760$ and $V_{S30} = 3000$ m/sec site profiles or between the $V_{S30} = 2000$ and $V_{S30} = 3000$ m/sec site profiles and use these as adjustment factors to correct the recorded GMIM values to the reference hard-rock site condition.

Figure 5.8 compares the site factors that were used to adjust the observed PSA values from the BSSA14 reference NEHRP B/C site condition, or alternatively from the Atkinson and Boore [2006] hard-rock site condition, to the CENA reference hard-rock site condition defined in this study. These factors include the effects of both crustal amplification and site attenuation. The top frame shows the PSA spectral ratio between the $V_{S30} = 760$ and $V_{S30} = 3000$ m/sec site profiles and the bottom frame shows the PSA spectral ratio between the $V_{S30} = 2000$ and $V_{S30} = 3000$ m/sec site profiles. These plots show that the adjustments can be relatively large for the NEHRP B/C site profile and almost negligible for the $V_{S30} = 2000$ m/sec site profile.

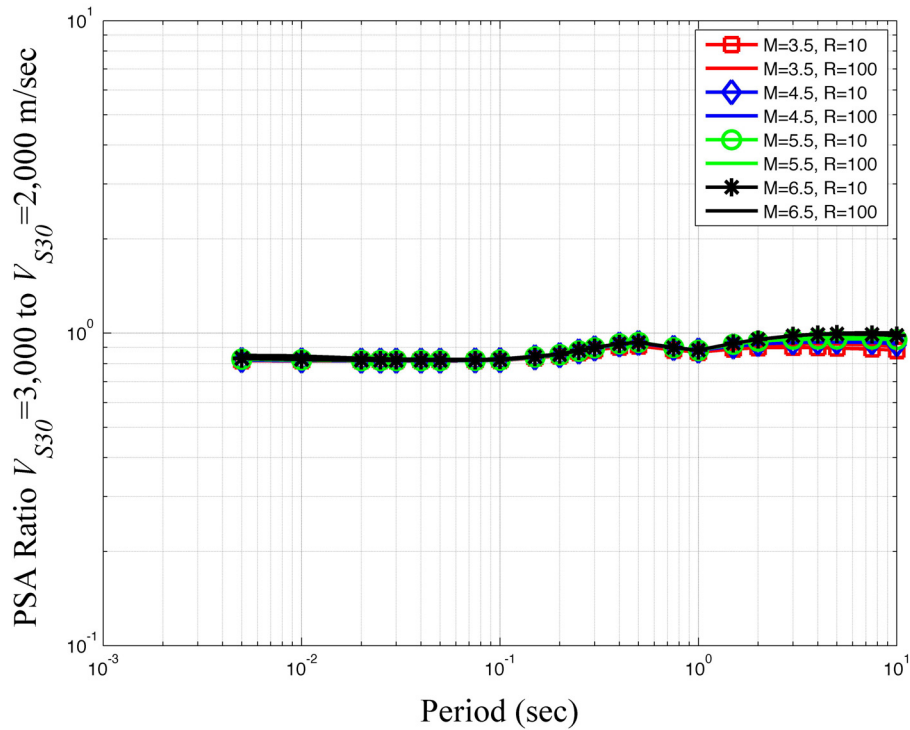
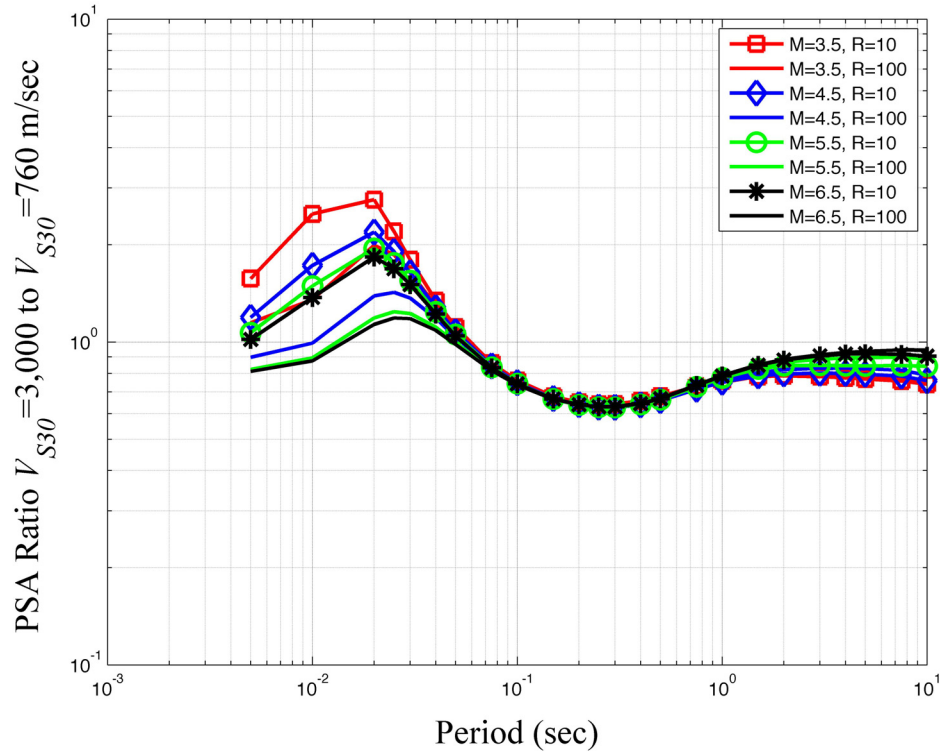


Figure 5.8 Comparisons of the site factors including amplification and damping effects used to adjust the selected CENA empirical observations to the CENA reference hard-rock site condition recommended by Hashash et al. [2014b].

Figure 5.9 compares the median predicted values of PSA from the GMPE developed in this study based on the stochastic-scaling approach versus the site-adjusted observed PSA at $T = 0.2, 1, \text{ and } 2$ sec for three one-unit magnitude bins centered at $M = 3.5, 4.5, \text{ and } 5.5$. These comparisons include the common log empirical calibration constant of 0.32 (factor of 2.09) that was used to adjust the GMIM predictions from the GMPE for the average misfit between the predictions and the site-adjusted observations over all magnitudes, distances, and spectral periods. In general, there is relatively good agreement (within about a factor of 2) between the PSA predictions and the observations, although there are some magnitudes and distances where the comparison is better than others. We note that there is a great deal of uncertainty associated with adjusting the observed GMIMs to the reference hard-rock site condition in CENA, which precludes making specific conclusions regarding their comparison with the predicted values.

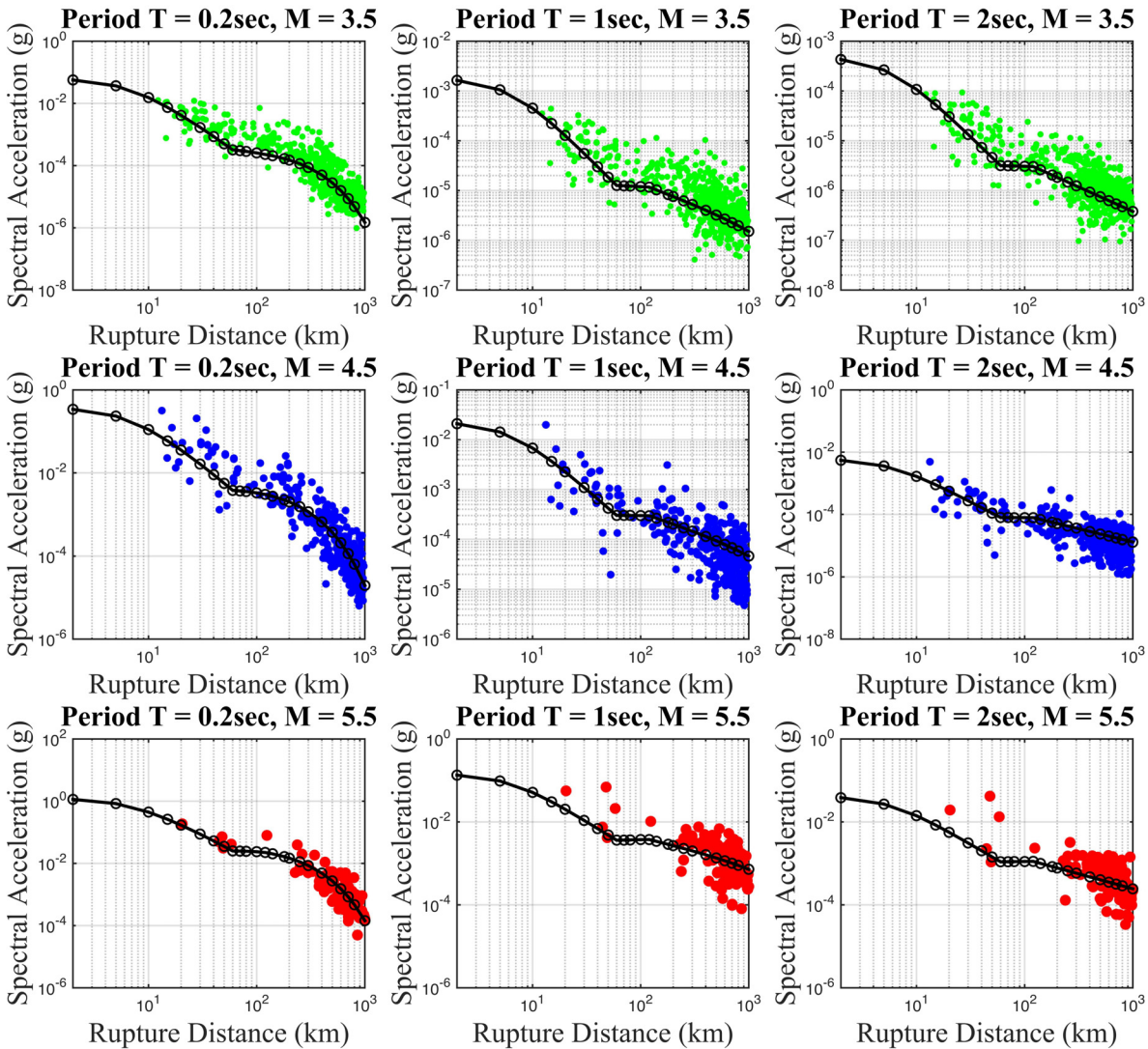


Figure 5.9 Comparisons of the predictions from the HEM-based GMPE developed in this study with the CENA site-adjusted observations for $T = 0.2, 1, \text{ and } 2$ sec and $M = 3.5 \pm 0.5, 4.5 \pm 0.5, \text{ and } 5.5 \pm 0.5$.

Figure 5.10 shows the total residuals of the predicted values of PSA from the GMPE developed in this study based on the stochastic-scaling approach as a function of distance for $T = 0.2, 1.0, \text{ and } 2.0$ sec. In this figure, the size of each circle and its color represents the magnitude of the earthquake. The squares represent the mean of the binned residuals and the error bars represent the 95th-percentile confidence limits of this mean. This figure shows that there is about a 50% statistically significant underestimation by the GMPE for binned distances ranging between 50 and 300 km, but this underestimation disappears at longer periods (lower frequencies). Otherwise there is no discernable trend in the total residuals with distance.

5.7 SUMMARY AND CONCLUSIONS

The hybrid empirical method of Campbell [2003] was used to develop two new GMPEs for CENA. These GMPEs are based on two alternative large-magnitude scaling approaches: (1) using HEM-based GMIM predictions for all magnitudes even though the stochastic simulations used to perform the regional adjustments were based only on seismological models that were constrained by data for $\mathbf{M} \leq 6.0$, referred to as the stochastic-scaling approach, and (2) using HEM-based GMIM predictions for $\mathbf{M} \leq 6.0$ and the magnitude scaling predicted by the NGA-West2 GMPEs for larger magnitudes, referred to as the empirical-scaling approach. The empirical-scaling approach eliminates or significantly reduces oversaturation of GMIM predictions at large magnitudes, short distances, and short periods and is, therefore, preferred over the stochastic-scaling approach.

The new GMPEs are valid for predicting PGA and 5%-damped PSA for $T = 0.01\text{--}10$ sec, $\mathbf{M} = 3.0\text{--}8.0$, and nominally for $R_{RUP} \leq 1000$ km. However, because the developers of the NGA-West2 GMPEs suggest that their models are mostly constrained by data at distances within about 300 km, we suggest that because the GMIM predictions from the GMPEs developed in this study become less reliable at $R_{RUP} > 300\text{--}400$ km, they should be used with caution at these larger distances. The GMIM predictions represent the reference CENA hard-rock site condition recommended by Campbell et al. [2014] and Hashash et al. [2014a,b], which corresponds to a site profile with $V_{S30} = 3000$ m/sec and $\kappa_0 = 0.006$ sec. The prediction of GMIMs for other site conditions requires using appropriate site-amplification factors, such as those used to adjust the CENA recordings to the CENA reference hard-rock site condition in this study or those that will be developed as part of the NGA-East project.

We consider our new GMPE to be a viable alternative to both the existing set of CENA GMPEs, such as those used by Petersen et al. [2008] in the development of the national seismic hazard model, and to other GMPEs that are being developed as part of the NGA-East project. Using a GMPE developed using the HEM approach will be an important contribution to the distribution of epistemic uncertainty of GMIM predictions in CENA.

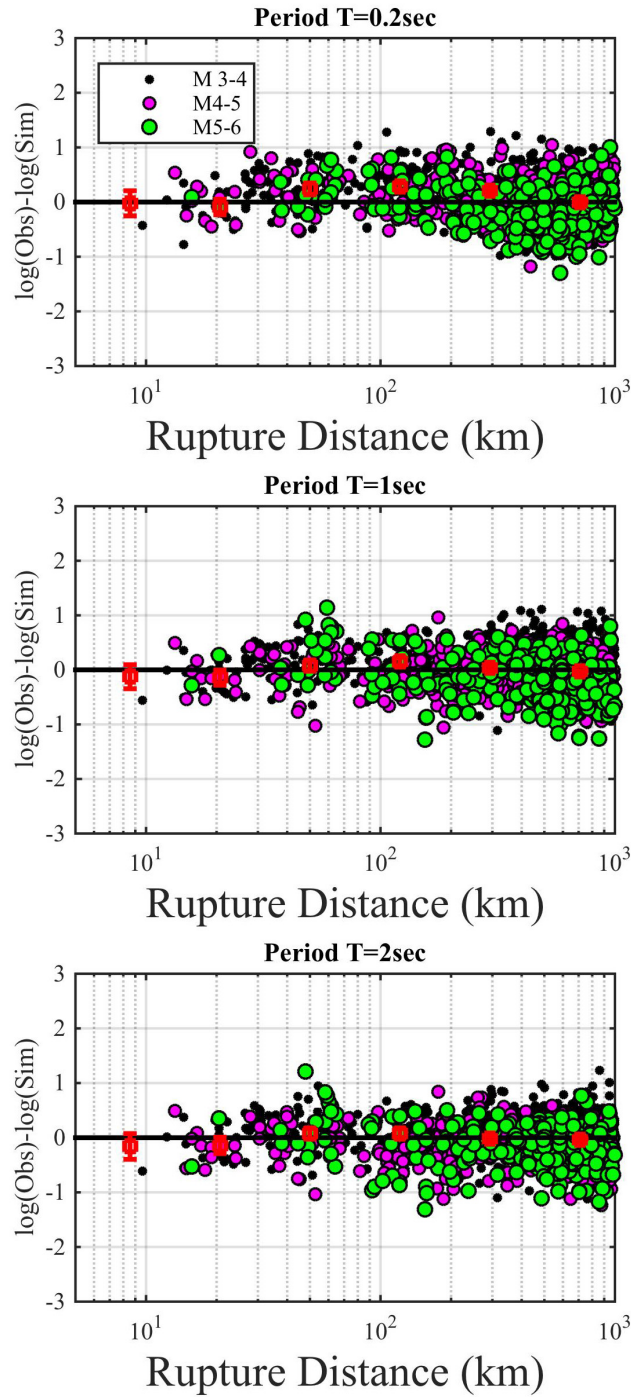


Figure 5.10 Plots showing the distribution of total residuals between the GMPE developed in this study and the sited-adjusted CENA observations as a function of rupture distance (R_{RUP}). The size of each circle and its color represent the magnitude of the event. The squares represent the mean of the binned residuals and the error bars represent the 95th-percentile confidence limits in this mean.

The application of the HEM approach in this study used WNA empirical GMPEs developed as part of the NGA-West2 project [Bozorgnia et al. 2014] to estimate GMIMs in the host region. These GMPEs were evaluated for a reference firm-rock site condition corresponding to $V_{S30} = 760$ m/sec and the default earthquake depths and basin effects recommended by the GMPE developers. For the WNA stochastic simulations, we used a consistent set of seismological parameters that were derived by inversion from the NGA-West2 GMPEs. For the CENA stochastic simulations, we used an updated set of internally consistent seismological parameters that were derived by various investigators.

The major assumption in the HEM approach is that the near-source scaling and saturation effects observed in active tectonic regions, such as WNA, is a general characteristic that can be extended to other tectonic regions, such as CENA. The empirical GMIM predictions from the host region were adjusted using stochastically simulated GMIM ratios that account for the differences in the source, path, and site response between the target (CENA) and the host (WNA) regions. These adjustment factors were evaluated using a point-source stochastic model with an effective point-source distance metric that mimics the distance from a finite-fault rupture plane, such as that used in the NGA-West2 GMPEs.

The GMIM predictions from the GMPEs developed in this study were compared with a selected set of observed GMIMs from the NGA-East database [Goulet et al. 2014] by evaluating the residuals between the predictions and the observations, after adjusting the latter to the CENA reference hard-rock site condition defined by [Hashash et al. 2014b]. In general, there is relatively good agreement between the GMPEs and the CENA observations, although we note that we also used the observations to calibrate our model with a calibration factor of 2.09 that was calculated as the mean bias over all magnitudes, distances, and spectral periods. We consider any disagreement between the model predictions and the site-adjusted observations to be acceptable (i.e., within about a factor of 2), considering the relatively large adjustments and associated uncertainty that was necessary to adjust the observations to the CENA reference hard-rock site condition. A comparison between the GMPE developed in this study with those developed previously by the authors shows that they closely agree at $M = 5.0$ and short periods, but the new models predict higher values of PSA at larger magnitudes and longer periods.

5.8 ACKNOWLEDGEMENTS

We want to express our appreciation to Yousef Bozorgnia, Christine Goulet, Norm Abrahamson, and Alireza Haji-Soltani for their helpful comments and support.

5.9 LIST OF ELECTRONIC APPENDICES FOR CHAPTER 5

- 5A Model Output: Model 1, stochastic-scaling approach (Excel workbook)
- 5B Model Output: Model 2, empirical-scaling approach (Excel workbook)

6 Ground-Motion Predictions for Eastern North American Earthquakes Using Hybrid Broadband Seismograms from Finite-Fault Simulations with Constant Stress-Drop Scaling

Arthur D. Frankel

U.S. Geological Survey
Seattle, WA

Abstract

Broadband seismograms for $M_{4.5}$, 5.5, 6.5, 7.5, and 8.0 eastern North American (ENA) earthquakes were calculated from physically-plausible, finite-fault simulations for rupture distances of 2–1000 km. Pseudo-spectral acceleration (PSA) values were calculated from these synthetics, binned with respect to distance, and provided to the NGA-East project. The broadband synthetics were derived from combining deterministic synthetics for a plane-layered velocity model at low frequencies with stochastic synthetics at high frequencies using matched filters. This follows the procedure described in Frankel [2009], which has been validated for several earthquakes and against NGA-West1. The procedure uses a dynamic stress drop that is constant with magnitude for the low-frequency synthetics and a Brune stress drop that is constant with magnitude for the high-frequency synthetics. The stochastic synthetics assume a geometrical spreading of $1/R$ from 0 to 70 km distance. The 1 Hz pseudo-spectral accelerations (PSA) values controlled by the deterministic synthetics decay more steeply than predicted from a $1/R$ model, which is consistent with observations of Charlevoix earthquakes. The PSA values at higher frequencies exhibit saturation with magnitude at distances less than the rupture length. At larger distances, the PSA values at high frequencies are similar to the point source results of Frankel et al. [1996].

6.1 METHODOLOGY

The purpose of this study is to provide PSA values for eastern North American (ENA) earthquakes derived from broadband seismograms determined from physically-plausible source models and propagation parameters. The hybrid procedure (Figure 6.1) used in this study was

described in detail in Frankel [2009] and combines low-frequency, finite-fault (FF), deterministic synthetics for a plane-layered crustal model with high-frequency, FF, stochastic synthetics that are based on summing stochastic point-source synthetics from SMSIM [Boore 2005]. The deterministic and stochastic synthetics are combined using matched filters to produce broadband synthetic seismograms (see Hartzell et al. [1999]). Propagation and source parameters applied in the simulations were modified for ENA earthquakes from the Western U.S. (WUS) parameters used in Frankel [2009]. The PSA values in this ENA study are for hard-rock sites with a V_{S30} of 2.8 km/sec. Note that the methodology has some similarities to that of Graves and Pitarka [2004], but with significant differences in how the source is specified and propagation parameters. I use the terms PSA and SA interchangeably in this chapter. All PSA and SA values are the 5%-damped PSAs. The values are the geometrical mean of the PSA values of the two horizontal components.

Frankel [2009] demonstrated that the WUS synthetics derived from this method produced PSA values similar to those predicted by NGA-West1 GMPEs for M5.5, 6.5, and 7.5 earthquakes, over distances of 5–200 km. The methodology was also validated using the strong-motion recordings of the Northridge, Loma Prieta, and Izmit earthquakes [Hartzell et al. 2011]. Frankel [2015] showed that 1 Hz Fourier spectral amplitudes at distances of 10–80 km for the Rivière-du-Loup, Québec, earthquake were matched by the deterministic synthetics used in this procedure.

A key feature of the source model is constant stress drop scaling with moment. For the low-frequency deterministic synthetics and in keeping with observations of intensities and stress drops of ENA earthquakes, this is manifested by a constant dynamic stress drop for all magnitudes based on an average slip velocity of 5.4 m/sec, which is twice that used for WUS earthquakes in Frankel [2009]. Note that dynamic stress drop is proportional to slip velocity divided by rupture velocity. The average rupture velocity was also kept constant with magnitude. The average slip velocity and rupture velocity were not varied with depth. The high-frequency stochastic synthetics are derived from a summation of point-source (PS) synthetics each of which is calculated from a Brune [1970] stress drop of 200 bars, twice the value used for the WUS in Frankel [2009].

The low-frequency deterministic synthetics contain directivity effects from a propagating rupture, including forward directivity pulses, and also have the proper time delays for Moho reflections and surface waves. Low-frequency stochastic seismograms do not include the phasing of these essential features observed in actual seismograms. I used the southeastern Canada velocity and Q model of Hartzell et al. [1994] to construct the low-frequency synthetics (Table 6.1). The Q is independent of frequency.

Table 6.1 Velocity model used to make deterministic low-frequency synthetics (from Hartzell et al. [1994]).

V_p (km/sec)	V_s (km/sec)	Density (g/cm ³)	Thickness (km)	Q_p	Q_s
4.5	2.6	2.3	1.44	500	250
5.5	3.4	2.5	6.	1000	500
6.1	3.5	2.67	12.	4000	2000
6.6	3.7	2.85	14.	4000	2000
7.0	4.0	3.02	10.	4000	2000
8.2	4.7	3.35		4000	2000

The synthetics were generated using the frequency-wavenumber integration code of Zhu and Rivera [2002]. I developed random slip distributions with a wavenumber spectral falloff of k^2 , where k is the wavenumber. The correlation distance of slip for each magnitude was scaled from the values specified in Mai and Beroza [2002], adjusting for twice the static stress drop (i.e., divided by the cube root of 2), such that the ratio of the correlation distance to overall rupture dimension was equal to that used for the WUS. A rupture cell (sub-event) size of 250 m was used for all magnitudes. An average rupture velocity (v_{rave}) of 2.8 km/sec was applied for all magnitudes. The secant rupture velocity at a given point on the fault plane was taken to be dependent on the final slip at that point. This is consistent with the results of dynamic simulations that showed higher rupture velocity in areas with high slip (see Frankel [2009; 2013]). The initiation time of rupture of each cell (sub-event) i is specified by

$$t_i = x_i/v_{ri} + \sigma_i \varepsilon_j \quad (6.1)$$

where x_i is the distance between the cell and the hypocenter. v_{ri} is the secant rupture velocity for that cell, which is dependent on the difference between the slip of that cell u_i and the average slip u_{ave} such that

$$v_{ri} = v_{rave} + c(u_i - u_{ave}) \quad (6.2)$$

Here c is a constant determined by specifying a 20% standard deviation of v_r . The rupture velocity perturbation of each cell is capped at $\pm 0.4 v_{rave}$. In Equation (6.1), σ_i is a random value chosen from a uniform distribution from ± 0.2 sec. ε_j is a random value selected from a uniform distribution from ± 0.4 sec, applied to each square j with five cells on a side. This produces a small rupture velocity perturbation common within groups of neighboring cells.

The rise time of slip for each cell equals the final slip for that cell divided by the slip velocity at that point. A Brune pulse [1970] was used for each sub-event. Deterministic

simulations were done for vertical strike slip faults and 45° dipping thrust faults (Table 6.2). For the latter, runs were done for rupture towards and away from the receivers.

For the high-frequency stochastic synthetics, I used a geometrical spreading of R^{-1} out to 70 km, R^0 from 70–130 km, and $R^{-0.5}$ for distances greater than 130 km, based on Atkinson and Boore [1995]. Applying the R^{-1} geometrical spreading was motivated by recent analysis of a set of Charlevoix, Quebec, earthquakes; I found that the apparent geometrical spreading steeper than R^{-1} observed at 1 Hz [Fourier spectral amplitude (FAS)] at distances of less than 80 km could be explained by radiation pattern and directivity effects [Frankel 2015]. The high-frequency (14 Hz) observations for the Charlevoix earthquakes were consistent with a true geometrical spreading of R^{-1} . A $Q = 680f^{0.36}$ was applied in the stochastic synthetics, based on Atkinson and Boore [1995] and consistent with their geometrical spreading parameters. I used a V_{S30} of 2.8 km/sec and a κ of 0.006. The hard-rock shear-wave velocity profile used in the stochastic simulations was described in Frankel et al. [1996]. The point-source stochastic synthetics were multiplied by a factor corresponding to a random distribution of stress drop over the rupture based on a k^{-1} falloff of the wavenumber spectrum, using the same correlation distances and random number seed as the slip models (see Frankel [2009]). The moment of the sub-events was determined from the specified sub-event area assuming self-similar scaling such that area is proportional to (moment)^{2/3}. The sub-event areas fill the rupture area of the earthquake being simulated, which results in a scaling of high-frequency FAS with moment consistent with a ω^{-2} high-frequency displacement spectral falloff [Frankel 1995; 2009]. Before combining with the low-frequency synthetics, the stochastic synthetic is convolved with a relative slip velocity function to ensure that its FAS is flat with respect to frequency, for frequencies less than the corner frequency of the sub-event (see Frankel [1995]).

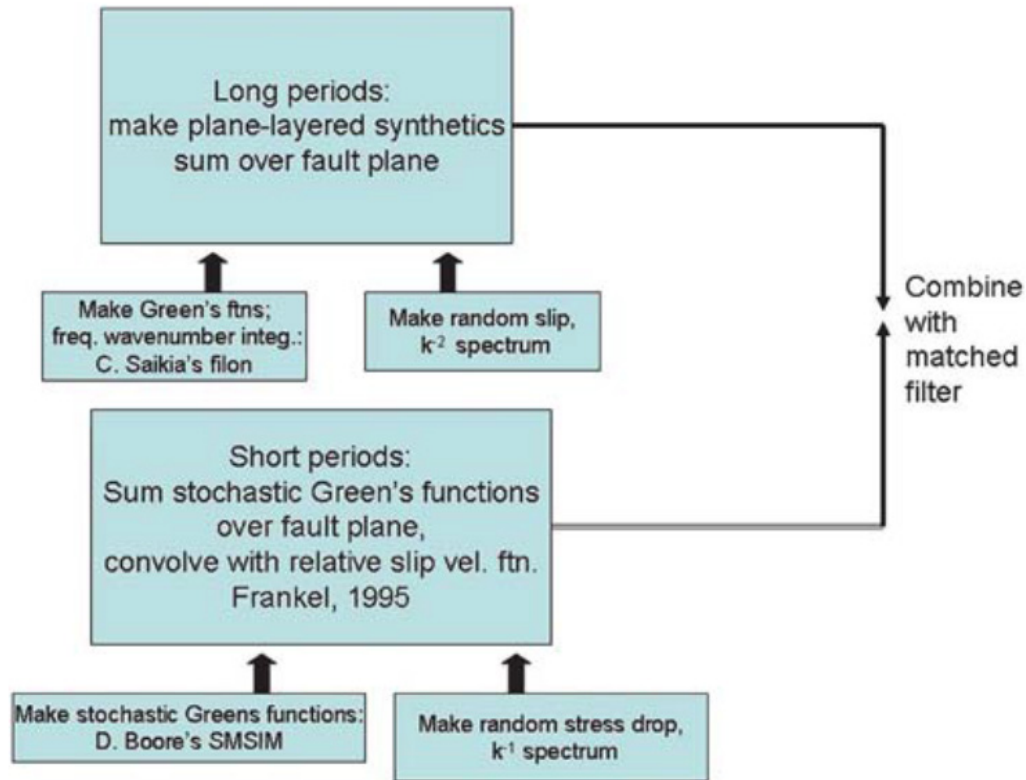


Figure 6.1 Flow chart of procedure to make hybrid broadband synthetics, from Frankel [2009]. The frequency-wavenumber integration code used in the ENA simulations was from Zhu and Rivera [2002].

The crossover frequency between the deterministic and stochastic synthetics varied with magnitude (see Frankel [2009]) to reflect the differences in rise time and sub-event size, although caps in this frequency were applied for the largest and smaller magnitudes studied. For the **M8.0** and **M7.5** simulations, the crossover frequency was set to 0.8 Hz. For the **M6.5** simulations, the crossover frequency was 2.4 Hz. For the **M5.5** and **M4.5** runs, the crossover frequency was 3.0 Hz.

For the **M4.5**, 5.5, and 6.5, and the “thin-fault” runs for **M7.5**, the fault dimensions are reduced from the WUS values used in Frankel [2009], assuming that the ENA static stress drop is twice that for WUS, based on intensity data and stress-drop determinations (see fault dimension in Table 6.2). The fault dimensions for **M4.5**, 5.5, and 6.5 WUS earthquakes were derived from the **M6.5** faulting dimensions found from empirical data by Wells and Coppersmith [1994] and using area proportional to (moment)^{2/3} [Frankel 2009]. Two geometries were used for the **M7.5** ruptures (“thin” and “thick” faults), reflecting a range of aspect ratios, maximum depth, and area of faulting. The “thin fault” runs use a length of 119 km and width of 12 km, based on scaling the WUS values in Frankel [2009]. The WUS fault length for **M7.5** was determined in Frankel [2009] from averaging the results of several empirical relations. For the “thick fault” ENA **M7.5** runs, I used a fault length of 80 km and fault width of 25 km from Leonard [2010]. The fault dimensions for the **M8.0** runs were also taken from the Leonard [2010], using the stable continental regions (SCRs) equations.

Table 6.2 Earthquake scenarios simulated to date. In some cases, multiple slip distributions and hypocenters were used for a given scenario.

Magnitude	Fault Dimensions (km)	Fault Mechanism	Z_{TOR} (km)	Approximate distance range (R_{RUP}, km)
8.0	160 × 40	Strike slip, 90° dip	1	2–1000
8.0	160 × 40	Thrust, 45° dip	1	2–200
8.0	160 × 40	thrust	5	5–200
8.0	160 × 40	Strike slip	5	5–1000
7.5	80 × 25	Strike slip	1	2–1000
7.5	80 × 25	thrust	1	2–200
7.5	119 × 12	Strike slip	5	5–1000
7.5	80 × 25	Strike slip	5	5–1000
7.5	80 × 25	thrust	5	5–200
6.5	14 × 10	Strike slip	5	5–1000
6.5	14 × 10	thrust	5	5–200
5.5	3.9 × 3.9	Strike slip	5	5–1000
5.5	3.9 × 3.9	thrust	5	5–200
5.5	3.9 × 3.9	Strike slip	9	9–200
4.5	1.2 × 1.2	Strike slip	5	5–1000
4.5	1.2 × 1.2	thrust	5	5–200
4.5	1.2 × 1.2	Strike slip	12	12–200

For most of the runs, the depth to top of rupture (Z_{TOR}) was 5 km (see Table 6.2). The **M8.0** and **M7.5** runs were for Z_{TOR} values of 1 and 5 km. There is one run with Z_{TOR} of 9 km for **M5.5** and one run with Z_{TOR} of 12 km for **M4.5** (Table 6.2). I have supplied the PSA values from the $Z_{TOR} = 1$ km and $Z_{TOR} \geq 5$ km runs in separate directories. Each PSA value shown is the geometrical average of the PSA values from the two horizontal components.

6.2 RESULTS

Synthetics were calculated for an array of sites at various distances and azimuths from the rupture, following Frankel [2009]. The distance metric used is nearest distance to the rupture, R_{RUP} . The PSA values were provided to the NGA-East project as median values in distance bins.

Figure 6.2 shows the 5 Hz PSA values from a sub-set of the simulations for **M4.5**, 5.5, 6.5, and 7.5. The results are compared with predictions (hard-rock sites) from Frankel et al. [1996] and Atkinson and Boore [2006]; the latter using their predictions based on their original stress drop of 140 bars, as well as their predictions for a stress drop of 200 bars. At large distances relative to the rupture dimension, the values from the FF simulations are very close to those predicted from the point-source model of Frankel et al. [1996]. This is expected since the propagation and stress drops for the high-frequency stochastic calculations were the same for the two models. At distances less than the rupture dimension, the PSA values from the simulations level off with decreasing distance. At any given distance, the new simulations generally predict higher 5-Hz PSA values than the models of Atkinson and Boore [2006] because I used a less steep geometrical spreading of $1/R$ in the first 70 km.

The 1-Hz PSA values from the simulations are largely controlled by the deterministic calculations, with the exception of the **M7.5** and **M8.0** results, where the crossover frequency is 0.8 Hz and both portions of the hybrid synthetics are important. Figure 6.3 shows that the 1-Hz PSA values from the simulations are less than those of Frankel et al. [1996] because they decay more steeply with distance in the first 70 km. This is caused by the effects of radiation pattern, directivity, and propagation through the flat-layered velocity model. The steep decay at 1 Hz is consistent with observations from the Charlevoix earthquakes studied by Frankel [2015]. The 1-Hz PSA values from the simulations are still a bit higher, at any given distance, than those predicted by Atkinson and Boore [2006].

Figures 6.4–6.7 compare the PSA values from the simulations with the values from recordings of ENA earthquakes, as provided in the NGA-East database [Goulet et al. 2014]. Here, I only plot the observed values for sites with $V_{S30} \geq 760$ m/sec. I have not adjusted these values to V_{S30} of 2800 m/sec. For the **M4.5** example, I used observed PSA values from **M4.0** to 5.0. For **M5.5**, I compared the predicted results with observed data from **M5.0–5.8**. I did not include observed PSA values from the **M5.8** Prague, Oklahoma, earthquake. The point of these plots is to show that the data are generally consistent with the predicted values for **M4.5** and **M5.5** earthquakes out to 1000 km, at least for 1-Hz and 5-Hz PSA. However, there is a cluster of data points for **M4.0–5.0** earthquakes at distance of 700–1000 km that are lower than the predicted values for **M4.5** (Figure 6.6). A more detailed comparison with the data needs to be done.

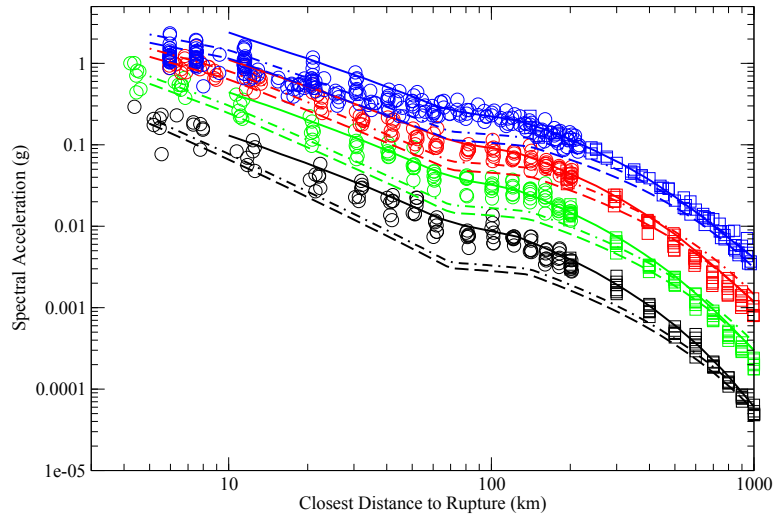


Figure 6.2 5-Hz PSA for **M4.5** (black circles), **M5.5** (green circles), **M6.5** (red circles), and **M7.5** (blue circles) from the simulations ($Z_{TOR} = 5\text{km}$). The plotted values are a representative sub-set of all the simulation results for that magnitude. Solid lines are predicted values from Frankel et al. [1996]. Dashed lines are predicted values from Atkinson and [2006]. Dot dash lines are predicted values from Atkinson and Boore [2006] using stress drop of 200 bars. Lines with predicted values are color-coded by magnitude.

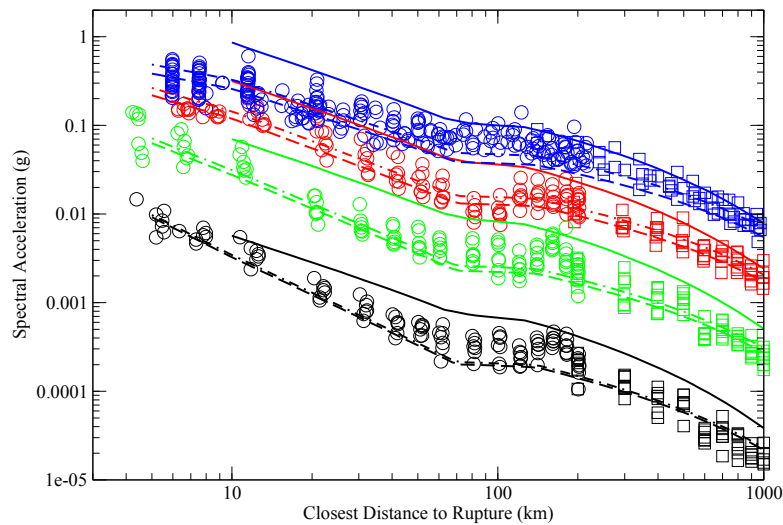


Figure 6.3 1-Hz PSA for **M4.5** (black circles), **M5.5** (green circles), **M6.5** (red circles), and **M7.5** (blue circles) from the simulations. The plotted values are a representative sub-set of all the simulation results for that magnitude. Solid lines are predicted values from Frankel et al. [1996]. Dashed lines are predicted values from Atkinson and [2006]. Dot dash lines are predicted values from Atkinson and Boore [2006] using stress drop of 200 bars. Lines with predicted values are color-coded by magnitude.

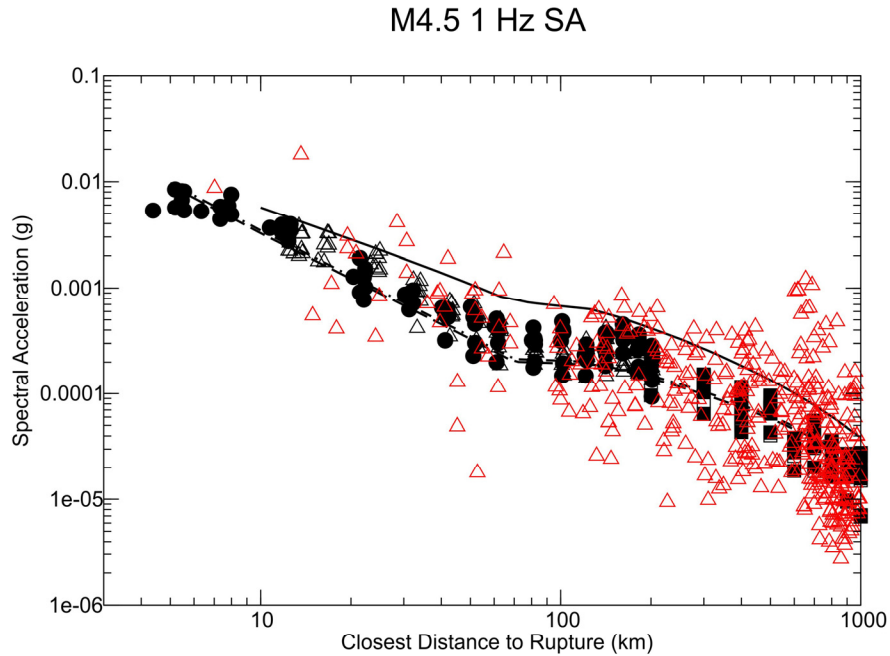


Figure 6.4 1-Hz PSA from M4.5 simulations plotted with observed values from NGA-East database (red triangles). Filled black circles (< 200 km distance) and filled squares (≥ 200 km distance) are for strike-slip simulation, $Z_{TOR} = 5$ km. Black open triangles are for strike-slip simulation with $Z_{TOR} = 12$ km. Only observed values for sites with $V_{S30} > 760$ m/sec were plotted. The observed values were not adjusted for V_{S30} . Solid lines are predicted values from Frankel et al. [1996]. Dashed lines are predicted values from Atkinson and [2006]. Dot dash lines are predicted values from Atkinson and Boore [2006] using stress drop of 200 bars.

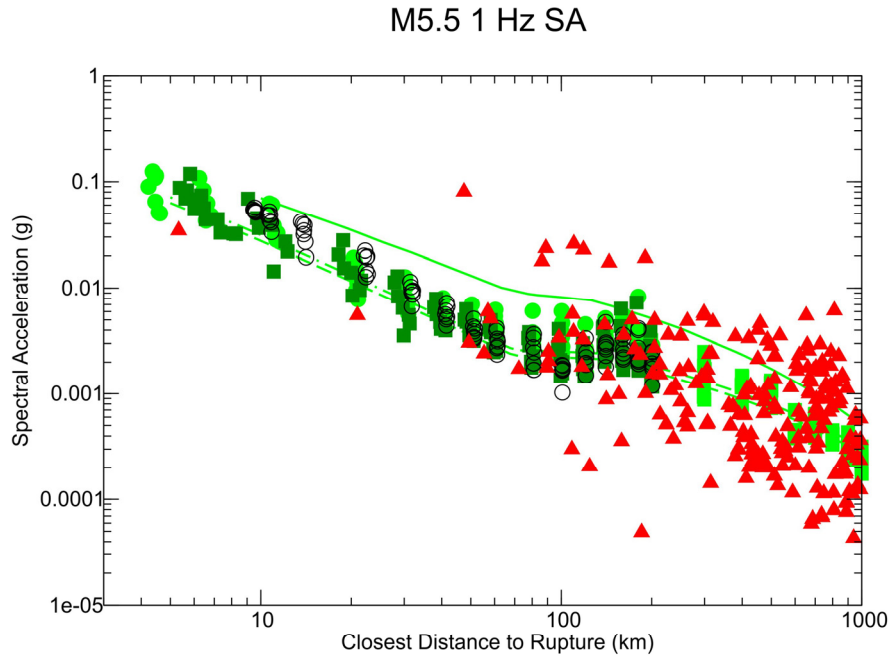


Figure 6.5 1-Hz PSA from M5.5 simulations plotted with observed values from NGA-East database (red triangles). Filled light green circles (< 200 km distance) and filled light green squares (≥ 200 km distance) are from strike-slip simulation with $Z_{TOR} = 5$ km. Filled dark green squares are for thrust fault simulation with $Z_{TOR} = 5$ km. Open black circles are for strike-slip simulation with $Z_{TOR} = 9$ km. Only observed values for sites with $V_{S30} > 760$ m/sec were plotted. The observed values were not adjusted for V_{S30} . Lines represent predictions from Frankel et al. [1996] and Atkinson and Boore [2006]; see caption for Figure 6.2.

M4.5 5 Hz SA

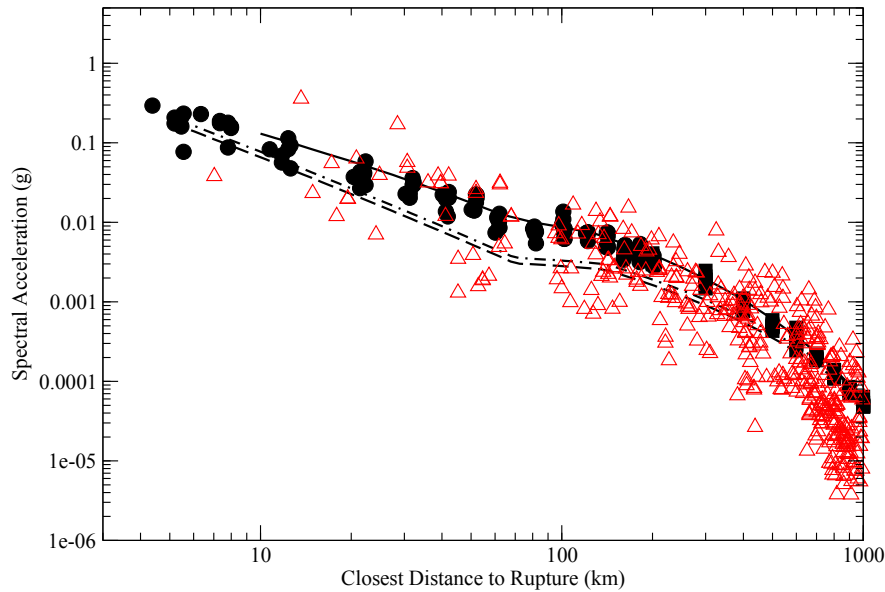


Figure 6.6 5-Hz PSA from M4.5 strike-slip simulations with $Z_{TOR} = 5\text{km}$ black symbols plotted with observed values from NGA-East database (red triangles). Filled black circles are simulation results for distances < 200 km and filled black squares are for distances ≥ 200 km. Only observed values for sites with $V_{S30} = 760$ m/sec were plotted. The observed values were not adjusted for V_{S30} . Solid lines are predicted values from Frankel et al. [1996]. Dashed lines are predicted values from Atkinson and [2006]. Dot dash lines are predicted values from Atkinson and Boore [2006]) using stress drop of 200 bars.

M5.5 5 Hz SA

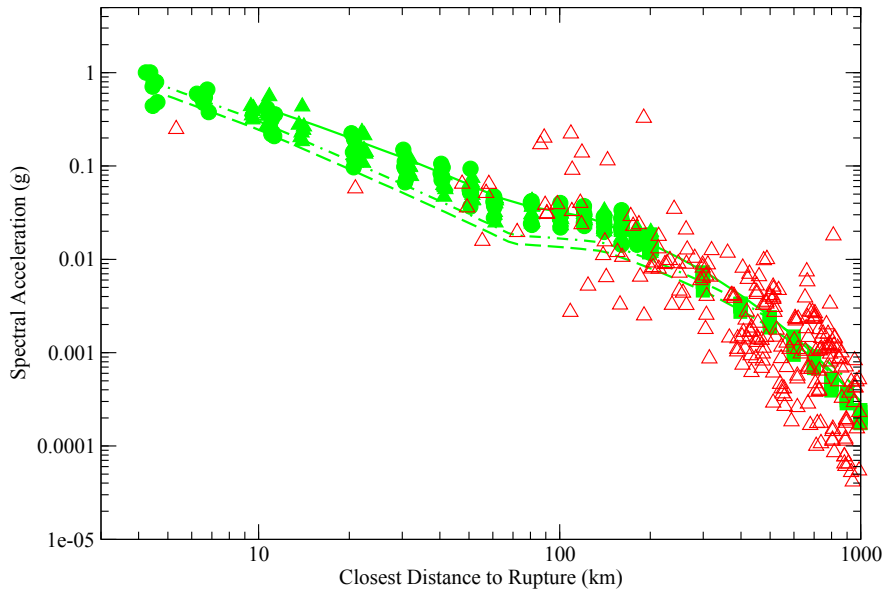


Figure 6.7 5-Hz PSA from **M5.5** simulations (green symbols) plotted with observed values from NGA-East database (red triangles). Filled green circles (distances < 200 km) and filled green squares (distances \geq 200 km) are from strike-slip simulation with $Z_{TOR} = 5$ km. Filled green triangles are from strike-slip simulation with $Z_{TOR} = 9$ km. Only observed values for sites with $V_{S30} = 760$ m/sec were plotted. The observed values were not adjusted for V_{S30} . Solid lines are predicted values from Frankel et al. [1996]. Dashed lines are predicted values from Atkinson and [2006]. Dot dash lines are predicted values from Atkinson and Boore [2006] using stress drop of 200 bars.

The variability of ground motions for different rupture parameters is illustrated in Figure 6.8. Here I show the 1-Hz PSA for **M7.5** using different aspect ratios of the rupture, focal mechanisms, hypocenters, and slip distributions. At this frequency, the PSA values are influenced by both the deterministic and stochastic parts of the broadband synthetics. Larger variability is observed at lower frequencies. The deterministic portion of the calculation produces more variability than the stochastic part, because it includes focal mechanism effects and stronger directivity effects.

For periods of 2 sec and longer, the PSA values from the simulations are affected by the depth of rupture. Figure 6.9 shows a case where the 3-sec PSA values are substantially decreased at distances of 40–200 km as the Z_{TOR} is increased from about 5 to 9 km, corresponding to hypocentral depths of 8 and 13 km, respectively. The more gradual decay with distance for the shallower source is probably caused by the larger surface waves for the shallower source. I found that increasing the Z_{TOR} from 1 to 5 km in the **M7.5** and **M8.0** simulations produced a significant decrease of PSA values at periods of 2 sec and longer. A key question is whether the intrinsic

and scattering Q values for surface waves are properly characterized in the crustal model used in the deterministic simulations.

The PSA values for each magnitude were binned by distance and the median and standard deviation (in ln units) for each bin have been calculated and supplied to the NGA-East project. Figure 6.10 shows the binned values for 1 Hz PSA for the **M4.5**, 5.5, 6.5, 7.5, and 8.0 simulations. The Moho reflection causes the increase of PSA values at 100–200 km for the **M4.5–6.5** results, which are controlled by the deterministic calculation at this frequency. For **M7.5** and 8.0 there is a leveling-off with distance of the PSA values in this distance range caused partly by the stochastic part of the calculation. In addition, the finiteness of the source tends to blur out the PSA peak from the Moho reflection in the deterministic synthetics. Figure 6.10 illustrates the saturation of 1-Hz PSA with increasing magnitude at close-in distances.

The PSA values were calculated at periods from 0.01 to 10 sec. Figure 6.11 is a plot of the binned PSA values at different periods from the **M7.5** simulations, as a function of distance. At distances greater than about 200 km the PSA values at higher frequencies tend to merge with those at lower frequencies, because of the effect of Q .

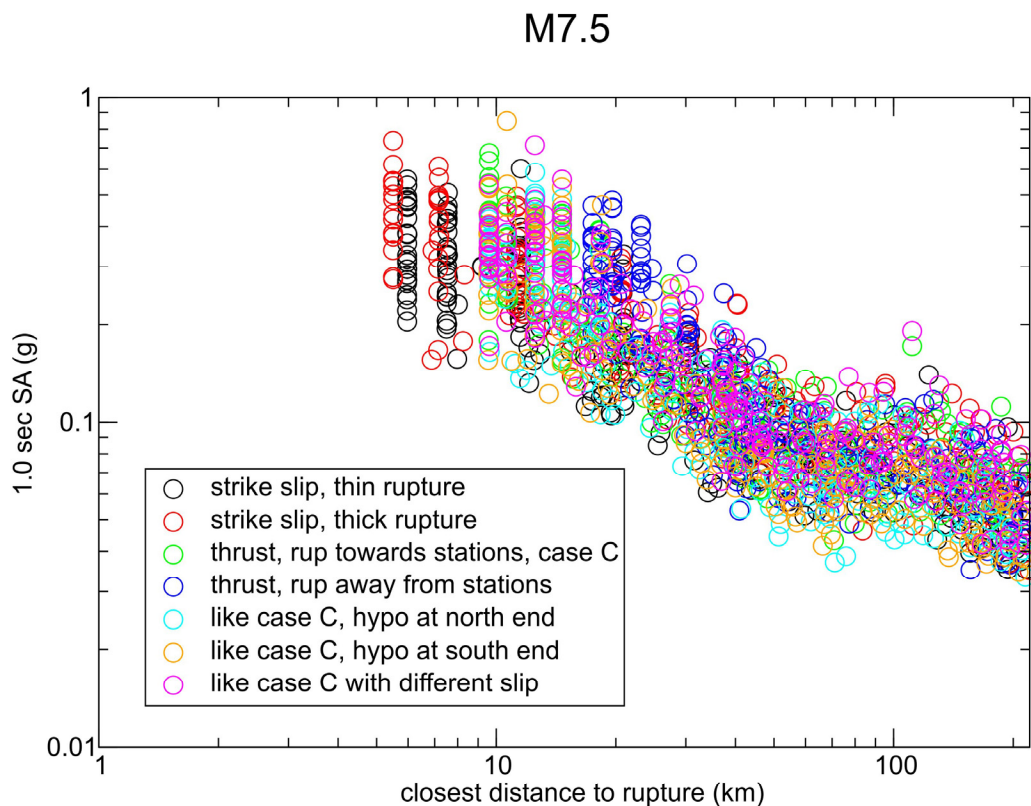


Figure 6.8 1.0-sec PSA values for the various **M7.5** simulations with different rupture characteristics.

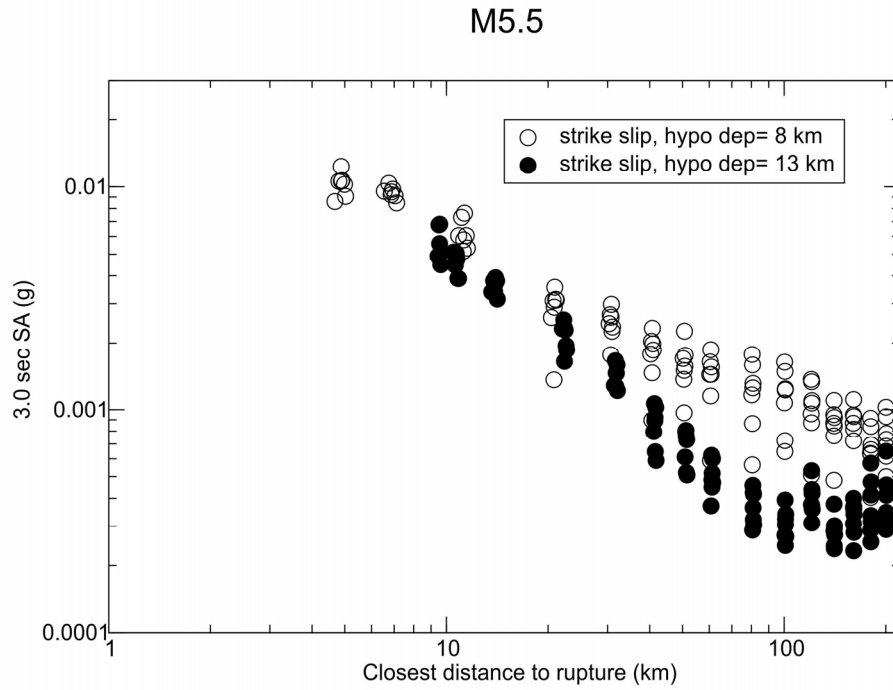


Figure 6.9 3.0-sec PSA values from two of the M5.5 simulations showing the effect of changing the depth of the rupture.

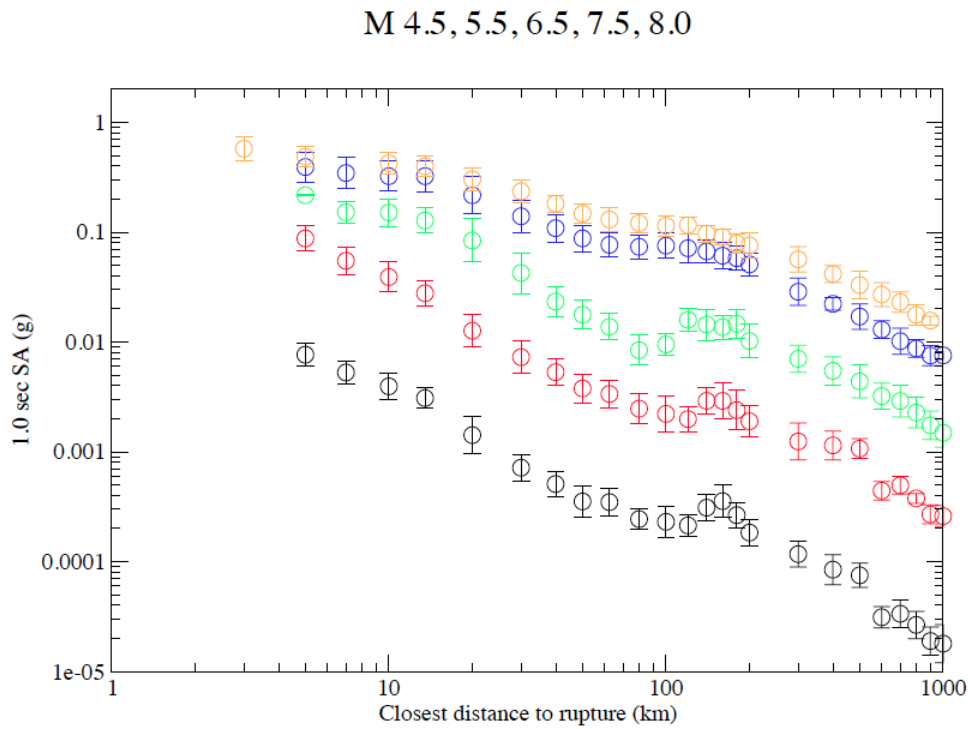


Figure 6.10 1.0-sec PSA values binned by distance, for all of the magnitudes studied. $Z_{TOR} \geq 5$ km.

M7.5

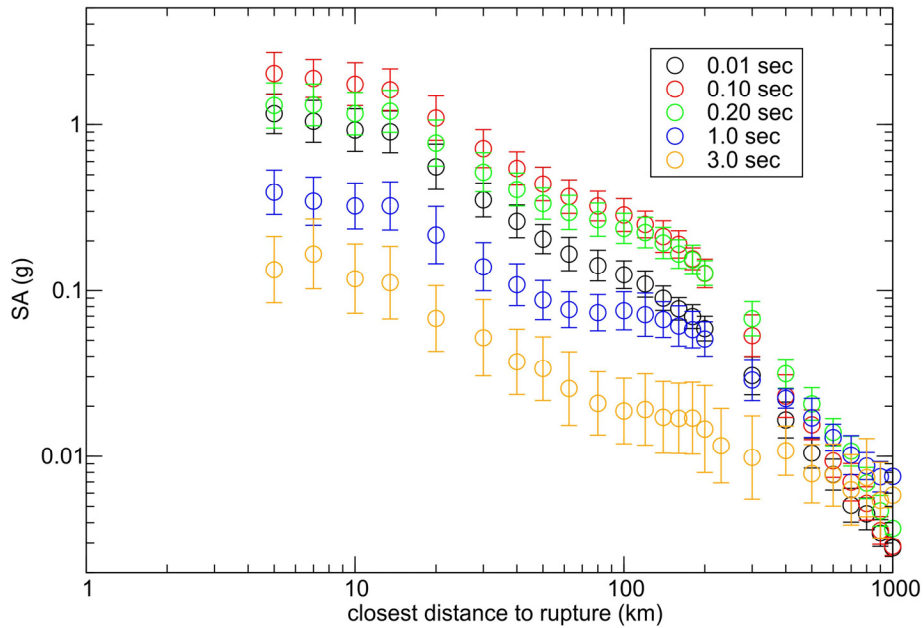


Figure 6.11 PSA values for various periods for the M7.5 simulations, binned by distance.

6.3 CONCLUSIONS

The PSA values derived in this study are based on a methodology that incorporates our knowledge of earthquake rupture histories and seismic-wave propagation. For low frequencies, the deterministic synthetics include phasing appropriate for earthquakes, including directivity effects and surface waves. The broadband synthetics essentially contain a frequency-dependent apparent geometrical spreading from 5 to 70 km distance, since the deterministic portion of the calculation includes radiation pattern and directivity that cause steeper decay than R^{-1} and the stochastic portion is based on R^{-1} spreading, consistent with observations. The PSA values derived from these finite-fault simulations are appropriate for use in seismic hazard assessment in ENA.

6.4 ACKNOWLEDGMENTS

I thank David Boore and Stephen Hartzell for helpful reviews that led to improvements in this chapter.

6.5 ELECTRONIC APPENDIX FOR CHAPTER 6

6A Model Output (Excel workbook)

7 Hybrid Empirical Ground-Motion Model for Central and Eastern North America using Hybrid Broadband Simulations and NGA-West2 GMPEs

Alireza Shahjouei

Shahram Pezeshk

**The University of Memphis
Memphis, Tennessee**

Abstract

We have proposed an alternative hybrid empirical ground-motion model (GMM) for the Central and Eastern North America (CENA) to update Pezeshk et al. [2011] ground-motion prediction equations (GMPE). Hybrid empirical estimates are calculated using the regional modification factors between two regions of Western North America (WNA) and CENA, referred to as host, and target regions, respectively, along with empirical GMPEs from the host region. We have incorporated the recent updated five empirical GMMs developed by PEER for the NGA-West2 project [Bozorgnia et al. 2014] in this study. Synthetic seismograms for both regions are generated through a hybrid broadband simulation technique and using a finite-fault method. Multiple earthquake shaking scenarios are defined applying the updated seismological and geological parameters and information and are implemented in simulations. The high-frequency and low-frequency parts of synthetics are calculated separately through a stochastic finite-fault method and kinematic source models along with the deterministic wave propagation, respectively. In the stochastic synthetics simulations for CENA, we have considered two alternative sets of parameters (such as geometrical spreading, anelastic attenuation, stress parameter, etc.) suggested by Atkinson and Boore [2014] and Pezeshk et al. [2011]. The results from these two sets are equally weighted and incorporated in this study. The average intensity measures (i.e., RotD50) of peak ground acceleration, peak ground velocity, and 5%-damped pseudo-spectral accelerations at spectral periods of 0.01–10 sec are derived from synthetics. The synthetics are generated from shaking scenarios in the magnitude range of M5.0–8.0 and are recorded at stations distributed in distances and azimuths with the R_{JB} distance range of 2–1000 km. The new GMPEs are developed for the reference rock site condition in CENA with

$V_{S30} = 3000$ m/sec. Although the aleatory variability of ground motions was modeled as part of the GMPE development, it is outside of the scope of the current report and not presented here.

7.1 INTRODUCTION

Ground-motion prediction equations provide the expected level of shaking in terms of ground-motion intensity measures as a function of earthquake magnitude, site-to-source distance, and local site parameters (and sometimes also as a function of style of faulting mechanism). Such GMMs are used in seismic hazard applications as well as site-specific engineering studies [Pezeshk et al. 2011; Campbell 2007]. The intensity measures or parameters mostly referred to as the peak ground motions include peak ground acceleration (PGA), peak ground velocity (PGV), and peak ground displacement (PGD), as well as a damped pseudo-absolute response spectral acceleration (PSA), usually 5%-damped PSA. In active crustal regions (ACRs) with high seismicity where strong ground motions are well recorded, such as the active tectonic area of Western North America (WNA), GMPEs are empirically developed from the recorded earthquakes by applying empirical regressions of observed amplitudes against predictor variables [Douglas 2003; 2011]. For regions with the historical seismicity but deficient recorded strong ground motions such as Central and Eastern North America (CENA), GMMs are theoretically or semi-empirically constructed [Pezeshk et al. 2011; Campbell 2007].

The examples of empirical ground-motion models (EGMM) in active crustal regions are GMPEs developed by Abrahamson et al. [2014], Boore et al. [2014b], Campbell and Bozorgnia [2014], Chiou and Youngs [2014], and Idriss [2014] as part of the Next Generation Attenuation project (i.e., NGA-West2) by the Pacific Earthquake Engineering Research Center (PEER) [Bozorgnia et al. 2014].

In regions where there are demands for engineering applications in structural analysis and design (such as nonlinear seismic analysis of structures) or seismological applications (such as GMPEs development) but lack of large earthquake recordings (e.g., CENA), synthetic generation is a promising solution. There are a number of approaches to generate synthetic earthquake seismograms in both engineering and seismological applications [Pezeshk et al. 2011; Ghodrati et al. 2011]. The stochastic method is a simulation approach commonly used by engineers and seismologists to generate strong ground motions for the desired earthquake magnitude and distance utilizing the seismological model in a simple yet powerful manner [Boore 1983, 2003; Hanks and McGuire 1981]. The point-source stochastic method predicts the ground motions by considering a random process over almost all frequencies, so it is deficient in capturing the inherent near-source characteristics (particularly in the long-period portion) usually observed in the recorded data. This shortage is improved by applying the stochastic double-corner frequency model [Atkinson and Silva 1997; Atkinson and Boore 1998] and more effectively by using the finite-fault (FF) stochastic model [Beresnev and Atkinson 1999, 2002; Motazedian and Atkinson 2005; and Atkinson and Boore 2006].

The hybrid broadband (HBB) simulation method is another earthquake simulation technique in which the broadband synthetics for the entire frequency band of interest are developed by combining deterministically generated long-period synthetics with high-frequency synthetics. Recent technological developments in high-performance computing enable researchers to utilize and extend the implementation of broadband simulation techniques in

broader applications. Examples of broadband models are proposed and/or used by Zeng et al. [1994], Hartzell et al. [2005], Liu et al. [2006], Frankel [2009], Graves and Pitarka [2004; 2010], Mai et al. [2010], Mena et al. [2010], Olsen [2012], and Shahjouei and Pezeshk [2013; 2014].

As discussed earlier, synthetic seismograms are implemented to develop GMPEs for CENA in the absence of insufficient appropriately recorded strong ground motions. A number of GMMs are currently available and are used in this region: the stochastic-based, hybrid empirical-based, reference empirical-based, and full wave-based (or numerical-based) models. Frankel et al. [1996], Toro et al. [1997], Toro [2002], and Silva et al. [2002] provide examples of the GMMs that used the stochastic method (with single-corner frequency). Atkinson and Boore [2006; 2011] developed their model based on the stochastic finite-fault simulations and considered the dynamic corner frequency. Campbell [2003; 2007], Tavakoli and Pezeshk [2005], and Pezeshk et al. [2011] proposed hybrid-empirical GMMs for Eastern North America (ENA). Atkinson [2008] suggested a reference empirical model based on regional ground-motion observations in ENA. Subsequently, she revised her model in light of new data and presented it in Atkinson and Boore [2011]. Somerville et al. [2001; 2009] incorporated a full waveform simulation technique in development of their GMMs.

National Seismic Hazard Maps (NSHMs) published by the U.S. Geological Survey (USGS) are reliable sources used by engineering design firms to estimate seismic loads in a region. Such estimations will be implemented in seismic provisions of national building codes for the purpose of seismic analysis and design of structures. Selected GMMs are significant contributions to the seismic hazard analysis, and consequently to NSHMs.

For the Central and Eastern U.S. (CEUS), 2014 update of the U.S. NSHMs [2014] incorporated the following models: Frankel et al. [1996], Toro et al. [1997], Toro [2002], Silva et al. [2002], Atkinson and Boore [2006; 2011], Campbell [2003], Tavakoli and Pezeshk [2005], Pezeshk et al. [2011], Somerville et al. [2001], and the revised model of Atkinson [2008] through a logic-tree process by assigning different weights to each model. The weights are assigned based on the model type, applicability of the model over the distance range and some CEUS parameters [Petersen et al. 2014].

Our goal in this study is to propose alternative hybrid empirical GMPEs for CENA to update Pezeshk et al. [2011] GMPEs model implementing the hybrid broadband simulation technique using the recent proposed empirical NGA-West2 GMPEs [Abrahamson et al. 2014; Boore et al. 2014b; Campbell and Bozorgnia 2014; Chiou and Young 2014; and Idriss 2014]. Synthetics are generated for both host (WNA) and target (CENA) regions using the hybrid broadband simulation approach [Shahjouei and Pezeshk 2013; 2014]. We have implemented the recent updated and suggested geological and seismological parameters in the synthetic simulations. The model is developed for the moment magnitude (M) in the range of 5–8, and for the Joyner-Boore distance (R_{JB} : horizontal distance to the surface projection of the rupture plane) in the range of 2–1000 km. The new model gives PGA (g), PGV (cm/sec), and 5%-damped PSA (g) in the spectral periods of 0.01–10 sec for a generic hard rock site condition with shear velocity of 3000 km/sec in CENA. The proposed model is compared with the available GMPEs and validated with the recorded data in the region.

7.2 REVIEW OF HYBRID EMPIRICAL METHOD

The hybrid empirical method (HEM) is a powerful technique to develop GMMs in regions with a shortage of recorded strong ground motions. The procedure was first proposed by Campbell [1981] to estimate ground motions in ENA. The idea also was implemented by Nuttli and Herrmann [1984] to develop GMMs in the Mississippi Valley. Abrahamson and Silva [2001] and Atkinson [2001] afterward used the HEM technique in ENA. Campbell [2003] provided a comprehensive mathematical framework for HEM and developed the GMPEs for this region. Tavakoli and Pezeshk [2005] applied the HEM technique and proposed GMMs for ENA using stochastic simulations. Later, Pezeshk et al [2011] revised their previous models using the updated seismological parameters and empirical GMMs provided in the NGA-West1 project [Power et al. 2008]. A complete review and evaluation of GMPEs that applied the HEM technique for ENA was presented in Campbell [2014].

The HEM has also been used in areas other than ENA to develop GMPEs. Examples of such regions are: western central Europe [Scherbaum et al. 2005]; the Pacific Northwest region of the U.S. and Canada [Atkinson 2005]; southern Spain; and Norway [Douglas et al. 2006].

7.2.1 Framework

The HEM derives the GMM for the desired region (target) based on some modifications on the empirical GMMs, which have already been developed in the well-recorded earthquake area (host). The modification is performed utilizing the regional adjustment factors, which are the ratios of the intensity measures of ground motions between two regions.

Selection of the host and target regions in HEM requires some considerations [Campbell 2003]. In this study, WNA is selected as the host since there are well constrained empirical GMPEs developed and are available to use for this region. Furthermore, seismological models used in synthetic simulations, which represent the earthquake source, wave propagation, site situation, and crustal structure models, exist for both the target (ENA) and host (WNA) regions. The regional modifications implemented in HEM account for the differences in seismological models used in synthetic simulations [Campbell 2007; Pezeshk et al. 2011].

The broadband synthetics for the two regions in this study are calculated using the HBB simulation technique. The applied model parameters will be described and presented in the following section. By applying adjustment factors the hybrid empirical estimates of ground motions are calculated and are then used to develop GMPEs for CENA.

7.3 GROUND-MOTION SIMULATION

In the previous applications of HEM, Tavakoli and Pezeshk [2005], Campbell [2003; 2007] and Pezeshk et al. [2011] used the stochastic method in synthetic simulations. Shahjouei and Pezeshk [2013; 2014] generated broadband synthetics for CENA using a proposed hybrid broadband simulation technique. In this study, we have extended the application of that procedure to develop broadband synthetics for both CENA and WNA in order to be applied in HEM. In the broadband procedure, the low-frequency portion of synthetics are obtained through a deterministic approach, implementing kinematic source models and the discrete

wavenumber-finite element method for wave propagation using the program COMPSYN [Spudich and Xu 2003]. The high-frequency portions are derived through a finite-fault stochastic simulation where the heterogeneous stress distribution over the fault—which is correlated to the slip distribution used in the low frequency portions—is used. We have implemented the SMSIM program [Boore 2005] to obtain the high-frequency part of the synthetics. These stochastic synthetics are summed up over the fault plane, scaled with the magnitude, and then combined with the long-period ones after passing the matched filters. To compute the intensity measures, two components of the broadband synthetics at each station, generated from each shaking scenario, are rotated, and the RotD50 intensity parameters of broadband synthetics are calculated. This is done using the package provided by David Boore in his website [Boore 2010; Boore et al. 2006]. The RotD50 is an alternative designation of the mean horizontal component that is orientation-independent, while spectral period-dependent. In other words, it is a single component across all non-redundant azimuths [Boore 2010]. The flowchart of the procedure is presented in Figure 7A.1 in appendix 7A.

To consider uncertainties associated with applying different parameters used in the kinematic source modeling, at any given magnitude of M5.0, 5.5, 6.0, 6.5, 7.0, 7.5, and 8.0, we have defined 9 and 18 source representations of strike slip faulting mechanisms for WNA and CENA, respectively. The variability includes the hypocenter locations, distributions of the slip, stress, rise time, slip velocity, and rupture propagation over the fault plane. We implemented recent proposed geological and seismological models and parameters proposed in the literature in our modeling.

In CENA, two sets of the stochastic parameters are defined to account for their variability. The broadband synthetics are separately calculated for both sets of parameters. Equal weight (50%) is assigned to each model to obtain the final results associated with CENA.

The intensity measures are achieved from synthetics generated from 63 (9 shaking scenarios for each 7 earthquake magnitudes) and 126 (18 shaking scenarios for each 7 earthquake magnitudes) source models in WNA and CENA, respectively. These synthetics are recorded at stations with a distance range of 2–1000 km distributed with different azimuths. All scenarios are defined for strike slip faulting mechanisms assuming a vertical fault plane (90° dip).

7.3.1 Long-Period Simulation Parameters

As discussed earlier, the low-frequency synthetics are calculated based on the mathematical framework of the discrete wavenumber-finite element technique provided in the COMPSYN package [Spudich and Xu 2003], which has been widely used in the literature. The software package generates the low-frequency Green's function based on the predefined source characteristics. In this study, kinematic source representation is used, as it will be discussed in more detail.

7.3.1.1 Fault Areas

There are few empirical equations that provide an estimate of the faulting areas and dimensions derived either from the indirect (e.g., rupture length) or direct (e.g., seismic radiation) earthquake measurements. Examples of the former type are equations by Wells and Coppersmith [1994],

measurements. Examples of the former type are equations by Wells and Coppersmith [1994], Working Group on California Earthquake Probabilities [WGCEP 2003], and Hanks and Bakun [2002]. The relations proposed by Somerville et al. [1999], Mai and Beroza [2000], and Somerville [2006] are examples of the latter type of equations. We employed the average results from the abovementioned models to calculate fault dimensions in the WNA as a tectonically active area. Somerville et al. [2001; 2009] suggested using smaller rupture areas for stable continental regions like ENA (as compared to active tectonic regions), which is also considered in some source modeling of CENA in this study. A summary of the fault geometry and rupture areas used in this study is provided in Table 7.1.

Table 7.1 The fault geometry used in synthetic simulations.

M	CENA (km)				WNA (km)			
	L	W	Z_{TOR}	Z_{Hypo}	L	W	Z_{TOR}	Z_{Hypo}
5.0	2	3	3–5	6.5±1.5	3.0	4	3–4	6.0±1.0
5.5	5	5	3–5	7.5±2.0	4.5	4.5	3–4	6.5±1.0
6.0	8	6	3–5	8.0±1.5	12	7	3–4	8.5±1.0
6.5	18	12	2–4	11.0±1.5	18	12	2–3	12±1.5
7.0	23	12	2–4	11.0±1.5	50	13	2–3	12±1.5
7.5	150	15	2–3	12.0±2.0	150	15	1–2	13.5±2
8.0	150	22	2–3	17.0±2.0	180	25	1–2	18±2

7.3.1.2 Slip, Rise Time, and Slip Rate Distributions

The estimated average of slip for a given magnitude and faulting area is distributed over the fault plane assuming a wavenumber-squared spectral decay, k^2 [Graves and Pitarka 2010]. The heterogeneous slip distribution is constructed using the von Karman auto correlation function (ACF) suggested by Mai and Beroza [2002] as a spatial random field model. Rupture initiated at a hypothetical location is propagated over the fault plane following the proposed approach by Graves and Pitarka [2010]. A depth-dependent rupture velocity is used in the procedure. The rupture front in this approach is calculated as a function of the local, maximum, and average of slip over the fault plane as well as the seismic moment.

The slip velocity is calculated using source time functions (STF) and the rise time parameter. The simulations are performed using different STFs in different simulations. Examples of STFs are boxcar, exponential, and Regularized Yoffe [Tinti et al. 2005; Liu et al. 2006]. In this study, the average rise time parameter for CEUS and WNA are calculated using the magnitude-dependent relations proposed by Somerville et al. [1999; 2001; 2009] and by Somerville [2006] and the dip-dependent modification suggested by Graves and Pitarka [2010]. The rise time is also heterogeneously distributed over the fault area implementing the approach suggested by Graves and Pitarka [2010]. This local slip-dependent and depth-dependent distribution approach accounts for the trade-off between assuming a constant slip velocity and a constant rise time.

7.3.1.3 Hypocenter Location and Seismogenic Zone

Usually the earthquake's depths distributed in the range of 3–15 km. The lower depth of the seismogenic zone, or depth of the top of rupture, Z_{TOR} , is a controversial topic [Stanislavsky and Garven 2002]. Atkinson and Boore [2011] used a magnitude-dependent equation ($Z_{TOR} = 21 - 2.5M$) to estimate Z_{TOR} . Frankel [2009] applied a 3 km depth in simulations for all magnitudes for WNA. Simulations of **M**7.4–7.4 New Madrid Seismic Zone (NMSZ) events are performed using 1 km as the minimum depth of rupture in the study of Olsen [2012]. In this study, we implemented a magnitude-dependent depth of 2–5 km and 1–4 km as Z_{TOR} for **M**8–5, in CENA and WNA, respectively.

Atkinson and Silva [2001] used a magnitude-dependent relation ($\log_{10} h = -0.05 + 0.15M$) to estimate the hypocenter depth to be incorporated in the PS stochastic simulations. The relation was revised to $\log_{10} h = \max(-0.05 + 0.15M, -1.72 + 0.43M)$ in the study of Yenier and Atkinson [2014]. Other magnitude-dependent relations to estimate the hypocenter depth are proposed by Scherbaum et al. [2004] for different styles of fault mechanism: $Z_{Hypo} = 5.63 + 0.68M$ for strike slip and $Z_{Hypo} = 11.24 + 0.2M$ for non-strike slip. Mai et al. [2005] suggested the hypocenter depth for crustal dip-slip earthquakes is about 60% down the fault depth. Based on the abovementioned recommendations, the hypocenter depth in our study varies in each shaking scenario in about 0.5–0.8 down the fault width. We have considered three hypothetical rupture initiation points (hypocenter locations) along the strike of the fault (L) as $L/4$ – $L/3$, $L/2$, and $2L/3$ – $3L/4$. For each hypocenter location, three slip distributions are assigned; therefore, a total of nine shaking scenarios for each magnitude are defined.

Figure 7A.2 in appendix 7A shows an example of the kinematic source model developed for one of the simulations of **M**7 in CENA. This figure represents distributions of the slip, rise time, and slip velocity as well as stress distribution over the finite-fault plane. In addition, the propagation of the rupture (rupture front) from the initiation point (hypothetical hypocenter) depicted by a star is represented by contours on the slip distribution panel. In Figure 7A.3, we have provided examples of several source models used for **M**7 simulations in CENA. The variability of slip distribution, rupture front, and hypocenter location in different simulations is depicted in this figure in order to account for uncertainties associated with these source parameters. A summary of some source parameters in our simulations is provided in Table 7.2.

Table 7.2 Summary of some parameters implemented in long-period synthetic simulations.

M	$\log_{10}(M_0)$ (N. m)	f_{cross} (Hz)	CENA		WNA	
			Ave. Slip (m)	Ave. Rise Time (sec)	Ave. Slip (m)	Ave. Rise Time (sec)
5.0	16.550	3.0	0.18	0.21	0.10	0.12
5.5	17.301	3.0	0.25	0.38	0.25	0.20
6.0	18.041	2.6	0.71	0.67	0.40	0.36
6.5	18.799	2.4	0.90	1.20	0.88	0.64
7.0	19.550	1.6	2.56	2.12	1.65	1.13
7.5	20.300	0.8	2.70	3.75	2.68	2.02
8.0	21.050	0.8	10.3	6.72	7.56	3.58

7.3.2 High-Frequency Simulation Parameters

High-frequency synthetics are calculated using stochastic FF simulations. The synthetics at each sub-fault are calculated through the stochastic method using the software package SMSIM [Boore 2005]. The stochastic synthetics at each station are computed by summing up the sub-fault stochastic synthetics over the fault plane (considering the appropriate delays accounted for by their arrival times) followed by convolving with a source time function using the Frankel [1995] approach. The stochastic point-source simulation at each sub-fault is developed using a different initial seed number.

The PS stochastic simulations at each sub-fault are incorporated the following equation proposed by Boore [2003] to derive the displacement Fourier amplitude spectrum $Y(M_0, R, f)$. The spectral amplitude includes different terms of the PS $E(M_0, f)$, path effect $P(R, f)$, local site response effect $G(f)$, and the type of ground motion $I(f)$.

$$Y(M_0, R, f) = E(M_0, f) \times P(R, f) \times G(f) \times I(f) \quad (7.1)$$

where R (km) is the distance, M_0 (dyne-cm) is the seismic moment, and f is the frequency.

The stochastic parameters used in the high-frequency simulations are given in Table 7.3 and Table 7.4 for CENA and WNA, respectively. Two sets of parameters are used in CENA to account for the different parameters proposed by investigators in this region.

Table 7.3 Two alternative sets of median parameters used in high-frequency stochastic synthetic simulations for CENA.

Parameter	CENA-Alternative 1	CENA-Alternative 2
Source spectrum model	Single corner frequency ω^{-2}	Single corner frequency ω^{-2}
Stress parameter, $\Delta\sigma$ (bars)	250	600
Shear-wave velocity at source depth, β_s (km/sec)	3.7	3.7
Density at source depth, ρ_s (gm/cc)	2.8	2.8
Geometric spreading, $Z(R)$	$\begin{cases} R^{-1.3} & R < 70 \text{ km} \\ R^{+0.2} & 70 \leq R < 140 \text{ km} \\ R^{-0.5} & R \geq 140 \text{ km} \end{cases}$	$\begin{cases} R^{-1.3} & R < 50 \text{ km} \\ R^{-0.5} & R \geq 50 \text{ km} \end{cases}$
Quality factor, Q	$\max(1000, 893 f^{0.32})$	$525 f^{0.45}$
Source duration, T_s (sec)	$1/f_a$	$1/f_a$
Path duration, T_p (sec)	$\begin{cases} 0 & R \leq 10 \text{ km} \\ +0.16R & 10 < R \leq 70 \text{ km} \\ -0.03R & 70 < R \leq 130 \text{ km} \\ +0.04R & R > 130 \text{ km} \end{cases}$	$\begin{cases} 0 & R \leq 10 \text{ km} \\ +0.16R & 10 < R \leq 70 \text{ km} \\ -0.03R & 70 < R \leq 130 \text{ km} \\ +0.04R & R > 130 \text{ km} \end{cases}$
Site amplification, $A(f)$	Atkinson and Boore [2006] Boore and Thompson [2015]	Atkinson and Boore [2006] Boore and Thompson [2015]
Kappa, κ_0 (sec)	0.005	0.005

Table 7.4 Median parameters used in high-frequency stochastic synthetic simulations for WNA.

Parameter	WNA
Source spectrum model	Single corner frequency ω^{-2}
Stress parameter, $\Delta\sigma$ (bars)	80
Shear-wave velocity at source depth, β_s (km/sec)	3.5
Geometric spreading, $Z(R)$	$\begin{cases} R^{-1.0} & R < 40 \text{ km} \\ R^{-0.5} & R \geq 40 \text{ km} \end{cases}$
Quality factor, Q	$180f^{0.32}$
Source duration, T_s (sec)	$1/f_a$
Path duration, T_p (sec)	0.05R
Site amplification, $A(f)$	Boore and Joyner [1997] Boore and Thompson [2015]
Kappa, κ_0 (sec)	0.04
Quality factor, Q	$180f^{0.32}$

7.3.2.1 Earthquake Source Term

In this study, the Brune ω -square source spectrum as a single corner-frequency source spectrum is used for both host and target regions. The key element in this source model is the stress parameter ($\Delta\sigma$), which controls the amplitude of spectrum at high frequencies. The geometric mean of the stress parameter in each region is given in Table 7.3 and Table 7.4.

The FF simulations at each sub-fault are performed using a local stress parameter assigned at each point on the fault. The correlation between the stress and slip distribution used in high-frequency and low-frequency simulations, respectively, needs to be taken into account. In this study, we used the stress distribution procedure proposed by Ripperger and Mai [2004] and Andrews [1980] in simulations. This technique correlates the local slip to the local stress at a given point over the fault plane. The final stress distribution is achieved by applying a scaling factor to match the geometric mean of the stress over the fault to the desired values given in Table 7.3 and Table 7.4. An example of the stress distribution is shown in Figure A7.2 along with kinematic source representations.

Campbell [2003] and Tavakoli and Pezeshk [2005] used five stress parameters in ENA in the range of 105–215 bars, with different assigned weights to each one. Atkinson and Boore [2006] applied $\Delta\sigma = 140$ bars in FF stochastic simulations using the EXSIM package by Motazedian, and Atkinson [2005]. Further studies by Atkinson et al. [2009] and Boore [2009] suggested $\Delta\sigma = 250$ bars in ENA based on observations from the recorded data. Pezeshk et al.

[2011] used $\Delta\sigma = 250$ bars in their HEM simulations for ENA. Recently, Atkinson and Boore [2014] suggested the stress term of 600 bars for $M > 4.5$. Following the previous discussion, we have used 250 and 600 bars to represent the overall stress parameter in our two alternative models for CENA.

In WNA, Campbell [2003; 2007] used 100 bars stress parameters in his HEM model. Atkinson and Silva [2000] suggested $\Delta\sigma = 80$ bars for a single-corner frequency source model, which also was implemented by Pezeshk et al. [2011]. We used the same stress parameter ($\Delta\sigma = 80$ bars) in our simulations.

7.3.2.2 Path Effects

The path term takes into account two effects of geometrical spreading, $Z(R)$ and anelastic attenuation (known as quality factor, Q). Note that the selection of stress parameter is correlated with the geometrical spreading implemented in the model [Boore et al. 2010]. Simulations in Atkinson and Boore [2006] were performed using a trilinear geometrical spreading as R^b where b is -1.3, +0.2, and -0.5 for $R < 70$, $70 < R < 140$, and $R > 140$, respectively. They used the quality factor of $Q = 893f^{0.32}$ (with the minimum value of 1000) as the anelastic attenuation following Atkinson [2004]. Similar parameters are incorporated in the study of Pezeshk et al. [2011] for simulations in ENA. Atkinson and Boore [2014] suggested the bilinear geometrical spreading with different attenuation rates for distances beyond 50 km (i.e., $R^{-1.3}$ for $R < 50$ km and $R^{-0.5}$ for $R > 50$ km). In addition, they proposed the quality factor of $Q = 525f^{0.45}$ compatible with updated parameters for stochastic simulations. Following the previous discussion and to be consistent with implementing two different stress parameters applied in this study, we employed two alternative sets of geometrical spreading and quality factor relations. The similar distance-dependent path duration in CENA used in Campbell [2003; 2007] and Pezeshk et al. [2011] is applied in this study.

Western North America stochastic simulations by Campbell [2003] were performed using a bilinear geometrical spreading (i.e., $R^{-1.0}$ for $R < 40$ km and $R^{-0.5}$ for $R > 40$ km) and the anelastic attenuation of $Q = 180f^{0.45}$. The parameters originally derived in the study by Raof et al. [1999] were based on the evaluation of about 180 earthquakes in Southern California. These parameters were supported by further studies by Malagnini et al. [2007] by considering a larger earthquake dataset. Similar path term relations were applied in Pezeshk et al. [2001] and this study. A simple path duration ($T_p = 0.05R$) was suggested by Herrmann [1985], which has been widely used in the literature. Boore and Thompson [2014] proposed longer path duration based on their observations on NGA-West2 database. Similar to Atkinson and Silva [2000], Campbell [2003; 2007] and Pezeshk et al. [2011], we applied ($T_p = 0.05R$) as the path duration in our simulations for WNA.

7.3.2.3 Site Effects

The local site effects incorporated two terms of amplification factor, $A(f)$, which is the amplification relative to the source, and a near-surface attenuation that represents the loss of energy in high frequencies as a path-independent function [Boore 2003]. This attenuation could

be applied through a low-pass filter characterized by the decay parameter of κ_0 , which has significant effects on the high-frequency slope of spectrum [Boore 1983].

The ENA simulations in studies by Campbell [2003] and Tavakoli and Pezeshk [2005] were performed using site amplification factors proposed by Boore and Joyner [1997] for the hard-rock site condition with $V_{s30} = 2900$ m/sec. They considered variability in the κ_0 (0.012, 0.003, and 0.006 in their models). Campbell [2007] generated synthetics in ENA for the national earthquake hazards reduction program (NEHRP) B-C site condition with $V_{s30} = 760$ m/sec.. He used site amplification factors derived by Atkinson and Boore [2006] for this site condition along with $\kappa_0 = 0.02$. Siddiqqi and Atkinson [2002] derived empirical amplification factors for hard-rock site conditions with $V_{s30} = 2000$ m/sec (NEHRP site class A). These factors along, with $\kappa_0 = 0.005$ were implemented in the ENA simulations of Atkinson and Boore [2006] and Pezeshk et al. [2011]. Recently, Hashash et al. [2014a, b] and Campbell et al. [2014] proposed the shear wave velocity of 3000 m/sec and the compatible kappa ($\kappa_0 = 0.006$) as the reference rock site condition for CENA. The parameters are derived applying the quarter-wavelength theory, using the data include the geographic regions of the Atlantic coast, the Appalachian Mountains, and the continental interior (the Gulf Coast region is not included). Atkinson and Boore [2014] set $\kappa_0 = 0.005$ along with their proposed new Q factor for ENA. Boore and Thompson [2015] revised the Boore and Joyner [1997] site amplification factors and provided two new sets of amplification factors for the generic very hard rock site condition with $V_{s30} = 3000$ m/sec as well as the generic rock site with $V_{s30} = 620$ m/sec. In this study, we used $\kappa_0 = 0.005$ along with the site amplification factors similar to what was used in Atkinson and Boore [2006] and Pezeshek et al. [2011], along with considering the Boore and Thompson [2015] amplification factors to account for $V_{s30} = 3000$ m/sec. Currently, the NGA-East working group are investigating to come up with reliable site amplification factors corresponding to $V_{s30} = 3000$ m/sec.

The site amplification factors in WNA proposed by Boore and Joyner [1997] derived from the quarter-wavelength method for a generic rock site condition with $V_{s30} = 620$ m/sec. These factors have been used in the WNA simulations by Atkinson and Silva [2000], Campbell [2003; 2007], Tavakoli and Pezeshk [2005], and Pezeshk et al. [2011]. A modification to these amplification factors have been provided by Boore and Thompson [2015] and was used in this study. Anderson and Hough [1984] suggested the average κ parameter for WNA in the range of 0.02–0.04 for the hard rock site condition. In this study, we utilized $\kappa_0 = 0.04$ in WNA, considering compatibility with the other parameters used and following Atkinson and Silva [1997], Campbell [2003; 2007], Pezeshk et al. [2011], and Al Atik et al. [2014, and *personal communication*].

7.4 HYBRID BROADBAND

The high-frequency stochastic and long-period synthetics constructed through the abovementioned procedures are combined and filtered to make broadband synthetics. The synthetics are filtered by passing through the matched second-order low-pass and high-pass Butterworth filters. In this study, a magnitude-dependent transition frequency (f_{cross}) between

high-frequency and low-frequency synthetics was applied as proposed by Frankel [2009] for **M5.5**, 6.5, and 7.5. We set f_{cross} for **M5** and 8 to be the same as for **M5.5**, and 7.5, respectively (i.e., 0.8 Hz for **M7.5**, and 8, 3.0 Hz for **M5** and 5.5); the f_{cross} for **M6** and 7 are calculated from interpolation.

Due to computational limitations associated with the generation of deterministic long-period synthetics at far distances, the broadband synthetics are computed for near-fault stations with R_{JB} distance of less than 200 km. Those are supplemented with synthetics generated for stations beyond 200 km through the finite-fault simulations in which the identical kinematic stress distributions are used (as was defined at each shaking scenario).

The synthetics generated from each individual 63 and 126 kinematic source models in CENA and WNA, respectively, were recorded at 490–670 (varies with magnitude) stations distributed in distance (2–1000 km) and azimuths (0–180°). The numbers of stations are listed in Table 7.5. For a given shaking scenario and a given station from 2–1000 km, two components of synthetics were rotated using the software package by Boore [2010], and the RotD50 intensity measures were calculated. These intensity parameters PGA, PGV, and 5%-damped PSA (0.02–10 sec) were used along with empirical GMMs of WNA in the development of HEM for CENA. The massive computations were accomplished using high performance computing at the University of Memphis Penguin Computing Cluster Servers.

The crustal structure used in CENA and WNA are given in Table 7.6, and Table 7.7, respectively. We used the continent velocity model suggested by Mooney et al. [2012] and Mooney [*personal communication*, 2013] for CEUS. In WNA, the crustal structure used by Frankel [2009], which represents a mean for the Western U.S. is implemented in this study.

Table 7.5 The number of stations where the synthetic seismograms are generated; the stations are distributed in distance and azimuth.

M	$R \leq 200$ km		$R > 200$ km	Total	
	CENA	WNA	Both regions	CENA	WNA
5.0	346	342	140	486	482
5.5	384	384	140	524	384
6.0	380	363	140	520	363
6.5	438	438	140	578	438
7.0	404	355	140	544	355
7.5	459	459	140	599	459
8.0	520	459	140	660	459

Table 7.6 The crustal model used in simulations for WNA (source: Frankel [2009]).

Z (km)	V_p (km/sec)	V_s (km/sec)	ρ (g/cm ³)
0.0	1.9	1.0	2.1
0.1	2.6	1.6	2.1
0.2	3.3	1.9	2.1
0.3	4.0	2.0	2.4
1.3	5.5	3.2	2.7
3.8	6.3	3.6	2.8
18.0	6.8	3.9	2.9
30.0	7.8	4.5	3.3

Table 7.7 The mid-continent crustal structure model used in simulations for CENA (source: Mooney et al. [2012; 2013]).

Z (km)	V_p (km/sec)	V_s (km/sec)	ρ (g/cm ³)
0.0	4.9	2.83	2.52
1.0	6.1	3.52	2.74
10.0	6.5	3.75	2.83
20.0	6.7	3.87	2.88
40.0	8.1	4.68	3.33

7.5 EMPIRICAL GROUND-MOTION MODELS IN WNA

One of the key elements in HEM technique is applying appropriate empirical GMMs developed for the host region. Pezeshk et al. [2011] incorporated the GMPEs from the PEER NGA-West1 project [Power et al. 2008] as empirical GMMs for WNA in their HEM model. Recently, the NGA-West1 model developers updated their GMPEs as part of the NGA-West2 project [Bozorgnia et al. 2014] in light of additional data available in the NGA-West2 database. This database includes well-recorded shallow crustal earthquakes that occurred worldwide (in the Western U.S. as well as other similar tectonically active regions).

We have used the following proposed 5 NGA-West2 GMPEs in this study for WNA: (1) Abrahamson et al. [2014], (2) Boore et al. [2014b], (3) Campbell and Bozorgnia [2014], (4) Chiou and Young [2014], and (5) Idriss [2014] models which hereafter are referred to as ASK14, BSSA14, CB14, CY14, and I14, respectively. The weighted geometric mean of the abovementioned GMPEs is computed to represent the median empirical ground motion in WNA. The similar weights used in the 2014 update of the U.S. national seismic hazard maps [Petersen et al. 2014] are assigned to each NGA-West2 GMPE in this study. The weights are distributed

evenly between all GMPEs except for I14 with the lower weight. The assigned weights are 0.22 for each of the ASK14, BSSA14, CB14, and CY14 models, and 0.11 for the I14 model.

The intensity measures in NGA-West2 GMPEs are computed using RotD_{50} parameters, unlike GMRotI50 (the period-independent geometric mean of two horizontal motions) used in the NGA-West1 project. The RotD_{50} is an alternative designation of the mean horizontal component that is independent of sensor orientation, but in contrast to GMRotI50, it is spectral period-dependent [Boore 2010].

Except for the BSSA14 model developed for R_{JB} distance, the other GMMs used the closest distance to the rupture plane (R_{RUP}). As the proposed model in this study is based on the R_{JB} distance metric, we converted R_{RUP} to R_{JB} in the ASK14, CB14, CY14, and I14 models, using the suggested conversion equations by Scherbaum et al. [2004].

The intensity measures of empirical GMMs were attained for the generic rock site of NEHRP B-C site condition with $V_{s30} = 760$ m/sec. This study used a generic style of faulting to evaluate the empirical ground motions, and the hanging wall effect was excluded. Other parameters were set to be calculated by each model (if applicable) assuming no other information was available.

7.6 PROPOSED GROUND-MOTION PREDICTION EQUATIONS FOR CENA

7.6.1 Hybrid Empirical Ground-Motion Estimates in CENA

The median hybrid empirical estimates of ground motion for CENA are calculated by applying regional modification factors that properly scale the empirical ground motions in WNA. To generate synthetics for both the target and host region, the model is calibrated for the same sets of magnitude (M5.0 to M8.0 in 0.5 magnitude increments), distances ($2.0 \leq R_{JB} \leq 1000$ km in 33 R_{JB} distances of 2, 5, 10, 15, 20, 30, 40, 50, 60, 70, 80, 90, 100, 110, 120, 140, 150, 160, 180, 200, 250, 300, 350, 400, 450, 500, 550, 600, 650, 700, 800, 900, and 1000 km) and the ground-motion parameters used to obtain empirical GMPEs in the host region.

The regional modification factors are calculated based on the ratios of intensity measures of CENA to WNA. Synthetics are generated and then used to derive the intensity measures in both target and host regions. In each region, median intensity measures at a particular magnitude, distance, and spectral period are calculated considering all shaking scenarios (for that magnitude) and all stations distributed in different azimuths. The median intensity measures in CENA are obtained by applying equal weight (50%) to results from two alternative models as defined in this region.

There are some restrictions and issues that need to be considered in developing the hybrid empirical ground-motion estimates. One refers to the range of validity of empirical ground motion used. Table 7A.1 (appendix 7A) lists the range in which NGA-West2 GMPEs were developed in terms of magnitude, distance, and site condition based on their developers' suggestions. It can be inferred that these empirical ground motion are not valid for distances beyond 300–400 km, so it is inappropriate to implement them beyond that distance range. Another issue originated from the difference of the attenuation rates between CENA and WNA

regions used in the synthetic generations (see Tables 7.3 and 7.4). The lower attenuation rate in CENA in the distance range of about 70–140 km causes higher amplitudes of ground motions at larger distances, resulting in higher estimations of the hybrid empirical ground motion at larger distances.

Considering the abovementioned issues, the hybrid empirical method for CENA is limited to distances up to about 70 km in which reliable hybrid empirical estimates can be developed. In order to avoid this constraint and extend our GMPEs model up to 1000 km, we followed the procedure proposed by Campbell [2003] and used by Campbell [2007] and Pezeshk et al. [2011]. The procedure supplements hybrid empirical estimates beyond 70 km by intensity measures of generated synthetics. In this regard, for a given magnitude, the intensity measures of synthetics beyond 70 km are scaled by a factor that fits the hybrid empirical estimate to the median of synthetics' intensity measure at $R_{JB} = 70$ km in CENA.

The completed set of hybrid empirical ground-motion estimates are then used to develop GMPEs in CENA for distances of 2–1000 km and magnitudes of 5–8. It include intensity measures of PGA, PGV, and 5%-damped PSAs at spectral periods of 0.01–10 sec, which were computed using RotD_{50} parameters for the generic hard rock site condition with $V_{s30} = 3000$ m/sec. We did not include PGD equations because none of the empirical NGA-West2 GMPEs implemented in this study provided such equations in their model. In addition, Boore et al. [2014b] observed that low-cut filtering has a significant influence on the PGD parameter.

7.7 THE FUNCTIONAL FORM

In this study, our effort was to keep the functional form as similar as that presented in Pezeshk et al. [2011]. However, there are two main changes to the functional form as compared to the median function of Pezeshk et al. [2011]: (1) we used R_{JB} distance instead of rupture distance (R_{RUP}); and (2) the range of distance in which the rate of attenuation is decayed has been changed from 70–140 km to 60–120 km based on recent observation of recorded data [Boore and Thompson 2015]. The following equation represents our functional form used herein to predict the median ground motion for CENA:

$$\begin{aligned} \log(\bar{Y}) = & c_1 + c_2\mathbf{M} + c_3\mathbf{M}^2 + (c_4 + c_5\mathbf{M}) \times \min\{\log(R), \log(60)\} \\ & + (c_6 + c_7\mathbf{M}) \times \max\left[\min\{\log(R/60), \log(120/60)\}, 0\right] \\ & + (c_8 + c_9\mathbf{M}) \times \max\{\log(R/120), 0\} + c_{10}R \end{aligned} \quad (7.2)$$

and

$$R = \sqrt{R_{JB}^2 + c_{11}^2} \quad (7.3)$$

where \bar{Y} represents the median value of ground-motion intensity measure in CGS units (i.e., PSA (g), PGA (g), or PGV (cm/sec)), \mathbf{M} is the moment magnitude, R_{JB} (km) is the closest horizontal distance to the vertical projection of the rupture plane, and c_1 to c_{11} are the coefficients of the functional form that fits the hybrid empirical estimates of ground motion in CENA. The

coefficients are derived from a nonlinear least-squares regression and are tabulated in Table 7.8; $PSA(g)$ signifies the pseudo-spectral accelerations for 5% damping and for spectral periods of 0.01 to 10.0 sec. The resulting GMM is valid for $5.0 \leq \mathbf{M} \leq 8.0$, $5.0, 2.0 \leq R_{JB} \leq 1000$ km, and is developed for the generic hard rock site with $V_{s30} = 3000$ m/sec.

Table 7.8 Regression coefficients for the proposed hybrid empirical model.

T (sec)	C_1	C_2	C_3	C_4	C_5	C_6	C_7	C_8	C_9	C_{10}	C_{11}	C_{12}	C_{13}	C_{14}
PGA	1.4621	6.809E-02	-1.490E-02	-3.1827	2.861E-01	-1.199E+00	9.093A-02	-2.9089	2.503A-01	-5.781E-04	5.121E+00	-2.407E-02	4.247E-01	2.882E-01
PGV	-0.9273	8.713A-01	-4.999E-02	-3.0414	3.093A-01	-2.954E-01	-1.167E-02	-2.6440	3.205E-01	-5.377E-04	6.060E+00	-1.783A-02	3.804E-01	2.652E-01
0.010	1.4276	6.458E-02	-1.452E-02	-3.1747	2.871E-01	-1.110E+00	8.313A-02	-2.8809	2.503A-01	-6.084E-04	4.966E+00	-2.431E-02	4.264E-01	2.883A-01
0.020	1.7005	4.014E-02	-1.078E-02	-3.1103	2.614E-01	-1.636E+00	1.291E-01	-3.0448	2.516E-01	-4.333A-04	5.863A+00	-2.429E-02	4.269E-01	2.890E-01
0.030	1.8545	-4.291E-03	-8.502E-03	-3.1347	2.798E-01	-9.440E-01	3.427E-02	-3.4069	2.663A-01	-3.681E-04	5.099E+00	-2.505E-02	4.358E-01	2.934E-01
0.040	1.7859	7.902E-03	-9.799E-03	-3.1386	2.914E-01	-5.341E-01	-1.466E-02	-3.4676	2.619E-01	-4.136E-04	4.674E+00	-2.506E-02	4.407E-01	2.989E-01
0.050	1.6066	4.692E-02	-1.249E-02	-3.1186	2.959E-01	-3.417E-01	-3.267E-02	-3.3679	2.487E-01	-5.017E-04	4.466E+00	-2.508E-02	4.455E-01	3.042E-01
0.075	1.0249	1.729E-01	-2.008E-02	-3.0198	2.912E-01	-2.626E-01	-2.598E-02	-2.9064	2.078E-01	-7.414E-04	-4.347E+00	-2.436E-02	4.493A-01	3.131E-01
0.100	0.4682	2.905E-01	-2.658E-02	-2.9118	2.790E-01	-3.268E-01	-5.395E-03	-2.4515	1.734E-01	-9.288E-04	-4.449E+00	-2.454E-02	4.552E-01	3.178E-01
0.150	-0.4215	4.745E-01	-3.626E-02	-2.7416	2.545E-01	-3.875E-01	1.604E-02	-1.8167	1.307E-01	-1.138E-03	-4.838E+00	-2.428E-02	4.516E-01	3.142E-01
0.200	-1.0998	6.142E-01	-4.352E-02	-2.6270	2.354E-01	-3.165E-01	1.257E-02	-1.4684	1.108E-01	-1.211E-03	-5.261E+00	-2.433A-02	4.488E-01	3.105E-01
0.250	-1.6625	7.309E-01	-4.975E-02	-2.5450	2.209E-01	-1.815E-01	-2.760E-03	-1.2861	1.026E-01	-1.215E-03	-5.638E+00	-2.331E-02	4.412E-01	3.093A-01
0.300	-2.1603	8.351E-01	-5.549E-02	-2.4803	2.095E-01	-3.014E-02	-2.184E-02	-1.1963	1.002E-01	-1.185E-03	-5.954E+00	-2.220E-02	4.368E-01	3.118E-01
0.400	-3.0450	1.022E+00	-6.626E-02	-2.3761	1.923A-01	2.393A-01	-5.741E-02	-1.1475	1.025E-01	-1.087E-03	-6.436E+00	-2.043A-02	4.289E-01	3.149E-01
0.500	-3.8326	1.191E+00	-7.630E-02	-2.2889	1.795E-01	4.249E-01	-8.235E-02	-1.1638	1.070E-01	-9.805E-04	-6.800E+00	-1.920E-02	4.261E-01	3.198E-01
0.750	-5.4816	1.547E+00	-9.803A-02	-2.1117	1.565E-01	5.619E-01	-9.995E-02	-1.2235	1.130E-01	-7.674E-04	-7.585E+00	-1.667E-02	4.202E-01	3.302E-01
1.000	-6.7391	1.818E+00	-1.145E-01	-1.9803	1.403A-01	4.249E-01	-7.933A-02	-1.2253	1.111E-01	-6.361E-04	-8.477E+00	-1.364E-02	4.050E-01	3.343A-01
1.500	-8.3135	2.147E+00	-1.333A-01	-1.8396	1.199E-01	-7.694E-02	-6.935E-03	-1.1269	9.884E-02	-5.167E-04	-1.087E+01	-9.864E-03	3.833A-01	3.370E-01
2.000	-8.9502	2.267E+00	-1.384E-01	-1.8493	1.128E-01	-5.042E-01	5.307E-02	-1.0238	8.902E-02	-4.782E-04	1.402E+01	-7.980E-03	3.720E-01	3.377E-01
3.000	-8.5940	2.149E+00	-1.260E-01	-2.1748	1.302E-01	-8.038E-01	8.808E-02	-0.9878	9.075E-02	-4.494E-04	2.022E+01	-8.203A-03	3.731E-01	3.375E-01
4.000	-7.5122	1.833A+00	-1.021E-01	-2.5766	1.708E-01	-5.200E-01	3.744E-02	-1.1502	1.133A-01	-4.079E-04	2.283A+01	-6.930E-03	3.604E-01	3.326E-01
5.000	-6.3964	1.501E+00	-7.863A-02	-2.9617	2.188E-01	4.749E-02	-5.068E-02	-1.4038	1.437E-01	-3.491E-04	2.330E+01	-6.642E-03	3.586E-01	3.326E-01
7.500	-5.5543	1.154E+00	-5.334E-02	-3.4138	2.864E-01	1.166E+00	-2.141E-01	-1.8555	1.967E-01	-2.523A-04	2.123A+01	-6.207E-03	3.541E-01	3.309E-01
10.000	-7.6258	1.734E+00	-9.512E-02	-3.5309	2.870E-01	4.274E-01	-9.501E-02	-1.4464	1.613A-01	-3.943A-04	2.244E+01	-7.381E-03	3.570E-01	3.267E-01

7.8 RESULTS AND MODEL EVALUATION

This next section presents and evaluates the results of the proposed model. Validation and evaluation of the results in this study are accomplished by the comparisons of the proposed GMPEs with the previous GMMs as well as recorded data in CENA.

Figure 7.1 shows comparison examples of 5%-damped response spectral accelerations derived from the hybrid broadband simulations with five NGA-West2 GMPEs as well as their weighted geometric mean. The response spectra are presented for two magnitudes of $M=6$ and 7 at the distance of $R_{JB} = 40$ km. The WNA spectral accelerations are calculated from the generated broadband synthetics using the parameters discussed earlier. A comparison shows a good agreement between the weighted geometric mean of empirical NGA models and the WNA simulations.

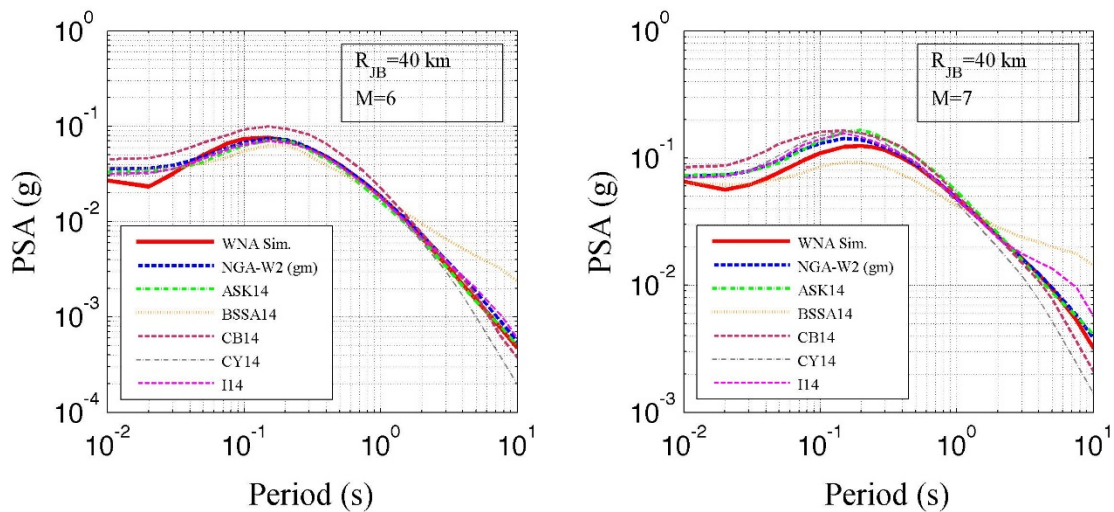


Figure 7.1 Comparison of spectral accelerations (5%-damped-PSA) from broadband simulations in this study and predicted values from NGA-West2 GMPEs. Plots include the individual GMMs of ASK14, BSSA14, CB14, CY14, and I14, along with their weighted geometric mean at $R_{JB} = 40$ km, and for magnitudes of $M=6$ (left panel) and $M=7$ (right panel).

7.8.1 Comparison with Previous Models

Figure 7.2 and Figure 7.3 represent the comparison of the GMPE results in this study (hereafter SP14) with two GMMs available in CENA: Pezeshk et al. [2011] and Atkinson and Boore [2006; 2011], hereafter referred to as PZT11 and AB06', respectively. The GMPE model comparisons are given in Figure 7.3 for $M=5$ and $M=7$ and for intensity measures of PGA and spectral periods of 0.2, 1.0, and 5.0 sec. In Figure 7.4 similar comparisons are made, but for different magnitude sets of $M=6$ and $M=8$. At very close distances and for PGA and higher-frequency spectral accelerations (e.g., at the spectral period of 0.2 sec), the magnitude saturation effects are observed in HEM results herein. In addition, we perceived over-saturation effects in the results from the broadband synthetics simulations, which is compatible with simulation results from

other investigators and observations from the recorded data [Shahjouei and Pezeshk 2013; 2014]. As discussed earlier, the stochastic finite-fault simulations of AB06' and the stochastic point-source model of PZT11 for ENA are based on using the stress parameters of 140 and 250 bars, respectively. The results reported herein are derived from the equally weighted simulations, which used the stress parameter of 250 and 600 bars in the high-frequency part of synthetics. The distance conversion relations for generic fault style by Scherbaum et al. [2004] is implemented on AB06' and PZT11 in order to compare with the results in this study.

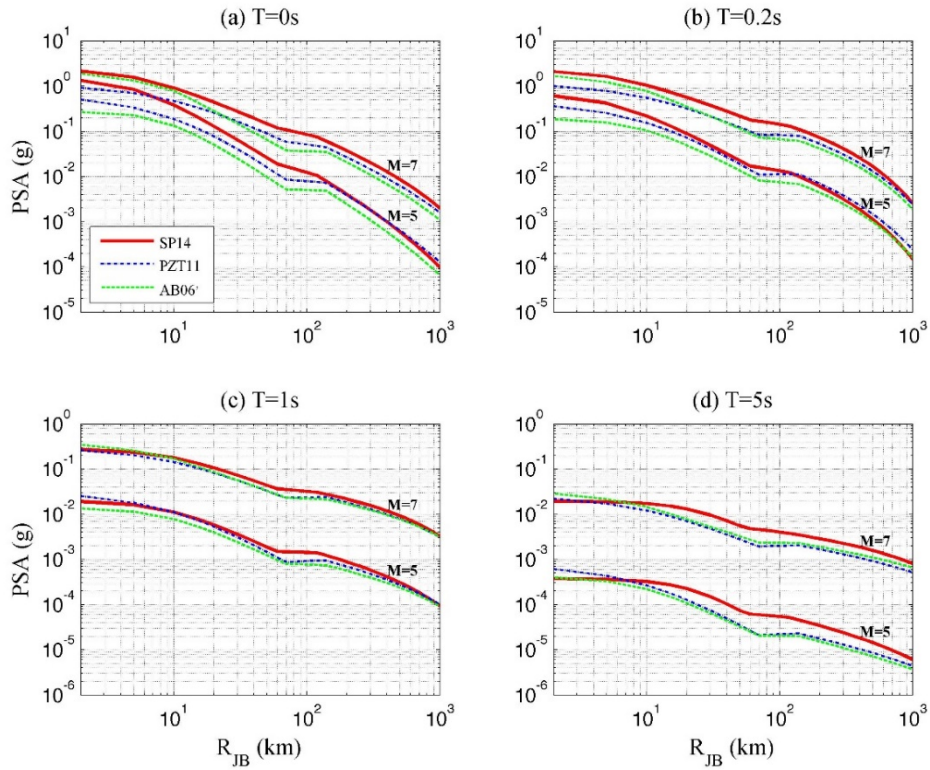


Figure 7.2 GMPEs developed in this study and comparison with AB06' and PZT11 GMMs for M5, and M7 at PGA ($T = 0$ sec) and spectral periods of 0.2, 1.0, and 5.0 sec.

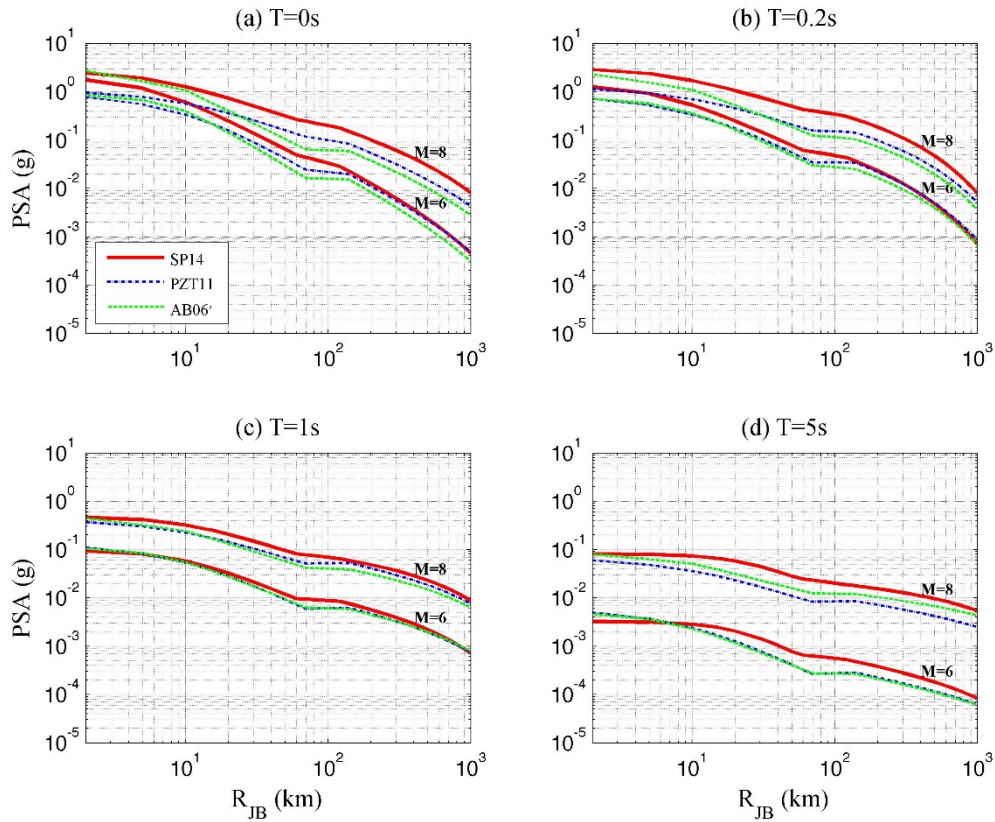


Figure 7.3 Similar to Figure 7.2 but for different magnitudes: **M6** and **M8**.

7.8.2 Comparison with Recorded Ground Motions

The new prediction model is compared and calibrated against the NGA-East database [Goulet et al. 2014]. In this comparison the data from the Gulf coast region and potentially-induced events (PIEs) are excluded. In addition, we used the data with quality flag of zero recorded at stations with $V_{s30} = 180$ m/sec. Figures 7.4–7.6 show comparisons of the results of this study with the small to moderate magnitude recorded earthquake data available in the NGA-East database. The NGA-East database was corrected for site conditions following Boore et al. [2014b] and Boore and Thompson [2015]. Figure 7.4 shows the comparison for the spectral period of 0.2 sec in different magnitude bins of **M4.5**, **5**, **5.5**, and **6**. Similar evaluations are shown in Figure 7.5 and Figure 7.6 but for different spectral periods of 1.0 and 4.0 sec. In order to make the appropriate assessment, intensity measures of the NGA-East database are adjusted for $V_{s30} = 3000$ m/sec. This scaling is performed by using the ratios of amplification factors that scale the calculated intensity measures at stations with local shear wave velocities to the reference rock site condition used in this study (i.e., $V_{s30} = 3000$ m/sec). Comparisons show a good agreement between the proposed model and small to moderated magnitude recorded data in the NGA-East database.

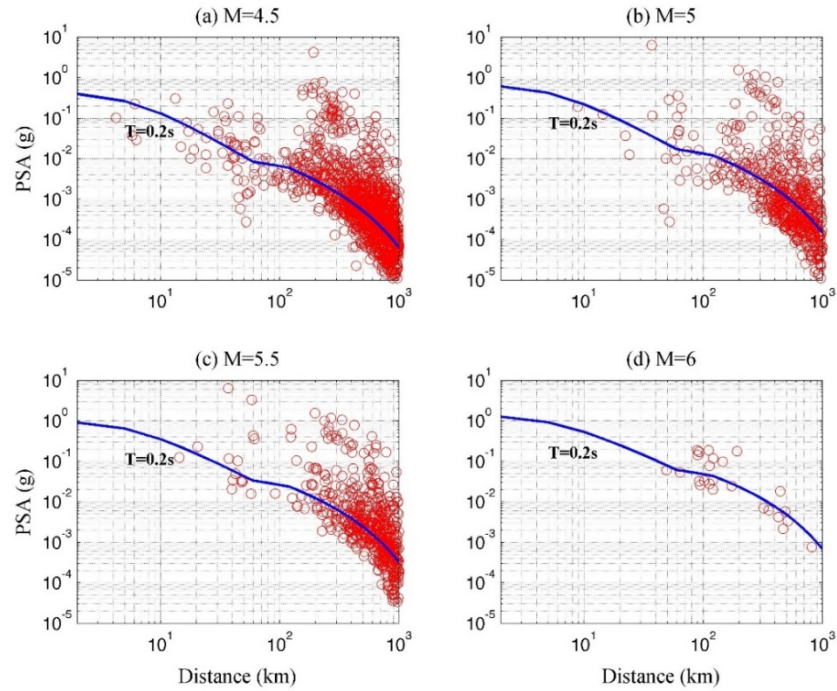


Figure 7.4 Comparison of the developed GMPEs with the recorded earthquakes available in NGA-East database for the spectral period of 0.2 sec in magnitude bins of M4.5, 5.0, 5.5, and 6.

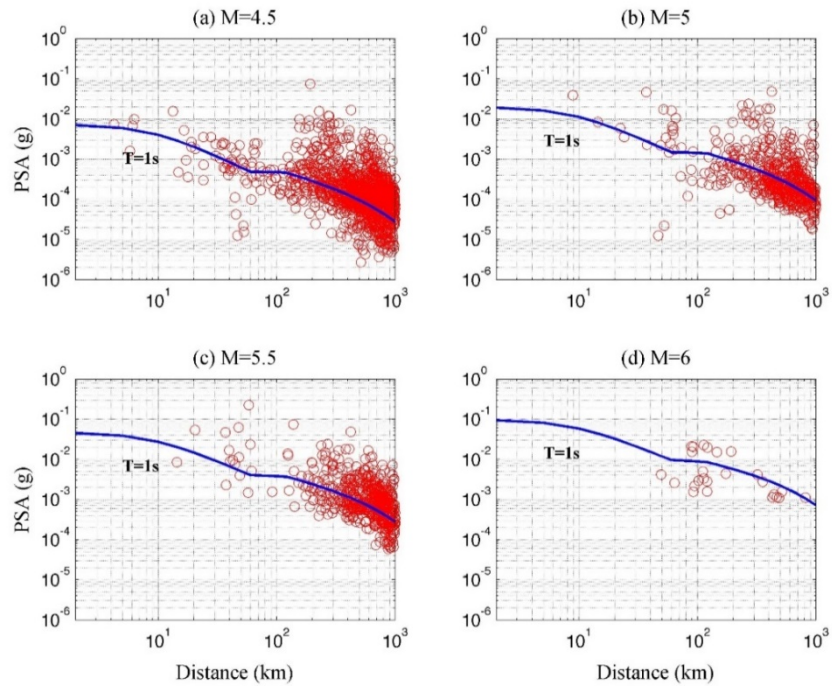


Figure 7.5 Similar to Figure 7.4 but for different spectral period of 1.0 sec.

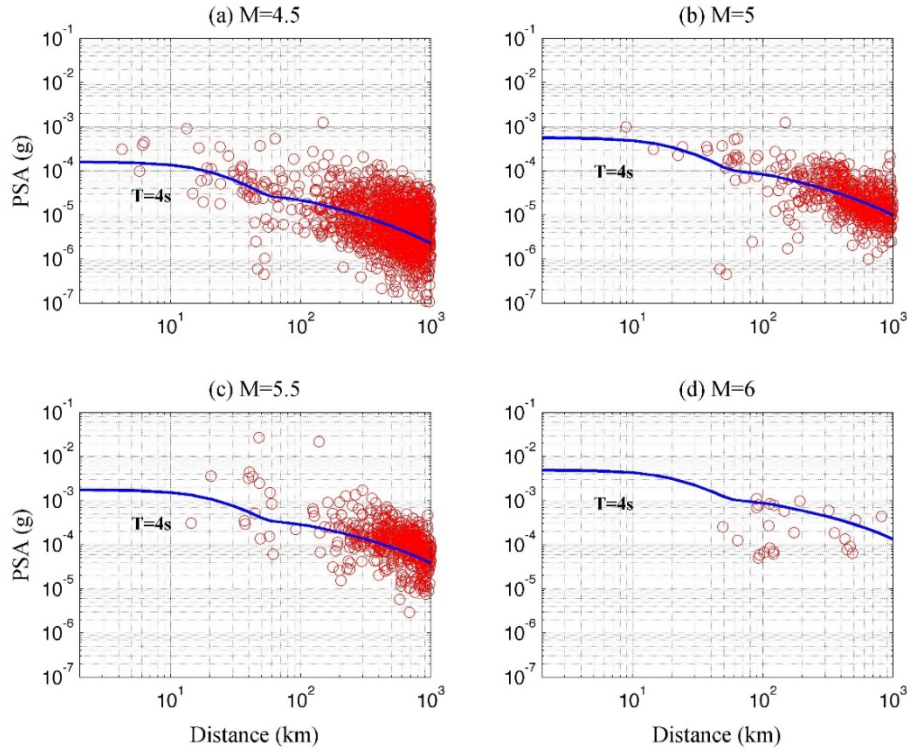


Figure 7.6 Similar to Figure 7.4 but for different spectral period of 4.0 sec.

Figures 7.7–7.9 show some examples of the residual analysis performed in this study. The residuals represent the differences between predicted (simulated) and the earthquake recorded data in the NGA-East database. Figure 7.7 shows the distribution of residuals with respect to the distance for spectral accelerations at periods of 0.2, 1.0, and 4 sec. The distribution of residuals with respect to the magnitude at the similar spectral periods is given in Figure 7.8. In Figure 7.9 the residuals are presented in classified terms of the inter-event (between-event) and intra-event (within-event) residuals for the same periods of 0.2, 1.0, and 4 sec. This classification demonstrates the effects of very small magnitude earthquakes included in the catalog. Additionally, the effects of local site condition on residuals are illustrated in Figure 7.9. The corrected residuals are obtained after applying the scaling factors to represent all intensity measures with the reference rock site condition. The plots show no significant trends in residuals obtained from the predicted model and the NGA-East database.

The response spectral accelerations from the proposed model are compared with those from the AB06' and PZT11 GMMs in Figure 7.10. The spectra are shown for earthquake magnitudes of M5, 6, 7, and 8 at distance of $R_{JB} = 40$ km for spectral periods up to 10 sec. At this close distance to the fault, we observed the higher spectral amplitudes compared to PZT11, particularly for longer periods.

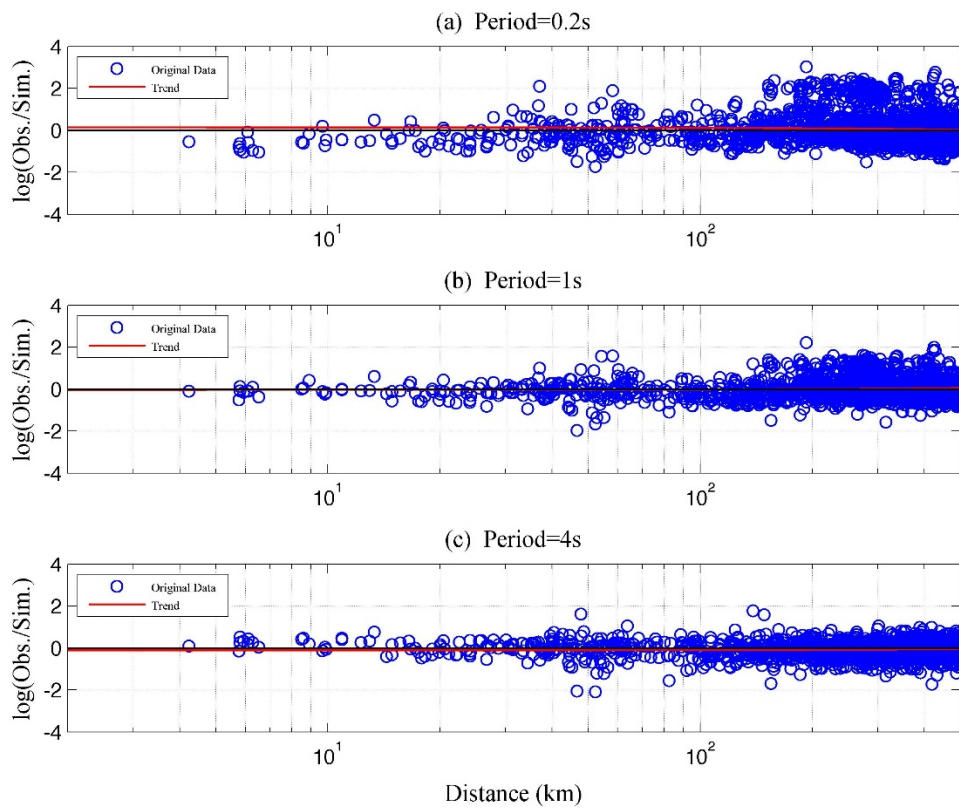


Figure 7.7 Residuals with respect to the distance for spectral periods of $T = 0.2, 1.0,$ and 4 sec. The total residuals represent the difference between observed and the predicted spectral accelerations.

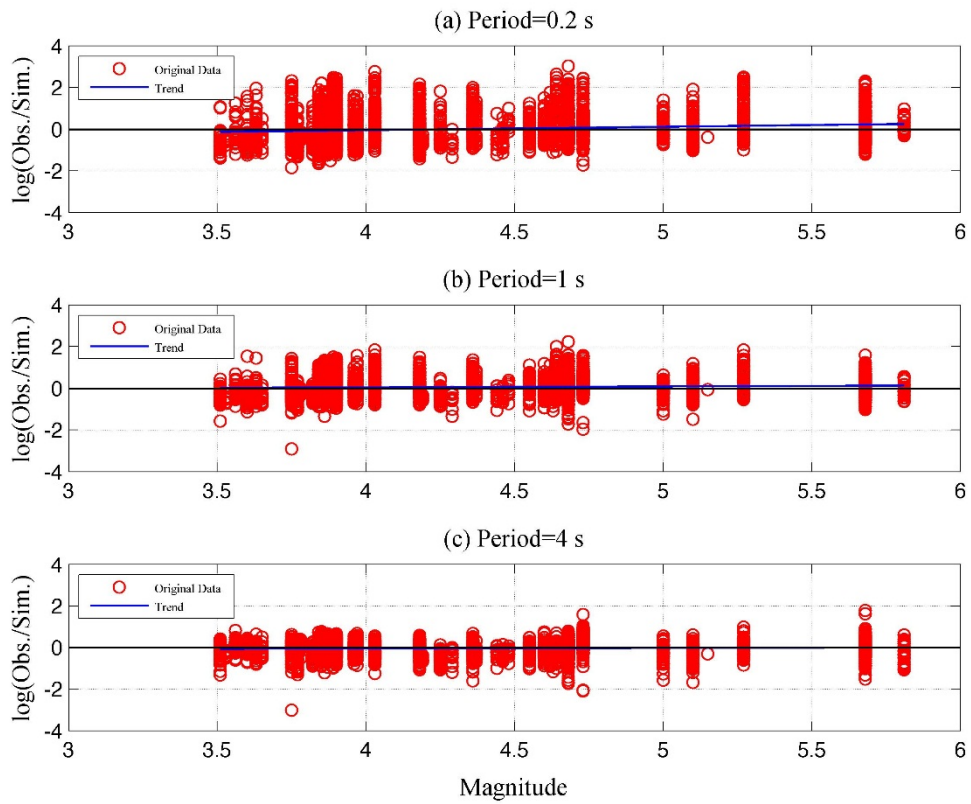


Figure 7.8 Residuals with respect to the magnitude for same spectral periods of $T = 0.2, 1.0,$ and 4 sec as was presented in Figure 7.7. The total residuals represent the difference between observed and the predicted spectral accelerations.

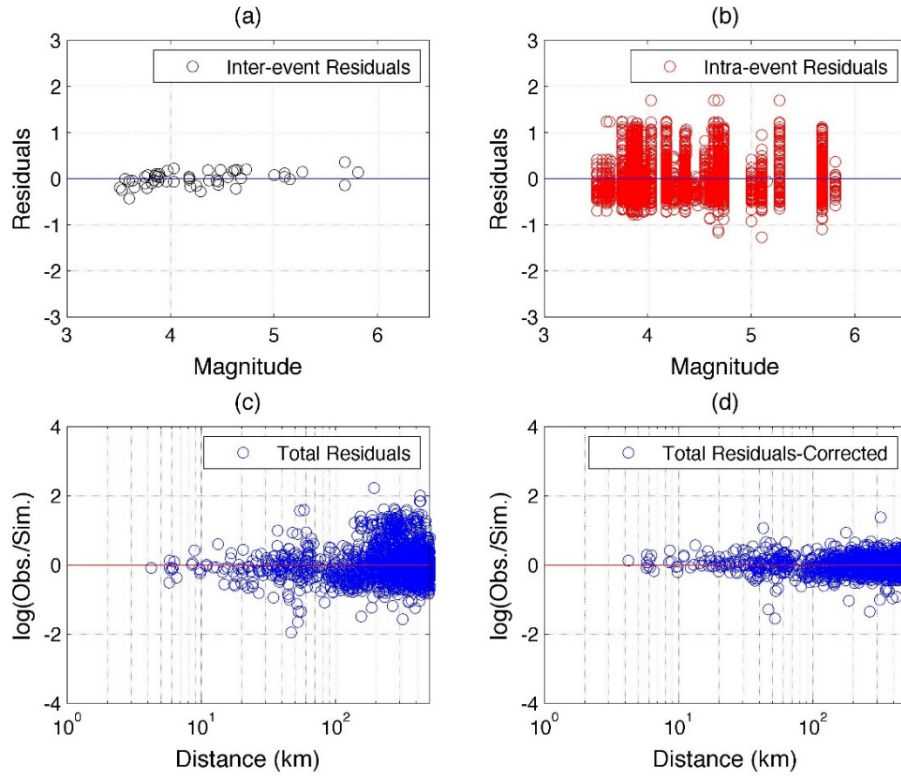


Figure 7.9 Residuals are presented in terms of (a) inter-event residuals and (b) intra-event residuals for spectral periods of $T = 0.2, 1.0,$ and 4 sec; (c) shows the total residuals without considering the local individual site condition; and (d) the corrected residuals take into account local site conditions when compared with the predicted model.

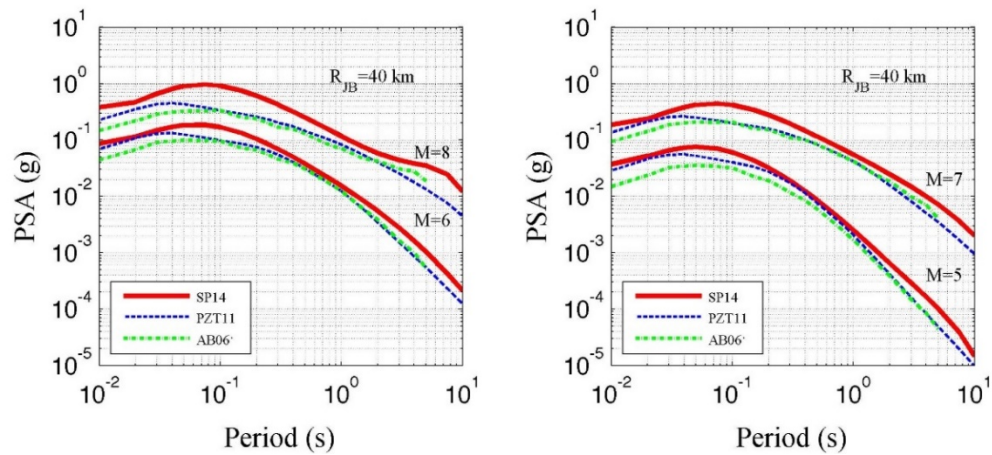


Figure 7.10 Comparison of the 5%-damped pseudo-spectral accelerations derived from the GMPEs developed in this study for CENA and those obtained from AB06' and PZT11 models. PSAs are shown at distance of $R_{JB} = 40$ km, and for magnitudes of **M6**, and **8** (left) and **M5**, and **7** (right).

7.9 DISCUSSIONS AND CONCLUSIONS

A hybrid empirical GMM is proposed for CENA as an update to the Pezeshk et al. [2011] model, following the procedure proposed by Campbell [2003]. To be implemented in the HEM, earthquake broadband synthetics are generated through a hybrid broadband simulation technique using a FF method for both host (here, WNA) and target (here, CENA) regions. The high-frequency synthetics are produced through a stochastic FF method, and the low-frequency ones are constructed through the kinematic source models and deterministic wave propagation. Two sets of stochastic parameters for CENA are used in this study and are equally weighted to consider the variability in parameters. A detailed description of the synthetic generation approach and the parameters used is discussed in the ground-motion simulation part and is also available in Shahjouei and Pezeshk [2013; 2014]. We have used the updated seismological and geological parameters suggested in the literature in synthetic simulations.

The HEM used the empirical GMMs for the host region. The recent five updated empirical GMPEs for WNA, called NGA-West2 GMPEs, were incorporated in this study as the element of HEM. These models are in Abrahamson et al. [2014], Boore et al. [2014b], Campbell and Bozorgnia [2014], Chiou and Young [2014], and Idriss [2014]. These empirical models are weighted following the procedure adopted by the 2014 U.S. NSHMs [Petersen et al. 2014].

The new GMPEs are developed for R_{JB} distances up to 1000 km, for the moment magnitude range of $M5-8$, and for the suggested generic hard rock site condition with $V_{s30} = 3000$ m/sec [Hashash et al. 2014a, b] for CENA. Applying the proper site amplification factors, a GMM could be estimated for other site conditions.

The predicted new GMPEs and the associated spectral accelerations are compared with the GMMs of Pezeshk et al. [2011] and Atkinson and Boore [2006; 2011]. The inter-event and intra-event residuals that represent the differences between the predicted and observed ground-motion intensity measures do not display a discernible trend. The residual analyses are performed on the small-moderate earthquakes in CENA available in the NGA-East dataset with respect to the magnitude and distance.

The new sets of coefficients are provided to be used in the functional form of the GMPE. The uncertainties associated with the new model are discussed and delivered. The aleatory uncertainty incorporated the uncertainties in NGA-West2 GMPEs and the regression analysis used to derive the GMPE coefficients. The minimum additional epistemic uncertainty suggested to be used along with the median of NGA-West2 GMPEs [Al Atik and Youngs 2014] as well as the variation of some parametric modeling are provided in this study.

The proposed GMPE, as an alternative GMM together with the other available models, can be implemented in order to better characterize the ground-motion estimations and to effectively signify the epistemic uncertainty in the CENA.

7.10 DATA AND RESOURCES

The COMPSYN sxv3.11 software package provided by its author (Dr. Paul Spudich) is used for long-period simulations. We have used and modified the rupture model generator package by Dr. Martin Mai (some codes are available at www.ces.kaust.edu.sa/Pages/Software.aspx, last

accessed August 2013). The SMSIM program along with some other FORTRAN subroutines available at www.daveboore.com (last accessed May 2013) have been incorporated in this study. The NGA-East database (November 12, 2014 version) for comparison was obtained from Goulet et al. [2014].

7.11 ACKNOWLEDGMENTS

The authors would like to acknowledge Dr. Paul Spudich and Dr. Martin Mai for providing us with their software packages, and their continuous constructive supports and suggestions, which helped us in earthquake simulations. We have benefitted from interactions with and comments received from Drs. Kiran K. Thingbaijam and Hugo C. Jimenez in discussions on earthquake source modeling.

7.12 LIST OF ELECTRONIC APPENDICES FOR CHAPTER 7

- 7A Supplemental Documentation (PDF document)
- 7B Model Output (Excel workbook)

8 Empirical Ground-Motion Prediction Equations for Eastern North America

Md. Nayeem Al Noman

Chris H. Cramer

**CERI, University of Memphis
Memphis, Tennessee**

Abstract

Our GMPE is an empirical model, based on the two-stage regression approach of Joyner and Boore [1993; 1994]. Besides ground-motion observations from the latest NGA-East RotD50 flatfile (2014-11-18), we included ground-motion observations from the 1976 **M**6.8 Gazli and 2001 **M**7.6 Bhuj earthquakes plus intensities converted to ground-motion estimates by Ogweno and Cramer [2014] for **M** > 6 ENA historical earthquakes (1811–1812 New Madrid, 1886 Charleston, South Carolina, 1925 Charlevoix, and 1929 Grand Banks earthquakes). Magnitudes for historical events were taken from Cramer and Boyd [2014] for the 1811–1812 and 1886 **M**7 earthquakes and from Bent [1992; 1995] for the 1925 and 1929 earthquakes. The Cramer and Boyd [2014] magnitude estimates have 95% confidence levels of ± 0.3 magnitude units. The prediction equations are for peak ground acceleration, peak ground velocity, and 5% damped pseudo-absolute acceleration spectra at 21 periods between 0.1 sec to 10 sec. Empirical observations were restricted to mid-continent crustal regions, avoiding Gulf Coast and Western U.S. Q regions for both earthquakes and recording stations. The reference V_{s30} is 760 m/sec. Geometrical spreading is modeled by a single term due to the limited observations at distances less than 50 km. We included a magnitude-dependent geometrical spreading term to help model magnitude saturation at large magnitudes. Alternative terms are also provided for focal mechanism type (reverse, strike-slip, and undefined). The observations did not constrain a depth factor h for distance ($R^2 = R_{RUP}^2 + h^2$), so it was fixed at 10 km.

8.1 INTRODUCTION

There has been a paucity of earthquake strong-motion recordings in Eastern North America (ENA) due to the low rate of seismicity. Traditionally ENA ground-motion prediction equations (GMPEs) used in engineering and earthquake hazard applications have been based on stochastic, finite rupture, and hybrid empirical models (e.g., Atkinson and Boore [1995], Somerville et al.

finite rupture, and hybrid empirical models (e.g., Atkinson and Boore [1995], Somerville et al. [2001], and Campbell [2003]). Since 2000, the number of earthquake strong-motion recordings has increased remarkably, making possible the compilation of the Next Generation Attenuation (NGA) East ground-motion database [Cramer et al. 2011; 2013]; however, the NGA-East database of ground-motion recordings is still limited to earthquake magnitudes less than moment magnitude (M) 6.

We developed ENA empirical GMPEs to explore the limitations of the NGA-East database of ground motions [Al Noman 2013]. We included strong motion observations for the 1976 $M6.8$ Gazli, 1985 $M6.9$ Nahanni, and the 2001 $M7.6$ Bhuj, India, earthquakes to provide some constraint on the empirical GMPEs from $M > 6$ earthquakes. Now we are including ground-motion estimates from intensity observations for historical $M > 6$ ENA earthquakes to better constrain our empirical GMPEs at large magnitudes. Ogweno and Cramer [2014] specifically developed ground motion from intensity conversion equations (GMICE) for ENA to provide the relevant $M > 6$ ground-motion observations for ENA empirical GMPE development.

In this chapter, we review the empirical dataset used in our GMPE development, summarize the GMICE of Ogweno and Cramer [2014] as it applies to our GMPE development, discuss our methodology, present our functional form for our GMPEs, and present our resulting GMPEs. As part of our results, we show comparisons to observations, scaling relationships, and comparisons with other recent ENA GMPEs.

8.2 DATASET

8.2.1 NGA-East Database

The data used for developing empirical GMPEs in this study are from the database compiled by the NGA-East Project. The data have been extracted from the NGA-East RotD₅₀ (geometric mean horizontal component, rotation dependent, median values) flatfile (version 2014-11-18), including the 1985 $M6.9$ Nahanni and 1976 $M6.8$ Gazli earthquake recordings. We also included ground-motion observations from the 2001 $M7.6$ Bhuj earthquakes [Cramer and Kumar 2003] to help constrain the ground motions for large magnitude earthquakes.

To make a more suitable GMPE model for ENA, we used those records (Figure 8.1) that were not influenced by the relatively higher attenuating areas of the Gulf Coast and Western North America (WNA). The Gulf Coast and WNA regions are delineated using initial results found in a study defining the major crustal attenuation boundaries of the continental U.S. [Cramer et al. 2014], and data outside these more attenuating regions are defined as north of 35°N and east of 100°W. The data with ray paths through the more attenuating regions are removed from the dataset. As a result, a total of 6048 records from 78 earthquakes are available and were used in the GMPE regressions. An additional 13 recordings are available from the 2001 $M7.6$ Bhuj earthquake but only for peak ground acceleration (PGA), 0.4 sec, 0.75 sec, 1.0 sec, and 1.25 sec [Cramer and Kumar 2003]. Bodin et al. [2004] demonstrate that the Bhuj area Q is similar to ENA Q at distances less than 300 km, which corresponds to the Cramer and Kumar [2003] dataset.

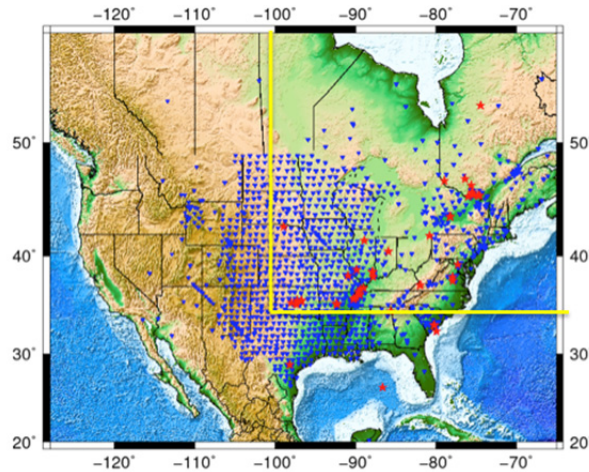


Figure 8.1 Recording stations (blue inverted triangles) and ENA earthquakes (red stars) from NGA-East database used in the regression analysis for developing empirical GMPEs for ENA. Only stations and events north and east of the yellow lines have been selected.

The selected dataset has a good number of earthquakes of reverse-slip and strike-slip fault types; however, it has only one normal-slip earthquake, which is not adequate for accounting for normal-slip fault type as an independent variable in the regression analysis. Therefore, the data from this one earthquake are included in the strike-slip records. Twenty-five earthquakes also have unknown focal mechanism parameters. As the number of such records is large in the database, they are classified as unspecified focal mechanism in the regression. Thus, the three fault type variables (reverse-slip, strike-slip, and unspecified) have sufficient data to be constrained in the prediction model by the amount of the records for each fault type.

8.2.2 Intensity Data

We have also included ground-motion estimates from intensity observations from $M > 6$ ENA earthquakes. We selected the intensity data from the 1811–1812 M 7.5, 7.3, and 7.7 New Madrid, the 1886 M 7.0 Charleston, the 1925 M 6.2 Charlevoix, and the 1929 M 7.2 Grand Banks earthquakes. The magnitudes for the New Madrid and Charleston earthquakes are from Cramer and Boyd [2014] and have a 95% confidence interval of ± 0.3 magnitude units. The magnitudes for the Charlevoix and Grand Banks earthquakes are taken from Bent [1992; 1995]. We used intensity observations from all distances, except for the offshore Grand Banks earthquake for which we used intensity observations from modified Mercalli Intensity II and III to avoid any distance bias from missing higher intensities at closer-in distances.

Each of the 1921 intensity observations selected were converted to an estimate of ground motion for each period for which we regressed for a GMPE. The GMICE of Ogweno and Cramer [2014] were used for the conversion from intensity to an estimate of ground motion. Ogweno and Cramer [2014] fit linear regressions to median \log_{10} ground motions versus Modified Mercalli Intensity (MMI), with Community Internet intensity (CII) observations (Did You Feel It?) corrected to MMI using the approach suggested by Hough [2014a]. Basically, Hough's suggestion is to use the difference between Bakun and Hopper's [2004] preferred

intensity prediction equation (IPE) for MMI and Atkinson and Wald's [2007] IPE dominated by CII data. At close-in distances we capped the difference at 0.6 intensity units based on Figure 6 of Hough [2013], which shows an average difference of 0.3 to 0.5 intensity units by our calculations. Figure 8.2 shows an example of the residual trends with magnitude and distance for peak ground velocity (PGV).

Ogweno and Cramer [2014] found correlated magnitude and distance trends in the residuals for the observations fit to their linear regressions. Fitting a linear trend to the residuals as a function of magnitude effectively eliminated the residual trend with distance; see Figure 8.3. The magnitude corrections of Ogweno and Cramer [2014] were applied to correct the ground-motion estimates for each period for the observed magnitude-dependent effect, possibly due to the shift in source corner frequency with magnitude. The magnitude correction is capped above **M5.7** to the value at **M5.7** because there is no data above **M5.9**. The magnitude correction is largest for long periods away from the shorter-period frequencies represented by intensity observations. The magnitude correction is necessary for obtaining proper levels of ground motion at close-in distances from the GMPE regressions, especially at longer periods.

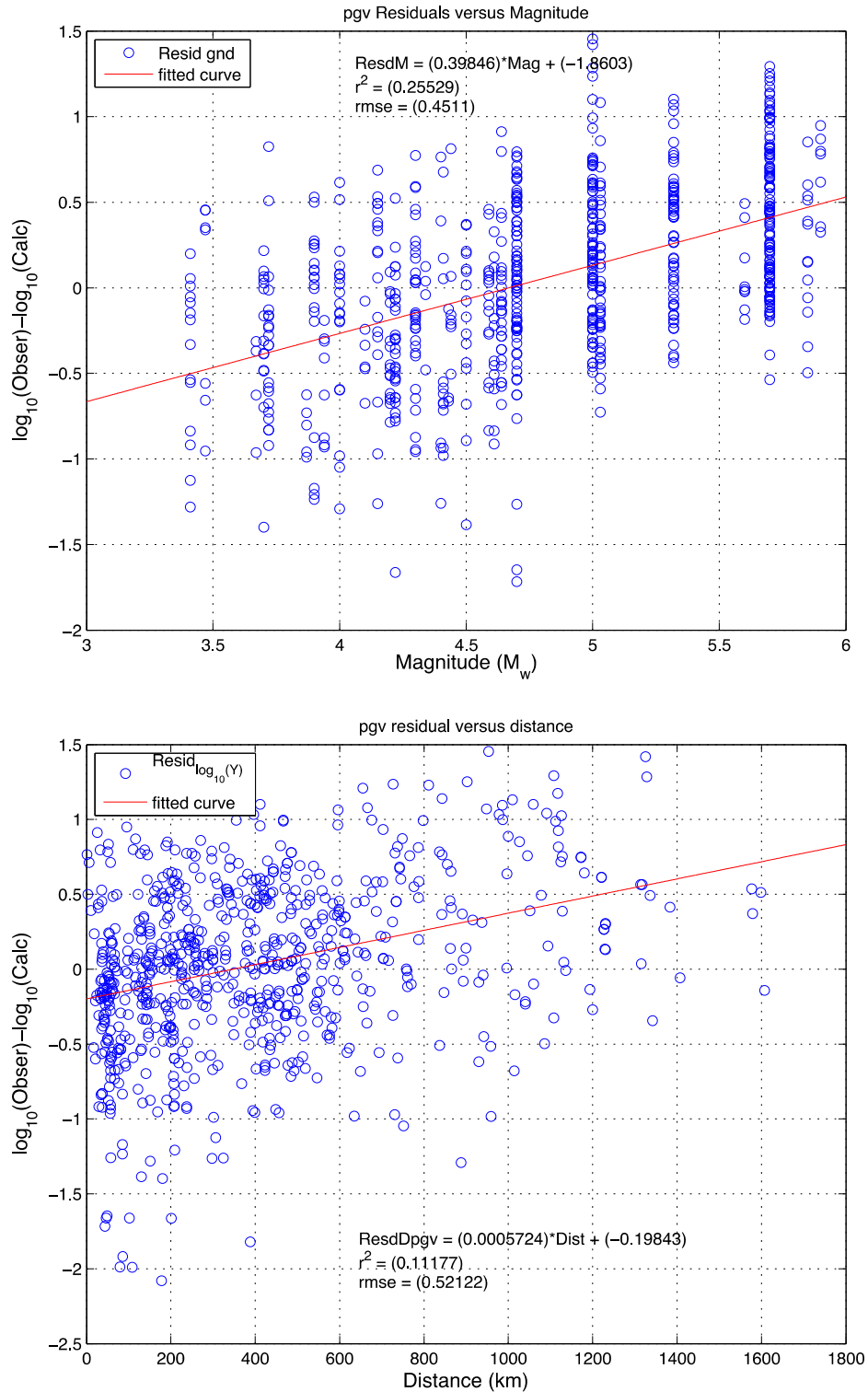


Figure 8.2 Peak ground velocity residual trends with magnitude (top) and distance (bottom) from Ogweno and Cramer [2014]; also shown are linear fits to the trends.

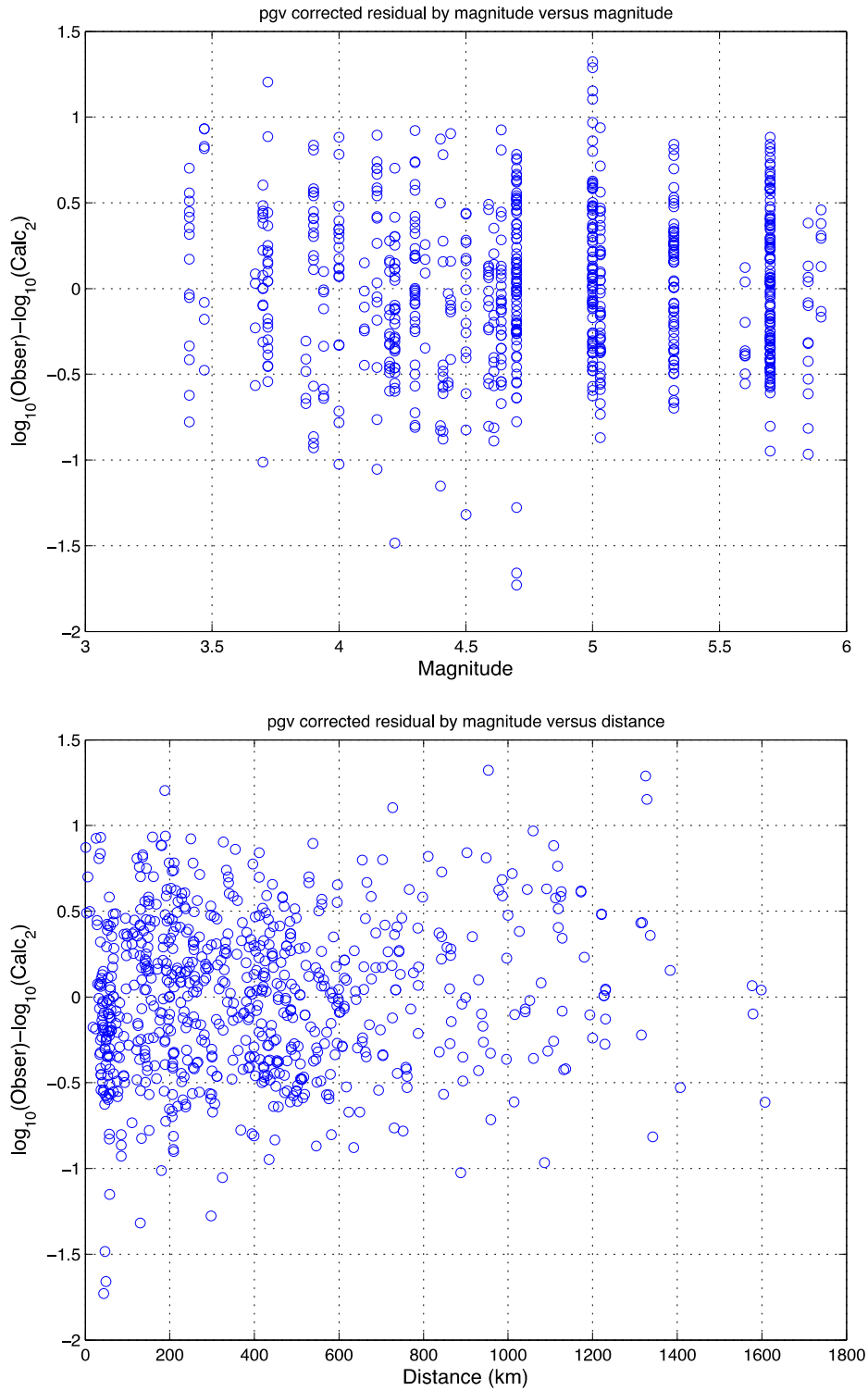


Figure 8.3 Peak ground velocity residual trends after applying the magnitude correction to the data shown in Figure 8.2.

8.2.3 Data Distribution

The distribution of data used to develop the GMPEs is shown in Figure 8.4 by M and distance. The observational data have a similar pattern for the two fault types (reverse and strike-slip) with a good representation of records for $M < 6$ with a distance range of less than 10 km up to 3500 km at all response variables (PGA, peak ground velocity (PGV), and pseudo-spectral acceleration (PSA) at selected periods). With the intensity data, the observations used in our regressions cover a magnitude range of $M_{2.5} - 7.7$ and a distance range of less than 10 km to over 2000 km, although the observational data coverage at distances less than 50 km is sparse, particularly at large magnitudes.

V_{S30} estimates for the NGA-East recording sites are provided by the NGA-East project. V_{S30} site estimates for the 2001 Bhuj observations are based on geology information in Cramer and Kumar [2003] with Quaternary, Tertiary, and Older site geology represented as NEHRP site class D, C, and B midpoint V_{S30} values, respectively. For the ENA intensity observations, V_{S30} estimates at observation sites were based on Wald and Allen [2007]; see USGS Global V_{S30} Map Server at <http://earthquake.usgs.gov/hazards/apps/vs30/>.

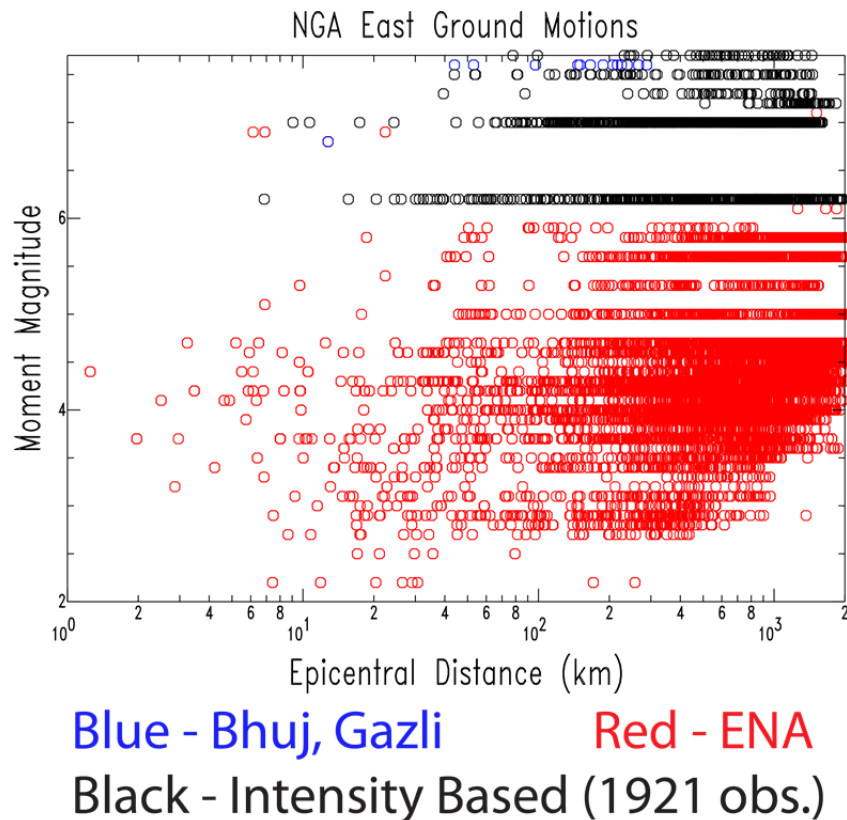


Figure 8.4 Magnitude versus distance distribution of NGA-East database and intensity data from $M > 6$ ENA historical earthquakes.

8.3 METHODOLOGY AND FUNCTIONAL FORM

Our GMPE is an empirical model, based on the two-stage regression approach of Joyner and Boore [1993; 1994]. This approach provides both within event and between event variability along with event and site terms. The functional form for our regressions is

$$\log Y = f(R) + f(\mathbf{M}) \quad (8.1)$$

where \log is a base-10 logarithm. The distance dependent terms are

$$f(R) = (c_1 + c_2 \mathbf{M}) \log R + c_3 (R - R_0) + d_1 \log(V_{S30}/760) + \phi \quad (8.2)$$

where R_0 is a reference distance set equal to 1 km, V_{S30} is the average travel-time V_S for the top 30 m at the desired location in m/sec, and ϕ is the within event variability. The reference V_{S30} in our regressions is 760 m/sec. We have included a magnitude dependent geometrical spreading term to model magnitude saturation at large magnitudes. R_0 does not change the functional behavior of our regression form and provides the added advantage of a reference to ground-motion amplitude on hard rock. The magnitude dependent terms of our functional form are

$$f(M) = a_1 U + a_2 RR + a_3 SS + b_1 \mathbf{M} + b_2 \mathbf{M}^2 + \tau \quad (8.3)$$

where U , RR , and SS are set to one for undefined, reverse, and strike-slip focal mechanisms, respectively, and zero otherwise, and τ is the between event variability. Total variability (uncertainty) σ is given by

$$\sigma^2 = \phi^2 + \tau^2 \quad (8.4)$$

The distance metric R in the regression is given by from the observed rupture distance (R_{RUP}) by

$$R^2 = R_{RUP}^2 + h^2 \quad (8.5)$$

where the pseudo-depth term is fixed at 10 km. Because the value of h could not be determined as an independent variable by the regression, it was arbitrarily fixed at 10 km.

8.4 RESULTS

Table 8.1 provides the regression results at 23 periods: PGA, PGV, and 0.1, 0.2, 0.3, 0.4, 0.5, 0.6, 0.7, 0.75, 0.8, 0.9, 1.0, 2.0, 3.0, 4.0, 5.0, 6.0, 7.0, 7.5, 8.0, 9.0, and 10.0 sec.

Figures 8.5–8.6 present comparisons to observations used in the regression at selected periods for **M5.9** and **M7.6**. Also shown are regression results without the intensity data to

Figures 8.5–8.6 present comparisons to observations used in the regression at selected periods for **M5.9** and **M7.6**. Also shown are regression results without the intensity data to demonstrate the impact of adding the intensity data. The addition of the intensity observations to the regression has only a small effect at **M5.9** due to the large amount of actual ground-motion observations available in the NGA-East database for $M < 6.0$. At **M7.6** (large magnitudes) the addition of the intensity observations has a greater impact, particularly when **M7.6** Bhuj observations are not available for that period. The Bhuj observations are limited to PGA and 0.4, 0.75, 1.0, and 1.25 sec [Cramer and Kumar 2003]. Figure 8.7 shows the variability (total, within, and between) as a function of period.

Table 8.1 Regression coefficients for rupture distance.

Prd σ	a_1	a_2	a_3	b_1	b_2	c_1	c_2	c_3	d_1	ϕ	τ_u	τ_S	σ_u	σ_S
PGA	-0.3299	-0.3114	-0.3320	0.3498	-0.0294	-2.7994	0.2734	-0.0005	-0.3827	0.37	0.21	0.21	0.43	0.43
PGV	-2.1381	-2.1783	-2.0687	1.1144	-0.0546	-1.9363	0.1168	-0.0002	-0.4009	0.35	0.25	0.24	0.43	0.43
0.1	-0.2668	-0.1818	-0.1818	0.3552	-0.0290	-2.7560	0.2745	-0.0007	-0.3582	0.41	0.33	0.32	0.53	0.52
0.2	-2.7091	-2.6836	-2.7055	0.9790	-0.0783	-2.2082	0.2338	-0.0009	-0.4671	0.37	0.19	0.19	0.42	0.42
0.3	-4.7196	-4.7032	-4.7026	1.3647	-0.0934	-1.6744	0.1635	-0.0009	-0.4806	0.37	0.18	0.18	0.41	0.41
0.4	-4.9014	-4.8831	-4.8816	1.3784	-0.0928	-1.6297	0.1610	-0.0009	-0.4793	0.36	0.18	0.18	0.40	0.40
0.5	-6.9327	-6.9433	-6.8870	1.7776	-0.1046	-1.1403	0.0718	-0.0007	-0.5026	0.36	0.17	0.17	0.39	0.39
0.6	-7.6378	-7.6631	-7.5752	1.9103	-0.1069	-0.9828	0.0370	-0.0006	-0.4846	0.35	0.17	0.16	0.39	0.39
0.7	-8.1431	-8.1790	-8.0684	2.0129	-0.1087	-0.8880	0.0100	-0.0005	-0.4665	0.35	0.17	0.16	0.39	0.39
0.75	-8.3065	-8.3426	-8.2284	2.0331	-0.1076	-0.8559	0.0013	-0.0004	-0.4595	0.35	0.17	0.16	0.39	0.39
0.8	-8.4903	-8.5311	-8.4116	2.0693	-0.1086	-0.8231	-0.0078	-0.0004	-0.4491	0.35	0.17	0.16	0.39	0.39
0.9	-8.7111	-8.7537	-8.6314	2.1039	-0.1088	-0.8046	-0.0164	-0.0003	-0.4464	0.35	0.17	0.16	0.39	0.39
1.0	-9.0908	-9.1444	-8.9996	2.0875	-0.0985	-0.6406	-0.0369	-0.0004	-0.3739	0.41	0.18	0.16	0.45	0.44
2.0	-9.7846	-9.8518	-9.6785	2.1573	-0.0912	-0.6332	-0.0886	0.0000	-0.3308	0.35	0.20	0.18	0.40	0.39
3.0	-9.8723	-9.9454	-9.7638	1.9783	-0.0625	-0.4997	-0.1264	0.0000	-0.2872	0.36	0.22	0.20	0.42	0.41
4.0	-10.1578	-10.2337	-10.0468	1.8871	-0.0433	-0.2989	-0.1671	0.0000	-0.2524	0.37	0.23	0.22	0.44	0.43
5.0	-10.4501	-10.5383	-10.3268	1.9112	-0.0425	-0.2665	-0.1788	0.0001	-0.2279	0.38	0.25	0.23	0.45	0.44
6.0	-10.2955	-10.3912	-10.1737	1.7375	-0.0172	-0.2683	-0.1851	0.0001	-0.2631	0.38	0.25	0.23	0.46	0.44
7.0	-10.7313	-10.8358	-10.6028	1.9333	-0.0446	-0.3925	-0.3252	0.0001	-0.2154	0.38	0.26	0.24	0.46	0.45
7.5	-10.7639	-10.8663	-10.6376	1.9388	-0.0461	-0.3602	-0.1723	0.0001	0.2166	0.38	0.26	0.23	0.46	0.44
8.0	-10.7802	-10.8796	-10.6550	1.9382	-0.0467	-0.3925	-0.1683	0.0001	-0.2197	0.38	0.25	0.23	0.45	0.44
9.0	-10.8158	-10.9130	-10.6880	1.9436	-0.0490	-0.4607	-0.1588	0.0001	-0.2234	0.38	0.25	0.23	0.45	0.44
10.0	-10.8617	-10.9603	-10.7341	1.9515	-0.0511	-0.5116	-0.1525	0.0002	-0.2258	0.37	0.25	0.22	0.45	0.43

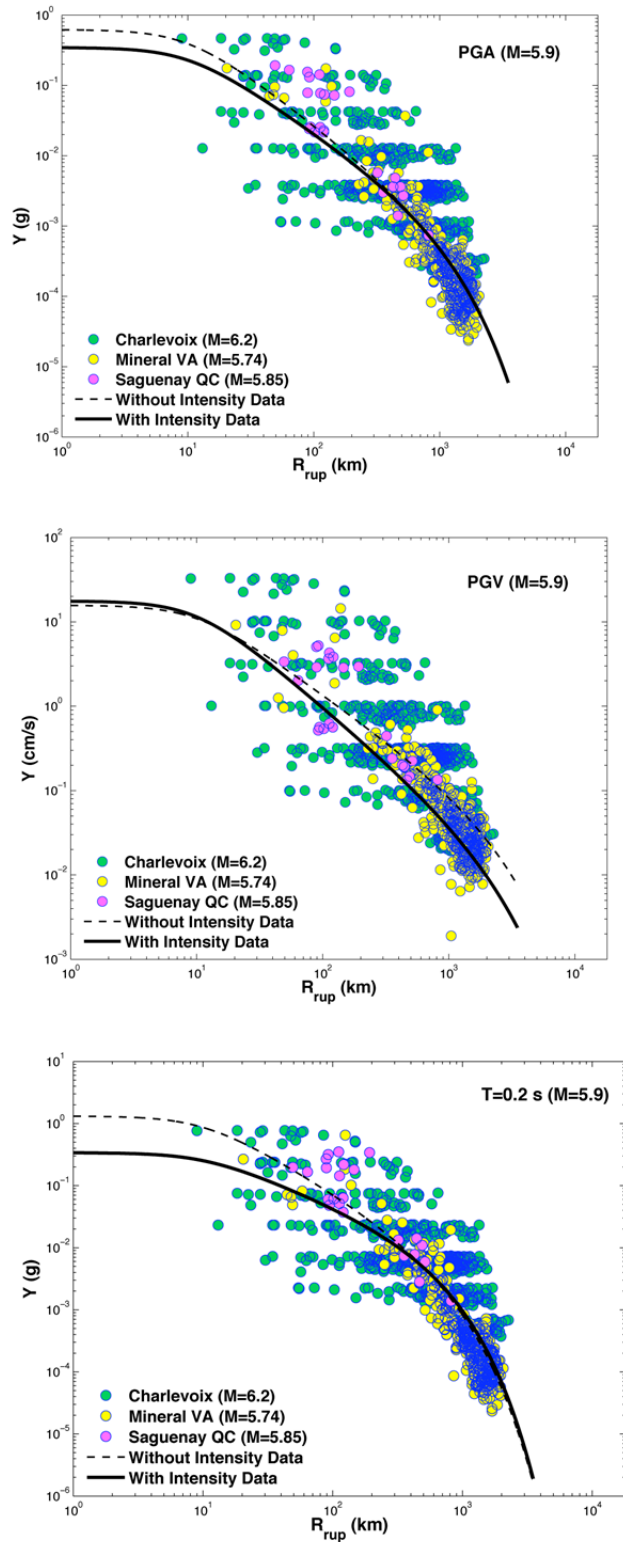


Figure 8.5 Comparison of observations near M5.9 with our M5.9 regression curves with and without intensity data for PGA (top), PGV (middle), and 0.2 sec PSA (bottom).

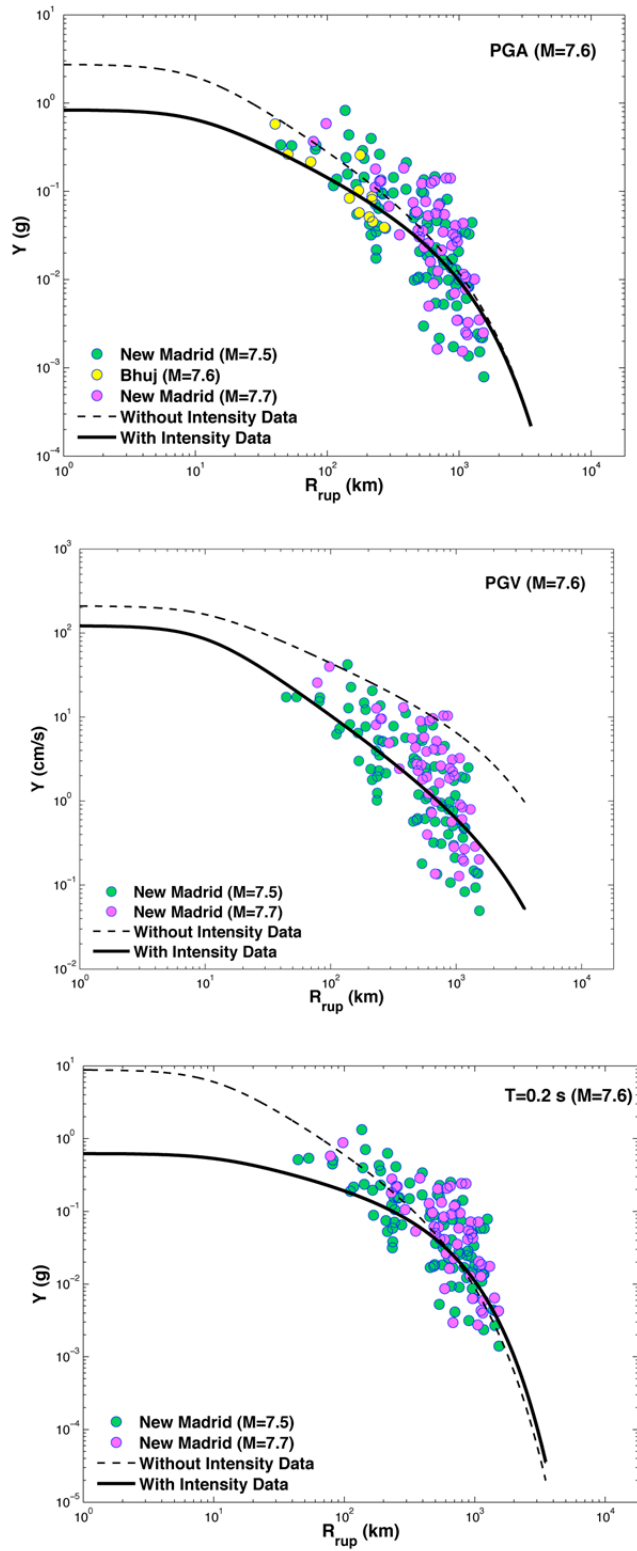


Figure 8.6 Comparison of observations near **M7.6** with our **M7.6** regression curves with and without intensity data for PGA (top), PGV (middle), and 0.2 sec PSA (bottom).

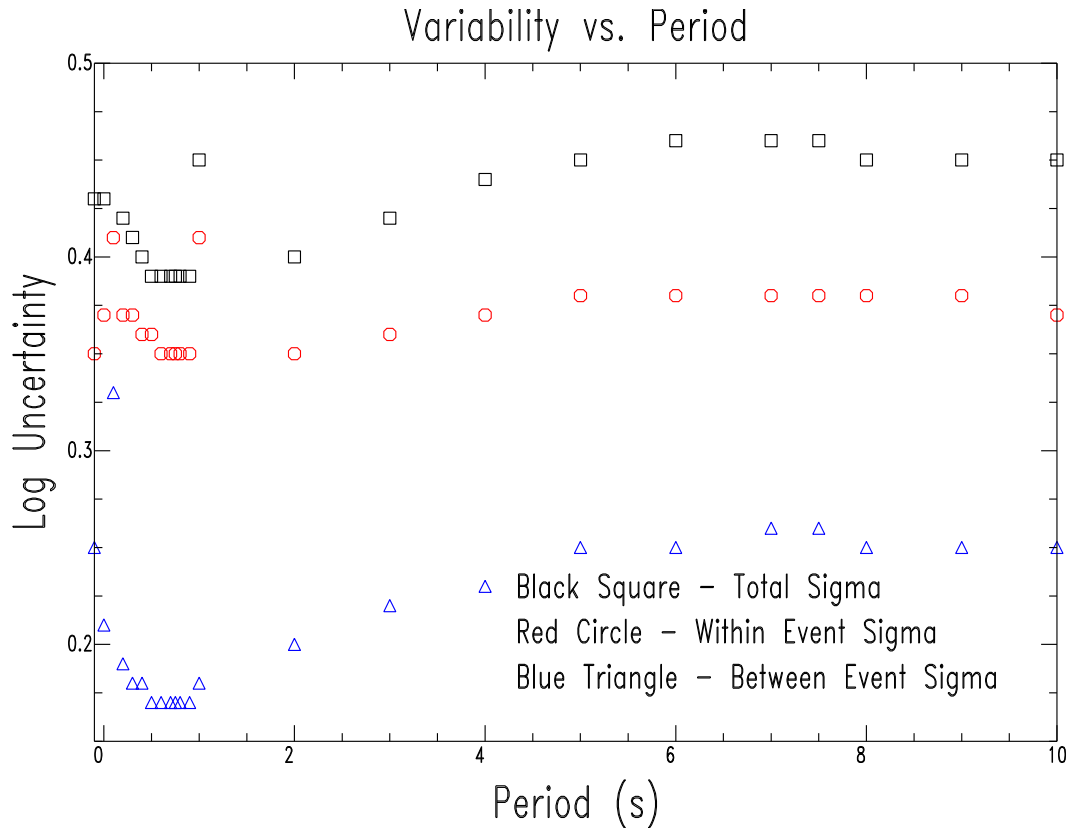


Figure 8.7 Regression variability as a function of period, where -0.1 is PGV and 0.0 is PGA.

8.4.1 Scaling

Scaling with V_{S30} , magnitude, and distance for all 23 periods is presented in Figures 8.8–8.11. The line color and type are common to these four figures. Ground-motion saturation is demonstrated in Figure 8.12 with stronger saturation at short periods than at long periods. Also at short periods, saturation is obviously a function of magnitude and distance, while at long periods it is dominantly a function of magnitude.

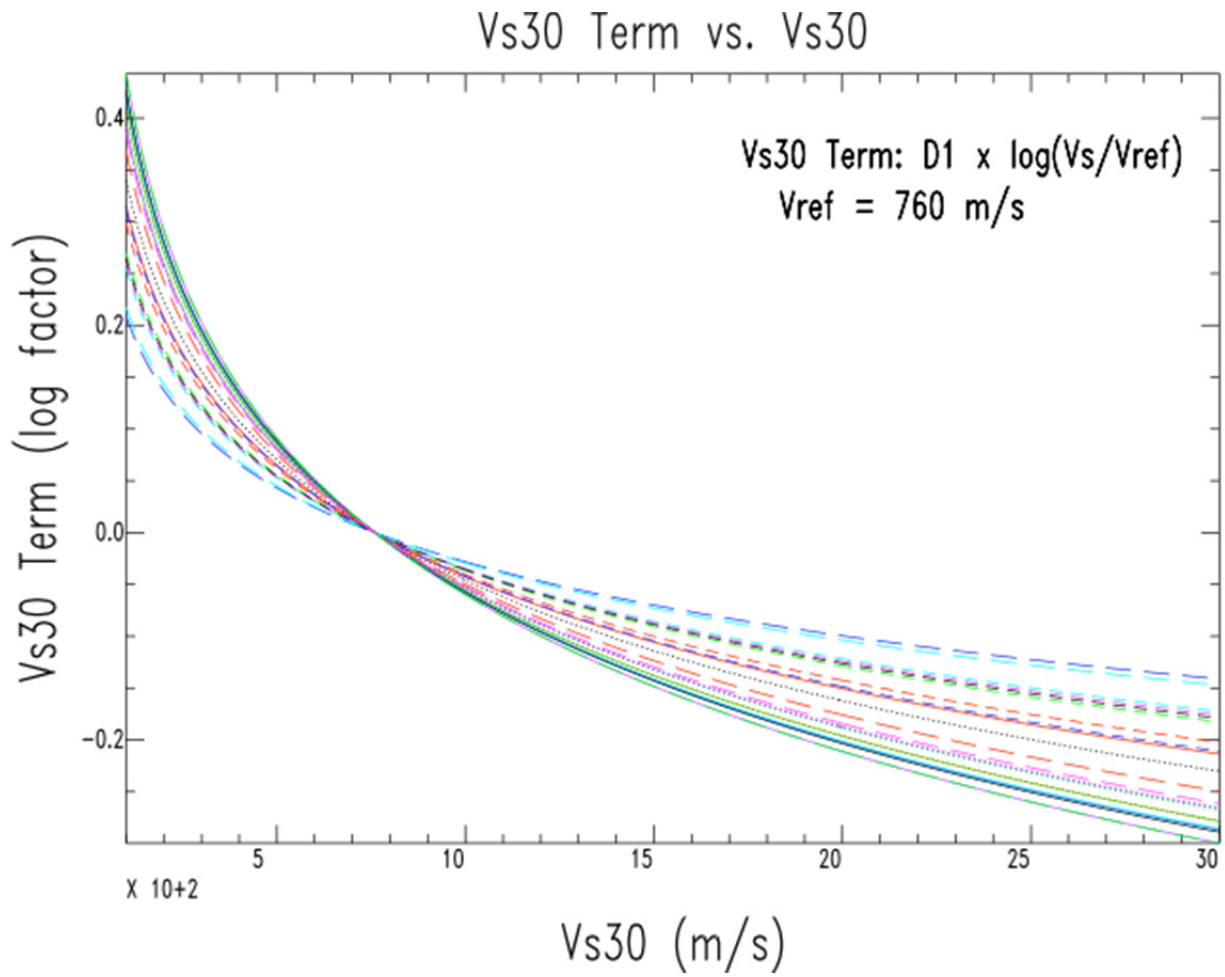


Figure 8.8 V_{s30} scaling for all 23 periods. Solid lines: red = 0.1 sec, green = 0.2 sec, blue = 0.3 sec, cyan = 0.4 sec, magenta = 0.5 sec, and black = 0.6 sec. Dotted lines: red = 0.7 sec, green = 0.8 sec, blue = 0.9 sec, cyan = 1.0 sec, magenta = 2.0 sec, and black = 3.0 sec. Short dashed lines: red = 4.0 sec, green = 5.0 sec, blue = 6.0 sec, cyan = 7.0 sec, magenta = 8.0 sec, and black = 9.0 sec. Long dashed lines: red = PGA, green = 0.75 sec, blue = 7.5 sec, cyan = 10.0 sec, magenta = PGV.

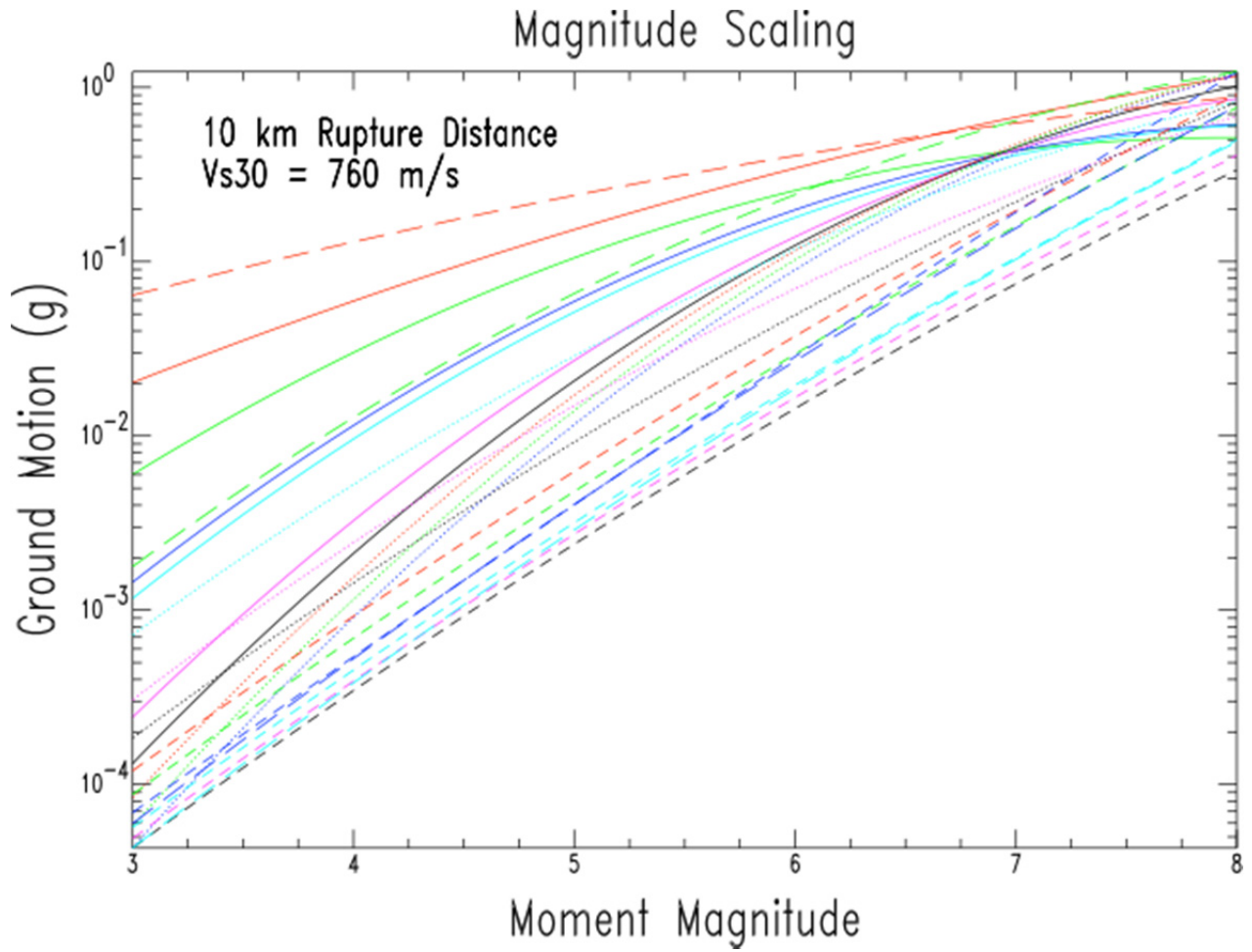
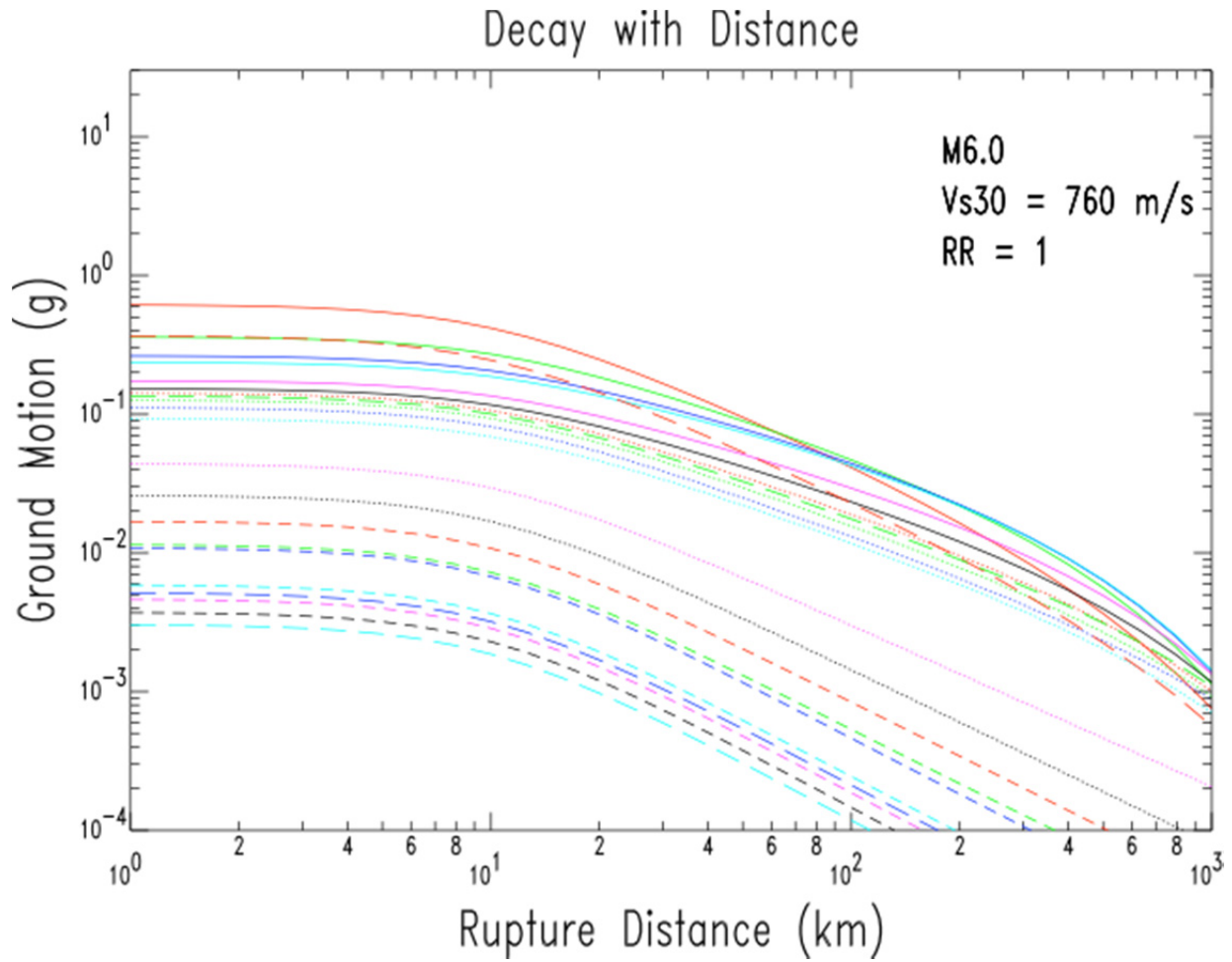
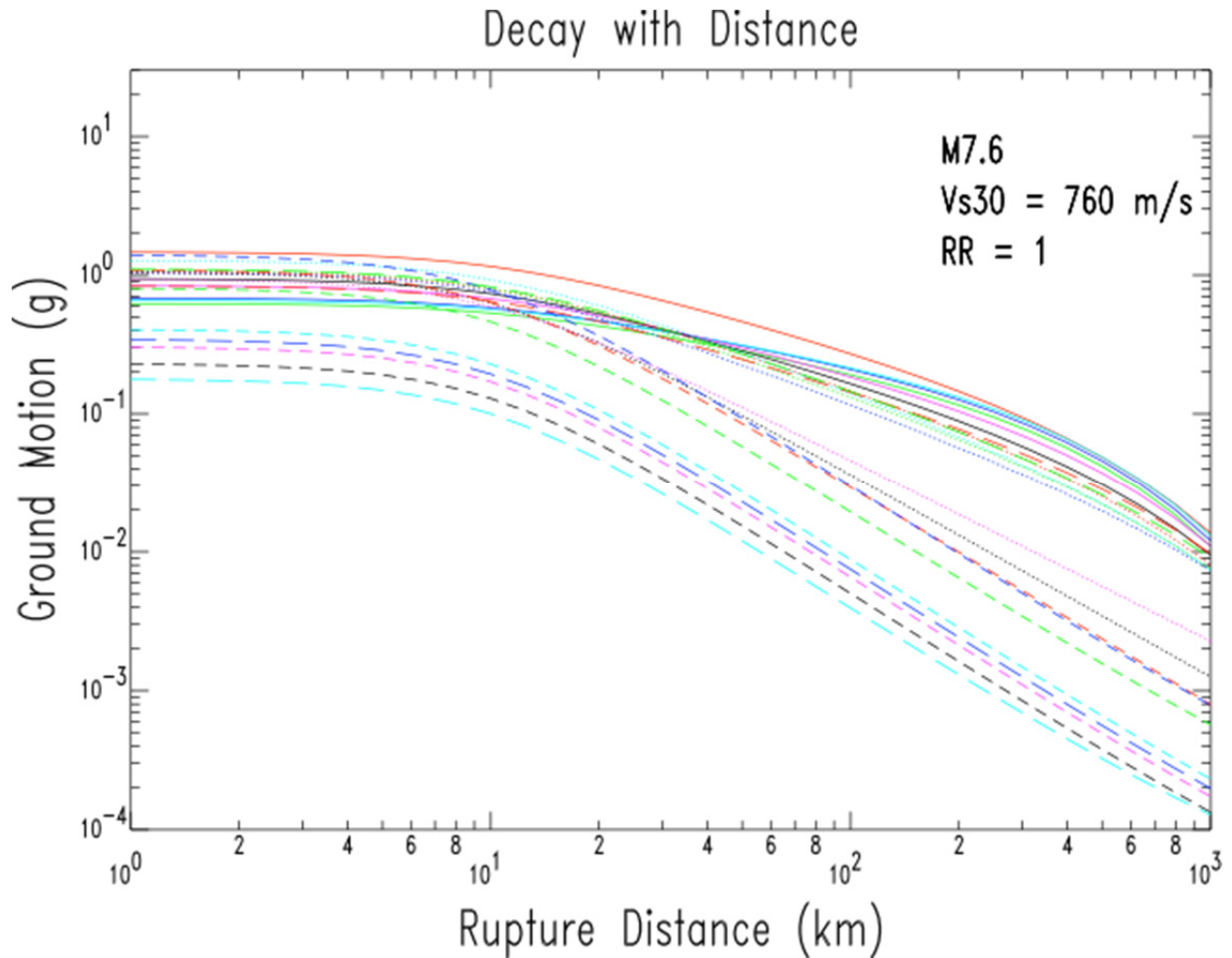


Figure 8.9 Magnitude scaling for 22 periods. Period representation by line color and type is the same as Figure 8.8, except PGV is not shown due to different units and scale.



Figures 8.10 Predicted decay with distance at 22 periods at M6.0. Period representation by line color and type is the same as Figure 8.8, except PGV is not shown due to different units and scale.



Figures 8.11 Predicted decay with distance at 22 periods at **M7.6**. Period representation by line color and type is the same as Figure 8.8, except PGV is not shown due to different units and scale.

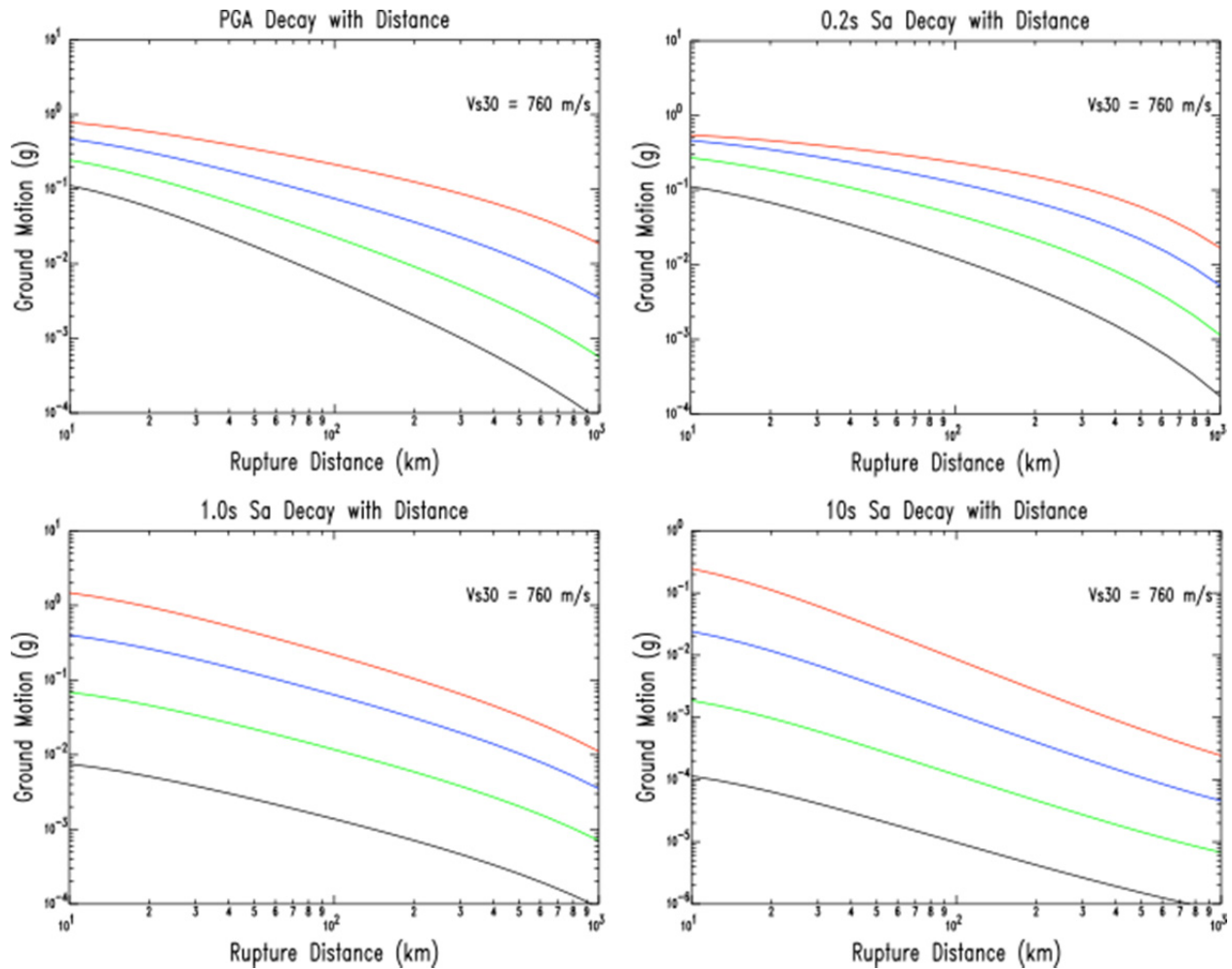


Figure 8.12 Ground-motion saturation for PGA (upper left), 0.2 sec (upper right), 1.0 sec (lower left), and 10.0 sec (lower right). Decay with distance is shown for **M8.0** (red), **M7.0** (blue), **M6.0** (green), and **M5.0** (black).

8.4.2 Comparison to other GMPEs

For the comparison of our GMPE to other ENA GMPEs, we chose the ENA GMPEs of the USGS NSHMP 2014 seismic hazard model [Petersen et al. 2014]. We have purposely not identified the other ENA GMPEs in our plots, only our own. The use of the other ENA GMPEs is to provide a range of predictions for comparison to our own. Figures 8.13–8.14 presents these comparisons for selected periods in separate plots for **M6.0** and **M7.6**. Generally, our GMPEs tend to under predict ground motions at close-in distances and over predict at large distances, possibly due to our functional form using a simple linear geometrical spreading term due to the lack of observations at larger magnitudes for distances less than 50 km.

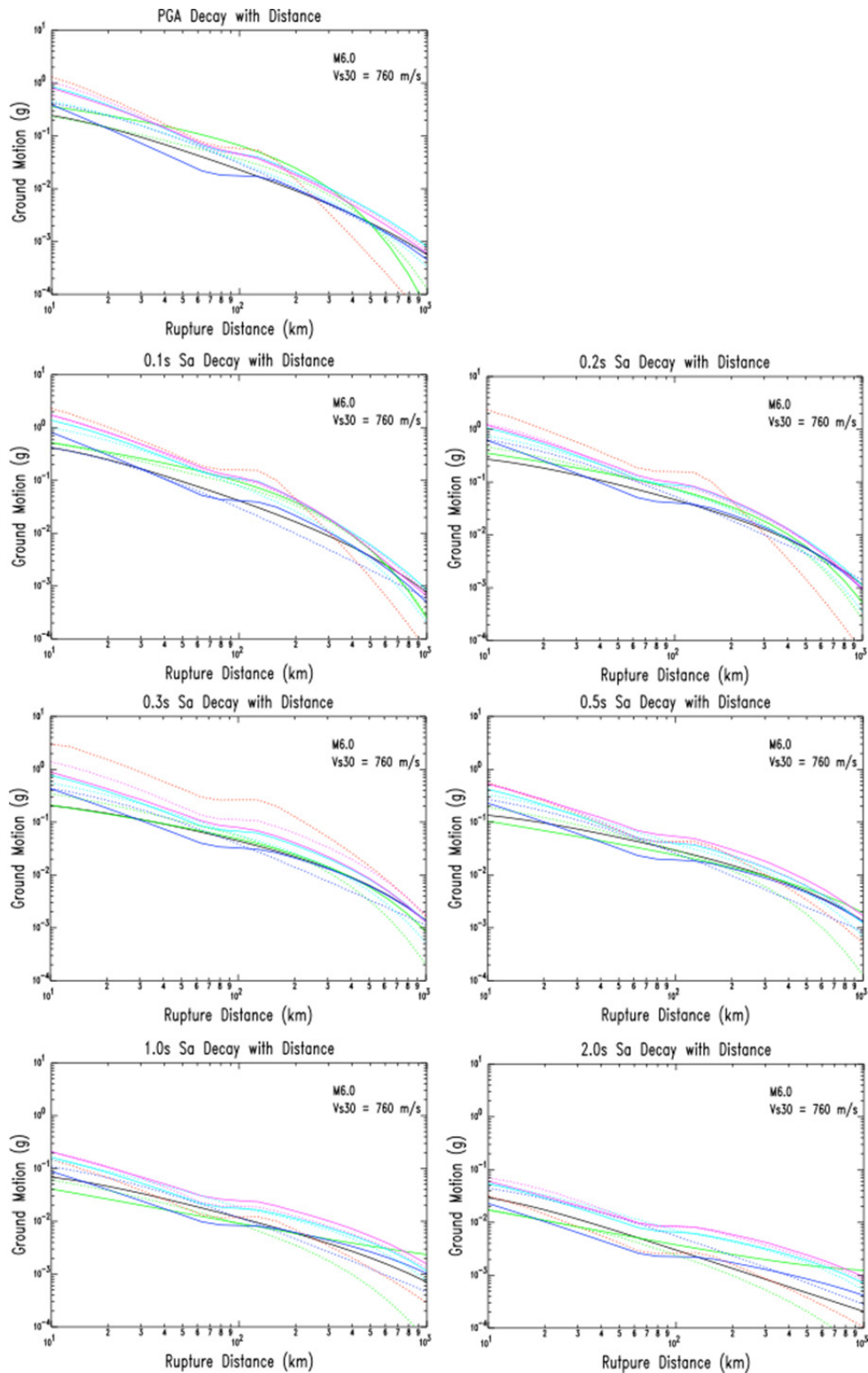


Figure 8.13 Comparison for **M6.0** and selected periods of our GMPE (solid black) with other ENA GMPEs (colored) used in Petersen et al. [2014].

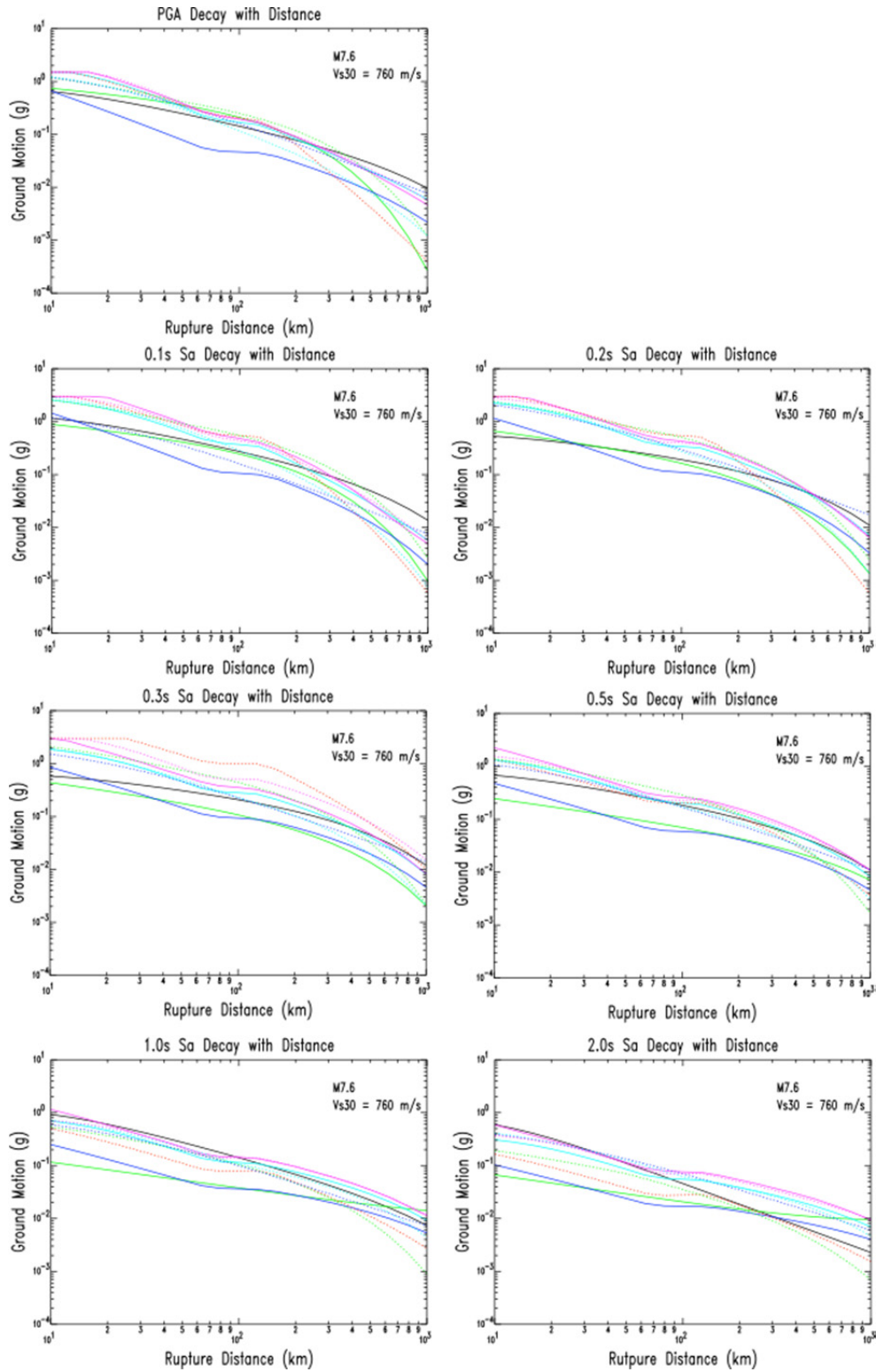


Figure 8.14 Comparison for M7.6 and selected periods of our GMPE (solid black) with other ENA GMPEs (colored) used in Petersen et al. [2014].

8.5 SUMMARY

We have developed ENA empirical GMPEs at 23 periods including PGA and PGV. The main source of ground-motion observations is the NGA-East ground-motion database, which is basically limited to observations from $M < 6.0$ earthquakes. Ground-motion observations from the 2001 $M7.6$ Bhuj earthquakes were added to our regression database. We have also included intensity observations for ENA historical earthquakes greater than $M6.0$ to help constrain the GMPEs at large magnitudes ($M > 6.0$). For the regressions, the observed intensities were converted to ground-motion estimates using the GMICEs of Ogweno and Cramer [2014]. Our resulting GMPEs thus have observational coverage from $M2.5$ to 7.7 over a distance range of less than 10 km to over 2000 km. The addition of intensity-based estimates of ground motion does help constrain the GMPEs at large magnitudes, particularly for periods where there are not observations available for the $M7.6$ Bhuj earthquake. However, the improvement comes with the cost of increase uncertainty in the regressions that include the intensity observations because of the larger scatter in those observations.

8.6 ACKNOWLEDGMENTS

Figures in this report were generated using GMT [Wessel and Smith 1991 and SAC [Goldstein et al. 2003]].

8.7 ELECTRONIC APPENDIX FOR CHAPTER 8

8A Model Output (Excel workbook)

9 Ground-Motion Prediction Equations for the Central and Eastern United States

Vladimir Graizer

U.S. Nuclear Regulatory Commission

Abstract

A new median ground-motion prediction equation (GMPE) G-14 model for the Central and Eastern U.S. (CEUS) is presented based on the modular filter based approach developed by Graizer and Kalkan [2007; 2009] for active tectonic environment in the Western U.S. (WUS). The G-14 model is based on the NGA-East database for the horizontal peak ground acceleration and 5%-damped pseudo spectral acceleration RotD_{50} component [Goulet et al. 2014]. In contrast to the active tectonic environment, the database for the CEUS stable continental environment is not sufficient for creating purely empirical GMPEs covering the range of magnitudes and distances required for seismic hazard assessments. Recorded data collected in the NGA-East database are sparse and cover mostly a range of moment magnitudes $\mathbf{M} < 6.0$ with limited amount of near-fault recordings. The functional form of the G-14 GMPE is derived from filters: each filter represents a particular physical phenomenon affecting the seismic wave radiation from the source. Main changes in the functional form for the CEUS model relative to the WUS model are a shift of maximum frequency of the acceleration response spectrum toward higher frequencies and an increase in the response spectrum amplitudes at high frequencies. I developed site corrections based on multiple runs of different representative V_{S30} profiles through SHAKE-type equivalent-linear (EQL) programs using time histories and random vibration theory (RVT) approaches. Site amplification functions are calculated for different V_{S30} relative to hard rock definition used in nuclear industry ($V_{S30} = 2800$ m/sec).

The number of predictors used in the model is limited to a few measurable parameters: moment magnitude \mathbf{M} , closest distance to fault rupture plane R_{RUP} , average shear-wave velocity in the upper 30 m of the geological profile V_{S30} , and anelastic attenuation factor Q_0 . Incorporating anelastic attenuation Q_0 as an input parameter allows adjustments based on the regional crustal properties. The model covers the range of magnitudes $4.0 < \mathbf{M} < 8.2$, distances of $0 < R_{RUP} < 1000$ km, S -wave velocities in the upper 30 m of $450 < V_{S30} < 2800$ m/sec and period range of $0.01 < T < 10$ sec. Comparison are made of the G-14 model with existing CEUS

GMPEs. In general, the G-14 model produces results lower than the median EPRI [Cramer et al. 2013] model at high frequencies ($f > 10$ Hz) and higher amplitudes for frequencies lower than 2.5 Hz.

9.1 INTRODUCTION

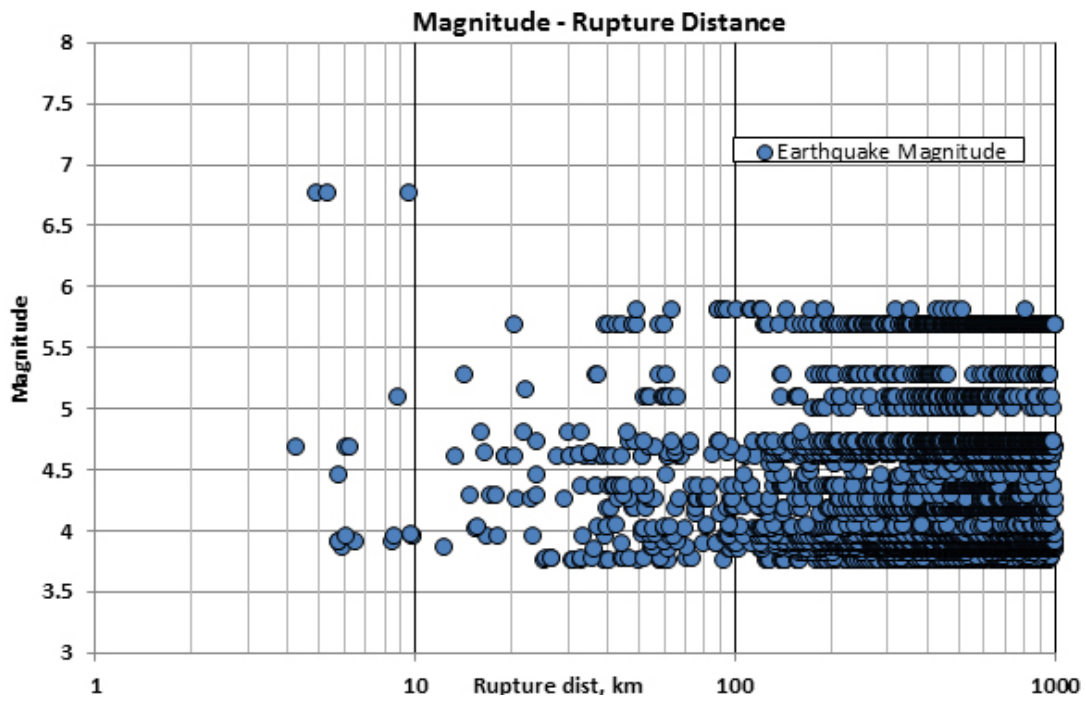
In contrast to the active tectonic environment in the Western U.S. (WUS) the strong-motion record database for the stable continental environment in the Central and Eastern U.S. (CEUS) is not sufficient for creating purely empirical (GMPEs) covering range of magnitudes and distances required for seismic hazard assessments. Recorded data collected in the NGA-East database [Goulet et al. 2014] are sparse and cover mostly a limited range of moment magnitudes $M < 6.0$ with only three data points with $M > 6$ from the 1985 $M = 6.8$ Nahanni earthquakes. There are also only few near-fault recordings, which complicates constraining the GMPE even more (Figure 9.1).

I started the development of the GMPE by using the first version of the database created under the NGA-East project provided by the Electric Power Research Institute (EPRI) at the beginning of 2013 [EPRI 2013]. It is the same database that was used to update the previous EPRI [2004; 2006] GMPEs [EPRI 2013]. I also originally used GMPE models prepared by EPRI [2013] and Pezeshk et al. [2011] as main constraints especially for large magnitudes. This allowed me to create a “pilot” GMPE by adjusting functional forms and magnitude scaling function developed for the WUS to the CEUS [Graizer 2014b]. Later, I switched to the November 2014 NGA-East database [Goulet et al. 2014].

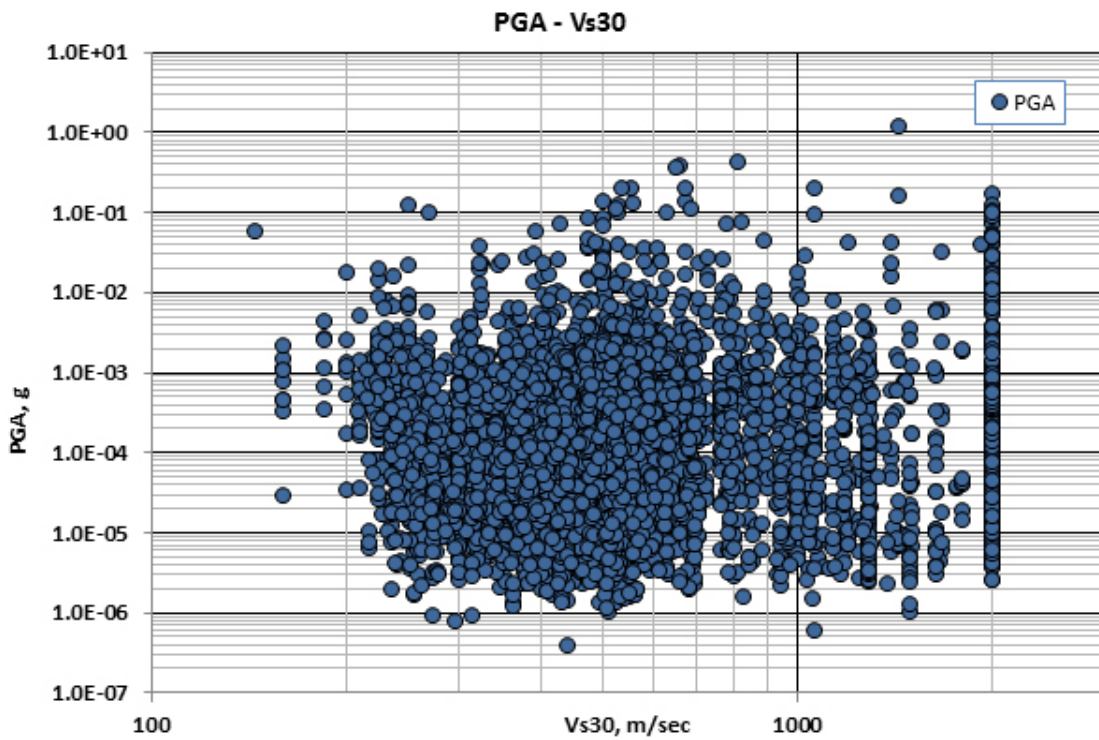
My GMPE model for the CEUS is based on the same modular filter-based approach developed by Graizer and Kalkan for active tectonic environment [2007; 2009; 2011; and Graizer 2014a]. The important characteristics of these GMPEs developed for active tectonic environment are:

- The number of predictors used in the model was limited to a few measurable parameters: moment magnitude (M), closest distance to fault rupture plane (R_{Rup}), average shear-wave velocity in the upper 30 m of the geological profile (V_{s30}) style of faulting, anelastic attenuation factor (Q_0), and if available basin depth defined as depth to the 1.5 km/sec shear-wave velocity isosurface ($Z_{1.5}$).
- The predictive model for pseudo-spectral acceleration (PSA) is a continuous function of spectral period (T), which eliminates the standard matrix of estimator coefficients, and allows for calculation of PSA at any period of interest within the model range, which is 0.01 to 10 sec. I use SA in the figures, but all spectral accelerations are PSA.
- The functional form of the GMPEs is derived from filters: each filter represents a particular physical phenomenon affecting the seismic wave radiation from the source.

The filter-based approach in modeling ground-motion attenuation is shown to provide accuracy (expected median prediction without significant bias) and efficiency (relatively small standard deviation of predictions).



(a)



(b)

Figure 9.1 Subset of the NGA-East database used considering earthquakes with $M \geq 3.75$ and a total of 5026 data points: (a) magnitude versus rupture distance; and (b) PGA versus V_{s30} .

There are a number of simplifications relative to the original WUS model in my CEUS model:

- No bump in the near field since there are no data to support it.
- No basin effect.
- No distinguishing between different fault styles.

Main changes in the functional form for the CEUS are a shift of the acceleration response spectrum shape toward higher frequencies and an increase in the response spectrum amplitude at high frequencies.

The G-14 model is based on the NGA-East database for the horizontal peak ground acceleration (PGA) and 5%-damped pseudo spectral acceleration (PSA) RotD_{50} component [Goulet et al. 2014]. Figure 9.1 demonstrates a subset of 5026 data points from this database with $M \geq 3.75$ and fault distances $R_{RUP} \leq 1000$ km used to constrain the G-14 model. The dataset includes 48 earthquakes from different regions in the CEUS with no distinction made between the mid-continent and Gulf Coast regions. Mid-continent data dominate the dataset. I did not use data with lower magnitudes and larger distances. I also included six data points from the recent $M = 4.8$ 11/12/2014 Kansas earthquake recorded by high-quality strong-motion instruments at the epicentral distances of 18 to 162 km (<http://www.strongmotioncenter.org/>).

9.2 PGA ATTENUATION MODEL

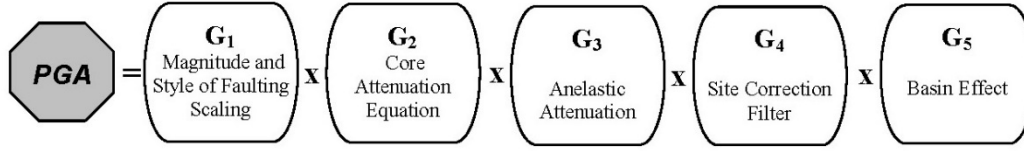
In this approach [Graizer and Kalkan 2007, 2011, 2015; and Graizer 2014a), a GMPE is expressed as a series of filters: each filter represents a certain physical phenomenon affecting the radiation of seismic waves from the source. In this representation, filters [denoted as G_n in Equation (9.1), where n is the filter number] are in multiplication form (cascade of filters). This way simplifies controlling their relative contributions on resultant ground-motion intensity measures.

$$\text{PGA} = G_1 G_2 G_3 G_4 G_5 \sigma_Y \quad (9.1)$$

In Equation (9.1), $G_{1..n}$ is a function of a set of independent parameters representing, magnitude, distance, style of faulting (F), shallow site conditions, basin, and other parameters affecting the physical process of ground-motion distance attenuation with standard deviation σ_Y . The latest Graizer-Kalkan GMPE for PGA was composed of five different filters [Equation (9.1)] [Graizer 2014a; Graizer and Kalkan 2015). For consistency, I am keeping same number of filters for the G-14 CEUS GMPE (Figure 9.2).

In my new model the first filter, G_1 is for magnitude scaling and style of faulting scaling with the same approximation function type as for WUS [Graizer and Kalkan 2007]:

$$A(M, F) = [c_1 \arctan(M + c_2) + c_3] F \quad (9.2)$$



$$\ln(PGA) = \ln(G_1) + \ln(G_2) + \ln(G_3) + \ln(G_4) + \ln(G_5) + \sigma_{\ln(PGA)}$$

Modules

$$\ln(G_1) = \ln([c_1 \arctan(M + c_2) + c_3] F)$$

$$\ln(G_2) = -0.5 \ln[(1 - r_2)^2 + 4D_2^2 r_2]$$

$$\ln(G_3) = -\frac{c_{11} + c_{12}M}{Q_0} R$$

$$\ln(G_4) = 0$$

$$\ln(G_5) = 0$$

where

$$r_2 = R / R_2$$

$$R_2 = c_4 M + c_5 \quad D_2 = 0.7$$

Estimator Coefficients

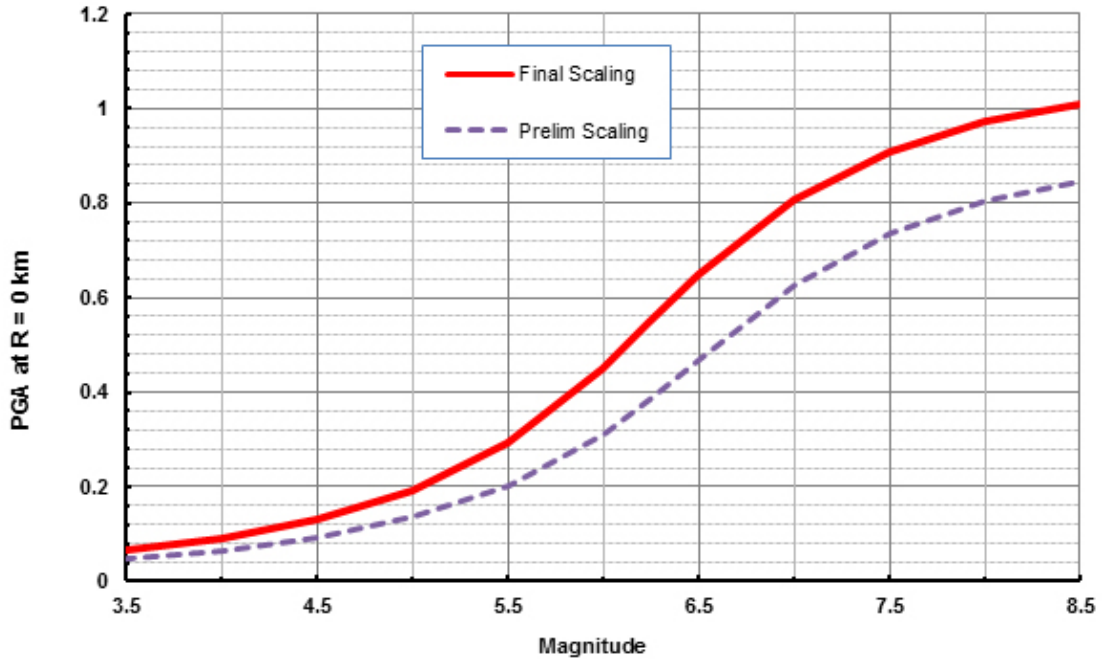
c_1	c_2	c_3	c_4	c_5	c_6	c_7	c_8	c_9
0.40	-6.25	0.55	2.237	-7.542	-0.125	1.19	-6.13	0.60

c_{11}	c_{12}	F	σ
3.9	-0.3445	2.232	0.53

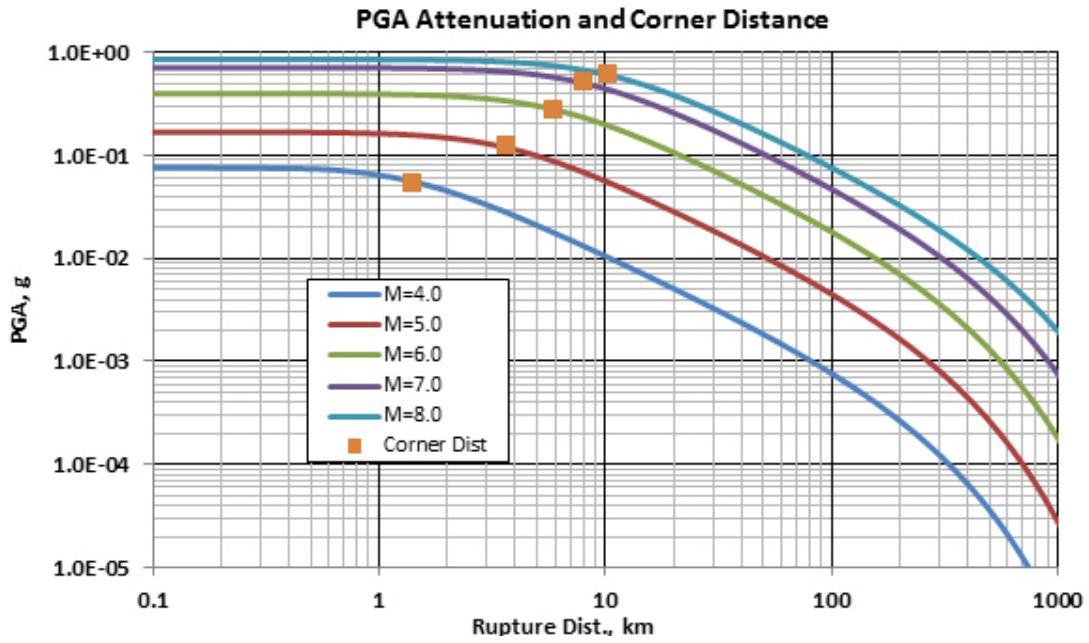
Note: R = Closest fault distance and M = Moment magnitude

Figure 9.2 G-14 PGA model for the free-field horizontal component of ground motion.

Equation (9.2) and Figure 9.3(a) and (b) demonstrate PGA scaling with magnitude at zero rupture distance for the hard rock ($V_s = 2800$ m/sec). The coefficients c_n are adjusted based on a combination of: (1) ratios of amplitude of earthquakes $3.75 < M < 6$ from the NGA-East database relative to the NGA-West; (2) average stress-drop ratio between WUS and CEUS; and (3) checked against recent ground-motion simulations ratios between $M5.0$ and higher M (see Section 1.3.4 and Appendix 1B, Goulet et al. [2015]; Atkinson and Assatourians [2015]; Graves and Pitarka [2015]; and Olsen and Takedatsu [2015]). Comparisons with ground-motion simulations are discussed in more detail later.



(a)



(b)

Figure 9.3 PGA scaling (a, b) and corner distance dependence from magnitude for the hard rock conditions ($V_s = 2800$ m/sec).

The G_2 filter models the distance attenuation of ground-motion and is similar to the frequency response function of a damped single-degree-of-freedom (SDOF) oscillator. This filter is expressed as:

$$G_2(M, R, C_2) = \frac{1}{\sqrt{[1 - (R/R_2)]^2 + 4D_2^2(R/R_2)}} \quad (9.3)$$

where R_2 is the corner distance in the near-source defining the plateau without significant attenuation of ground-motion. This parameter is directly proportional to earthquake magnitude; the larger is \mathbf{M} , the wider is the plateau defined by R_2 . Corner distance is proportional to the moment magnitude \mathbf{M} with scaling law previously developed for the active tectonic environment [Graizer and Kalkan 2007]; see Figures 9.2 and 9.3(b):

$$R_2 = c_4 M + c_3 \quad (9.4)$$

There is an analogy between R_2 and the corner frequency defined in Brune's model [1970; 1971] since both are related to the earthquake magnitude. Equation (9.3) and (9.4) imply that for larger magnitudes, the turning point on the attenuation curve occurs at larger distances; see Figure 9.3. In my new model for the CEUS, I kept this turning point same as for the WUS [Graizer and Kalkan 2007] since there is not enough information to constrain it based on CEUS data. I assigned parameter $D_2 = 0.7$, which is equivalent to no "bump" (increase in amplitude of ground motion at certain distance from the fault) on PGA attenuation with smooth transition from plateau to the R^{-1} attenuation.

The G_3 filter adjusts distance attenuation rate by including anelastic attenuation given as:

$$G_3 = \exp \left[\left(-\frac{c_{11} + c_{12}M}{Q_0} \right) R \right] \quad (9.5)$$

where Q_0 is the regional quality-factor for propagation of seismic waves from source to the site at a frequency of 1 Hz, and c_{11} and c_{12} are coefficients. Equation (9.5) changes the PGA attenuation rate after it is plugged into Equation (9.1). The value for Q_0 varies regionally and is about 650–1000 for the CEUS [Mitchell and Hwang 1987; Erickson et al. 2004; and Pasyanos 2013]. Based on my previous tests [Graizer 2014a], I concluded that it is reasonable to use a constant Q_0 typical for a given region/path (usually that for Lg or Coda waves). In my CEUS model, I assume frequency-independent Q . I expect that my model can be adjusted to other stable tectonic regions by using Q_0 values typical for that region.

To fit the data I had to assume anelastic attenuation to be magnitude dependent with higher magnitudes, thus producing lower PGA decay. The simplest explanation for this is that larger magnitude events generate wider spectrum of waves with longer period waves attenuating slower and creating more converted waves. Pasyanos [2011; 2013] demonstrated that incorporating laterally variable Q into a GMPE without even taking into account the effect of V_{s30} improves agreement between empirical data and model predictions.

After experimenting with geometrical spreading and varying it from R^{-1} to $R^{-1.3}$, I found that R^{-1} fits NGA-East data best. Similarly to the WUS, the CEUS PGA practically saturates with $\mathbf{M} = 8$ (Figure 9.3). This plot is shown for the hard rock of $V_s = 2800$ m/sec.

9.3 SITE CORRECTION

The G_4 filter models ground-motion amplification due to shallow site conditions (V_{s30}). I developed my own site correction based on multiple runs of different representative profiles through SHAKE-type equivalent-linear (EQL) programs using time histories and random vibration theory (RVT) approaches [Kottke and Rathje 2008], and an EQL RVT type code developed at the U.S. Nuclear Regulatory Commission. Site amplification functions are calculated for different V_{s30} relative to hard rock definition used in nuclear industry ($V_{s30} = 2800$ m/sec):

$$Lin_Amp = 1 + \frac{k_{V_{s30}}}{\sqrt{\left[1 - (f_{V_{s30}} / f)\right]^2 + 1.96(f_{V_{s30}} / f)}}$$

$$k_{V_{s30}} = -0.5 \ln(V_{s30} / 2800)$$

$$f_{V_{s30}} = V_{s30} / 120 - 1.6$$
(9.6)

Here, f is frequency. I checked my site correction from $V_{s30} = 760$ m/sec to hard rock ($V_{s30} = 2800$ m/sec) conditions against Atkinson and Boore [2006; 2011]. Equation (9.6) produces transfer function with results between those presented in these two publications; see Figure 9.4. This linear site amplification function covers the range of $450 < V_{s30} < 2800$ m/sec, but practically can be applied to all data in the subset of the NGA-East database used since data with even lower V_{s30} have very low amplitudes and are not expected to produce nonlinearity; see Figure 9.1(b).

I also developed a nonlinear site effects model similar to that of Abrahamson et al. [2014]. Nonlinearity starts at $V_{s30} = 450$ m/sec and site amplification decreases proportionally to PGA (PSA), starting from accelerations higher than 0.05g (real effect starts being visible for $PGA > 0.1g$).

The G_5 filter is for basin effect and was developed and calibrated based on California data [Graizer 2014a; Graizer and Kalkan 2015]. This filter is a function of three parameters: (1) depth to 1.5 km/sec shear-wave velocity isosurface under the site, denoted as $Z_{1.5}$; (2) distance from the earthquake source; and (3) period (T). It is set to one and does not produce any effect on attenuation in the current GMPE version.

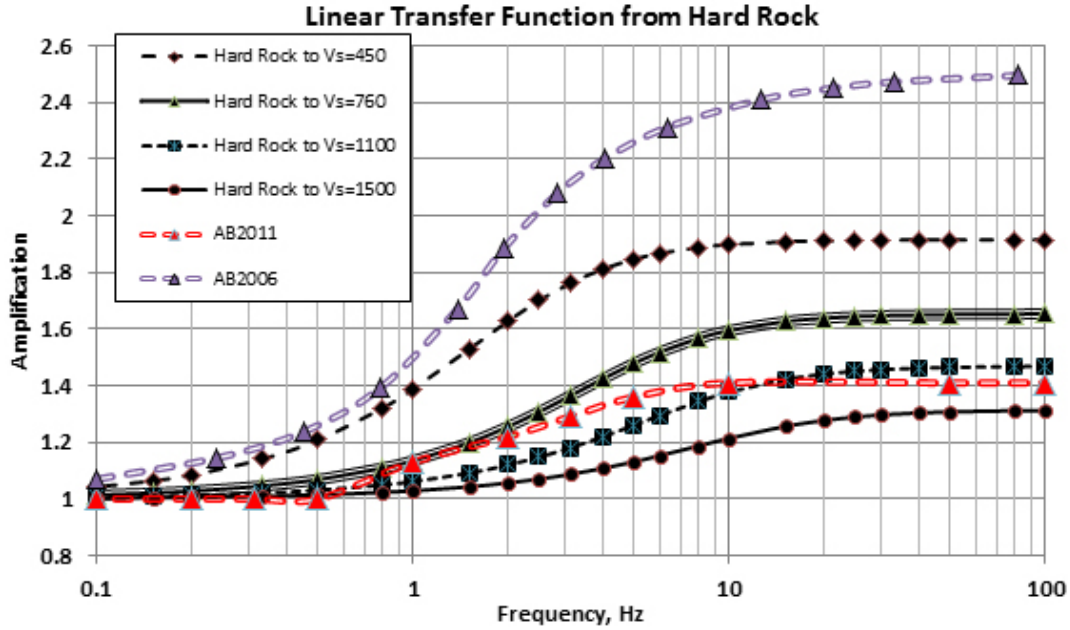


Figure 9.4 V_{s30} site amplification relative to hard rock (2800 m/sec) and comparison with Atkinson and Boore [2006; 2011] correction from hard rock to $V_{s30} = 760$ m/sec..

9.4 PGA-BASED PREDICTIVE MODEL FOR SPECTRAL ACCELERATION

Following the approach developed in Graizer and Kalkan [2009] for WUS, a spectral acceleration prediction model that explicitly integrates PGA as a scaling factor for the spectral shape was developed, which is a continuous function of spectral period (or frequency). Thus, it allows for prediction of PSA at any period of interest within the model range of 0.01 to 10 sec or even longer periods; Figure 9.5 summarizes this model.

Summation of a modified lognormal probability density function with an altered SDOF oscillator transfer function (Figure 9.5) eventually provides the desired shape with enough flexibility to fit into wide range of spectral shapes of real recordings. Each one of these functions simulates certain spectral behavior, and their combination results in a working predictive model.

I made a number of modifications to the WUS model to fit the CEUS data. For example, in current model, spectral slope ζ at long periods is \mathbf{M} dependent, resulting in slower decay for larger \mathbf{M} for $\mathbf{M} > 5.25$. The fastest slope is 2.25 for small events with $\mathbf{M} \leq 5.25$; the slowest of 1.5 is for large $\mathbf{M} \geq 8.0$ events.

I also observed the same tendency as seen in the WUS, with a shift of the peak of response spectra with distance toward lower frequencies; see Figures 9.6 and 9.7. Comparisons of average RS at different distances from the fault clearly demonstrates shift of the maxima to longer periods with increasing distance to the source. I did not observe this tendency in the EPRI [2013] model.

$$SA(T) = \text{PGA} \times \left[SA_{norm}(T / M, R, V_{S30}) \right] \quad \begin{array}{l} R = \text{Closest fault distance} \\ M = \text{Moment magnitude} \end{array}$$

$$SA_{norm}(T / M, R, V_{S30}) = I(M, R) e^{-\frac{1}{2} \left(\frac{\ln(T) + \mu(M, R, V_{S30})}{S(M, R)} \right)^2} + \left[\left(1 - \left(\frac{T}{T_{sp,0}} \right)^\zeta \right)^2 + 4D_{sp}^2 \left(\frac{T}{T_{sp,0}} \right)^\zeta \right]^{-1/2}$$

$$\mu(M, R, V_{S30}) = m_1 R + m_2 M + m_3$$

$$I(M, R) = 1.4$$

$$S(M, R) = s_1 R - (s_2 M + s_3)$$

$$T_{sp,0}(M, R, V_{S30}) = t_1 R + t_2 M + t_3$$

$$\zeta(M) = a_1 M^2 + a_2 M + a_3$$

m_1	m_2	m_3	m_4	a_1	a_2	a_3	D_{sp}
-0.002	-0.12	3.0	0.0	0.0347	-0.5542	3.694	0.75

t_1	t_2	t_3	t_4	s_1	s_2	s_3
0.0008	0.16	0.0	-0.4875	0.0	0.077	0.3251

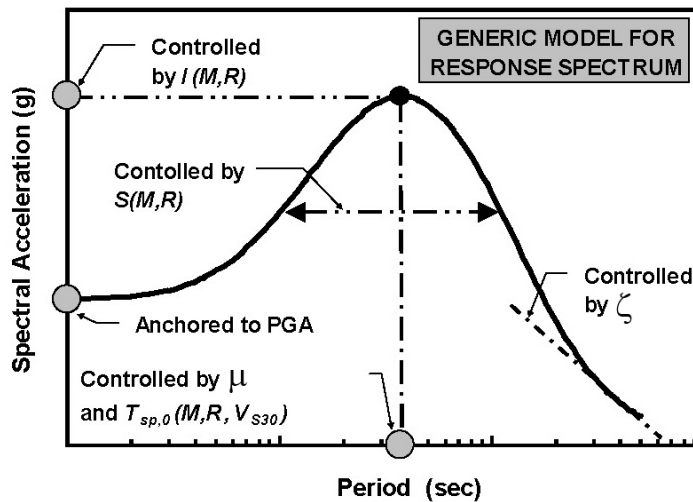


Figure 9.5 PGA-based G-14 model for 5%-damped pseudo spectral acceleration RotD₅₀ component.

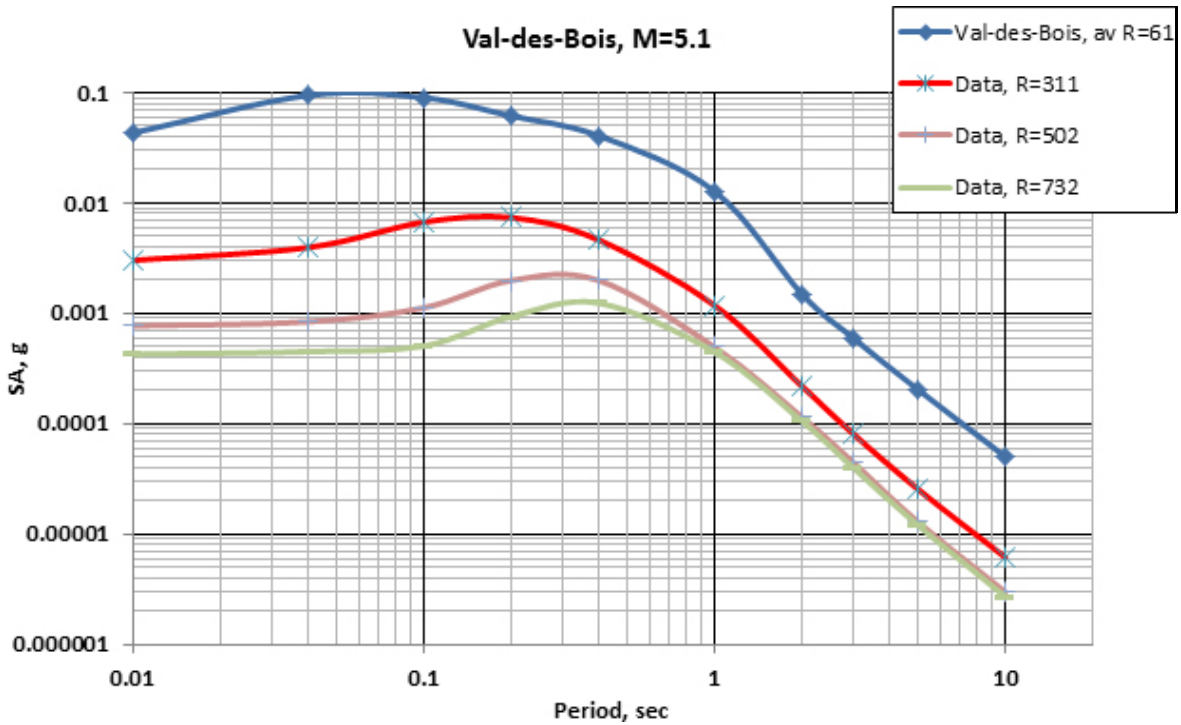
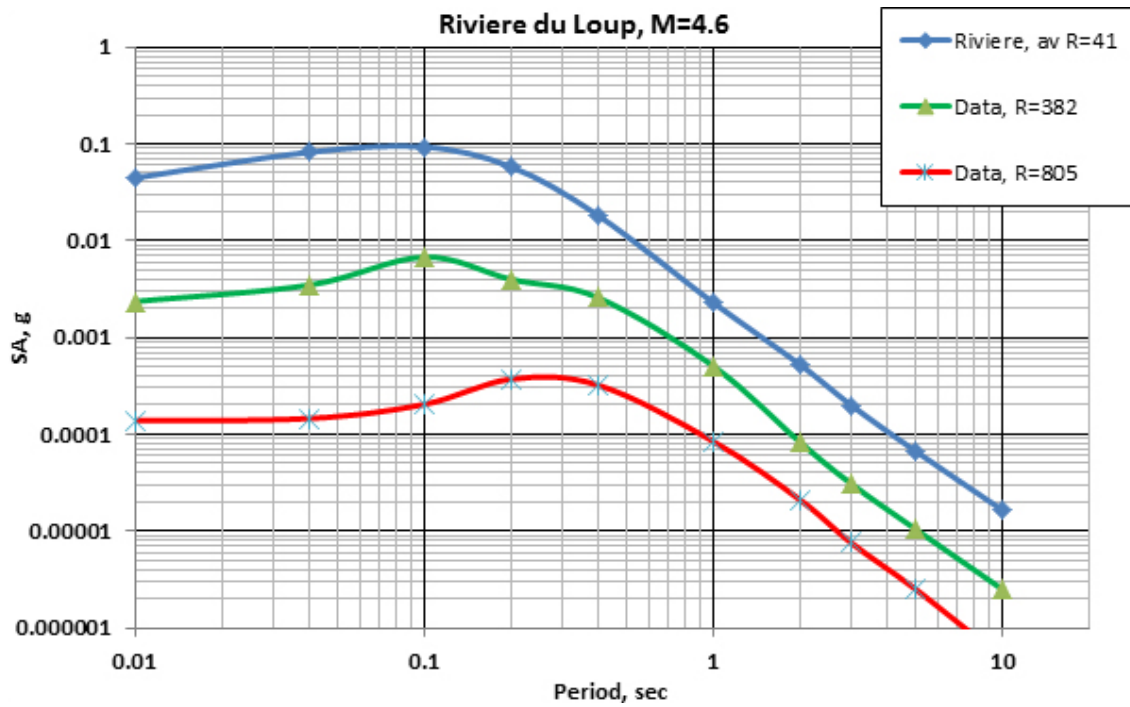


Figure 9.6 Comparisons of average response spectra at different distances from the fault for the Riviere-du-Loup and Val-des-Bois events, demonstrating shift of the maxima to longer periods with increasing rupture distance.

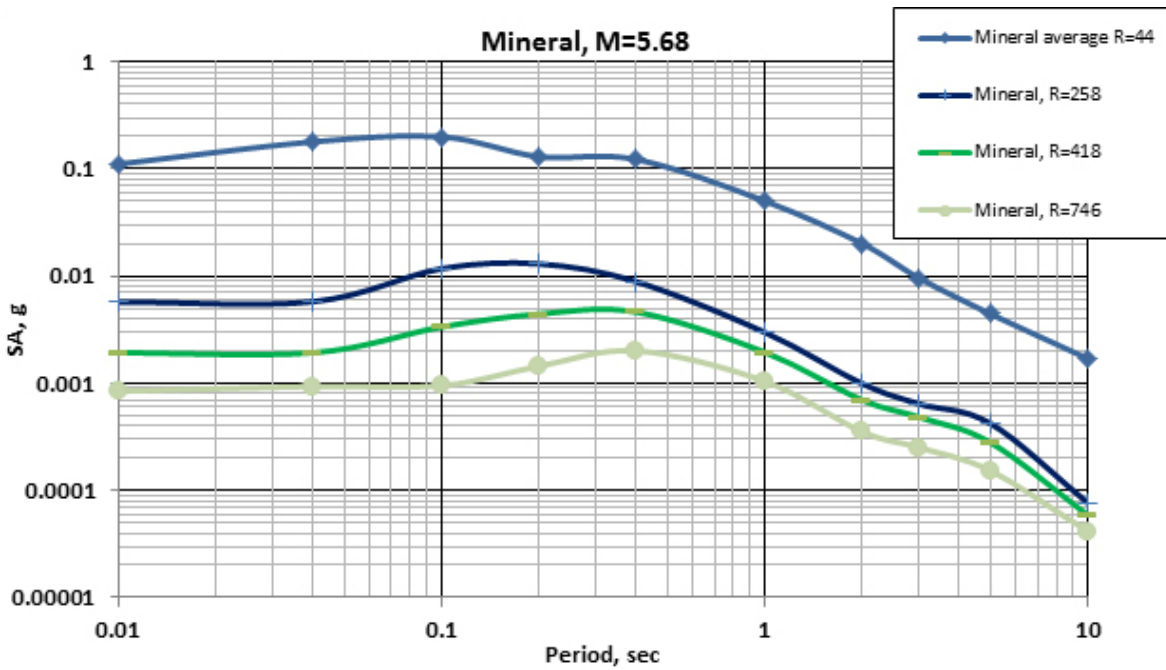
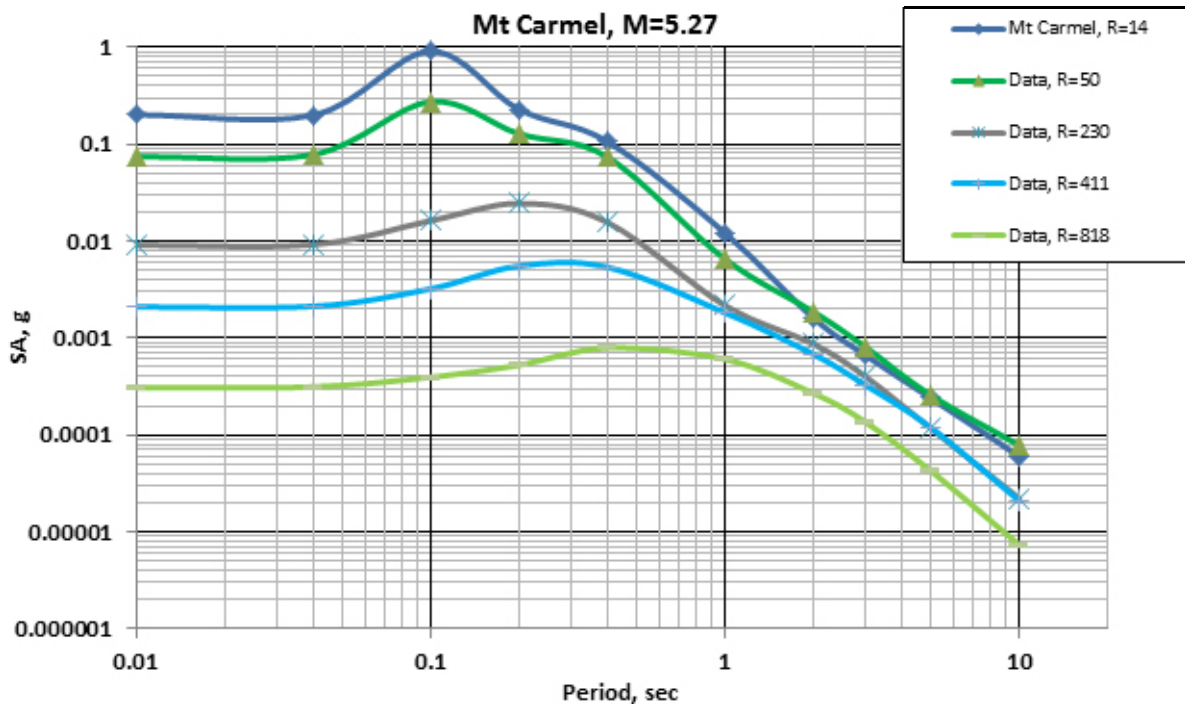


Figure 9.7 Comparisons of average response spectra at different distances from the fault for the Mount Carmel and Mineral events, demonstrating shift of the maxima to longer periods with increasing rupture distance.

Figure 9.8 demonstrates examples of the spectral acceleration functions for magnitudes $4.5 \leq M \leq 7.5$ at fault distances of 1 and 20 km. Note: in contrast to the WUS, the CEUS response spectra flatten at much higher frequencies.

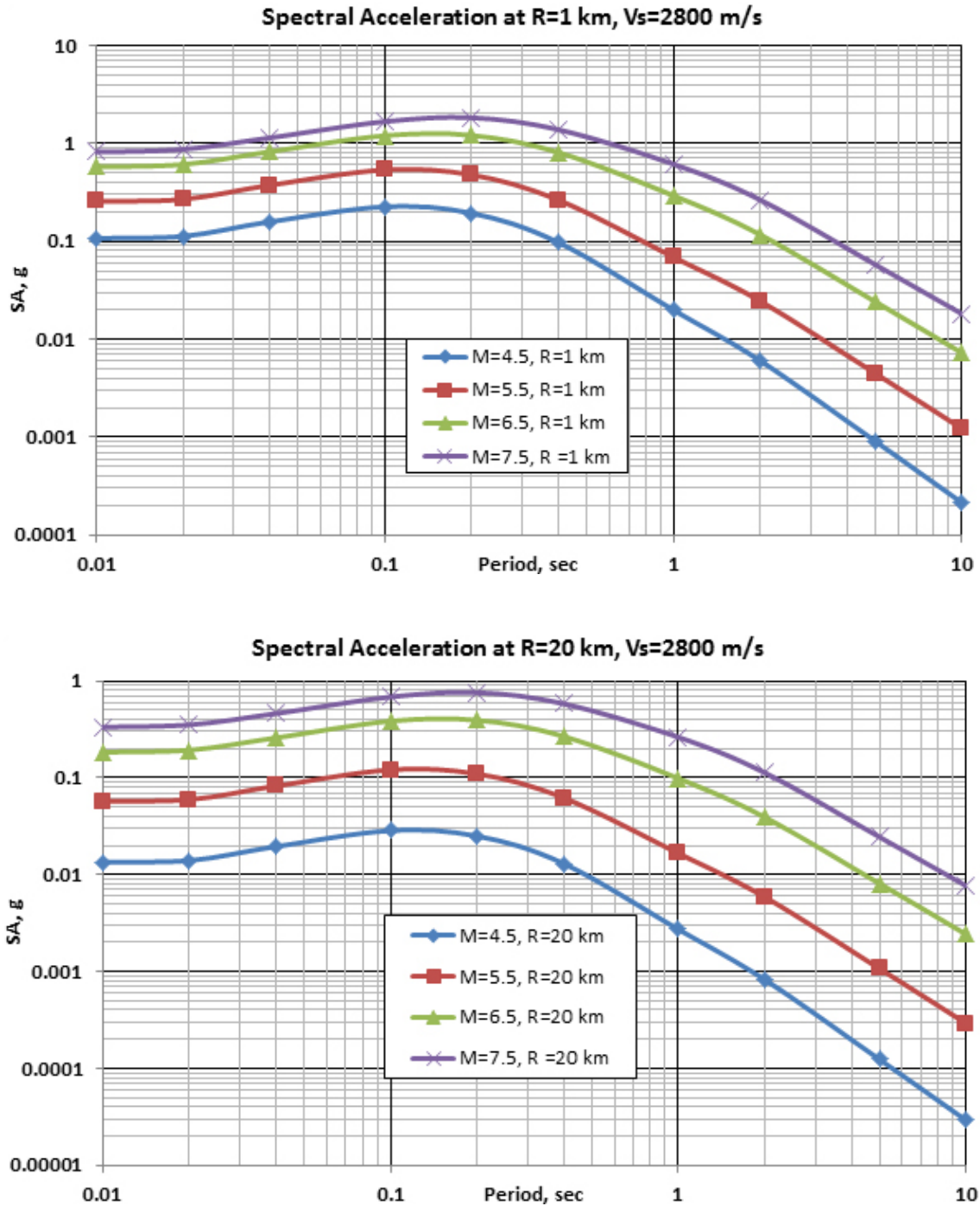


Figure 9.8 Examples of the spectral acceleration functions for magnitudes $4.5 < M < 7.5$ at fault distances of 1 and 20 km for hard rock conditions.

Figure 9.9 demonstrates comparisons of the G-14 spectral acceleration functions for the CEUS with GK-14 for the WUS at rupture distances of 5 and 50 km for the average $V_{s30} = 760$ m/sec. As shown in this figure, high-frequency amplitudes of the G-14 PSA functions are few times higher than that of GK-14, while the low-frequency amplitudes are similar. Similarities of low-frequency PSA values are expected up to certain distances. At larger distances, low frequencies in the west are expected to be lower because of lower Q_0 .

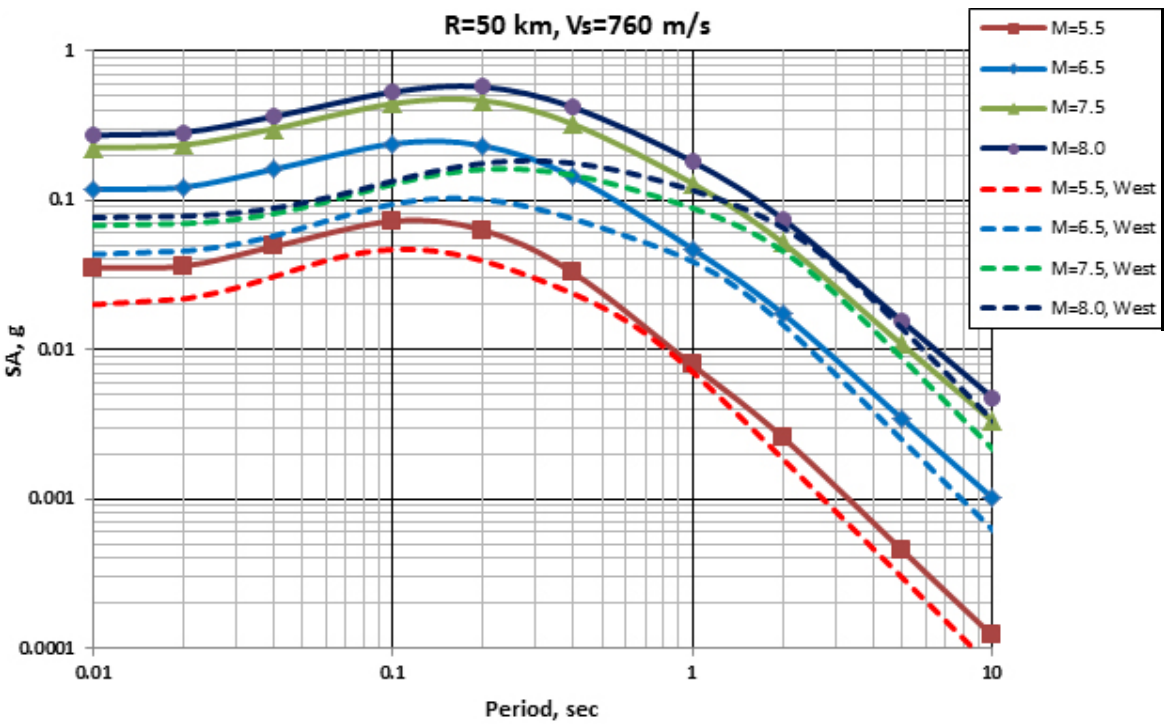
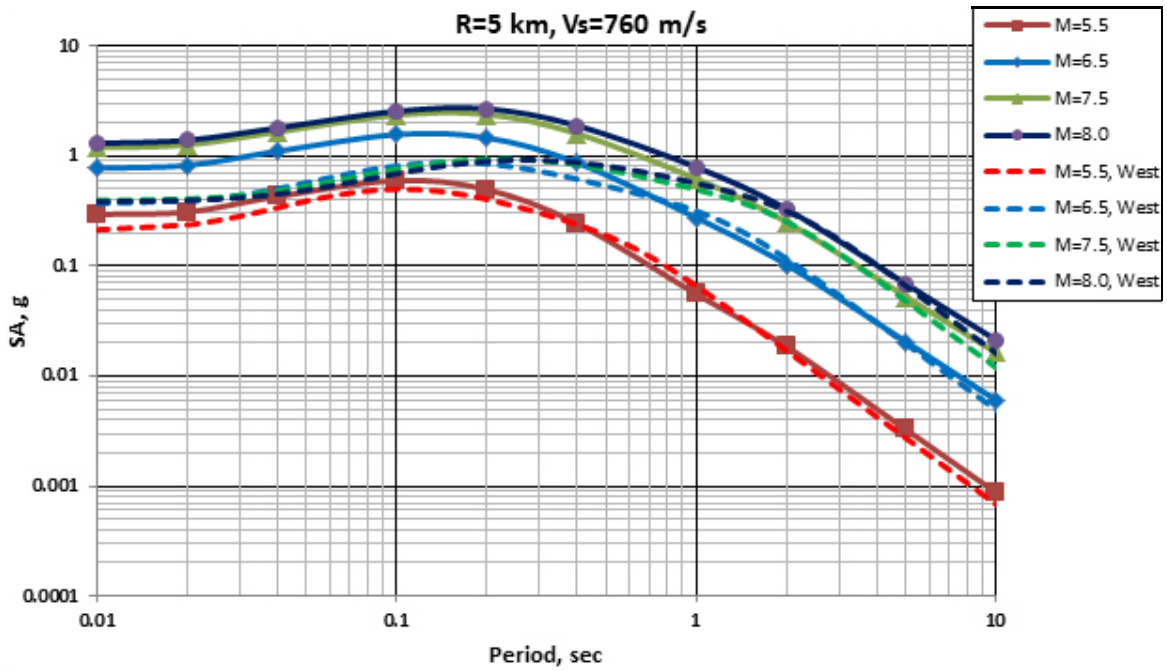


Figure 9.9 Comparisons of the G-14 spectral acceleration functions for the CEUS with GK-14 for the WUS at rupture distances of 5 and 50 km for the average $V_{s30} = 760$ m/sec.

Figure 9.10 shows magnitude scaling for PGA and PSA of 10, 2.5, and 0.5 Hz. Figure 9.11 demonstrates comparisons of the average scaling ratios relative to $\mathbf{M} = 5.0$ from ground-motion simulations (EXSIM, GP, SD) for $Z_{TOR} = 5$ km (dashed lines) [Goulet et al. 2015; Atkinson and Assatourians 2015; Graves and Pitarka 2015; and Olsen and Takedatsu 2015] with that of the G-14 model (solid lines) at rupture distances of 50 and 100 km. It compares well in terms of amplitudes and shapes for frequencies higher than 2 Hz. For lower frequencies, G-14 generally compares well in terms of shape of behavior, but predicts lower ratios relative to $\mathbf{M} = 5.0$.

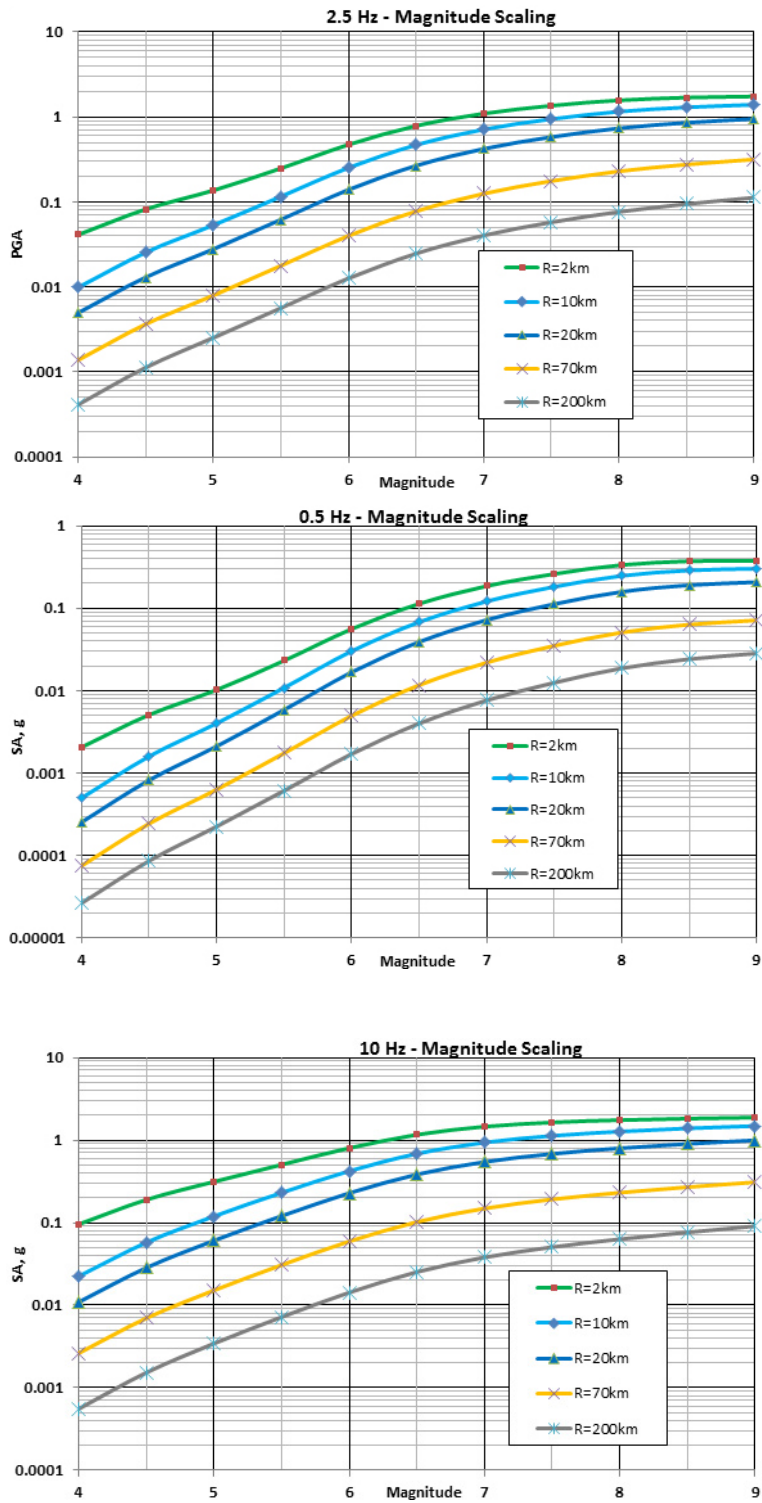
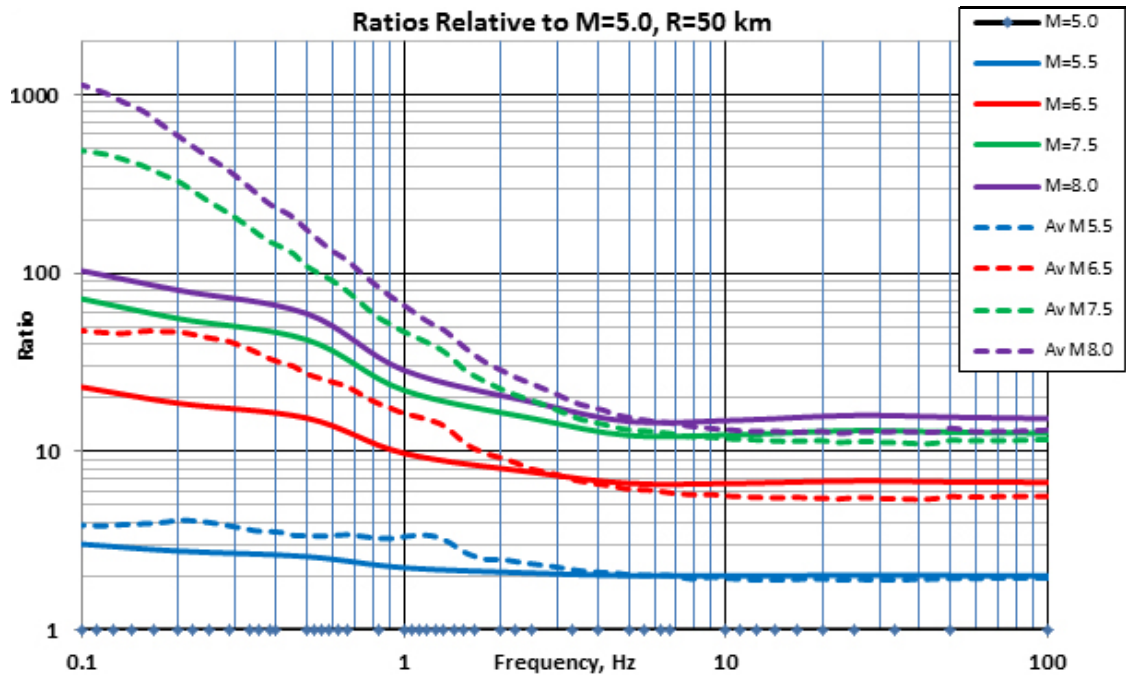
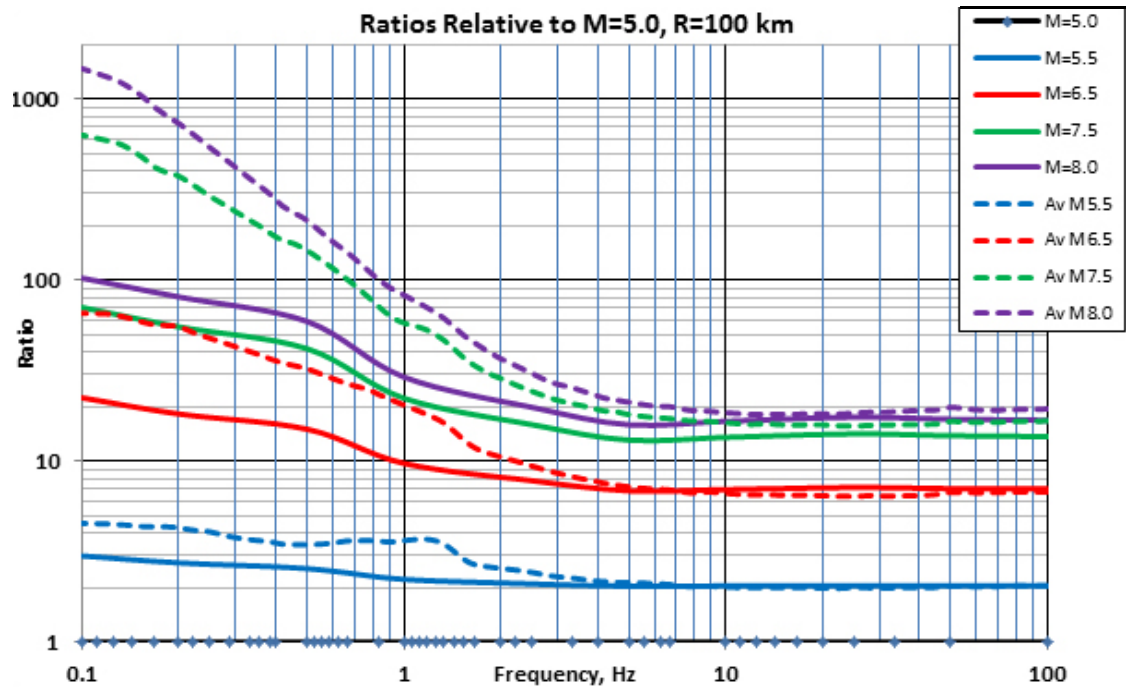


Figure 9.10 Magnitude scaling at PGA and PSA of 10, 2.5, and 0.5 Hz for hard rock conditions.



(a)



(b)

Figure 9.11 Comparisons of the average scaling ratios relative to $M = 5.0$ from simulations (EXSIM, GP, SD) for $Z_{TOR} = 5$ km (dashed lines) with that of the G-14 model (solid lines) at rupture distances of (a) 50 and (b) 100 km.

As stated earlier, the pilot version of the model was designed based on EPRI [2013] and Pezeshk et al. [2011] models. Figures 9.12–9.15 demonstrate comparison of my model for the CEUS with the above-mentioned models for magnitudes $M = 5.0$ and $M = 7.5$ for the seven frequencies of interest in nuclear industry. In general, the G-14 model produces results lower than the median EPRI 2013 model at high frequencies ($f > 10$ Hz) and higher amplitudes for frequencies lower than 2.5 Hz.

Figures 9.16-9.18 compares G-14 model with previously published individual seven models for CEUS [Somerville et al. 1997; Toro et al. 1997; Campbell 2003; Silva et al. 2003; Tavakoli and Pezeshk 2005; and Atkinson and Boore 2011] for magnitudes 5.5, 6.5, and 7.5 at PGA, and spectral frequencies of 10 Hz and 1 Hz. Figures 9.8 and 9.10–9.18 are shown for hard rock conditions.

Figures 9.19-9.22 demonstrate the model behavior (spectral acceleration decay with rupture distance) for different frequencies (from 0.1 to 100 Hz) compared to recorded data from the NGA-East database. These G-14 curves are shown for $V_{s30} = 640$ m/sec – average V_{s30} in the database used.

Figure 9.23 demonstrates examples comparisons of G-14 model predictions with a number of recorded data from Nahani $M6.76$, Mineral Virginia $M5.68$, Au Sable Forks $M5.0$, and Kansas $M4.8$ earthquakes.

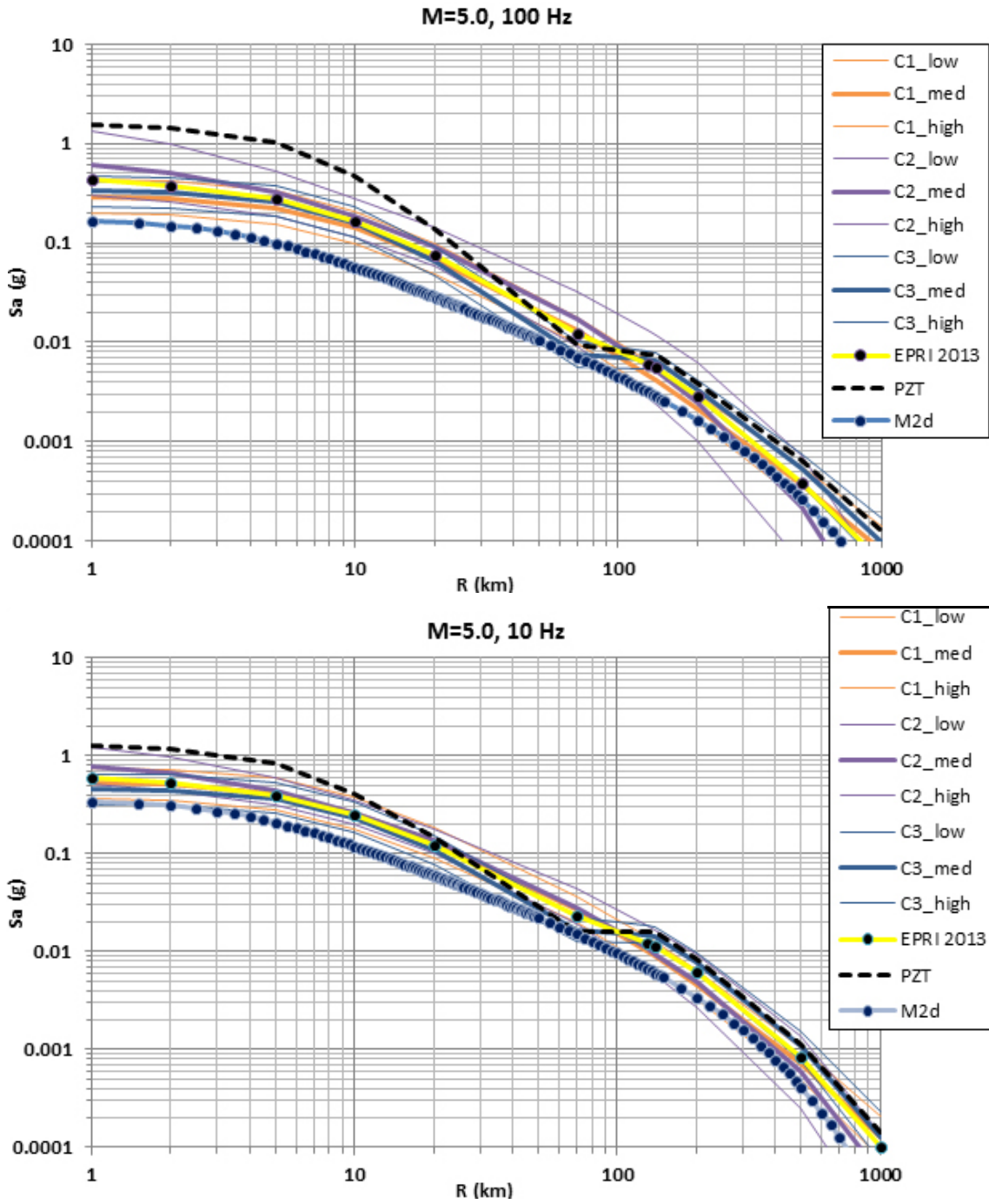


Figure 9.12 Comparison of the G-14 (M2d) model for the CEUS with the median EPRI 2013 model and low, median and high EPRI clusters for magnitude $M = 5.0$ for PGA and PSA of 10 Hz.

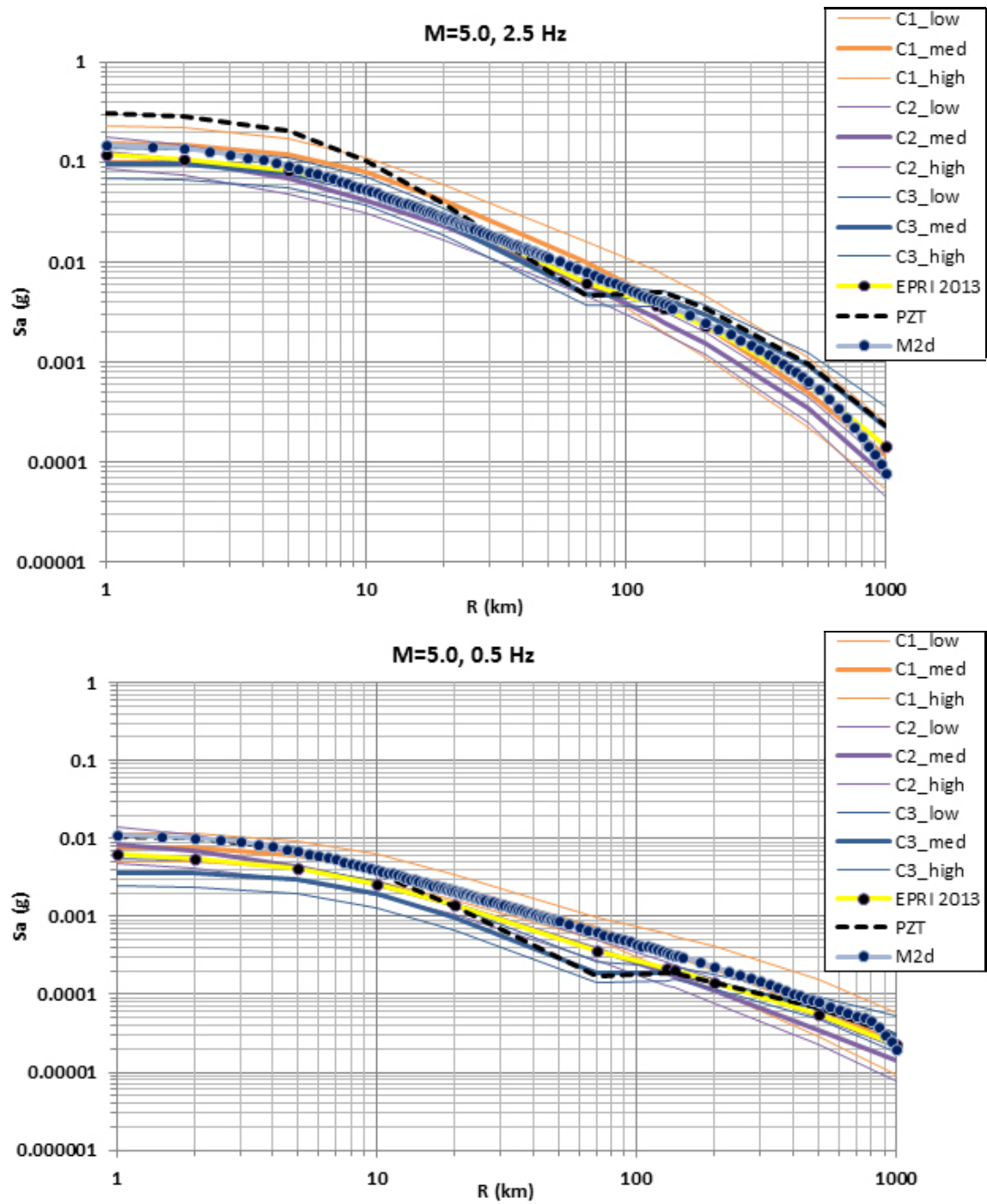


Figure 9.13 Comparison of the G-14 (M2d) model for the CEUS with the median EPR1 2013 model and low, median and high EPR1 clusters for magnitude $M = 5.0$ for PSA of 2.5 and 0.5 Hz.

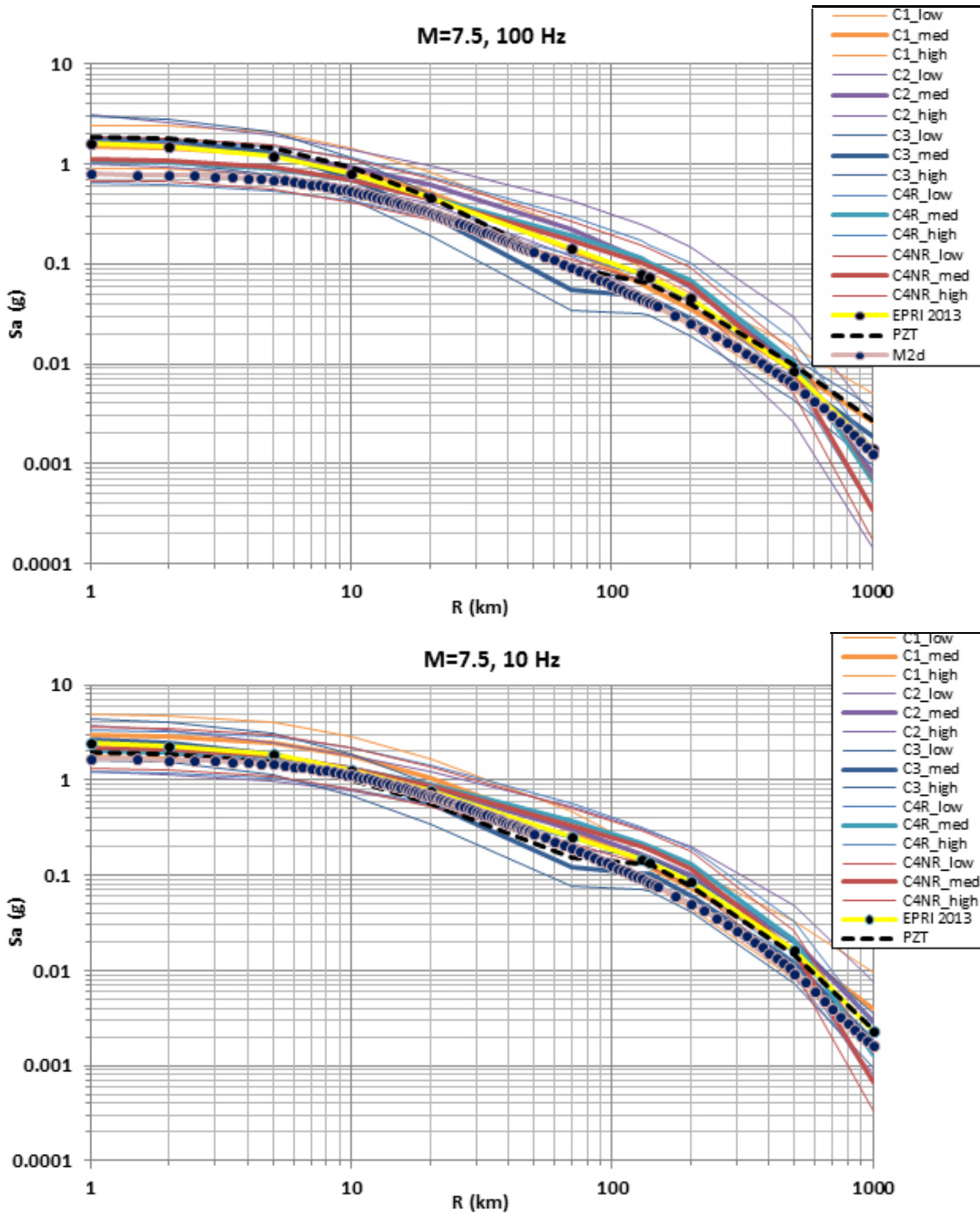


Figure 9.14 Comparison of the G-14 model for the CEUS with the median EPRI 2013 model and low, median and high EPRI clusters for magnitude $M = 7.5$ for PGA and PSA of 10 Hz.

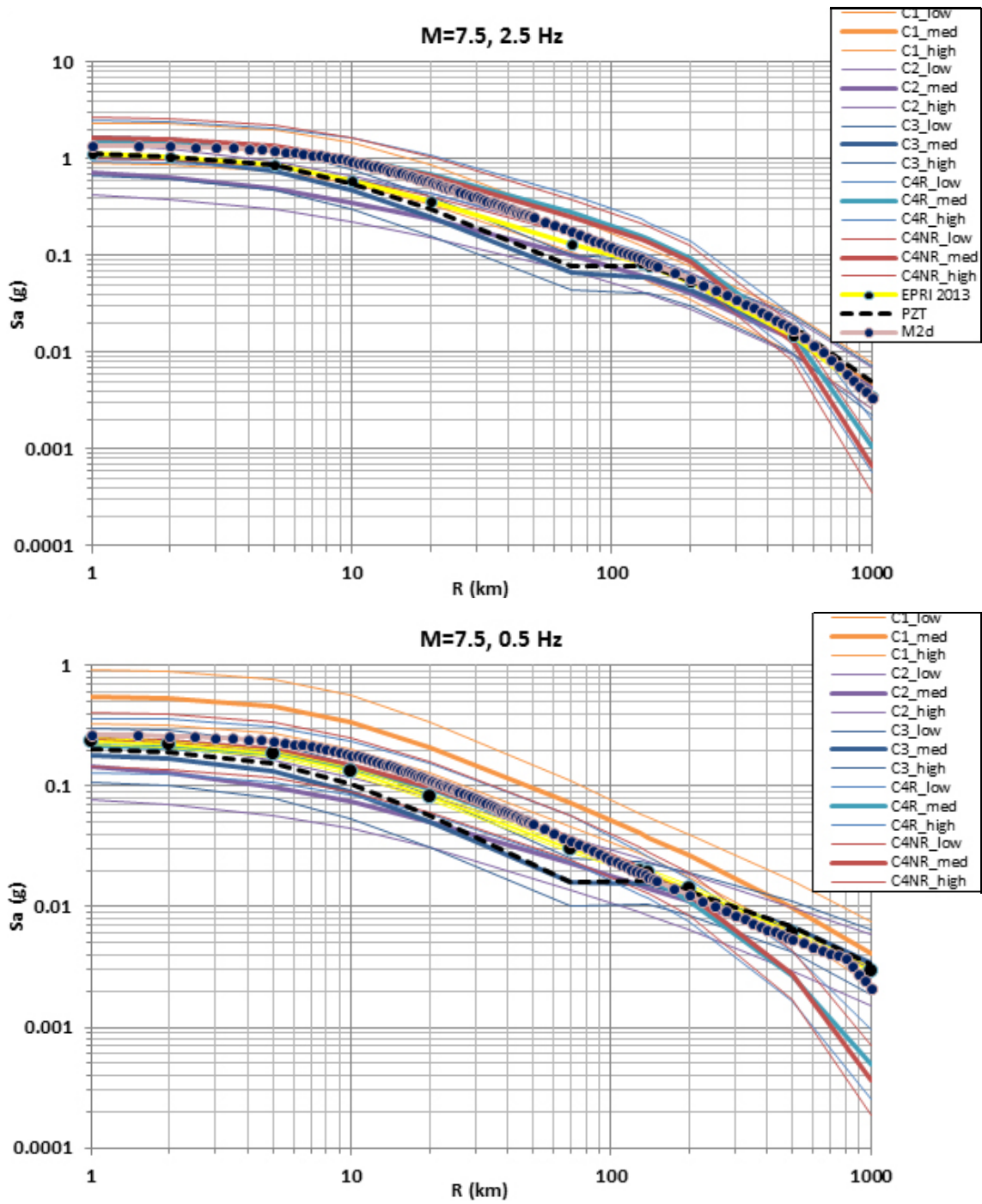


Figure 9.15 Comparison of the G-14 model for the CEUS with the median EPRI 2013 model and low, median and high EPRI clusters for magnitude $M = 7.5$ for PSA of 2.5 and 0.5 Hz.

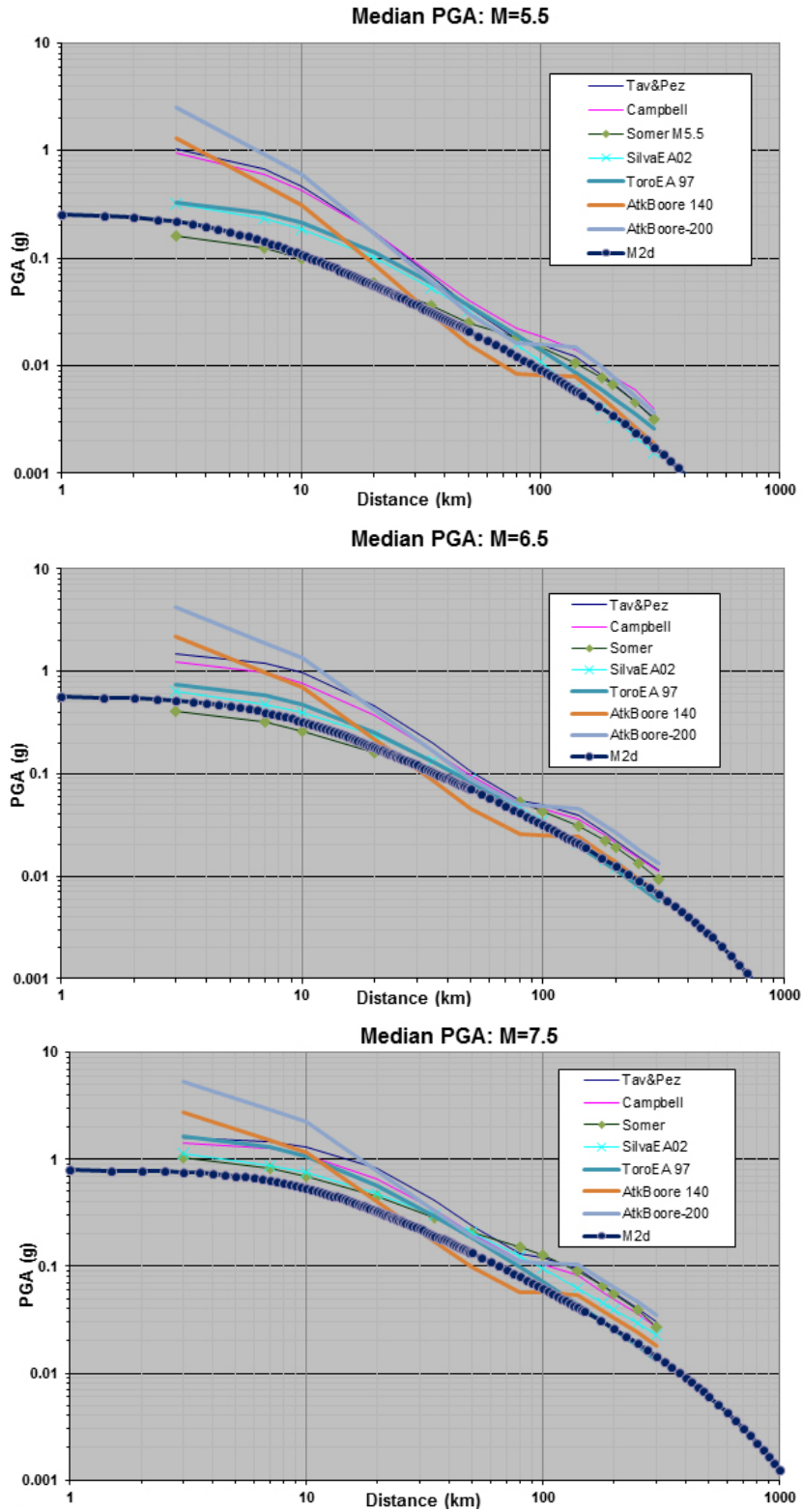


Figure 9.16 Comparison of the G-14 (M2d) model with the individual seven CEUS models for magnitudes 5.5, 6.5, and 7.5 at PGA.

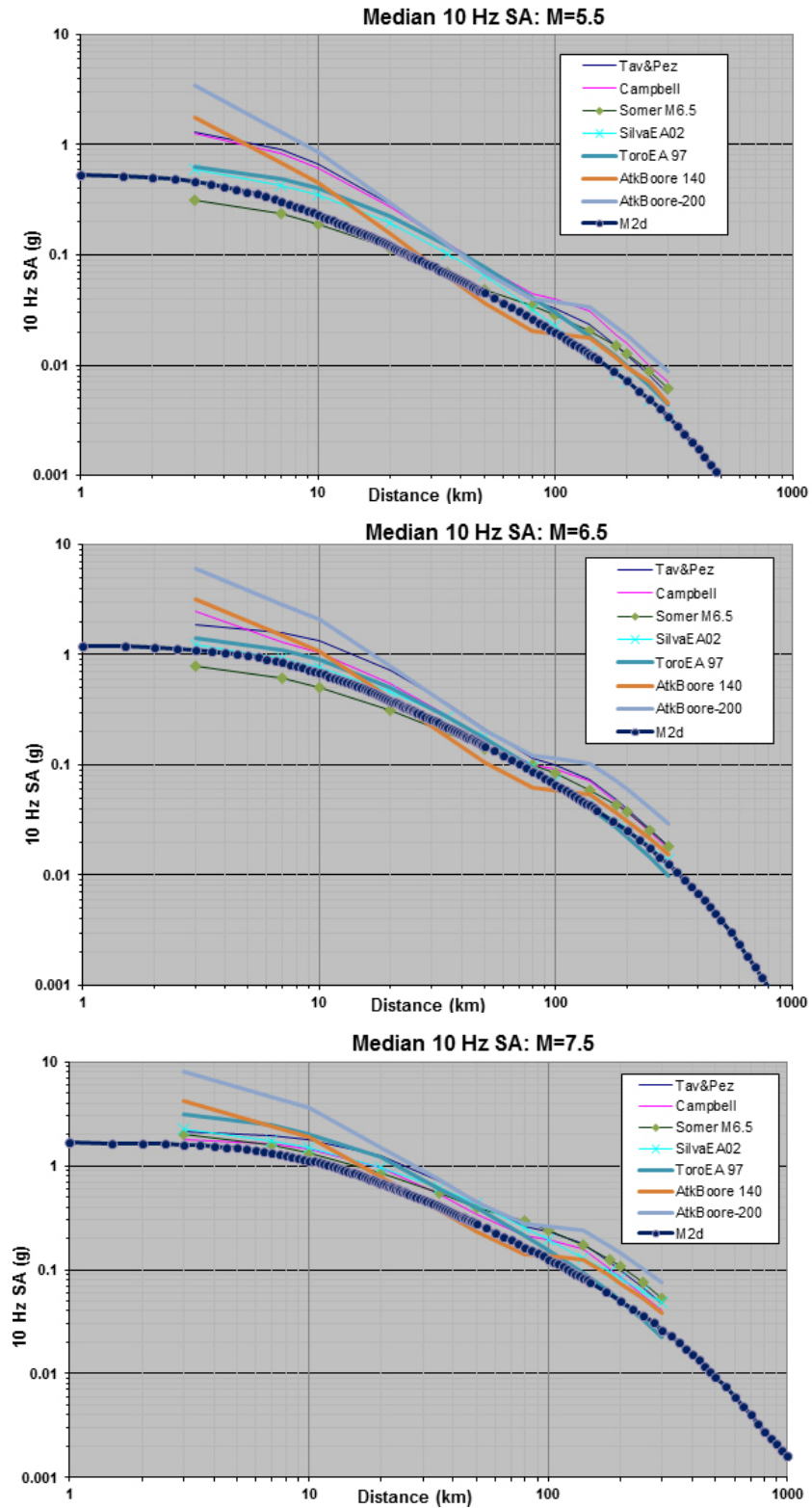


Figure 9.17 Comparison of the G-14 (M2d) model with the individual seven CEUS models for magnitudes 5.5, 6.5, and 7.5 at PSA of 10 Hz.

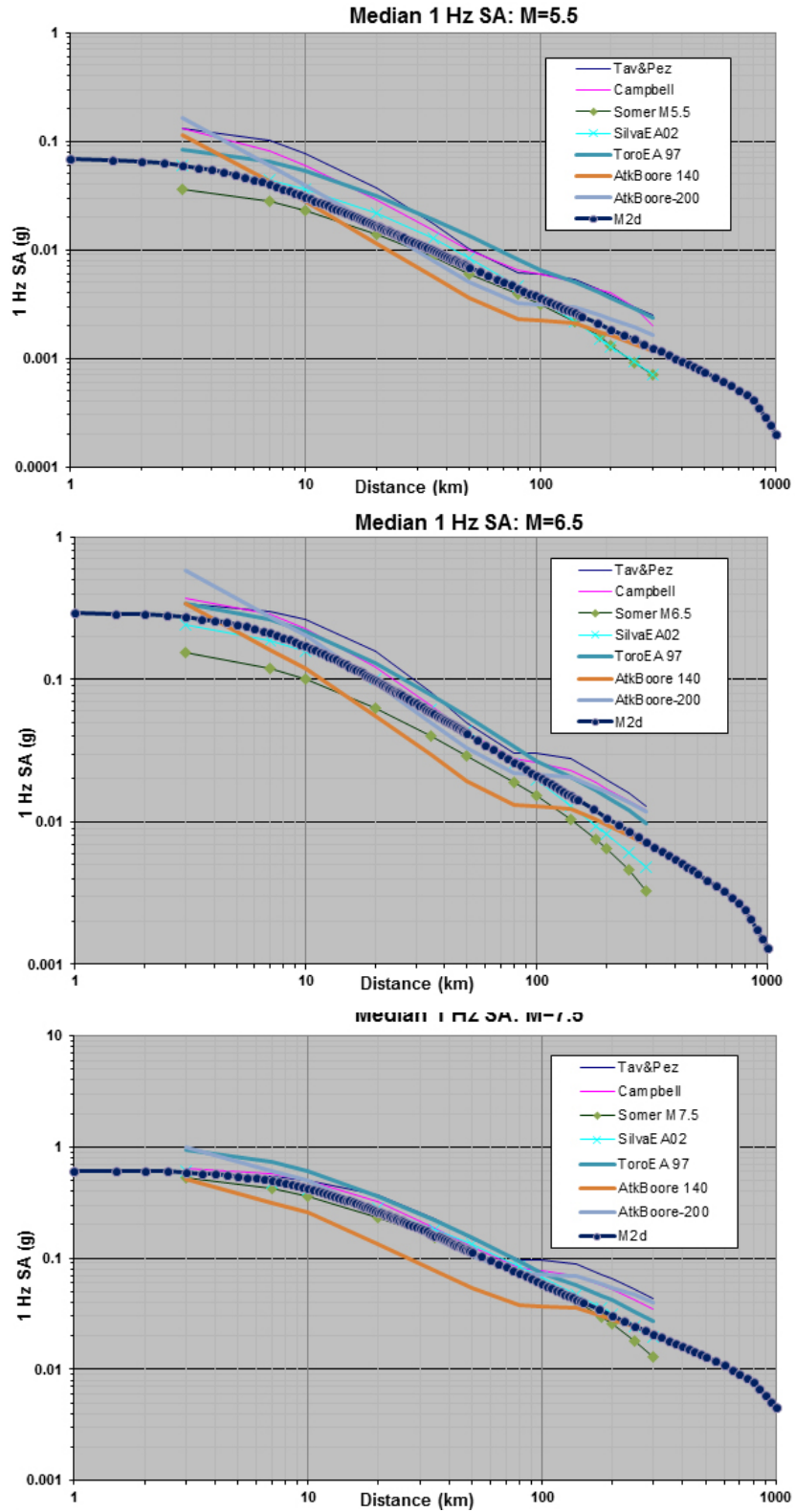


Figure 9.18 Comparison of the G-14 (M2d) model with the individual seven CEUS models for magnitudes 5.5, 6.5, and 7.5 at PSA of 1 Hz.

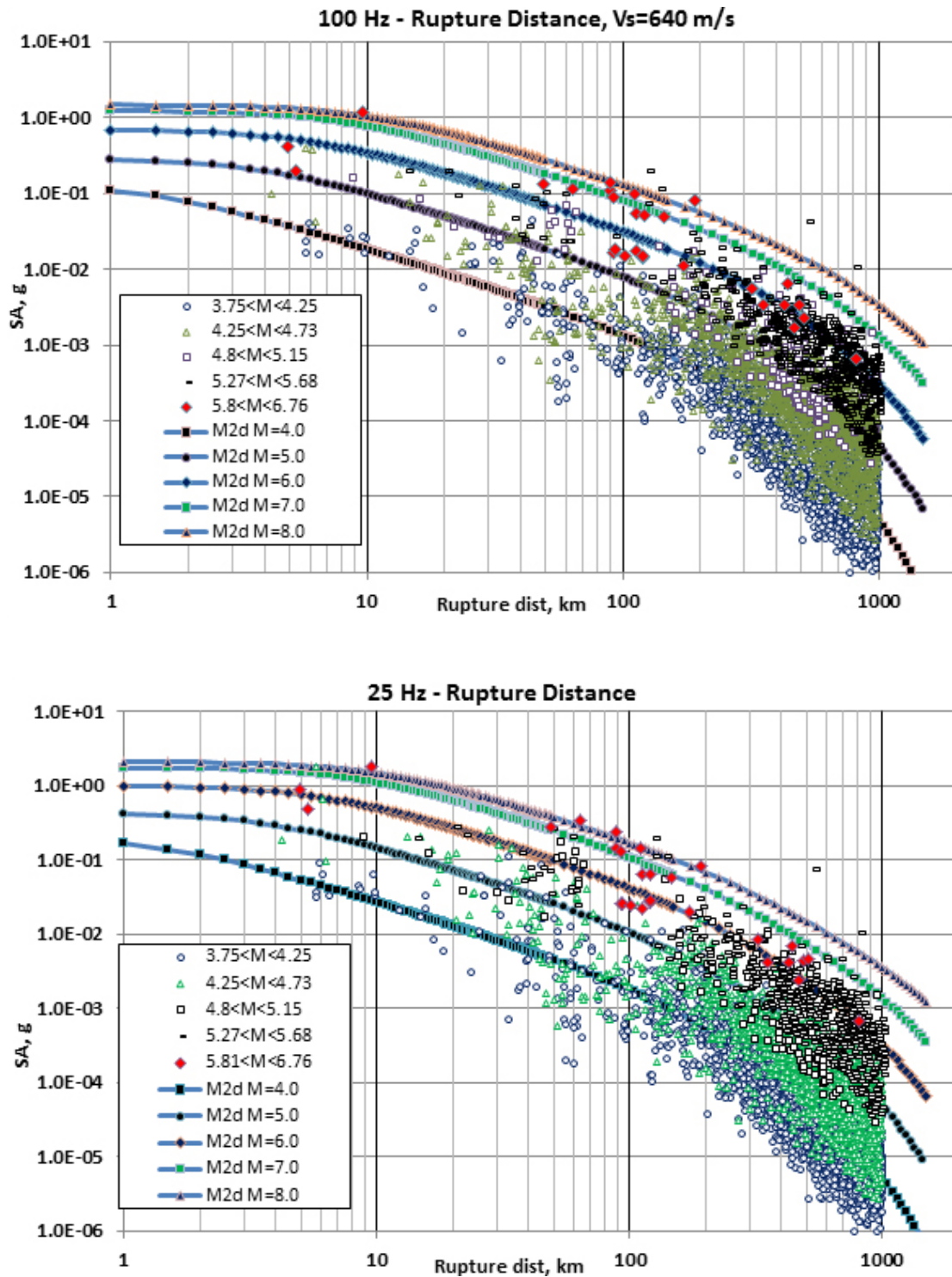


Figure 9.19 Model behavior (spectral acceleration decay with rupture distance) for different 100 and 25 Hz compared to recorded data.

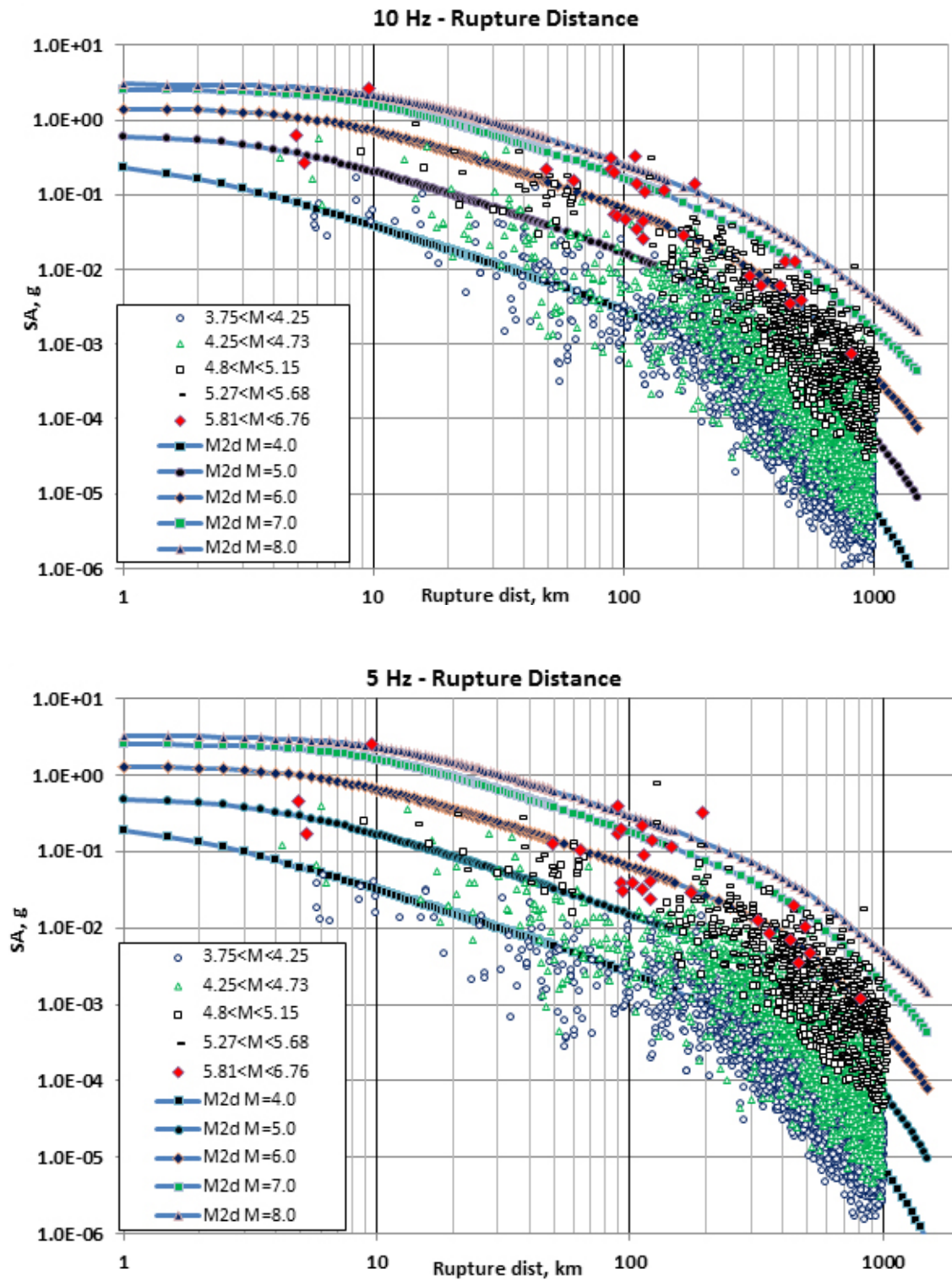


Figure 9.20 Model behavior (spectral acceleration decay with rupture distance) for different 10 and 5 Hz compared to recorded data.

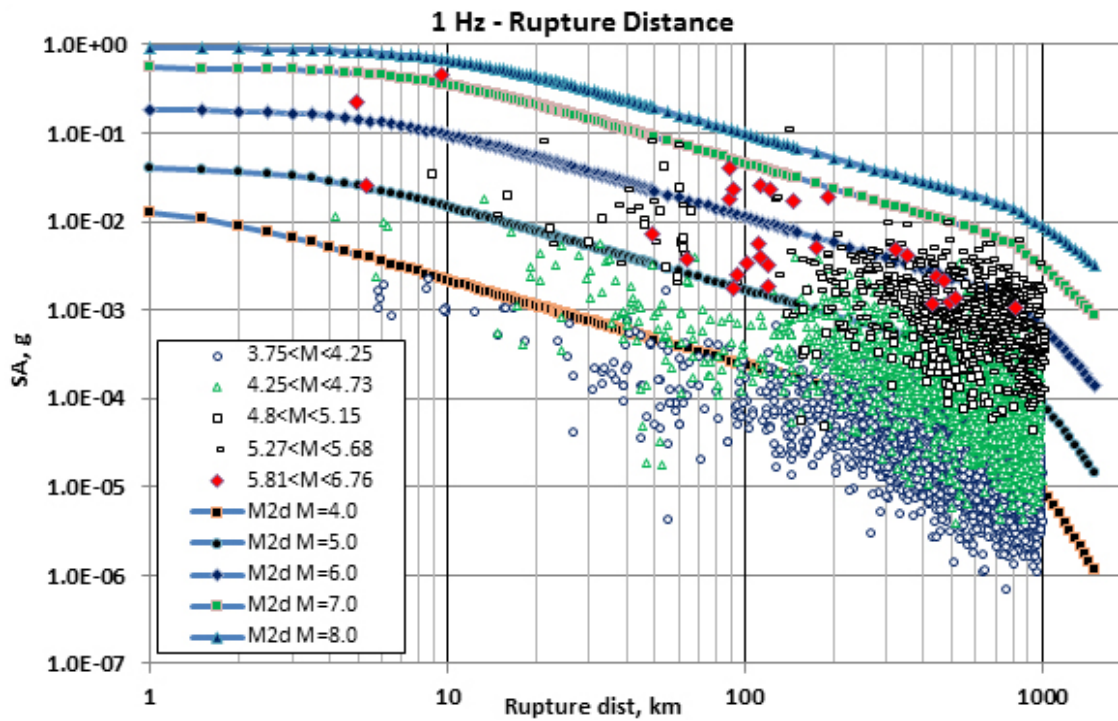
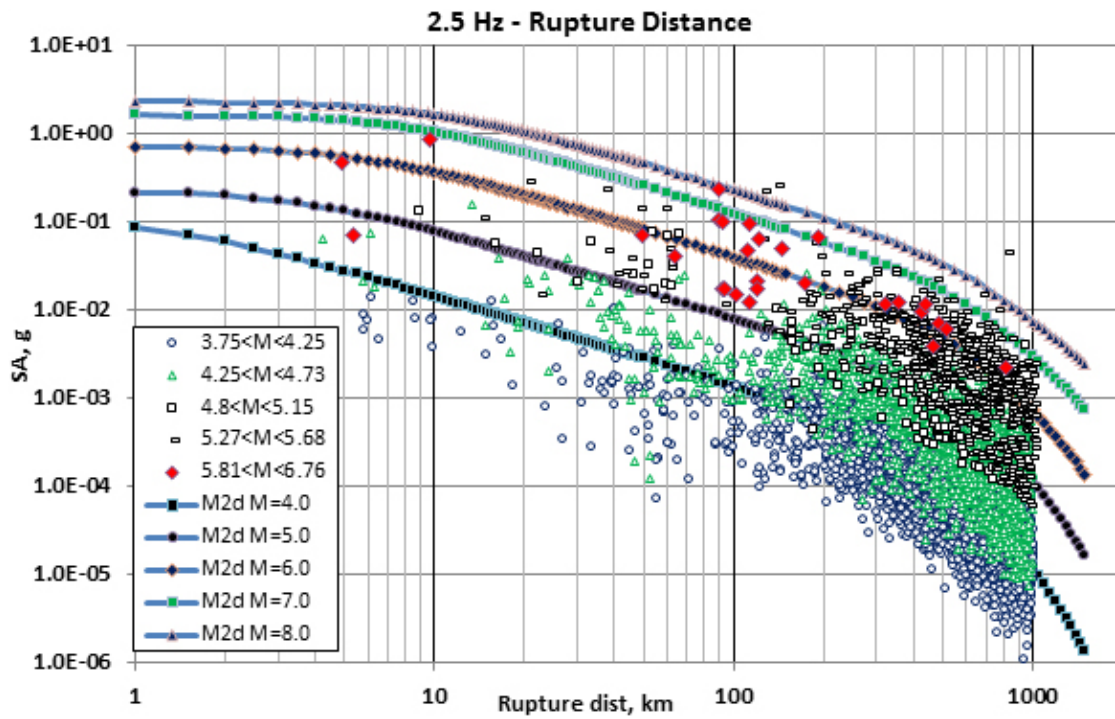


Figure 9.21 Model behavior (spectral acceleration decay with rupture distance) for different 2.5 and 1 Hz compared to recorded data.

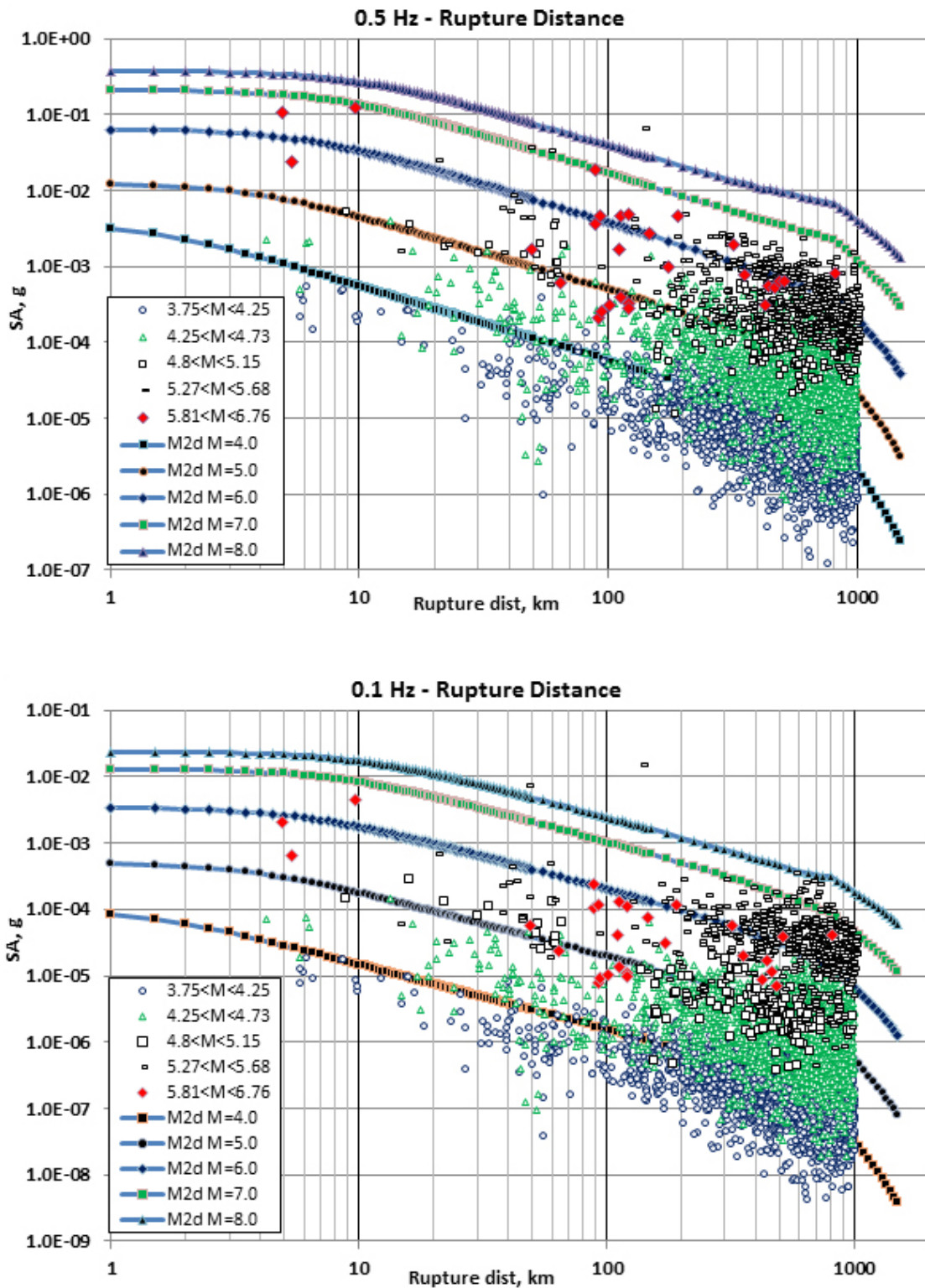


Figure 9.22 Model behavior (spectral acceleration decay with rupture distance) for different 0.5 and 0.1 Hz compared to recorded data.

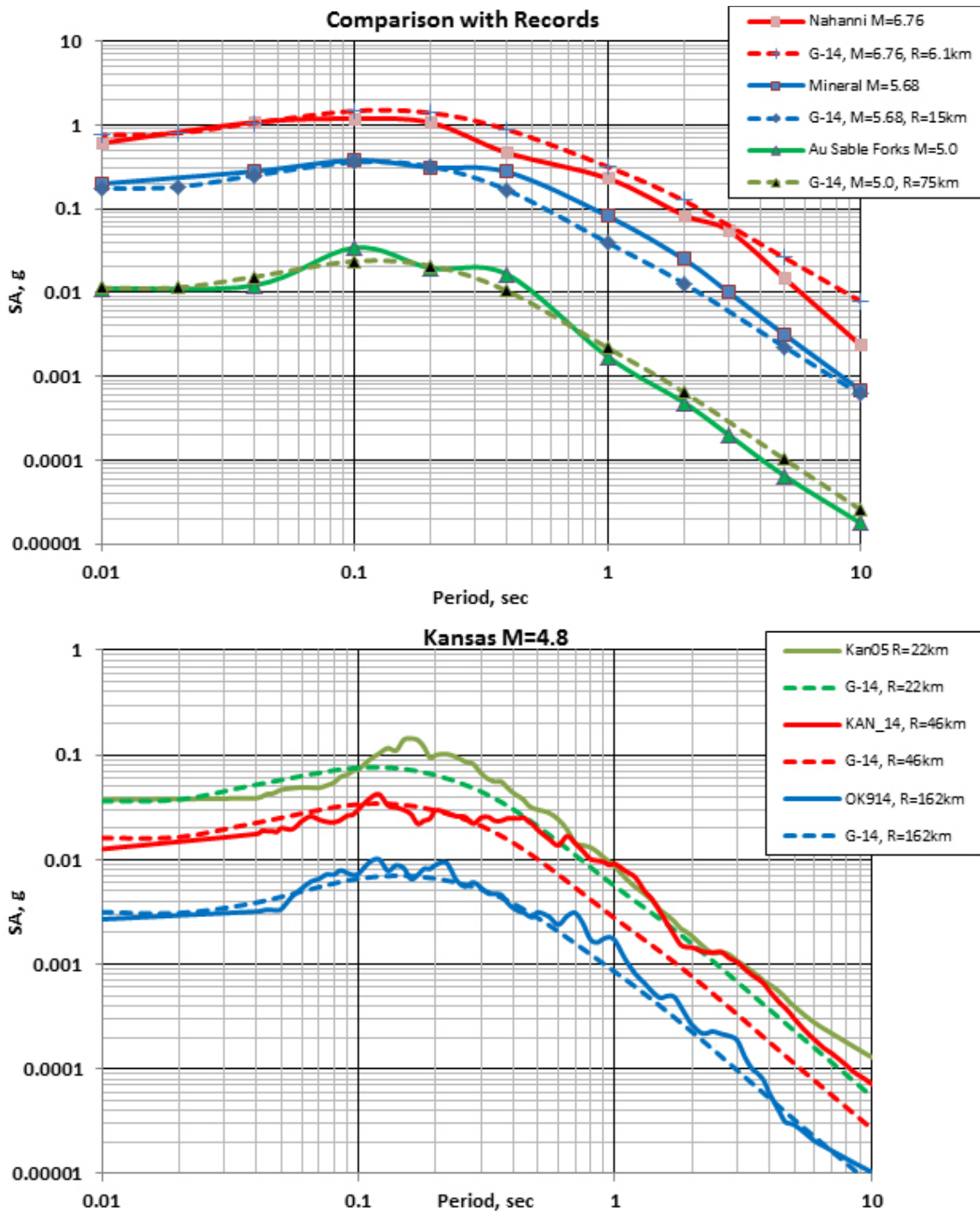


Figure 9.23 Examples comparisons of G-14 model predictions with recorded data from the Nahani M6.76, Mineral Virginia M5.68, Au Sable Forks M5.0, and Kansas M4.8 earthquakes.

9.5 RESIDUALS

Evidently, it is difficult to create a GMPE working in the range of 0 to 1000 km. In this case of CEUS, I first attempted to have the G-14 model with the coefficients shown in Figures 9.2 and 9.5 working at all frequencies, only to discover that residual curves still have linear trends, over prediction at closer distances, and under prediction at large rupture distances. To correct for these trends, I added linear trend correction at each period of interest. Table 9.2 presents residuals corrections applied at 11 periods of interest; PGA is assigned $T = 0.001$ sec. Figure 9.24 demonstrates the final residuals after above-mentioned correction (removing linear trends). Standard errors of residuals are shown on Figure 9.25.

Table 9.2 Corrections for Residuals at Eleven periods.

$$SA_{cor}(T) = SA(T) / \text{Residual}(T)$$

Residual(0.001 sec) = $\exp(-0.000257R + 0.270)$
Residual(0.01 sec) = $\exp(-0.000257R + 0.270)$
Residual(0.02 sec) = $\exp(-0.000330R + 0.350)$
Residual(0.04 sec) = $\exp(-0.000421R + 0.428)$
Residual(0.1 sec) = $\exp(-0.000441R + 0.409)$
Residual(0.2 sec) = $\exp(-0.000141R + 0.300)$
Residual(0.4 sec) = $\exp(-0.000290R + 0.314)$
Residual(1.0 sec) = $\exp(-0.000569R + 0.368)$
Residual(2.0 sec) = $\exp(-0.000300R + 0.300)$
Residual(5.0 sec) = $\exp(-0.000250R + 0.500)$
Residual(10 sec) = $\exp(-0.000300R + 0.650)$

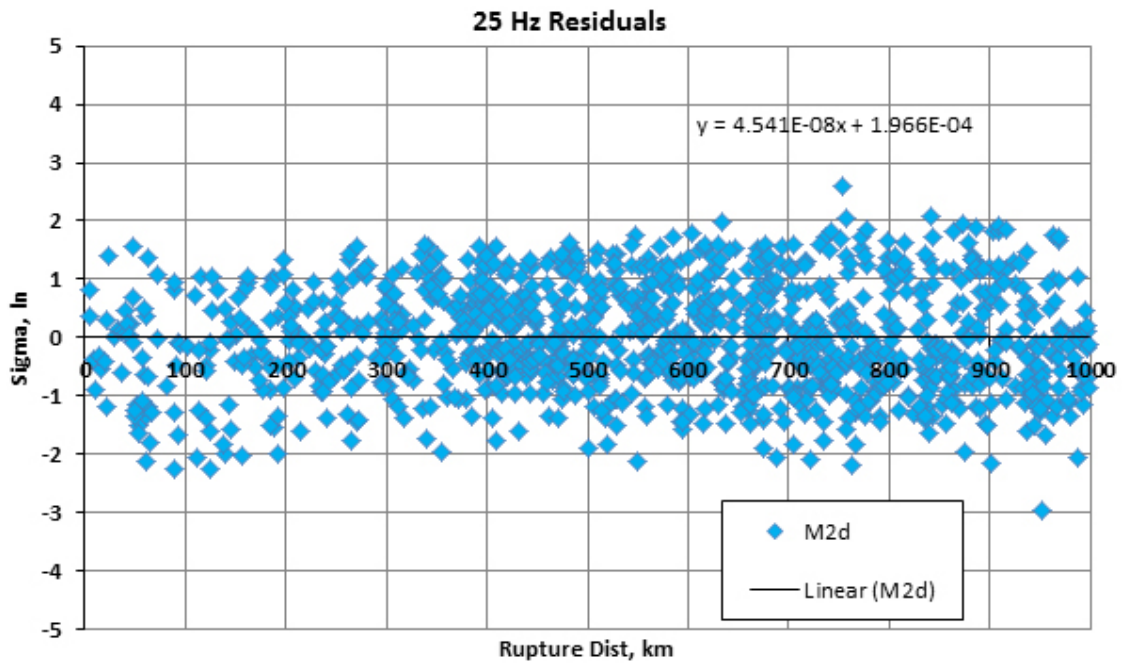
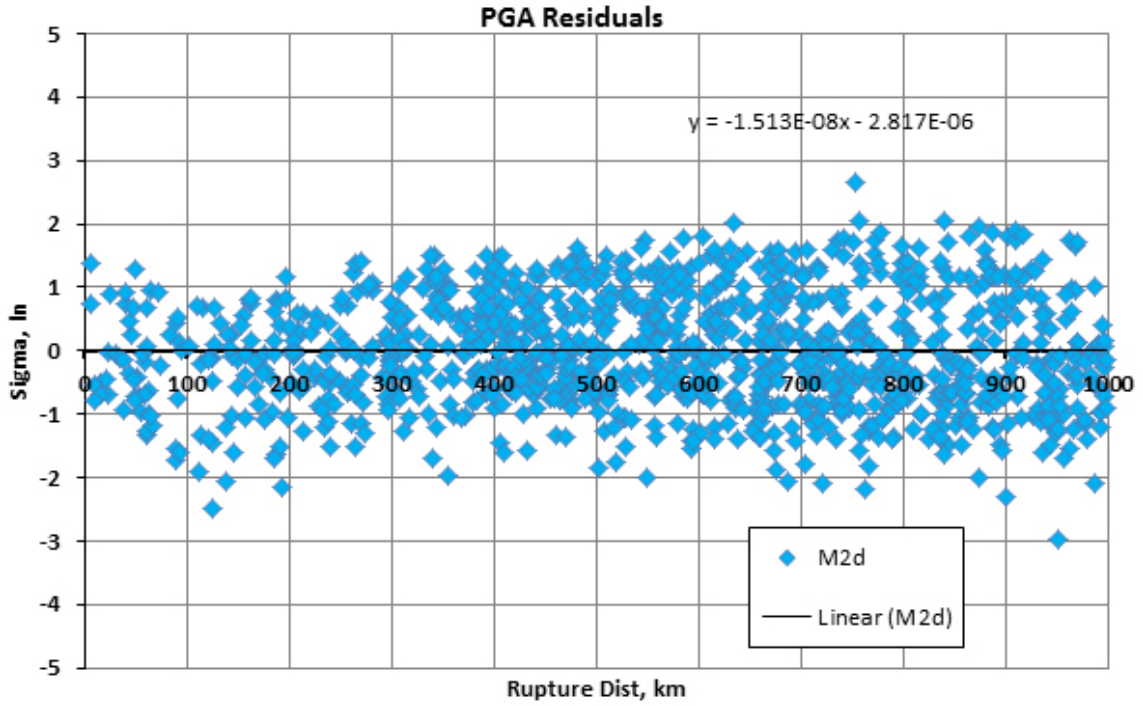


Figure 9.24 G-14 (M2d) residuals versus fault distance.

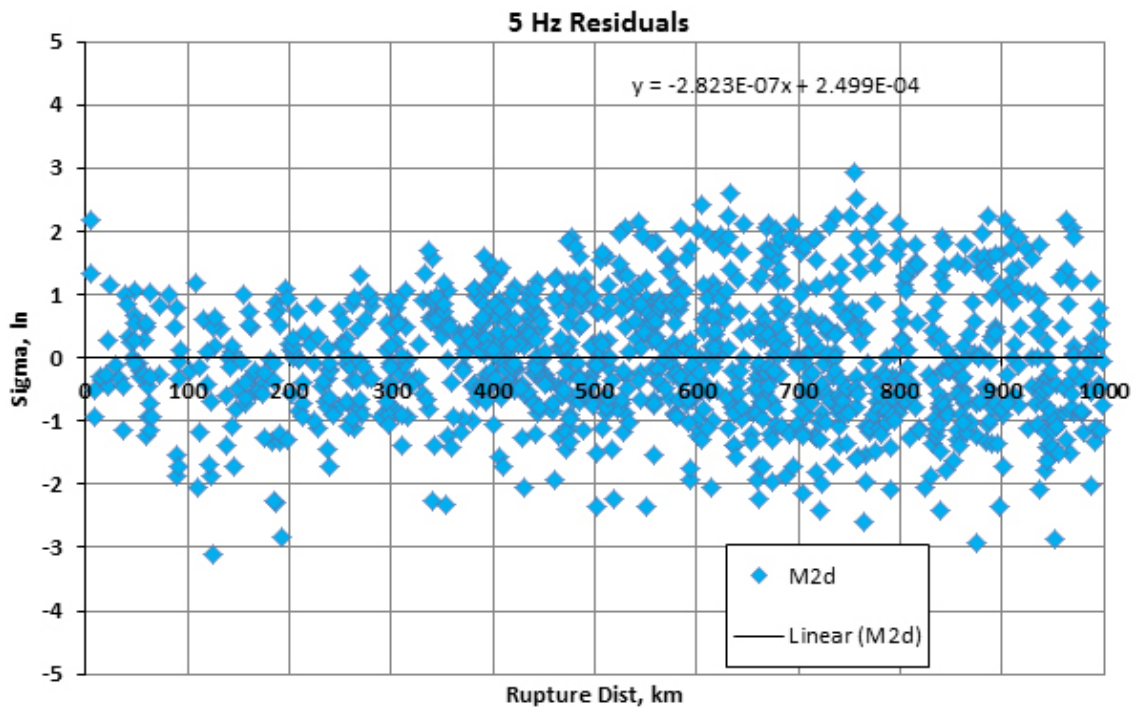
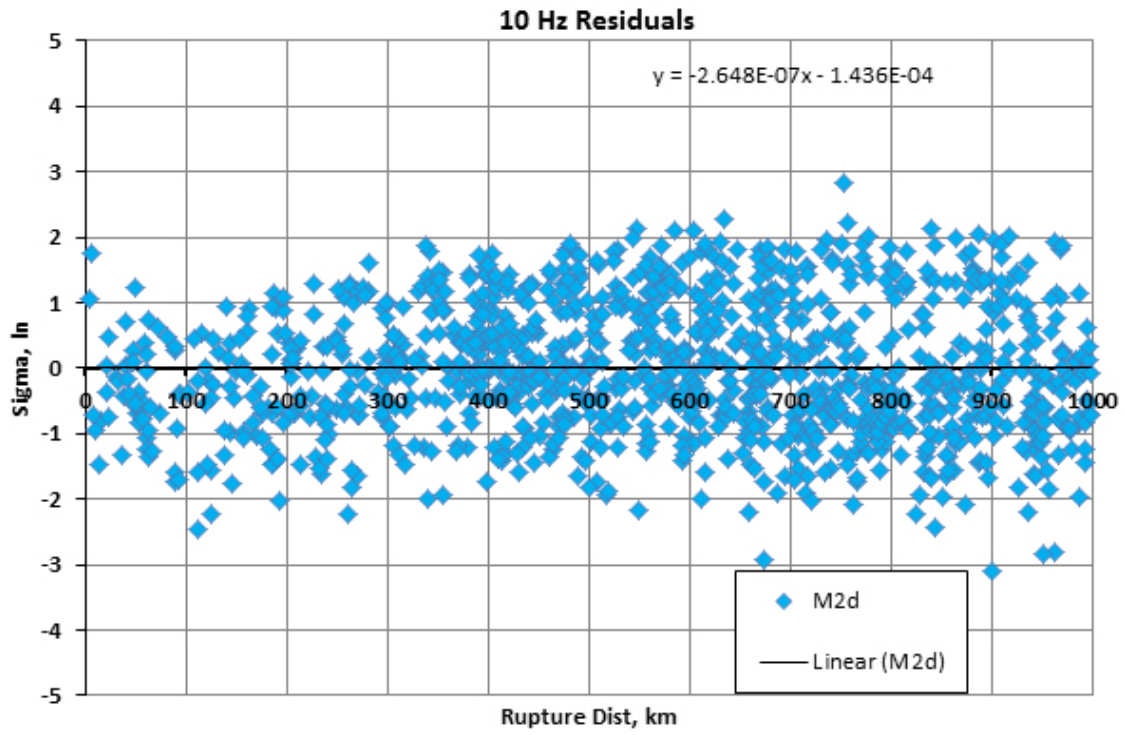


Figure 9.24 Continued.

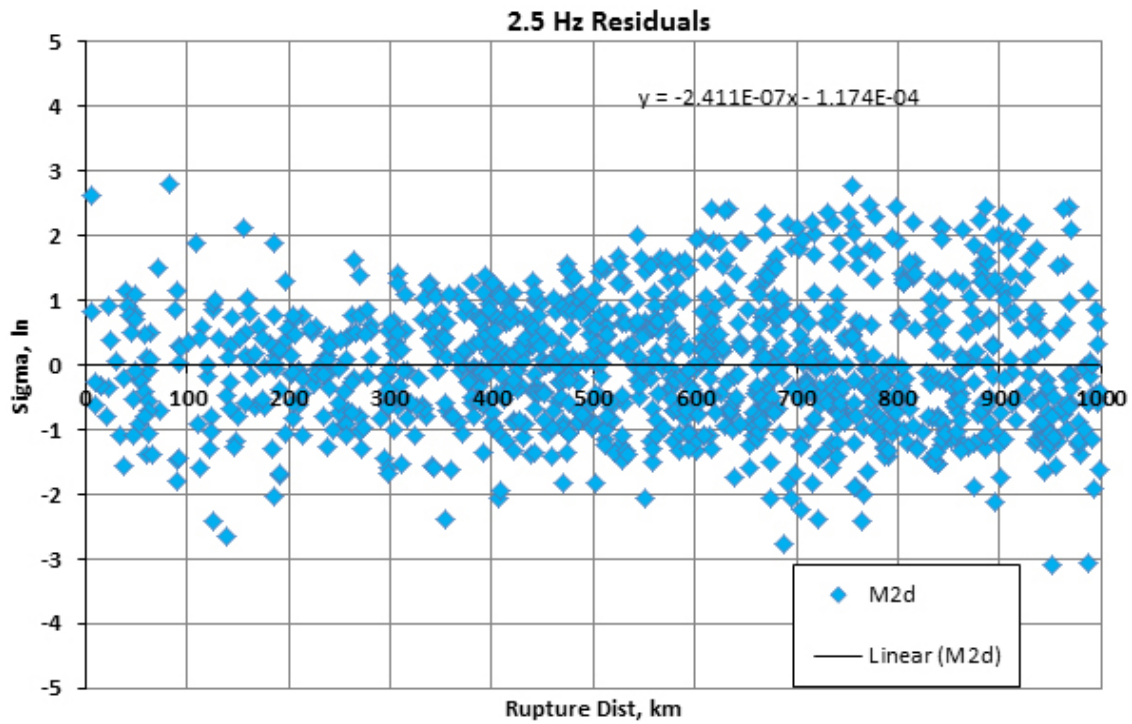


Figure 9.24 Continued.

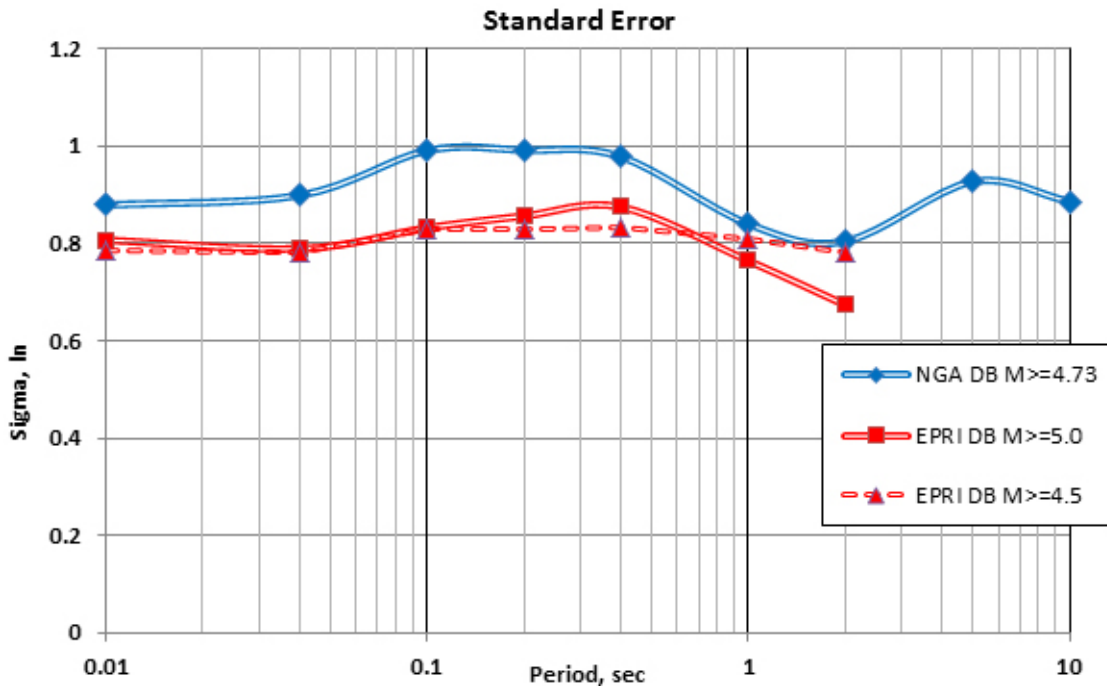


Figure 9.25 Standard error of G-14 model based on NGA-East and EPRI [2013] databases.

9.6 RESULTS

The new G-14 GMPE model for the CEUS is presented based on a filter-based approach first developed by Graizer and Kalkan [2007; 2009] for an active tectonic environment. The model uses same set of functions as in WUS, with calibration (coefficients) adjusted based on the NGA-East database of September 2014 for the horizontal PGA and 5%-damped PSA RotD_{50} component [Goulet et al. 2014].

In contrast to the active tectonic environment, this database for the CEUS stable continental environment is not sufficient to create purely empirical GMPEs covering the range of magnitudes and distances required for seismic hazard assessments. Recorded data collected in the NGA-East database are sparse and cover mostly range of magnitudes $\mathbf{M} < 6.0$, with limited amount of near-fault recordings. I used the subset of this database with $\mathbf{M} \geq 3.75$ and fault distances $R_{RUP} \leq 1000$ km with the addition of six data points from the recent $\mathbf{M} = 4.8$ 11/12/2014 Kansas earthquake recorded by high-quality strong-motion instruments at the epicentral distances of 18–162 km. The total number of earthquakes in the subset used is 48 with a number of 5026 recordings.

To constrain the model coefficients for larger magnitudes, I used a combination of: (1) ratios of amplitude of earthquakes with $3.75 < \mathbf{M} < 6$ from the NGA-East database relative to the enhanced NGA-West1 database; (2) average stress-drop ratio between WUS and CEUS; and (3) recent ground motion simulations ratios between $\mathbf{M} = 5.0$ and higher \mathbf{M} [Atkinson and Assatourians 2015; Graves and Pitarka 2015; and Olsen and Takedatsu 2015, see Appendix 1B]. The core function [Equation (9.3)] and the corner distance dependence function [Equation (9.4)] are taken from our findings for the WUS [Graizer and Kalkan 2007].

Comparisons were made of the G-14 model with the EPRI [2013] and a number of other published GMPEs. In general, the G-14 model compares reasonably well with most of the current models, but produces results lower than the median of the EPRI 2013 model at high frequencies ($f > 10$ Hz) and slightly higher amplitudes for frequencies lower than 2.5 Hz. These results are based on the NGA-East database.

I developed site correction based on multiple runs of different representative V_{S30} through SHAKE-type equivalent-linear programs using time histories and RVT approaches. Site amplification functions are calculated for different V_{S30} relative to hard rock definition used in nuclear industry ($V_s = 2800$ m/sec). Model is covering the range of $450 < V_{S30} = 2800$ m/sec.

The model is easy to use with a limited number of measurable parameters: moment magnitude \mathbf{M} , closest distance to fault rupture plane R_{RUP} , average shear-wave velocity in the upper 30 m of the geological profile V_{S30} , and anelastic attenuation factor Q_0 . Incorporating anelastic attenuation Q_0 as an input parameter allows adjustments based on the regional crustal properties.

The model covers the range of moment magnitudes of $4.0 < \mathbf{M} < 8.2$, distances of $0 < R_{RUP} < 1000$ km, S -wave velocities of $450 < V_{S30} = 2800$ m/sec and period range of 0.01 to 10 sec.

The Graizer-14 ground-motion prediction models for PGA and PSA are available from the author in MatLab format.

9.7 ACKNOWLEDGMENTS

I am grateful to Dogan Seber for critical review and valuable comments that helped improving the quality of the manuscript. I thank Scott Stovall for his help in programming tools of testing the model, and Scott Stovall, Thomas Weather and Jon Ake for providing EQL RVT type code for site response analysis.

9.8 DISCLAIMER

Any opinions, findings and conclusions expressed in this paper are those of the author and do not necessarily reflect the views of the U.S. Nuclear Regulatory Commission.

9.9 ELECTRONIC APPENDIX FOR CHAPTER 9

9A Model Output (Excel workbook)

10 Referenced Empirical Ground-Motion Model for Eastern North America

Behzad Hassani

Gail M. Atkinson

**Department of Earth Sciences
Western University, Ontario, Canada**

Abstract

We update ground-motion prediction equations (GMPEs) for Eastern North America (ENA) using the referenced empirical approach of Atkinson [2008]. The technique is based on the use of residual analysis that models differences between regional ground-motion observations and a reference GMPE developed for a data-rich region. The update is timely because the NGA-West2 GMPEs for shallow crustal earthquakes in active tectonic regions enable a significant improvement in the implementation of this model, relative to previous work (e.g., Atkinson and Boore [2011]). The predicted ground-motion amplitudes of the ENA referenced empirical model are very similar to the equivalent California values of Boore et al. [2014a] (BSSA 14) at close distances ($R \leq 50$ km), at low to moderate frequencies ($f \leq 5$ Hz). At regional distances ($R > 50$ km) and at high frequencies ($f > 5$ Hz), the ENA data suggest higher ground-motion amplitudes than the BSSA14 reference model, presumably due to lower attenuation and higher stress for ENA events relative to those in active tectonic regions. We also show that the referenced empirical approach predicts ground motions that are consistent with those produced by the hybrid empirical approach [Campbell 2003], considering recent equivalent point-source models that match both ENA and California ground-motion databases

10.1 INTRODUCTION

Ground-motion prediction equations (GMPEs) are simple functions that describe ground-motion amplitudes as a function of magnitude, distance and site condition, and which are key elements in seismic hazard modeling. The common approach to developing GMPEs in data-rich regions is to empirically correlate the observed ground-motion amplitudes to predictive variables that represent source, path, and site terms using a suitable functional form. An example of recent empirical GMPEs is the Pacific Earthquake Engineering Research Center's (PEER's) Next Generation Attenuation (PEER NGA-West1) equations, which have been developed for shallow

crustal earthquakes in active tectonic regions [Power et al. 2008; Bozorgnia et al. 2014]. The second generation of NGA equations was recently published as part of the NGA-West2 project, as described by Bozorgnia et al. [2014] and references contained therein. The NGA-West2 equations facilitate a fresh look at GMPEs for ENA. This is because the NGA-West2 equations are much more robust for small-to-moderate magnitude events than previous empirical GMPEs, enabling meaningful comparisons between eastern and western events in the magnitude range for which ENA data are plentiful. Note that although ENA data are relatively plentiful for small-to-moderate events, especially at regional distances, they are too sparse in the magnitude-distance range of engineering interest to allow direct regression of ground-motion amplitude data to determine robust empirical GMPEs.

In general, three different approaches have been proposed to develop GMPEs in ENA. The most widely used approach is the stochastic simulation-based method, in which a seismological model is used to model source, path, and site effects (e.g. Atkinson and Boore [1995, 2006, 2011]; Toro et al. [1997]; Silva et al. [2002]). Simulation-based GMPEs usually rely on a simple seismological model in which the underlying source, path, and site parameters are determined from small-to-moderate magnitude events, and then used to model expected motions over a wider range of magnitudes and distances.

Another popular approach is the hybrid empirical method [Campbell 2003; Tavakoli and Pezeshk 2005; Pezeshk et al. 2011]. In this method, GMPEs from host regions (active regions with robust empirical GMPEs) are adjusted to produce GMPE models for target regions (regions with poor ground-motion databases). This method also makes use of stochastic simulations: specifically, the adjustment factors are defined as the ratio of the simulated ground-motion amplitudes for the target region divided by the simulated ground-motion amplitudes for the host region.

A third method for development of GMPEs in data-poor regions is the referenced empirical method [Atkinson 2008]. In this method, sparse observational data are compared to an empirical GMPE model from a data-rich region [Atkinson 2008; Atkinson 2010; Atkinson and Boore 2011; and Atkinson and Motazedian 2013]. This method is similar in concept to the hybrid empirical method. The difference is that the adjustment factors are purely empirical, estimated using the ratio of the observed regional ground motions in the target region to the predicted values for the host region.

In both the hybrid empirical method and the referenced empirical method, we anchor our predictions to experience from data-rich regions. This approach is fundamentally robust, particularly in light of the growing body of evidence that regional differences in ground motions may not be as significant as once believed [Douglas 2004; Bommer et al. 2007; Atkinson and Morrison 2009]. The general similarity in ground motions between regions lends weight to the concepts implicit in such approaches. These concepts are that the magnitude scaling and overall near-source behavior should be the same in the host and the target regions, with regional differences being attributed to differences in fundamental source and attenuation parameters.

In this study, we use the referenced empirical method to develop a GMPE model for ENA, relative to the reference model of Boore et al. [2014; denoted BSSA14] which was developed as part of the NGA-West2 Project [Bozorgnia et al. 2014]. Any of the NGA-West equations could be used with relatively similar results, because the method is essentially a calibration of the GMPE to the database. The BSSA14 GMPE is especially convenient as all of

its necessary input parameters are available for the ENA database. Moreover, it is well constrained at low magnitudes ($M > 3.5$) and large distances $R \leq 400$ km, making comparisons to ENA data robust.

We could have developed a referenced empirical GMPE for each of the NGA-West2 equations, to include some measure of epistemic uncertainty due to the choice of the reference equation. However, this would represent only a partial source of epistemic uncertainty in the resulting GMPEs. The relative magnitude of this uncertainty can be judged by the comparisons given by Gregor et al. [2014] between the NGA-West2 models. We believe that other sources of epistemic uncertainty, especially those arising from limitations in the ENA database, are more important. Therefore, we choose to restrict the focus of this paper and do not aim to characterize epistemic uncertainty here. Rather, this paper presents one approach that can be used, alongside other approaches, in a broader evaluation of epistemic uncertainty.

The referenced empirical method has been previously used to develop GMPE models in ENA. Atkinson [2008] developed a referenced GMPE model (A08) for ENA based on the first generation of NGA GMPE equations [Boore and Atkinson 2008; denoted BA08], which was updated by Atkinson and Boore [2011] (with the updated model being denoted A08'). In this study, we make a major improvement on A08' by using a reference GMPE that is dramatically improved for small-to-moderate magnitudes, enabling a much more robust GMPE to be developed for ENA. Moreover, we show that the approach is in demonstrable agreement with predictions that would be made using the hybrid empirical approach for ENA, using recent validated equivalent point-source models for both the host and target regions. Thus we 'close the loop' between the referenced empirical and hybrid empirical methods.

10.2 THE GROUND-MOTION DATABASE FOR ENA

Our target region is ENA, defined here as North America east of 105° W longitude. The ENA database of this study is compiled from several different resources (see Section 10.5). Figure 10.1 is a map of recording stations and events used in this study. The ENA database consists of two separate regions, the central U.S. (designated Central), and southeastern Canada and northeastern U.S. (designated East). The regions differ in that data from the Central region is recorded predominantly on soil sites, while that from the East region is recorded predominantly on rock sites. We removed recorded ground motions in the Gulf Coast region (Figure 10.1) from our database because of significantly deep sediments in this region, which cause considerably different attenuation behavior [EPRI 2004].

The database of this study consists of peak ground-motion amplitudes (peak ground acceleration [PGA], peak ground velocity [PGV]) and response spectra (5%-damped pseudo-acceleration [PSA]) at frequencies from 0.1 to 20 Hz for horizontal components of ground motions. We used rotation-angle-independent geometric average of horizontal ground-motion amplitudes (RotD50) [Boore 2010] if available, and geometric mean of the two horizontal components if the RotD50 was not available (see Section 10.5). We used instrument-corrected response spectra and ground-motion amplitudes whenever available, and process time histories to calculate these ground-motion parameters when it was needed. The processing of the waveforms involved baseline correction, windowing, tapering, digital filtering, removing instrumental response, and obtaining response spectra and Fourier spectra at defined frequencies

instrumental response, and obtaining response spectra and Fourier spectra at defined frequencies band, as described by Assatourians and Atkinson [2010]. We retained data only for those frequencies with a signal-to-noise ratio greater than two. Moreover, we used only events with at least five records and having moment magnitudes (M) greater than three. The moment magnitudes of the events are either known (see Section 10.5) or can be reliably estimated (within 0.2 units) from the PSA amplitude at 1 Hz as described by Atkinson and Babaie Mahani [2013].

The ENA database consists of events with $M \leq 5.8$ with relatively few observations at close distances ($R \leq 50$ km). Therefore, for the ENA database we can assume that the closest distance to the surface projection of the rupture (R_{JB}) is approximately equal to the epicentral distance (R_{epi}), and that the closest distance to the rupture surface (R_{cd}) is equal to hypocentral distance (R_{hyp}). We consider records with $R_{epi} \leq 400$ km, to be consistent with NGA-West2 database [Boore et al. 2014b]. To consider site amplification effects following the format of the reference BSSA14 GMPEs, we characterized each site according to its time-averaged shear wave velocity in the upper 30 m (V_{s30}). V_{s30} information is extracted from the updated NGA-East database (see Section 10.5). According to the NGA-East database, V_{s30} values are either measured or estimated using two to five different proxies. The weighted average of these proxies provides more reliable estimate of V_{s30} comparing to the values obtained by a single proxy (e.g., such as the topographic slope method of Wald and Allen [2007]).

Figure 10.2 shows the magnitude-distance distribution of the database, distinguishing between different site classes based on their NEHRP (National Earthquake Hazards Reduction Program) site classification. Here, the histogram of number of sites in each site class is also shown for both regions (Note: NEHRP site classifications are based on V_{s30} values, where $V_{s30} \leq 180$ m/sec considered as site class E, $180 < V_{s30} \leq 360$ m/sec considered as site class D, $360 < V_{s30} \leq 760$ m/sec considered as site class C, $760 < V_{s30} \leq 1500$ m/sec considered as site class B, and $V_{s30} > 1500$ m/sec considered as site class A).

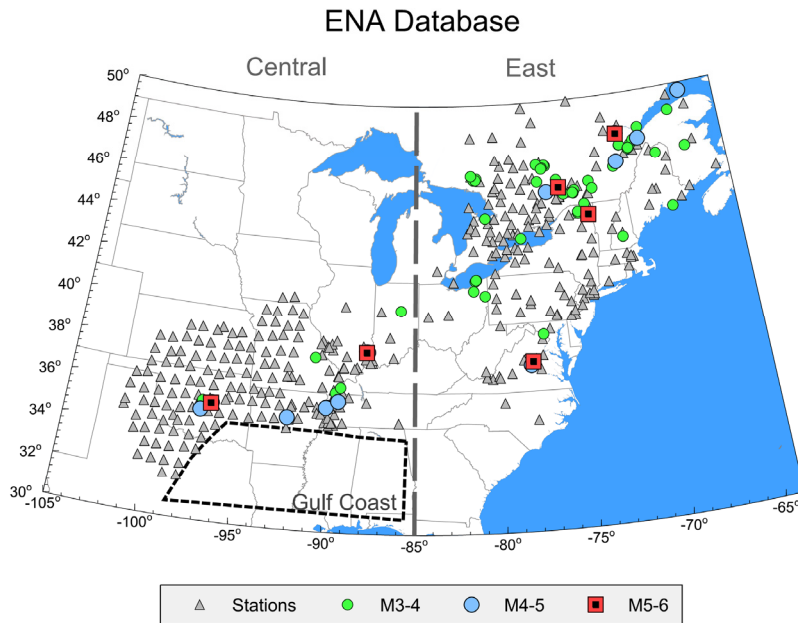


Figure 10.1 Geographic distribution of study events and stations.

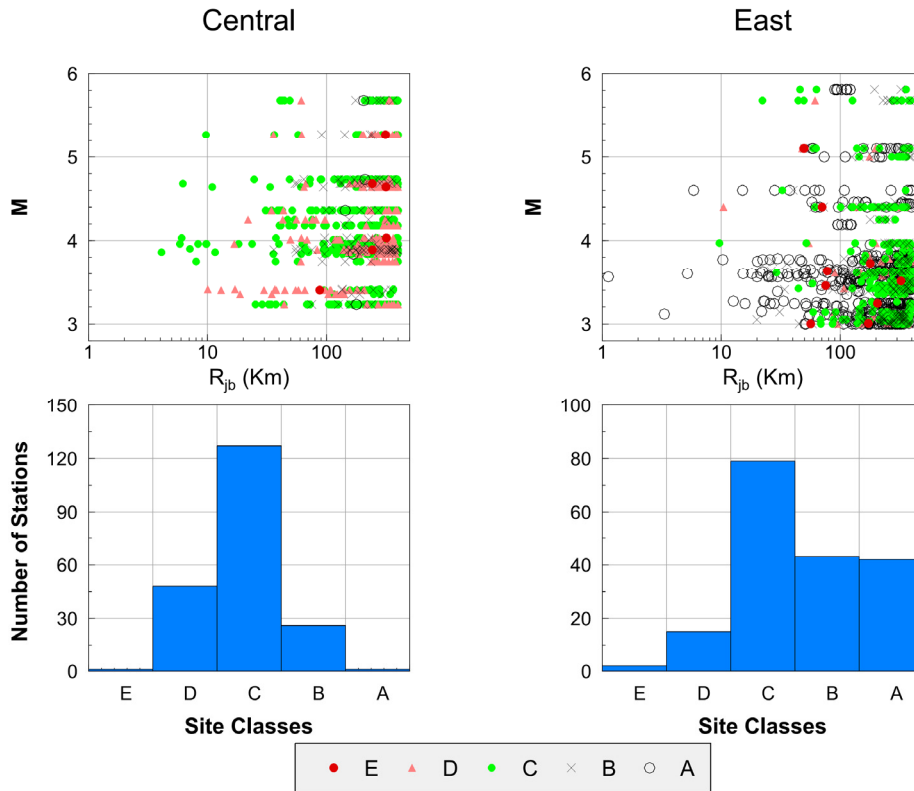


Figure 10.2 Top: Magnitude-distance distribution of the database, by NEHRP site classes; Bottom: Histogram of number of stations in each site class.

10.3 REFERENCED EMPIRICAL METHOD

The idea behind the referenced empirical approach is to adjust well-calibrated empirical GMPEs from a data-rich region (host region) to match the observed data in a target region. Applying this method, we can make the best use of both region-specific empirical ground-motion data and global experience from better-instrumented regions. The main assumption of this method is that the magnitude scaling and overall near-source behavior of ground motions are the same in the host and target regions, although the overall ground-motion levels at the source might be different (if the source parameters differ), and the attenuation might be different. Under these conditions, if we can establish the regional differences at moderate magnitudes, we can extend them to larger magnitudes. To proceed, we compute the residuals, defined as the difference (in log units) between the observed ground-motion parameters from the target region and the predicted ground-motion parameters of the host region GMPEs. Adjustment factors are defined to model the observed residual trends. The adjustment factors can modify the overall level of the reference GMPEs frequency-by-frequency, and possibly change their shape as a function of distance, in order to match the regional data. Adjustments to the overall level can accommodate regional variations in stress drop and event type, while adjustments to the distance coefficients can accommodate regional variation of attenuation parameters, including any differences in anelastic attenuation or geometrical spreading [Atkinson 2008; Atkinson 2010; Atkinson and Motazedian 2013].

The key inputs to construct referenced empirical GMPEs are regional ground-motion data from the target region and a set of reference GMPEs from the host region. The ground-motion database of this study is the ENA database as discussed in the previous section (horizontal components), while the reference GMPE is BSSA14 [Boore et al. 2014b]. Input parameters for BSSA14 are M , R_{JB} , V_{S30} , and source mechanism (assumed as unspecified). The outputs of BSSA14 are RotD50 [Boore 2010] of horizontal ground-motion amplitudes (PGA and PGV) and PSA at the defined frequency range (0.1 to 20 Hz), which is approximately the geometric mean of two randomly-oriented horizontal components.

The residuals (in log units) are computed for each record as the log (base10) of the ratio of the observed ENA horizontal ground motions to those predicted by BSSA14 reference model [i.e., $\log(\text{residual}) = \log(\text{observed ENA amplitude}/\text{predicted amplitude from BSSA14})$]. Figure 10.3 shows the residuals for Central and East regions at two selected frequencies (1 and 5 Hz) versus distance (R_{JB}), along with the function used to model the residuals (described in the following). Inspection of Figure 10.3 reveals that the averages of the residuals (filled squares) are positive in all distance bins, except at very close distances. This implies relatively higher ground-motion amplitudes in ENA in comparison to those in active regions, although at short distances ($R \leq 50$ km) the differences in amplitudes do not appear to be significant (at $f \leq 5$ Hz). There is an increasing residual trend at distances > 50 km, which is increasingly important, especially at high frequencies. The residual trends observed here agree with our general expectations, considering the slower attenuation of ENA motions at regional distances [Atkinson 2004]. At distances ≤ 50 km, the differences between ENA amplitudes and the predictions of BSSA14 model are not significant, at least at 1 and 5 Hz. The residual trends in the Central region are very similar to the equivalent values in the East region, which suggests similar ground-motion amplitudes for both regions. This agrees with a previous conclusion by Babaie Mahani and Atkinson [2012], and with expectations based on modeling studies by EPRI [2004]. Therefore, in order to develop more robust adjustment factors, the residuals for the East and Central regions are combined.

Figure 10.4 shows the residuals at four selected frequencies (0.5, 1, 5, and 10 Hz) for the whole ENA database. Here, the residual trends are defined as:

$$\begin{aligned} \log[F_{ENA}(f)]_{ij} &= C_1(f) + C_2(f)(R_{JB})_{ij} \\ &+ C_3(f) \max\left\{0, \log\left[\frac{\min((R_{JB})_{ij}, 150)}{50}\right]\right\} + \eta(f)_i + \varepsilon(f)_{ij} \end{aligned} \quad (10.1)$$

where $\log[F_{ENA}(f)]_{ij}$ is the residual estimated for recording j in event i as a function of frequency, $C_1(f)$ adjusts the overall level of BSSA14 reference GMPEs, $C_2(f)$ is a factor to model regional differences in anelastic attenuation, $C_3(f)$ is a factor to adjust the shape of the reference GMPEs (as a function of distance) to match the observed ground-motion attenuation shape in ENA in the transition zone from direct wave to Lg -spreading ($50 \leq R < 150$ km) and beyond, η_i is the random event term for event i , and ε_{ij} represents the within-event residual for

recording j in event i . Event terms have zero mean and standard deviation of τ (log10 units), while within-event errors have zero mean and standard deviation of ϕ (log10 units).

The adopted functional form of Equation (10.1) produces a relatively flat attenuation zone between 50 and 150 km, which is consistent with proposed tri-linear ENA empirical models (e.g., Atkinson and Mereu [1992] and Atkinson, [2004]). This functional form offers advantages in fitting the observed residuals over alternative bilinear forms, which are also commonly used (e.g., Boatwright and Seekins [2011] and Atkinson and Boore [2011]). The transition zone models the effect of reflections and refractions off the Moho discontinuity, which disrupts amplitude decay in the distance range from 50 to 200 km (e.g., Burger et al. [1987]).

To solve Equation (10.1), we applied a mixed effects regression of residuals according to Abrahamson and Youngs [1992]. An iterative regression was performed to maximize the likelihood of the model (Equation 3 in Abrahamson and Youngs [1992]) and estimate the adjustment factor coefficients $[C_1(f), C_2(f) \text{ and } C_3(f)]$ and $C_3(f)$, as well as the variability parameters ($\eta_i, \varepsilon_{ij}, \tau$, and ϕ). The total standard deviation σ is obtained as:

$$\sigma = \sqrt{\tau^2 + \phi^2} \quad (10.2)$$

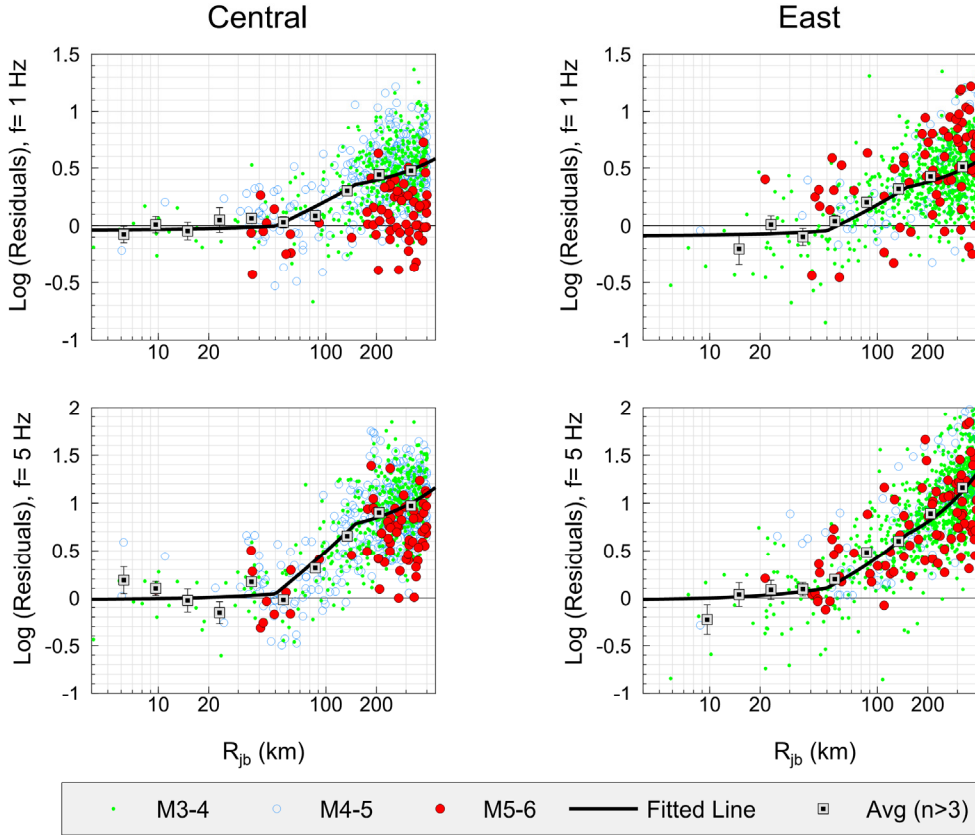


Figure 10.3 Residuals in Central and East regions compared to BSSA14 reference GMPE in log10 units for PSA at 1 and 5 Hz frequencies. The residuals are coded by magnitude. Filled squares show mean residuals in equally log-spaced distance bins with their corresponding standard error, and solid lines show the fit line to residuals [Equation (10.1)].

Table 10.1 shows the estimated coefficients for PGA, PGV, and PSA at 0.1 to 20 Hz frequencies, as well as the between-event standard deviation (τ), within-event standard deviation (ϕ), and total standard deviation (σ). The referenced empirical GMPE for ENA is given by:

$$Y'_{ENA} = F_{ENA} Y_{BSSA14} \quad (10.3)$$

where Y'_{ENA} is the predicted ground-motion parameter value (PGA, PGV, and PSA) in ENA, and Y_{BSSA14} is the predicted amplitude of the BSSA14 reference GMPEs. This equation should not be used at distances greater than 400 km as it is unconstrained. If the GMPE is to be extended beyond 400 km, a maximum value of 400 km should be used in defining the adjustment factor. Moreover, if the proposed GMPE is to be extended beyond 20 Hz (up to 50 Hz), the same adjustment factors estimated at 20 Hz should be used.

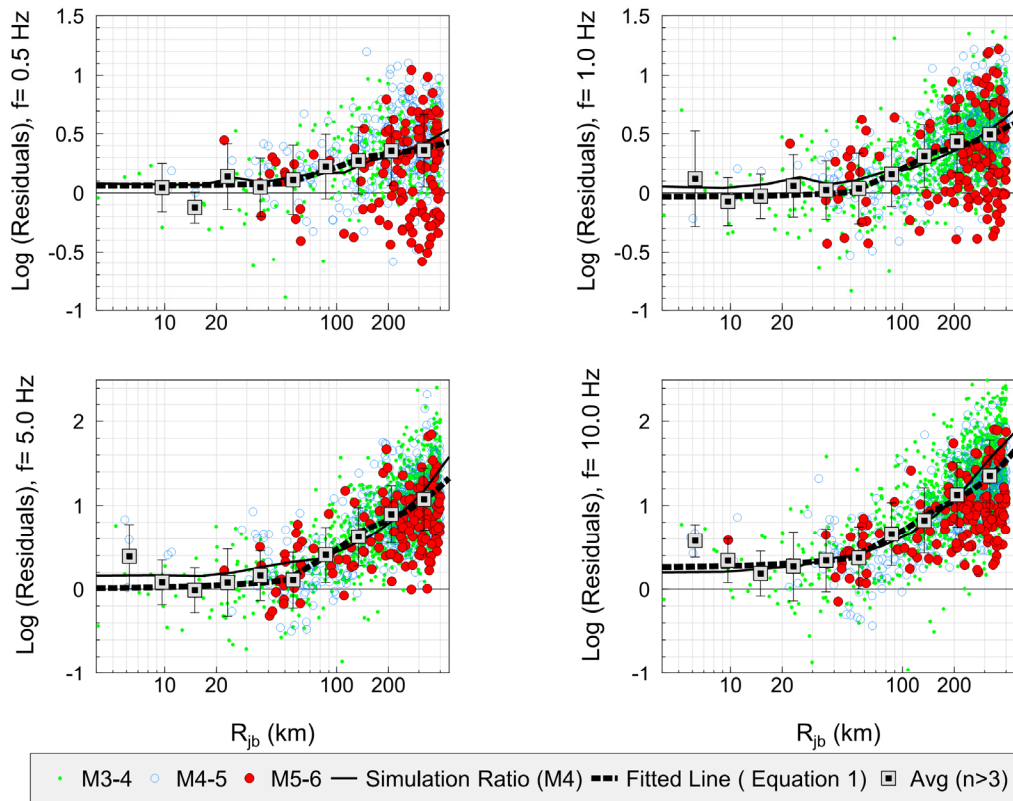


Figure 10.4 Residuals for the whole ENA database compared to BSSA14 reference GMPE in log10 units for PSA at 0.5, 1, 5, and 10 Hz frequencies. The residuals are coded by magnitude. Filled squares show mean residuals in equally log-spaced distance bins with their corresponding standard deviations, and dashed lines show the fit line to Equation (10.1). Solid lines shows the ratio obtained from proposed seismological models for ENA and WNA (predicted ground-motion parameter using ENA seismological model / predicted ground-motion parameter using WNA seismological model).

In Table 10.1, the quoted total standard deviation of the residuals is very large (0.29 to 0.40 log10 units). This is due to a variety of factors, including the combination of a wide range of regions and site classes, and the use of a wide range of magnitudes and distances, particularly including many data of $M < 4$. It has been shown that smaller-magnitude data have larger variability and that the use of larger distances increases variability (e.g., Boore et al. [2014b] and Campbell and Bozorgnia [2014]). By contrast, Atkinson [2013] obtained relatively low ground-motion variability when considering a more tightly constrained ENA database. To obtain more representative estimates of variability for the range of engineering interest, we computed the geomean residual for events of $M \geq 4$ recorded at distances < 70 km. The calculated variability parameters corresponding to the confined magnitude and distance ranges are smaller at some frequencies in comparison to the values obtained from the whole ENA dataset; however, the difference is not that significant. This may be because of the paucity of the data in the range of

engineering interest in the ENA database. Therefore, the same value of variability parameters is suggested for all of the magnitude and distance ranges.

Table 10.1 Values of adjustment factor coefficients and variability parameters (in log10 units) of Equations (10.1) and (10.2).

Frequency (Hz)	C_1	C_2	C_3	σ (ENA)	T	ϕ
PGV	0.166	0.0007	0.73	0.33	0.28	0.18
PGA	0.384	0.0017	0.63	0.41	0.30	0.27
0.10	0.065	0.0006	0.22	0.25	0.21	0.14
0.13	0.029	0.0006	0.27	0.28	0.21	0.19
0.16	0.010	0.0006	0.27	0.29	0.22	0.20
0.20	0.025	0.0006	0.22	0.29	0.22	0.18
0.25	0.052	0.0006	0.21	0.28	0.23	0.17
0.32	0.067	0.0005	0.27	0.28	0.23	0.16
0.40	0.061	0.0004	0.36	0.28	0.23	0.16
0.50	0.041	0.0004	0.44	0.28	0.24	0.15
0.63	0.020	0.0005	0.48	0.29	0.24	0.15
0.79	-0.009	0.0006	0.50	0.28	0.25	0.14
1.00	-0.043	0.0009	0.54	0.28	0.25	0.13
1.26	-0.067	0.0011	0.57	0.28	0.25	0.12
1.58	-0.077	0.0013	0.59	0.29	0.26	0.13
2.00	-0.068	0.0014	0.63	0.30	0.27	0.14
2.51	-0.053	0.0015	0.71	0.31	0.28	0.14
3.16	-0.036	0.0016	0.80	0.33	0.29	0.15
3.98	-0.016	0.0018	0.86	0.34	0.29	0.17
5.01	0.014	0.0020	0.89	0.35	0.30	0.18
6.31	0.074	0.0021	0.88	0.36	0.30	0.20
7.94	0.158	0.0022	0.81	0.38	0.30	0.22
10.00	0.264	0.0023	0.71	0.40	0.31	0.25
12.59	0.370	0.0024	0.61	0.42	0.32	0.28
15.85	0.439	0.0023	0.52	0.45	0.33	0.30
≥ 19.95	0.472	0.0022	0.44	0.47	0.36	0.32

As we discussed earlier, the referenced empirical approach is similar in concept to the hybrid empirical method of Campbell [2003]. Therefore, if we calculate the expected residual trends using calibrated simulation-based models in both regions, we expect to predict similar trends to those that we observed empirically. To test whether this is so, we used an equivalent point-source (PS) stochastic model that has recently been calibrated for applications in both western North America (WNA) and ENA [Atkinson et al. 2014]. The model uses the equivalent PS approach of Yenier and Atkinson [2014], with a bilinear attenuation model in both regions, characterized by geometric spreading of $R^{-1.3}$ at $R \leq 50$ km (where R is a generic distance measure, typically hypocentral distance), with $R^{-0.5}$ beyond, with typical regional Q models. The average stress drop is a factor of two higher in ENA in comparison to WNA. For both regions we neglected the effects of crustal and site amplification, as we are calculating only the ratio between two models; therefore, these factors approximately cancel each other under the assumption that they are similar. Simulations are generated over a range of magnitudes and distances using the SMSIM algorithm of Boore [2003] in the time domain, with the simulation parameters as given in Table 10.2. The predicted residual trends based on the hybrid empirical approach are determined from the log of the ratio of the simulated motions in ENA to the corresponding simulated motions in WNA.

Table 10.2 Seismological parameters used in the WNA and ENA stochastic models for a reference rock site [Atkinson et al. 2014].

Parameter	Western North America	Eastern North America
Source spectrum	Brune ω -square, point source [Brune 1970; 1971]	Brune ω -square, point source [Brune 1970; 1971]
Stress drop, $\Delta\sigma$ (bar)	300	600
Geometric attenuation	$R^{-1.3}$; $R < 50$	$R^{-1.3}$; $R < 50$
	$R^{-0.5}$; $R \geq 50$	$R^{-0.5}$; $R \geq 50$
Source duration, T_s (sec)	$1/f_0$	$1/f_0$
Path duration, T_p (sec)	$0.05R$	$0.05R$
Path attenuation, Q	$170f^{0.45}$ (minimum $Q = 100$)	$525f^{0.45}$
Shear velocity, β_s (km/sec)	3.7	3.7
Density, ρ_s (g/cc)	2.8	2.8
Site attenuation, κ_0 (sec)	0.02	0.02
Site amplification	no crustal or site amplifications are applied	no crustal or site amplifications are applied

In Figure 10.4, we compare the referenced empirical residuals to those predicted by the hybrid empirical approach for the ENA versus WNA simulation models for $\mathbf{M} = 4$, assuming (a) a focal depth of 10 km in both regions and (b) $R_{epi} = R_{JB}$. The trend lines obtained from the referenced empirical approach follow the predictions of the hybrid empirical method well overall (within 0.1 log units). Some differences are seen at near-source distances ($R \leq 50$ km) for low to moderate frequencies ($f \leq 5$ Hz), for which the hybrid-empirical approach would suggest relatively higher ground-motion amplitudes than would the referenced empirical method. However, it should be noted that the ENA database is sparse at close distances, hindering robust conclusions regarding ground-motion amplitudes at near-source distances. Moreover, we have not included consideration of any regional difference in the ‘calibration constant’ required to center the model predictions for the dataset (see Atkinson et al. [2014]). The offset between the referenced empirical and hybrid empirical lines on Figure 10.4 could be interpreted as an estimate of the difference in this calibration constant between the east and the west (i.e., about 0.1 log units).

Figure 10.5 shows the within-event residuals at four sample frequencies obtained from Equation (10.1). The residuals do not show any apparent distance or magnitude dependency, and the overall behavior of the residuals at all frequencies is satisfactory. This demonstrates that the model works well in matching the observed ENA ground-motion data.

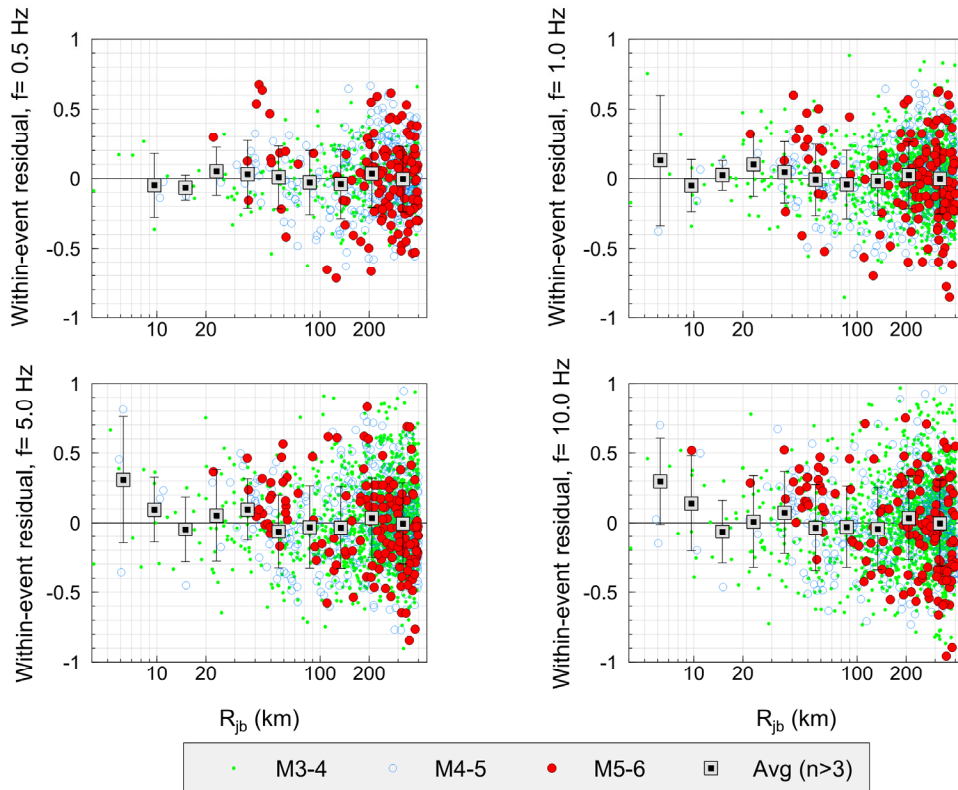


Figure 10.5 Within-event residuals ϵ for the whole ENA database for PSA at 0.5, 1, 5, and 10 Hz. The residuals are coded by magnitude. Filled squares show mean residuals in equally log-spaced distance bins with their corresponding standard deviations.

It is interesting to investigate the behavior of the within-event residuals in terms of the site conditions, to see how successfully the site correction factors of BSSA14, which are implicitly included in the GMPE, have removed the overall site effects. Figure 10.6 shows the within-event residuals as a function of V_{S30} for PSA at four sample frequencies. The general behavior of the residuals at all frequencies is acceptable. However, we note a small tendency to lower average residuals (overprediction of ENA amplitudes by ~ 0.1 log units) at softer sites (D and E sites) at lower frequencies. This may be because the western GMPEs that form the reference level are influenced to a greater extent at longer periods by deep sedimentary section effects, including basin effects. Moreover, it should be noted that the proposed site amplification model of BSSA14 was obtained based on sites in active tectonic regions, although there might be regional site response variations within these regions as discussed in Boore et al. [2014b]. However, there is little available information regarding expected differences in site response between ENA and the active regions considered in NGA-West2; inspection of the residuals shows no apparent trend corresponding to V_{S30} that we might attribute to such factors.

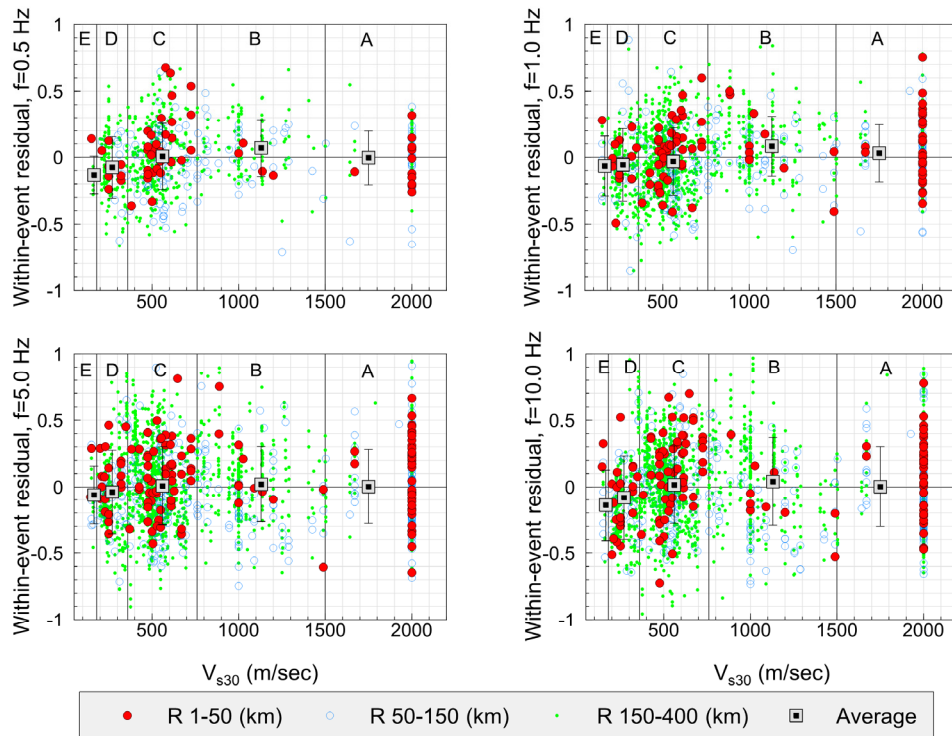


Figure 10.6 Within-event residuals ε for ENA as a function of V_{S30} of the stations. The residuals are coded by distance. Filled squares show mean residuals in NEHERP site classes with their corresponding standard deviations.

In Figure 10.7, the between-event residuals η are plotted as function of magnitude. The within-event residuals do not show any apparent magnitude dependency, and the overall behavior of the residuals at all frequencies is satisfactory. However, there is a tendency to lower average residuals (over prediction of amplitudes by ~ 0.2 log units) for $M > 5$. This is attributable mainly to the events that are located in Central region, near the boundaries of the Gulf coast region (Figures 10.1 and 10.2), where the stations are not symmetrically distributed around the events. Moreover, the database for $M > 5$ is too sparse to define any magnitude trends in a robust

way. Therefore, we assumed no magnitude dependence for the residuals in the proposed GMPE model. We note that we might expect a stress-drop effect on the adjustment factors, which could be significant for larger events at some frequencies, due to regional differences in stress drop between ENA and WNA. The difference in corner frequency between ENA and WNA (for the same magnitude) should theoretically result in regional variability in magnitude scaling between the corner frequencies. One could calculate the expected effect using the available simulation-based model in ENA and WNA, which is essentially what the hybrid-empirical model [Campbell 2003] does. However, we did not observe any noticeable magnitude trends based on the available data, and thus, under the referenced-empirical philosophy, we did not include any such effect. This unmodeled effect is a source of epistemic uncertainty in the referenced-empirical GMPE, the importance of which can be assessed by comparison of its predictions to those of hybrid-empirical model predictions.

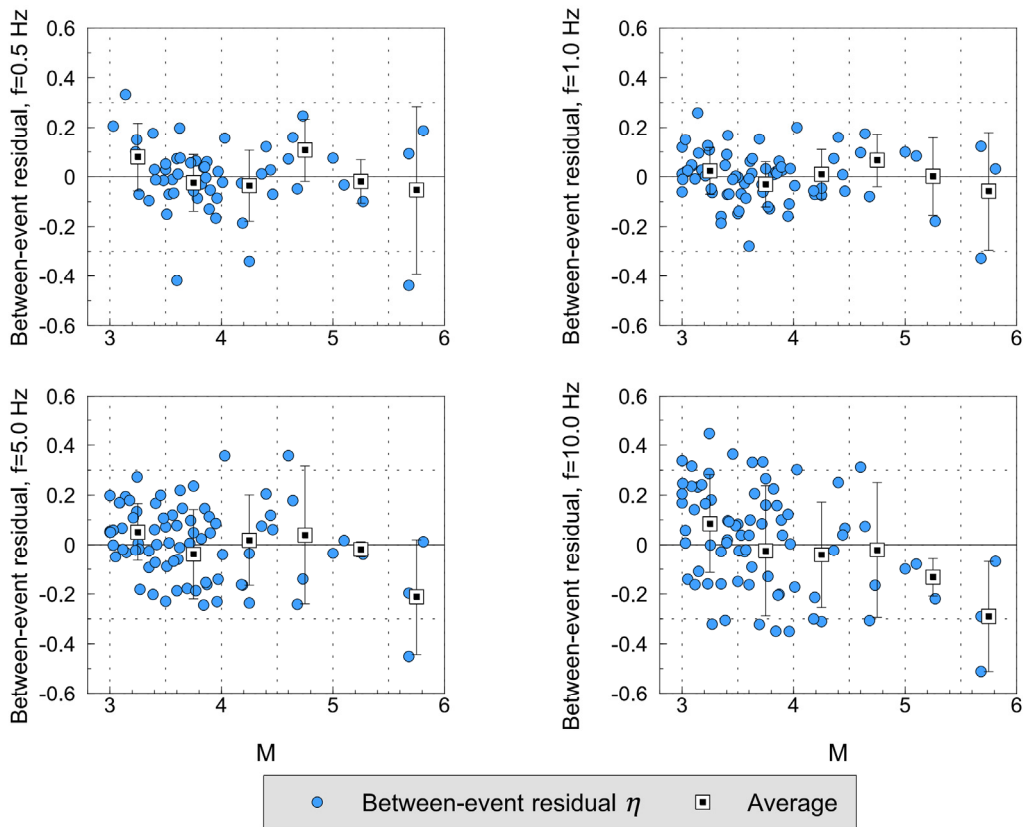


Figure 10.7 Between-event residuals η for ENA events as a function of magnitude. Filled squares show mean residuals in 0.5 magnitude bins with their corresponding standard deviations.

In Figures 10.8 and 10.9, we display the performance of the proposed referenced empirical GMPEs (HA14) against the observed ENA data. The observed data are all adjusted to equivalent amplitudes for B/C site condition ($V_{S30} = 760$ m/sec) using the site amplification model of BSSA14. We plot the GMPEs as a function of distance for **M4** and **M5** for an unspecified source mechanism and B/C site condition. GMPEs are plotted for the proposed referenced empirical model for ENA, the BSSA14 reference model, the stochastic simulation-

based GMPE of Atkinson and Boore [2011, denoted AB06'], and the former ENA referenced empirical model of Atkinson and Boore [2011, denoted AB08']. The proposed referenced empirical GMPE model for ENA matches the observed regional data at all distances, as we would expect from its definition. It is interesting and important to note that at close distances ($R \leq 50$ km), for $f \leq 5$ Hz, the referenced empirical model predicts the same level of ground-motion amplitudes as does the BSSA14 model, implying that differences between ENA and WNA motions are only important at high frequencies (all distances) and at regional distances (all frequencies). These trends are presumably due to the lower attenuation rate of ENA motions at regional distances and to the effects of higher stress drop in ENA (e.g., Atkinson and Boore [2014]). Comparison between the HA14 model and the referenced empirical model of A08' shows that at $R \leq 50$ km the A08' model predicts higher ground-motion amplitudes at all frequencies, which is more obvious for M4. This is likely because the previous generation of the NGA models were not originally developed for small magnitude events and do not model their amplitudes as well as the newer models. Comparing the referenced empirical model of this study with the simulation-based model of AB06' reveals that both models are similar in shape, although they predict different amplitudes—especially at close distances ($R \leq 50$ km)—where there are not enough data to constrain the prediction models.

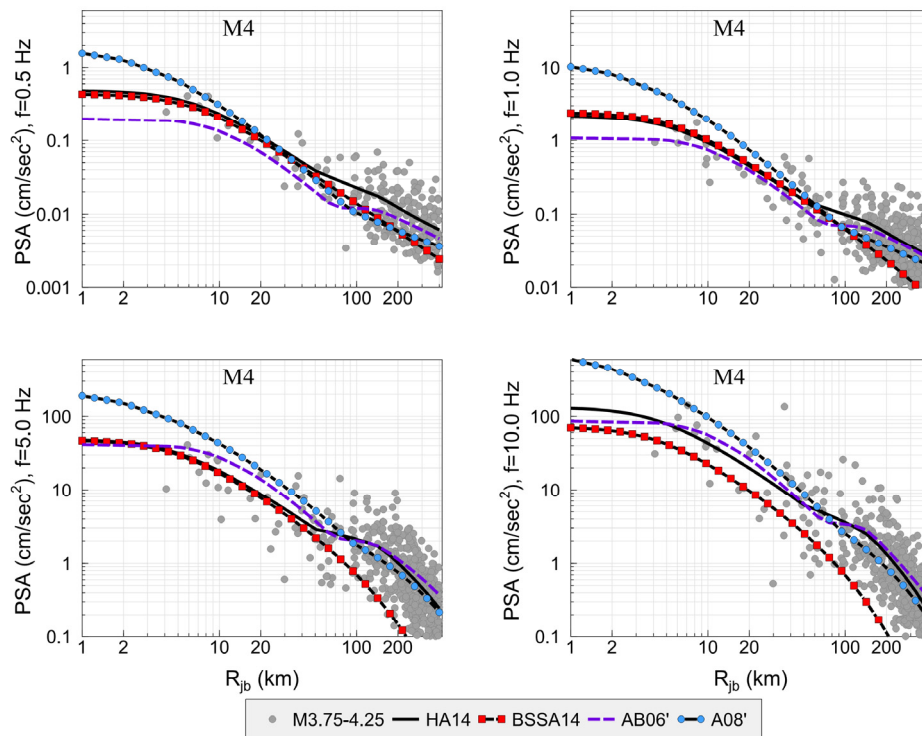


Figure 10.8 Proposed ENA referenced empirical GMPEs (HA14) for M4 assuming an unspecified focal mechanism and B/C site condition, compared to the observed data in ENA corrected for B/C site condition. Reference GMPEs of BSSA14, simulation-based GMPEs of AB06', and former referenced empirical GMPE of A08' are also shown for M4.

In Figure 10.10, we compare the proposed referenced empirical GMPE of this study with the BSSA14 reference model, the AB06' simulation-based GMPE, and the former referenced empirical GMPE of A08' for a large-magnitude event (**M7**, unspecified source mechanism, and B/C site condition) at four sample frequencies. As Equation (10.1) implies, there is no magnitude dependency for the adjustment factors. Therefore, the comparison between HA14 and BSSA14 models reveals the same features as discussed in Figures 10.8 and 10.9. Comparison of the HA14 and the A08' models shows that although both of the models predict similar ground-motion amplitudes at $R \leq 50$ km and $f > 5$ Hz, the HA14 model predicts higher ground-motion amplitudes at $f \leq 5$ Hz and $R < 50$ km. Comparison of the HA14 and the AB06' models shows that the HA14 model predicts smaller ground-motion amplitudes especially at $R \leq 20$ km. This suggests that near-distance saturation effects are stronger in the BSSA14 empirical equations than in the stochastic simulations employed by AB06'. However, at $f \geq 5$ Hz and $R > 50$ km, the referenced empirical model suggests higher ground-motion amplitudes in comparison to the AB06' model. This difference is a factor of two at $R > 200$ km, which in some cases could have significant implications for seismic hazard evaluations. As there are no direct ground-motion observations to justify this difference, it should be considered a source of epistemic uncertainty in seismic hazard applications.

In Figure 10.11, the predicted response spectra of a **M5** and a **M7** event at $R_{JB} = 10$ km and $R_{JB} = 100$ km (unspecified source mechanism, and B/C site condition) are plotted for the proposed referenced empirical GMPE of this study, to illustrate the overall frequency behavior of the model. Response-spectra of BSSA14, AB06', and A08' are also plotted for the same magnitudes and distances. The differences between the HA14 and BSSA14 response spectra were discussed above, based on the adjustment factors obtained in Equation (10.1). Comparison between the HA14 and AB06' and A08' response spectra shows that all of them present similar ground-motion amplitudes at $R_{JB} = 10$ for **M5** and **M7**. However, HA14 predicts higher ground-motion amplitudes at $R_{JB} = 100$ km, reflecting trends seen in regional seismographic data.

We also provide ground-motion predictions for very hard rock site condition ($V_{S30} = 3000$ m/sec). Atkinson [2012b] derived site factors that allow amplitude conversion between sites with $V_{S30} = 760$ m/sec and $V_{S30} \geq 2000$ m/sec, using the predictions of Atkinson and Boore [2006]. The site factors are given independent of distance, except for very high frequencies and PGA (Table 10.3). For $f \geq 40$ Hz, the site factor is given as a function of R_{epi} . We convert ground-motion predictions for $V_{S30} = 760$ m/sec to the equivalent motions for ($V_{S30} = 3000$ m/sec) based on the site factors of Atkinson [2012b]. Here, we assume that the amplitude difference between sites with $V_{S30} \geq 2000$ m/sec and ($V_{S30} = 3000$ m/sec) is small enough to neglect. We use R_{JB} - R_{epi} distance conversion method described in Atkinson [2012b] to evaluate site factors for $f \geq 40$ Hz and PGA. To switch from $V_{S30} = 760$ m/sec to ($V_{S30} = 3000$ m/sec) site condition, the values provided in Table 10.3 should be subtracted from predicted ground-motion parameters (log10 base) for $V_{S30} = 760$ m/sec.

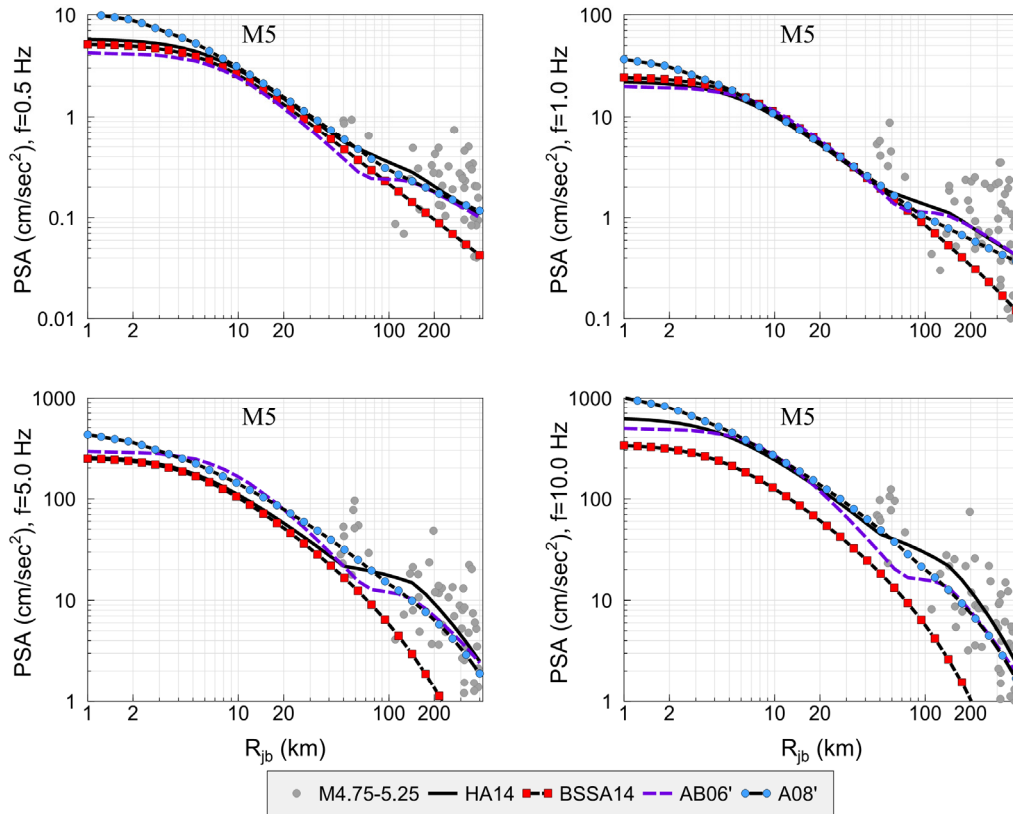


Figure 10.9 Proposed ENA referenced empirical GMPEs (HA14) for M5 assuming an unspecified focal mechanism and B/C site condition, compared to the observed data in ENA corrected for B/C site condition. Reference GMPEs of BSSA14, simulation-based GMPEs of AB06', and former referenced empirical GMPE of A08' are also shown for M5.

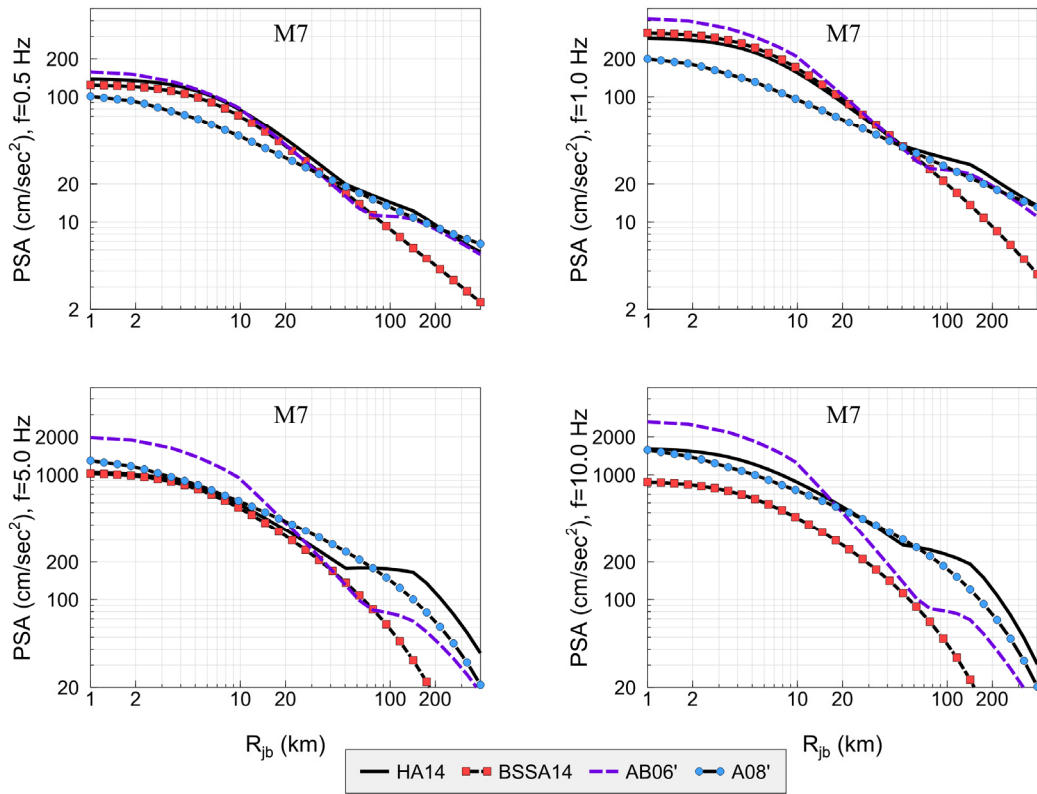


Figure 10.10 Proposed ENA referenced empirical GMPEs (HA14) for **M7** assuming an unspecified focal mechanism and B/C site condition compared to the Reference GMPEs of BSSA14, the simulation-based GMPEs of AB06', and the former referenced empirical GMPE of A08' for the same magnitude.

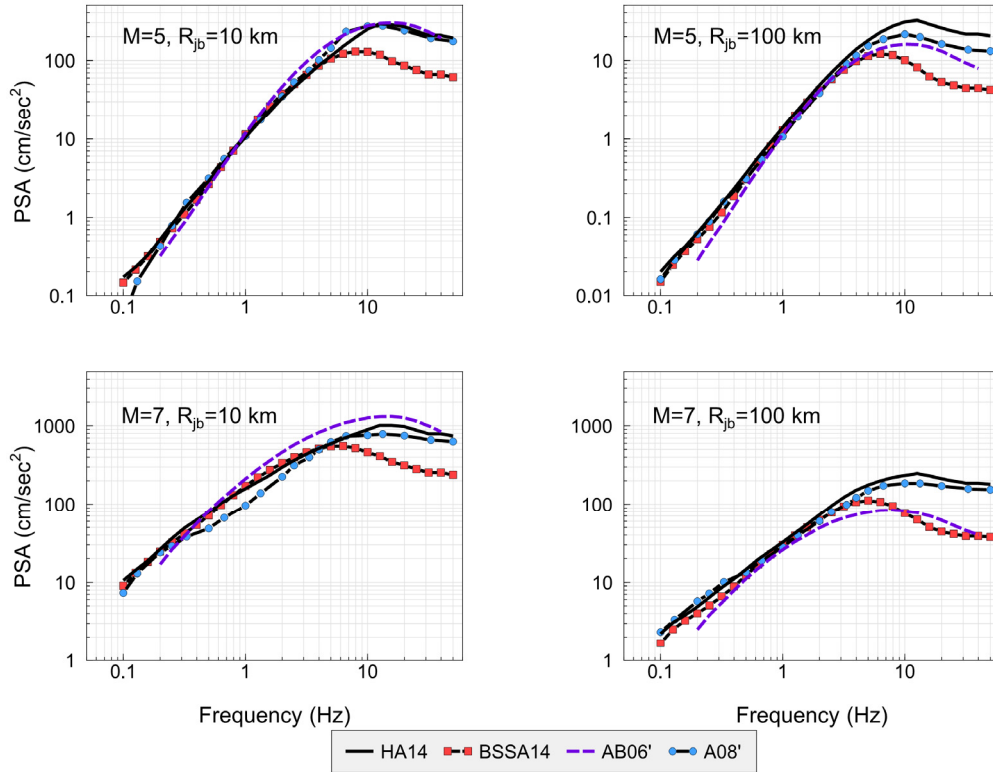


Figure 10.11 Response spectra of M_5 and M_7 at $R_{JB} = 10$ km and $R_{JB} = 100$ km for the proposed ENA referenced empirical GMPEs (HA14) for unspecified focal mechanism and B/C site condition compared to the Reference GMPEs of BSSA14, the simulation-based GMPEs of AB06', and the former referenced empirical GMPE of A08' for the same magnitude.

To extend the proposed GMPE model for higher frequencies (> 20 Hz) where number of reliable data reduces significantly, it is not rational to use the empirical data to develop adjustment factor. Therefore, we investigated the residual trends obtained from simulation-based models of Atkinson et al. [2014] (predicted ground-motion parameter using ENA seismological model/predicted ground-motion parameter using WNA seismological model) at higher frequencies for a sample event with $M = 4$, as shown in Figure 10.12. Here, we plotted the residual trends at five different frequencies, namely 20 Hz, 25 Hz, 30 Hz, 40 Hz, and 50 Hz. As we observe here, estimated residual trend at 20 Hz is a good approximation for higher frequencies (≥ 20 Hz), even though it may slightly overestimate the predicted ground-motion parameters at very high frequencies. Therefore, for $f \geq 20$ Hz, we suggest to use the adjustment factors obtained at 20 Hz.

Table 10.5 Site conversion factors from Atkinson [2012b].

f (Hz)	$\log[Y_{ENA}(V_{S30} - 760 \text{ m/sec})] - \log[Y_{ENA}(V_{S30} - 3000 \text{ m/sec})]$
PGV	0.09
PGA	$-0.3 + 0.15\log(R_{epi})$
≤ 0.2	0.06
0.5	0.09
1.0	0.11
2.0	0.14
3.0	0.14
5.0	0.12
10.0	0.03
20.0	-0.1
≥ 40	$-0.3 + 0.15\log(R_{epi})$

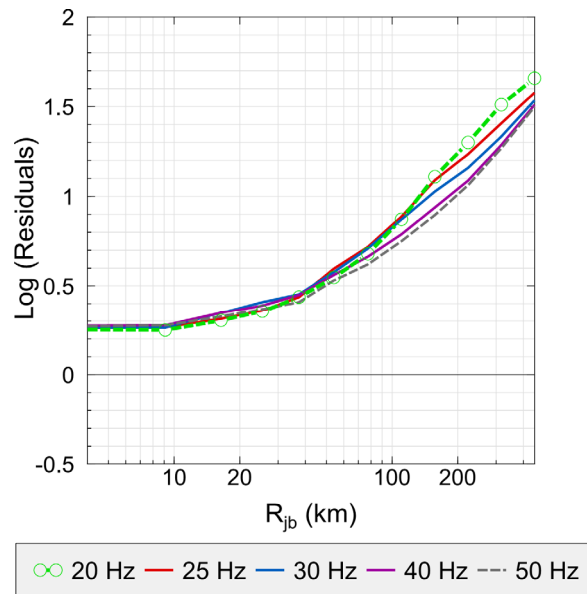


Figure 10.12 Residual trends obtained from proposed seismological models for ENA and WNA (predicted ground-motion parameter using ENA seismological model/prediction ground-motion parameter using WNA seismological model) at 20 Hz, 25 Hz, 30 Hz, 40 Hz, and 50 Hz.

10.4 CONCLUSIONS

The proposed referenced empirical GMPEs for ENA are in agreement with regional ground-motion data to a distance of 400 km, while being constrained to follow the overall scaling behavior of ground motion observed for larger events in active tectonic regions. The referenced empirical model of this study suggests that ground-motion amplitudes in ENA are similar to those predicted by the BSSA14 reference equations at distances smaller than 50 km at frequencies ≤ 5 Hz. At higher frequencies and larger distances, ENA ground-motion amplitudes are significantly higher than predicted by the BSSA14 model, reflecting higher stress drop and lesser attenuation in ENA relative to active tectonic regions.

10.5 DATA AND RESOURCES

Corrected ground-motion parameters (PGA, PGV, and PSA) for events in the central U.S. were obtained from the NGA-East database as provided by the NGA-East project [www.peer.berkeley.edu, last accessed Oct. 2014] which provides RotD50 response spectrum of horizontal ground motions; we used a pre-publication version of the database made available to project participants by C. Goulet [*Personal Communication* 2014]. Many of the event data for the East region were obtained from the Engineering Seismology Toolbox website which provides 3-component processed ground-motion parameters (www.seismotoolbox.ca, last accessed December [2013]). For recent unprocessed data from Canadian stations, horizontal velocity waveforms were obtained from the Automatic Data Request Manager Facility (AutoDRM of the Geological Survey of Canada (autodrm@seismo.nrcan.gc.ca, last contacted December [2013])). For unprocessed data of U.S. stations, including data from the U.S Transportable Array (TA) stations in southern Ontario, horizontal velocity waveforms were obtained from the IRIS AutoDRM (breq_fast@iris.washington.edu, last contacted December [2013]). Moment magnitude information was extracted from the same resources as the ground-motion database if available, and obtained from the following references if needed: (1) Global Centroid Moment Tensor project (www.globalcmt.org; last accessed December [2013]); (2) USGS earthquake catalogue (www.earthquake.usgs.gov; last accessed December [2013]), (3) regional moment Tensor solution by R. B. Herrmann (<http://www.eas.slu.edu/eqc/eqcmt.html>; last accessed December [2013]). Ground-motion simulations were performed using the SMSIM v3.8 software that is available at http://www.daveboore.com/software_online.html (last accessed November [2014]). We used MATLAB (www.mathworks.com, last accessed November [2014]) for regression of the ground-motion amplitudes and CoPlot (www.cohort.com, last accessed November [2014]) for making the figures.

10.6 ACKNOWLEDGMENTS

This study was supported by the Natural Sciences and Engineering Research Council of Canada, by the NGA-East project, and by the USGS NEHRP program under Grant G13AP00067. Any opinions, findings, and conclusions or recommendations expressed in this material are those of the authors and do not necessarily reflect those of the sponsoring agencies.

10.7 ELECTRONIC APPENDIX FOR CHAPTER 10

10A Model Output (Excel workbook)

11 PEER NGA-East Median Ground-Motion Models

Justin Hollenback, Nicolas Kuehn, Christine A. Goulet

**Pacific Earthquake Engineering Research Center
University of California, Berkeley**

Norman A. Abrahamson

**Pacific Gas and Electric Company
San Francisco, California**

Abstract

This chapter summarizes the development of a pair of ground-motion models (GMMs) for the NGA-East Project. The GMMs provide estimates of RotD_{50} 5%-damped pseudo-spectral acceleration (PSA) as well as peak ground acceleration (PGA) and velocity (PGV) from events in the magnitude (M) range of 4 to 8.2 within a distance of 1200 km. The models described here are applicable to the large Central Eastern North America (CENA) region that excludes the Gulf Coast. The GMMs are associated with a reference site condition of an average shear-wave velocity of 3000 m/sec in the upper 30 m of geomaterials (V_{s30}) with a corresponding kappa (κ) value of 0.006 sec. To overcome the problem of sparse recorded data available in CENA [Goulet et al. 2014], we are supplementing empirical data with seismological constraints. This is performed in Fourier amplitude spectral (FAS) space, which does not suffer from nonlinear complexities present in the PSA space, and builds on the work of Bora et al [2014]. Random vibration theory (RVT) is used, along with a calibrated RVT-duration model, to develop the final PSA, PGA, and PGV models from the FAS. The difference between the two GMMs developed in this chapter is the finite-fault simulation method used to constrain the magnitude scaling beyond $M5.5$, employing EXSIM [Atkinson and Assatourians 2015] for one GMM and Graves and Pitarka [2015] for the second model.

11.1 INTRODUCTION

11.1.1 Approach and Motivation

Two GMMs developed by a PEER team are presented in this chapter. The GMMs provide estimates of the following ground-motion intensity measures (GMIMs): 5%-damped pseudo-spectral acceleration (PSA) values for a wide range of frequencies, peak ground acceleration (PGA) and peak ground velocity (PGV) all for RotD50 horizontal components [Boore 2010]. The GMMs are applicable to sites in CENA (excluding the Gulf Coast) for a reference site condition with $V_{S30} = 3000$ m/sec associated with a kappa (κ) value of 0.006 sec. The GMMs development follows a fundamentally different approach when compared to the traditional empirical, simulations-based or hybrid empirical model developments and builds largely on the work of Bora et al. [2014]. First, a model is developed in acceleration Fourier Amplitude Spectral (FAS) space; then random vibration theory (RVT) is used to obtain the final PSA, PGA and PGV quantities. The approach consists of the following general steps

- Perform an empirical regression on FAS of acceleration in ranges for which the recorded data is reliable,
- Extend the empirical model (in terms of magnitude, distance and frequency coverage) using a combination of point-source (PS) stochastic model and FF simulations,
- Develop an empirically-calibrated RVT-duration (D_{RVT}) model, and
- Compute GMIMs for a wide range of magnitude and distances using RVT.

The motivation for this FAS-based approach came from known limitations of recorded data coverage in CENA [Goulet et al. 2014]. The most important data limitations are (1) lack of records from events with $M > 6$, and (2) lack of reliable amplitude data below 0.6 Hz and above 10.0 Hz. Developing the models on the FAS allows for an easier integration of seismological constraints for the extrapolation beyond the limits of the data (as well as direct κ adjustments).

The empirical regression is performed to constrain the spectral shape from 0.6 to 10 Hz. Since the NGA-East database is limited to records from $M < 6$ (with the exception of a handful of records from the 1985 Nahanni earthquake, $M6.76$), the M scaling is adopted from finite-fault (FF) simulations [Section 1.34 and Appendix 1B]. Frequencies beyond 10 Hz are populated using the point-source (PS) model for which the parameters were determined from inversions. The complete FAS spectra, which cover the frequency range from 0.01 Hz to 400 Hz, are used in conjunction with RVT and a calibrated RVT-duration model to compute the final PSA, PGA and PGV models.

11.1.2 Effective Amplitude Spectrum: Orientation-Independent Average Fourier Amplitude Spectrum

The GMMs are to predict RotD50 GMIM values, which are independent of the orientation of the recording instrument at a given station. Thus, the FAS metric used in modeling should also be independent of the orientation of the recording instrument. We use the effective amplitude spectrum (EAS), as defined in Kottke et al. [2015] as:

$$\text{EAS}(f) = \sqrt{\frac{1}{2} [\text{FAS}_{HC1}(f)^2 + \text{FAS}_{HC2}(f)^2]} \quad (11.1)$$

where FAS_{HC1} and FAS_{HC2} are the FAS of the first and second as-recorded horizontal components of a three-component acceleration time series. By definition, this metric is independent of the orientation of the instrument.

11.2 DEVELOPMENT OF EMPIRICAL EAS MODEL

The empirical EAS model is derived from recorded ground motions in the 0.6–10 Hz range. This range was defined based on the CENA empirical data limitations. Below 0.6 Hz, the data have issues with processing-induced truncation (for a given \mathbf{M} and distance, very low ground motions are excluded due to poor signal-to-noise ratio and only relatively large ground motions remain, leading to a bias). A large majority of records in the NGA-East database are from the Transportable Array (TA), which has a sampling rate of 40 samples per second. The TA effectively has an upper usable limit of around 16 Hz, a limit that is further reduced for a wide range of magnitude, distance, and site condition combinations. Remaining records above 10 Hz are dominated by sites located on hard rock ($V_{S30} > 1200$ m/sec), which are primarily in northeastern U.S. and southeastern Canada. Most of the high-frequency data is, thus correlated with a specific region and hard rock conditions. If the results of our empirical regression were to show differences in scaling with respect to predictive parameters for the high-frequency bandwidth, it would be impossible to discern whether these differences are applicable to the entire CENA region or if they are a result of the regional correlation in the available data.

11.2.1 Selected Data and Regional Constraints

Selected CENA Data

The main dataset used for the GMM development is the NGA-East database [Goulet et al. 2014]. We chose to limit the events to only those with $\mathbf{M} > 2.5$ and records to closer than 300 km rupture distance (R_{RUP}), with at least one recording per event within 200 km. Records from smaller events and/or from larger distances tend to have poor signal-to-noise ratios and data truncation issues (Only events with large event terms for these \mathbf{M} and R_{RUP} can exceed the noise threshold level, effectively biasing the ground-motions distribution.). We required events to have at least one record within 200 km to prevent the event term from being biased by a regional difference in distance attenuation. This difference would potentially appear as an event-specific effect if there were not enough data recorded at moderate to close distance to recognize the difference in slope that appears at larger distances. We have included events flagged as “potentially-induced events” (PIE) in the selected dataset. The model is developed for path region 2 (Central North America, CNA, as defined in Section 1.3.1.2). Data from other CENA regions were also used to better constrain the regionally varying parameters.

Additional Data from the NGA-West2 Database

The data in the NGA-East database only include one event with M larger than 6 (Nahanni 1985, $M6.76$), preventing the development of a purely empirical model up to $M8.2$. A subset of the NGA-West2 database [Ancheta et al. 2014] was included in the analysis, covering a broad range of M and R_{RUP} ; this helps constrain both the empirical EAS model and the calibrated RVT-duration model (Section 11.4).

The subset of data from the NGA-West2 database was divided into sub-regions based on the geographic location of the data (numbering was continued from the NGA-East path-region numbers, Section 1.3.1.2). The grouping is as follows: Region 7 includes California and Nevada, Region 8 includes other locations in the western U.S (WUS), Region 9 includes Taiwan, Region 10 includes Italy, Region 11 includes the Middle East, Region 12 includes China, and Region 13 includes Japan. Using a broader dataset allows better constraints in the regression and helps reduce the effect of correlations present in the target region dataset (path region 2, CNA).

11.2.2 Regression Approach

We fit the EAS data frequency-by-frequency. Therefore, there is no assumption about spectral shape for our model. However, this also assumes the amplitudes are independent across frequency. This correlation is easily recoverable after the regression is performed (as is done for conventional PSA-based models).

We used a Bayesian regression scheme to estimate the coefficients of the empirical EAS model. This technique was implemented using the STAN modeling language [Stan Development Team 2014]. This method allowed us to build a hierarchical model designed to recognize any differences in data across regions; however, we will only be presenting results for the model for CNA in this chapter. Other advantages of performing the regression using this method are:

- The full joint posterior distribution of model coefficients is obtained
- Random effects can be added to the model at multiple levels and/or as cross or nested effects
- Constraints on coefficients can be easily enforced
- Subjective information can be imposed on the model through implementation of informative prior distributions

The disadvantage of the approach is that it is computationally intensive when implemented in the STAN modeling language relative to more traditional regression algorithms. The regression was performed for three random-effects simultaneously: grouping by event, region, and site.

11.2.3 Empirical EAS Model

As mentioned above, subsets of data from the NGA-West2 database [Ancheta et al. 2014] were included in the regression of the EAS. This was necessary because of the lack of data for large earthquakes in the NGA-East database. There should be differences in the ground motions between these two datasets. Furthermore, we expect there to be difference in ground motion

between the six path regions defined in Section 1.3.1.2. However, we assumed that the magnitude scaling is the same between the two datasets and across the different path regions sampled by the combined datasets. The portion of the model that is empirically defined will only be used for magnitudes below 5, and the large magnitude data from the NGA-West2 database is needed to help constrain the shape of the magnitude scaling. Without this large-magnitude data, the shape of the magnitude scaling—defined empirically—did not transition smoothly to the magnitude scaling defined by the FF simulations. Regionally-grouped random effects were added to the model to account for the expected differences in ground motion while “borrowing strength” from the large magnitudes in the NGA-West2 dataset. To allow for better estimation of regionally grouped random effects, we grouped the NGA-West2 data by the sub-regions defined in Section 11.2.1.

Our regression model has the following base functional form:

$$\ln\left[Y\left(f, \mathbf{M}, H_{Dep}, R_{RUP}, V_{S30}\right)\right] = \left(c_1 + c_{1,R}\right) + F_1\left(\mathbf{M}, Z_{HYP}\right) + F_2\left(R_{RUP}, \mathbf{M}\right) + F_3\left(V_{S30}\right) + \eta_e + \eta_s + \varepsilon \quad (11.2)$$

where $Y\left(f, \mathbf{M}, Z_{HYP}, R_{RUP}, V_{S30}\right)$ is the ground-motion distribution predicted EAS at frequency f , c_1 is the model constant, F_1 is the median source scaling model, F_2 is the median distance scaling model, F_3 is the median site scaling model, η_e is a random variable representing the between-event variability, η_s is a random variable representing the site-to-site variability, and ε is a random variable representing the single-station within-event variability. All three of these variables are normally distributed with zero means, and for which the variance of η_e is τ^2 , the variance of η_s is ϕ_{S2S}^2 , and the variance of ε is ϕ_{SS}^2 . The subscript R is used to identify regionally derived regression coefficients and to differentiate them from the global model coefficients. The absence of a regional coefficient reflects the assumption that no regional differences are modeled for the term.

The median source-scaling model, F_1 , is defined as:

$$F_1 = c_2 \mathbf{M} + c_3 \mathbf{M}^2 + c_9 \left(\frac{Z_{HYP}}{20}\right). \quad (11.3)$$

where Z_{HYP} is the hypocentral depth, in km. The median distance-scaling model, F_2 , is defined as follows, with two breaks at R_{RUP} of 50 km and 150 km, respectively:

For $R_{RUP} \leq 50$ km :

$$F_2 = \left\{ \left(c_4 + c_{4,R} \right) + c_5 \max\left[\left(\mathbf{M} - 5 \right), 0 \right] \right\} \ln\left(\sqrt{R_{RUP}^2 + c_6^2} \right) + \left(c_7 + c_{7,R} \right) \sqrt{R_{RUP}^2 + c_6^2} \quad (11.4)$$

For $50 \text{ km} < R_{RUP} \leq 150 \text{ km}$:

$$F_2 = C_{50} + \left\{ (c_{4h} + c_{4h,R}) + c_5 \max[(\mathbf{M} - 5), 0] \right\} \left[\ln\left(\sqrt{R_{RUP}^2 + c_6^2}\right) - \ln\left(\sqrt{50^2 + c_6^2}\right) \right] + (c_7 + c_{7,R}) \sqrt{R_{RUP}^2 + c_6^2} \quad (11.5)$$

and for $150 \text{ km} < R_{RUP}$:

$$F_2 = C_{50} + C_{150} + c_{4h2} \left[\ln\left(\sqrt{R_{RUP}^2 + c_6^2}\right) - \ln\left(\sqrt{150^2 + c_6^2}\right) \right] + (c_7 + c_{7,R}) \sqrt{R_{RUP}^2 + c_6^2} \quad (11.6)$$

The C_{50} and C_{150} terms in Equations (11.4)–(11.6) are defined as follows:

$$C_{50} = \left\{ (c_4 + c_{4,R}) + c_5 \max[(\mathbf{M} - 5), 0] \right\} \ln\left(\sqrt{50^2 + c_6^2}\right) \quad (11.7)$$

$$C_{150} = \left\{ (c_{4h} + c_{4h,R}) + c_5 \max[(\mathbf{M} - 5), 0] \right\} \left[\ln\left(\sqrt{150^2 + c_6^2}\right) - \ln\left(\sqrt{50^2 + c_6^2}\right) \right] \quad (11.8)$$

This F_2 formulation allows breaks in the geometrical spreading effects (terms associated with c_4 , c_{4h} , and c_{4h2}) at R_{RUP} of 50 km and 150 km, respectively. The distance region between 50 and 150 km was selected to capture the effect of waves reflected from the Moho discontinuity (a.k.a. the Moho-bounce phenomenon). Ground motions at distances larger than 150 km are controlled by a combination of geometrical spreading and anelastic attenuation of the crust. The median site scaling model, F_3 , is defined as:

$$F_3 = c_8 \ln(V_{S30}) \quad (11.9)$$

All the regression terms are a function of frequency. The terms c_1 , c_2 , c_3 , c_4 , c_{4h} , c_7 , c_8 , and c_9 are “global” model coefficients and the terms $c_{1,R}$, $c_{4,R}$, $c_{4h,R}$, and $c_{7,R}$ are region-specific model coefficients that are estimated from regression. The “global” model coefficients are applicable everywhere in CENA, while each of the region-specific coefficients are applicable to one of the six regions defined in Section 1.3.1.2. The terms c_{4h2} , c_5 , and c_6 were all fixed prior to running the Bayesian regression (constraints of these three terms are discussed in later sections) and were obtained from a simpler and faster regression code; they are frequency-independent. The four region-specific coefficients are additive to the global coefficients (see equations above) and correspond to a mean bias term ($c_{1,R}$), two geometrical spreading slopes ($c_{4,R}$, $c_{4h,R}$), and a large distance scaling term ($c_{7,R}$). For the purpose of this chapter, we only show regional results for path region 2 (CNA) in addition to the global effects.

Mean Bias and Model Variability

The combined effect of global and regional mean bias (c_1 and $c_{1,R}$ for path region 2) is plotted in Figure 11.1.

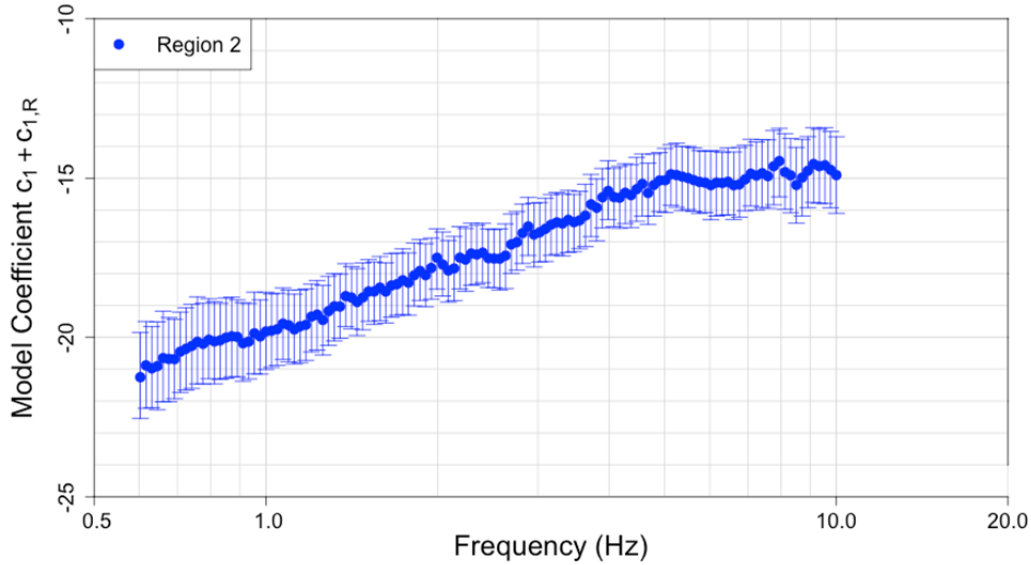


Figure 11.1 Model constant term for path region 2 (CNA), the combined effect of the global coefficient c_1 and path region 2 specific $c_{1,R}$ against frequency.

The partitioned variance terms are computed as part of the regression analysis. The between-event, site-to-site, and single-station within-event variance, τ^2 , ϕ_{S2S}^2 , and ϕ_{SS}^2 respectively, are different than their counterparts for PSA. The NGA-East Sigma Working Group will quantify the ground-motion variability for PSA separately. These terms are included in the model to convert the median EAS to the mean EAS (required for RVT computations of PSA, Section 11.4). These terms are also necessary for the regression to account for the uneven sampling of regions, events, and sites. This was achieved by adding three different random effects to the global constant term in the model, c_1 , during regression for path region, event, and site. The random effect grouped by path region is represented by coefficient $c_{1,R}$ in the base model. The random effects grouped by event and site are represented by the terms $c_{1,e}$ and $c_{1,s}$, respectively (which are realizations of the random variables η_e and η_s). The variances of these two terms along with the single-station within-event variance and the within-event variance are plotted in Figure 11.2. The terms $c_{1,e}$ and $c_{1,s}$ represent the average difference in ground motion for event e and site s , and are referred to as the event-term and site-term (or the between-event residual and the site-to-site residual). These are estimated during regression for every event and site. These terms are represented by the random variables η_e and η_s in Equation (11.2) since they cannot be known for a future event or for a site without any prior recordings.

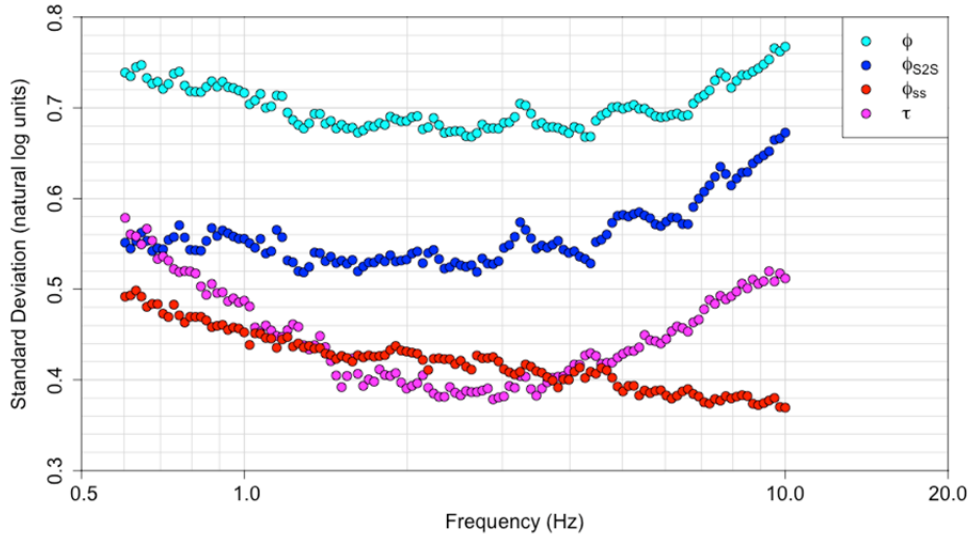


Figure 11.2 Standard deviations τ , ϕ_{S2S} , and ϕ_{SS} , for $c_{1,e}$, $c_{1,s}$, and ε respectively.

Source Scaling Model

The median source-scaling term, F_1 [Equation (11.3)], is a simple quadratic magnitude-scaling model with a linear depth term, where c_2 is the linear magnitude scaling term, c_3 is the quadratic magnitude scaling term, and c_9 is the depth scaling term. Figures 11.3–11.5 show plots of c_2 , c_3 , and c_9 against frequency, respectively. Figures 11.6–11.7 show plots of $c_{1,e}$ (between-event residuals) against \mathbf{M} and Z_{HYP} for a subset of frequencies. There are no biases or strong trends in the event terms with \mathbf{M} or Z_{HYP} . At large values of Z_{HYP} (> 20 km), $c_{1,e}$ shows a slight bias for 10 Hz. This implies that the depth scaling may need to be constrained to be constant for $Z_{HYP} > 20$ km.

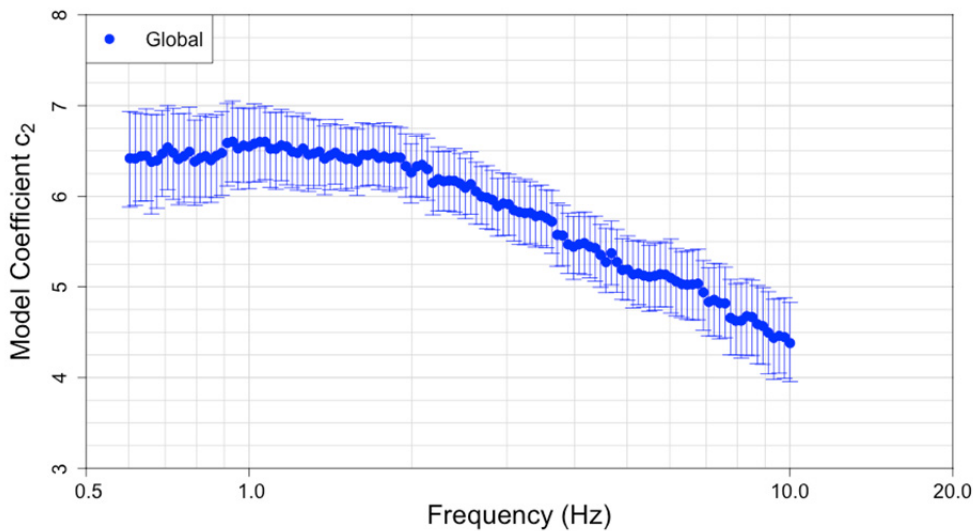


Figure 11.3 Global linear magnitude scaling term, c_2 , against frequency.

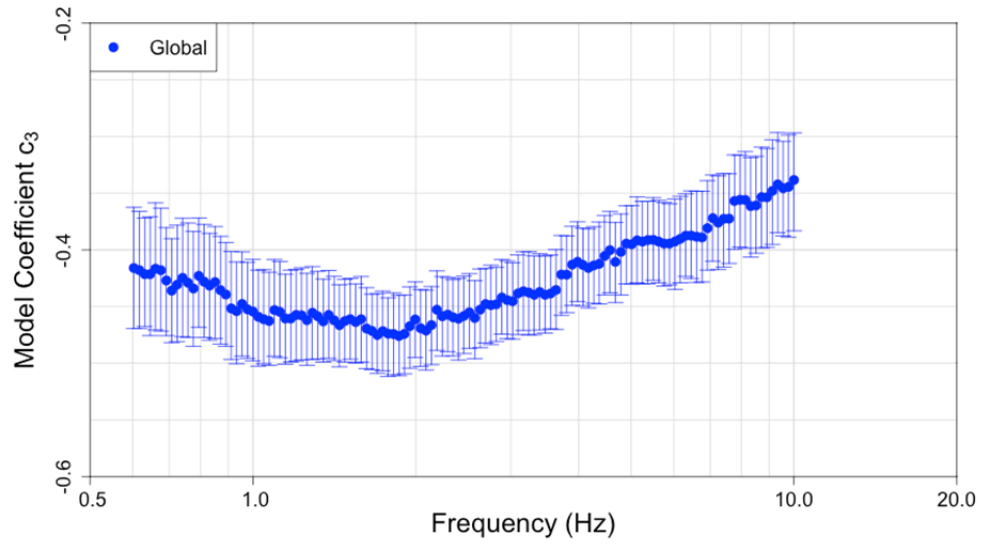


Figure 11.4 Global quadratic magnitude scaling term, c_3 , against frequency.

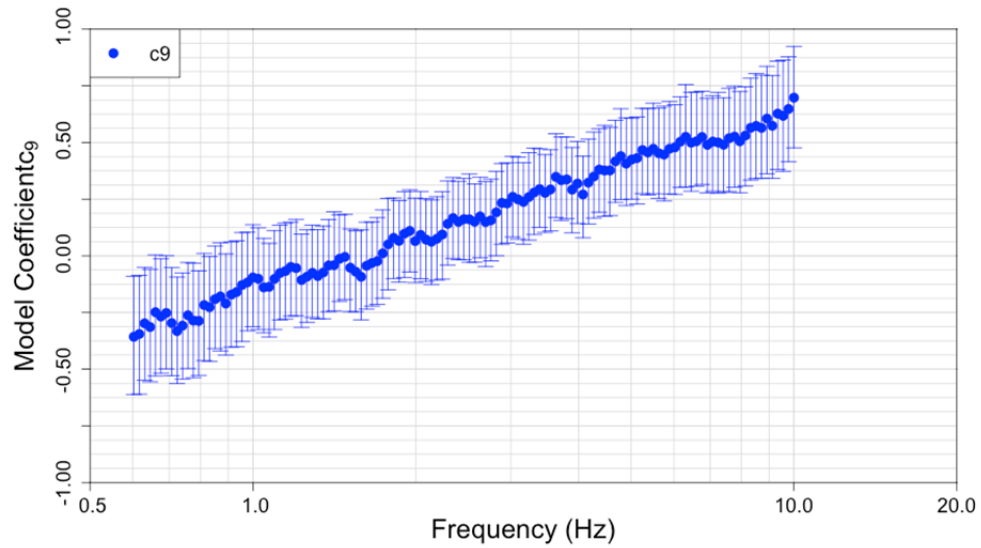


Figure 11.5 Global hypocentral depth scaling term, c_9 , against frequency.

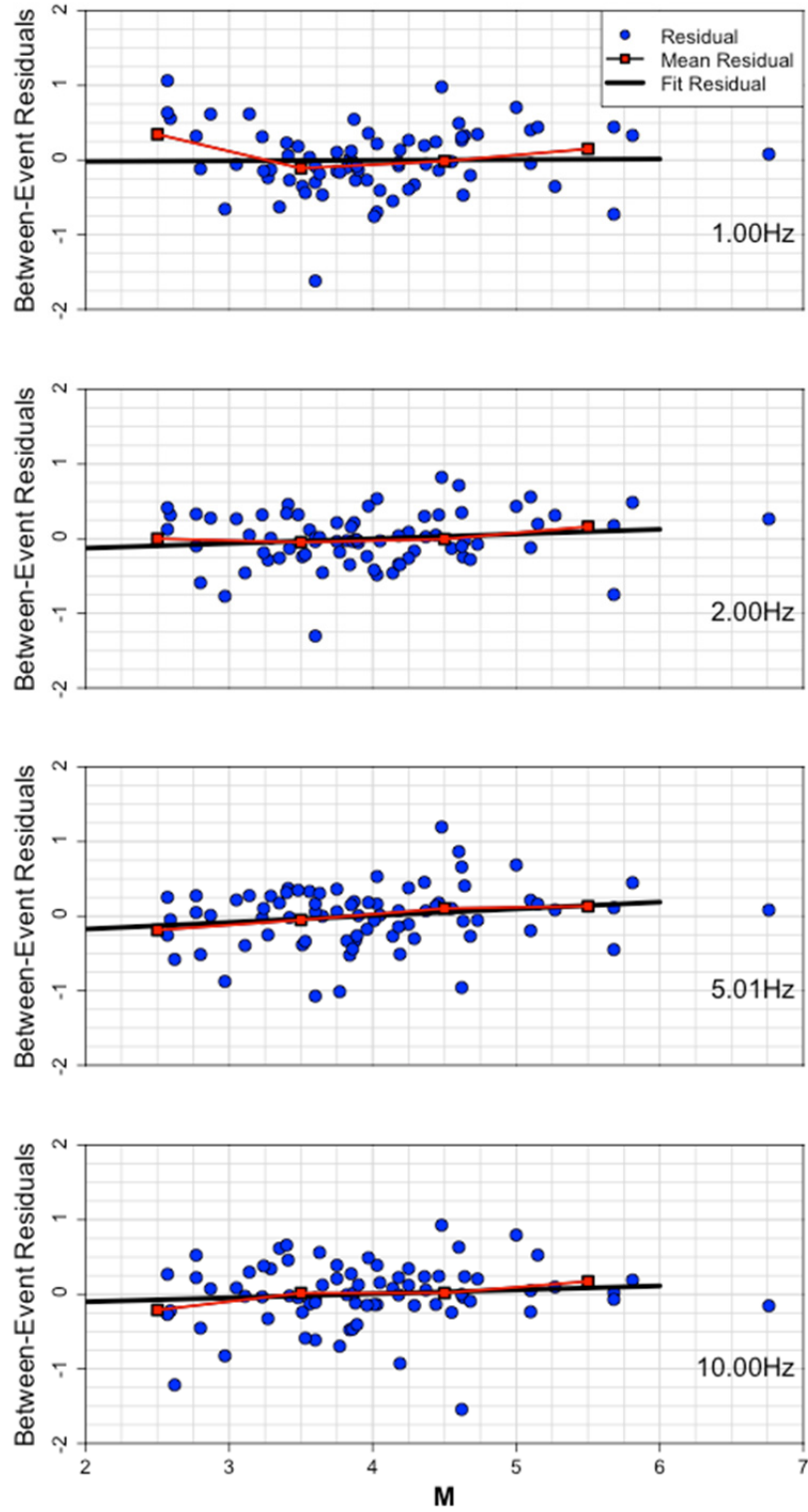


Figure 11.6 Between-event residuals against M for 1, 2, 5, and 10 Hz. Also shown are a linear trend (black) and a binned mean trend (red).

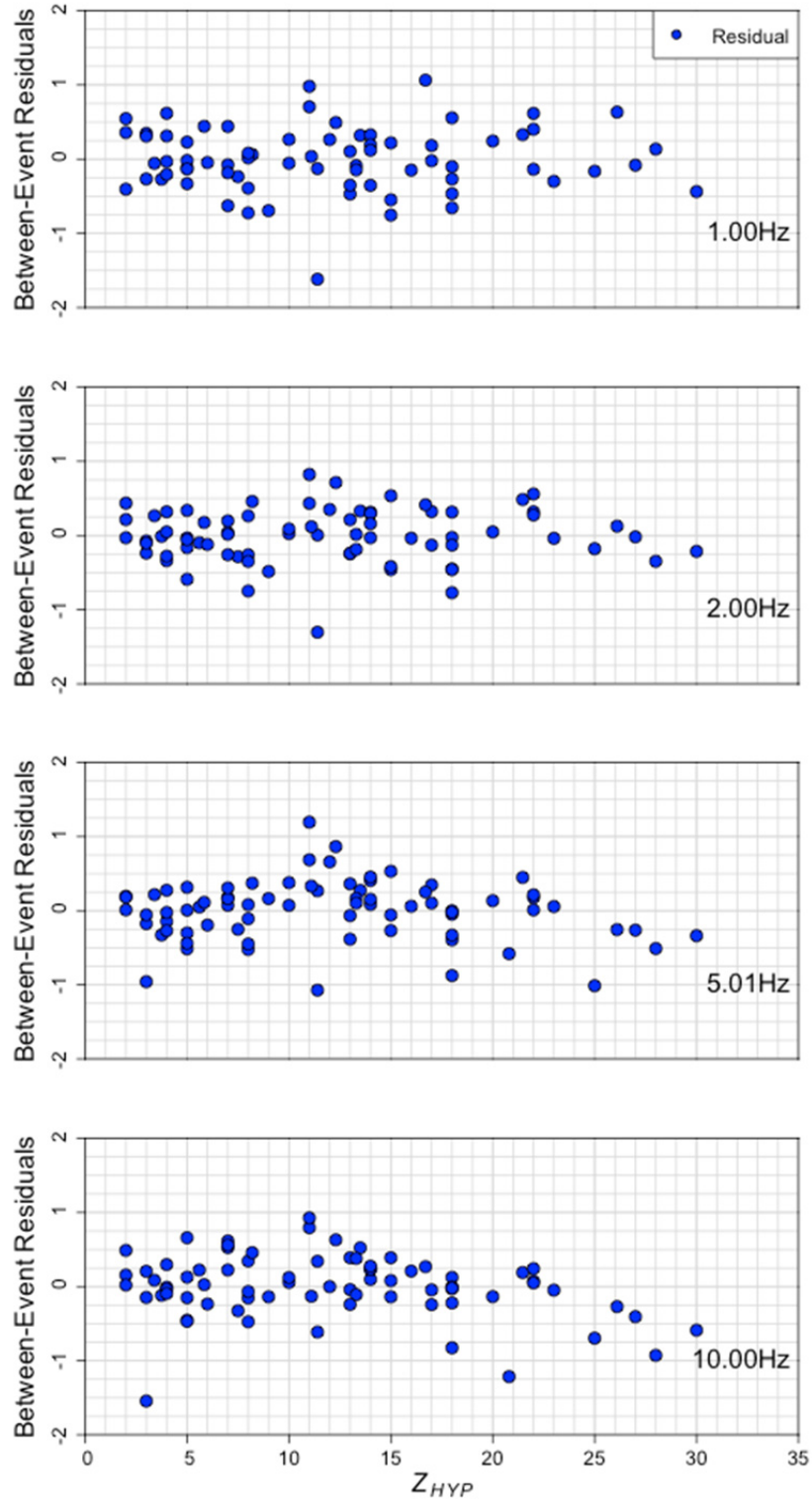


Figure 11.7 Between-event residuals against Z_{HYP} for 1, 2, 5, and 10 Hz.

Distance Scaling Model

The median distance-scaling term, F_2 [Equations (11.4)–(11.8)], has both a geometrical spreading term and a linear attenuation term. The term c_4 is the magnitude-independent portion of the geometrical spreading slope within 50 km for the global model, and $c_{4,R}$ is the regional difference of c_4 in path region R . The coefficient c_4 of the global model is fixed at -1.1, which was chosen as a representative value of the regressed term over a wide frequency range, and the random effects $c_{4,R}$ are constrained such that their mean is equal to the global value of c_4 . The term c_{4h} is the magnitude-independent portion of the geometrical spreading slope between 50 and 150 km for the global model, and $c_{4h,R}$ is the regional difference of c_{4h} in region R . The term c_5 represents the magnitude dependence of the geometrical spreading slope up to 150 km. This was fixed at 0.2 based on preliminary regression runs from the NGA-West2 data. This term only showed a statistically significant difference from zero for $M > 5$, which is reflected in the distance attenuation model. The term c_{4h2} is the geometrical spreading slope beyond 150 km. The c_7 term is the linear distance attenuation slope for the global model, and $c_{7,R}$ is the regional difference of c_7 in path region R . The combined effect of these parameters was constrained to be less than zero for all regions.

The geometrical spreading is assumed to be trilinear in shape with hinge points at 50 and 150 km. Both linear and bilinear shapes of the geometrical spreading were also examined. However, both resulted in unrealistic values for the linear attenuation coefficient, c_7 and the trilinear shape was selected. The coefficient c_{4h2} is fixed at -0.5 for all frequencies. This is a common assumption in attenuation studies (e.g., Boatwright and Seekins [2011] and Atkinson [2004]) and is consistent with theoretical surface-wave decay (e.g., Chun et. al [1987]). The locations of the two hinge locations were fixed to reasonable values prior to regression as they were difficult to constrain through regression. Summary plots show the frequency-dependent combined effect of c_{4h} and $c_{4h,R}$, (Figure 11.8) and c_7 and $c_{7,R}$ (Figure 11.9) for path region 2 (CNA). Figure 11.10 shows the single-station within-event residuals against R_{RUP} for frequencies 1, 2, 5 and 10 Hz. There are no observed biases or trends in the residuals with distance.

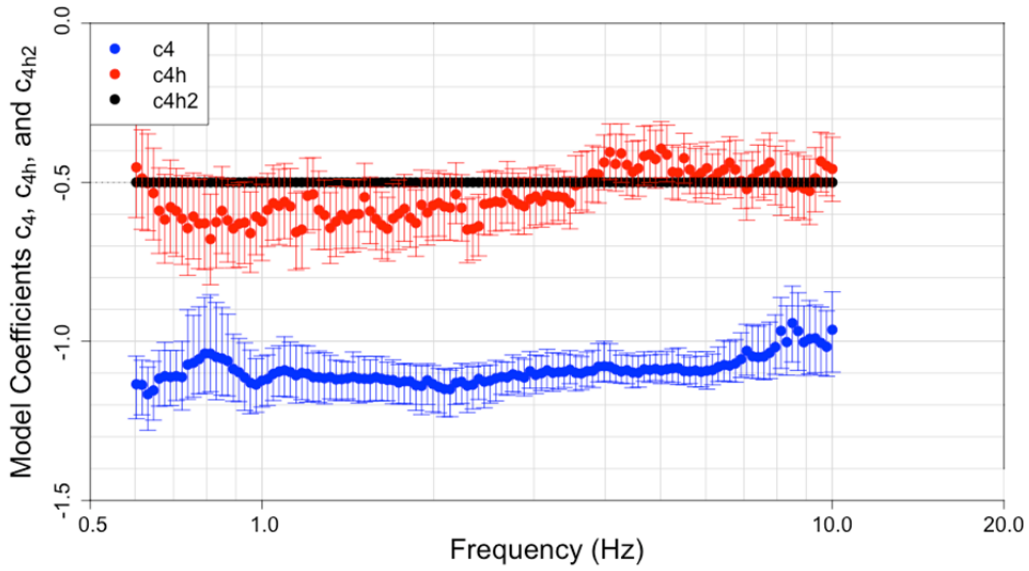


Figure 11.8 Geometrical spreading coefficients for path region 2 (CNA) within 50 km, (combined effect of c_4 and path region 2 specific $c_{4,R}$ in blue), between 50 and 150 km (combined effect of c_{4h} and path region 2 specific $c_{4h,R}$ in red) and the beyond 150 km (c_{4h2} in black) against frequency.

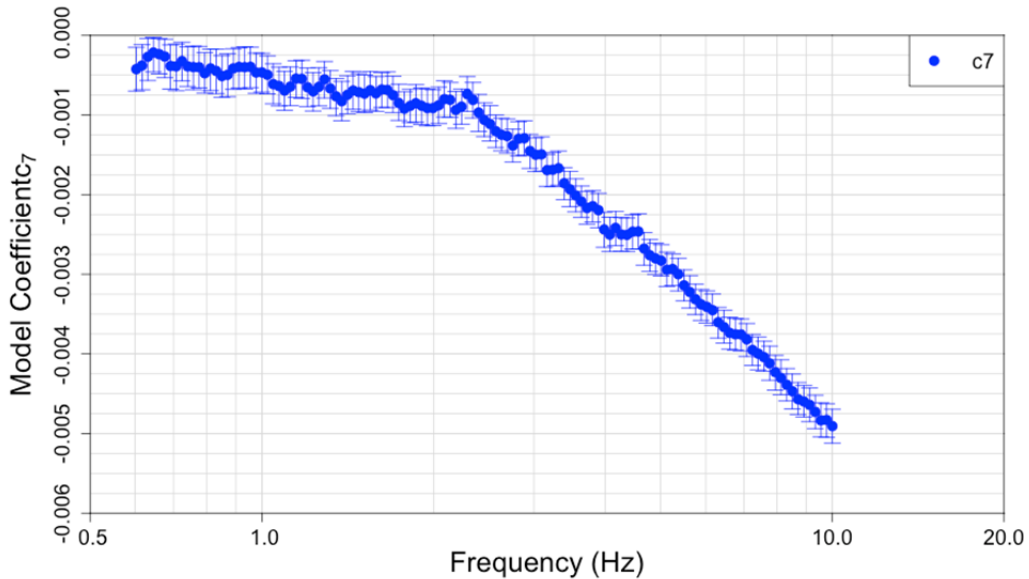


Figure 11.9 Linear distance scaling coefficient for path region 2 (CNA), combined effect of coefficients c_7 and path region 2 specific $c_{7,R}$, against frequency.

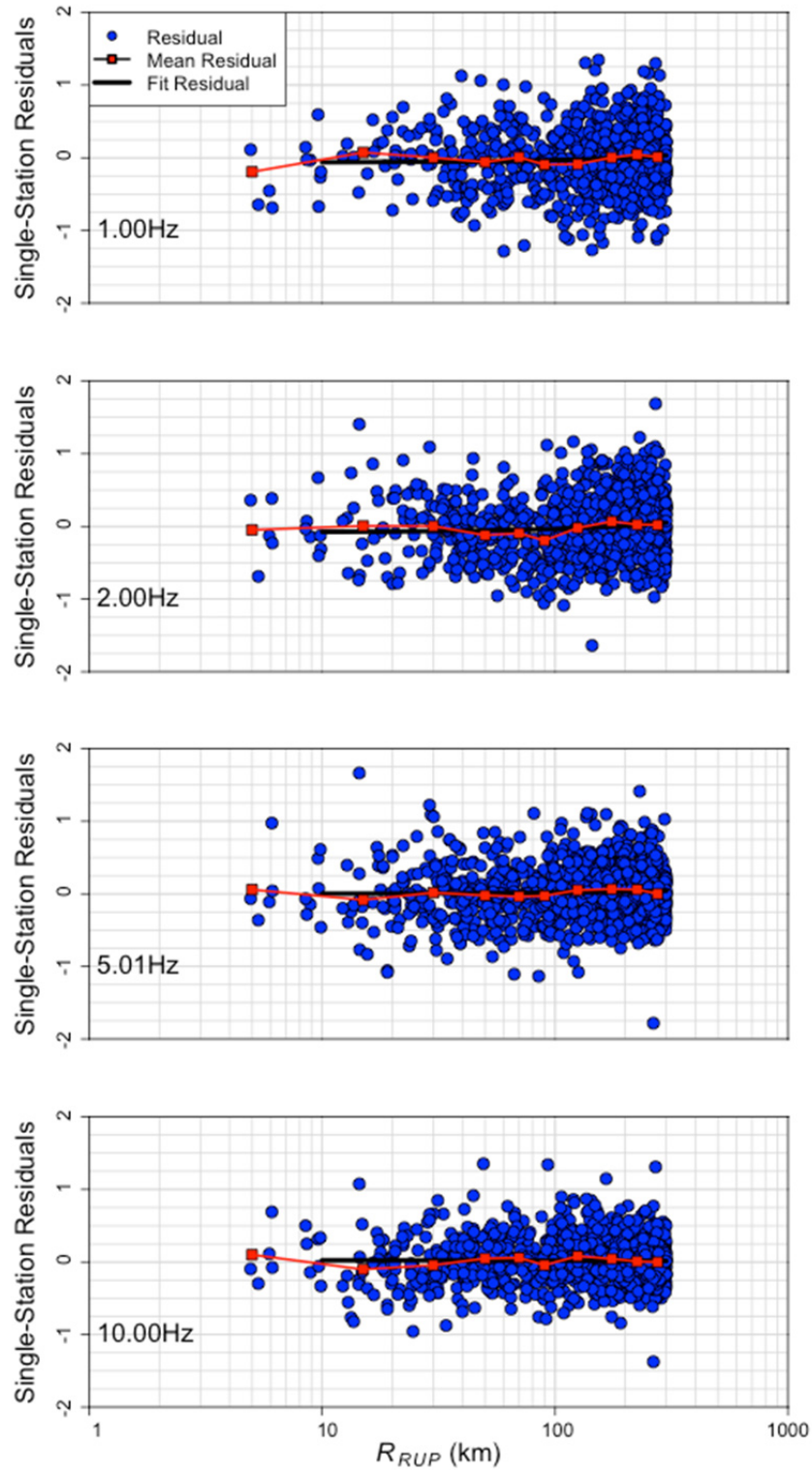


Figure 11.10 Single-station within-event residuals against R_{RUP} for 1, 2, 5, and 10 Hz. Also shown are a linear trend (black) and a binned mean trend (red).

Coefficient c_6 represents the short distance saturation effect, which is incorporated into the model to account for the finite size of earthquake rupture. This is often referred to as the fictitious depth term; however we are avoiding this terminology, as it can be misleading. There is not enough data at close distances to large earthquakes to constrain this term adequately from regression. In addition, it is highly correlated with the magnitude dependence of the geometrical spreading in the distance-scaling model. Therefore, we adopt the model for the equivalent point source depth from Atkinson and Silva [2000], which is plotted in Figure 11.11 and is given by:

$$c_6 = 10^{(-0.05+0.15M)} \quad (11.10)$$

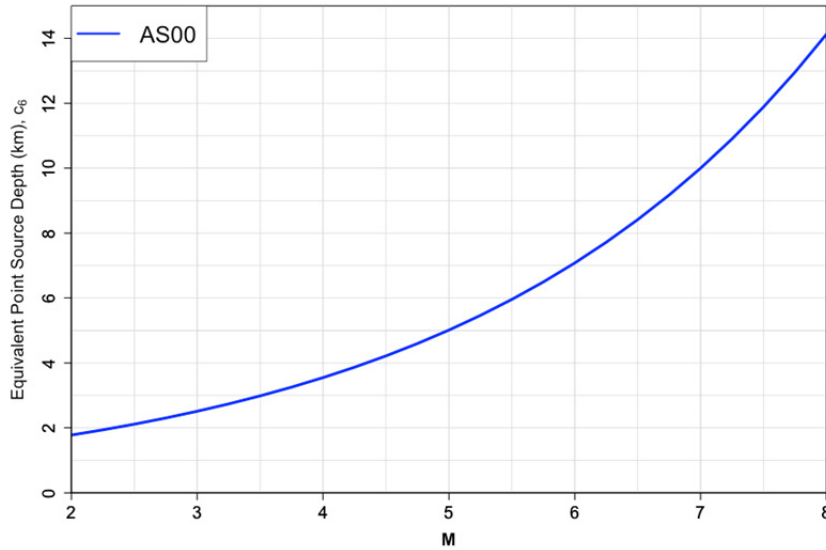


Figure 11.11 Atkinson Silva [2000] equivalent point-source depth.

Site Effects Scaling Model

The median site-scaling term, F3 [Equation (11.9)], is a simple function of V_{S30} . It is included primarily to provide stability in estimating the site-specific random effects through the regression. If this term were not present, it would be more difficult for the regression algorithm to correctly partition event, site, and region specific random effects. Note that there is no regionally grouped random effect on the site-scaling coefficient, c_8 , which is plotted against frequency in Figure 11.12. If the site-scaling model were to be used in the forward sense, a random effect would be necessary. However, the regionally grouped random effect ($c_{1,R}$) will capture any regional differences relative to the average V_{S30} scaling and the site-terms ($c_{1,S}$), will account for any site-specific differences in scaling. Figure 11.13 shows the single-station within-event residuals against V_{S30} for four frequencies. There are no biases or strong trends in the residuals with V_{S30} .

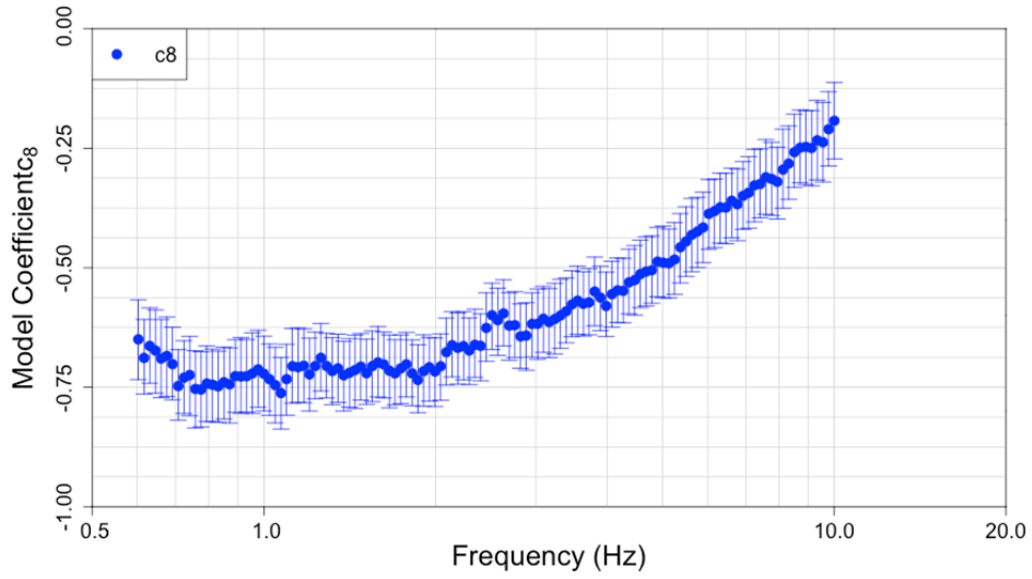


Figure 11.12 The global V_{S30} scaling coefficient, c_8 , against frequency.

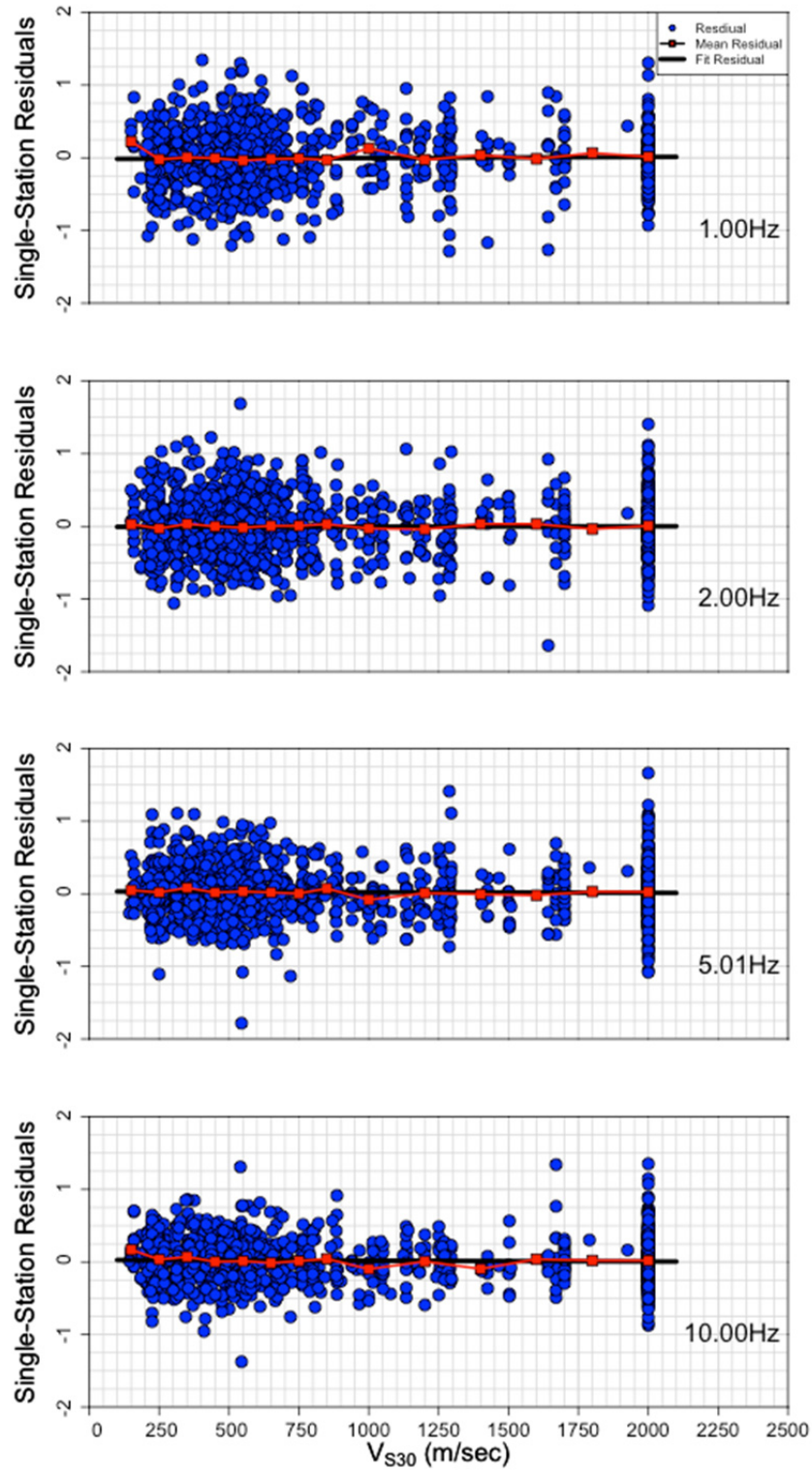


Figure 11.13 Single-station within-event residuals against V_{S30} for 1, 2, 5, and 10 Hz. Also shown are a linear trend (black) and a binned mean trend (red).

Model Variability and Adjustment to Mean EAS

The mean EAS is required for generating response spectral values using RVT [Kottke et al. 2015]. The final step in the empirical model development is the correction of the EAS from the median to the mean. The EAS at a given frequency is assumed to follow a log-normal distribution. The adjustment to the mean EAS is given by:

$$\ln\left[Y(f, \mathbf{M}, Z_{HYP}, R_{RUP}, V_{S30})_{mean}\right] = \ln\left[Y(f, \mathbf{M}, Z_{HYP}, R_{RUP}, V_{S30})\right] + \frac{\phi_{ss}^2 + \tau^2}{2} \quad (11.11)$$

where $Y(f, \mathbf{M}, Z_{HYP}, R_{RUP}, V_{S30})_{mean}$ is the *mean* EAS, $Y(f, \mathbf{M}, Z_{HYP}, R_{RUP}, V_{S30})$ is the median EAS, ϕ_{ss} is the single-station within-event standard deviation and τ is the between event standard deviation. The values of partitioned residuals shown on Figure 11.2 were used for this conversion. Note that we are explicitly excluding the site-to-site variability, ϕ_{S2S} , from the conversion [Equation (11.11)]. This additional variability is not applicable to the conversion to the mean EAS for use in RVT because we are correcting the model to a reference site condition (described in later sections).

11.3 EXTENSION OF EMPIRICAL EAS MODEL USING SEISMOLOGICAL THEORY AND MODELS

The EAS empirical model described above is limited to frequencies from 0.6 to 10 Hz and to events with $\mathbf{M} < 6$. The model needs to be extrapolated and “filled-up” for a full frequency range before GMIMs are computed using RVT. This section summarizes the steps taken to extend the EAS model to the full-range of applicability (in terms of magnitude and frequency).

11.3.1 Extension of Empirical EAS Model from 0.6 Hz down to 0.01 Hz

The extrapolation from 0.6 to 0.01 Hz is performed on the empirical predictions for $\mathbf{M} \leq 5.0$. The corner frequency of each $\mathbf{M} \leq 5.0$ is defined based on the Brune [1970, 1971] model with:

$$f_c = 4.9 \times 10^6 \beta \left(\frac{\Delta\sigma}{M_0} \right)^{1/3} \quad (11.12)$$

where β is the shear-wave velocity km/sec in the vicinity of the source, $\Delta\sigma$ is the Brune stress parameter in bars, and M_0 is the seismic moment in dyne-cm. We performed a simple inversion based on predictions of the EAS for $\mathbf{M} = 5$ to estimate the stress parameter. Given the stress parameter we obtained (48 bars), the corner frequency is above 0.6 Hz for all $\mathbf{M} \leq 5$ and we extended the spectrum to fall off at a rate of $2 \cdot \log(f)$, below the corner frequency, f_c .

The mean prediction of EAS that has been extrapolated to frequencies beyond the band limitations of the empirical model is referred to as $Y(f)_B$. Figure 11.14 shows the $Y(f)_B$ for $f \leq 10$ Hz against frequency at $\mathbf{M} = 5$, $R_{RUP} = 10$ km, $V_{S30} = 760$ m/sec, $H_{Dep} = 10$ km and path region 2 (CNA).

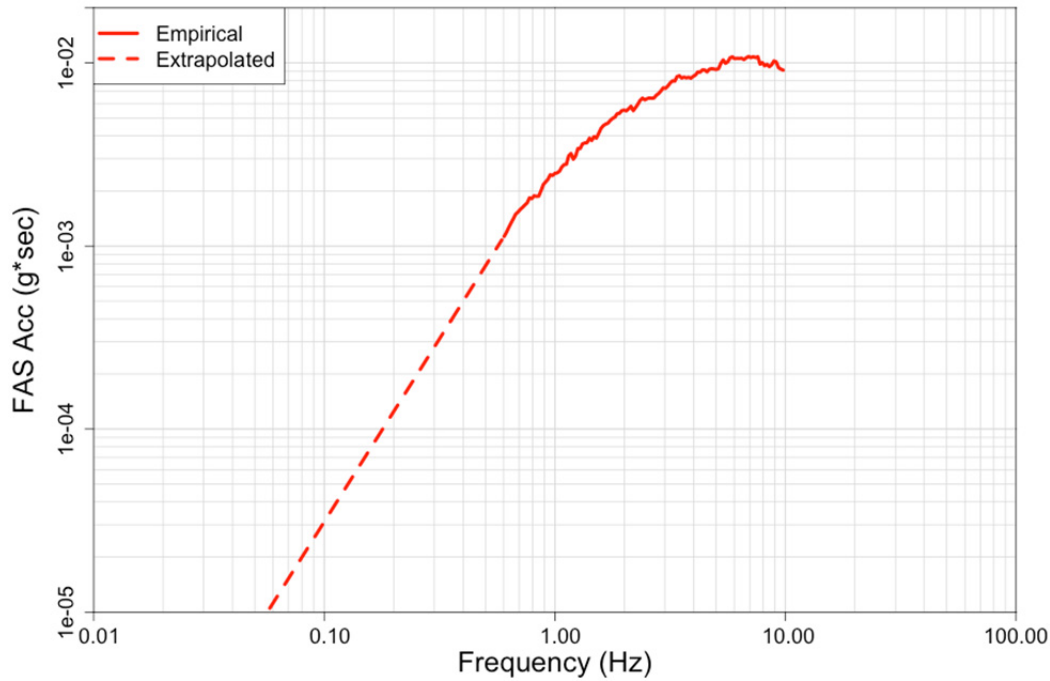


Figure 11.14 The EAS, $Y(f)_B$, extrapolated down to 0.01 Hz and up to 100 Hz for $\mathbf{M} = 5$, $R_{Rup} = 10$ km, $V_{S30} = 760$ m/sec, $Z_{HYP} = 10$ km, and path region 2 (ENA).

11.3.2 Extension of Empirical EAS Model to Large \mathbf{M} from 0.01 to 10 Hz

Constraining how the GMMs extrapolate to magnitudes beyond the range of empirical data ($\mathbf{M} > 6$) was an important step and was accomplished through the use of FF simulations [Section 1.3.4 and Appendix 1B]. We originally developed empirically-based magnitude scaling to magnitude 7.9 (with additional extrapolation to 8.2) using the empirical data from NGA-West2. However, an initial trial of this approach led to unreasonable PSA spectral shapes, characterized by a large and relatively wide peak at low frequencies. We concluded that this approach would require more work to be applicable to NGA-East and it was discarded for the current model development.

The FAS \mathbf{M} -scaling spectral ratio from FF simulations [Appendix 1B] is employed for extrapolation to large magnitudes. The ratio is defined as:

$$\alpha(f, \mathbf{M} = m, R_{RUP}, Z_{TOR})_{sim} = \frac{FAS(f, \mathbf{M} = m, R_{RUP}, Z_{TOR})}{FAS(f, \mathbf{M} = 5, R_{RUP}, Z_{TOR})} \quad (11.13)$$

where α is a function of frequency f , magnitude, \mathbf{M} , rupture distance, R_{Rup} , and the depth to top of rupture, Z_{TOR} .

We evaluated the FF simulations (Appendix 1B) and selected EXSIM (EX) [Atkinson and Assatourians 2015], and Graves and Pitarka (GP) [Graves and Pitarka 2015] for our GMM development. The median prediction of EAS at frequency f extrapolated to magnitude above 5 for a given simulation method is defined as:

$$Y(f)_{sim,B} = \alpha(f, \mathbf{M} = m, R_{RUP}, Z_{TOR}) * Y_B(f, \mathbf{M} = 5, Z_{HYP}, R_{RUP}, V_{S30}) \quad (11.14)$$

where $Y(f)_{sim,B}$ is the mean EAS extrapolated to $\mathbf{M} > 5.0$ based on simulation method sim and extrapolated to frequencies beyond the band limitations of the empirical model. Following an evaluation of the scaling ratios from FF simulations, we defined their range of applicability to frequencies above 0.07 Hz. Therefore, below this frequency, the EAS is constrained to fall off at a rate of $2 * \log(f)$. The scaling ratios are used up to 10 Hz.

The ratios were provided to for discrete combinations of \mathbf{M} , R_{Rup} , Z_{TOR} , and f , for which a scaling model was developed. We used Model 2 [Appendix 1B], which includes Z_{TOR} as a parameter. We applied Model 2 using a magnitude-dependent Z_{TOR} distribution based on the CEUS SSC Project [EPRI/DOE/NRC 2012; R. Youngs *Personal Communication* 2014]. The distribution of Z_{TOR} is shown on Figure 11.15; $Z_{TOR} = 0$ for all $\mathbf{M} \geq 7$.

Figures 11.16–11.18 show how the empirical magnitude scaling up to $\mathbf{M} = 5$ and the extrapolation with the two different simulation methods selected, for a subset of distances and frequencies.

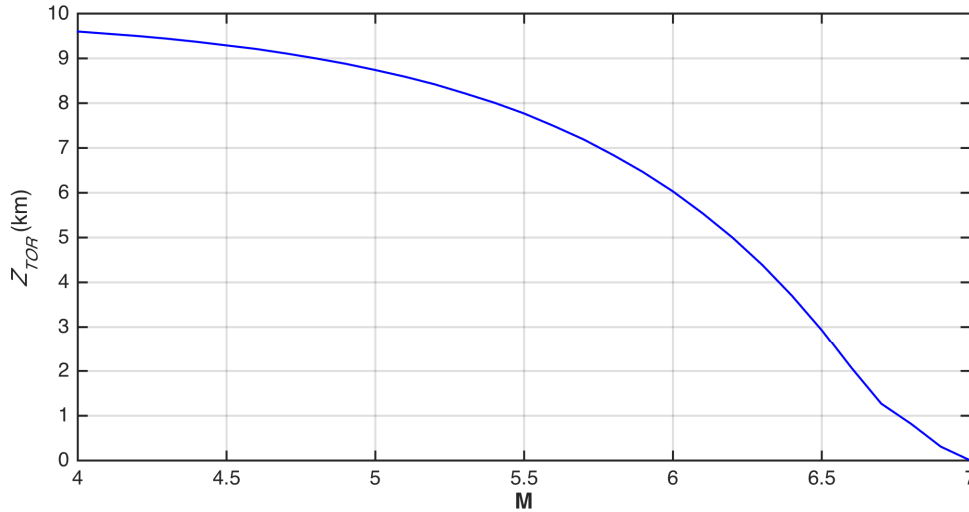


Figure 11.15 Average Z_{TOR} value as a function of \mathbf{M} , based on the CEUS SSC distribution [R. Youngs *Personal Communication* 2014].

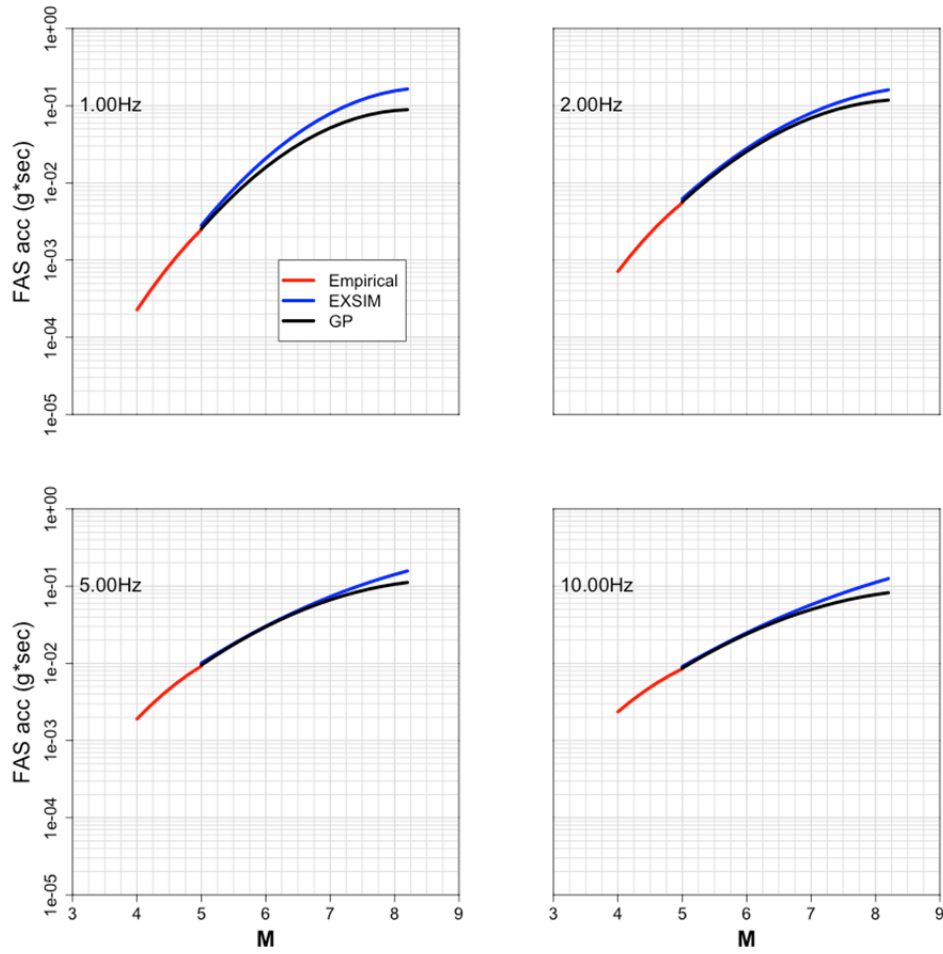


Figure 11.16 Empirical magnitude scaling model, extrapolated to large magnitude, compared with the simulation based extrapolation at $R_{Rup} = 10$ km at frequencies 1, 2, 5, and 10 Hz.

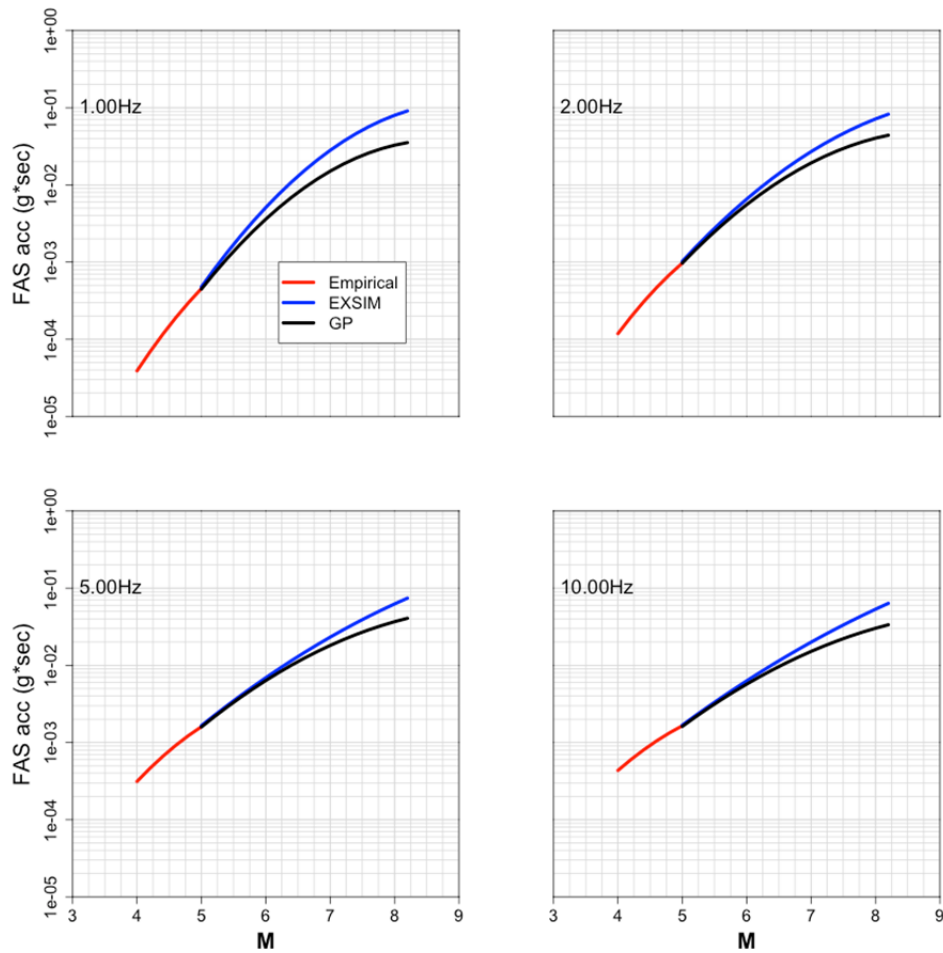


Figure 11.17 Empirical magnitude scaling model, extrapolated to large magnitude, compared with the simulation based extrapolation at $R_{Rup} = 50$ km at frequencies 1, 2, 5, and 10 Hz.

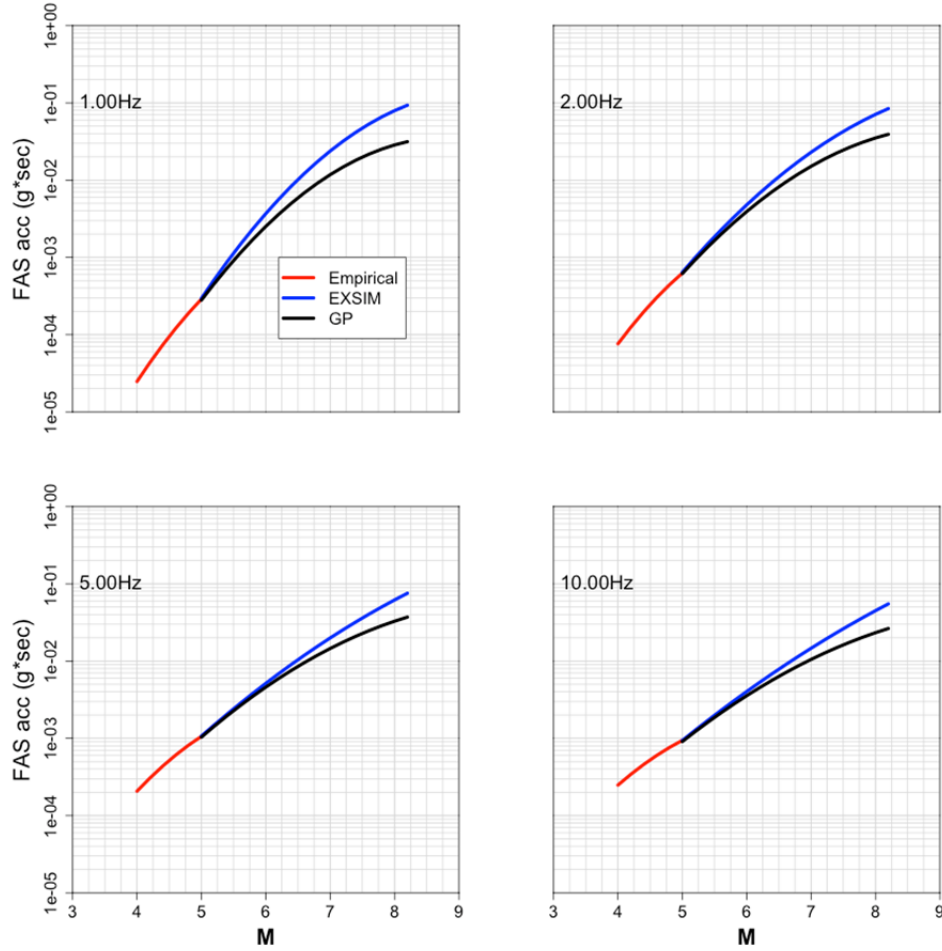


Figure 11.18 Empirical magnitude scaling model, extrapolated to large magnitude, compared with the simulation based extrapolation at $R_{rup} = 100$ km at frequencies 1, 2, 5, and 10 Hz.

11.3.3 Extension of Empirical EAS Model from 10 to 400 Hz

At high frequencies, the shape of the FAS is generally controlled by kappa (κ) and anelastic attenuation Q [Al Atik et. al 2014], which has more of an effect at larger distances. In order to extrapolate the model to high frequencies, we need to know these two parameters. In the empirically derived model from 0.6–10 Hz the term $(c_7 + c_{7,R})$ can be equated to a frequency dependent $Q(f)$ as

$$(c_7 + c_{7,R}) = \frac{-\pi f \beta}{Q(f)} = \frac{-\pi f \beta}{Q_0 f^\eta} = \frac{-\pi f^{1-\eta} \beta}{Q_0} \quad (11.15)$$

where β is the shear-wave velocity of the crust, and η and Q_0 are parameters of the frequency-dependent Q model. Shear-wave velocity β is assumed to be 3.5 km/sec, c_7 is the linear distance attenuation coefficient for the global, and $c_{7,R}$ is the regional random effect on the linear distance

attenuation from path region 2 (CNA). The parameters η and Q_0 were solved for by least squares. Q_0 was found to be approximately 1700, while η was effectively 0.

We assumed that for an EAS prediction at $V_{S30} = 760$ m/sec, $\kappa = 0.025$. To verify this assumption, we inverted median EAS predictions from magnitude 3 to 5, in half magnitude steps, at 10 km R_{Rup} for stress parameter and frequency-dependent amplification factors. For this inversion, the geometrical spreading and $Q(f)$ were fixed at the values of the empirical model for path region 2 (CNA). The amplifications were very close to one, confirming that the initial assumption of kappa was reasonable, given that our model was for 760 m/sec.

The κ assumed has a much larger effect on the ground motion at high frequencies when compared to the effect of $Q(f)$, even at larger distances. Therefore to extrapolate the median EAS above 10 Hz, κ was the only parameter applied. This extrapolation was applied to all predictions up to M 8.2, at all distances, and $V_{S30} = 760$ m/sec.

The EAS extrapolated to frequencies beyond the band limitations of the empirical model and to large magnitude, $Y(f)_{sim,B}$, is plotted for the two simulation-based extrapolations (Figure 11.19).

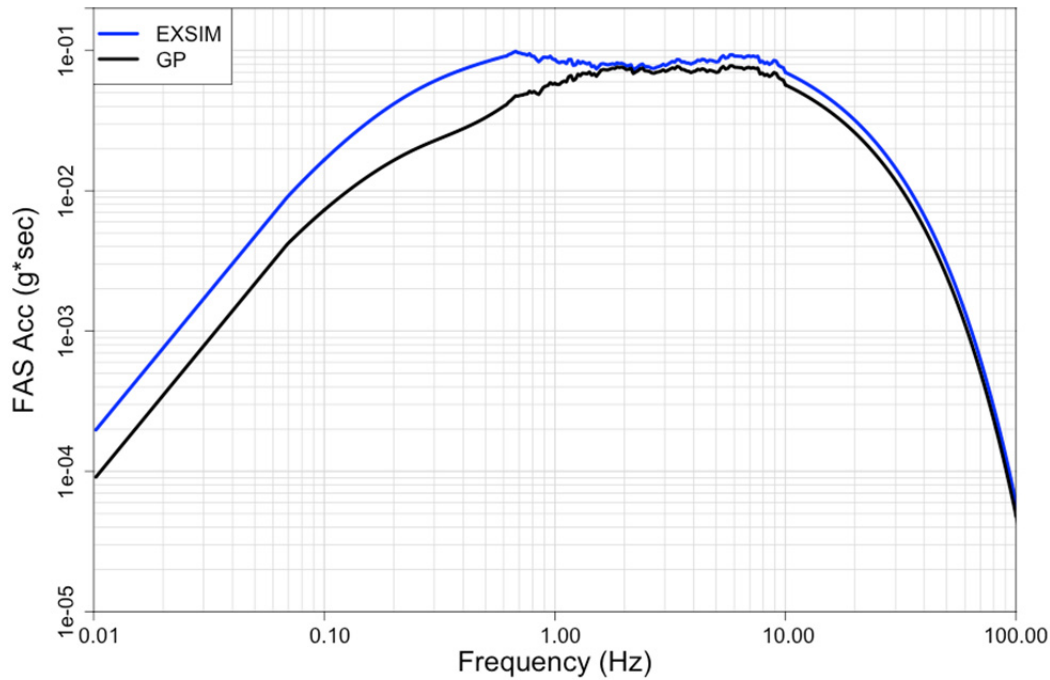


Figure 11.19 The EAS, $Y(f)_{sim,B}$, extrapolated down to 0.01 Hz and up to 100 Hz for $M = 7$, $R_{Rup} = 10$ km, $V_{S30} = 760$ m/sec, $Z_{HYP} = 10$ km, and path region 2 (CNA). Extrapolations based on finite-fault models EXSIM and GP are plotted.

11.3.4 Correction to Reference Site Conditions

The reference site conditions for NGA-East GMM development were established in a separate task as $V_{S30} = 3000$ m/sec and kappa of 0.006 sec [Hashash et al. 2014a,b and Campbell et al. 2014]. Since a reasonable κ was used to extrapolate the median EAS to frequencies above 10 Hz the κ adjustment is performed as in Al Atik et al. [2014] given by

$$Y(f)_{B,\kappa_t} = Y(f)_B e^{\left[-\pi f(\kappa_t - \kappa_h)\right]} \quad (11.16)$$

where $Y(f)_{B,\kappa_t}$ is the mean predicted EAS, extrapolated to large magnitude and frequencies above and below the band limitation of the data, and corrected to $\kappa = \kappa_t$; here, κ_t is the target kappa value and κ_h is the host kappa value, which was defined above as 0.025. The model is corrected from $V_{S30} = 760$ m/sec to $V_{S30} = 3000$ m/sec with amplification factors for FAS developed in [Boore 2015] by

$$Y(f)_{B,\kappa_t,3000} = Y(f)_{B,\kappa_t} AMP(f)_{3000/760} \quad (11.17)$$

where $Y(f)_{B,\kappa_t,3000}$ is the mean EAS, extrapolated to large magnitude and frequencies above and below the band limitation of the data, and corrected to $\kappa = 0.006$ and $AMP(f)_{3000/760}$ are the frequency-dependent FAS amplification factors for adjusting to from $V_{S30} = 760$ m/sec to $V_{S30} = 3000$ m/sec. Figure 11.20 shows the $Y(f)_{sim,B}$, which has been adjusted to the reference site condition for both magnitude extrapolation methods.

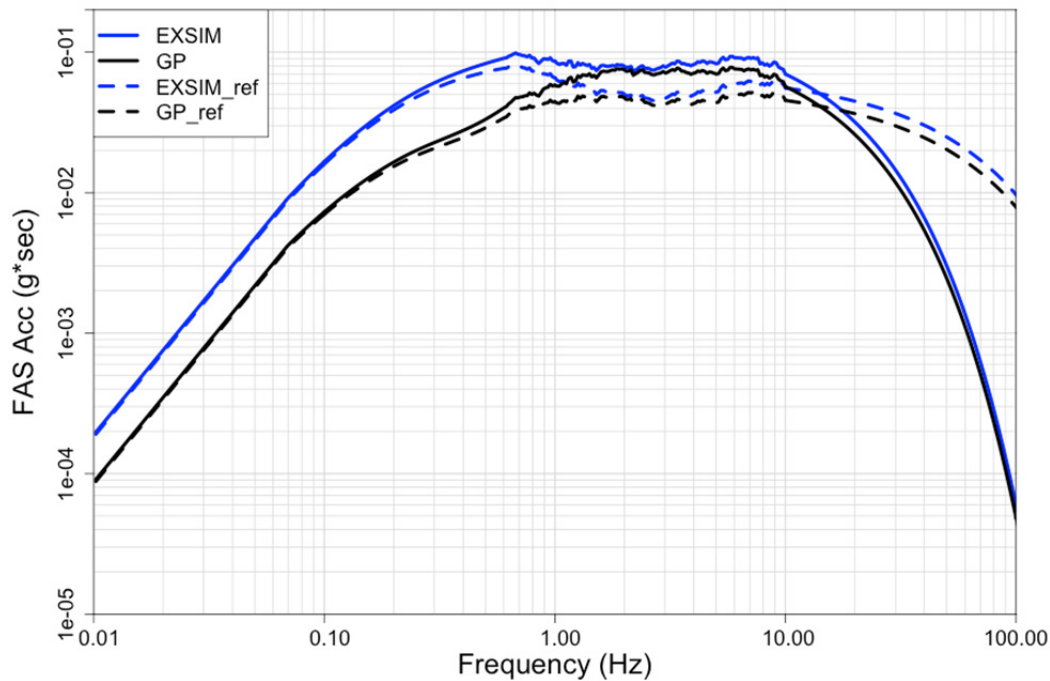


Figure 11.20 The EAS, $Y(f)_{sim,B}$, corrected (dashed lines) to the reference site condition of $\kappa = 0.006$ and $V_{S30} = 3000$ m/sec extrapolated down to 0.01 Hz and up to 100 Hz for $M = 7$, $R_{RUP} = 10$ km, $Z_{HYP} = 10$ km, and path region 2 (CNA).

Note on Site Effects in CENA

The majority of the sites in the NGA-East database were assigned V_{S30} values through proxy methods [Goulet et al 2014], as opposed to measured. This led to a concern that site effects defined on the basis of *uncertain* V_{S30} values could be biased. Additionally, many of the sites may not have exhibited site response that can be explained well from a simple $\ln(V_{S30})$ scaling model. This would be the case, for example, for sites with large impedance contrasts, such as many in the glaciated regions of CENA. To address this issue, we defined as “reliable site” those sites for which the site effects were well captured by the model. The segregation of “reliable sites” was performed by visual inspection of trends of site-term against frequency for all sites included in the regression analysis. Through this process, a total of 93 sites were given the “reliable site” designation. If the simple $\ln(V_{S30})$ scaling was applicable to the bulk of sites in the NGA-East database, the trends in residuals for the two classes of sites should be similar, and near zero. The single-station within-event residuals for all of the records from both groups of sites were re-regressed to identify any mean offset. Figure 11.20 shows that average site term against frequency for the sites designated “reliable,” while Figure 11.21 shows that the adjustment factor regressed for the reliable sites is close to zero for all frequencies. Figure 11.22 shows the average site term for the sites that were not designated “reliable.” These sites also did not show a prominent trend in site terms with frequency. The average V_{S30} values for both categories were also very close. Although there is some scatter, this analysis provided us with the reassurance that no systematic bias was introduced, in average, by the use of the $\ln(V_{S30})$ site effects scaling.

Future improvement to site effects modeling would require better site characterization and the consideration of additional site parameters, such as the site period or a metric that captures the large impedance contrasts encountered in many places in CENA.

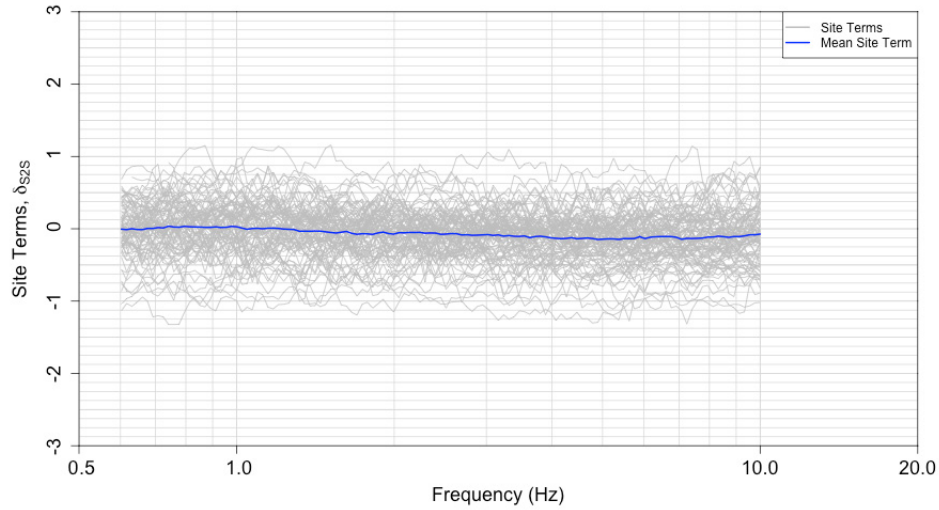


Figure 11.21 Average site terms against frequency for sites designated reliable.

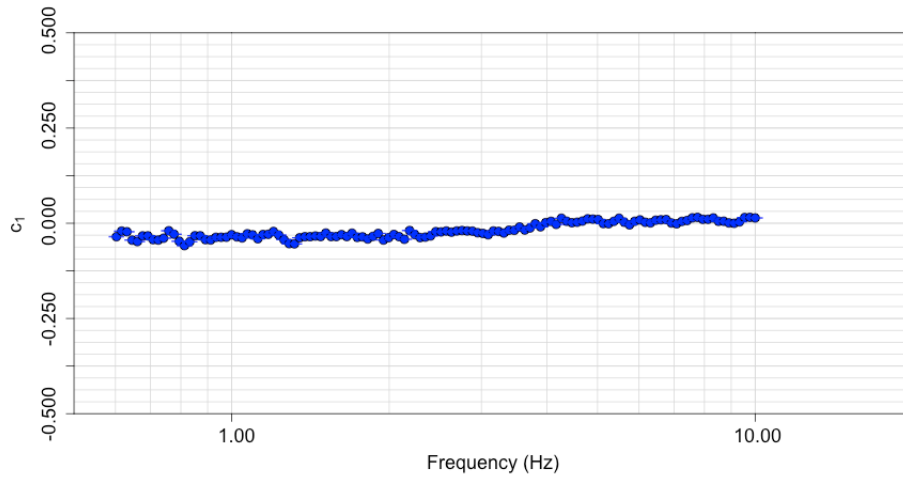


Figure 11.22 Reliable site correction term against frequency. This term is negligible across frequency.

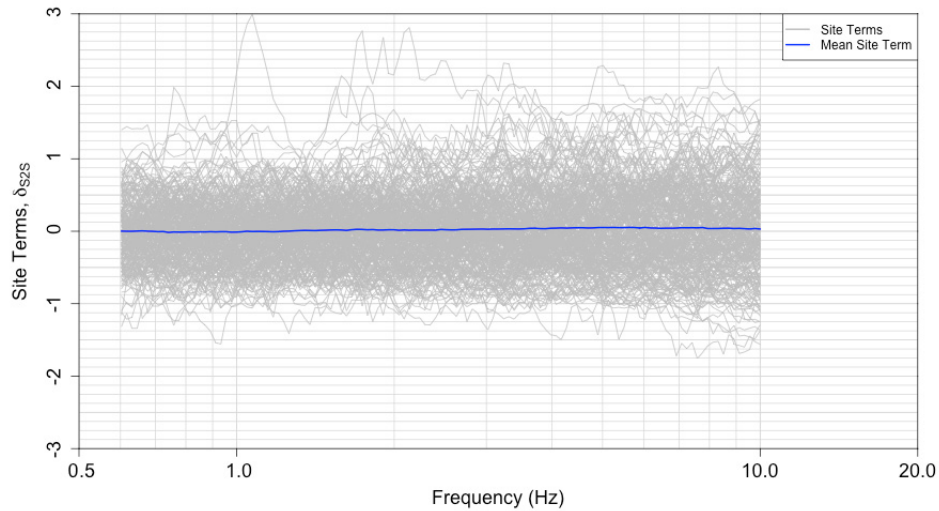


Figure 11.23 Average site terms against frequency for sites not designated reliable.

11.4 RANDOM VIBRATION THEORY AND CALIBRATED DURATION MODEL

As stated earlier, RVT was used to calculate GMIM predictions from the FAS (or EAS) model. The key elements of the RVT approach are described below (details are available in Kottke et al. [2015]). We also summarize the development of a calibrated duration model specific to this project.

11.4.1 RVT Overview

The use of RVT to calculate PSA is common in engineering seismology and earthquake engineering. Examples of RVT use include the program SMSIM [Boore 2003] to calculate PSA from various PS models and the program STRATA [Kottke and Rathje 2008] for performing site response analysis in the frequency domain. It is also used in the hybrid empirical method [e.g., Campbell 2003] to adjust GMMs from a host to a target region. Conceptually, the steps in RVT used to calculate PSA at an oscillator period T are as follows:

1. Apply the appropriate transfer function to the square of the FAS to obtain the frequency response function of the single degree-of-freedom (SDOF) oscillator with 5%-damping ratio and a natural period equal to T .
2. Calculate the 0th spectral moment of the frequency response function, which is used to calculate the root-mean-square (RMS) of the response.
3. Use the appropriate peak factor relationship along with the ground-motion duration to calculate the peak response from the RMS response.

The above steps are repeated for a range of T to create an entire response spectrum. As per the recommendation of the NGA RVT Working Group [Kottke et al. 2015], we used the Vanmarke [1975] peak factor relationship. A significant challenge in calculating PSA in this way is that the FAS need to be known for a very broad range of frequencies. To calculate PSA at

short periods (e.g., $T < 0.01$ sec), the FAS must be known out to frequencies beyond 100 Hz, depending on site conditions and distance. This, along with the desire to capture the true PGA value, was the motivation for extending the model to 400 Hz.

11.4.2 Development of Calibrated RVT-Duration Model

Step 3 in the previous section requires a duration model. The duration model presented here, the RVT-duration, D_{RVT} , is not developed for a traditional definition of ground-motion duration, e.g., D_{5-95} or D_{5-75} . Rather, D_{RVT} , is defined as the duration that minimizes the squared error (in natural log units) between response spectra calculated from recorded EAS via RVT and response spectra calculated directly from the time series (averaged over the usable period range for PSA). Hence, D_{RVT} is more a parameter than a physical quantity (see Bora et al. [2014]).

We model the dependence of D_{RVT} on magnitude, distance and hypocentral depth using the following functional form:

$$\ln(D_{RVT}) = (a_0 + a_{0,R}) + b_1 \mathbf{M} + b_2 Z_{HYP} + [(a_1 + a_{1,R}) + a_2 \mathbf{M}] \ln(\sqrt{R_{RUP} + a_3}) + \eta_{RVT,e} + \eta_{RVT,s} + \varepsilon_{RVT} \quad (11.18)$$

where $\eta_{RVT,e}$ represents the between-event variability of the model, $\eta_{RVT,s}$ represents the site-to-site variability, and ε_{RVT} represents the single-station within-event variability of the model. Global coefficient are a_0 , a_1 , a_2 , a_3 , b_1 , and b_2 , while $a_{0,R}$, and $a_{1,R}$ are region-specific random effects.

The CENA data are not sufficient to develop a model for D_{RVT} that would perform well to magnitude 8.2. A subset of the NGA-West2 database [Ancheta et al 2014] was included in this analysis to help constrain how D_{RVT} scaled to magnitudes outside the range of the NGA-East data, as was done for the EAS model development itself. Differences in durations versus distance were observed, this was expected due to the different attenuation rates in the different tectonic environments. Where the data overlapped, the trends in duration with \mathbf{M} from both dataset (NGA-East and NGA-West2) were similar. To account for the differences between the datasets while borrowing strength from the large magnitude data in the NGA-West2 dataset, two random effects, grouped by dataset (East or West2), were included in the model. They are $a_{0,R}$, and $a_{1,R}$ where $a_{0,R}$ is an additive term to the model constant, and $a_{1,R}$ is an additive term on the magnitude independent portion of the distance scaling. These two terms each take on one of two values, depending on where the model is to be applied.

All model coefficients are independent of the PSA frequency. A better match between RVT response spectra and time series response spectra could have been achieved if frequency-dependent ground-motion durations were calculated for each record; however, the match provided by the frequency-independent ground-motion duration proved to be sufficient. The marginally improved match provided by frequency-dependent ground-motion duration model did not justify the additional complication.

We used the same Bayesian regression scheme mentioned above to estimate the coefficients of the calibrated duration model. The regression for duration was performed in two

steps: Terms b_1 and b_2 and the between-event residuals (realizations of the variable $\eta_{RVT,e}$) were estimated from data with $R_{RUP} < 50$ km and fixed. The remaining model coefficients were estimated based on all of the data.

The magnitude scaling terms, b_1 and b_2 , and the between-event residuals were solved from data within 50 km because the majority of the recordings in CENA are dominated by small-to-moderate magnitudes and large distances. These durations are dominated by the contribution from the path, which makes it difficult to resolve the source contributions. Solving for the magnitude scaling terms and between-event residuals with the short distance data leads to much more stable results and a better partition of the source and path contributions to durations. Figures 11.24 and 11.25 show the between-event residuals plotted against magnitude and the within-event residuals plotted against distance, respectively.

The mean of D_{RVT} is used in the computation of PSA and is calculated in the same way as the mean of the EAS [Equation (11.11)], considering only the variances of $\eta_{RVT,e}$ and ϵ_{RVT} .

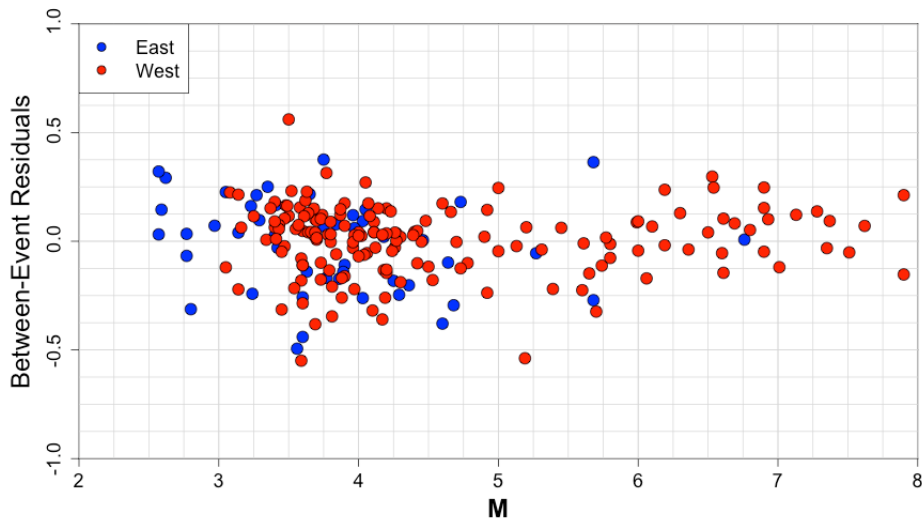


Figure 11.24 Between-event residuals against M for the calibrated D_{RVT} model.

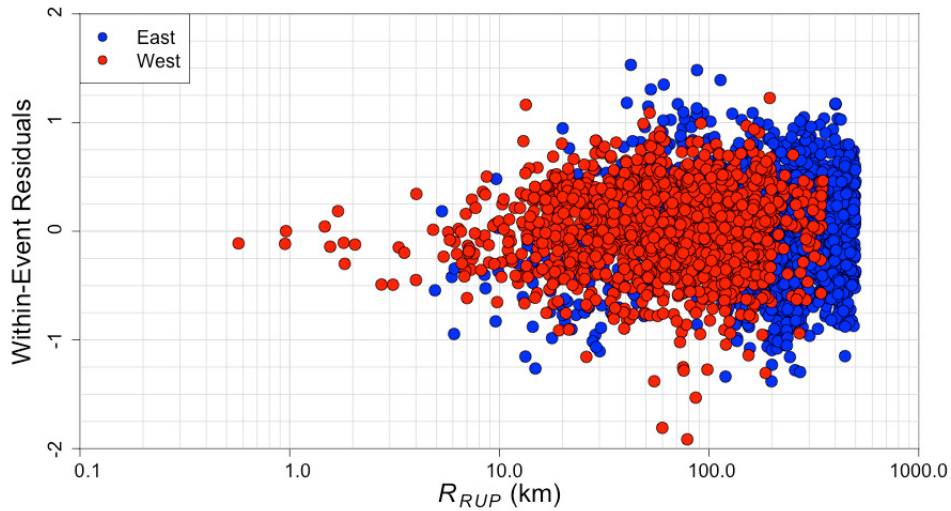


Figure 11.25 Within-event residuals against R_{Rup} for the calibrated D_{RVT} model.

11.5 FINAL MODEL RESULTS: PSA, PGA, AND PGV

The final GMIMs are obtained by taking the EAS model from Section 11.3 and applying the RVT approach summarized in Section 11.4. The results for all the GMIMs defined in Chapter 1 are provided in tables as an electronic appendix. Figures 11.26–11.28 present the PSA model as a function of magnitude. Figures 11.29–11.30 show the distance scaling for the PSA estimates of the two GMMs. The extrapolation to large magnitudes using the current set of FF simulations leads to models that have unrealistic distance scaling within 5–10 km (ground motions decrease from approximately 5 km into 1 km, as shown in Figures 11.29–11.30). It is difficult to evaluate the behavior of the models given the lack of recordings within 5 km R_{Rup} of an earthquake, but we do not recommend the models to be used within 5 km. Outside of this very short distance range, these two GMMs consist in credible alternative median models for predicting GMIMs for the NGA-East Project.

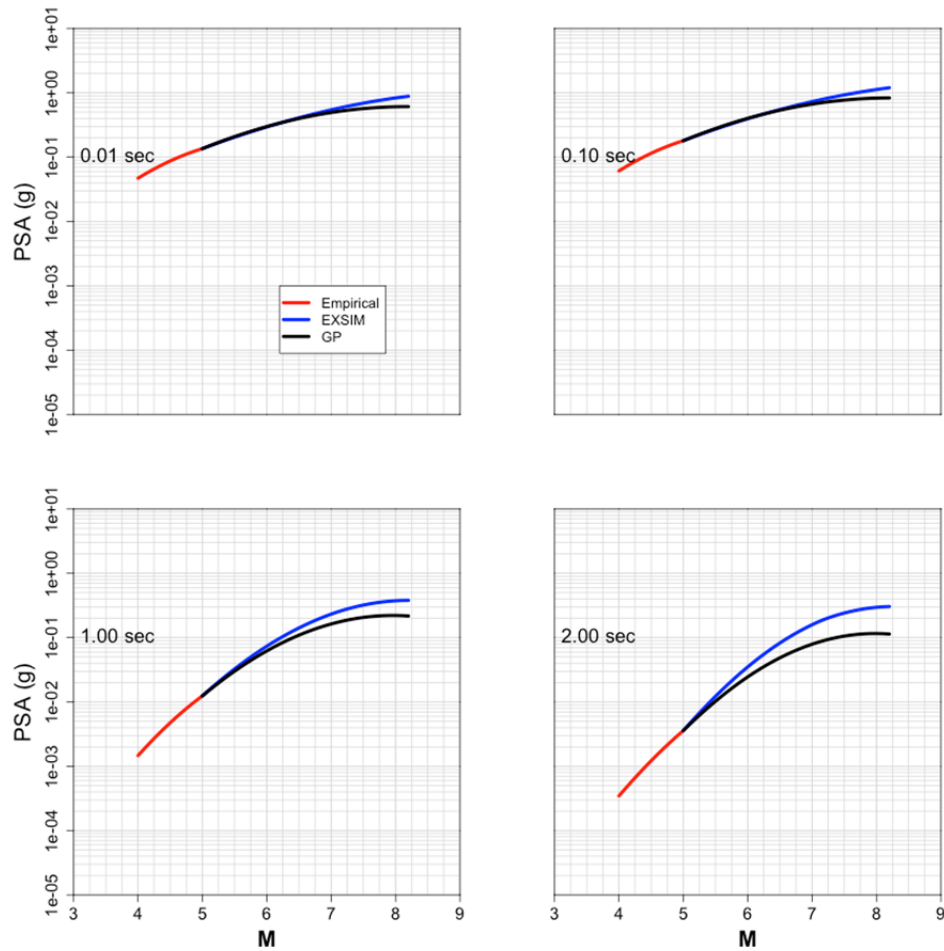


Figure 11.26 Magnitude scaling of median PSA model predictions plotted for the reference site condition and $R_{Rup} = 10$ km.

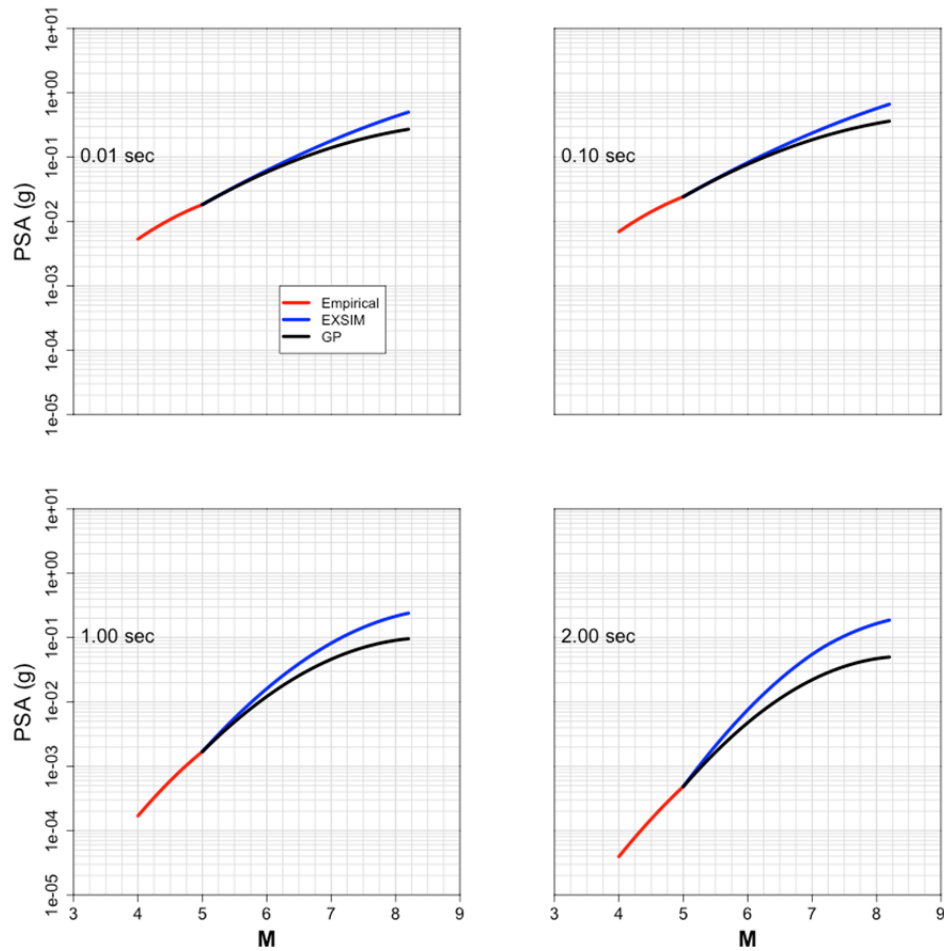


Figure 11.27 Magnitude scaling of median PSA model predictions plotted for the reference site conditions and $R_{Rup} = 50$ km.

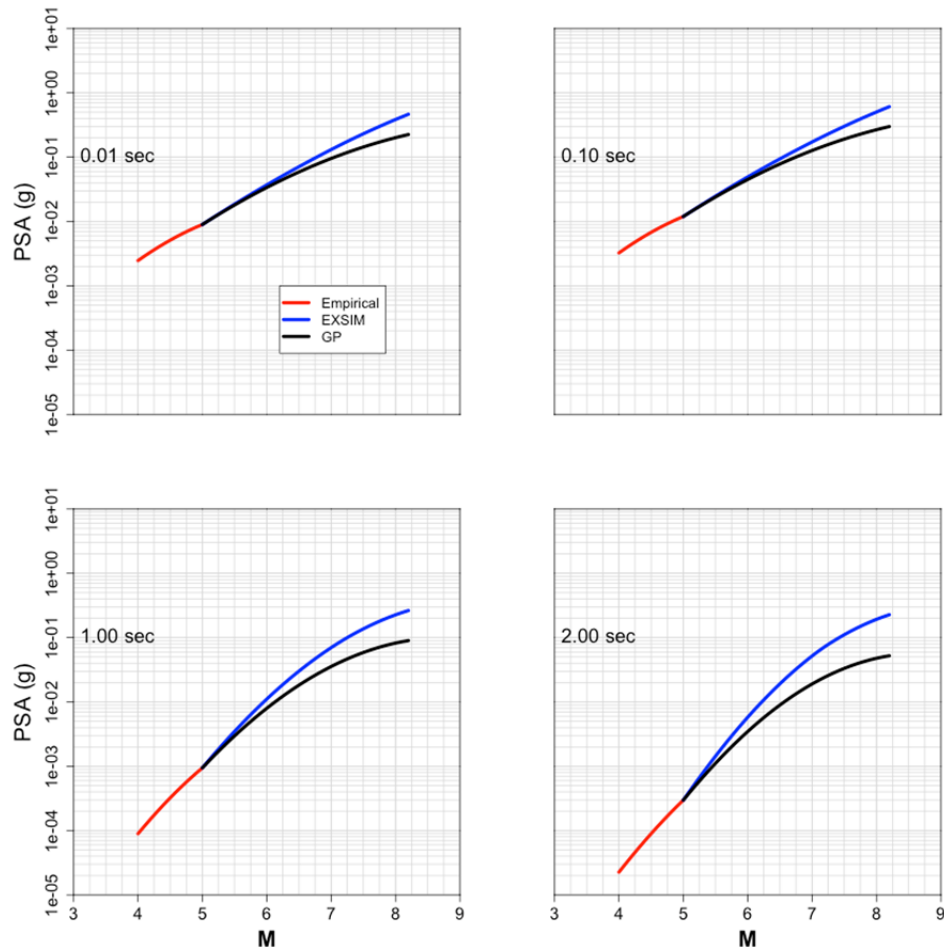


Figure 11.28 Magnitude scaling of median PSA model predictions plotted for the reference site conditions and $R_{Rup} = 100$ km.

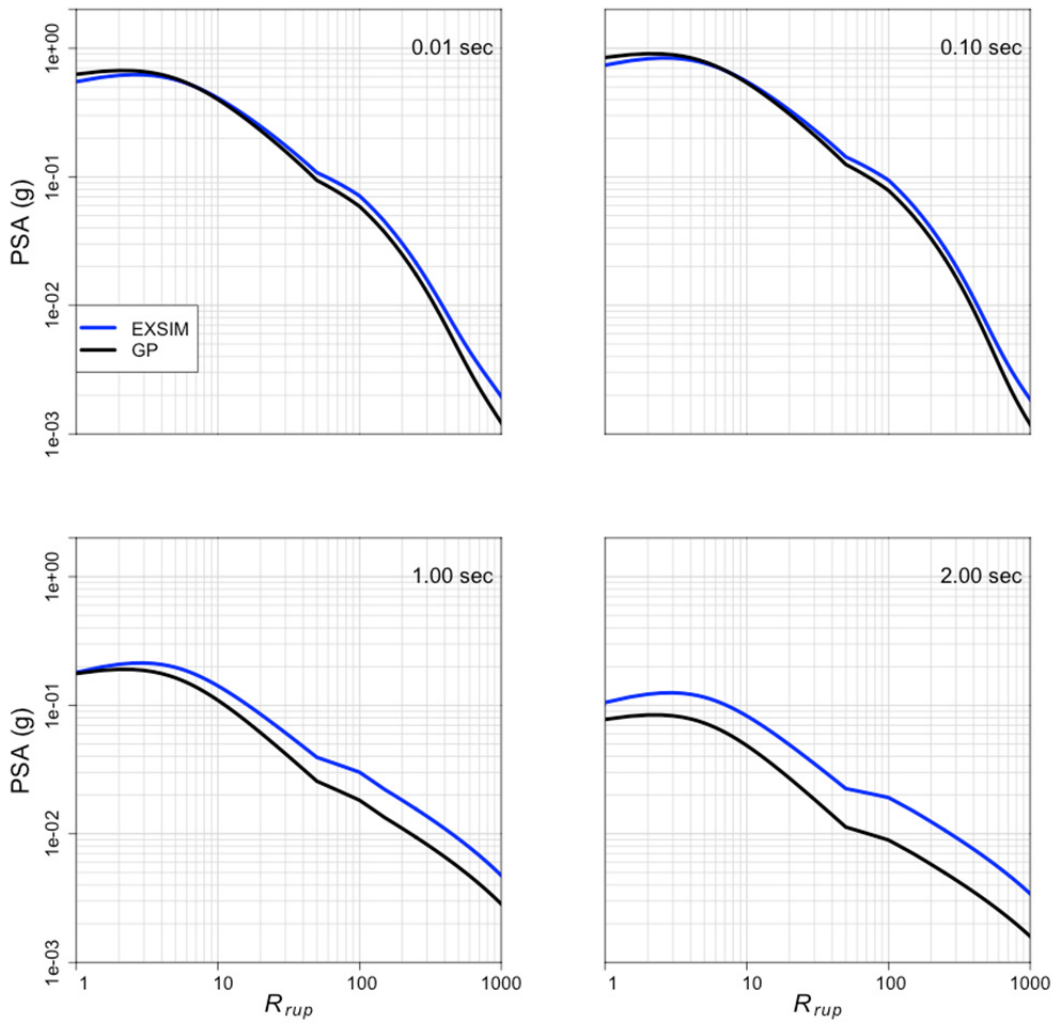


Figure 11.29 Distance scaling of median PSA model predictions plotted for the reference site conditions and $M = 6.5$.

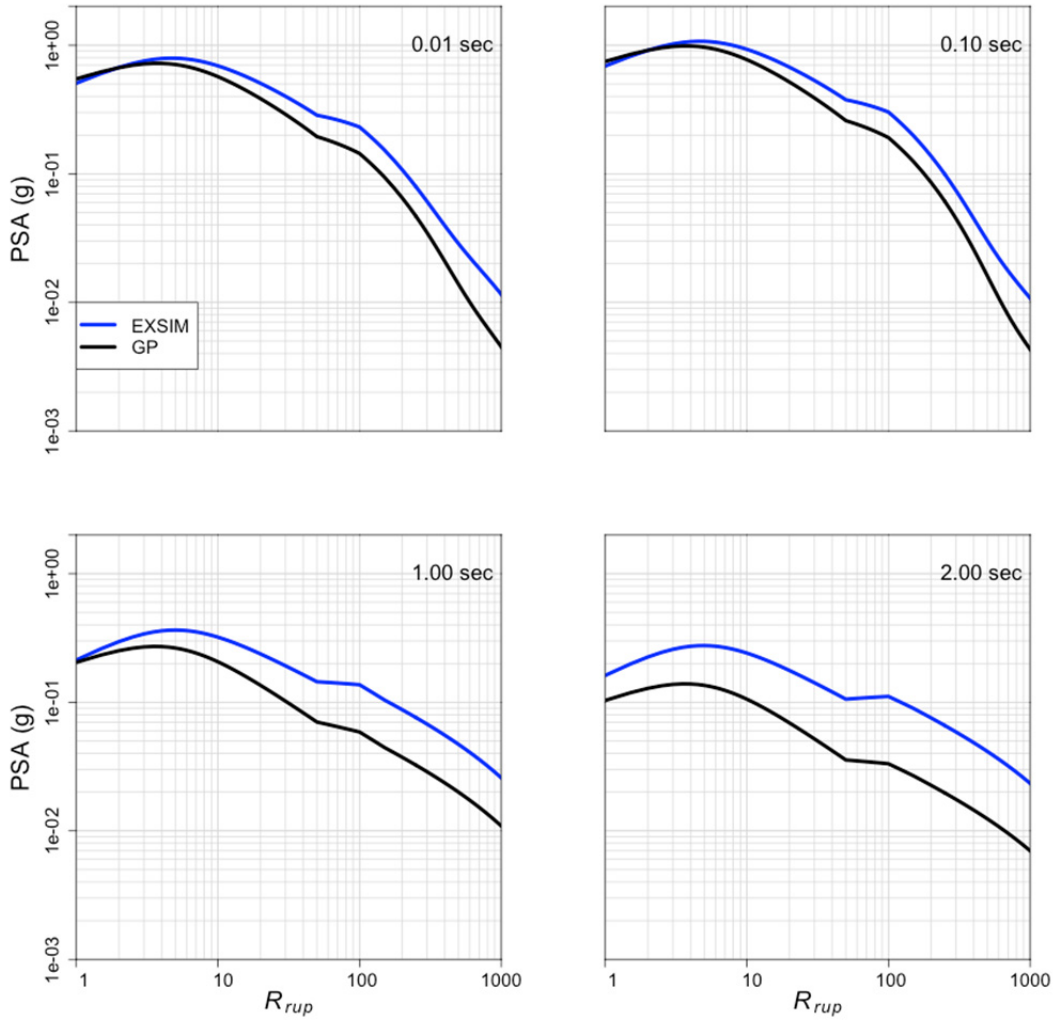


Figure 11.30 Distance scaling of median PSA model predictions plotted for the reference site conditions and $M = 7.5$.

11.6 CONCLUSIONS

The strong ground-motion data available in CENA [Goulet et al. 2014] have limitations on usable frequency band, source-to-site distance, magnitude (overall lack of large magnitude data), and reliable site characterization. These limitations required innovative development strategies to make the models applicable to $M4-8.2$ events in CENA. We have developed models based on the available empirical data where the data are reliable, and integrated both simple and more complex seismological theory and models to constrain the extrapolation of the models to large magnitudes. Development in FAS space allowed us to integrate these pieces without the complication of nonlinearity that PSA presents. For the empirical part of the FAS model, the NGA-East database [Goulet et al. 2014] was supplemented by data selected from the NGA-West2 database [Ancheta et al. 2014]. The combination of data from various path regions in CENA and from additional regions represented in the NGA-West2 database allowed a more stable and reliable regression model. A Bayesian regression that utilized a hierarchical model for event-, region- and station-specific mixed effects regression was employed to “borrow strength” from the larger dataset to constrain the model specific to CENA path region 2 (CNA). Two alternative GMMs were developed through this process, each reflecting epistemic differences in magnitude scaling from independent FF simulation methodologies from Atkinson and Assatourians [2015] and Graves and Pitarka [2015].

11.7 ACKNOWLEDGEMENTS

Constructive comments provided by Yousef Bozorgnia are greatly appreciated.

11.8 ELECTRONIC APPENDIX FOR CHAPTER 11

- 11A Model Output, magnitude scaling based on Graves and Pitarka [2015] (Excel workbook)
- 11B Model Output, magnitude scaling based on EXSIM, Atkinson and Assatourians [2015] (Excel workbook)

12 REFERENCES

- Abrahamson N.A., Silva W.J. (1997). Empirical response spectral attenuation relations for shallow crustal earthquakes, *Seismol. Res. Lett.*, 68(1): 94–127.
- Abrahamson N.A., Silva W.J. (2001). Empirical attenuation relations for central and eastern U.S. hard and soft rock and deep soil site conditions, *Seism. Res. Lett.* 72, 282.
- Abrahamson N.A., Silva W.J, Kamai R. (2014). Summary of the ASK14 ground-motion relation for active crustal regions, *Earth. Spectra*, 30(3): 1025–1055,
- Abrahamson N.A., Youngs R.R. (1992). A stable algorithm for regression analysis using the random effects model, *Bull. Seismol. Soc. Am.*, 82: 505–510.
- Al Atik L. (2014). *Personal Communication*.
- Al Atik L., Abrahamson N.A., Bommer J.J., Scherbaum F., Cotton F., Kuehn N. (2010). The variability of ground-motion prediction models and its components, *Seismol. Res. Lett.*, 81: 794–801.
- Al Atik L., Kottke A., Abrahamson N.A., Hollenback J. (2014). Kappa (k) scaling of ground-motion prediction equations using an inverse random vibration theory approach, *Bull. Seismol. Soc. Am.*, 104: 336–346.
- Al Atik L., Youngs R.R. (2014). Epistemic uncertainty for NGA-West2 models, *Earthq. Spectra*, 30(3): 1301–1318.
- Al Noman M.N. [2013]. *Ground Motion Modeling for Eastern North America: An Empirical Approach with the NGA-East Database*, M.S. thesis, University of Memphis, 54 pgs.
- Allen T., Cummins P., Dhu T., Schneider J. (2007). Attenuation of ground-motion spectral amplitudes in southeastern Australia, *Bull. Seismol. Soc. Am.*, 97: 1279–1292.
- Ancheta T., Darragh R.B., Stewart J.P., Seyhan E., Silva W.J., Chiou B.-S.J., Wooddell K., Graves R.W., Kottke A.R., Boore D.M., Kishida T., Donahue J. (2014). PEER NGAWest2 database, *Earthq. Spectra*, 30: 989–1006.
- Andrews D.J. (1980). A stochastic fault model: 1. Static case, *J. Geophys. Res.*, 85: 3867–3877.
- Anderson J.G., Hough S.E. (1984). A model for the shape of the Fourier amplitude spectrum of acceleration at high frequencies, *Bull. Seismol. Soc. Am.*, 74(5): 1969–1993.
- Assatourians K., Atkinson G.M. (2010). Database of processed time series and response spectra data for Canada: An example application to study of 2005 MN5.4 Riviere du Loup, Quebec, earthquake, *Seismol. Res. Lett.*, 81, 1013–1031.
- Atkinson G.M. (2001). An alternative to stochastic ground-motion relations for use in seismic hazard analysis in eastern North America, *Seismol. Res. Lett.*, 72: 299–306.
- Atkinson G.M. (2004). Empirical attenuation of ground-motion spectral amplitudes in southeastern Canada and the northeastern United States, *Bull. Seismol. Soc. Am.*, 94: 1079–1095.
- Atkinson G.M. (2005). Ground motions for earthquakes in southwestern British Columbia and northwestern Washington: crustal, in-slab, and offshore events, *Bull. Seismol. Soc. Am.*, 95: 1027–1044.
- Atkinson G.M. (2008). Ground motion prediction equations for eastern North America from a referenced empirical approach: Implications for epistemic uncertainty, *Bull. Seismol. Soc. Am.*, 98: 1304–1318.

- Atkinson G.M. (2010). Ground-motion prediction equations for Hawaii from a referenced empirical approach, *Bull. Seismol. Soc. Am.*, 101: 1304–1318.
- Atkinson G.M. (2012a). Evaluation of attenuation models for the northeastern United States/southeastern Canada, *Seismol. Res. Lett.* 83, 166–178.
- Atkinson G.M. (2012b). White paper on proposed ground-motion prediction equations (GMPEs) for 2015 national seismic hazard maps, http://www.seisemtoolbox.ca/GMPEtables2012/r12_GMPEs9b.pdf (last accessed in January 2015).
- Atkinson G.M. (2013). Empirical evaluation of aleatory and epistemic uncertainty in eastern ground motions, *Seismol. Res. Lett.*, 84: 130–138.
- Atkinson G.M., Assatourians K. (2010). Attenuation and source characteristics of the 23 June 2010 M 5.0 Val-des-Bois, Quebec, earthquake, *Seismol. Res. Lett.*, 81: 849–860.
- Atkinson G.M., Assatourians, K. (2015). Implementation and validation of EXSIM (a stochastic finite-fault ground-motion simulation algorithm) on the SCEC broadband platform, *Seismol. Res. Lett.*, 86(1): 48–60.
- Atkinson G.M., Babaie Mahani A. (2013). Estimation of moment magnitude from ground motions at regional distances, *Bull. Seismol. Soc. Am.*, 103: 107–116.
- Atkinson G.M., Bommer J.J., Abrahamson N.A. (2014). Alternative approaches to modeling epistemic uncertainty in ground motions in probabilistic seismic hazard analysis, *Seismol. Res. Lett.*, 85: 1141–1144.
- Atkinson G.M., Boore D.M. (1995). Ground motion relations for eastern North America, *Bull. Seismol. Soc. Am.*, 85: 17–30.
- Atkinson G.M., Boore D.M. (1997). Some comparisons between recent ground-motion relations, *Seismol. Res. Lett.*, 68(1): 24–40.
- Atkinson G.M., Boore D.M. (2006). Earthquake ground-motion prediction equations for eastern North America, *Bull. Seismol. Soc. Am.*, 96: 2181–2205.
- Atkinson G.M., Boore D.M. (2011). Modification to existing ground-motion prediction equations in light of new data, *Bull. Seismol. Soc. Am.*, 101(3): 1121–1135.
- Atkinson G.M. Boore D.M. (2014). The attenuation of Fourier amplitudes for rock sites in eastern North America, *Bull. Seismol. Soc. Am.*, 104: 513–528.
- Atkinson G.M., Boore D.M., Assatourians K., Campbell K.W., Motazedian D. (2009). A guide to differences between stochastic point-source and stochastic finite-fault simulations, *Bull. Seismol. Soc. Am.*, 99: 3192–3201.
- Atkinson G.M., Greig D., Yenier E. (2014). Estimation of moment magnitude (M) for small events ($M < 4$) on local networks, *Seismol. Res. Lett.*, 85: 1116–1124.
- Atkinson G.M., Mereu R. (1992). The shape of ground motion attenuation curves in southeastern Canada, *Bull. Seismol. Soc. Am.*, 82: 2014–2031.
- Atkinson G.M., Morrison M. (2009). Regional variability in ground motion amplitudes along the west coast of North America, *Bull. Seismol. Soc. Am.*, 99: 2393–2409.
- Atkinson G.M., Motazedian D. (2013). Ground-motion amplitudes for earthquakes in Puerto Rico, *Bull. Seismol. Soc. Am.*, 103: 1846–1859.
- Atkinson G.M., Silva W.J. (1997). An empirical study of earthquake source spectra for California earthquakes, *Bull. Seismol. Soc. Am.*, 87: 97–113.
- Atkinson G.M., Silva W.J. (2000). Stochastic modeling of California ground motions, *Bull. Seismol. Soc. Am.*, 90: 255–274.
- Atkinson G.M., Wald D.J. (2007). “Did you feel it?” intensity data: a surprisingly good measure of earthquake ground motion, *Seismol. Res. Lett.*, 78: 362–368.
- Babaie Mahani A., Atkinson G.M. (2012). Evaluation of functional forms for the attenuation of small-to-moderate-earthquake response spectral amplitudes in North America, *Bull. Seismol. Soc. Am.* 102: 2714–2726.

- Babaie Mahani A., Atkinson G.M. (2013). Regional differences in ground-motion amplitudes of small-to-moderate earthquakes across North America, *Bull. Seismol. Soc. Am.*, 103(5): 2604–2620.
- Bakun W.H. Hopper M.G. (2004). Magnitudes and locations of the 1811–1812 New Madrid, Missouri, and the 1886 Charleston, South Carolina, Earthquakes, *Bull. Seismol. Soc. Am.*, 94: 64–75.
- Baltay A.S., Hanks T.C. (2014). Understanding the magnitude dependence of PGA and PGV in NGA-West2 Data, *Bull. Seismol. Soc. Am.*, 104: 2851–2865.
- Bent A.L. (1992). A re-examination of the 1925 Charlevoix, Quebec, earthquake, *Bull. Seismol. Soc. Am.*, 82: 2097–2113.
- Bent, A.L. (1995). A complex double-couple source mechanism for the Ms 7.2 1929 Grand Banks earthquake, *Bull. Seismol. Soc. Am.*, 85: 1003–1020.
- Beresnev I.A., Atkinson G.M. (1999). Generic finite-fault model for ground motion prediction in eastern North America, *Bull. Seismol. Soc. Am.*, 89: 608–625.
- Beresnev I.A., Atkinson G.M. (2002). Source parameters of earthquakes in eastern and western North America based on finite-fault modeling, *Bull. Seismol. Soc. Am.*, 92: 695–710.
- Boatwright J., Seekins L. (2011). Regional spectral analysis of three moderate earthquakes in northeastern North America, *Bull. Seismol. Soc. Am.*, 101: 1769–1782.
- Bodin, P., Malagnini L., Akinci A. (2004). Ground-motion scaling in the Kachchh Basin, India, deduced from aftershocks of the 2001 Mw 7.6 Bhuj earthquake, *Bull. Seismol. Soc. Am.*, 94: 1658–1669.
- Bommer, J., Stafford P., Alarcon J., Akkar S. (2007). The influence of magnitude range on empirical ground-motion prediction, *Bull. Seismol. Soc. Am.*, 97: 2152–2170.
- Boore D.M. (1983). Stochastic simulation of high-frequency ground motions based on seismological models of the radiated spectra, *Bull. Seismol. Soc. Am.*, 73: 1865–1894.
- Boore D.M. (2003). Prediction of ground motion using the stochastic method, *Pure Appl. Geophys.* 160: 635–676.
- Boore D.M. (2005). SMSIM—Fortran programs for simulating ground motions from earthquakes: Version 2.3—A revision of OFR 96-80-A, U.S. Geological Survey open-file report, *U. S. Geological Survey Open-File Report 00-509*, revised 15 August 2005, 55 pgs.
- Boore D.M. (2009). Comparing stochastic point-source and finite-source ground-motion simulations: SMSIM and EXSIM, *Bull. Seismol. Soc. Am.*, 99: 3202–3216.
- Boore D.M. (2010). Orientation-independent, non geometric-mean measures of seismic intensity from two horizontal components of motion, *Bull. Seismol. Soc. Am.*, 100: 1830–1835.
- Boore D.M. (2012). Updated determination of stress parameters for nine well-recorded earthquakes in Eastern North America, *Seismol. Res. Lett.*, 83: 190–199.
- Boore D.M. (2013). The uses and limitations of the square-root impedance method for computing site amplification, *Bull. Seismol. Soc. Am.*, 103: 2356–2368.
- Boore D.M. (2015). Adjusting PSA amplitudes to $V_{s30} = 3.0$ km/sec, PEER Report, *in preparation*.
- Boore D.M., Atkinson G.M. (1987). Stochastic prediction of ground motion and spectral response parameters at hard-rock sites in eastern North America, *Bull. Seismol. Soc. Am.*, 77(2): 440–467.
- Boore D.M., Boatwright J. (1984). Average body-wave radiation coefficients, *Bull. Seismol. Soc. Am.*, 74: 1615–1621.
- Boore D.M., Campbell K.W., Atkinson G.M. (2010). Determination of stress parameters for eight well-recorded earthquakes in eastern North America, *Bull. Seismol. Soc. Am.*, 100: 1632–1645.
- Boore D.M., Di Alessandro C., Abrahamson N.A. (2014a). A generalization of the double-corner-frequency source spectral model and its use in the SCEC BBP validation exercise, *Bull. Seismol. Soc. Am.*, 104: 2387–2398.
- Boore D.M., Joyner W.B. (1997). Site amplifications for generic rock sites, *Bull. Seismol. Soc. Am.*, 87: 327–341.
- Boore D.M., Stewart J.P., Seyhan E., Atkinson G.M. (2014b). NGA-West2 equations for predicting response spectral accelerations for shallow crustal earthquakes, *Earthq. Spectra*, 30: 1057–1085.

- Boore D.M., Thompson E.M. (2014). Path durations for use in the stochastic-method simulation of ground motions, *Bull. Seismol. Soc. Am.*, 104: 2541–2552. DOI: 10.1785/0120140058
- Boore D.M., Thompson E.M. (2015). Revisions to some parameters used in stochastic-method simulations of ground motion, *Bull. Seismol. Soc. Am.*, Vol. 105 (in press).
- Boore, D.M., Watson-Lamprey J., Abrahamson N.A. (2006). Orientation-independent measures of ground motion, *Bull. Seismol. Soc. Am.*, 96: 1502–1511.
- Bora S.S., Scherbaum F., Kuehn N., Stafford P. (2014) Fourier spectral- and durations models for the generation of response spectra adjustable to different source-, propagation-, and site conditions, *Bull. Earthq. Eng.*, 12: 467–493.
- Bozorgnia Y., Abrahamson N.A., Al Atik L., Ancheta T.D., Atkinson G.M., Baker J., Baltay A., Boore D.M., Campbell K.W., Chiou B.-S.J., Darragh R.B., Day S., Donahue J., Graves R.W., Gregor N., Hanks T., Idriss I.M., Kamai R., Kishida T., Kottke A., Mahin S.A., Rezaeian S., Rowshandel B., Seyhan E., Shahi S., Shantz T., Silva W.J., Spudich P., Stewart J.P., Watson-Lamprey J., Wooddell K.E., Youngs R.R. (2014). NGA-West2 research project, *Earthq. Spectra*, 30(3): 973–987.
- Brune J.N. (1970). Tectonic stress and the spectra of seismic shear waves from earthquakes, *J. Geophys. Res.*, 75: 4997–5009.
- Brune, J. (1971). Correction, *J. Geophys. Res.*, 76: 5002.
- BSSC (2009). NEHRP Recommended Seismic Provisions for New Buildings and Other Structures (FEMA P-75), 2009 ed., Building Seismic Safety Council, Washington, D.C.
- Burger R.W., Somerville P.G., Barker J.S., Herrmann R.B., Helmberger D.V. (1987). The effect of crustal structure on strong ground motion attenuation relations in eastern North America, *Bull. Seismol. Soc. Am.*, 77: 420–439.
- Campbell, K. W. (1981). A ground motion model for the central United States based on near source acceleration data, in Proceedings of the Conference on Earthquakes and Earthquake Engineering—the Eastern United States, Ann Arbor Science Publishers, Ann Arbor, Michigan, Vol. 1, 213–232.
- Campbell K.W. (2002). Development of semi-empirical attenuation relationships for the CEUS, Report to U.S. Geological Survey, *NEHRP Award No.01HQGR0011*.
- Campbell K.W. (2003). Prediction of strong ground motion using the hybrid empirical method and its use in the development of ground-motion (attenuation) relations in eastern North America, *Bull. Seismol. Soc. Am.*, 93: 1012–1033.
- Campbell K.W. (2007). Validation and update of hybrid empirical ground motion (attenuation) relations for the CEUS, report to the U.S. Geological Survey, *National Earthquake Hazards Reduction External Research Program, Award No. 05HQGR0032*.
- Campbell K.W. (2008). Hybrid empirical ground motion model for PGA and 5% damped linear elastic response spectra from shallow crustal earthquakes in stable continental regions: Example for eastern North America, *Proceedings, 14th World Conference on Earthquake Engineering*, Paper No. S03-001, Beijing, China.
- Campbell K.W. (2009). Estimates of shear-wave Q and κ_0 for unconsolidated and semiconsolidated sediments in eastern North America, *Bull. Seismol. Soc. Am.*, 99: 2365–2392.
- Campbell K.W. (2011). Ground motion simulation using the hybrid empirical method: Issues and insights, in *Earthquake Data in Engineering Seismology: Predictive Models, Data Management and Networks*, S. Akkar, P. Gulkan, T. van Eck (eds.), Geotechnical, Geological and Earthquake Engineering Series, Springer, London, 14: 81–95.
- Campbell K.W. (2014). An evaluation of eastern North America ground-motion models developed using the hybrid empirical method, *Bull. Seismol. Soc. Am.*, 104: 347–359.
- Campbell K.W., Bozorgnia Y. (2008). NGA ground motion model for the geometric mean horizontal component of PGA, PGV, PGD and 5% damped linear-elastic response spectra for periods ranging from 0.01 to 10.0 s, *Earthq. Spectra*, 24: 139–171.

- Campbell K.W., Bozorgnia Y. (2014). NGA-West2 ground motion model for the average horizontal components of PGA, PGV, and 5% damped linear acceleration response spectra, *Earthq. Spectra*, 30(3): 1087–1115.
- Campbell K.W., Hashash Y.M.A., Kim B., Kottke A.R., Rathje E.M., Silva W.J., Stewart J.P. (2014). Reference-rock site conditions for Central and Eastern North America: Part II – Attenuation definition, *PEER Report 2014-12*, Pacific Earthquake Engineering Research Center, University of California, Berkeley, CA, 80 pgs.
- Chapman M.C. (2013). On the rupture process of the 23 August 2011 Virginia earthquake, *Bull. Seismol. Soc. Am.*, 103: 613–628.
- Chapman M.C., Godbee R.W. (2012). Modeling geometrical spreading and the relative amplitudes of vertical and horizontal high-frequency ground motions in eastern North America, *Bull. Seismol. Soc. Am.*, 102: 1957–1975.
- Chapman M.C., Pezeshk S., Hosseini M., Conn A. (2014). Regional study of Fourier amplitude drop of *Lg*-wave acceleration in central United States, *Proceedings, Seismological Society of America Annual Meeting*, Anchorage, AK.
- Chiou B.-S.J., Youngs R.R. (2014). Update of the Chiou and Youngs NGA model for the average horizontal component of peak ground motion and response spectra, *Earthq. Spectra*, 30(3): 1117–1153.
- Chun K., West G.F., Kokoski R.J., Samson C. (1987) A novel technique for measuring *Lg* attenuation results from Eastern Canada Between 1 to 10 Hz, *Bull. Seismol. Soc. Am.*, 77(2): 398–419.
- Cramer C.H., Al Noman M.N., DeShon H.R. (2014). Improving regional ground motion attenuation boundaries and models using EarthScope USArray data for use in the National Seismic Hazards Mapping Project, *Final Technical Report to the USGS under grant G12AP20018*, 19 pgs.
- Cramer C.H., Boyd O.S. (2014). Why the New Madrid earthquakes are M7-8 and the Charleston earthquake is ~M7, *Bull. Seismol. Soc. Am.*, 104: 2884–2903.
- Cramer C.H., Kumar A. (2003). 2001 Bhuj, India earthquake engineering seismoscope recordings and eastern North America ground-motion attenuation relations, *Bull. Seismol. Soc. Am.*, 93, 1390–1394.
- Cramer C.H., Kutliroff J.R., Dangkua D.T. (2011). *Next Generation Attenuation East Initial Flat Files for Eastern North America*, Report to PEER accompanying NGA-East flat files and time series under subagreement 7140,
- Cramer, C.H., Kutliroff, J.R., Dangkua, D.T., and Al Noman, M.N. (2013). *Completing the NGA-East CENA/SCR Ground Motion Database*, Report prepared for the Pacific Earthquake Engineering Research Center by the Center for Earthquake Research and Information, University of Memphis under Subagreement 7140, April 5, 2013, 18 pgs.,
<https://umdrive.memphis.edu/ccramer/public/NGAeast/> Documentation/NGAEastDbPEERFinalReport.docx
- Der Kiureghian A. (1980). Structural response to stationary excitation, *J. Eng. Mech. Div.*, EM6: 1195–1213.
- Douglas J. (2003). Earthquake ground motion estimation using strong-motion records: A review of equations for the estimation of peak ground acceleration and response spectral ordinates, *Earth-Science Reviews*, 61(1–2): 43–104.
- Douglas J. (2004). An investigation of analysis of variance as a tool for exploring regional differences in strong ground motions, *J. Seismol.*, 8: 484–496.
- Douglas J. (2011). Ground motion prediction equations 1964–2010, *PEER Report 2011/102*, Pacific Earthquake Engineering Research Center, University of California, Berkeley, CA.
- Douglas J., Bungum H., Scherbaum F. (2006). Ground-motion prediction equations for southern Spain and southern Norway obtained using the composite model perspective. *J. Earthq. Eng.*, 10: 33–72.
- Dreger D.S., Beroza G.C., Day S.M., Goulet C.A., Jordan T.H., Spudich P.A., Stewart J.P. (2015). Validation of the SCEC broadband platform v14.3 simulation methods using pseudospectral acceleration data, *Seismol. Res Lett.* 86: 39–47.
- Dreiling J., Isken M.P., Mooney W.D., Chapman M.C., Godbee R.W. (2014). *NGA-East regionalization report: comparison of four crustal regions within central and eastern north america using waveform modeling and 5%-*

- damped pseudo-spectral acceleration response, *PEER Report No. 2014/15*, Pacific Earthquake Engineering Research Center, University of California, Berkeley, CA.
- Erickson D., McNamara D.E., Benz H.M. (2004). Frequency-dependent $L_g Q$ within the continental United States. *Bull. Seismol. Soc. Am.*, 94: 1630–1643.
- EPRI (1993). Guidelines for determining design basis ground motions, *EPRI TR-102293*, Vol 1–5, Electric Power Research Institute, Palo Alto, CA.
- EPRI (2004). CEUS ground motion project final report. *Technical Report 100968*,. Electric Power Research Institute, Dominion Energy, Glen Allen, VA, Entergy Nuclear, Jackson, MS, and Exelon Generation Company, Kennett Square, PA. Palo Alto, CA
- EPRI (2006). Program on Technology Innovation: Truncation of the Lognormal Distribution and Value of the Standard Deviation for Ground Motion Models in the Central and Eastern United States, EPRI Report 1013105, Technical Update, February, Palo Alto, Calif.
- EPRI (2013). EPRI 2004-2006 Ground-Motion Model (GMM) Review Project 3002000717, Final Report. June 2013, Electric Power Research Institute, Palo Alto, CA.
- EPRI/DOE/NRC (2012). Technical Report: Central and Eastern United States Seismic Source Characterization for Nuclear Facilities, NUREG-2115.
- Fatehi A., Herrmann R.B. (2008). High-frequency ground-motion scaling in the Pacific Northwest and in northern and central California, *Bull. Seismol. Soc. Am.*, 98: 709–721.
- Frankel A. (1995). Simulating strong motions of large earthquakes using recordings of small earthquakes: the Loma Prieta mainshock as a test case, *Bull. Seismol. Soc. Am.*, 85: 1144–1160.
- Frankel A. (2009). A constant stress-drop model for producing broadband synthetic seismograms—Comparison with the Next Generation Attenuation Relations, *Bull. Seismol. Soc. Am.*, 99: 664–681.
- Frankel A. (2013). Rupture history of the 2011 M9 Tohoku Japan earthquake determined from strong-motion and high-rate GPS recordings, sub-events radiating energy in different frequency bands, *Bull. Seismol. Soc. Am.*, 103: 1290–1306.
- Frankel A. (2015). Decay of S-wave amplitudes with distance for earthquakes in the Charlevoix, Quebec area: effects of radiation pattern and directivity, *Bull. Seismol. Soc. Am.*, DOI.101785/0120140249.
- Frankel A., Mueller, C. Barnhard T., Perkins D., Leyendecker E.V., Dickman N., Hanson S., Hopper M. (1996). National seismic hazard maps—Documentation June 1996, *U.S. Geological Survey Open File Report 96-532*, Menlo Park, CA, 110 pgs.
- Ghodrati G., Shahjouei A., Saadat S., Ajallooeian M. (2011). Implementation of genetic algorithm, MLFF neural network, principal component analysis and wavelet packet transform in generation of compatible seismic ground acceleration time histories, *J. Earthq. Eng.*, 15(1): 50–76.
- Goldstein P., Dodge D., Firpo M., Minner L. (2003). SAC2000: Signal processing and analysis tools for seismologists and engineers, Invited contribution to *The IASPEI International Handbook of Earthquake and Engineering Seismology*, Edited by W.H.K. Lee, H. Kanamori, P.C. Jennings, and C. Kisslinger (eds.), Academic Press, London.
- Goulet C.A., Boore D.M. (2014). *Personal Communication*.
- Goulet C.A., Abrahamson N.A., Somerville P.G., Wooddell K.E. (2015). The SCEC broadband platform validation exercise: Methodology for code validation in the context of seismic hazard analyses, *Seismol. Res. Lett.*, 86(1): 17–26.
- Goulet C.A., Kishida T. Ancheta T D., Cramer C.H., Darragh R.B., Silva W.J., Hashash Y.M.A., Harmon J., Stewart J.P., Wooddell K.E., Youngs R.R. (2014). PEER NGA-East database, *PEER Report 2014/17*, Pacific Earthquake Engineering Research Center, University of California, Berkeley, CA.

- Graizer V. (2014a). Updated Graizer-Kalkan ground-motion prediction equations for Western United States, *Proceedings, 10th National Conference on Earthquake Engineering*, Earthquake Engineering Research Institute, Anchorage, AK.
- Graizer V. (2014b). Preliminary ground motion prediction equations for the Central and Eastern United States. Abstract, *American Geophysical Union Annual Meeting*, San Francisco, CA.
- Graizer V. Kalkan E. (2007). Ground-motion attenuation model for peak horizontal acceleration from shallow crustal earthquakes, *Earthq. Spectra*, 23(3): 585–613.
- Graizer V. Kalkan E. (2009). Prediction of response spectral acceleration ordinates based on PGA attenuation, *Earthq. Spectra*, 25(1): 39–69.
- Graizer V. Kalkan E. (2011). Modular filter-based approach to ground-motion attenuation modeling, *Seismol. Res. Lett.*, 82(1): 21–31.
- Graizer V. Kalkan E. (2015). Update of the Graizer-Kalkan ground-motion prediction equations for shallow crustal continental earthquakes, *U.S. Geological Survey Open-File Report 2015-1009*, <http://dx.doi.org/10.3133/ofr20151009>.
- Graves R.W., Pitarka A. (2004). Broadband time history simulation using a hybrid approach, *Proceedings, 13th World Conference on Earthquake Engineering*, Paper No., 1098. Vancouver, B.C., Canada.
- Graves R.W., Pitarka A. (2010). Broadband ground-motion simulation using a hybrid approach, *Bull. Seismol. Soc. Am.*, 100: 1197–1210.
- Graves R.W., Pitarka A. (2015). Refinements to the Graves and Pitarka (2010) broadband ground motion simulation method, *Seismol. Res. Lett.*, 86(1) 75–80.
- Gregor N., Abrahamson N.A., Atkinson G.M., Boore D.M., Bozorgnia Y., Campbell K.W., Chiou B.-S.J., Idriss I.M., Kamai R., Seyhan E., Silva W.J., Stewart J.P., Youngs R.R. (2014). Comparison of NGA-West 2 GMPEs, *Earthq. Spectra*, 30: 1179–1197.
- Hanks T.C. (1982). f_{\max} , *Bull. Seismol. Soc. Am.*, 72: 1867–1879.
- Hanks T.C., Bakun W.H. (2002). A bilinear source-scaling model for M–log A observations of continental earthquakes, *Bull. Seismol. Soc. Am.*, 92: 1841–1846.
- Hanks T.C., Kanamori H. (1979). A moment magnitude scale, *J. Geophys. Res.*, 84: 2348–2350.
- Hanks T.C., McGuire R.K. (1981). The character of high–frequency strong ground motion, *Bull. Seismol. Soc. Am.*, 71: 2071–2095.
- Hartzell S.W., Langer C., Mendoza C. (1994). Rupture histories of Eastern North American earthquakes, *Bull. Seismol. Soc. Am.*, 84(6): 1703–1724.
- Hartzell S.H., Frankel A., Liu P., Zeng Y., Rahman S. (2011). Model and parametric uncertainty in source-based kinematic models of earthquake ground motion, *Bull. Seismol. Soc. Am.*, 101: 2431–2452.
- Hartzell S.H., Guatteri M., Mariagiovanna G., Mai P.M., Liu P.C., Fisk M. (2005). Calculation of broadband time histories of ground motion, Part II: Kinematic and dynamic modeling using theoretical Green’s functions and comparison with the 1994 Northridge earthquake, *Bull. Seismol. Soc. Am.*, 95: 614–645.
- Hartzell S.H., Harmsen S., Frankel A., Larsen S. (1999). Calculation of broadband time histories of ground motion: Comparison of methods and validation using strong motion from the 1994 Northridge earthquake, *Bull. Seismol. Soc. Am.*, 89: 1484–1504.
- Hashash Y.M.A., Kottke A.R., Stewart J.P., Campbell K.W., Kim B., Rathje E.M., Silva W.J. (2014a). Reference-rock site conditions for Central and Eastern North America: Part I – Velocity Definition, *PEER Report 2014-No. 11*, Pacific Earthquake Engineering Research Center, University of California, Berkeley, CA, 188 pgs.
- Hashash Y.M.A., Kottke A.R., Stewart J.P., Campbell K.W., Kim B., Rathje E.M., Silva W.J. (2014b). Reference rock site condition for central and eastern North America, *Bull. Seismol. Soc. Am.*, 104: 684–701.
- Hassani B. Atkinson G.M. (2014). Referenced empirical ground-motion model for eastern North America, *Seismol. Res. Lett.* (in review).

- Herrmann R.B. (1985). An extension of random vibration theory estimates of strong ground motion to large distances, *Bull. Seismol. Soc. Am.*, 75: 1447–1453.
- Hough S.E. (2014a). Earthquake intensity distributions: a new view (abstract), *Seismol. Res. Lett.*, 85: 526–527.
- Hough S.E. (2014b). Shaking from injection-induced earthquakes in the central and eastern United States, *Bull. Seismol. Soc. Am.*, 104: 2619–2626.
- Idriss I.M. (2014). An NGA-West2 empirical model for estimating the horizontal spectral values generated by shallow crustal earthquakes, *Earth. Spectra*, 301(3): 1155–1177.
- Joyner W.B., Boore D.M. (1993). Methods for regression analysis of strong motion data, *Bull. Seismol. Soc. Am.*, 83: 469–487.
- Joyner W.B., Boore D.M. (1994). Errata: Methods for regression analysis of strong-motion data, *Bull. Seismol. Soc. Am.* 84: 955-956
- Kamai R., Abrahamson N.A., Silva W.J. (2013). Nonlinear horizontal site response for the nga-west2 project, *PEER Report 2013/12*, Pacific Earthquake Engineering Research Center, University of California, Berkeley, CA, 69 pgs.
- Kottke A., Rathje E., Boore D.M., Thompson E., Hollenback J., Kuehn N., Goulet C.A., Abrahamson N.A., Bozorgnia Y., Der Kiureghian A., Silva W.J., Wang X. (2015). Selection of random vibration procedures for the NGA East Project, PEER report, *in preparation*.
- Kottke A.R., Rathje E.M. (2008). Technical manual for Strata, *PEER Report 2008/10*, Pacific Earthquake Engineering Research Center, University of California, Berkeley, CA, 95 pgs.
- Ktenidou O.J., Cotton F., Abrahamson N.A., Anderson J.G. (2014). Taxonomy of κ : A review of definitions and estimation approaches targeted to applications, *Seismol. Res. Lett.*, 85: 135–146.
- Leonard M. (2010). Earthquake fault scaling self-consistent relations of rupture length, width, average displacement and moment release, *Bull. Seismol. Soc. Am.*, 100: 1971–1988.
- Liu P., Archuleta R., Hartzell S.H. (2006). Prediction of broadband ground motion time histories: Frequency method with correlation random source parameters, *Bull. Seismol. Soc. Am.*, 96: 2118–2130.
- Maechling P.J., Silva F., Callaghan S., Jordan T.H. (2015). SCEC broadband platform: system architecture and software implementation, *Seismol. Res. Lett.*, 86(1): 27–38.
- Mai P.M., Beroza G.C. (2000). Source scaling properties from finite-fault rupture models, *Bull. Seismol. Soc. Am.*, 90(3): 604–615.
- Mai P.M., Beroza G.C. (2002). A spatial random field model to characterize complexity in earthquake slip, *J. Geophys. Res.*, 107(B11): 1–21.
- Mai P.M., Imperatori W., Olsen K.B. (2010). Hybrid broadband ground-motion simulations: combining long-period deterministic synthetics with high-frequency multiple S-to-S backscattering, *Bull. Seismol. Soc. Am.*, 100(5): 2124–2142.
- Mai P.M., Spudich P., Boatwright J. (2005). Hypocenter locations in finite-source rupture models, *Bull. Seismol. Soc. Am.*, 95: 965–980.
- Malagnini L., Mayeda K., Uhrhammer R., Akinci A., Herrmann R.B. (2007). A regional ground-motion excitation/attenuation model for the San Francisco region, *Bull. Seismol. Soc. Am.*, 97: 843–862.
- Mena B., Mai P.M., Olsen K.B., Purvance M.D., Brune J.N. (2010). Hybrid broadband ground-motion simulation using scattering Green's functions: Application to large-magnitude events, *Bull. Seismol. Soc. Am.*, 100(5A): 2143–2162.
- Mitchell B.J., Hwang H J. (1987). Effect of low Q sediments and crustal Q on Lg attenuation in the United States, *Bull. Seismol. Soc. Am.*, 77: 2095–2123.
- Mooney W., Chulick D.G., Ferguson A., Radakovich A., Kitaura K., Detweiler S. (2012). NGA-East: Crustal Regionalization. *NGA-East Working Meeting: Path and Source Issues*, Oct. 16 2012, University of California, Berkeley, CA.

- Mooney W. (2013). *Personal Communication*.
- Motazedian D., Atkinson G.M. (2005). Stochastic finite-fault modeling based on a dynamic corner frequency, *Bull. Seismol. Soc. Am.*, 95: 995–1010.
- NEHRP (2000). *NEHRP Recommended provisions for seismic regulations for new buildings and other structures, Part 1, Provisions, FEMA 368*, Federal Emergency Management Agency, Washington, D.C.
- Nuttli O.W., Herrmann R.B. (1984). Ground motion of Mississippi Valley earthquakes, *J. Tech. Topics Civil Eng.*, 110: 54–69.
- Ogweno L.P., Cramer C.H. (2014). Regression relationships between modified Mercalli intensities and ground motion parameters (abstract), *Program and Abstracts, 86th annual meeting, Eastern Section of the Seismological Society of America*, Charleston, SC.
- Ojo S., Mereu R. (1986). The effect of random velocity functions on the travel times and amplitudes of seismic waves, *Geophys. J. Royal Astro. Soc.*, 84: 607–618.
- Olsen K.B. (2012). 3D broadband ground motion estimation for large earthquakes on the New Madrid seismic zone, Central US, *Final Report to the U.S. Geological Survey, Award # G10AP00007*.
- Olsen K.B., Takedatsu R. (2015). The SDSU broadband ground-motion generation module BBtoolbox Version 1.5. *Seismol. Res. Lett.*, 86(1): 81–88.
- Ou G.-B., Herrmann R.B. (1990). A statistical model for ground motion produced by earthquakes at local and regional distances, *Bull. Seismol. Soc. Am.*, 80: 1397–1417.
- Pasyanos M.E. (2011). A case for the use of 3D attenuation models in ground-motion and seismic-hazard assessment, *Bull. Seismol. Soc. Am.*, 101: 1965–1970.
- Pasyanos M.E. (2013). A lithospheric attenuation model of North America, *Bull. Seismol. Soc. Am.*, 103: 3321–3333.
- Petersen M.D., Moschetti M.P., Powers P.M., Mueller C.S., Haller K M., Frankel A.D., Zeng Y., Rezaeian S., Harmsen S.C., Boyd O.S., Field N., Chen R., Rukstales K.S., Luco N., Wheeler R.L., Williams R.A., Olsen A.H (2014). Documentation for the 2014 update of the United States national seismic hazard maps: *U.S. Geological Survey Open-File Report 2014–1091*, 243 pgs.
- Pezeshk S., Zandieh A., Tavakoli B. (2011). Hybrid empirical ground-motion prediction equations for eastern North America using NGA models and updated seismological parameters, *Bull. Seismol. Soc. Am.*, 101: 1859–1870.
- Power M., Chiou B.-S.J., Abrahamson N.A., Bozorgnia Y., Shantz T., Roblee C. (2008). An overview of the NGA project, *Earthq. Spectra*, 24: 3–21.
- Raoof M., Herrmann R.R., Malagnini L. (1999). Attenuation and excitation of three-component ground motion in southern California, *Bull. Seismol. Soc. Am.*, 89: 888–902.
- Ripperger J., Mai P.M. (2004). Fast computation of static stress changes on 2D faults from final slip distributions, *Geophys. Res. Lett.*, 31: L18610.
- Scherbaum F., Bommer J.J., Bungum H., Cotton F., Abrahamson N.A. (2005). Composite ground motion models and logic trees: Methodology, sensitivities, and uncertainties, *Bull. Seismol. Soc. Am.*, 95: 1575–1593.
- Scherbaum, F., Cotton F., Staektk H. (2006). The estimation of minimum-misfit stochastic model from empirical ground-motion prediction equations, *Bull. Seismol. Soc. Am.* 96: 417–445.
- Scherbaum F., Schmedes J., Cotton F. (2004). On the conversion of source-to-site distance measures for extended earthquake source models, *Bull. Seismol. Soc. Am.*, 94: 1053–1069.
- Schneider J.F., Silva W.J., Stark C.L. (1993). Ground motion model for the 1989 M 6.9 Loma Prieta earthquake including effects of source, path and site, *Earthq. Spectra*, 9(2): 251–287.
- Shahjouei A., Pezeshk S. (2013). Producing broadband synthetic time histories for Central and Eastern North America, *Proceedings, Structures Congress 2013*, pp. 1767–1776.
- Shahjouei A., Pezeshk S. (2014). Synthetic seismogram simulations using a hybrid broadband ground-motion simulation approach: Application to central and eastern United States, *Bull. Seismol. Soc. Am.* (accepted).

- Siddiqi J., Atkinson G.M. (2002). Ground motion amplification at rock sites across Canada, as determined from the horizontal-to-vertical component ratio, *Bull. Seismol. Soc. Am.*, 92: 877–884.
- Silva W.J., Gregor N., Darragh R.B. (2002). Development of regional hard rock attenuation relations for central and eastern North America, *Report to Pacific Engineering and Analysis*, El Cerrito, CA.
- Silva W.J., Gregor N., Darragh R.B. (2003). Development of regional hard rock attenuation relations for Central and Eastern North America, Mid-continent and Gulf Coast areas. *Pacific Engineering Report*, 80 pgs.
- Silva et al. (1996). See page 52.
- Somerville P.G. (2006). Review of magnitude-area scaling of crustal earthquakes, *Report to Working Group on California Earthquake Probabilities*, 22 pgs., URS Corp., Pasadena, CA.
- Somerville P.G., Collins N., Abrahamson N.A., Graves R.W., Saikia C. (2001). Ground motion attenuation relations for the central and eastern United States, Report to U.S. Geological Survey, *NEHRP Award No. 99HQGR0098*, 36 pgs.
- Somerville P.G., Graves R.W., Collins N., Song S.-G., Ni S., Cummins P. (2009). Source and ground motion models of Australian earthquakes, *Proceedings, 2009 Annual Conference of the Australian Earthquake Engineering Society*, Newcastle, Australia.
- Somerville P.G., Irikura K., Graves R.W., Sawada S., Wald D., Abrahamson N.A., Iwasaki Y., Smith N., and Kowada A. (1999). Characterizing crustal earthquake slip models for the prediction of strong ground motion, *Seismol. Res. Lett.* 70: 59–80.
- Somerville P.G., McLaren J., Saikia C., Helmberger D. (1990). The 25 November 1988 Saguenay, Quebec earthquake: Source parameters and the attenuation of strong ground motion, *Bull. Seismol. Soc. Am.*, 80: 1118–1143.
- Somerville P.G., Smith N., Graves R.W., Abrahamson N.A. (1997). Modification of empirical strong ground motion attenuation relations to include the amplitude and duration effects of rupture directivity, *Seismol. Res. Lett.*, 68: 199–222.
- Spudich P., Xu L. (2003). Software for calculating earthquake ground motions from finite-faults in vertically varying media, In *IASPEI International Handbook of Earthquake and Engineering Seismology*, W.H.K. Lee, H. Kanamori, P.C. Jennings, and C. Kisslinger (eds.), Chapter 85.14, Academic Press, New York, pp. 1633–1634.
- STAN Development Team (2014). *Stan Modeling Language Users Guide and Reference Manual, Version 2.5.0*.
- Stanislavsky E. Garven G. (2002). The minimum depth of fault failure in compressional environments, *Geophys. Res. Lett.*, 29(24): 8-1–8-4.
- Tavakoli B., Pezeshk S. (2005). Empirical–stochastic ground–motion prediction for eastern North America, *Bull. Seismol. Soc. Am.*, 95: 2283–2296.
- Tinti E., Fukuyama E., Piatanesi A., Cocco M. (2005). A kinematic source-time function compatible with earthquake dynamics, *Bull. Seismol. Soc. Am.*, 95: 1211–1223.
- Toro G.R. (1996). Probabilistic models of site velocity profiles for generic and site-Sspecific ground motion amplification studies, Appendix C of Silva, W.J., N. Abrahamson, G. Toro and C. Costantino. (1996). "Description and validation of the stochastic ground motion model." Report Submitted to Brookhaven National Laboratory, Associated Universities, Inc. Upton, New York 11973, *Contract No. 770573*. Available on-line at http://www.pacificengineering.org/bnl/Bnl_rpt.zip.
- Toro G.R. (2002). Modification of the Toro et al. (1997) attenuation equations for large magnitudes and short distances, *Risk Engineering Technical Report*, 10 pgs.
- Toro G., Abrahamson N.A., Schneider J. (1997). Model of strong ground motion in eastern and central North America: best estimates and uncertainties, *Seismol. Res. Lett.*, 68: 41–57.
- Toro G.R. McGuire R.K. (1987). An investigation into earthquake ground motion characteristics in eastern North America, *Bull. Seismol. Soc. Am.*, 77(2): 468–489.

- Vanmarcke E.H. (1975). Distribution of first-passage time for normal stationary random processes, ASME, *J Appl. Mech.-Trans.*, 42: 215–220.
- Wald D.J., Allen T.I. (2007). Topographic slope as a proxy for seismic site conditions and amplification, *Bull. Seismol. Soc. Am.*, 97: 1379–1395.
- Wells D.L., Coppersmith K.J. (1994). New empirical relationships among magnitude, rupture length, rupture width, and surface displacements, *Bull. Seismol. Soc. Am.*, 84: 974–1002.
- Wessel P., Smith W.H.F. (1991). Free software helps map and display data, *EOS Trans. AGU*, 72: 441–446
- Working Group on California Earthquake Probabilities (2003). Earthquake probabilities in the San Francisco Bay region, 2002–2031, *U.S. Geological Survey Open-File Report 03-214*, 235 pgs.
- Yenier E., Atkinson G.M. (2014). Equivalent point-source modeling of moderate- to-large magnitude earthquakes and associated ground-motion saturation effects, *Bull. Seismol. Soc. Am.*, 104: 1458–1478.
- Yenier E., Atkinson G.M. (2015a). Regionally-adjustable generic ground-motion prediction equation based on equivalent point-source simulations: Application to Central and Eastern North America, *Bull. Seismol. Soc. Am.*, submitted for review.
- Yenier E., Atkinson G.M. (2015b). Modeling source and attenuation attributes of the 2010–2012 Christchurch, New Zealand, earthquakes based on equivalent point-source modeling technique in preparation.
- Yenier E., Atkinson G.M. (2015c). An equivalent point-source model for stochastic simulation of earthquake ground motions in California, *Bull. Seismol. Soc. Am.*, Accepted for publication.
- Zandieh A., Pezeshk S. (2015). The estimation of seismological parameters for use in a stochastic point source model for western United States using an inversion technique to match the median NGA-West2 GMPEs, *Bull. Seismol. Soc. Am.*, in preparation.
- Zeng Y. (1999). *Personal Communication*.
- Zeng Y., Anderson J.G., Yu G. (1994). A composite source model for computing realistic synthetic strong ground motions, *Geophys. Res. Lett.*, 21: 725–728.
- Zhu L., Rivera L. (2002). Computation of dynamic and static displacement from a point source in multi-layered media, *Geophys. J. Int.*, 148: 619–627.

PEER REPORTS

PEER reports are available as a free PDF download from http://peer.berkeley.edu/publications/peer_reports_complete.html. Printed hard copies of PEER reports can be ordered directly from our printer by following the instructions at http://peer.berkeley.edu/publications/peer_reports.html. For other related questions about the PEER Report Series, contact the Pacific Earthquake Engineering Research Center, 325 Davis Hall mail code 1792, Berkeley, CA 94720. Tel.: (510) 642-3437; Fax: (510) 665-1655; Email: peer_editor@berkeley.edu

- PEER 2015/04** *NGA-East: Median Ground-Motion Models for the Central and Eastern North America Region.* April 2015.
- PEER 2015/03** *Single Series Solution for the Rectangular Fiber-Reinforced Elastomeric Isolator Compression Modulus.* James M. Kelly and Niel C. Van Engelen. March 2015.
- PEER 2015/02** *A Full-Scale, Single-Column Bridge Bent Tested by Shake-Table Excitation.* Matthew J. Schoettler, José I. Restrepo, Gabrielle Guerrini, David E. Duck, and Francesco Carrea. March 2015.
- PEER 2015/01** *Concrete Column Blind Prediction Contest 2010: Outcomes and Observations.* Vesna Terzic, Matthew J. Schoettler, José I. Restrepo, and Stephen A Mahin. March 2015.
- PEER 2014/20** *Stochastic Modeling and Simulation of Near-Fault Ground Motions for Performance-Based Earthquake Engineering.* Mayssa Dabaghi and Armen Der Kiureghian. December 2014.
- PEER 2014/19** *Seismic Response of a Hybrid Fiber-Reinforced Concrete Bridge Column Detailed for Accelerated Bridge Construction.* Wilson Nguyen, William Trono, Marios Panagiotou, and Claudia P. Ostertag. December 2014.
- PEER 2014/18** *Three-Dimensional Beam-Truss Model for Reinforced Concrete Walls and Slabs Subjected to Cyclic Static or Dynamic Loading.* Yuan Lu, Marios Panagiotou, and Ioannis Koutromanos. December 2014.
- PEER 2014/17** *PEER NGA-East Database.* Christine A. Goulet, Tadahiro Kishida, Timothy D. Ancheta, Chris H. Cramer, Robert B. Darragh, Walter J. Silva, Youssef M.A. Hashash, Joseph Harmon, Jonathan P. Stewart, Katie E. Wooddell, and Robert R. Youngs. October 2014.
- PEER 2014/16** *Guidelines for Performing Hazard-Consistent One-Dimensional Ground Response Analysis for Ground Motion Prediction.* Jonathan P. Stewart, Kioumars Afshari, and Youssef M.A. Hashash. October 2014.
- PEER 2014/15** *NGA-East Regionalization Report: Comparison of Four Crustal Regions within Central and Eastern North America using Waveform Modeling and 5%-Damped Pseudo-Spectral Acceleration Response.* Jennifer Dreiling, Marius P. Isken, Walter D. Mooney, Martin C. Chapman, and Richard W. Godbee. October 2014.
- PEER 2014/14** *Scaling Relations between Seismic Moment and Rupture Area of Earthquakes in Stable Continental Regions.* Paul Somerville. August 2014.
- PEER 2014/13** *PEER Preliminary Notes and Observations on the August 24, 2014, South Napa Earthquake.* Grace S. Kang (Editor), Stephen A. Mahin (Editors). September 2014.
- PEER 2014/12** *Reference-Rock Site Conditions for Central and Eastern North America: Part II – Attenuation (Kappa) Definition.* Kenneth W. Campbell, Youssef M.A. Hashash, Byungmin Kim, Albert R. Kottke, Ellen M. Rathje, Walter J. Silva, and Jonathan P. Stewart. August 2014.
- PEER 2014/11** *Reference-Rock Site Conditions for Central and Eastern North America: Part I - Velocity Definition.* Youssef M.A. Hashash, Albert R. Kottke, Jonathan P. Stewart, Kenneth W. Campbell, Byungmin Kim, Ellen M. Rathje, Walter J. Silva, Sissy Nikolaou, and Cheryl Moss. August 2014.
- PEER 2014/10** *Evaluation of Collapse and Non-Collapse of Parallel Bridges Affected by Liquefaction and Lateral Spreading.* Benjamin Turner, Scott J. Brandenberg, and Jonathan P. Stewart. August 2014.
- PEER 2014/09** *PEER Arizona Strong-Motion Database and GMPEs Evaluation.* Tadahiro Kishida, Robert E. Kayen, Olga-Joan Ktenidou, Walter J. Silva, Robert B. Darragh, and Jennie Watson-Lamprey. June 2014.
- PEER 2014/08** *Unbonded Pretensioned Bridge Columns with Rocking Detail.* Jeffrey A. Schaefer, Bryan Kennedy, Marc O. Eberhard, John F. Stanton. June 2014.
- PEER 2014/07** *Northridge 20 Symposium Summary Report: Impacts, Outcomes, and Next Steps.* May 2014.
- PEER 2014/06** *Report of the Tenth Planning Meeting of NEES/E-Defense Collaborative Research on Earthquake Engineering.* December 2013.
- PEER 2014/05** *Seismic Velocity Site Characterization of Thirty-One Chilean Seismometer Stations by Spectral Analysis of Surface Wave Dispersion.* Robert Kayen, Brad D. Carkin, Skye Corbet, Camilo Pinilla, Allan Ng, Edward Gorbis, and Christine Truong. April 2014.

- PEER 2014/04** *Effect of Vertical Acceleration on Shear Strength of Reinforced Concrete Columns.* Hyerin Lee and Khalid M. Mosalam. April 2014.
- PEER 2014/03** *Retest of Thirty-Year-Old Neoprene Isolation Bearings.* James M. Kelly and Niel C. Van Engelen. March 2014.
- PEER 2014/02** *Theoretical Development of Hybrid Simulation Applied to Plate Structures.* Ahmed A. Bakhaty, Khalid M. Mosalam, and Sanjay Govindjee. January 2014.
- PEER 2014/01** *Performance-Based Seismic Assessment of Skewed Bridges.* Peyman Kaviani, Farzin Zareian, and Ertugrul Taciroglu. January 2014.
- PEER 2013/26** *Urban Earthquake Engineering. Proceedings of the U.S.-Iran Seismic Workshop.* December 2013.
- PEER 2013/25** *Earthquake Engineering for Resilient Communities: 2013 PEER Internship Program Research Report Collection.* Heidi Tremayne (Editor), Stephen A. Mahin (Editor), Jorge Archbold Monterossa, Matt Brosman, Shelly Dean, Katherine deLaveaga, Curtis Fong, Donovan Holder, Rakeeb Khan, Elizabeth Jachens, David Lam, Daniela Martinez Lopez, Mara Minner, Geffen Oren, Julia Pavicic, Melissa Quinonez, Lorena Rodriguez, Sean Salazar, Kelli Slaven, Vivian Steyert, Jenny Taing, and Salvador Tena. December 2013.
- PEER 2013/24** *NGA-West2 Ground Motion Prediction Equations for Vertical Ground Motions.* September 2013.
- PEER 2013/23** *Coordinated Planning and Preparedness for Fire Following Major Earthquakes.* Charles Scawthorn. November 2013.
- PEER 2013/22** *GEM-PEER Task 3 Project: Selection of a Global Set of Ground Motion Prediction Equations.* Jonathan P. Stewart, John Douglas, Mohammad B. Javanbarg, Carola Di Alessandro, Yousef Bozorgnia, Norman A. Abrahamson, David M. Boore, Kenneth W. Campbell, Elise Delavaud, Mustafa Erdik and Peter J. Stafford. December 2013.
- PEER 2013/21** *Seismic Design and Performance of Bridges with Columns on Rocking Foundations.* Grigorios Antonellis and Marios Panagiotou. September 2013.
- PEER 2013/20** *Experimental and Analytical Studies on the Seismic Behavior of Conventional and Hybrid Braced Frames.* Jiun-Wei Lai and Stephen A. Mahin. September 2013.
- PEER 2013/19** *Toward Resilient Communities: A Performance-Based Engineering Framework for Design and Evaluation of the Built Environment.* Michael William Mieler, Bozidar Stojadinovic, Robert J. Budnitz, Stephen A. Mahin and Mary C. Comerio. September 2013.
- PEER 2013/18** *Identification of Site Parameters that Improve Predictions of Site Amplification.* Ellen M. Rathje and Sara Navidi. July 2013.
- PEER 2013/17** *Response Spectrum Analysis of Concrete Gravity Dams Including Dam-Water-Foundation Interaction.* Arnkjell Løkke and Anil K. Chopra. July 2013.
- PEER 2013/16** *Effect of hoop reinforcement spacing on the cyclic response of large reinforced concrete special moment frame beams.* Marios Panagiotou, Tea Visnjic, Grigorios Antonellis, Panagiotis Galanis, and Jack P. Moehle. June 2013.
- PEER 2013/15** *A Probabilistic Framework to Include the Effects of Near-Fault Directivity in Seismic Hazard Assessment.* Shrey Kumar Shahi, Jack W. Baker. October 2013.
- PEER 2013/14** *Hanging-Wall Scaling using Finite-Fault Simulations.* Jennifer L. Donahue and Norman A. Abrahamson. September 2013.
- PEER 2013/13** *Semi-Empirical Nonlinear Site Amplification and its Application in NEHRP Site Factors.* Jonathan P. Stewart and Emel Seyhan. November 2013.
- PEER 2013/12** *Nonlinear Horizontal Site Response for the NGA-West2 Project.* Ronnie Kamai, Norman A. Abramson, Walter J. Silva. May 2013.
- PEER 2013/11** *Epistemic Uncertainty for NGA-West2 Models.* Linda Al Atik and Robert R. Youngs. May 2013.
- PEER 2013/10** *NGA-West 2 Models for Ground-Motion Directionality.* Shrey K. Shahi and Jack W. Baker. May 2013.
- PEER 2013/09** *Final Report of the NGA-West2 Directivity Working Group.* Paul Spudich, Jeffrey R. Bayless, Jack W. Baker, Brian S.J. Chiou, Badie Rowshandel, Shrey Shahi, and Paul Somerville. May 2013.
- PEER 2013/08** *NGA-West2 Model for Estimating Average Horizontal Values of Pseudo-Absolute Spectral Accelerations Generated by Crustal Earthquakes.* I. M. Idriss. May 2013.
- PEER 2013/07** *Update of the Chiou and Youngs NGA Ground Motion Model for Average Horizontal Component of Peak Ground Motion and Response Spectra.* Brian Chiou and Robert Youngs. May 2013.
- PEER 2013/06** *NGA-West2 Campbell-Bozorgnia Ground Motion Model for the Horizontal Components of PGA, PGV, and 5%-Damped Elastic Pseudo-Acceleration Response Spectra for Periods Ranging from 0.01 to 10 sec.* Kenneth W. Campbell and Yousef Bozorgnia. May 2013.

- PEER 2013/05** *NGA-West 2 Equations for Predicting Response Spectral Accelerations for Shallow Crustal Earthquakes.* David M. Boore, Jonathan P. Stewart, Emel Seyhan, Gail M. Atkinson. May 2013.
- PEER 2013/04** *Update of the AS08 Ground-Motion Prediction Equations Based on the NGA-West2 Data Set.* Norman Abrahamson, Walter Silva, and Ronnie Kamai. May 2013.
- PEER 2013/03** *PEER NGA-West2 Database.* Timothy D. Ancheta, Robert B. Darragh, Jonathan P. Stewart, Emel Seyhan, Walter J. Silva, Brian S.J. Chiou, Katie E. Wooddell, Robert W. Graves, Albert R. Kottke, David M. Boore, Tadahiro Kishida, and Jennifer L. Donahue. May 2013.
- PEER 2013/02** *Hybrid Simulation of the Seismic Response of Squat Reinforced Concrete Shear Walls.* Catherine A. Whyte and Bozidar Stojadinovic. May 2013.
- PEER 2013/01** *Housing Recovery in Chile: A Qualitative Mid-program Review.* Mary C. Comerio. February 2013.
- PEER 2012/08** *Guidelines for Estimation of Shear Wave Velocity.* Bernard R. Wair, Jason T. DeJong, and Thomas Shantz. December 2012.
- PEER 2012/07** *Earthquake Engineering for Resilient Communities: 2012 PEER Internship Program Research Report Collection.* Heidi Tremayne (Editor), Stephen A. Mahin (Editor), Collin Anderson, Dustin Cook, Michael Erceg, Carlos Esparza, Jose Jimenez, Dorian Krausz, Andrew Lo, Stephanie Lopez, Nicole McCurdy, Paul Shipman, Alexander Strum, Eduardo Vega. December 2012.
- PEER 2012/06** *Fragilities for Precarious Rocks at Yucca Mountain.* Matthew D. Purvance, Rasool Anooshehpour, and James N. Brune. December 2012.
- PEER 2012/05** *Development of Simplified Analysis Procedure for Piles in Laterally Spreading Layered Soils.* Christopher R. McGann, Pedro Arduino, and Peter Mackenzie-Helnwein. December 2012.
- PEER 2012/04** *Unbonded Pre-Tensioned Columns for Bridges in Seismic Regions.* Phillip M. Davis, Todd M. Janes, Marc O. Eberhard, and John F. Stanton. December 2012.
- PEER 2012/03** *Experimental and Analytical Studies on Reinforced Concrete Buildings with Seismically Vulnerable Beam-Column Joints.* Sangjoon Park and Khalid M. Mosalam. October 2012.
- PEER 2012/02** *Seismic Performance of Reinforced Concrete Bridges Allowed to Uplift during Multi-Directional Excitation.* Andres Oscar Espinoza and Stephen A. Mahin. July 2012.
- PEER 2012/01** *Spectral Damping Scaling Factors for Shallow Crustal Earthquakes in Active Tectonic Regions.* Sanaz Rezaeian, Yousef Bozorgnia, I. M. Idriss, Kenneth Campbell, Norman Abrahamson, and Walter Silva. July 2012.
- PEER 2011/10** *Earthquake Engineering for Resilient Communities: 2011 PEER Internship Program Research Report Collection.* Eds. Heidi Faison and Stephen A. Mahin. December 2011.
- PEER 2011/09** *Calibration of Semi-Stochastic Procedure for Simulating High-Frequency Ground Motions.* Jonathan P. Stewart, Emel Seyhan, and Robert W. Graves. December 2011.
- PEER 2011/08** *Water Supply in regard to Fire Following Earthquake.* Charles Scawthorn. November 2011.
- PEER 2011/07** *Seismic Risk Management in Urban Areas. Proceedings of a U.S.-Iran-Turkey Seismic Workshop.* September 2011.
- PEER 2011/06** *The Use of Base Isolation Systems to Achieve Complex Seismic Performance Objectives.* Troy A. Morgan and Stephen A. Mahin. July 2011.
- PEER 2011/05** *Case Studies of the Seismic Performance of Tall Buildings Designed by Alternative Means.* Task 12 Report for the Tall Buildings Initiative. Jack Moehle, Yousef Bozorgnia, Nirmal Jayaram, Pierson Jones, Mohsen Rahnama, Nilesh Shome, Zeynep Tuna, John Wallace, Tony Yang, and Farzin Zareian. July 2011.
- PEER 2011/04** *Recommended Design Practice for Pile Foundations in Laterally Spreading Ground.* Scott A. Ashford, Ross W. Boulanger, and Scott J. Brandenburg. June 2011.
- PEER 2011/03** *New Ground Motion Selection Procedures and Selected Motions for the PEER Transportation Research Program.* Jack W. Baker, Ting Lin, Shrey K. Shahi, and Nirmal Jayaram. March 2011.
- PEER 2011/02** *A Bayesian Network Methodology for Infrastructure Seismic Risk Assessment and Decision Support.* Michelle T. Bensi, Armen Der Kiureghian, and Daniel Straub. March 2011.
- PEER 2011/01** *Demand Fragility Surfaces for Bridges in Liquefied and Laterally Spreading Ground.* Scott J. Brandenburg, Jian Zhang, Pirooz Kashighandi, Yili Huo, and Minxing Zhao. March 2011.
- PEER 2010/05** *Guidelines for Performance-Based Seismic Design of Tall Buildings.* Developed by the Tall Buildings Initiative. November 2010.
- PEER 2010/04** *Application Guide for the Design of Flexible and Rigid Bus Connections between Substation Equipment Subjected to Earthquakes.* Jean-Bernard Dastous and Armen Der Kiureghian. September 2010.

- PEER 2010/03** *Shear Wave Velocity as a Statistical Function of Standard Penetration Test Resistance and Vertical Effective Stress at Caltrans Bridge Sites.* Scott J. Brandenberg, Naresh Bellana, and Thomas Shantz. June 2010.
- PEER 2010/02** *Stochastic Modeling and Simulation of Ground Motions for Performance-Based Earthquake Engineering.* Sanaz Rezaeian and Armen Der Kiureghian. June 2010.
- PEER 2010/01** *Structural Response and Cost Characterization of Bridge Construction Using Seismic Performance Enhancement Strategies.* Ady Aviram, Božidar Stojadinović, Gustavo J. Parra-Montesinos, and Kevin R. Mackie. March 2010.
- PEER 2009/03** *The Integration of Experimental and Simulation Data in the Study of Reinforced Concrete Bridge Systems Including Soil-Foundation-Structure Interaction.* Matthew Dryden and Gregory L. Fenves. November 2009.
- PEER 2009/02** *Improving Earthquake Mitigation through Innovations and Applications in Seismic Science, Engineering, Communication, and Response. Proceedings of a U.S.-Iran Seismic Workshop.* October 2009.
- PEER 2009/01** *Evaluation of Ground Motion Selection and Modification Methods: Predicting Median Interstory Drift Response of Buildings.* Curt B. Haselton, Ed. June 2009.
- PEER 2008/10** *Technical Manual for Strata.* Albert R. Kottke and Ellen M. Rathje. February 2009.
- PEER 2008/09** *NGA Model for Average Horizontal Component of Peak Ground Motion and Response Spectra.* Brian S.-J. Chiou and Robert R. Youngs. November 2008.
- PEER 2008/08** *Toward Earthquake-Resistant Design of Concentrically Braced Steel Structures.* Patxi Uriz and Stephen A. Mahin. November 2008.
- PEER 2008/07** *Using OpenSees for Performance-Based Evaluation of Bridges on Liquefiable Soils.* Stephen L. Kramer, Pedro Arduino, and HyungSuk Shin. November 2008.
- PEER 2008/06** *Shaking Table Tests and Numerical Investigation of Self-Centering Reinforced Concrete Bridge Columns.* Hyung IL Jeong, Junichi Sakai, and Stephen A. Mahin. September 2008.
- PEER 2008/05** *Performance-Based Earthquake Engineering Design Evaluation Procedure for Bridge Foundations Undergoing Liquefaction-Induced Lateral Ground Displacement.* Christian A. Ledezma and Jonathan D. Bray. August 2008.
- PEER 2008/04** *Benchmarking of Nonlinear Geotechnical Ground Response Analysis Procedures.* Jonathan P. Stewart, Annie On-Lei Kwok, Youssef M. A. Hashash, Neven Matasovic, Robert Pyke, Zhiliang Wang, and Zhaohui Yang. August 2008.
- PEER 2008/03** *Guidelines for Nonlinear Analysis of Bridge Structures in California.* Ady Aviram, Kevin R. Mackie, and Božidar Stojadinović. August 2008.
- PEER 2008/02** *Treatment of Uncertainties in Seismic-Risk Analysis of Transportation Systems.* Evangelos Stergiou and Anne S. Kiremidjian. July 2008.
- PEER 2008/01** *Seismic Performance Objectives for Tall Buildings.* William T. Holmes, Charles Kircher, William Petak, and Nabih Youssef. August 2008.
- PEER 2007/12** *An Assessment to Benchmark the Seismic Performance of a Code-Conforming Reinforced Concrete Moment-Frame Building.* Curt Haselton, Christine A. Goulet, Judith Mitrani-Reiser, James L. Beck, Gregory G. Deierlein, Keith A. Porter, Jonathan P. Stewart, and Ertugrul Taciroglu. August 2008.
- PEER 2007/11** *Bar Buckling in Reinforced Concrete Bridge Columns.* Wayne A. Brown, Dawn E. Lehman, and John F. Stanton. February 2008.
- PEER 2007/10** *Computational Modeling of Progressive Collapse in Reinforced Concrete Frame Structures.* Mohamed M. Talaat and Khalid M. Mosalam. May 2008.
- PEER 2007/09** *Integrated Probabilistic Performance-Based Evaluation of Benchmark Reinforced Concrete Bridges.* Kevin R. Mackie, John-Michael Wong, and Božidar Stojadinović. January 2008.
- PEER 2007/08** *Assessing Seismic Collapse Safety of Modern Reinforced Concrete Moment-Frame Buildings.* Curt B. Haselton and Gregory G. Deierlein. February 2008.
- PEER 2007/07** *Performance Modeling Strategies for Modern Reinforced Concrete Bridge Columns.* Michael P. Berry and Marc O. Eberhard. April 2008.
- PEER 2007/06** *Development of Improved Procedures for Seismic Design of Buried and Partially Buried Structures.* Linda Al Atik and Nicholas Sitar. June 2007.
- PEER 2007/05** *Uncertainty and Correlation in Seismic Risk Assessment of Transportation Systems.* Renee G. Lee and Anne S. Kiremidjian. July 2007.
- PEER 2007/04** *Numerical Models for Analysis and Performance-Based Design of Shallow Foundations Subjected to Seismic Loading.* Sivapalan Gajan, Tara C. Hutchinson, Bruce L. Kutter, Prishati Raychowdhury, José A. Ugalde, and Jonathan P. Stewart. May 2008.

- PEER 2007/03** *Beam-Column Element Model Calibrated for Predicting Flexural Response Leading to Global Collapse of RC Frame Buildings.* Curt B. Haselton, Abbie B. Liel, Sarah Taylor Lange, and Gregory G. Deierlein. May 2008.
- PEER 2007/02** *Campbell-Bozorgnia NGA Ground Motion Relations for the Geometric Mean Horizontal Component of Peak and Spectral Ground Motion Parameters.* Kenneth W. Campbell and Yousef Bozorgnia. May 2007.
- PEER 2007/01** *Boore-Atkinson NGA Ground Motion Relations for the Geometric Mean Horizontal Component of Peak and Spectral Ground Motion Parameters.* David M. Boore and Gail M. Atkinson. May. May 2007.
- PEER 2006/12** *Societal Implications of Performance-Based Earthquake Engineering.* Peter J. May. May 2007.
- PEER 2006/11** *Probabilistic Seismic Demand Analysis Using Advanced Ground Motion Intensity Measures, Attenuation Relationships, and Near-Fault Effects.* Polsak Tothong and C. Allin Cornell. March 2007.
- PEER 2006/10** *Application of the PEER PBEE Methodology to the I-880 Viaduct.* Sashi Kunnath. February 2007.
- PEER 2006/09** *Quantifying Economic Losses from Travel Forgone Following a Large Metropolitan Earthquake.* James Moore, Sungbin Cho, Yue Yue Fan, and Stuart Werner. November 2006.
- PEER 2006/08** *Vector-Valued Ground Motion Intensity Measures for Probabilistic Seismic Demand Analysis.* Jack W. Baker and C. Allin Cornell. October 2006.
- PEER 2006/07** *Analytical Modeling of Reinforced Concrete Walls for Predicting Flexural and Coupled-Shear-Flexural Responses.* Kutay Orakcal, Leonardo M. Massone, and John W. Wallace. October 2006.
- PEER 2006/06** *Nonlinear Analysis of a Soil-Drilled Pier System under Static and Dynamic Axial Loading.* Gang Wang and Nicholas Sitar. November 2006.
- PEER 2006/05** *Advanced Seismic Assessment Guidelines.* Paolo Bazzurro, C. Allin Cornell, Charles Menun, Maziar Motahari, and Nicolas Luco. September 2006.
- PEER 2006/04** *Probabilistic Seismic Evaluation of Reinforced Concrete Structural Components and Systems.* Tae Hyung Lee and Khalid M. Mosalam. August 2006.
- PEER 2006/03** *Performance of Lifelines Subjected to Lateral Spreading.* Scott A. Ashford and Teerawut Juirnarongrit. July 2006.
- PEER 2006/02** *Pacific Earthquake Engineering Research Center Highway Demonstration Project.* Anne Kiremidjian, James Moore, Yue Yue Fan, Nesrin Basoz, Ozgur Yazali, and Meredith Williams. April 2006.
- PEER 2006/01** *Bracing Berkeley. A Guide to Seismic Safety on the UC Berkeley Campus.* Mary C. Comerio, Stephen Tobriner, and Ariane Fehrenkamp. January 2006.
- PEER 2005/16** *Seismic Response and Reliability of Electrical Substation Equipment and Systems.* Junho Song, Armen Der Kiureghian, and Jerome L. Sackman. April 2006.
- PEER 2005/15** *CPT-Based Probabilistic Assessment of Seismic Soil Liquefaction Initiation.* R. E. S. Moss, R. B. Seed, R. E. Kayen, J. P. Stewart, and A. Der Kiureghian. April 2006.
- PEER 2005/14** *Workshop on Modeling of Nonlinear Cyclic Load-Deformation Behavior of Shallow Foundations.* Bruce L. Kutter, Geoffrey Martin, Tara Hutchinson, Chad Harden, Sivapalan Gajan, and Justin Phalen. March 2006.
- PEER 2005/13** *Stochastic Characterization and Decision Bases under Time-Dependent Aftershock Risk in Performance-Based Earthquake Engineering.* Gee Liek Yeo and C. Allin Cornell. July 2005.
- PEER 2005/12** *PEER Testbed Study on a Laboratory Building: Exercising Seismic Performance Assessment.* Mary C. Comerio, editor. November 2005.
- PEER 2005/11** *Van Nuys Hotel Building Testbed Report: Exercising Seismic Performance Assessment.* Helmut Krawinkler, editor. October 2005.
- PEER 2005/10** *First NEES/E-Defense Workshop on Collapse Simulation of Reinforced Concrete Building Structures.* September 2005.
- PEER 2005/09** *Test Applications of Advanced Seismic Assessment Guidelines.* Joe Maffei, Karl Telleen, Danya Mohr, William Holmes, and Yuki Nakayama. August 2006.
- PEER 2005/08** *Damage Accumulation in Lightly Confined Reinforced Concrete Bridge Columns.* R. Tyler Ranf, Jared M. Nelson, Zach Price, Marc O. Eberhard, and John F. Stanton. April 2006.
- PEER 2005/07** *Experimental and Analytical Studies on the Seismic Response of Freestanding and Anchored Laboratory Equipment.* Dimitrios Konstantinidis and Nicos Makris. January 2005.
- PEER 2005/06** *Global Collapse of Frame Structures under Seismic Excitations.* Luis F. Ibarra and Helmut Krawinkler. September 2005.

- PEER 2005/05** *Performance Characterization of Bench- and Shelf-Mounted Equipment.* Samit Ray Chaudhuri and Tara C. Hutchinson. May 2006.
- PEER 2005/04** *Numerical Modeling of the Nonlinear Cyclic Response of Shallow Foundations.* Chad Harden, Tara Hutchinson, Geoffrey R. Martin, and Bruce L. Kutter. August 2005.
- PEER 2005/03** *A Taxonomy of Building Components for Performance-Based Earthquake Engineering.* Keith A. Porter. September 2005.
- PEER 2005/02** *Fragility Basis for California Highway Overpass Bridge Seismic Decision Making.* Kevin R. Mackie and Božidar Stojadinović. June 2005.
- PEER 2005/01** *Empirical Characterization of Site Conditions on Strong Ground Motion.* Jonathan P. Stewart, Yoojoong Choi, and Robert W. Graves. June 2005.
- PEER 2004/09** *Electrical Substation Equipment Interaction: Experimental Rigid Conductor Studies.* Christopher Stearns and André Filiatrault. February 2005.
- PEER 2004/08** *Seismic Qualification and Fragility Testing of Line Break 550-kV Disconnect Switches.* Shakhzod M. Takhirov, Gregory L. Fenves, and Eric Fujisaki. January 2005.
- PEER 2004/07** *Ground Motions for Earthquake Simulator Qualification of Electrical Substation Equipment.* Shakhzod M. Takhirov, Gregory L. Fenves, Eric Fujisaki, and Don Clyde. January 2005.
- PEER 2004/06** *Performance-Based Regulation and Regulatory Regimes.* Peter J. May and Chris Koski. September 2004.
- PEER 2004/05** *Performance-Based Seismic Design Concepts and Implementation: Proceedings of an International Workshop.* Peter Fajfar and Helmut Krawinkler, editors. September 2004.
- PEER 2004/04** *Seismic Performance of an Instrumented Tilt-up Wall Building.* James C. Anderson and Vitelmo V. Bertero. July 2004.
- PEER 2004/03** *Evaluation and Application of Concrete Tilt-up Assessment Methodologies.* Timothy Graf and James O. Malley. October 2004.
- PEER 2004/02** *Analytical Investigations of New Methods for Reducing Residual Displacements of Reinforced Concrete Bridge Columns.* Junichi Sakai and Stephen A. Mahin. August 2004.
- PEER 2004/01** *Seismic Performance of Masonry Buildings and Design Implications.* Kerri Anne Taeko Tokoro, James C. Anderson, and Vitelmo V. Bertero. February 2004.
- PEER 2003/18** *Performance Models for Flexural Damage in Reinforced Concrete Columns.* Michael Berry and Marc Eberhard. August 2003.
- PEER 2003/17** *Predicting Earthquake Damage in Older Reinforced Concrete Beam-Column Joints.* Catherine Pagni and Laura Lowes. October 2004.
- PEER 2003/16** *Seismic Demands for Performance-Based Design of Bridges.* Kevin Mackie and Božidar Stojadinović. August 2003.
- PEER 2003/15** *Seismic Demands for Nondeteriorating Frame Structures and Their Dependence on Ground Motions.* Ricardo Antonio Medina and Helmut Krawinkler. May 2004.
- PEER 2003/14** *Finite Element Reliability and Sensitivity Methods for Performance-Based Earthquake Engineering.* Terje Haukaas and Armen Der Kiureghian. April 2004.
- PEER 2003/13** *Effects of Connection Hysteretic Degradation on the Seismic Behavior of Steel Moment-Resisting Frames.* Janise E. Rodgers and Stephen A. Mahin. March 2004.
- PEER 2003/12** *Implementation Manual for the Seismic Protection of Laboratory Contents: Format and Case Studies.* William T. Holmes and Mary C. Comerio. October 2003.
- PEER 2003/11** *Fifth U.S.-Japan Workshop on Performance-Based Earthquake Engineering Methodology for Reinforced Concrete Building Structures.* February 2004.
- PEER 2003/10** *A Beam-Column Joint Model for Simulating the Earthquake Response of Reinforced Concrete Frames.* Laura N. Lowes, Nilanjan Mitra, and Arash Altoontash. February 2004.
- PEER 2003/09** *Sequencing Repairs after an Earthquake: An Economic Approach.* Marco Casari and Simon J. Wilkie. April 2004.
- PEER 2003/08** *A Technical Framework for Probability-Based Demand and Capacity Factor Design (DCFD) Seismic Formats.* Fatemeh Jalayer and C. Allin Cornell. November 2003.
- PEER 2003/07** *Uncertainty Specification and Propagation for Loss Estimation Using FOSM Methods.* Jack W. Baker and C. Allin Cornell. September 2003.

- PEER 2003/06** *Performance of Circular Reinforced Concrete Bridge Columns under Bidirectional Earthquake Loading.* Mahmoud M. Hachem, Stephen A. Mahin, and Jack P. Moehle. February 2003.
- PEER 2003/05** *Response Assessment for Building-Specific Loss Estimation.* Eduardo Miranda and Shahram Taghavi. September 2003.
- PEER 2003/04** *Experimental Assessment of Columns with Short Lap Splices Subjected to Cyclic Loads.* Murat Melek, John W. Wallace, and Joel Conte. April 2003.
- PEER 2003/03** *Probabilistic Response Assessment for Building-Specific Loss Estimation.* Eduardo Miranda and Hesameddin Aslani. September 2003.
- PEER 2003/02** *Software Framework for Collaborative Development of Nonlinear Dynamic Analysis Program.* Jun Peng and Kincho H. Law. September 2003.
- PEER 2003/01** *Shake Table Tests and Analytical Studies on the Gravity Load Collapse of Reinforced Concrete Frames.* Kenneth John Elwood and Jack P. Moehle. November 2003.
- PEER 2002/24** *Performance of Beam to Column Bridge Joints Subjected to a Large Velocity Pulse.* Natalie Gibson, André Filiatrault, and Scott A. Ashford. April 2002.
- PEER 2002/23** *Effects of Large Velocity Pulses on Reinforced Concrete Bridge Columns.* Greg L. Orozco and Scott A. Ashford. April 2002.
- PEER 2002/22** *Characterization of Large Velocity Pulses for Laboratory Testing.* Kenneth E. Cox and Scott A. Ashford. April 2002.
- PEER 2002/21** *Fourth U.S.-Japan Workshop on Performance-Based Earthquake Engineering Methodology for Reinforced Concrete Building Structures.* December 2002.
- PEER 2002/20** *Barriers to Adoption and Implementation of PBEE Innovations.* Peter J. May. August 2002.
- PEER 2002/19** *Economic-Engineered Integrated Models for Earthquakes: Socioeconomic Impacts.* Peter Gordon, James E. Moore II, and Harry W. Richardson. July 2002.
- PEER 2002/18** *Assessment of Reinforced Concrete Building Exterior Joints with Substandard Details.* Chris P. Pantelides, Jon Hansen, Justin Nadauld, and Lawrence D. Reaveley. May 2002.
- PEER 2002/17** *Structural Characterization and Seismic Response Analysis of a Highway Overcrossing Equipped with Elastomeric Bearings and Fluid Dampers: A Case Study.* Nicos Makris and Jian Zhang. November 2002.
- PEER 2002/16** *Estimation of Uncertainty in Geotechnical Properties for Performance-Based Earthquake Engineering.* Allen L. Jones, Steven L. Kramer, and Pedro Arduino. December 2002.
- PEER 2002/15** *Seismic Behavior of Bridge Columns Subjected to Various Loading Patterns.* Asadollah Esmaeily-Gh. and Yan Xiao. December 2002.
- PEER 2002/14** *Inelastic Seismic Response of Extended Pile Shaft Supported Bridge Structures.* T.C. Hutchinson, R.W. Boulanger, Y.H. Chai, and I.M. Idriss. December 2002.
- PEER 2002/13** *Probabilistic Models and Fragility Estimates for Bridge Components and Systems.* Paolo Gardoni, Armen Der Kiureghian, and Khalid M. Mosalam. June 2002.
- PEER 2002/12** *Effects of Fault Dip and Slip Rake on Near-Source Ground Motions: Why Chi-Chi Was a Relatively Mild M7.6 Earthquake.* Brad T. Aagaard, John F. Hall, and Thomas H. Heaton. December 2002.
- PEER 2002/11** *Analytical and Experimental Study of Fiber-Reinforced Strip Isolators.* James M. Kelly and Shakhzod M. Takhirov. September 2002.
- PEER 2002/10** *Centrifuge Modeling of Settlement and Lateral Spreading with Comparisons to Numerical Analyses.* Sivapalan Gajan and Bruce L. Kutter. January 2003.
- PEER 2002/09** *Documentation and Analysis of Field Case Histories of Seismic Compression during the 1994 Northridge, California, Earthquake.* Jonathan P. Stewart, Patrick M. Smith, Daniel H. Whang, and Jonathan D. Bray. October 2002.
- PEER 2002/08** *Component Testing, Stability Analysis and Characterization of Buckling-Restrained Unbonded Braces™.* Cameron Black, Nicos Makris, and Ian Aiken. September 2002.
- PEER 2002/07** *Seismic Performance of Pile-Wharf Connections.* Charles W. Roeder, Robert Graff, Jennifer Soderstrom, and Jun Han Yoo. December 2001.
- PEER 2002/06** *The Use of Benefit-Cost Analysis for Evaluation of Performance-Based Earthquake Engineering Decisions.* Richard O. Zerbe and Anthony Falit-Baiamonte. September 2001.

- PEER 2002/05** *Guidelines, Specifications, and Seismic Performance Characterization of Nonstructural Building Components and Equipment.* André Filiatrault, Constantin Christopoulos, and Christopher Stearns. September 2001.
- PEER 2002/04** *Consortium of Organizations for Strong-Motion Observation Systems and the Pacific Earthquake Engineering Research Center Lifelines Program: Invited Workshop on Archiving and Web Dissemination of Geotechnical Data, 4–5 October 2001.* September 2002.
- PEER 2002/03** *Investigation of Sensitivity of Building Loss Estimates to Major Uncertain Variables for the Van Nuys Testbed.* Keith A. Porter, James L. Beck, and Rustem V. Shaikhutdinov. August 2002.
- PEER 2002/02** *The Third U.S.-Japan Workshop on Performance-Based Earthquake Engineering Methodology for Reinforced Concrete Building Structures.* July 2002.
- PEER 2002/01** *Nonstructural Loss Estimation: The UC Berkeley Case Study.* Mary C. Comerio and John C. Stallmeyer. December 2001.
- PEER 2001/16** *Statistics of SDF-System Estimate of Roof Displacement for Pushover Analysis of Buildings.* Anil K. Chopra, Rakesh K. Goel, and Chatpan Chintanapakdee. December 2001.
- PEER 2001/15** *Damage to Bridges during the 2001 Nisqually Earthquake.* R. Tyler Ranf, Marc O. Eberhard, and Michael P. Berry. November 2001.
- PEER 2001/14** *Rocking Response of Equipment Anchored to a Base Foundation.* Nicos Makris and Cameron J. Black. September 2001.
- PEER 2001/13** *Modeling Soil Liquefaction Hazards for Performance-Based Earthquake Engineering.* Steven L. Kramer and Ahmed-W. Elgamal. February 2001.
- PEER 2001/12** *Development of Geotechnical Capabilities in OpenSees.* Boris Jeremić. September 2001.
- PEER 2001/11** *Analytical and Experimental Study of Fiber-Reinforced Elastomeric Isolators.* James M. Kelly and Shakhzod M. Takhirov. September 2001.
- PEER 2001/10** *Amplification Factors for Spectral Acceleration in Active Regions.* Jonathan P. Stewart, Andrew H. Liu, Yoojoong Choi, and Mehmet B. Baturay. December 2001.
- PEER 2001/09** *Ground Motion Evaluation Procedures for Performance-Based Design.* Jonathan P. Stewart, Shyh-Jeng Chiou, Jonathan D. Bray, Robert W. Graves, Paul G. Somerville, and Norman A. Abrahamson. September 2001.
- PEER 2001/08** *Experimental and Computational Evaluation of Reinforced Concrete Bridge Beam-Column Connections for Seismic Performance.* Clay J. Naito, Jack P. Moehle, and Khalid M. Mosalam. November 2001.
- PEER 2001/07** *The Rocking Spectrum and the Shortcomings of Design Guidelines.* Nicos Makris and Dimitrios Konstantinidis. August 2001.
- PEER 2001/06** *Development of an Electrical Substation Equipment Performance Database for Evaluation of Equipment Fragilities.* Thalia Agninos. April 1999.
- PEER 2001/05** *Stiffness Analysis of Fiber-Reinforced Elastomeric Isolators.* Hsiang-Chuan Tsai and James M. Kelly. May 2001.
- PEER 2001/04** *Organizational and Societal Considerations for Performance-Based Earthquake Engineering.* Peter J. May. April 2001.
- PEER 2001/03** *A Modal Pushover Analysis Procedure to Estimate Seismic Demands for Buildings: Theory and Preliminary Evaluation.* Anil K. Chopra and Rakesh K. Goel. January 2001.
- PEER 2001/02** *Seismic Response Analysis of Highway Overcrossings Including Soil-Structure Interaction.* Jian Zhang and Nicos Makris. March 2001.
- PEER 2001/01** *Experimental Study of Large Seismic Steel Beam-to-Column Connections.* Egor P. Popov and Shakhzod M. Takhirov. November 2000.
- PEER 2000/10** *The Second U.S.-Japan Workshop on Performance-Based Earthquake Engineering Methodology for Reinforced Concrete Building Structures.* March 2000.
- PEER 2000/09** *Structural Engineering Reconnaissance of the August 17, 1999 Earthquake: Kocaeli (Izmit), Turkey.* Halil Sezen, Kenneth J. Elwood, Andrew S. Whittaker, Khalid Mosalam, John J. Wallace, and John F. Stanton. December 2000.
- PEER 2000/08** *Behavior of Reinforced Concrete Bridge Columns Having Varying Aspect Ratios and Varying Lengths of Confinement.* Anthony J. Calderone, Dawn E. Lehman, and Jack P. Moehle. January 2001.
- PEER 2000/07** *Cover-Plate and Flange-Plate Reinforced Steel Moment-Resisting Connections.* Taejin Kim, Andrew S. Whittaker, Amir S. Gilani, Vitelmo V. Bertero, and Shakhzod M. Takhirov. September 2000.

- PEER 2000/06** *Seismic Evaluation and Analysis of 230-kV Disconnect Switches.* Amir S. J. Gilani, Andrew S. Whittaker, Gregory L. Fenves, Chun-Hao Chen, Henry Ho, and Eric Fujisaki. July 2000.
- PEER 2000/05** *Performance-Based Evaluation of Exterior Reinforced Concrete Building Joints for Seismic Excitation.* Chandra Clyde, Chris P. Pantelides, and Lawrence D. Reaveley. July 2000.
- PEER 2000/04** *An Evaluation of Seismic Energy Demand: An Attenuation Approach.* Chung-Che Chou and Chia-Ming Uang. July 1999.
- PEER 2000/03** *Framing Earthquake Retrofitting Decisions: The Case of Hillside Homes in Los Angeles.* Detlof von Winterfeldt, Nels Roselund, and Alicia Kitsuse. March 2000.
- PEER 2000/02** *U.S.-Japan Workshop on the Effects of Near-Field Earthquake Shaking.* Andrew Whittaker, ed. July 2000.
- PEER 2000/01** *Further Studies on Seismic Interaction in Interconnected Electrical Substation Equipment.* Armen Der Kiureghian, Kee-Jeung Hong, and Jerome L. Sackman. November 1999.
- PEER 1999/14** *Seismic Evaluation and Retrofit of 230-kV Porcelain Transformer Bushings.* Amir S. Gilani, Andrew S. Whittaker, Gregory L. Fenves, and Eric Fujisaki. December 1999.
- PEER 1999/13** *Building Vulnerability Studies: Modeling and Evaluation of Tilt-up and Steel Reinforced Concrete Buildings.* John W. Wallace, Jonathan P. Stewart, and Andrew S. Whittaker, editors. December 1999.
- PEER 1999/12** *Rehabilitation of Nonductile RC Frame Building Using Encasement Plates and Energy-Dissipating Devices.* Mehrdad Sasani, Vitelmo V. Bertero, James C. Anderson. December 1999.
- PEER 1999/11** *Performance Evaluation Database for Concrete Bridge Components and Systems under Simulated Seismic Loads.* Yael D. Hose and Frieder Seible. November 1999.
- PEER 1999/10** *U.S.-Japan Workshop on Performance-Based Earthquake Engineering Methodology for Reinforced Concrete Building Structures.* December 1999.
- PEER 1999/09** *Performance Improvement of Long Period Building Structures Subjected to Severe Pulse-Type Ground Motions.* James C. Anderson, Vitelmo V. Bertero, and Raul Bertero. October 1999.
- PEER 1999/08** *Envelopes for Seismic Response Vectors.* Charles Menun and Armen Der Kiureghian. July 1999.
- PEER 1999/07** *Documentation of Strengths and Weaknesses of Current Computer Analysis Methods for Seismic Performance of Reinforced Concrete Members.* William F. Cofer. November 1999.
- PEER 1999/06** *Rocking Response and Overturning of Anchored Equipment under Seismic Excitations.* Nicos Makris and Jian Zhang. November 1999.
- PEER 1999/05** *Seismic Evaluation of 550 kV Porcelain Transformer Bushings.* Amir S. Gilani, Andrew S. Whittaker, Gregory L. Fenves, and Eric Fujisaki. October 1999.
- PEER 1999/04** *Adoption and Enforcement of Earthquake Risk-Reduction Measures.* Peter J. May, Raymond J. Burby, T. Jens Feeley, and Robert Wood.
- PEER 1999/03** *Task 3 Characterization of Site Response General Site Categories.* Adrian Rodriguez-Marek, Jonathan D. Bray, and Norman Abrahamson. February 1999.
- PEER 1999/02** *Capacity-Demand-Diagram Methods for Estimating Seismic Deformation of Inelastic Structures: SDF Systems.* Anil K. Chopra and Rakesh Goel. April 1999.
- PEER 1999/01** *Interaction in Interconnected Electrical Substation Equipment Subjected to Earthquake Ground Motions.* Armen Der Kiureghian, Jerome L. Sackman, and Kee-Jeung Hong. February 1999.
- PEER 1998/08** *Behavior and Failure Analysis of a Multiple-Frame Highway Bridge in the 1994 Northridge Earthquake.* Gregory L. Fenves and Michael Ellery. December 1998.
- PEER 1998/07** *Empirical Evaluation of Inertial Soil-Structure Interaction Effects.* Jonathan P. Stewart, Raymond B. Seed, and Gregory L. Fenves. November 1998.
- PEER 1998/06** *Effect of Damping Mechanisms on the Response of Seismic Isolated Structures.* Nicos Makris and Shih-Po Chang. November 1998.
- PEER 1998/05** *Rocking Response and Overturning of Equipment under Horizontal Pulse-Type Motions.* Nicos Makris and Yiannis Roussos. October 1998.
- PEER 1998/04** *Pacific Earthquake Engineering Research Invitational Workshop Proceedings, May 14-15, 1998: Defining the Links between Planning, Policy Analysis, Economics and Earthquake Engineering.* Mary Comerio and Peter Gordon. September 1998.
- PEER 1998/03** *Repair/Upgrade Procedures for Welded Beam to Column Connections.* James C. Anderson and Xiaojing Duan. May 1998.

- PEER 1998/02** *Seismic Evaluation of 196 kV Porcelain Transformer Bushings.* Amir S. Gilani, Juan W. Chavez, Gregory L. Fennes, and Andrew S. Whittaker. May 1998.
- PEER 1998/01** *Seismic Performance of Well-Confined Concrete Bridge Columns.* Dawn E. Lehman and Jack P. Moehle. December 2000.

ONLINE PEER REPORTS

The following PEER reports are available by Internet only at http://peer.berkeley.edu/publications/peer_reports_complete.html.

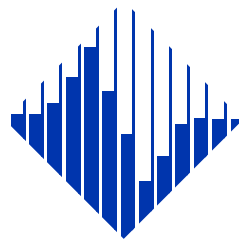
- PEER 2012/103** *Performance-Based Seismic Demand Assessment of Concentrically Braced Steel Frame Buildings.* Chui-Hsin Chen and Stephen A. Mahin. December 2012.
- PEER 2012/102** *Procedure to Restart an Interrupted Hybrid Simulation: Addendum to PEER Report 2010/103.* Vesna Terzic and Božidar Stojadinovic. October 2012.
- PEER 2012/101** *Mechanics of Fiber Reinforced Bearings.* James M. Kelly and Andrea Calabrese. February 2012.
- PEER 2011/107** *Nonlinear Site Response and Seismic Compression at Vertical Array Strongly Shaken by 2007 Niigata-ken Chuetsu-oki Earthquake.* Eric Yee, Jonathan P. Stewart, and Kohji Tokimatsu. December 2011.
- PEER 2011/106** *Self Compacting Hybrid Fiber Reinforced Concrete Composites for Bridge Columns.* Pardeep Kumar, Gabriel Jen, William Trono, Marios Panagiotou, and Claudia Ostertag. September 2011.
- PEER 2011/105** *Stochastic Dynamic Analysis of Bridges Subjected to Spatially Varying Ground Motions.* Katerina Konakli and Armen Der Kiureghian. August 2011.
- PEER 2011/104** *Design and Instrumentation of the 2010 E-Defense Four-Story Reinforced Concrete and Post-Tensioned Concrete Buildings.* Takuya Nagae, Kenichi Tahara, Taizo Matsumori, Hitoshi Shiohara, Toshimi Kabeyasawa, Susumu Kono, Minehiro Nishiyama (Japanese Research Team) and John Wallace, Wassim Ghannoum, Jack Moehle, Richard Sause, Wesley Keller, Zeynep Tuna (U.S. Research Team). June 2011.
- PEER 2011/103** *In-Situ Monitoring of the Force Output of Fluid Dampers: Experimental Investigation.* Dimitrios Konstantinidis, James M. Kelly, and Nicos Makris. April 2011.
- PEER 2011/102** *Ground-motion prediction equations 1964 - 2010.* John Douglas. April 2011.
- PEER 2011/101** *Report of the Eighth Planning Meeting of NEES/E-Defense Collaborative Research on Earthquake Engineering.* Convened by the Hyogo Earthquake Engineering Research Center (NIED), NEES Consortium, Inc. February 2011.
- PEER 2010/111** *Modeling and Acceptance Criteria for Seismic Design and Analysis of Tall Buildings.* Task 7 Report for the Tall Buildings Initiative - Published jointly by the Applied Technology Council. October 2010.
- PEER 2010/110** *Seismic Performance Assessment and Probabilistic Repair Cost Analysis of Precast Concrete Cladding Systems for Multistory Buildings.* Jeffrey P. Hunt and Božidar Stojadinovic. November 2010.
- PEER 2010/109** *Report of the Seventh Joint Planning Meeting of NEES/E-Defense Collaboration on Earthquake Engineering. Held at the E-Defense, Miki, and Shin-Kobe, Japan, September 18–19, 2009.* August 2010.
- PEER 2010/108** *Probabilistic Tsunami Hazard in California.* Hong Kie Thio, Paul Somerville, and Jascha Polet, preparers. October 2010.
- PEER 2010/107** *Performance and Reliability of Exposed Column Base Plate Connections for Steel Moment-Resisting Frames.* Ady Aviram, Božidar Stojadinovic, and Armen Der Kiureghian. August 2010.
- PEER 2010/106** *Verification of Probabilistic Seismic Hazard Analysis Computer Programs.* Patricia Thomas, Ivan Wong, and Norman Abrahamson. May 2010.
- PEER 2010/105** *Structural Engineering Reconnaissance of the April 6, 2009, Abruzzo, Italy, Earthquake, and Lessons Learned.* M. Selim Günay and Khalid M. Mosalam. April 2010.
- PEER 2010/104** *Simulating the Inelastic Seismic Behavior of Steel Braced Frames, Including the Effects of Low-Cycle Fatigue.* Yuli Huang and Stephen A. Mahin. April 2010.
- PEER 2010/103** *Post-Earthquake Traffic Capacity of Modern Bridges in California.* Vesna Terzic and Božidar Stojadinović. March 2010.
- PEER 2010/102** *Analysis of Cumulative Absolute Velocity (CAV) and JMA Instrumental Seismic Intensity (I_{JMA}) Using the PEER–NGA Strong Motion Database.* Kenneth W. Campbell and Yousef Bozorgnia. February 2010.
- PEER 2010/101** *Rocking Response of Bridges on Shallow Foundations.* Jose A. Ugalde, Bruce L. Kutter, and Boris Jeremic. April 2010.
- PEER 2009/109** *Simulation and Performance-Based Earthquake Engineering Assessment of Self-Centering Post-Tensioned Concrete Bridge Systems.* Won K. Lee and Sarah L. Billington. December 2009.

- PEER 2009/108** *PEER Lifelines Geotechnical Virtual Data Center.* J. Carl Stepp, Daniel J. Ponti, Loren L. Turner, Jennifer N. Swift, Sean Devlin, Yang Zhu, Jean Benoit, and John Bobbitt. September 2009.
- PEER 2009/107** *Experimental and Computational Evaluation of Current and Innovative In-Span Hinge Details in Reinforced Concrete Box-Girder Bridges: Part 2: Post-Test Analysis and Design Recommendations.* Matias A. Hube and Khalid M. Mosalam. December 2009.
- PEER 2009/106** *Shear Strength Models of Exterior Beam-Column Joints without Transverse Reinforcement.* Sangjoon Park and Khalid M. Mosalam. November 2009.
- PEER 2009/105** *Reduced Uncertainty of Ground Motion Prediction Equations through Bayesian Variance Analysis.* Robb Eric S. Moss. November 2009.
- PEER 2009/104** *Advanced Implementation of Hybrid Simulation.* Andreas H. Schellenberg, Stephen A. Mahin, Gregory L. Fenves. November 2009.
- PEER 2009/103** *Performance Evaluation of Innovative Steel Braced Frames.* T. Y. Yang, Jack P. Moehle, and Božidar Stojadinovic. August 2009.
- PEER 2009/102** *Reinvestigation of Liquefaction and Nonliquefaction Case Histories from the 1976 Tangshan Earthquake.* Robb Eric Moss, Robert E. Kayen, Liyuan Tong, Songyu Liu, Guojun Cai, and Jiaer Wu. August 2009.
- PEER 2009/101** *Report of the First Joint Planning Meeting for the Second Phase of NEES/E-Defense Collaborative Research on Earthquake Engineering.* Stephen A. Mahin et al. July 2009.
- PEER 2008/104** *Experimental and Analytical Study of the Seismic Performance of Retaining Structures.* Linda Al Atik and Nicholas Sitar. January 2009.
- PEER 2008/103** *Experimental and Computational Evaluation of Current and Innovative In-Span Hinge Details in Reinforced Concrete Box-Girder Bridges. Part 1: Experimental Findings and Pre-Test Analysis.* Matias A. Hube and Khalid M. Mosalam. January 2009.
- PEER 2008/102** *Modeling of Unreinforced Masonry Infill Walls Considering In-Plane and Out-of-Plane Interaction.* Stephen Kadsiewicz and Khalid M. Mosalam. January 2009.
- PEER 2008/101** *Seismic Performance Objectives for Tall Buildings.* William T. Holmes, Charles Kircher, William Petak, and Nabih Youssef. August 2008.
- PEER 2007/101** *Generalized Hybrid Simulation Framework for Structural Systems Subjected to Seismic Loading.* Tarek Elkhoraibi and Khalid M. Mosalam. July 2007.
- PEER 2007/100** *Seismic Evaluation of Reinforced Concrete Buildings Including Effects of Masonry Infill Walls.* Alidad Hashemi and Khalid M. Mosalam. July 2007.

The Pacific Earthquake Engineering Research Center (PEER) is a multi-institutional research and education center with headquarters at the University of California, Berkeley. Investigators from over 20 universities, several consulting companies, and researchers at various state and federal government agencies contribute to research programs focused on performance-based earthquake engineering.

These research programs aim to identify and reduce the risks from major earthquakes to life safety and to the economy by including research in a wide variety of disciplines including structural and geotechnical engineering, geology/seismology, lifelines, transportation, architecture, economics, risk management, and public policy.

PEER is supported by federal, state, local, and regional agencies, together with industry partners.



PEER Core Institutions:
University of California, Berkeley (Lead Institution)
California Institute of Technology
Oregon State University
Stanford University
University of California, Davis
University of California, Irvine
University of California, Los Angeles
University of California, San Diego
University of Southern California
University of Washington

PEER reports can be ordered at http://peer.berkeley.edu/publications/peer_reports.html or by contacting

Pacific Earthquake Engineering Research Center
University of California, Berkeley
325 Davis Hall, mail code 1792
Berkeley, CA 94720-1792
Tel: 510-642-3437
Fax: 510-642-1655
Email: peer_editor@berkeley.edu

ISSN 1547-0587X